Advanced pyrolysis of plastic waste for chemicals, fuel and materials

Laura Salvia Diaz Silvarrey

Supervisor: Dr Anh N Phan
Dr Kui Zhang

School of Engineering
Newcastle University

This dissertation is submitted for the degree of
Doctor of Philosophy

July 2019

Abstract

The constant increasing generation of plastic waste, alongside the lack of plastic waste recycling capacity and the health and environmental risks from their disposal in landfills and incineration, have contributed to the search for versatile alternative management solutions e.g. pyrolysis. Thermal pyrolysis of plastic waste is a well-known and mature technology yielding very little gas and solid residue and high low quality wax (mixed C_6-C_{25} hydrocarbons) with limited direct application as transportation fuels. Zeolites are often introduced as catalysts for plastic waste pyrolysis to improve the quality of the wax and reduce operation temperature. However, they rapidly deactivate via coking and are expensive, opening up the search for alternative catalysts/technologies. In this thesis thermal, catalytic and cold plasma assisted pyrolysis, were evaluated in terms of the type of products obtained. Although scarcely used, sulphated zirconia, Ni/Al_2O_3 and char from waste biomass pyrolysis as catalysts and cold plasma proved to be potential improvements for plastic waste pyrolysis.

A kinetic model of individual plastic waste, developed via iso-conversional methods and linear model fitting, showed their thermal decomposition was complex and allowed predictions for the design and operation of pyrolysis systems. The combination of waste high density polyehtylene and waste polypropylene pyrolysis with cold plasma yielded high-value chemicals e.g. ethylene (up to 55 times compared to thermal pyrolysis of waste high density polyethylene), hydrogen (40 times the H_2 generation flow rate compared to waste polypropylene thermal pyrolysis) and carbon nanotubes (30-40 nm diameter from waste polypropylene), improving the overall profitability of pyrolysis. Cold plasma and catalysts (HZMS-5, sulphated zirconia and Ni/Al_2O_3) showed a synergistic effect promoting the recovery of ethylene and hydrogen from waste high density polyehtylene and waste polypropylene respectively. Sulphated zirconia catalyst (0-10 wt%) improved the recovery of up to 27-32 wt% of benzoic acid, a precursor in the food and beverage industry, alongside other high-value products recovered in the gas (CH_4 and C_2-C_3 hydrocarbons) from waste PET catalytic pyrolysis. Biochar, derived from waste biomass pyrolysis, as a catalysts for unsorted mixed plastic waste two-stage pyrolysis significantly enhanced the cracking process compared to non-catalytic thermal by increasing the gas (up to 85 wt%), hydrogen (up to 3.25 wt%) and methane yields (up to 55 wt%). Therefore, this thesis successfully proved the novel use of cold plasma and sulphated zirconia and biochar as catalysts to improve the value of plastic waste pyrolysis products, opening up opportunities to develop a sustainable and efficient process to re-engineer plastic wastes.

List of publications

List of publications from this thesis:

1. L.S. Diaz-Silvarrey and A.N. Phan. Kinetic study of municipal plastic waste. International Journal of Hydrogen Energy, 41(37):16352–16364, 2016

2. L.S. Diaz-Silvarrey, A. McMahon, and A. Phan. Benzoic acid recovery via waste poly(ethylene terephthalate)(PET) catalytic pyrolysis using sulphated zirconia catalyst. Journal of Analytical and Applied Pyrolysis, 134:621–631, 2018

3. L.S. Diaz-Silvarrey, K. Zhang, and A.N. Phan. Monomer recovery through advanced pyrolysis of waste high density polyethylene (HDPE). Green Chemistry, 20:1813–1823, 2018

4. L.S. Diaz-Silvarrey, Anh N. Phan, and Kui Zhang. Direct production of carbon nanotubes and hydrogen from plastic waste using cold plasma pyrolysis. Submitted to *ACS Sustainable Sustainable Chemistry & Engineering*

5. L.S. Diaz-Silvarrey, L. Dixon, P. Prasertcharoensuka, A.N. Phan. Waste to wealth: pyrolysis of unsorted plastic waste using a waste derived catalyst. Submitted to *Applied Energy* and revised

List of conference poster and oral presentations from this thesis:

1. Oral presentation titled 'Kinetic Study of Municipal Plastic Waste' at 8^{th} International Conference on Sustainable Energy and Environmental Protection (SEEP), Paisley, UK, 9-12 June 2015

2. Poster presentation titled 'Pyrolysis of Municipal Plastic Waste for Fuels and Chemicals' at 4^{th} UK-Japan Engineering Education League (UKJEEL) Workshop, Tokyo, Japan, 5-8 August 2016

3. Poster presentation 'Cold plasma assisted pyrolysis of waste high density polyethylene for monomer recovery' at ChemEngDayUK 2017, Birmingham, UK, 27-28 March 2017

To my parents, my sister and Sergio.

Acknowledgements

I thank my supervisors, Dr Anh N. Phan and Dr Kui Zhang, for their supervision, mentorship and insightful contributions to this work. I also express my gratitude to:

- O'Brien Recycling Solutions (Wallsend, UK) for providing the plastic waste materials.
- Advanced Chemical and Materials Analysis (ACMA) at Newcastle University: Dr Isabel Arce Garcia for SEM images and EDX analysis, Maggie White for XRD analysis and Richard Baron for CHN analysis on plastic waste.
- Department of Chemistry at Sheffield University for providing CHN analysis of biochar.
- Chris Ottley from the Department of Earth Sciences at Durham University for ICP analysis on biochar.
- National EPSRC XPS Users' Service (NEXUS) at Newcastle University for X-ray photoelectron spectra.
- Dr Duc-The Ngo from the Electron Microscopy Centre at University of Manchester for HRTEM and EDXS images of carbon nanotubes.
- The Application of Ion Transport Group at Newcastle University: Dr Greg Mutch for Raman spectroscopy analysis and Dr Kalliopi Kousi for temperature programmed oxidation (TPO) test of spent Ni/Al_2O_3 catalysts.
- Dr Jiri Kislinger and Robert Dent at Mettler Toledo for TGA/MS analysis on sulphated zirconia.
- CEAM technical, IT and administrative members of staff.
- Process Intensification Group (PIG) members for their useful contributions and shared knowledge.

I thank my parents, Carmen and Antonio, and my sister Elena for all their invaluable help and support. Lastly, I express my deepest gratitude to Sergio for all his support, understanding and encouragement during the past four years.

Table of contents

List of figures

List of tables

Chapter 1 Introduction

1.1 Background

Plastics, one of the most popular materials of the 21^{st} Century due to their versatility, low cost and durability, have increasing annually and, subsequently, so has plastic waste generation at about 9 % per year (Raynaud, 2014). The plastics most globally used i.e. commodity plastics, are polyethylene (PE), both high density (HDPE) and low density (LDPE); polypropylene (PP); polystyrene (PS); polyvinyl chloride (PVC); and polyethylene terephthalate (PET). Plastic waste often account for 9-15 wt% of the total household waste stream (Department for Environment Food & Rural Affairs, 2011; Karak et al., 2012) depending on the region, living standards, season, etc. (Eurostat, 2015*b*, n.d.; Karak et al., 2012). Of that fraction, 19.3 wt% (4.6 million tonnes) was PP, 17.5 wt% (4.2 million tonnes) LDPE, 12.3 wt% (2.9 million tonnes) HDPE, 10 wt% (2.4 million tonnes) PVC, 7.4 wt% (1.8 million tonnes) PET, 6.7 wt% (1.6 million tonnes) PS and 26.8 wt% (6.4 million tonnes) other plastic types (e.g. polyurethane, acrylonitrile butadiene styrene, etc.) in the UK in 2017 (Plastic Europe, 2017).
Environmental waste policies e.g. the Waste Framework Directive (WFD) (Directive 2008/98/EC), try to maximize the efficient use of resources by opting for prevention, re-use and recycling of waste (target of 70 wt% recycling by 2030 (European Comission, 2015)) while incineration without energy recovery and landfill disposal are the least desirable options according to the pyramidal waste hierarchy. However, the recycling rate in the EU has slowly grown at about 1 % per year (European Environmental Agency (EEA), 2013; Eurostat, 2015*c*) in the last 14 years with approximately 75 wt% of the packaging plastic waste generated in the UK either disposed in landfills or incinerated with energy recovery (EuroStat, 2015*a*; U.S. Environmental Protection Agency (EPA), 2016). Plastic waste mechanical recycling is limited by: (i) the presence of additives or contaminants, (ii) the mixture of plastic types for the manufacture of daily products, (iii) a relatively small market for some recycled plastic products, and (iv) the lack of domestic recycling capacity to cope with the entirety of the plastic waste generated. There is an international plastic waste trade of the plastic waste generated in developed countries e.g. USA, the EU, Japan, etc. (Velis, 2014) although, the recycling methods and/or their real environmental impact is unknown (Velis, 2014). Imported plastic waste are vastly reprocessed in small familiar business with poor technologies and without any pollution controls, suggesting that even the recycled fraction of plastic waste could contribute enormously to the global detriment of the environment. This fact is worsen as most plastic products

consumed, often in the form of packaging, agricultural films and disposable consumer items, have an average life of just less than a month (Lopez et al., 2017). In addition, virgin plastic manufacturing industry accounts for 10 % of worldwide oil and gas usage (Hopewell et al., 2009) for feedstock and energy. All the reasons above, along with long term accumulation of plastic waste as debris in the form of micro particles in the environment (Barnes et al., 2009; Hopewell et al., 2009; Kreith and Tchobanoglous, 1994; Kyrikou and Briassoulis, 2007; Verma et al., 2016), have contributed to plastic waste becoming a key global environmental issue. Advanced thermochemical processes e.g. pyrolysis or gasification, have been thereby considered as desirable management alternatives with notable advantages over incineration (Al-Salem et al., 2009; Panda et al., 2010). This research focuses on the production of high-value products from unsorted mixed and individual plastic wastes pyrolysis in a simple one or two-stage pyrolysis set-up. Pyrolysis of mixed plastics would reduce the need for extensive separation and cleaning in upstream processes and could cope with plastic products manufactured from various plastic types. Pyrolysis produces a gas, liquid/wax and solid residue fraction. The proportion and composition in individual fractions are dependent upon the feedstock composition, reactor type and process conditions (Achilias et al., 2007). High temperature (>700 °C) maximises the yield of monomer i.e. ethylene and propylene (Achilias et al., 2007), which could be used as feedstock for polymer industry. This could be desirable as HDPE, LDPE and PP account for a major share of the global plastic consumption (Hujuri et al., 2008; Plastic Europe, 2017). In contrast, low temperature pyrolysis (<500 °C) promotes the the liquid/wax fraction, often with the purpose of fuels for the transport sector, and the solid residue. Catalytic pyrolysis of plastic waste presents advantages over thermal pyrolysis because: (i) it reduces the activation energy of the reaction and thus, the temperature and energy requirements and (ii) it narrows the hydrocarbon distribution in the liquid/wax so it is more similar to fossil fuels (gasoline and diesel) (Sharuddin et al., 2016). Heterogeneous acid catalysts e.g. nanocrystalline zeolites (Aguado et al., 2006, 2007; Serrano et al., 2004), metals with a carbon support (Acomb et al., 2016; Uemichi et al., 1989), basic oxides (Kumar et al., 2017) and silica-alumina catalysts (Sharuddin et al., 2016) are more commonly used in plastic waste pyrolysis (PWP) as they do not require catalyst separation, their ion exchange properties and selectivity. The very reactive environment and unique properties of cold plasma to promote thermodynamically unfavoured reactions, has spike its application to assist multiple processes including hydrocarbon reforming, air pollution and gas streams treatment, volatile organic compounds (VOC) decomposition, waste water treatment and disinfection and even medical applications.

1.2 Research scope

Despite catalytic pyrolysis of plastic waste being extensively investigated, most studies focus primarily on the use of zeolites. However, their deactivation and high costs opens up opportunities to look for other inexpensive cracking catalysts. This thesis explores the use of sulphated zirconia and char derived from waste biomass pyrolysis. Sulphated zirconia

application to plastic waste pyrolysis is very limited, despite the similar nature to zeolite and positive performance in similar processes. Activated carbon-based catalysts have been scarcely applied to plastic waste pyrolysis but there is little information on the use of non-activated carbon-based catalysts for this purpose despite their good performance for biomass tar cracking. Cold plasma ability to promote radical chain scission reactions has been suggested, however its use for plastic waste pyrolysis is null, creating another research gap investigated in this thesis.

1.3 Aim and objectives

The purpose of this thesis was to explore novel techniques i.e. cold plasma, and the utilisation of waste/cheap materials as catalysts to enhance the economics and sustainability of plastic waste management. To do so, the following objectives were set:

1. Study the thermal behaviour and reactivity of plastic waste for the determination of pyrolysis operation conditions: heating rate, pyrolysis temperature and holding time. Development of a kinetic model to describe and predict the behaviour of plastic waste during pyrolysis.
2. Investigate the effect of operating conditions and different catalysts (zeolites, sulphated zirconia, Ni/Al_2O_3 and char from waste biomass pyrolysis) on the yield and composition of plastic waste catalytic pyrolysis.
3. Study the effect of novel technologies such as cold plasma on the yield and composition of thermal and catalytic plastic waste pyrolysis.
4. Investigate the synergistic effect of acid catalysts (zeolite, sulphated zirconia and Ni/Al_2O_3) and cold plasma to recover high-value products i.e. monomer, hydrogen and high-value carbon products.
5. Study the feasibility of inexpensive waste materials as catalysts i.e. char derived from waste biomass for mixed plastic waste catalytic pyrolysis.
6. Study the reusability of catalysts (zeolite, sulphated zirconia and char from waste biomass pyrolysis) and novel catalyts regeneration methods.

1.4 Thesis outline and novelty

This thesis is divided into ten chapters:

- Chapter 1 presents and overview of plastic waste generation, management and PWP as well as sets this thesis purpose, scope, outline and novelty.
- Chapter 2 extends, synthesises and critically reviews the research context.

- Chapter 3 presents the characterisation of all the materials used in modelling and laboratory experiments as well as the experimental set-up and analysis techniques used to perform all pyrolysis experiments, to collect the initial data for the model section and to characterise all the materials.
- Chapter 4 explains the specific background for the development of the kinetic model of plastic waste, the methodology and steps used and the results. The contents of this chapter have been published in Diaz-Silvarrey and Phan (2016).
- Chapter 5 compiles results and discussion on monomer recovery from waste HDPE pyrolysis. The contents of this chapter have been published in Diaz-Silvarrey, Zhang and Phan (2018).
- Chapter 6 studies waste PP thermal, catalytic and cold plasma assisted pyrolysis to recover hydrogen and high-value carbon. Some of the contents of this chapter have been submitted for publication to ACS Sustainable Chemistry and Engineering.
- Chapter 7 compiles findings from catalytic waste PET pyrolysis to recover benzoic acid. This chapter has been published in Diaz-Silvarrey, McMahon and Phan (2018).
- Chapter 8 studies the use of char derived from waste biomass as a catalyst for one-stage and two-stage mixed plastic catalytic pyrolysis. It is also focused on the reusability of catalysts during several mixed plastic waste two-stage catalytic pyrolysis cycles. Some of the contents of this chapter have been submitted for publication to Applied Energy and it is currently under review after revision.
- Chapter 9 creates an outlook of the key points regarding PWP technical and economic challenges.
- Chapter 10 clearly and concisely captures the main key findings emerging from this thesis.

The novelty of this thesis is explained at the beginning of chapters 4 to 8. Below is a summary of the novelty of each chapter:

- Chapter 4 develops a kinetic model for all common plastic waste types unlike most literature kinetic studies. This model involved the use of exhaustive methods to obtain the full kinetic triplet (activation energy, pre-exponential factor and decomposition model) instead of making the common, and untrue, assumption of first order decomposition, allowing for more accurate predictions of the process.
- Chapter 5 assessed the use of cold plasma to assist waste HDPE pyrolysis to recover the monomer for the first time. The synergistic effect of sulphated zirconia catalyst, an uncommon but suitable catalyst used for PWP, and cold plasma was also exploited for the time applied to PWP.

- Chapter 6 built on the novel approach to introduce cold plasma to assist PWP observed in chapter 5. The synergistic effect of cold plasma and Ni/Al_2O_3 catalyst was explored through an innovative method to recover high-value carbon products and hydrogen in this chapter.
- Chapter 7 involves the use of waste PET, often forgotten in literature, to recover benzoic acid from wate PET catalytic pyrolysis was using sulphated zirconia as catalysts. The effect of the catalyst, pyrolysis temperature and their interaction on the yield of benzoic acid constitutes a novel approach in terms of the range of products recovered from PWP.
- Chapter 8 novelly tested char derived from waste biomass pyrolysis as a catalysts for mixed plastic waste catalytic pyrolysis. In addition, this chapter includes a reusability assessment of the catalyst which are scarce on literature.

Chapter 2 A Review of Municipal Plastic Waste Management: conventional, catalytic and non-thermal plasma pyrolysis

This chapter explains the rationale and background and reviews the state-of-the-art of plastic waste pyrolysis including thermal or conventional, catalytic and cold plasma assisted. It reviews plastic waste management technologies and compares the existing methods with pyrolysis from a life cycle assessment perspective. It also discusses the suitability of plastic waste pyrolysis for several applications including conversion to fuels for transportation and/or other valuable chemicals.

2.1 Plastics and the Environment

Commodity plastics are manufactured from petrochemical products and represent around 2-4 % of the global oil consumption (Thompson et al., 2009). Thermoplastics i.e. PE, PP, PS and PVC represent the majority of commodity plastics (50 % of the global production in 2015 i.e 242.67 million tonnes with an expected growth rate of 4.1 % by 2020 (Mordor Intelligence, 2016)). They are mainly manufactured by China (26 % in 2014), followed by Europe (20 % in 2014), USA (19 % in 2014) and the rest of Asia (16 % in 2014) (Plastic Europe, 2015). Most of commodity plastics are used in packaging (39.5 %) followed by building and construction (20.1 %); automotive (8.6 %); electrical and electronic (5.7 %); agriculture (3.4 %) and other applications (22.7 %) (Plastic Europe, 2015).
HDPE, LDPE are directly manufactured from ethylene by polymerisation (Aguado and Serrano, 1999; Intratec, 2016) while PP (propylene), PS (ethylene and benzene) and PVC (ethylene and chlorine) are synthesised by polymerisation of ethylene manufacture by-products or directly from reaction of ethylene and other reactants. Therefore, ethylene is a key chemical blocks for plastic manufacture (about 60 % of the global production (Intratec, 2016)) and a raw material for multiple processes. Figure 2.1 summarises the main routes around ethylene production and consumption for plastic products.
On the other hand, PET, vastly used in food packaging and in the form of fibres in textile applications, is not a thermoplastic but a polyester. PET is not synthesised by polymerisation but from either esterification of monoethylene glycol (MEG) and terephthalic acid (TPA) or via transesterification of the former with dimethyl terephthalate (DMT). The first process is more common for general PET products due to lower costs while the second process provides better adhesion quality and is often used for PET film manufacture. The product of both processes is

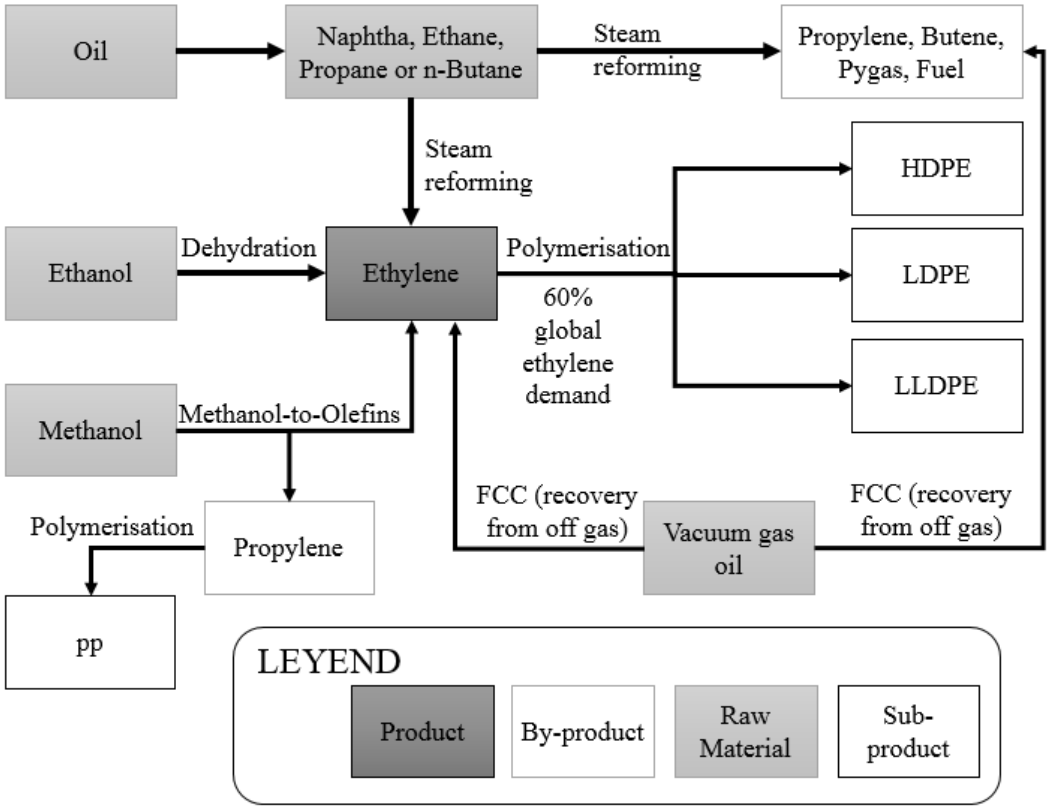

Figure 2.1 Main streams for ethylene production and utilisation. Adapted from (Intratec, 2016)

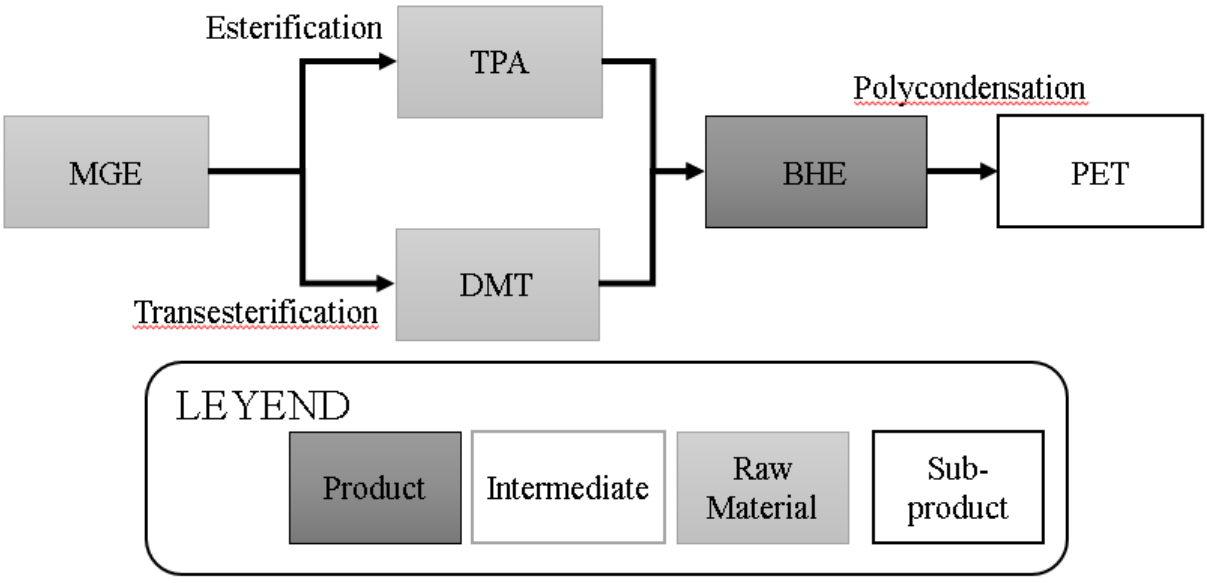

Figure 2.2 PET manufacturing routes

bis(2-hydroxyethyl) terephthalate (BHE) i.e. the PET monomer, which then undergoes polycondensation as shown in Figure 2.2.

Although plastics are one of the most popular materials in modern society due to their versatility, low cost and durability, the management of their waste is becoming a global concern. A large proportion of plastic waste all over the world is still being disposed in landfills e.g. 31 % in the UK in 2014 (Plastic Europe,, 2016) or 83 % in the USA in the same year (Themelis and Mussche, 2014). This is a substantial deprivation of valuable resources, occupies a large volume of land and creates a hazard for human and wildlife (Verma et al., 2016).

There has been an increasing trend on studies regarding the accumulation and transfer of plastic waste in the environment, particularly on large water bodies (Barnes et al., 2009; Jambeck et al., 2015; Ten Brink et al., 2018). This transfer causes the incursion of plastic waste nanoparticles (NPs) and microparticles (MPs) into the trophic chain posing a risk to wild and human life (Van Cauwenberghe and Janssen, 2014). It has been observed (Li et al., 2016) that the ingestion of MPs (>100 μm) causes physical and chemical imbalances on wildlife. These effects include blockage of the intestinal tract, inhibition of the gastric enzyme secretion, reduction of feeding stimuli, decrease of steroid hormone levels and delay in ovulation affecting reproduction. However, the risk goes beyond all these effects as plastics are known to transport airborne pollutants like persistent organic pollutants (POPs) (polychlorinated biphenyls, PCBs; polycyclic aromatic hydrocarbons, PAHs; and organochlorine pesticides) (Teuten et al., 2009) which are toxic, persistent in the environment, bioaccumulative, hydrophobic and have long-range transport potential (Li et al., 2016).

In addition to exposure via incursion in the trophic chain, MPs were discovered inside everyday products stored in plastic products. Recent studies suggested the presence of MPs, in particular PP, inside water and beer bottles and table salt across different brands from countries all over the world (Kosuth et al., 2018; Mason et al., 2018). Such discoveries contributed to a growing concern on the effect of NPs and MPs on human health due to their potential risk (Schirinzi et al., 2017). However, toxicity of NPs and MPs on human health has only been tested via *in vitro* studies and it is still unknown how that risk translates into human health due to a lack of *in vivo* studies. Soegijapranata Catholic University in Indonesia launched in May 2018 the very first study on the risk of MPs in human health through investigation of the presence of MPs on seafood and tracking the diet of 2000 individuals (David Shukman, BBC News, 2018). It is clear that the increasing use of short-lifespan plastic products accumulates plastic waste wastes on the environment with associated risks. That poses a growing concern on how countries manage plastic waste and opens up discussion for novel technologies capable of processing the vast amount of plastic waste generated globally.

2.2 Current plastic waste treatment

Al-Salem et al. (2009) and Panda et al. (2010) extensively reviewed and categorised plastic waste management into four generally accepted routes: primary, secondary, tertiary and

quaternary recycling. Each type corresponds with one of the four tiers of the waste hierarchy: re-use, recycling, other means of recovery and incineration with energy recovery respectively (Department for Environment Food & Rural Affairs (DEFRA), 2013). Primary recycling consists on the re-extrusion of plastic waste scrap to manufacture the same plastic product. This recycling method is very limited and mainly used in plastic products manufacturing industry to re-use faulty batches. Secondary or mechanical recycling is similar to primary recycling but the recovered product does not necessarily need to fulfil the same purpose. This method is limited due to waste contamination and therefore requires sorting, increasing costs. In the UK, around 9 wt% of the total plastic waste (237,000 tonnes (Al-Salem et al., 2009)) are currently recovered by secondary recycling.

The last two routes differ from the two previous ones as they involve a transformation of the chemical structure of the initial plastic. Tertiary or chemical recycling consists of the transformation of plastic waste into smaller molecules via thermal or chemical processes. These molecules can later be processed or upgraded to manufacture other chemicals. The advantage of tertiary recycling over secondary and primary is the acceptance of heterogeneous and contaminated plastic waste thereby decreasing separation and cleaning costs. Quaternary recycling implies energy recovery from plastic waste via incineration. Plastic waste have the potential to recover twice as much energy as that from coal and equivalent to that of diesel. However, quaternary recycling cannot recover the 'virgin' material and therefore has little contribution reducing the consumption of petrochemical resources.

The amount of data in regard to the percentage of each plastic type that is mechanically recycled is low. In the UK, the majority of local authorities (99 %) offer recycling schemes for plastic bottles (British Plastics Federation (BPF), 2019; Stephenson, 2018), which are mainly manufactured from HDPE and PET. Most local authorities (79 %) also offer recycling schemes for plastic pots, tubs and trays (British Plastics Federation (BPF), 2019; Stephenson, 2018), which are mainly manufactured from PP. The other plastic types present in the plastic waste mixture are not currently collected for mechanical recycling in the UK. This means that from the five plastic waste studied here; HDPE, LDPE, PP, PET and PS, only three (HDPE, PET and PP) are generally collected for mechanical recycled.

This statistic only refers to the percentage of local authorities that offer a recycling scheme. It does not however give any insight as to the actual percentage of HDPE, LDPE, PP, PET or PS that in fact ends up being mechanically recycled. Therefore, it is challenging to assess the amount of each plastic waste (HDPE, LDPE, PP, PET and PS) that it is mechanically recycled and it can only be assessed qualitatively, e.g. HDPE and PET are mostly mechanically recycled while LDPE and PS are not with PP being in the middle.

Amongst the four routes mentioned above, pyrolysis falls into tertiary or chemical recycling. In comparison to mechanical recycling (primary and secondary recycling), tertiary recycling routes such as pyrolysis of plastic waste are superior in some aspects. Pyrolysis is also superior to other tertiary (gasification) and quaternary recycling (incineration) routes in several aspects. Some of

the advantages of plastic waste pyrolysis against the other three methods aforementioned are listed below:

i. Unlike gasification and mechanical recycling, pyrolysis accepts heterogeneous and contaminated feedstock, therefore the need and costs for segregation and cleaning are eliminated;

ii. pyrolysis gases from advanced pyrolysis of plastic waste contain light hydrocarbons (C_1-C_4) and hydrogen, which are high-value products that can be used as fuels or upgraded into chemicals;

iii. compared to gasification, combustion or incineration no CO_2 and CO are produced, if PET is not present, reducing the carbon footprint;

iv. pyrolysis minimizes the emissions of toxic products (NO_x, SO_x and dioxins) due to moderate range of operating temperatures (450-650 °C) compared to incineration (> 800 °C); and

v. pyrolysis can produce versatile products ranging from feedstock for plastic manufacturing or other chemical processes to energy recovery and the production of fuels for transportation.

As the other plastic waste, waste PET management often consists on landfill disposal, energy recovery via incineration and mechanical recycling. However, PET is also chemically recycled via methanolysis, glycolysis or hydrolysis. Glycolysis, a very common PET chemical recycling method, yields BHTE monomer. Glycolysis consists on the depolymerisation of PET through the solvolytic chain cleavage into smaller molecules in the presence of ethylene glycol at temperature and pressure between 190-240 °C and 0.1-0.6 MPa over a long reaction time (0.5-8h) (Carta et al., 2003). It requires a basic liquid catalyst (metal acetates (Khoonkari et al., 2015; Yue et al., 2011), titanium-phosphates (Yue et al., 2011), solid super acids (Yue et al., 2011), metal oxides (Yue et al., 2011), ionic liquids (Khoonkari et al., 2015), hydrotalcites (Khoonkari et al., 2015), or enzymes (Khoonkari et al., 2015)) to obtain a reasonable yield of BHTE (6-100 %) at milder conditions (Duque-Ingunza et al., 2014; Karayannidis and Achilias, 2007; Nabid et al., 2017; Yue et al., 2011). However, these catalysts are toxic compounds (Yue et al., 2013), require additional extraction/filtration/crystallization steps to separate BHTE from the catalyst, the catalysts cannot be reused after separation increasing operation costs and finally, glycolysis cannot cope with contaminated, mixed waste PET. Carta et al. (2003); Karayannidis and Achilias (2007); Paszun and Spychaj (1997) provide very in-depth information on glycolysis that can satisfy the reader curiosity but it is not included here as it escapes the focus of this thesis.

2.2.1 Comparison of pyrolysis and other plastic waste management routes from a life cycle assessment perspective

Life cycle assessment (LCA) is a popular methodology to compare the environmental impact of various processes or scenarios. Gear et al. (2018) have developed a toolkit, using LCA methodology, to compare the environmental impact of pyrolysis of plastic waste (using Recycling Technologies RT7000 process to recover hydrocarbons, Plaxx) with incineration and landfill disposal. They have showed that pyrolysis of plastic waste is a better waste management alternative than both landfill and incineration with energy recovery in terms of lower environmental impact. Applying also a LCA to the management of mixed plastic waste in Singapore, Khoo (2019) have reported that the environmental impact of plastic waste pyrolysis was equal to that of mechanical recycling and lower than that of incineration and landfill disposal.

The main environmental impact for plastic waste management is global warming potential i.e. the amount of CO_2 emitted (Shonfield, 2008). This is true for pyrolysis and also all the other common waste management techniques (landfill, incineration and mechanical recycling). Shonfield (2008) showed that from a LCA perspective, landfill disposal is by far the worst way of managing plastic waste as it presents a negative impact for all emissions (CO_{2eq}, energy consumption, PO_{4eq}^{+}, SO_{2eq}, human toxicity, ozone creation and ozone layer depletion). This means that landfill disposal of plastic waste should be avoided. However, landfill is still the main way of managing plastic waste in some areas, e.g. USA, Cyprus or India.

Although slightly better than landfill, Shonfield (2008) have showed that incineration with energy recovery was a negative option in terms of CO_2 emissions. Despite this, several countries including the UK, are investing in the creation of waste-to-energy plants. However, from a LCA perspective Shonfield (2008) have reported that it is much beneficial, in terms of minimising the environmental impact of plastic waste management, to separate plastic waste and recover them as much as possible e.g. mechanical recycling or pyrolysis.

Al-Salem et al. (2014) have reported similar conclusions to the ones of Gear et al. (2018); Khoo (2019) mentioned above. However, they have mentioned an additional point in terms of the financial, or other, incentives available. The lack of these incentives for pyrolysis of plastic waste and its products have hindered the view of this technology as a profitable process. This means that, despite the environmental impact of pyrolysis of plastic waste being equal to that of mechanical recycling and lower than that of landfill and incineration with energy recovery, the former is still considered somewhat inferior.

However, the growing popular concern about the use of plastic product and the management of plastic waste may change this perception. This is believed because of the growing interest of NGOs and the wider public on how household plastic waste are managed and what are their true environmental impacts. This concerns could put pressure to Governments to create new policies and incentives to shift the focus from plastic waste management into the recovery of plastic waste value. If this is the case, interest into plastic waste pyrolysis may grow and push further the implementation of this technology.

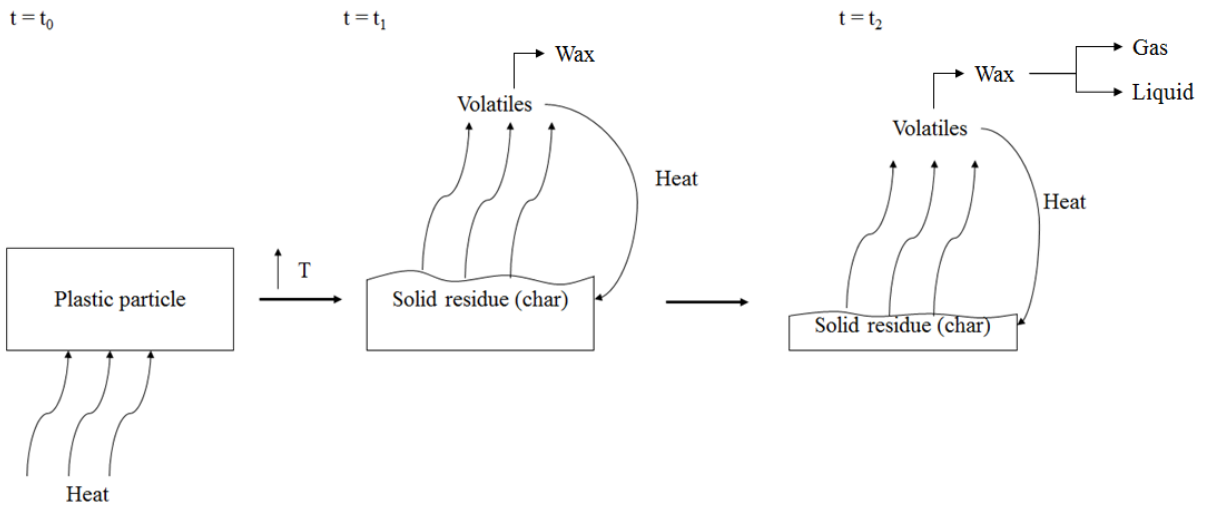

Figure 2.3 Plastic waste pyrolysis mechanism adapted from Babu and Chaurasia (2003)

2.3 Pyrolysis of plastic waste

Although some common plastic waste types present oxygen in their structure e.g. PET (33 wt%), they are mainly only formed by carbon (80 wt%) and hydrogen (12 wt%) (Diaz-Silvarrey and Phan, 2016) making them an ideal feedstock for chemical recycling. In pyrolysis, plastic wastes are decomposed to hydrogen, methane, light hydrocarbons (C_2 to C_4), liquid/wax hydrocarbons (C_5 to C_{35+}) and a small amount of solid residue depending on the type of plastic (Miskolczi et al., 2004; Pinto et al., 1999*a*; Sakata et al., 1996; Williams and Williams, 1997*a*, 1999). The difference in the amount of the aforementioned components depends both on the operating conditions (temperature, heating rate, pressure, residence time and type of reactor (Chen et al., 2014; Sharuddin et al., 2016)) and the operating methods (depolymerisation, partial oxidation or cracking) (Al-Salem et al., 2009; Panda et al., 2010).

Figure 2.3 illustrates the mechanism behind plastic waste pyrolysis proposed by Babu and Chaurasia (2003). When they are heated in an inert atmosphere the heat is first transferred towards the interior of the plastic molecule increasing its temperature. As the plastic internal temperature increases, the reaction is initiated via the cleavage of the weakest C-C bonds in the plastic chain. The first products of the reaction are shorter hydrocarbon chains than in the original plastic but still long. As those long-chain hydrocarbons suffer further cracking they reach a point when they are short enough to volatilise (volatiles). The volatiles released are at high temperature and they transfer part of that heat into the feedstock. After a certain time, all the feedstock is transformed into volatiles with the remaining non-volatile fraction forming a solid residue. Secondary cracking reactions occur where volatiles are further cracked into non-condensible gases. As volatiles loose heat they condense and form liquid and wax products.

2.3.1 Kinetic parameters

Kinetic analysis of plastic waste pyrolysis are scattered and inconsistent. Kinetic studies on HDPE, LDPE, PP and PS are more common than other plastic waste e.g. PET or PVC due to their abundance (over two thirds) (Miskolczi et al., 2004; Westerhout et al., 1997). Kinetic studies were often simplify as a first order decomposition reaction or performed single heating rate experiments (Garcia et al., 1995; Grammelis et al., 2009; Perez-Maqueda et al., 2014; Sorum et al., 2001). However, according to Westerhout et al. (1997) these simplifications could only describe plastic waste pyrolysis at high levels of conversion (over 70 %) and low pyrolysis temperatures (<450 °C), which do not represent real conditions of plastic waste pyrolysis. Thermal decomposition of plastic waste occurs via a complex mechanism, random scission, where the plastic chains break at random C-C bonds into smaller molecules yielding a wide range of compounds as products.
Sorum et al. (2001) reported the activation energy (E_a) for commercial grade HDPE, LDPE, PP and PS as 445.1 kJ/mol, 340.8 kJ/mol, 336.7 kJ/mol, and 311.5 kJ/mol respectively. In contrast, lower values of 233-326 kJ/mol for HDPE, 194-206 kJ/mol for LDPE, 184-265 kJ/mol for PP, and 172 kJ/mol for PS were reported by Wu et al. (1993). Saha and Ghoshal (2005) found that E_a and pre-exponential values (A) for different PET drinking bottles were in a range of 162.15-338.98 kJ/mol and $2.83 \cdot 10^{11}$-$1.18 \cdot 10^{25}$ s^{-1} depending on bottle type and kinetic method applied. A method to develop a kinetic model for plastic waste pyrolysis is discussed later on in chapter 4. This chapter shows that activation energy of waste HDPE, LDPE, PP, PS and PET was 375.59, 267.61, 261.22, 192.61 and 197.61 kJ/mol respectively (Diaz-Silvarrey and Phan, 2016). These findings agreed well with Wu et al. (1993) but not with Sorum et al. (2001). Even though plastic products are made of the same type of plastic, they could behave differently during pyrolysis due to different manufacturing processes and incorporation of additives to improve their properties. Unlike E_a, most kinetic studies agreed on the decomposition temperature of individual plastic waste: HDPE = 425-565 °C, LDPE = 443-535 °C, PP = 415-540 °C, PET = 395-520 °C and PS = 372-452 °C. Decomposition temperature ranges increase with heating rate and plastic type in the order HDPE>LDPE>PP>PET>PS due to substitution groups (Diaz-Silvarrey and Phan, 2016). Most of pyrolysis experiments are therefore performed around 500 °C as shown in Table 2.1 as a compromising temperature for a mixture of plastic waste.

2.3.2 Thermal (conventional) plastic pyrolysis

Thermal (conventional) pyrolysis is the thermo-chemical decomposition of plastic waste without any advanced technologies such as catalysts, microwaves, plasma, etc. This process has been extensively studied focusing on pyrolysis at moderate temperatures (500 °C) to maximise the yield of pyrolysis liquid/wax/oil (PPO) for transportation fuels (Al-Salem et al., 2010; Madorsky, 1964; Meier et al., 2013; Scheirs and Kaminsky, 2006). In 19991, Kaminsky (1991) showed that the PPO fraction obtained from pyrolysis of mixed PE, PP and PS at 450 °C was suitable for internal combustion engines. Since then, several authors continued plastic waste

pyrolysis research for fuels and hydrocarbons (Aguado et al., 2014*a*, 2003; Angyal et al., 2007; Artetxe et al., 2015, 2010; Barbarias et al., 2016; Bhaskar et al., 2004, 2005, 2003; Borsodi et al., 2011; Costa et al., 2007, 2010; Csukas et al., 2013; Miranda et al., 2011, 2012; Miskolczi, 2014; Miskolczi et al., 2009, 2008, 2004; Miskolczi and Nagy, 2012; Pinto et al., 1999*a*, 2013; Sakata et al., 1996; Singh et al., 2012; Williams and Williams, 1997*a*; Williams and Bagri, 2004; Williams and Slaney, 2007; Williams, 2006; Williams and Williams, 1998, 1999; Wu et al., 2014,?; Wu and Williams, 2010*a*). The main work on thermal pyrolysis of plastic waste is summarised in Table 2.1.

Table 2.1 Research on thermal/conventional pyrolysis of plastic waste

Reference	Plastic	Conditions	Products	Notes
Williams and Williams (1997*a*); Williams (2006); Williams and Williams (1998, 1999)	LDPE, HDPE, PP, PS, PET, PVC	10-25 °C/min 500-700 °C	Gas (9.79 - 88.76 %): H_2, CH_4, C_2H_4, C_2H_6, C_3H_6, C_3H_8, C_4H_8 and C_4H_{10}, CO_2(only PET), CO (only PET), HCl (only PVC) Oil/Wax (18.44 - 57.11 %): HDPE, LDPE and PP yield aliphatic oil; PVC, PS and PET increased aromatic content	Temperature and heating rate are the main parameters affecting plastic waste pyrolysis: 1) Low temperature (≤550 °C) and high residence time (10 s - 10 min) promote heavy wax similar to crude oil; 2) Higher temperature (≥550 °C), high heating rate and low residence time (<1 s) enhance aromatic content in wax; 3) Temperature over 700 °C enhance the gas yield and the PPO obtained resembles gasoline
Williams and Bagri (2004)	PS	10 °C/min 500 °C 20 min at maximum temperature	Gas (0.1 %): CH_4, C_2H_4, $2H_6$, C_3H_6, C_3H_8, C_4H_8 and C_4H_{10} Oil (96.6 %): Styrene and aromatic hydrocarbons	Oil from PS: high amounts of polycyclic aromatic hydrocarbons and monomer (styrene = 80 %)
Wu and Williams (2010*a*)	Real world MPW mixture Ni-Mg-Al catalyst	40 °C/min 500 °C Catalyst:Plastic = 0.5-2.0 g/g	Gas yield = 49.4-228.6 wt% Oil/Wax yield = 40 wt% Solid yield = 5.2-19.4 wt%	Catalyst:Plastic ratio does not have a significant effect on gas products yield Higher temperatures and water injection enhances gas yield

Wu et al. (2014)	HDPE and regranulated HDPE from PVC	Ni-Mn-Al catalyst: Plastic = 2:1 Catalyst bed: 40 °C/min to 800 °C Pyrolysis reactor: 40 °C/min to 500 °C	5.5-18.4 wt% H_2	Hydrogen from gas and carbon nanotubes form solid residue
Williams and Slaney (2007)	MPW mixture simulating real world distribution	5 °C/min 500 °C 1 h at maximum temperature 10 MPa	Gas (0.5-4.3 %): light hydrocarbons and hydrogen Oil/wax (48.7-72.3 %): considerable aromatic fraction Solid residue (23.3-50.2 %)	Higher pressure in pyrolysis reactor increases oil/wax yield and also operation costs
Pinto et al. (1999*a*)	PE:PP:PS = 4:1:1; 1:4:1; 1:1:4; 1:1:1 and individual plastics	430 °C 3.5 MPa 20 min at maximum temperature	Gas yield < 10 % (C_1-C_4 hydrocarbons) Gas average calorific value 50 MJ/kg Oil/Wax yield > 90 % (C_5-C_{17} hydrocarbons) Oil/Wax calorific value 43-46 MJ/kg	PE promotes alkanes in oil/wax PP promotes alkenes in oil/wax PS enhances oil/wax yield and its aromatic content (toluene, ethylbenzene and m-xylene Oil/Wax distillation curve between gas oil and gasoline PS increases the RON number of oil/wax (RON = 100) while PE decrease this value (RON = 20) RON for transportation fuels between 85-100

Costa et al. (2007, 2010)	LDPE and HDPE and PE:PP:PS = 1:1:1	PE: 29.5±2 °C/min, 400-470 °C, 13-910 s Plastic mixtures: 37±3 °C/min, 380-420 °C, 34-724 s	As temperature increases: Light oil (B.P.<150 °C) = 14.9 - 85.7 wt% for PE and 27 - 71 wt% for mixture Heavy oil (B.P.>150 °C) = 26.2 - 1.9 wt% for PE and 30 - 10 wt% for mixture Solid residue = 59.5 - 11.1 wt% for PE and 40 - 16 wt% for mixture Gas (C_1-C_4) by difference	Reaction time and temperature promote light oil and gas instead of heavy oil and solid residue PE pyrolysis mechanism comprises of nine first order series and parallel reactions with activation energy between 185.0-301.2 kJ/mol depending on the reaction PS alters pyrolysis initiation for PE and PP and yields are more similar to PP individual pyrolysis that PE or PS pyrolysis
Pinto et al. (2013)	10 % pine, 10 % scrap tyres and 80 % recycled plastic (56 %PE, 27 %PP and 17 %PS)	5.5 °C/min 350-450 °C 10-30 min 0.21-1.03 MPa	Total PPO yield = 76.3-91.6 wt% Maximum PPO yield at 350 °C, 30 min and 0.2 MPa	Low temperature and pressure and high reaction time increase total PPO yield

Miskolczi et al. (2004)	PE, PP, PS, PUR, EPC, PA	500 - 550 °C 0.6-1.2h residence time	Gas: C_2-C_4 hydrocarbons PPO: C_5 - C_{24} aliphatic hydrocarbons and benzene, toluene, xylene, ethyl-benzene and styrene (if PS present)	High temperature and residence time increase PPO yield but do not affect non-condensable gas PE and PP promote alkanes (ethylene, ethane) PS enhances aromatic content in PPO product but also harmful compounds such as benzene or toluene
Angyal et al. (2007)	PP and PS	510-520 °C 15-30 min residence time	PPO yield = 20 - 60 % increasing with residence time and PS content Gas: C_3 followed by C_2, CH_4 and C_4	Volatiles formed by heavy oil (≈60 %) followed by middle distillates (≈10 %), naphtha (≈20 %), light oil (≈5 %) and non-condensable gas (≈5 %) PS increases reaction rate of reaction, PP degradation and aromatic content of the PPO fraction Middle distillates fraction have low BMCI (Bureau of Mines Correlation Index) and moderate olefin content
Miskolczi et al. (2009)	Agricultural and packaging MPW	520 °C Feeding rate = 9.0 kg/h of plastic waste Commercial ZSM-5 at 5 wt% of plastic waste	Gasoline yield (C_5 - C_{15}) = 20 - 48 % Light oil yield (C_{12} - C_{28}) = 17-36 %	Zeolite enhances long chain cracking increasing lighter fractions yields Nature and origin of plastic waste highly affect pyrolysis products e.g. agricultural plastic waste have high concentrations of N, S, P and Ca hindering the quality of pyrolysis oil

Csukas et al. (2013)	HDPE	465-545 °C 6-20 g/min feeding rate	Four-step degradation yielding four products: gas, naphtha, middle distillate and heavy oil formed by paraffins, olefins and aromatic compounds	Main factor limiting plastic waste pyrolysis is effective heat transfer between the reactor and the plastic waste When scaling up hollow tubular reactors present worst heat transfer than laboratory scale reducing the cracking process considerably
Sakata et al. (1996)	HDPE, PVC, PET	430 °C	Gas = 8.5 wt% for HDPE, 64.4 wt% for PVC and 33.4 wt% for PE PPO (C_5-C_{25}) = 70 wt% for HDPE, 4.7 wt% for PVC and 0 wt% for PET Solid residue = 22.3 wt% for HDPE, 32 wt% for PVC and 66.6 wt% for PET	PET and PVC decrease the PPO yield however they enhance PE pyrolysis into low molecular weight hydrocarbons
Bhaskar et al. (2003)	PE/PP/PS/PVC/PET	430 °C	Gas = 25-34 wt% PPO = 53-70 wt% Solid residue = 5-16 wt%	PET decreases the PPO yield and facilitates the formation of organic chlorine compounds instead of inorganic chlorine typical of PVC decomposition
Artetxe et al. (2015)	PS	450-600 °C	Styrene yield = 70.6 wt%	Polystyrene monomer recovery highly depends on the temperature ranging from 55-70 wt% PS pyrolysis also yields monoaromatics and PAH in the PPO, no solid residue and low gas yield

Barbarias et al. (2016)	HDPE	Pyrolysis: 500 °C Steam reforming: 600-700 °C Steam/Plastic = 3-5	38.1 g of H_2/100g HDPE at 700 °C, steam/plastic=5	Plastic waste pyrolysis for hydrogen generation if combined with steam reforming

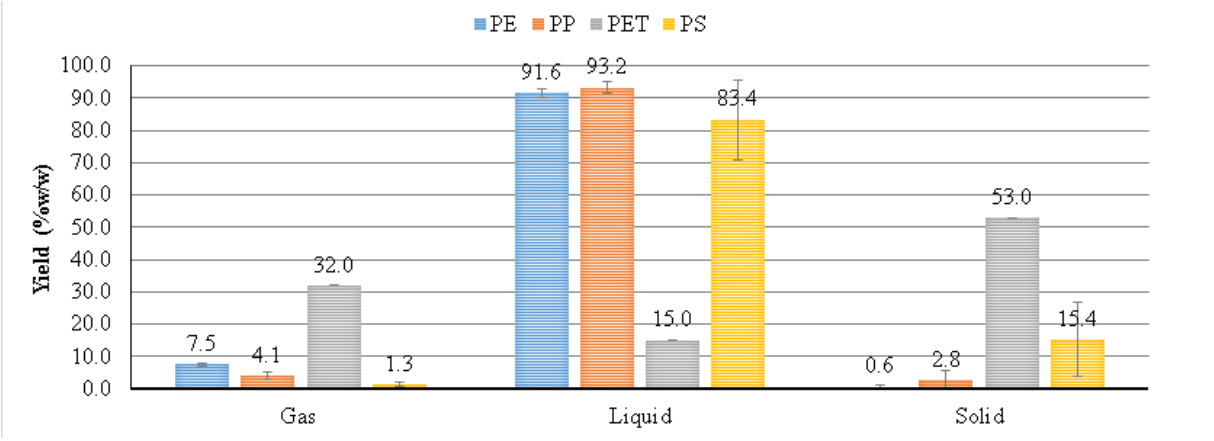

Figure 2.4 Gas, liquid/wax and solid residue yield of PE, PP, PS and PET pyrolysis. Adapted from Williams and Slaney (2007)(2-5 mm diameter virgin plastics and 5-10 mm plastic waste at 500 °C and 5 °C/min) and Pinto et al. (1999*a*) (3 mm virgin plastic particles, 20 min pyrolysis time, 430 °C and 3.5 MPa)

Table 2.1 shows that most research on plastic waste focuses on maximising the PPO fraction for transportation fuels by altering operating parameters i.e. temperature, heating rate and pressure. However, there is a lack of studies assessing the suitability of PPO performance in engines. Recently, Bukkarapu et al. (2018) reviewed the use of PPO as a fuel in diesel engines. They reported that pyrolysis oil presents a higher density and lower heating value, viscosity and break thermal efficiency than diesel. Therefore, direct use in engines is not recommended meaning PPO needs to be blended with diesel. A blend of 80 % PPO and 20 % diesel showed the most similar performance in terms of thermal efficiency to pure diesel at full engine load (Bukkarapu et al., 2018; Mani et al., 2011). However, the introduction of PPO in diesel engines also increased the amount of NO_x by 25 %, CO by 5 % and hydrocarbons by 15 % in the exhaust gases (Mani et al., 2011). These higher emissions were due to a longer ignition delay, higher carbon to hydrogen ratio and lower oxygen availability on the fuel mixture respectively (Bukkarapu et al., 2018). A reduction in emissions could be done by replacing 10 % of the PPO with either 2-methoxy ethyl acetate (MEA) or diethyl ether (DEE) (Bridjesh et al., 2018). Despite transportation fuels being the main focus, most studies neither characterised the PPO obtained nor test its suitability on engines. This fact, along with the lack of legislation/standards covering PPO, hinders the industrial implementation of this technology. Thereby, it is obvious that as long as studies do not extent their approach into the next step i.e. viability assessment of pyrolysis products, this technology cannot move forward for plastic waste management.

In recent years the main focus of plastic waste pyrolysis has shifted towards the production of other high value products such as hydrogen (Barbarias et al., 2018; Wu et al., 2014), carbon nanotubes (Aboul-Enein et al., 2018; Liu, Jiang, Yu and Tang, 2011; Mishra et al., 2012; Wu and Williams, 2009*a*), activated carbon for water treatment (Gopu et al., 2018) or monomer recovery (Artetxe et al., 2015; Diaz-Silvarrey, Zhang and Phan, 2018).

Figure 2.4 shows the average yield of the three plastic waste thermal/conventional pyrolysis products: gas, liquid/wax and solid residue of individual plastic waste (average between

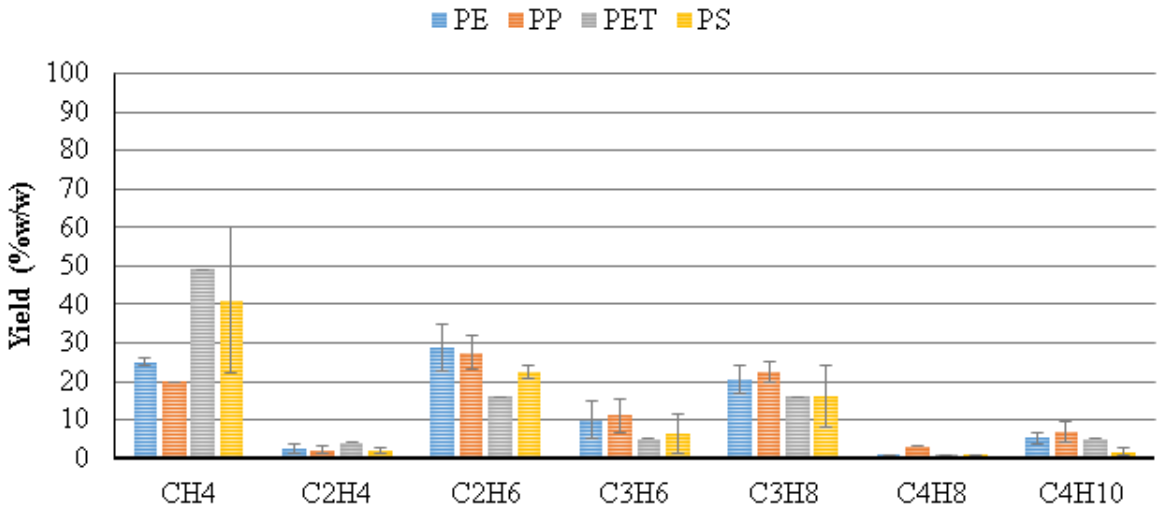

Figure 2.5 Average hydrocarbon product gas distribution from the pyrolysis of PE, PP, PS and PET pyrolysis. Adapted from Williams and Slaney (2007)(2-5 mm diameter virgin plastics and 5-10 mm plastic waste at 500 °C and 5 °C/min) and Pinto et al. (1999*a*) (3 mm virgin plastic particles, 20 min pyrolysis time, 430 °C and 3.5 MPa)

pyrolysis of 3 mm virgin plastic particles, 20 min pyrolysis time, 430 °C and 3.5 MPa (Pinto et al., 1999*a*) and 2-5 mm diameter virgin plastics mixed with 5-10 mm plastic waste particles at 500 °C at a heating rate of 5 °C/min (Williams and Slaney, 2007)). Thermal pyrolysis of PE, PP and PS was characterized by high liquid/wax yield (83-93 wt%) and low gas and solid residue yields (1-7 wt% and 0.5-15 wt% respectively). PET presented a different behaviour with low liquid/wax yield (15 wt%) and relatively high gas and solid residue yields (32 wt% and 53 wt% respectively). The difference between PE, PP, PS and PET product yields was due to their structure. As PE and PP are both manufactured by polymerisation of ethylene and propylene respectively to form a linear chain, their thermal decomposition is similar and occurs via random scission of C-C bonds to form smaller hydrocarbons (alkanes, alkenes and dienes).
Jung et al. (2010) reported that solid residue from PE and PP thermal pyrolysis comprised of over 90 wt% inorganic compounds with the remaining fraction being carbon. Therefore, applications of plastic waste pyrolysis solid residue are limited, mainly as building material or sometimes for co-combustion with coal (Bernardo, 2011; Sharuddin et al., 2016)).
High temperature and long residence time of volatiles increase the gas fraction at the expense of the liquid/wax due to secondary cracking (Sharuddin et al., 2016). The main components in the gas fraction are methane, ethane and propane (Pinto et al., 1999*a*; Williams and Slaney, 2007) as shown in Figure 2.5. The proportion of these components depends on feedstock composition, pyrolysis temperature, heating rate and residence time. Onwudili et al. (2009) showed that the addition of LDPE and PET in the feedstock increased the gas fraction whereas PS reduced the amount of gas produced. However, the presence of PET in the feedstock decreased the quality of the gas fraction due to the formation of CO and CO_2 while feedstock comprising of HDPE, LDPE, PP and PS produces mostly hydrocarbons (C_2-C_4) (Williams and Williams, 1999) with high calorific value (45-50 MJ/kg (Sharuddin et al., 2016)). Although, the ethylene (C_2H_4) and

propylene (C_3H_6) can be recovered for poleolefin manufacture, the amount in the gas fraction derived from thermal pyrolysis is low, therefore the main application of the gas phase is as heat source.

The condensible fraction from plastic waste pyrolysis i.e. liquid, wax or oil interchangeably (referred to as wax in this thesis), is often a wax or tick paste. The composition of the wax fraction strongly depends upon feedstock composition. For example, the presence of the methyl group in PP chain promotes the formation of C=C bonds i.e. more alkenes, compared to HDPE and LDPE (Pinto et al., 1999*a*). HDPE and LDPE produced around 70 %(v/v) of alkanes and 20 %(v/v) of alkenes (Pinto et al., 1999*a*) whereas PS and PET pyrolysis yielded mostly aromatic compounds (96 %v/v (Pinto et al., 1999*a*)) with a majority of toluene (27 %v/v (Pinto et al., 1999*a*), 7 wt% (Demirbas, 2004) and 22-28 wt% (Onwudili et al., 2009)) and ethyl benzene (15 %v/v (Pinto et al., 1999*a*) and 33-39 wt% (Onwudili et al., 2009)). PS presents an aromatic ring in the structure causing alterations on the thermochemical decomposition mechanism and increasing the aromatic content in the wax fraction (Pinto et al., 1999*a*). Under high temperature, PET ester link is broken yielding vinyl ester and carboxyl groups, altering product yields and composition (Du et al., 2016; Venkatachalam et al., 2012). If the desired product is the recovery of wax for transportation fuels as Table 2.1 suggested, then the proportion of each plastic waste in the feedstock is key. In addition, the desired carbon distribution of the wax fraction i.e. gasoline-like or diesel-like, also plays an important role.

Depending on the applications, feedstock composition should be adjusted. Although HDPE, LDPE and PP yield high wax fraction at low temperature (<500 °C), the wax is of bad quality for transportation fuels (Demirbas, 2004). Gasoline-like fuels used in internal combustion engines are classified according to their Research Octane Number (RON). RON measures the resistance of the gasoline to autoignition which is a phenomenon that shortens the life of the engine. The higher the RON the higher the power output and therefore the better quality of the gasoline. If the wax fraction is meant to substitute gasoline from fossil fuels it must present equivalent RON thereby, PS would need to be in pyrolysis feedstock to increase the aromatic content and hence the RON. PET pyrolysis produces mainly a yellow powder comprising of benzoic acid and terephthalic acid (Du et al., 2016; Sakata et al., 1996) alongside other aromatic and carboxylic compounds increasing the acidity of the wax fraction and its quality (Mani et al., 2011). PET recycling rate is already quite high compared to the other plastic waste due to the easy segregation by density difference with the other plastic waste (PE and PP = 0.9-1 g/cm^3, PS = 1.0-1.1 g/cm^3 and PET = 1.2-1.3 g/cm^3 (Gent et al., 2009)). Chemical recycling of PET via glycolysis/hydrolysis is the main route to recover high-value products.

Temperature also has a strong effect on the composition of thermal pyrolysis products. High pyrolysis temperature (>700 °C) increases the aromatic content of the wax fraction for the same feedstock composition (Kaminsky and Kim, 1999; Li et al., 1999) via either unimolecular cyclization reactions followed by dehydrogenation (pyrosynthesis) or Diels-Alder reactions followed by dehydrogenation (Bockhorn et al., 1999; Kalargaris et al., 2017). Kalargaris et al. (2017) showed that the wax recovered from pyrolysis of mixed plastic waste at 900 °C presented

a worst performance in diesel engines than the one obtained from pyrolysis of the same plastic waste mix at 700 °C. The wax obtained at 900 °C presented lower cetane number and higher emissions (NO_x, CO, CO_2) than the equivalent obtained at 700 °C. Therefore, if the desired product is the liquid/wax fraction for transportation fuel then both the feedstock and pyrolysis temperature need to be careful controlled.
Due to thermal pyrolysis challenges in terms of product application, the introduction of catalysts was studied. Catalysts often decrease pyrolysis activation energy allowing the operation at lower temperatures for equivalent product yield. In addition, catalysts have the potential to increase the selectivity of the desired hydrocarbon range in the wax fraction. Lastly, the addition of catalysts increases the amount of gas recovered and therefore the amount of ethylene and propylene expanding the applications of the gas fraction.

2.3.3 Catalytic pyrolysis of plastic waste

Catalytic cracking of plastic waste is well-known and mainly focused on single virgin plastic: PE (Aguado et al., 2007; Bagri and Williams, 2002; Olazar et al., 2009; Sakata et al., 1999), PP (Chaianansutcharit et al., 2007; Kaminsky and Zorriqueta, 2007; Sakata et al., 1999) and PS (Serrano et al., 2000; Williams and Bagri, 2004) and binary/ternary mixtures of waste PE, PP and PS (Bhaskar et al., 2003; Buekens and Huang, 1998; de Marco et al., 2009; Kassargy et al., 2018; Lee, 2009; López, De Marco, Caballero, Laresgoiti and Adrados, 2011; Pinto et al., 1999*b*; Siddiqui and Redhwi, 2009; Vasile et al., 2001) at a temperature range between 400-600 °C. The aim of the catalyst was to reduce pyrolysis temperature, decrease the wax fraction carbon number distribution compared to thermal pyrolysis (e.g. from C_6-C_{20} to C_6-C_{10} (Buekens and Huang, 1998; de Marco et al., 2009)) or produce ethylene or propylene (Burange et al., 2015; Rahimi and Karimzadeh, 2011). Zeolites e.g. HZSM-5, HY, USY, are commonly used in plastic waste pyrolysis (Aguado et al., 2009, 2007; Bagri and Williams, 2002; de Marco et al., 2009; Pinto et al., 1999*b*; Sakata et al., 1999; Serrano et al., 2000; Vasile et al., 2001; Williams and Bagri, 2004) due to their ion exchange properties, acidity and selectivity. However, zeolites rapidly deactivate after very few plastic waste pyrolysis cycles due to blockage of small pores by bulky volatile hydrocarbons (Serrano et al., 2012) and coking (Adrados et al., 2012; Ciesielski et al., 2018; Diaz-Silvarrey, Zhang and Phan, 2018; López, De Marco, Caballero, Adrados and Laresgoiti, 2011). Removal of coke by regeneration in air at 550 °C for 5 h is possible (López, De Marco, Caballero, Adrados and Laresgoiti, 2011; Serrano et al., 2007) but it adds energy requirements and costs to the pyrolysis process. Zeolite deactivation and high costs ($30-$120 per tonne for natural zeolites (Virta, 1997)) lead to the investigation of re-used catalyst (fluid catalytic cracking catalysts, FCC) (Ali et al., 2002; Cardona and Corma, 2000; Lee, 2008; Lin and Yang, 2007*b*; Salmiaton and Garforth, 2007) or waste materials from other processes (e.g. red mud, fly ash or carbide slag) (López, De Marco, Caballero, Laresgoiti, Adrados and Aranzabal, 2011). Table 2.2 summarises catalytic pyrolysis of individual and mixed plastic waste.

Table 2.2 Research on catalytic pyrolysis of plastic waste

Reference	Plastic	Catalyst	Conditions	Products	Notes
Lopez-Urionabarrenechea et al. (2012)	PE, PP, PS, PET and PVC	Zeolite	440 °C	56.9±3.0 wt% liquid yield; 40.4±1.9 wt% gas yield and 3.0±0.3 wt% solid yield	
Siddiqui and Redhwi (2009)	PS with LDPE, HDPE, PP, and PET	Hydroprocessing catalyst (MgO_3+NiO)	430-440 °C	50-75 % liquid yield; 25-75 % gas yield and solid by mass balance	
López, De Marco, Caballero, Laresgoiti, Adrados and Aranzabal (2011)	Virgin: 40 wt% PE, 35 wt% PP, 18 wt% PS and waste: 4 wt% PET, 3 wt% PVC	ZSM-5 Red Mud	20 °C/min 400-500 °C	Gas = 17.7-58.4 wt% Liquid = 39.8-79.3 wt%	ZSM-5 lowered operation temperature from 500 to 440 °C Red Mud catalyst activity comparable to ZSM-5 but required higher temperature (>500 °C) to be activated Red Mud increased gas yield, decreased viscosity of liquid and promoted aromatization

Yanik et al. (2001)	Virgin PP, PS, PE and PVC	Red Mud	3 °C/min to 120 °C and 60 min hold 3 °C/min to 300 °C and 60 min hold 3 °C/min to 430 °C	Gas: 2.2 wt% for PS, 15.0 wt% for PE and 15.4 wt% for PP Liquid: C_5-C_{25} for PE and PP and C_8-C_{10}, styrene, α-methyl styrene and toluene for PS	Red Mud fixed HCl from PVC and had an effect on organic chlorine compounds Red Mud had little effect on the carbon distribution of liquid
Cardona and Corma (2000)	Virgin PP	Zeolite USY and HY Amorphous silica-alumina Spent FCC	Pre-treatment at 210 °C for 70 minutes to melt plastic 10 °C/min to 380 °C Catalyst introduced at 380 °C	Gas <15 wt% for all tested conditions Gasoline >70 wt% for all tested conditions Diesel+gas oil = mass difference	Neither total number nor strength of the acid sites play a relevant role in PP cracking but the formation of mesopores Both amorphous SiO_2-Al_2O_3 and FCC catalysts were very active catalyst with good selectivity, comparable to zeolites but with lower costs

Lin and Yang (2007*a*)	62 wt% PE 30 wt% PP 7 wt% PS 1 wt% PVC	USY (Si/Al = 5.7), ZSM-5 (Si/Al = 17.5), amorphous SiO_2-Al_2O_3 (Si/Al = 3.6), silicate (Si/Al > 1000) and equilibrium catalysts	340 - 460 °C	Gas = 5.1 - 85.7 wt% Liquid = 0.3 - 6.9 wt% Residue = 9.7 - 94.1 wt%	FCC catalyst gave the highest conversion of waste plastic waste to volatile hydrocarbons Selectivity of olefin and iso-olefin products increased with low temperatures and short reaction times as well as with equilibrium catalysts
Lin and Yang (2008)	Virgin PP	Regenerated FCC catalyst (Si/Al = 2.1), ZSM-5 (Si/Al = 17.5), HUSY (Si/Al = 13.6), amorphous SiO_2-Al_2O_3 (Si/Al = 3.6) and silicate (Si/Al > 1000)	3,5,10 and 20 °C/min 497 °C Hold = 120 minutes Catalyst heated to 597 °C at 10 °C/min in air	Gas = 15.3 (silicate) - 89.7 (ZSM-5) wt% Liquid = 2.6 (silicate) - 5.4 (FCC) wt% Residue = 5.0 (ZSM-5) - 81.9 (silicate) wt%	Silicate showed little catalytic activity Activation energy of PP catalytic cracking: silicate (143.4 kJ/mol) > amorphous SiO_2-Al_2O_3 (91.7 kJ/mol) > FCC (87.1 kJ/mol) > HUSY (76.4 kJ/mol) > ZSM-5 (72.5 kJ/mol) FFC decreased activation energy to allowing PP cracking at lower temperature but at lower cost than HUSY and ZSM-5 FCC deactivates exponentially due to coking

Na et al. (2006)	Virgin LDPE	Fly ash-derived silica–alumina catalyst (FSA)	5 °C/min 600 °C	No product yield or product distribution	FSA catalyst decreased the boiling point distribution of liquid compared to thermal pyrolysis and diesel and was the same as zeolite HY catalyst
Benedetti et al. (2017)	Waste electrical and electronic equipment (WEEE): 64 wt% ABS, 33 wt% HIPS and 3 wt% PBT	Fly ash powder from coal gasification HUSY HZSM-5	400 °C Plastic/Catalyst weight ratio = 2:1 Hold = 30-45 minutes	Gas = 2 - 4 wt% Light oil = 59 - 83 wt% Heavy oil = 2 - 28 wt% Residue = 11.4 - 19 wt%	Mechanically and chemically treated fly ash improved WEEE pyrolysis yields in terms of quality of light oil Fly ash did not significantly altered degradation temperature Chemically processed fly ash increased H_2 from 0 (thermal pyrolysis) to 35 vol%
Rotliwala and Parikh (2012)	HDPE	Bituminous coal Bagasse fly ash Coal combustion fly ash De-oiled jatropha cake	10 °C/min to 450 °C Hold = 1 hour	Gas = 7.3 - 38 wt% Liquid = 54 - 79.1 wt% Residue = 8 - 20 wt%	The addition of all catalyst increased the liquid yield from 54 wt% to 63-79.1 wt% due to the presence of Fe, Ca, etc. Bagasse and coal combustion fly ash increased the gasoline-like fraction in liquid The addition of all catalysts tested increased the oxygenated in liquid up to 15 wt%

Ali et al. (2002) found that reactivated FCC catalysts could be reused for HDPE pyrolysis yielding similar products as commercial zeolites but at a fraction of the cost (operation costs around 9 M$/year for reactivated FFC catalysts compared to 200-700 M$/year for commercial zeolites). Amorphous SiO_2/Al_2O_3 catalysts were also used on single plastic waste and binary mixtures (San Miguel et al., 2009; Wang and Wang, 2011). Si/Al ratios up to 1:3 decreased gas yield and enhance light hydrocarbons in the liquid/wax due to the change in the catalyst pore acidity. Red Mud (a by-product of the Bayer process for alumina manufacture) was studied as an alternative catalyst (Adrados et al., 2012) due to its high surface area, sintering and poisoning resistance and low costs (Sushil and Batra, 2008). Red Mud catalyst has lower acidity and porosity than zeolites and needs higher temperature to be activated (>500 °C) for real mixed plastic waste pyrolysis (40 % PE, 35 % PP, 18 % PS, 4 % PET and 3 % PVC) (López, De Marco, Caballero, Laresgoiti and Adrados, 2011). However, the aromatic product (C_5-C_{16}) in the liquid/wax and high heating value (48-53 MJ/kg) of the gas product were very similar as to the one obtained with zeolites. Sulphated zirconia (SZ) ($Zr(SO_4)_2$-ZrO_2) presented good catalytic activity for polystyrene thermal cracking (Yadav and Nair, 1999) and for thermal decomposition of HDPE and coal mixtures (Liu and Meuzelaar, 1996).

Hydrogen has been identified as a very high-value product due to its potential as energy carrier i.e. transmitter of energy, in future transport, heat and industry supply (Balat, 2008; Staffell and Dodds, 2017). It is commercially produced from steam methane reforming (about 96 % (Wu and Williams, 2009*b*)), coal gasification and oil reforming (Ewan and Allen, 2005). However, alternative sources to produce hydrogen, such as plastic waste catalytic pyrolysis/gasification over transition metal catalysts have recently attracted attention: nickel-based catalyst (Ni/Al_2O_3, Ni-Mg-Al catalyst, Ni/MgO, Ni/CeO_2, Ni/ZSM-5 and $Ni/CeO_2/Al_2O_3$) (Alvarez et al., 2014; Jiao et al., 2016; Namioka et al., 2011; Wu and Williams, 2009*a*,*b*, 2010*b*) or rubidium-based catalyst at lower pyrolysis temperature (200 °C) compared to Ni-based catalysts but higher catalyst costs (Namioka et al., 2011).

One of the main disadvantages of Ni-based catalyst used in cracking reactions is the deactivation of the catalyst due to coking (Sehested, 2006). However, several studies have shifted that disadvantage into a perk by recovering carbon nanotubes (CNT) from the coke deposited on spent metal catalysts using plastic waste as a carbon source (Bazargan and McKay, 2012). CNTs are hollow cylinders formed by carbon with diameters ranging from 0.1-100 nm and lengths that could go over 100 m used in multiple applications: electronics, biosensors, energy storage or reinforced composites (Zhang, Zhang, Liu, Phan and Luo, 2017). They are conventionally manufactured via high pressure chemical vapour deposition (CVD) at high temperature (700-1200 °C) using hydrocarbons, mainly methane and ethylene, as carbon source and a catalyst containing Fe, Co or Ni (Tripathi et al., 2017; Zhang, Zhang, Liu, Phan and Luo, 2017). Wu et al. (2012) showed the potential recovery of up to 1 tonne/day of CNTs, along with up to 16800 Nm^3/day of H_2 via gasification of about 10 tonnes/day of waste PP. Pol and Thiyagarajan (2010) grew CNTs over cobalt acetate catalyst, recovering 0.4 g of CNTs per gram of waste HDPE and LDPE via thermal degradation at 700 °C. Liu, Jiang, Yu and Tang (2011) reported

that CNTs could be produced from a two-stage PP pyrolysis (PP catalytic pyrolysis at 550-750 °C over HZSM-5 zeolite followed by catalytic decomposition of pyrolysis gases at 500-800 °C over NiO). Wu and Williams (2009*a*) reported CNTs produced on $Ni/CeO_2/ZSM-5$ catalyst surface and a hydrogen rich gas stream (up to 65 vol% of H_2) alongside with CO_2 (5 vol%) and CO (25 vol%), using a two-stage PP pyrolysis/gasification system (500/800 °C pyrolysis/gasification temperatures respectively). Mishra et al. (2012) produced the purest CNTs from PP pyrolysis at 800 °C under argon and hydrogen atmosphere using 0.01 wt% of Ni catalyst compared to the CNTs recovered at 600 and 700 °C. The injection of steam in a two-stage steam gasification (600/800 °C respectively) using PP, LDPE and PS as carbon sources and Ni/Al_2O_3 as catalyst (Acomb et al., 2014) increased the amount of H_2 recovered however destroyed some CNTs. PS showed the largest yield of filamentous carbon i.e. CNTs (up to 32 wt%) followed by PP and LDPE (Acomb et al., 2014). Better quality CNTs, in terms of purity and graphitization, and higher H_2 yield were obtained with Fe-based catalysts instead of Ni-based ones (Yao et al., 2018) in a two-stage pyrolysis of mixed plastic waste heated at 10 °C/min up to 500 °C and 600/700/800 °C in the first and second stage respectively. Yao et al. (2018) confirmed that steam injection in the second stage increases the H_2 yield but decreases the amount of CNTs recovered.
None of the above studies on H_2 and CNTs production focused or discussed the wax/liquid. Bajad et al. (2016) reported up to 6.63 wt% CNTs, 69 vol% H_2 and 4.55 wt% wax/liquid from mixed plastic waste (i.e. 67.2 wt% HDPE, 11.2 wt% PP, 6.2 wt% PS, 5.2 wt% PVC and 10.2 wt% PET) catalytic pyrolysis (500-700 °C) over Ni/Mo/MgO catalyst (4:0.2:1 molar ratio). Conditions for optimum wax/liquid (up to 48 wt%) implied a reduction in CNTs and hydrogen to 5.69 wt% and 27.09 vol% respectively. Plastic waste, and PP in particular, are therefore a suitable feedstock to recover high-value products such as CNTs and hydrogen apart from pyrolysis liquid/wax for transportation fuels.

2.3.4 Catalytic pyrolysis mechanisms

Zeolites

Zeolites are a wide range of natural and artificial hydrated alumino-silicate structures that are an attractive option for plastic waste pyrolysis due to their ion exchange properties, acidity and selectivity. All zeolites are formed by well-defined frameworks of silicon and aluminium atoms tetrahedrally coordinated through oxygen atoms with cations and water molecules located inside the pores (Mortimer and Taylor, 2002) (Figure 2.6a). Zeolites structures differ depending on how the Si-O-Al tetrahedra are arranged forming either 6, 8, 10 or 12 ring apertures (Almutairi, 2013) (Figure 2.6b). Zeolites are classified into small (zeolite A, erionite), medium (ZSM-5 and ZSM-1) and large (zeolite X and Y) pores. However, not all zeolites are suitable for plastic waste pyrolysis. Small pore zeolites (<1-4 nm) prevent the bulky hydrocarbon chains (>1-4 nm) to be adsorbed inside the catalyst pores reducing its activity (Aguado et al., 2007; Serrano et al., 2000). Mesoporous zeolites (medium and large pores) e.g. nanocrystalline n-ZSM-5 or

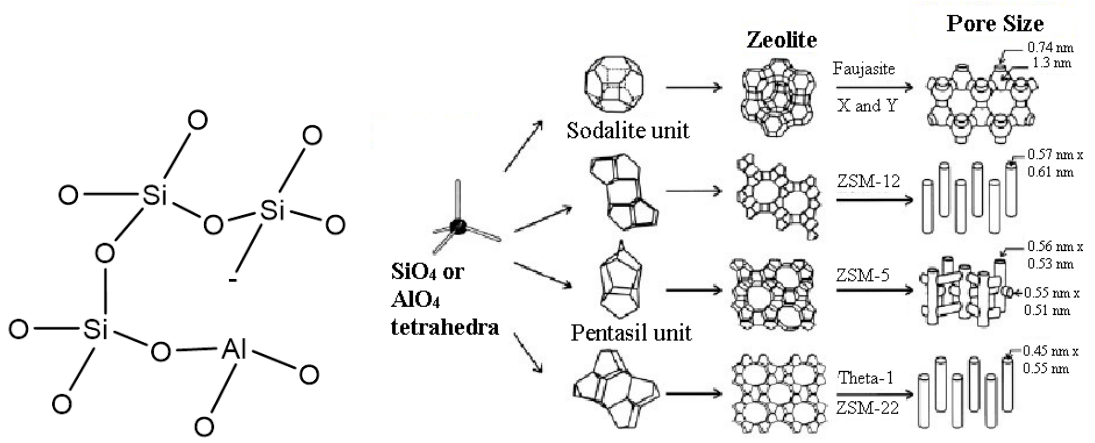

(a) Si-O-Al tetrahedral units forming zeolites (b) Zeolite ring apertures comprised of tetrahedral SiO_2-Al_2O_3 units. Adapted from Daramola et al. (2012)

Figure 2.6 Schematic representation of zeolites structure

HMCM-41, allow the entrance of long hydrocarbon chains into the larger pores, thereby can be used as catalysts for plastic waste pyrolysis.

The reactivity of zeolites towards hydrocarbons, e.g. plastic waste, is due to their Brønsted/Lewis acid sites which protonate/remove hydrogen ions from alkanes at high temperatures to form a carbonium/carbenium ion (Almutairi, 2013) respectively. Figure 2.6a shows the negative charge formed at an oxygen atom close to the lattice Al ion, which can be compensated by either a proton or a cation e.g. Na, Mg, etc. According to Almutairi (2013), when the charge is compensated by a proton, the acidity of the zeolite is higher than with a different cation, forming a Brønsted acid site in the proton. Opposite, Lewis acid sites are formed at cations loosely coordinated with the framework negative charge close to Al atoms and act as electron-pair acceptors. The presence of Lewis acid sites forms an electrostatic field which activates molecules like alkanes.

Generally, both Brønsted and Lewis acid sites contribute to the activation and cracking of the volatiles released from plastic waste pyrolysis (Elordi, Olazar, Lopez, Castaño and Bilbao, 2011) to form a carbonium ion i.e. a pentacoordinated carbon ion. Carbonium ions can then undergo further reactions via three pathways (Figure 2.7):

1. the zeolite proton activates a carbon atom in the alkane forming a carbenium ion followed by the released of a hydrogen atom attached to that carbon (path [1] in Figure 2.7) yielding the same original compounds;

2. the zeolite proton activates a carbon atom in the alkane molecule forming a carbenium ion and releasing a hydrogen that recombines with the proton to release H_2 (path [2] in Figure 2.7). The carbenium ion in the alkane chain can then undergo further cracking reactions like inter or intra molecular hydrogen transfer or β-scission;

3. the carbenium ion formed by the zeolite proton undergoes β-scission forming a shorter carbenium ion and a shorter olefin (path [3] in Figure 2.7).

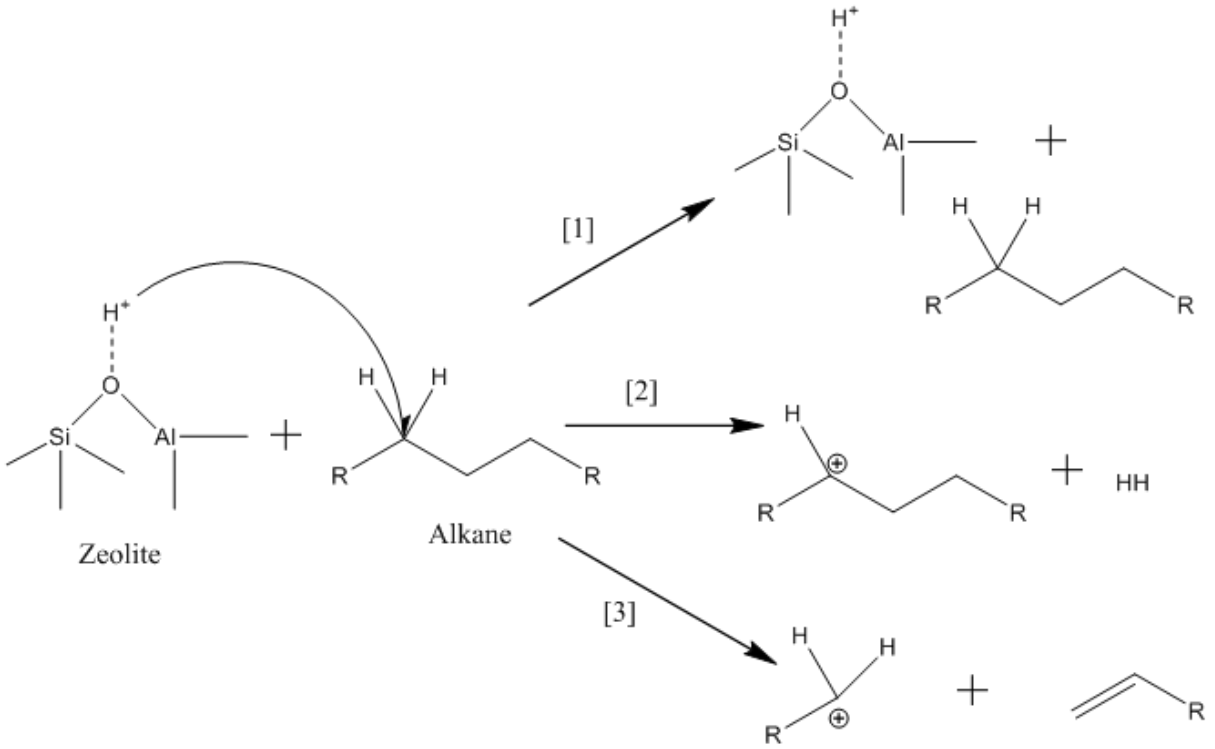

Figure 2.7 Schema of zeolite and alkane reaction pathways

The third pathway explains the increase in the yield of gas and the amount of light hydrocarbons (C_5-C_8) and aromatic compounds in the wax fraction (Adrados et al., 2012; Burange et al., 2015) using zeolites as catalysts in catalytic plastic waste pyrolysis. However, zeolite acidity also promotes coke formation causing their deactivation (reversible) after few pyrolysis runs (Elordi, Olazar, Lopez, Castaño and Bilbao, 2011). Coke deactivation also depends on the zeolite structure (Castaño et al., 2011). Smaller pores of HZSM-5 zeolite inhibited the growth of coke compared to HY and Hβ zeolites. Coke deposits on zeolite surface can be removed via combustion in air at temperatures >550 ° C, which is the minimum for coke removal, and below zeolite calcination temperature to avoid destruction of acid sites at high temperature (Gayubo et al., 2004; López, De Marco, Caballero, Adrados and Laresgoiti, 2011). However, continuous catalytic pyrolyis/zeolite regeneration cycles lead to the total deactivation of the catalyst because of the destruction of zeolite strong acid sites meaning permanent deactivation even at coke combustion <500 °C (Vitolo et al., 2001).

Sulphated zirconia

Yadav and Nair (1999) reviewed sulphated zirconia (SZ) catalysis activity and applications, which is the most extensive and complete available up to this time. SZ is a super acid catalyst suitable for catalysis of hydrocarbon cracking (Almustapha et al., 2017; Diaz-Silvarrey, Zhang and Phan, 2018; Yadav and Nair, 1999), alkylation (Vishwanathan et al., 2008; Yadav and Sengupta, 2002), esterification (Eterigho et al., 2011; Garcia et al., 2008; Lopez et al., 2008, 2005), isomerization (Davis et al., 1994; Iglesia et al., 1993; Ono, 2003), etc.

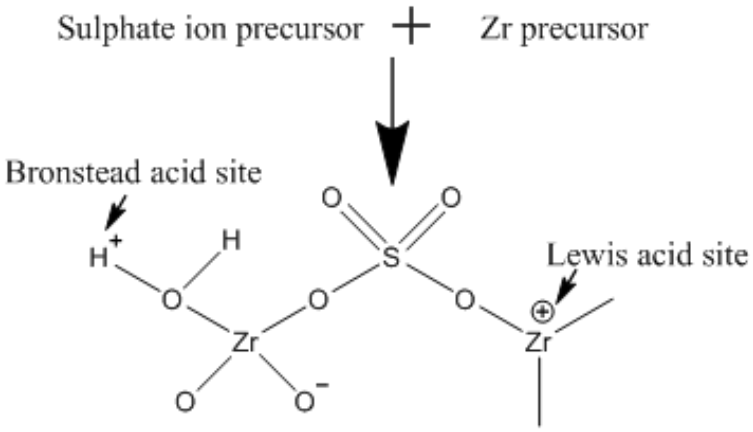

Figure 2.8 Schema of sulphated zirconia structure and acid sites

SZ is synthesised by the addition of SO_4^{2-} ion (from H_2SO_4, $(NH_4)_2SO_4$, SO_2, SO_3 or H_2S (Yamaguchi, 1990)) to a Zr precursor (e.g. $ZrCl_4$, $ZrOCl_2{\cdot}8H_2O$, $ZrO(NO_3)_2{\cdot}2H_2O$ (Comelli et al., 1995)). The addition of SO_4^{2-} ion provides the acidity due to the inductive effect of the S=O group which creates an electronic deficiency around the Zr atom i.e. creates Lewis acid sites (Almustapha et al., 2017; Comelli et al., 1995). Although there is still some debate about the exact nature of SZ acid sites (Yadav and Nair, 1999), it appears that SZ activity comes from the presence of both Brønsted and Lewis acid sites (Almustapha et al., 2017). According to Srinivasan et al. (1996), the amount of Brønsted acid sites in SZ catalyst depends both on the calcination temperature during SZ synthesis and the outgassing temperature used to determine the amount and type of acid sites via Fourier transform infrared spectroscopic with pyridine adsorption. It was reported that Brønsted acid sites are very susceptible to heating and fully disappeared when the catalyst is outgassed at temperatures above 500 °C, leaving the often reported Lewis acidity alone. However, this fact does not imply that Brønsted acid sites are not present in the catalyst before that analysis, hence the still ongoing debate.

Despite the aforementioned debate about SZ acidity, the most accepted hypothesis agrees with the one proposed by Yamaguchi (1990) and Arata and Hino (1990) as shown in Figure 2.8. They suggested Brønsted acid sites are formed due to the presence of adsorbed water molecules. This explains the reason behind the disappearance of Brønsted acid sites when SZ was outgassed at high temperatures as previously mentioned.

Almustapha et al. (2017) found that SZ catalyst lowered the onset temperature for HDPE thermal degradation from 337 °C to 187 °C and the temperature for maximum degradation from 494 °C to 419 °C. HDPE catalytic pyrolysis with SZ catalyst at 380 °C resulted in 38.5 wt% liquid yield comprised of C_7-C_{13} hydrocarbons with a 55 wt% aromatic fraction. These results were similar to those previously reported with more common catalysts e.g. zeolites (Miskolczi et al., 2006; Vasile et al., 2001). However, the gas contained mainly C_4-C_5 hydrocarbons with no traces of H_2, CH_4 or C_2-C_3 hydrocarbons which differed from previous studies (Miskolczi et al., 2006). Chandrasekaran et al. (2015) found that sulphated zirconia catalyst increased conversion of waste polyurethane foam (PUF) and waste PS catalytic pyrolysis up to 70-85 wt% with a temperature reduction of 10-15 %. Despite previous results suggested SZ as a suitable

catalyst for waste plastic cracking in terms of lowering pyrolysis temperature and improving products quality, there are no many studies using this catalyst. Therefore, there is a gap for further investigation applying SZ catalyst for plastic waste pyrolysis. Recently, SZ has been investigated in pyrolysis of waste HDPE for monomer recovery (Diaz-Silvarrey, Zhang and Phan, 2018) and waste PET for benzoic acid recovered (Diaz-Silvarrey, McMahon and Phan, 2018) which are discussed in more detail in chapters 5 and 7 respectively.
It was reported (Ng and Horvát, 1995; Strydom and Pretorius, 1993) that SZ catalyst partly looses its activity with reaction and temperature via a yet debatable mechanism. Yori et al. (1989) and Wang et al. (2016) proposed SZ deactivation mechanism occurring through a reduction of sulphate ion oxidation state from S^{+6} to lower states (S^{+4}, S^{+2}, S^{-2}). This reduction released water and hydrogen and consequently reduced the Lewis acidity due to a loss of the inductive effect of S=O as the oxidation state decreased. Chen et al. (1993) and Nascimento et al. (1993) suggested SZ deactivation was caused by coke deposition at the surface of the catalyst. During plastic waste both deactivation mechanism are likely to occur and, in a similar way as zeolite catalyst, SZ catalyst would loose its activity with consecutive pyrolysis cycles (Diaz-Silvarrey, Zhang and Phan, 2018).

Ni/Al_2O_3

Alumina (Al_2O_3) is a widely used catalyst support due to the low costs, stability at high temperature, high surface area and controlled pore-size distribution (Ángel-Soto et al., 2017; Guczi and Erdôhelyi, 2012; Robinson, 2010). Ni-based catalysts are also used for a myriad of industrial processes such as hydrogenation, steam reforming or methanation (Robinson, 2010). Ni presents a catalytic activity capable of C-C bond cleavage (Ángel-Soto et al., 2017) and thus, it has been extensively studied for hydrocarbon reforming reactions (Liu, Ye, Jiang and Pan, 2011; Rostrup-Nielsen, 1973; Takeguchi et al., 2002) and plastic waste pyrolysis (Wang and Wang, 2011; Wu and Williams, 2009*a*; Zhang, Nahil, Wu and Williams, 2017).
Ni/Al_2O_3 catalysts present both strong Lewis and weak Brønsted acid sites (Benbenek et al., 1993). Their acidity is enhanced when Ni is added compared to the original acidity of the support i.e. Al_2O_3. The reason behind that enhancement is a higher overall positive charge of the $NiAl_2O_4$ spinel (Benbenek et al., 1993), meaning that stronger Lewis acid sites are formed at Al^{+3} ions at the catalyst surface. Brønsted acid sites are formed by protons bonded to the external oxygen atoms. Despite presenting the same type of acidity as zeolites and SZ, the presence of the transition metal (Ni) varies the mechanism of catalytic cracking reaction.
Ni atoms in the catalyst add an extra initial step into the mechanism: alkane chains first loose a hydrogen atom (dehydrogentaion) forming an alkene chain and hydrogen (Kissin, 2001). The alkene chain then undergoes a carbenium-ion mechanism, in a similar manner as zeolites and SZ followed, as described in the third path in Figure 2.7 where a β-scission yields a shorter alkene and carbenium-ion chain, which repeats the second and third steps (Kissin, 2001). The first extra step also explains the higher amount of H_2 recovered using Ni/Al_2O_3 instead of zeolite and SZ catalysts for plastic waste pyrolysis.

CNTs can be grown on Ni/Al_2O_3 catalysts as mentioned above due to the Ni-based catalyst arguable disadvantage of coking (Sehested, 2006; Wu et al., 2016). This process occurs via one of the two following mechanism: base growth or tip growth (Mo et al., 2001; Tripathi et al., 2017), with the former being dominant. The tip growth mechanism requires requires a weak $Ni\text{-}Al_2O_3$ support bond which is not very frequent (Mo et al., 2001). The main difference between the two mechanisms is the position of the Ni atom during the CNTs growth. The Ni atom remains attached to the Al_2O_3 support and CNTs grow on top of the Ni atom in the direction normal to the support in the base growth mechanism while CNTs grow underneath the Ni atom separating this atom from the support in the tip growth mechanism.

Activated carbon and biomass char

Traditionally, plastic waste catalytic pyrolysis involves the use of acid catalyst e.g. zeolites, SZ, Ni/Al_2O_3, etc. However, these catalysts are well known for their deactivation via coking. Therefore, alternative carbon-based catalysts with comparable catalytic activity to traditional ones have gained popularity (González et al., 2011; Juliastuti et al., 2018; Kumar et al., 2017; Prathiba et al., 2018). Although carbon-based catalytic cracking mechanism differs from that of acid catalysts, there is a scarcity of studies on the topic and the exact mechanism is still unknown. Carbon-based catalysts, like activated carbon and char derived from lignocellulosic materials (biomass), own their catalytic activity to their high surface area (Abu El-Rub et al., 2004; Gilbert et al., 2009; Hervy et al., 2018) as well as to the presence of surface oxygen-containing functional groups (Abu El-Rub et al., 2004; Ducousso et al., 2015; Hervy et al., 2018; Klinghoffer et al., 2012; Lu et al., 2017; Wang et al., 2014) and their mineral content (Abu El-Rub et al., 2004; Hervy et al., 2018; Klinghoffer et al., 2012). Active sites are formed on the surface oxygen-containing groups and in the alkali and alkaline earth (AAEM) metals e.g. Na, K, Mg, etc (Sun et al., 2018).

Catalytic cracking mechanism on carbon-based catalysts varies depending on whether the carbon-based catalysts has been chemically activated or not (Sun et al., 2018). For non-activated carbon-based catalysts, the mechanism is initiated via hydrogen transfer from the hydrogen-rich hydrocarbon chain into the hydrogen-deficient biomass char. Therefore, the catalytic activity in this type of catalyst is enhanced when the hydrocarbons are alkanes as more hydrogen is available than for saturated hydrocarbons e.g. alkenes, dienes, etc. Biomass char promotes the cracking of alkanes into shorter alkenes as well as cycloalkanes and dienes. However, it does not promote the formation of aromatic compounds. Activated carbon-based catalysts increase the yield of aromatic compounds however the reaction mechanism varies depending on the activation agent used. For activated carbon catalysts with strong bases e.g. KOH, the catalytic cracking mechanism is initiated through hydrogen transfer followed by cyclisation reactions. When carbon-based catalysts are activated with transition metals e.g. Zn, or strong acids e.g. H_3PO_4, the activation agents create Lewis acid sites. The presence of these Lewis acid sites enhance the formation of aromatic compounds via Diels-Alder reactions. Sun et al. (2018) also suggested the possible existence of Brønsted acid sites at the surface oxygen-containing

functional groups, particularly when the carbon-based catalysts are activated with strong acids . However, this statement was not confirmed with any analysis. The existence of Brønsted acid sites could promote Diels-Alder reactions and Friedel-Crafts alkylations increasing the yield of aromatic compounds.

2.3.5 Plasma assisted pyrolysis

Plasma, the fourth state of matter, is defined as an electrically neutral ionized gas. When a gas passes through a strong electric field, the electrons impact on gas molecules causing ionization, dissociation and excitation of the source gas forming active radicals and ionic and excited atomic and molecular species that can initiate plasma chemical reactions (Fridman, 2008; Tendero et al., 2006). Plasma technologies are classified, according to the gas temperature, into high temperature or thermal plasma and non-thermal or cold plasma. In thermal plasma, electrons, ions and neutral species are in local thermodynamic equilibrium (LTE) and are at the same temperature (T_p = 10^6-10^8 K). In non-thermal or cold plasma, those species do not reach total LTE resulting in a difference between electrons and ions and neutral species temperature. The temperature of the energetic electrons in cold plasma ranges between 10^4-10^6 K (1-10 eV) while the gas remains closer to room temperature (Chen et al., 2008; Huang and Tang, 2007; Tendero et al., 2006).

Cold plasma

In cold plasma the operating gas, its pressure, the distance between the electrodes and the duration of the discharge (pulse or continuous) are important factors that produce different species in the plasma zone (Bogaerts et al., 2002). Cold plasma discharges include: corona, glow, arc, radio frequency (RF), dielectric barrier (DBD) and gliding discharges (Eliezer and Eliezer, 2001). Corona discharge is produced at atmospheric pressures when very low currents (10^{-11}-10^{-6} A) and very high voltages (about 1 kV) are applied. Glow discharge happens at low currents (<1 A) and high voltage (>100 V). Arc discharge generates by high current (1-10^5 A) and low voltage (10 V). RF operates at low pressures, high voltage and frequencies in the order of kHz. DBD is characterised by a dielectric barrier placed between the two electrodes powered by high voltages (10 kV) from a high frequency power source unit. Gliding arc combines the property of thermal and cold plasma at atmospheric pressure when the gas is passed through two divergent electrodes. The discharge starts at the shortest distance between the electrodes (thermal plasma) when high voltages are applied (5 kV) and moves along their length with the gas flow to cold plasma (Eliezer and Eliezer, 2001; Kogelschatz et al., 1997; Lie et al., 2006). DBD is a popular cold plasma discharge method (Kraus et al., 2001; Tu and Whitehead, 2012) due to the simple design, operation at atmospheric pressure and simple scalability (Kogelschatz, 2003). DBD comprises of two metal electrodes (black in Figure 2.9) separated by one or two dielectric barriers (orange in Figure 2.9) creating a few millimetres gap. The dielectric barrier can be made of glass, ceramics, enamel or polymer materials (Kogelschatz, 2003). When a voltage is applied between the two electrodes, cold plasma is generated in the gap in the form of

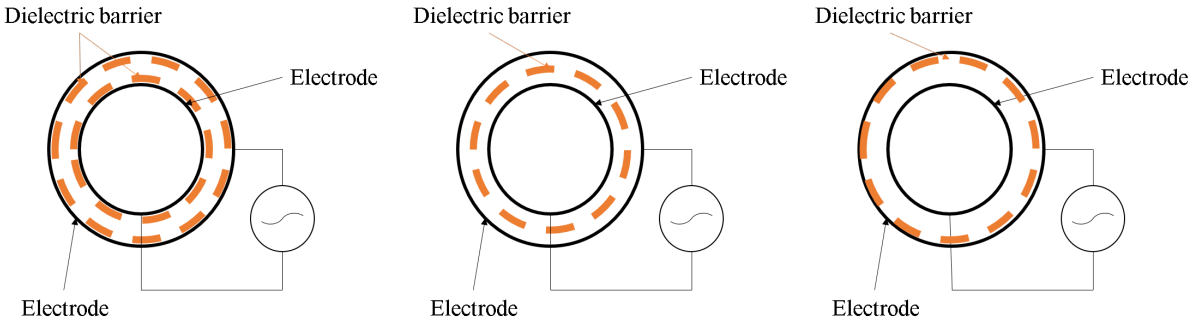

(a) Double dielectric barrier coating both electrodes

(b) Single dielectric barrier in the centre of gap

(c) Single dielectric barrier coating one electrode

Figure 2.9 Basic coaxial dielectric barrier discharge configurations (electrodes = solid black line and dielectric barrier layer = dotted orange line)

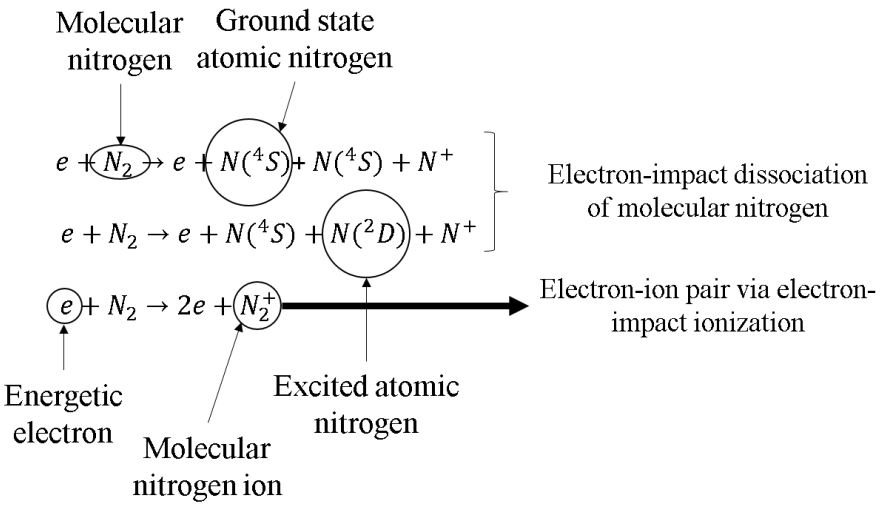

Figure 2.10 Schematic reaction pathways in N_2 cold plasma to generate reactive species

a large number of micro arcs or micro discharges (Kogelschatz, 2003; Schutze et al., 1998) in the shape of a cylinder which spreads into a surface discharge at the dielectric barrier layer (Kogelschatz, 2003).

According to Kogelschatz (2003) at the early stages of cold plasma micro discharges, an array of excitation and dissociation processes generate multiple ionic and excited species. However, in DBD discharges those species have a very short life-span. Therefore, cold plasma generated via DBD presents neutral atoms and molecular fragments as well as excited molecules and energised electrons capable of initiating chemical reactions via a free-radical mechanism. Penetrante et al. (1997) explained that cold plasma chemical activity occurs firstly through the creation of free radicals and electron-ion pairs via ionization and dissociation reactions, initiated by collisions between energetic primary electrons and the gas molecules. Secondly, the free-radicals and electron-ion pairs react with the pollutant molecules, hydrocarbons, VOCs, etc. to initiate the appropriate process that cold plasma is assisting e.g. removal of pollutants from gas/water, pyrolysis, gasification, steam reforming, etc. Figure 2.10 shows the reactive species formed in cold plasma with nitrogen gas.

Due to its unique properties, cold plasma is well known for assisting thermodynamically unfavourable reactions (Zhang, Zhang, Liu, Phan and Luo, 2017), which has guided most of its applications. The ionized/excited molecules in the gas and the energetic electrons formed create a very reactive environment which can initiate chemical reactions. Hence, cold plasma systems have been applied for reforming system (Chen et al., 2008; Petitpas et al., 2007), hydrocarbon conversion into hydrogen for fuel cells (National Energy Technology Laboratory (NETL), 2017; Paulmier and Fulcheri, 2005) and high-value carbon products such as carbon nanotubes, fullerenes, etc. (Ahmed et al., 2009; Deminsky et al., 2002), VOC decomposition (Harling et al., 2008; Mustafa et al., 2018; Urashima and Chang, 2000), gas streams cleaning (Van Durme et al., 2008) and air pollution treatment (Hackam and Aklyama, 2000; Jung and Kim, 2017). Cold plasma is also applied for decontamination, sterilization and purification systems (Bruggeman and Leys, 2009) in waste water treatment (Aziz et al., 2016) and for medical applications (Fridman et al., 2006; Kang et al., 2017). Meichsner et al. (2012), Kogelschatz (2003) and Kogelschatz et al. (1997) have very extensive reviews on cold plasma applications different from plastic waste pyrolysis.

Cold plasma can also substitute/complement acid or metal-based catalyst in plastic waste pyrolysis for monomer recovery (Diaz-Silvarrey, Zhang and Phan, 2018) or hydrogen/syngas generation but with lower environmental impact due to the reduction of the amount of catalyst. In addition, cold plasma can be used to regenerate spent catalysts deactivated by coking (Fan et al., 2015). Khani et al. (2014) demonstrated that cold plasma (DBD) decomposed n-hexadecane into ethylene (6.91 cm^3/min of ethylene) and lubricating oil (C_{13}-C_{42}) into C_4-C_{12} light oil (56.8 % reduction) at temperatures up to 250 °C. Hao et al. (2015) suggested the cracking of heavy crude oil into light crude oil via cold plasma (DBD at 200 °C) with an increase in the light crude oil yield from 0.56 wt% to 8.5 wt%.

Thermal plasma pyrolysis has been used for decades to treat organic municipal and hazardous waste (Bogaerts et al., 2002; Dave and Joshi, 2010; Guddeti et al., 2000*a*,*b*; Huang and Tang, 2007; Kowalska et al., 2008; Nema and Ganeshprasad, 2002; Punčochář et al., 2012; Tang and Huang, 2007; Tang et al., 2003; Vyas et al., 2011). In thermal plasma assisted pyrolysis, organic matter (such as plastic waste) is quickly heated by the plasma jet where the volatile matter is cracked into hydrogen and light hydrocarbons (Huang and Tang, 2007). Thermal plasma has been proven to recover the monomer from plastic waste pyrolysis: 93.7 vol% of propylene from PP (Guddeti et al., 2000*b*) and 22.24 vol% ethylene from PE pyrolysis (Guddeti et al., 2000*a*) when a rapid quench process (1000 K/s) was applied. Without rapid quenching, about 62 vol% of propylene was recovered from PP pyrolysis (Tang et al., 2003). Steam injection on the volatiles after pyrolysis increased the amount of hydrogen in the gas product from to 15 vol% to 27 vol% (Tang and Huang, 2007; Tang et al., 2003). Apart from monomer recovery, other high-value products such as CNTs and fullerenes can be recovered from thermal plasma assisted plastic waste pyrolysis (Knight et al., 2002). However, the capital costs of thermal plasma are high and this process requires complex quenching systems to minimise mechanical stress on the

electrodes. This makes thermal plasma a very energy intensive process which can hinder plastic waste pyrolysis profitability and sustainability.

Unlike thermal plasma, so far studies on cold plasma assisted plastic or other municipal waste pyrolysis/gasification are extremely limited (Diaz-Silvarrey, Zhang and Phan, 2018) despite being proved to enhance hydrocarbons decomposition (Ahmed et al., 2009; Deminsky et al., 2002; Hao et al., 2015; Khani et al., 2014; Prieto et al., 2001; Van Durme et al., 2008). Previous studies (Fan et al., 2018; Long et al., 2008; Tu and Whitehead, 2012; Van Durme et al., 2008), showed a significant synergistic effect between catalysts and cold plasma to reduce breakdown cold plasma voltage, energy losses, and improve the reactivity. Cold plasma could also reduce the amount of coke formed in the catalyst surface increasing its activity for further pyrolysis cycles (Fan et al., 2018).

2.4 Summary

Thermal pyrolysis is a very well-known mature technology with extensive literature describing the optimum operating conditions and product composition, in particular to produce wax/liquid/oil for transportation. This fact demonstrates that pyrolysis can successfully convert plastic waste into high-value products. Although wax/liquid/oil is the predominant fraction from thermal pyrolysis and attracts the most attention, it has low quality and needs further upgrading to replace fossil fuels. Despite the high interest on the liquid/wax/oil fraction as fuels for transportation, there is a lack of studies that test that fraction in engines to investigate its performance.

Pyrolysis products can be improved by adding catalysts. Traditionally, zeolites are the most common catalysts for plastic waste pyrolysis due to their acidity and shape selectivity. They increase the gas yield and reduce the wax/liquid/oil yield. However, the acidity of zeolites also makes them susceptible of coke formation on the surface. Coking deactivates zeolites and thus, increases operation costs as either catalyst regeneration or addition of fresh catalyst is required. There are a myriad of zeolites available with different Si/Al ratios and pore size distribution but microporous zeolites (<4 nm) are not suitable for plastic waste pyrolysis. The plastic waste chains are too bulky to enter zeolite micropores and therefore, reaction can only occurs at the surface reducing zeolite catalytic activity.

Other acid catalyst like amorphous SiO_2/Al_2O_3, sulphated zirconia or Ni/Al_2O_3 have been used with promising results however, information is not as extensive compared to zeolites. Wastes from other processes e.g. char from waste biomass or red mud, could provide a sustainable and affordable source for catalysts explaining the recent interest towards their use in plastic waste pyrolysis.

Plastic waste pyrolysis can also be improved by advanced techniques such as cold plasma assisted pyrolysis. Unlike thermal plasma, the application of cold plasma to plastic waste or other solid waste pyrolysis is not well reported. The addition of a catalyst to cold plasma

pyrolysis creates a synergistic effect between the high product selectivity of the catalysis and the rapid start-up from cold plasma to tune up chemicals or H_2 production.

Chapter 3 Materials and Methods

This chapter describes the characterisation of all the materials i.e. plastic waste and catalysts used during this research. Below are described the experimental methods used to collect the raw data for the kinetic model (Chapter 4), however, for clarity purposes the detailed description of the kinetic model is explained in Chapter 4 along with the model results. This chapter provides a general description of thermal, catalytic and cold plasma assisted pyrolysis experiments. Specific modifications to the general pyrolysis set-up description are described next to the results in chapters 5 to 8 to assist the reader. Technical specifications for the pieces of equipment mentioned in this chapter are collected in Appendix B.

3.1 Materials

3.1.1 Plastic waste characterisation

All plastic materials used in this thesis were plastic wastes. Plastic wastes were chosen as feedstock instead of virgin polymers to simulate real pyrolysis conditions as much as possible. One of the purposes of this thesis was the study of novel techniques that may improve the profitability of plastic waste pyrolysis in the context of a potential operational plant. If these studies would had been conducted on virgin polymers, the results obtained could not had been evaluated in this context. This is because virgin polymers do not accurately represent the composition and nature of plastic waste. Virgin polymers may had offered ideal and non-realistic yields that would not had translated into the context of a potential operational plastic waste pyrolysis plant. Therefore, the discussion of the viability of the new techniques explored would may have been misleading.
Plastic waste samples of the five most common types in the municipal plastic waste mixture, i.e. HDPE, LDPE, PP, PS and PET, were collected from O'Brien Recycling Solutions (Wallsend, Newcastle upon Tyne, United Kingdom). Upon arrival to this facility, plastic waste were separated from papers and cans by trommels and then manually sorted into HDPE, LDPE, PP and PET. Prior to experiments, plastic waste materials were thoroughly washed with soap and water to remove contaminants, i.e. food waste, labels, adhesives, etc., to minimise any possible effect on results and then cut into smaller pieces of different size depending on the analysis due to perform. The specific size is mentioned in the description of each specific analysis/experimental method. Figure 3.1 shows examples of plastic waste samples used in pyrolysis experiments.

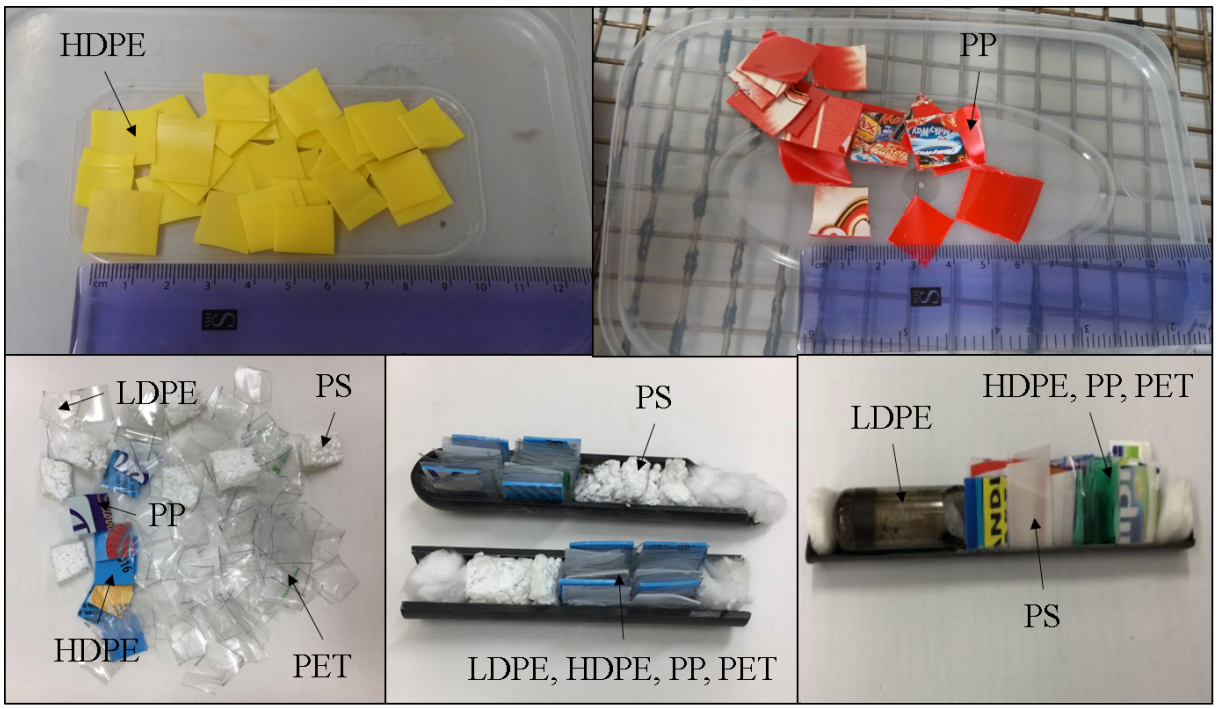

Figure 3.1 Examples of plastic waste samples used for thermal, catalytic and cold plasma assisted pyrolysis experiments

Elemental Analysis

Elemental analysis of individual plastic waste was performed in a Carlo Erba EA 1108 Elemental Analyser at the Advanced Chemical and Materials Analysis (ACMA), Newcastle University. Analysis of 1.000-2.000 $\pm$ 0.001 mg of round 1 mm diameter samples of individual plastic waste were carried out to quantify the total amount of carbon, nitrogen and hydrogen. This instrument comprised of a flash combustion furnace and a gas chromatographic oven coupled with a thermal conductivity detector (TCD). Samples were introduced into a quartz combustion chamber for flash combustion at 1020 °C. Flues gases were carried into an oxidizing area (tungstenic oxide -WO_3- catalyst) where products were oxidise into CO_2, H_2O and NO_x. After, they passed into a reduction area (elemental copper at 860 °C) to trap all the oxygen and reduce them to their elemental form i.e. CO_2, N_2 and H_2. Quantification of the elemental forms is done at the TCD detector. Experiments were duplicated for each sample. Table 3.1 shows the results from the elemental analysis.

The main components in all plastic waste samples were carbon (average of 78.60 $\pm$ 10.62 wt%) and hydrogen (average of 11.59 $\pm$ 5.67 wt%) with the exception of PET which showed oxygen of 32.94 wt% and PS with a nitrogen content of 2.17 wt%. The H/C ratio is a simple parameter to characterise hydrocarbon fuels. It measures the proportion of paraffins, naphthenes and aromatics giving an indication of their calorific value among other properties (Yue et al., 2016). Figure 3.2 adapts Van Krevelen plot to compare the H/C against the O/C ratio for plastic waste and several hydrocarbon fuels. Plastic waste (HDPE, LDPE, PP and PS) presented a heating value higher than coal and wood suggesting they are a good feedstock for thermal processes such as pyrolysis. PET differed from the other plastic waste tested due to the presence of oxygen

Table 3.1 Plastic waste elemental analysis (H/C = Hydrogen/Carbon mole ratio and O/C = Oxygen/Carbon mole ratio)

wt%	HDPE	LDPE	PP	PS	PET
Carbon	73.33±0.43	83.67±0.51	83.25±0.45	89.81±0.61	62.95±0.45
Hydrogen	13.28±0.43	16.33±0.51	16.75±0.45	7.47 ±0.44	4.12 ±0.46
Nitrogen	0.00±0.42	0.00 ±0.42	0.00 ±0.42	2.71 ±0.70	0.00 ±0.42
Oxygen [a]	13.39±0.74	0.00 ±0.83	0.00 ±0.76	0.00 ±1.03	32.94±0.77
H/C	2.17±0.09	2.34±0.21	2.41±0.14	1.00±0.13	0.79±0.18
O/C	0.14±0.03	0.00±0.00	0.00±0.00	0.00±0.00	0.39±0.06

[a] Calculated by mass difference

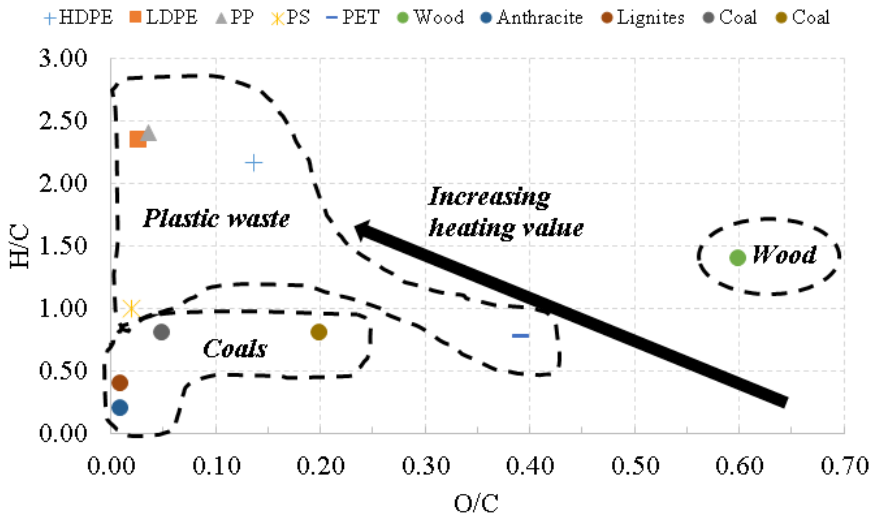

Figure 3.2 Adaptation of Van Krevelen plot to compare plastic waste with other hydrocarbon fuels

in the structure (32.94 wt%). The H/C ratio (0.79) was similar to that of coal and lower than that of wood (0.8 and 1.4 respectively (Van der Stelt et al., 2011)) implying a very low hydrogen content due to the existence the aromatic rings, ester and carboxylic group.

A 13.40 wt% oxygen content was found by HDPE elemental analysis, however, HDPE is formed by a C-H straight chain polymerised from ethylene (CH_2=CH_2). Therefore, the oxygen content could be due to presence of additives (adhesives, paint, etc.) added to alter the plastic product quality during manufacture and/or the mix of various virgin/recycled plastic types to manufacture the plastic product tested (plastic bag) (Wrap, 2018). As a result, various HDPE characteristics such as ash content, kinetic parameters and elemental composition could vary as well as release small amounts of CO_2 and CO during pyrolysis. However, not all HDPE waste products had this high oxygen content and this was only observed when waste HDPE plastic bags were used as feedstock. Other waste HDPE products, such as milk or bleach bottles, had a lower amount of oxygen (5.30±0.54 wt%) and therefore were used as feedstock in all tested conditions. These findings exemplified the reason why plastic waste were chosen as feedstock instead of virgin polymer materials. If the latter would had been chosen then the ash content,

kinetic parameters, elemental composition and pyrolysis yield would not have been representative of real conditions.

The use of plastic waste products instead of virgin polymer materials may introduce an uncertainty on results that needs to be considered. Comparison of the average elemental analysis results with those of others using plastic waste showed little difference (79.77 % of carbon, 15.47 % of hydrogen and 2.76 % of nitrogen for a mixture of 58.6 % HDPE and LDPE, 26.9 % PP, 5.6 % PET and 8.8 % PS (Singh et al., 2019) compared to 78.6 wt% of carbon and 11.59 wt% of hydrogen showed in Table 3.1). This suggests that even when the feedstock comprises of a different plastic waste mixture formed by different plastic waste products the elemental analysis remains. This means that the values found in Table 3.1 can be considered the ones corresponding to plastic waste material and therefore representative of this type of feedstock. Ciliz et al. (2004) compared the pyrolysis products of virgin and waste PP reaching to the conclusion that plastic waste impurities affect the decomposition temperatures and weight loss. This confirms the assumption that using virgin polymer materials as feedstock may provide unrealistic results not suitable to be discussed in the context of a potential operational plastic waste pyrolysis plant.

Proximate Analysis

Proximate analysis was carried out to determine moisture, ash and volatile matter content based on British Standard BS 1016-104.3:1998 (Appendix C). The moisture, ash and volatile matter content were calculated through equations 3.1 to 3.3. Fixed carbon was calculated by mass difference according to Equation 3.4.

$$Moisture(wt\%) = \frac{Water\ removed}{Original\ sample} = \frac{m_0 - m_f}{m_0 - m_C} \cdot 100 \tag{3.1}$$

$$Ash(wt\%) = \frac{Residue}{Original\ sample} = \frac{m_f - m_C}{m_0 - m_C} \cdot 100 \tag{3.2}$$

$$Volatile\ Matter(wt\%) = \frac{Volatilised\ matter}{Original\ sample} = \frac{m_0 - m_f}{m_0 - m_C} \cdot 100 - Moisture(wt\%) \tag{3.3}$$

$$Fixed\ Carbon(wt\%) = 100wt\% - Volatile\ Matter(wt\%) - Ash(wt\%) \tag{3.4}$$

For the moisture content, 1.0000±0.1000 g of each plastic waste were evenly spread over the bottom of a clean known-weight crucible (m_C). The crucible with the sample (m_0) was introduced into an oven set at 105-110 °C for an hour, then removed from the oven and placed into a desiccator until cool down at room temperature (20 °C) and finally weighted (m_f). The same procedure was repeated three times.

The ash content was determined by weighting and placing the dried samples (m_0) in a pre-weight combustion boat (m_C) inside a quartz tube. The tube was inserted into a Vecstar VCTF1 furnace set at 750 °C and burnt in oxidant atmosphere for 1 h after which the combustion boat was removed, left to cool down in a desiccator to room temperature and weighted (m_f). The same procedure was repeated twice.

Table 3.2 Plastic waste proximate analysis (VM=Volatile matter, A=Ash, FC=Fixed Carbon and M=Moisture)

wt%	HDPE	LDPE	PP	PS	PET
VM	77.70±1.64	99.78±0.67	97.69±0.04	98.77±0.16	85.73±7.29
A	10.36±0.30	0.00±0.00	0.00±0.00	0.00±0.00	8.31±0.15
FC [a]	11.94±1.67	0.22±0.60	2.31±0.20	1.23±0.52	5.96±1.93
M	0.10±0.07	0.01±0.15	0.11±0.05	0.36±0.23	1.01±0.39

[a] Calculated by mass difference

For volatile matter the dried sample was weighted (m_0) and placed in a pre-weight combustible boat (m_C) which was introduced in the left side of a quartz tube inside the furnace but outside the heating zone. Prior to analysis, the quartz tube was heated to 925 °C and continuously purged with N_2 at 50mL/min for 30 min to remove any trace of oxidant atmosphere. After purging, the quartz tube was slid to the right placing the combustion boat in the centre of the heated zone and kept there for exactly 7 minutes. After that time, the quartz tube was slid back left removing the combustion boat from the heated zone and left to cool down in a nitrogen atmosphere for 5 minutes until it could be handled. Then the combustible boat was removed from the quartz tube, placed in a dissacator and left to cool down to room temperature. The combustion boat with the residue was weighted (m_f) to calculate the volatile matter content. The same procedure was repeated twice.
Table 3.2 shows that plastic waste comprised of mainly volatile matter (average of 93.48 wt%) with very low ash (average of 2.59 wt%) and fixed carbon (average of 3.93 wt%) content and almost negligible moisture content (average of 0.31 wt%) reinforcing them as good feedstock for thermal degradation processes. Ash content of HDPE was very high (10.36 wt%) which could be explained due to additives or the presence of other virgin/recycled plastic types in the waste HDPE product tested (plastic bags). These substances e.g. ink, adhesives, etc. increase the mineral content and therefore ash content.

Calorimetry

Calorific value of individual plastic waste was determined using a CAL2k-ECO. Approximately 50.0±0.1 mg of each individual plastic were added into a stainless steel crucible at a time. The crucible with the sample was introduced into a vessel and placed into direct contact with a cotton wire, attached to a firing wire and connected to two electrodes for ignition. The vessel was pressurised to 3000 kPa with pure oxygen and introduced in the calorimeter chamber where the sample was ignited and combusted. Prior to displayed results the calorimeter cooled the products of the reaction back to room temperature and thereby, the value measured was the high calorific value (HHV) of the sample. The experiment was repeated twice for each individual plastic waste type.
Table 3.3 shows that HHV of waste HDPE, LDPE, PP and PS was in a range of 38.54-46.52 MJ/kg, which was similar to others (Environment and Plastics Industry Council (EPIC), 2004; Sarker et al., 2011; Themelis and Mussche, 2014). These values were close to the HHV of

Table 3.3 High heating value of plastic waste obtained by calorimetry (HHV=High Calorific Value)

MJ/kg	HDPE	LDPE	PP	PS	PET
HHV	44.81±0.36	46.52±0.01	46.50±0.11	38.54±0.36	22.96±0.03

Table 3.4 Differential scanning calorimetry analysis of plastic waste (T_g=Glass Transition Temperature, T_m=melting Temperature and ΔH_m=melting heat)

	HDPE	LDPE	PP	PS	PET
T_g/[°C]	N/A	N/A	N/A	110.58±3.88	70.75±0.62
T_m/[°C]	126.66±0.25	121.41±0.25	161.80±0.14	245.70±27.00	249.02±0.28
ΔH_m/[J/g]	125.20±22.34	66.83±5.75	105.00±0.99	5.08±0.48	42.89±3.11

kerosene (46.50 MJ/kg (Williams and Williams, 1997*b*)), gas oil (45.20 MJ/kg (Williams and Williams, 1997*b*)) or heavy oil (42.50 MJ/kg (Williams and Williams, 1997*b*)). PET had the lowest HHV (22.96 MJ/kg), similar to that of bituminous (17-23MJ/kg) or lignite coal (15-27 MJ/kg) because PET contained 32.94 wt% of oxygen.

Differential Scanning Calorimetry (DSC)

Differential Scanning Calorimetry (DSC) analysis, performed to study plastic waste thermal transitions, was carried out in a TA instruments DSC Q20. Round samples of 5mm diameter of each individual plastic waste (HDPE, LDPE, PP, PET and PS) were placed into a standard Tzero aluminium pan, weighted, and covered with an aluminium lid using a press. Analysis was carried out between 30-400 °C at 20 °C/min in a pre-set and fixed N_2 flow rate of 50 ml/min. The experiment was repeated twice for all types of plastic waste.
During analysis two heating plates situated inside the cell: front for sample and back for reference, were heated at the set heating rate up to the same temperature but supplying different heat flows to each pan due to the two different materials (air for the reference and plastic waste samples for the other one). The difference between the two heat flows was the heat absorbed by the plastic waste sample. DSC curves plotted the heat absorbed by the plastic waste sample against temperature. A DSC curve provides glass transition temperature (T_g), melting temperature (T_m) and melting heat (ΔH_m). Table 3.4 presents DSC results i.e. T_g, T_m and ΔH_m for all plastic waste types.
Table 3.4 shows that only PET (70.75 °C) and PS (110.58 °C) showed a glass transition region. According to Mark (2007), PE, PP, PET and PS have a T_g of -21, -13, 69 and 100 °C respectively. Therefore, the glass transition region for HDPE, LDPE and PP was out of the explored range. Below the T_g, plastic waste are in amorphous form i.e. disorganised chains, thereby plastics are brittle (as PET and PS). Over T_g, plastic waste became crystalline and more flexible. When plastic waste reach T_m, they melt transforming into a disorganised liquid. The T_m for HDPE (126.66 °C), LDPE (121.41 °C), PP (161.80 °C), PS (245.70 °C) and PET (249.02 °C) was in the range of previous reported values (137, 115, 176, 250 and 239 °C respectively

Table 3.5 Thermogravimetric analysis of plastic waste (T_p=temperature decomposition range, E_a=activation energy, n=order of reaction, A=pre-exponential factor and f(α)=thermal decomposition equation)

	HDPE	LDPE	PP	PS	PET
T_p/[°C]	428-564	443-535	412-541	372-490	396-519
E_a/[kJ/mol]	375.59±39.69	267.61±3.23	261.22±5.13	192.61±0.76	197.61±2.27
n	1.70	0.95	0.75	0.90	2.80
A/10^{16}[s^{-1}]	3.23±2.63	7860±5260	303000±317000	0.055±0.001	0.05±0.02
f_α	$(1-\alpha)^{1.70}$	$(1-\alpha)^{0.95}$	$(1-\alpha)^{0.75}$	$(1-\alpha)^{0.90}$	$(1-\alpha)^{2.80}$

(Institut für Arbeitsschutz der Deutschen Gesetzlichen Unfallversicherung, 2015; Kalpakjian et al., 2008; Olabisi and Adewale, 2016)).

Thermogravimetric Analysis (TGA)

Thermal decomposition data was obtained by thermogravimetric analysis (TGA) using a Perkin Elmer STA 6000 to complete the kinetic model explained in Chapter 4. Round waste HDPE, LDPE, PP and PET samples of 1 mm diameter were evenly spread into the bottom of an alumina crucible and placed on the balance of the TGA analyser. Round waste PS samples of 4mm diameter were prepared from wet waste PS materials to minimise the high electrostatic charge. Only PS samples were then dried at 105 °C for 30 min prior to TGA analysis. All samples were purged with N_2 (30 mL/min) for 15 minutes prior to analysis, to allow the TGA balance to stabilise after loading the crucible, and then heated in nitrogen from 30-700 °C at four different heating rates: 5, 10, 20 and 40 °C/min. This procedure was repeated for every type of plastic waste at least twice for reproducibility. TGA outcomes were temperature (T/[°C]), weight loss (W/[wt%]), derivative weight loss (dW/dt/[wt%/min]) and heat flow (HF/[mW]). Mass (m_i) and reacted fraction or conversion (α) were calculated by Equations 3.5 and 3.6 respectively (m_0=initial sample mass and m_f=residue mass at the end of TGA analysis).

$$m_i = W * m_0 \tag{3.5}$$

$$\alpha = \frac{m_0 - m_i}{m_0 - m_f} \tag{3.6}$$

Table 3.5 summarises the decomposition temperature range and the kinetic parameters (activation energy, order of reaction, pre-exponential factor and thermal decomposition equation) obtained from the kinetic model in chapter 4.

3.1.2 Fresh catalyst characterisation

This section describes all the analysis techniques used to characterised the six different types of catalysts used in this thesis: two types of commercial zeolite HZSM-5, zeolite HY, sulphated zirconia (SO_4-ZrO, SZ), nickel alumina (Ni-Al_2O_3) and biomass char (biochar) from waste

biomass pyrolysis. The analysis performed on each catalyst varied depending on their morphology and composition. Section 3.1.3 below discusses the results applicable to each catalyst type.

Transmission electron microscopy (TEM)

Morphology of SZ and Ni/Al_2O_3 catalysts was studied in a Philips CM100 Transmission Electron Microscopy (TEM) with Compustage and high resolution digital image capture at Electron Microscopy Research Services, Faculty of Medical Science, Newcastle University. A small amount of the catalyst samples were suspended in water. A small drop of the suspension was then placed onto an EM grid and dried for 2-3 seconds. The EM grid was position at the TEM microscope and several images were taken from various regions. TEM images also allowed the determination of catalyst particle size distribution via image processing with ImageJ software.

Scanning Electron Microscopy (SEM)

Scanning electron microscopy (SEM) was performed in a JEOL JSM-5610LV SEM operating at low-vacuum, with an energy dispersive X-ray spectroscopy (EDX) module attached, over non coated catalysts samples (both HZSM-5, HY and SZ) at the Advanced Chemical and Materials Analysis (ACMA), Newcastle University. SEM images of uncoated biochar were collected on a Hitachi S2400 Scanning Electron Microscope at School of Mechanical Engineering, Newcastle University. No prior preparation of catalyst was required for SEM images.

Surface area and pore characterisation

Surface area, total pore volume and pore size distribution for all tested catalysts were obtained by N_2 physisorption isotherms determined at 77K using a Thermo Scientific Surfer porosimeter. Samples were outgassed at high vacuum prior to analysis to remove any physisorbed materials at various conditions depending on the catalyst: 1) 12 h at 150 °C for SZ and Ni/Al_2O_3, 2) 8 h at 250 °C for zeolites HZSM-5 and HY, and 3) 8 h at 150 °C for biochar. The outgassing conditions selected for each catalyst were based on thermal stability of catalysts and on prior tests conducted at various temperatures/times until a stable vacuum of about 10^{-4} torr was achieved (Rouquerol et al., 1994) which implied a clean catalyst surface. After outgassed, the volume of nitrogen adsorbed at certain constant relative pressures was measured and plotted to construct the catalyst isotherm. The isotherm data was processed using Surfer software to calculate the total pore volume and size distribution (Barrett-Joyner-Halenda (BJH) method) and surface area (Brunauer-Emmett-Teller (BET) equation).

X-ray diffraction (XRD)

X-ray diffractograms (XRD) were obtained in a Panalytical X'Pert Pro Multipurpose Diffractometer (MPD) fitted with an X'Celerator and a secondary monochromator (Cu-Kα

Table 3.6 Surface area and silica/alumina (SiO_2/Al_2O_3) ratio of zeolites HZSM-5 and HY

	HZ_1	HZ2	HY
Surface Area / [m^2/g]	211	336	667
SiO_2/Al_2O_3 /[mol]	312	137	5.2

radiation, wavelength (λ) = 1.54 Å generated at 40 kV and 40 mA) over a 2θ range of 2-70° from 2-100 °C. Analysis was carried out at Advanced Chemical and Materials Analysis (ACMA) at Newcastle University. XRD analysis studied the crystallinity of the samples and therefore only those catalyst subject to have crystalline phases i.e. SZ and Ni/Al_2O_3 were analysed by XRD.

Elemental and proximate analysis

Elemental analysis of biochar was performed in a Elementar Vario MICRO Cube CHN/S Elemental Analyser at Sheffield University since the one used for plastic waste was not available at the time the catalyst was analysed. However, the procedure was the same as the one explained in section 3.1.1. Proximate analysis of biochar was performed following the same procedure described in Section 3.1.1. Due to the composition of the other five catalysts, only biochar was analysed by these methods.

Inductively coupled plasma mass spectrometry (ICP/MS analysis)

Inductively coupled plasma mass spectrometry (ICP/MS) analysis of biochar was performed in a Perkin Elmer Sciex Elan 6000 at Durham University to characterised the number and concentration of AAEM metals present in the sample. No other catalyst was tested by this method due to the lack of AAEM metals in their composition.

Fourier-transform infrared spectroscopy (FTIR)

Fourier-transform infrared spectroscopy (FTIR) was obtained in an Agilent Cary 630 in the 4000-600 cm^{-1} range using KBr as background reference to analyse the functional groups present in SZ (S=O and S-O) and biochar (C=O and C-O) catalysts.

3.1.3 Results from fresh catalysts characterisation

Zeolites

Three types of synthetic commercial zeolites were used in this work: two types of HZSM-5 i.e. HZ_1 and HZ_2 (Sigma Aldrich) with different silica to alumina ratio (Si/Al=312 and 137 respectively) and Zeolite Y, HY (Si/Al = 5.2, Alfa Aesar). HZ_1, HZ_2 and HY were characterised by SEM with EDX and N_2 adsorption isotherms analysis (section 3.1.2). Table 3.6 summaries the surface area calculated by N_2 isotherms at 77K and BET equation and the silica to alumina molar ratio obtained from SEM/EDX for the three tested zeolites. BET analysis of HZ_1, HZ_2 and HY showed zeolites pore size in the range of 2.71-34.4 nm with over 64 % of them between 4.1-16.38nm and the remaining fraction almost evenly distributed between 2.71-4.1 nm and

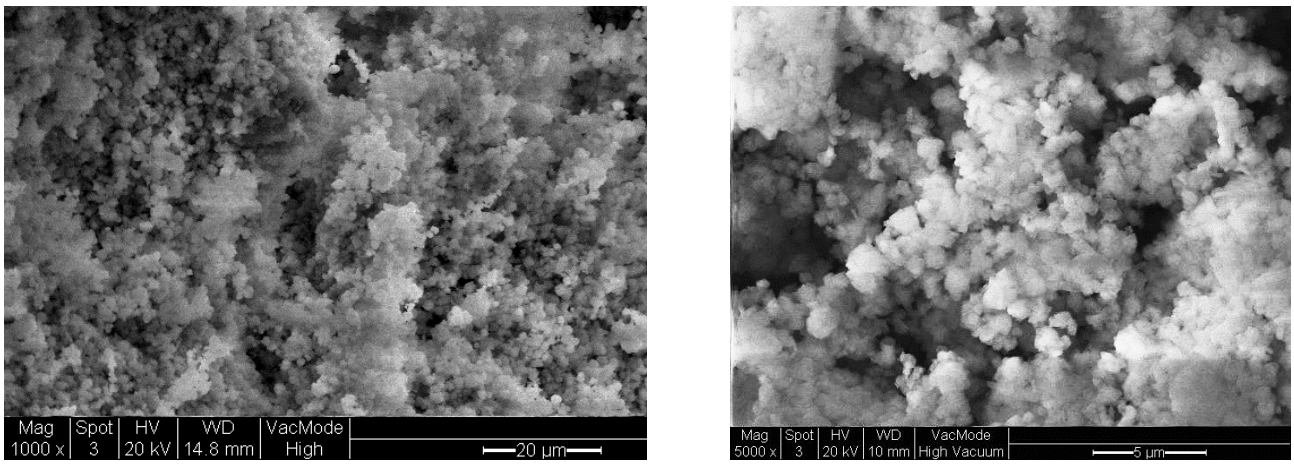

(a) HZSM-5 zeolite (x1000) (b) HY zeolite (x5000)

Figure 3.3 SEM images of fresh HZSM-5 zeolite (left) and HY zeolite (right)

16.38-34.4 nm. This suggests a mesoporous pore structure catalyst therefore, suitable for catalytic cracking of plastic waste as bulky volatile hydrocarbons (>1-4 nm (Ratnasari et al., 2017)) released from plastic waste pyrolysis can enter the catalyst pores.
EDX analysis in Table 3.6 confirmed the Si/Al ratio of the three commercial zeolites tested i.e. 312 for HZ_1, 137 for HZ_2 and 5.2 for HY. Zeolites catalytic activity depends on several factors including the radius and valence of the exchanged cation (sodium, calcium, magnesium, hydrogen) and the Si/Al ratio (Ward, 1970). When the Si/Al ratio increases, some aluminium atoms are substituted by silicon ones decreasing the Al content in the overall zeolite framework. As this happens, a cation is required to satisfy the zeolite structure and if it happens to be a proton, as in all tested zeolited in this thesis, it becomes a Brønsted acid site. Therefore, increasing the Si/Al ratio increases the Brønsted acidity. On the other hand, higher aluminium content, i.e. lower Si/Al ratio, translates into an overall negative charge of the zeolite due to the oxygen atoms attached to the aluminium ones as well as extra aluminium atoms not tetrahedrally bound to the zeolite framework. Those extra aluminium atoms are often linked to the formation of Lewis acid sites which provide an overall higher acidity of the zeolite as Lewis acid sites are somewhat stronger than Brønsted acid sites (Coster et al., 1994).
SEM images of HZ_1 and HY in Figure 3.3 were processed using ImageJ software to quantify particle size. Rectangular particles of average size of 0.94 ± 0.24 μm x 0.57 ± 0.16 μm were found.

Sulphated Zirconia

SZ catalyst was synthesised using the solvent-free direct mix of zirconium (IV) oxychloride octahydrate (Sigma Aldrich) and ammonium sulfate (Sigma Aldrich) method proposed by Eterigho et al. (2011). Both reactants were mixed in a 1:6 molar ratio followed by 18 h ageing at controlled temperature (25 °C) inside a Vecstar VCTF1 furnace. The sample was then calcined in air at 500 °C for 6 h in the same furnace. This solvent-free method was chosen due to the simplicity, the improved catalyst characteristics (larger surface area and higher Brønsted acidity)

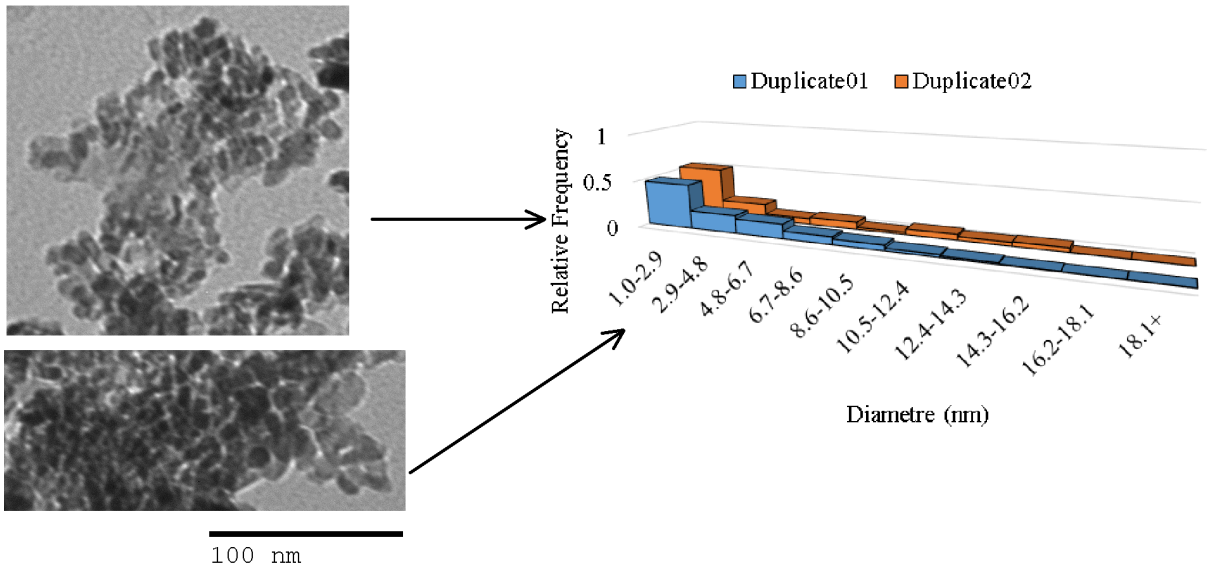

Figure 3.4 TEM images (180000x, HV=100.0kV, scale=100nm) of two fresh SZ catalyst random sections and particle size distribution obtained with ImageJ

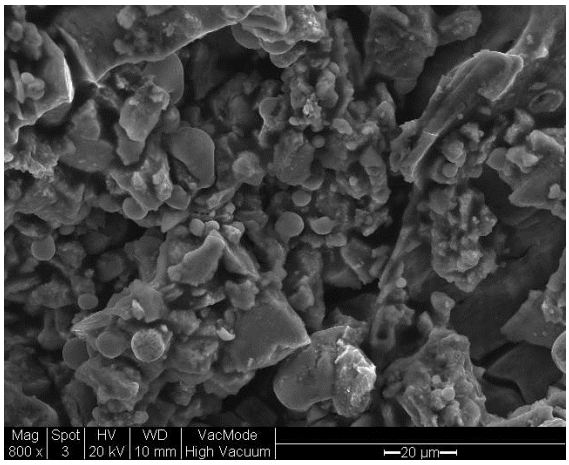

(a) SEM image (x800, scale=20 μm)

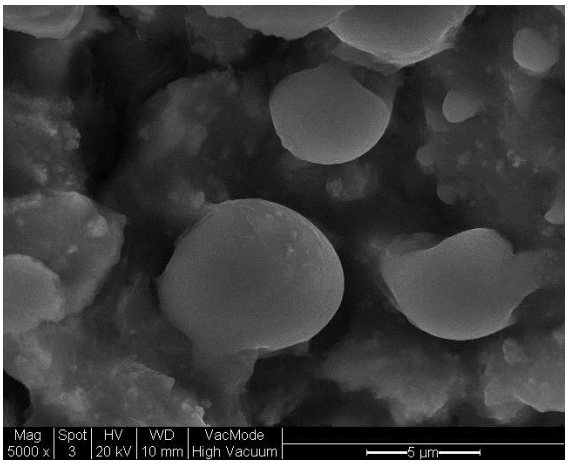

(b) SEM image (x5000, scale=5 μm)

Figure 3.5 SEM images of fresh SZ catalyst (x800 and x5000)

compare to conventional wet synthesis methods and the promoted triglycerides trans-esterification activity into saturated and unsaturated methyl esters reported (Eterigho, 2012; Eterigho et al., 2011). SZ solvent-free synthesis methods are reported to form a stronger interaction between the sulphate ion (SO_4^{2-}) and ZrO_2 which reduces the deactivation of the catalyst (Wang and Xiao, 2015).

SZ morphology was studied by SEM images (Figure 3.5) with EDX and TEM images (Figure 3.4) processed with ImageJ software. TEM images showed the majority of SZ particles (60 %) were between 1-2.9 nm in size. About 15 % ranged between 2.9-4.8 nm, 10 % between 4.8-6.7 nm and the remaining 15 % was distributed between 6.7-18.1 nm. SEM images showed SZ surface was not as uniform as zeolites surface (Figure 3.3). They show sputtered circular granules fused to the catalyst surface which have been previously reported for fusion sputtered SZ catalyst (Ewais et al., 2014). They appeared to be formed by tetragonal ZrO_2 (Li et al., 2012).

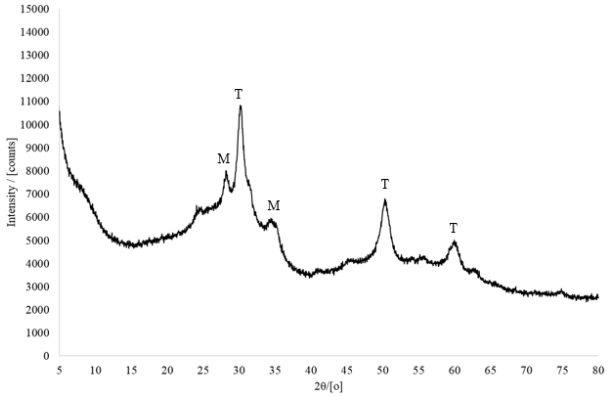

Figure 3.6 X-ray diffraction spectra of fresh SZ catalyst (T=tetragonal crystal and M=monoclinic crystal)

EDX analysis results showed that fresh SZ catalyst comprised of 43 wt% Zr, 39 wt% O and 18 wt% S which translates into a S/Zr molar ratio of 0.18 or a 9 mol% of SO_4^{2-}.
XRD spectra in Figure 3.6 confirmed the sample was mainly amorphous with low intensity peaks at 2θ of 28.25 and 34.30^o characteristic of monoclinic ZrO_2 and at 30.16, 50.11 and 60.10^o showing tetragonal ZrO_2. These findings agreed well with previous results (Eterigho, 2012; Eterigho et al., 2011; Mat et al., 2014).
SZ had a low surface area (10.43 ± 0.05 m^2/g) compared to some previously reported values (108 m^2/g (Eterigho et al., 2011) and 119.3 m^2/g (Tangchupong et al., 2010)) but agreed well with others (26 m^2/g (Chen et al., 1993)). The difference could be due to variation of catalyst preparation conditions such as ageing temperature and time, sulphur content, sulphating agent and zirconia precursor highly affect SZ surface area. Hamouda et al. (2000) and Stichert and Schüth (1998) reported that SZ surface area can dramatically vary from 19 m^2/g (no ageing) to 104 m^2/g (1 day ageing at 423K). Qi et al. (2009) also observed a variation in SZ surface area from 27.1 to 105.1 m^2/g after sulphate treatment and calcination at 600 °C. Yadav and Nair (1999) showed that using ammonia instead of urea and amorphous hydrous zirconia instead of precrystallized zirconia as reagents increased SZ surface area. Despite the low surface area, BET analysis also showed 74.61 % of SZ pores were between 4.10-16.38 nm with the remaining fraction between 16.38-34.40 nm. This suggested SZ pores were bigger than plastic waste pyrolysis volatiles (1-4 nm (Aguado et al., 2006)) and therefore, a suitable catalyst.
Previous studies suggested SZ catalyst can be sensitive to thermal decomposition (Strydom and Pretorius, 1993) via the loss of hydrated water molecules (<330 °C) and zirconia (>540 °C). Therefore DSC analysis with a final temperature of 550 °C, repeated twice, was used to characterise SZ thermal behaviour. Figure 3.7 shows four exothermic peaks at 82.58, 177.43, 455.53 and 525.17 °C. The first two peaks occurring between 80 and 180 °C corresponded to the loss of molecules of hydrated water from the zirconium sulphate hydrate ($Zr(SO_4)_2\cdot xH_2O$) according to the following reaction: $Zr(SO_4)_2 \cdot xH_2O \rightarrow Zr(SO_4)_2 \cdot yH_2O$ where y<x. The third peak at about 455 °C could be caused by further SZ dehydration; however, according to others (Strydom and Pretorius, 1993), this dehydration could take place at temperature below 300 °C. Therefore, the third and fourth endothermic peaks occurring between 455 and 525 °C were

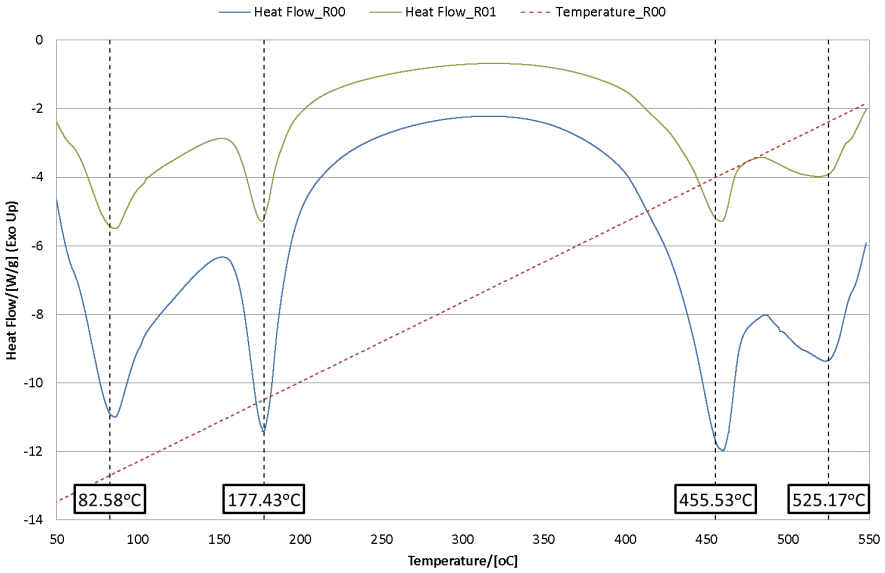

Figure 3.7 DSC analysis of fresh SZ catalyst for thermal behaviour

either caused by the formation of tetragonal ZrO_2 according to: $Zr(SO_4)_2 \rightarrow ZrO_2 + gases$ or by the decomposition of the sulphate into SO_x gases and O_2. Further analysis on SZ decomposition during plastic waste pyrolysis is discussed later on chapters 5, 6 and 8. Although studies have not found an agreement yet as to how or why SZ catalyst deactivates, the most accepted two theories or SZ deactivation are: 1) the reduction of the surface sulphate groups from S^{+6} to lower oxidation states at temperatures above 400 °C resulting in lower acidity and therefore activity and 2) the blockage of SZ pores due to the formation of coke deposits during reaction (Ng and Horvát, 1995). Wang et al. (2016) studied this process in detail suggesting that, under N_2, the sulphur content of the catalyst start to decrease at temperatures above 500 °C which explains the DSC peak obtained at 525.17 °C and possibly at 455.53 °C. Hence, SZ catalytic pyrolysis temperature should be lower than 500 °C to prevent deactivation of the catalyst due to the reduction of surface sulphate and consequent released of sulphur gases and catalytic activity reduction. However, Wang et al. (2016) also reported that, in the presence of an oxidizing atmosphere such as air or O_2, SZ catalytic activity and sulphate content are fully recovered again at temperatures above 700 °C. Unfortunately, this findings were only discovered after the use of SZ catalyst for waste HDPE (chapter 5) and waste PP (chapter 6) cold plasma assisted pyrolysis experiments and thereby, temperatures higher than 500 °C were tested in this thesis.

Nickel Alumina: Ni/Al_2O_3

Ni/Al_2O_3 catalyst was prepared by wet impregnation method of nickel nitrate hexahydrate ($Ni(NO_3)_2 \cdot 6H_2O$, 99.9 % purity, Sigma Aldrich) onto high surface area alumina support pellets, Al_2O_3 (180 m^2/g, Alfa Aesar) following the method proposed by Bartholomew and Farrauto (1976). A known amount of Al_2O_3 was mixed in a 1 M solution of nickel nitrate hexahydrate at a molar ratio of Al_2O_3:$Ni(NO_3)_2 \cdot 6H_2O$ of 10:1 for 1 h under constant vigorous stirring at 60

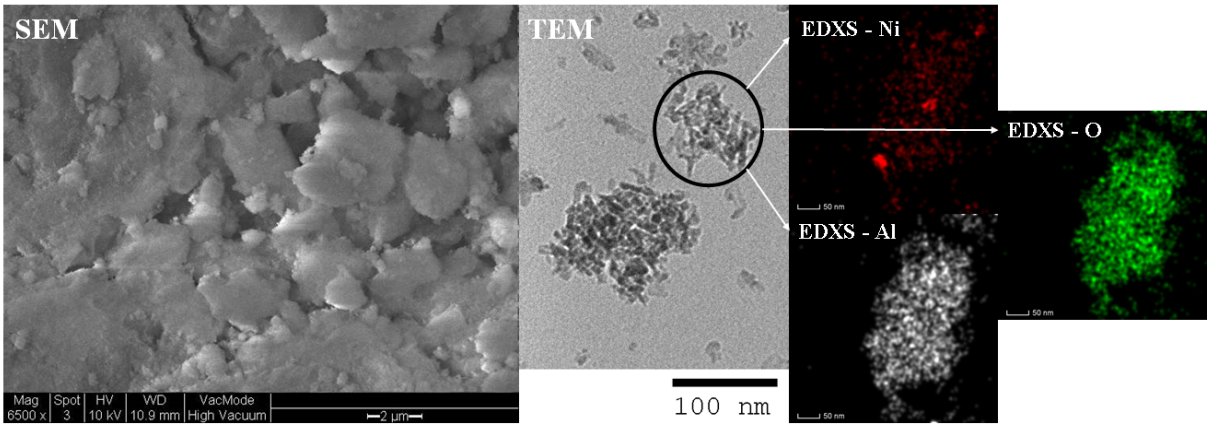

Figure 3.8 SEM image (left), TEM image (middle) and EDXS mapping (right) of fresh Ni/Al_2O_3 catalyst

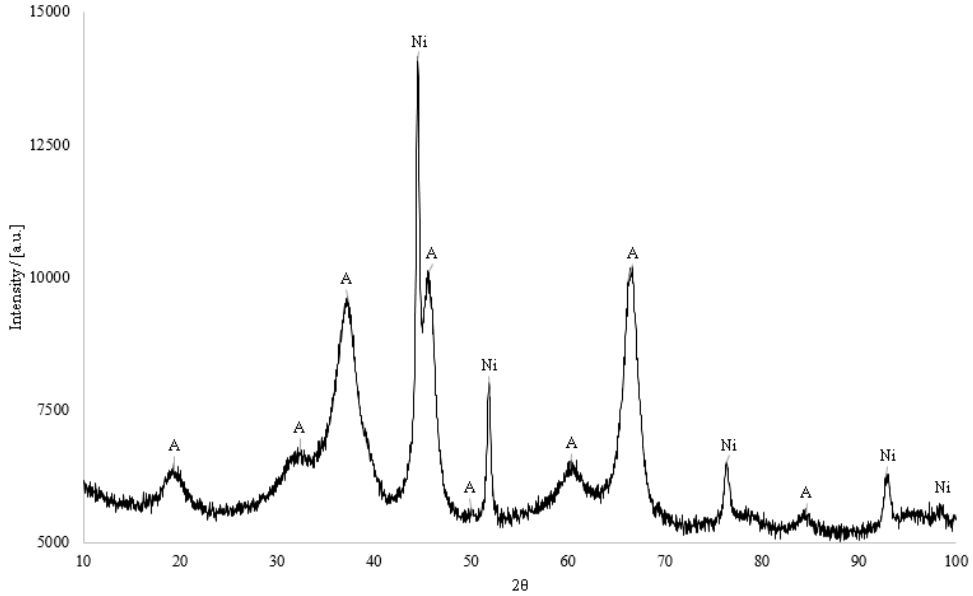

Figure 3.9 XRD spectrum of fresh Ni/Al_2O_3 catalyst (A=cubic Al_2O_3 and Ni=cubic nickel)

°C. The resulted slurry was dried at 105-110 °C for 24 h and then the dried Ni/Al_2O_3 catalyst was calcined at 550 °C for 5 h in air followed by an overnight reduction in hydrogen at 550 °C to reduce NiO to Ni. The catalyst was left to cool down to room temperature under a hydrogen stream to prevent reoxidation and finally grounded to a 0.5–1 mm size.

Morphology and composition of the fresh Ni/Al_2O_3 catalyst were analysed by SEM, TEM, EDXS and XRD. Figure 3.8 shows SEM and TEM images of fresh catalyst as well as elemental mapping obtained from EDXS. SEM image showed the surface of Ni/Al_2O_3 where Ni particles were distributed on top of Al_2O_3 surface. TEM images showed a fairly uniform particle distribution of Ni/Al_2O_3 with the catalyst forming conglomerates smaller than 100 nm in size, which agreed well with previous studies by Li et al. (2006). Processing of TEM image with ImageJ showed that over 90 % of the catalyst particles were between 1.2-13.0 nm with an average particle size of 8.8±3.6 nm, maximum particle size of 51.4 nm and minimum particle size of 1.2 nm. EDXS mapping of Ni/Al_2O_3 catalyst showed that 20-30 nm Ni particles were uniformly distributed on Al_2O_3 surface.

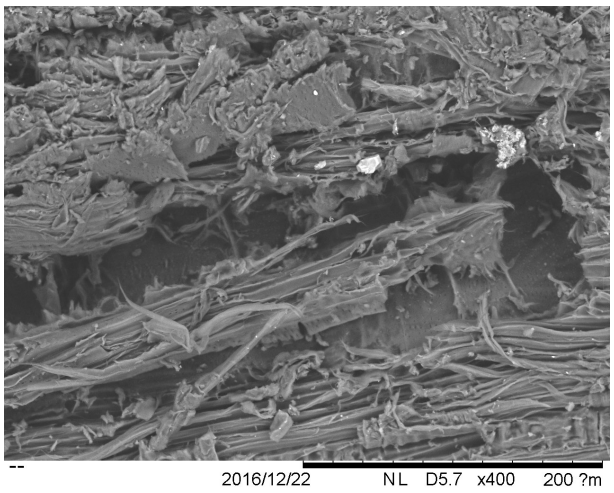

Figure 3.10 SEM image (x400) of fresh biochar catalyst (scale=200 μm)

Ni/Al_2O_3 XRD spectrum (Figure 3.9) presented cubic Al_2O_3 (2θ = 19.31, 32.34, 37.26, 45.61, 50.02, 60.48, 66.40 and 84.42^o) and cubic nickel (2θ = 44.48, 51.86, 76.39 and 92.90^o). Although NiO was reported to be formed during Ni/Al_2O_3 synthesis (Li et al., 2006), this fraction was not observed in this study due to the hydrogen reduction step.
Ni/Al_2O_3 had a surface area of 92 m^2/g which was obtained from N_2 isotherms at 77K and BET equation. It was slightly lower than that reported in previous studies (118 m^2/g for 13 wt% Ni load (Li et al., 2006) and 124 m^2/g for 48 wt% Ni load (Wen et al., 2009)). On the other hand, Ni/Al_2O_3 surface area was higher than that reported by others (Bartholomew and Farrauto, 1976) where the surface area of Ni/Al_2O_3 catalyst varied between 4.3-10.3 m^2/g depending on the amount of Ni dispersed on the surface (9-26 wt%).

Biochar derived from waste biomass pyrolysis

Biochar was obtained from in-house pyrolysis of waste wood at 900 °C. The waste biomass was collected from Sustainable Campus at Newcastle University and cut into 1 cm^3 cubic particles. Approximately 25 g of waste biomass cubic particles were placed in a 33 mm diameter and 830 mm long Inconel 600 fixed bed reactor and heated up to 900 °C. When the set temperature reached 900 °C, the system was held for a further 15 min before being switched off. The biomass char residue was collected, weighted and stored in glass containers until it was used as a catalyst in this work without any other activation/pre-treatment.
As shown in Figure 3.10, biochar internal channels had a diameter of 24 μm for each of the two parallel channels sides. According to N_2 isotherms at 77K, the average pore size of biochar was between 7-12 nm, suggesting a sufficient pore size to accommodate the large plastic waste pyrolysis volatiles (>1-4 nm Aguado et al. (2006); Ratnasari et al. (2017)). The total pore volume was 0.07 cm^3/g of which 64 % were micropores (<30 nm). Biochar had a BET surface area of 124.0$\pm$12.1 m^2/g.
Biochar proximate analysis showed that it contained up to 95.2$\pm$0.3% fixed carbon with low volatile (2.3$\pm$0.6%) and ash content (2.5$\pm$0.1%) which agreed well with previous reported

values (Mitsuoka et al., 2011). Empirical formula was $C_{6.00}H_{1.16}O_{0.52}N_{0.03}$ via elemental analysis. ICP/MS analysis showed that the main AAE in the sample were calcium (4117±165 ppm), potassium (1782±46 ppm), magnesium (1153±33 ppm), sodium (339±28 ppm) and silicon (142±26 ppm) as expected (Mitsuoka et al., 2011) alongside traces of phosphorus, aluminum, barium, manganese, iron, zinc, strontium, lead and boron. Dupont et al. (2011) analysed 21 different types of biomass char and reported that, although concentration of AAE metals varied among biomass types, they all present calcium, potasium, magnesium, sodium and silicon in this order. Klinghoffer (2013) demonstrated biochar as a suitable catalyst for the cleavage of C-C and C-H bonds in light hydrocarbons (methane and propane) pyrolysis up to a temperature at around 900 °C, due to the presence of AAE metals. They also reported that, above 900 °C and in the absence of CO and CO_2, the oxygen-containing functional groups in biochar structure can migrate to the surface of the catalyst and desorb CO and CO_2.

3.1.4 Spent catalyst characterisation

Spent catalysts from pyrolysis experiments in chapter 6 (Ni/Al_2O_3) and in chapter 8 (biochar, SZ and zeolite HY) were characterised to compare morphology and composition with the fresh ones. Additional analysis applied to Ni/Al_2O_3 catalyst included high resolution transmission electron microscopy (HRTEM), performed in a FEI Tecnai T20 (G2, 200 kV), energy-dispersive X-ray spectroscopy (EDXS), performed in a FEI Talos F200A TEM/STEM, temperature programmed oxidation (TPO) and Raman Spectroscopy. To ease the flow of this thesis and for better understanding, spent catalyst characterisation results are not included in this chapter but are however discussed in the relevant sections of chapters 6 and 8. This way, spent catalyst characterisation is discussed closer to the results from pyrolysis experiments.
TPO was performed to quantify the amount and reactivity towards oxygen of the different carbonaceous species deposited on the spent Ni/Al_2O_3 catalyst. Samples of 75 mg, placed inside a quartz reactor, were linearly heated at a rate of 10 °C/min from room temperature to 850 °C under a constant flow (45 mL/min) of an oxidizing gas mixture (5% O_2 in He) for TPO analysis. The gases at the reactor outlet were analysed by continuous recording of the mass spectrometry signals at m/z = 32 (O_2), 28 (CO) and 44 (CO_2) on an on-line Hiden Analytical Mass Spectrometer previously calibrated with known gas mixtures of 5% O_2, CO and CO_2 in He respectively. Raman Spectroscopy was conducted in a Horiba HR800 Confocal Raman Microscope at 10 accumulations of 10 second, with 21.6 mW power at sample, a wavelength of 532 nm at Raman shifts between 1200 and 2700 cm^{-1}.

3.2 Pyrolysis set up

Pyrolysis of plastic waste was carried out in this study with small variations depending on the type or types of plastic used and/or the addition of a catalyst or cold plasma. In all scenarios, pyrolysis experiments yielded three fractions i.e. a carbonaceous solid residue, a condensable vapour fraction (named wax) and a non-condensable gaseous fraction (called gas).

The yield of the carbonaceous solid residue was low in most cases and similar to the ash content in Table 3.2. This suggested that this fraction comprised of the inorganic and non-volatile material present on the initial plastic waste sample. Due to the low amount which made its collection and analysis very difficult and its few potential application this fraction was not analysed in this thesis. This is however an area for further work if any high value applications are found in the future.
The wax collected on each pyrolysis experiment varied in appearance and composition depending on the feedstock composition, pyrolysis temperature and presence of catalyst or cold plasma. Waste HDPE, LDPE and PP yield a thick wax product with an appearance similar to that of wax from a candle. Higher temperatures, acid catalysts and cold plasma decreased the viscosity of the wax to a consistency similar to that of a paste. The wax collected from PS presented the appearance of a dark brown viscous liquid. This difference was because of the presence of aromatic compounds in the case of PS which were absent for HDPE, LDPE and PP. In the case of PET, the wax fraction was very different in appearance and composition, as discussed later on in Chapter 7. The appearance of the waste PET wax fraction was a yellow powder which often was deposited not only in the condenser but also in the pipeline connecting the outlet of the pyrolysis reactor and the condenser. The wax yields discussed later on in Chapter 7 referred to total wax including the one collected from the condenser and the one scrapped from the pipeline mentioned above.
Due to the differences in consistency between experiments the term 'wax' was chosen to unify them for comparison purposes. This fraction is sometimes named as 'liquid' in literature. However, this term was discarded in this thesis as the appearance and viscosity did not resemble what the general knowledge would understand for a liquid and therefore, was considered to be misleading. Despite the difference in nomenclature, the fraction remains the same i.e. the condensable vapour fraction which condenses after pyrolysis experiments and therefore was compared with literature values which adjusted to this description.
The remaining fraction is the non-condensable or gas fraction. This comprised of a mixture of permanent gases (CO_2, H_2, O_2, CH_4 and CO) and light hydrocarbons (C_2-C_4). The amount of each compound greatly varied again depending on the feedstock composition, pyrolysis temperature and presence of catalyst or cold plasma. The nomenclature of this fraction was in agreement with literature. This fraction is one of the main focuses of this thesis due to the lower discussion found in literature despite the presence of high-value products in it (ethylene, propylene, hydrogen).
The experimental set-up used for each particular type of experiments is described below and summarised in Table 3.7 to ease the reader.

3.2.1 Cold plasma assisted thermal and catalytic pyrolysis

Cold assisted pyrolysis of plastic waste was carried out in a two-stage reactor comprising of an initial pyrolysis section followed by cold plasma treatment of the released volatiles as shown in Figure 3.11 and in more detail in Appendix D. The two-stage pyrolysis/cold plasma reactor

Table 3.7 Summary of experimental set-up, materials and correlation with results discussion chapters

Experimental set-up	Plastic waste	Results
Cold plasma assisted pyrolysis	HDPE and PP	Chapters 5 and 6
Thermal pyrolysis quartz reactor	HDPE and PP	Chapters 5 and 6
Catalytic pyrolysis quartz reactor	HDPE and PP	Chapters 5 and 6
Catalytic pyrolysis quartz reactor	PET	Chapter 7
Catalytic pyrolysis stainless steel reactor	Mixed plastic waste	Chapter 8

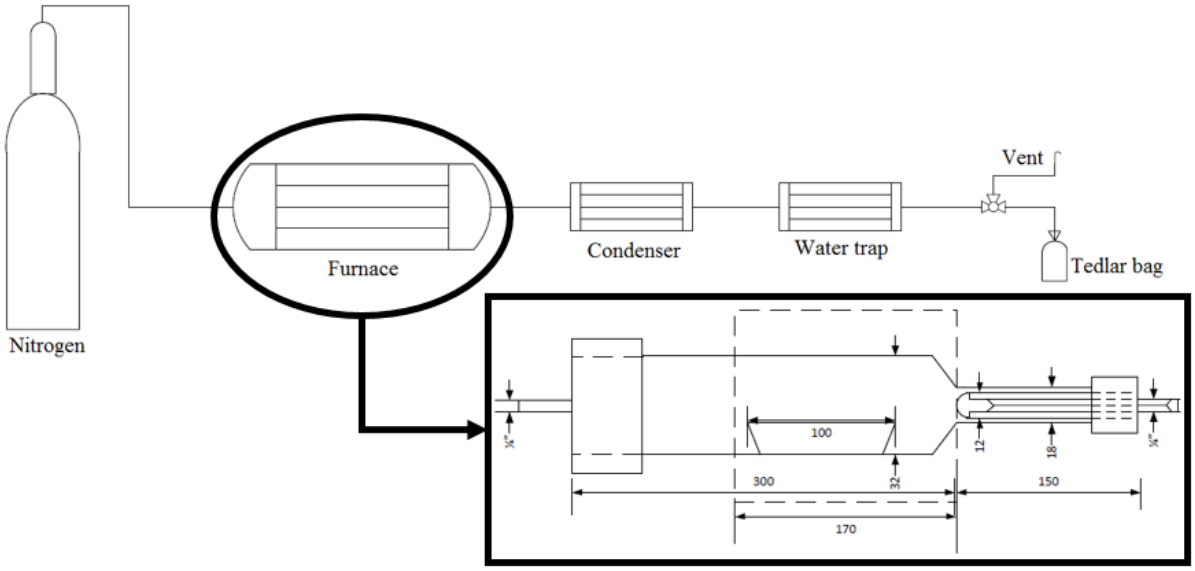

Figure 3.11 Cold plasma assisted catalytic and thermal pyrolysis experimental set up (not to scale)

comprised of a 32 mm O.D. quartz tube jointed to a 18 mm O.D. quartz tube both with a 1.5 mm wall thickness. The reactor was centred inside a horizontal VECSTAR VCTF1 furnace (heated length = 170 mm and chamber diameter = 38 mm). Plastic waste samples were placed in a quartz combustible boat in the centre of the pyrolysis section. The pyrolysis/cold plasma reactor was heated in an inert atmosphere (N_2at 20 ml/min) at various set heating rates ranging from 30-75 °C/min, depending on the experiments being performed, up to the desired pyrolysis temperature (450-700 °C) after which was hold for 15 minutes. The temperature range selected was based on TGA results (chapter 4) and previous studies to operate at plastic waste decomposition range. Temperatures above 525 °C were selected to study the secondary cracking of hydrocarbons at high temperature. In all tested conditions the plastic waste sample released gases and volatiles at temperatures above 390-410 °C. These were carried out by N_2 through a dielectric barrier discharge (DBD) reactor in the cold plasma section and then out of the furnace into the condenser, kept in an ice bath around 0 °C.

The DBD reactor in the cold plasma section comprised of two coaxial quartz tubes: an outer 18mm O.D. tube and an inner 12mm O.D. tube, both with a 1.5 mm wall thickness, creating a gap spacing of 1.5mm between the two coaxial quartz tubes. The gap was filled with rock wool. For cold plasma assisted catalytic pyrolysis a catalyst i.e. HZ_1, HZ_2, SZ or Ni/Al_2O_3 was evenly distributed on top of the rock wool filling the entire gap volume. The exterior of the outer tube and the interior of the inner tube were covered with a 316L stainless steel mesh and a stainless steel sheet respectively to create the two electrodes. The total length of the cold plasma discharge was 12cm and was kept at the same temperature as the plastic waste sample to eliminate wax condensation. The cold plasma was generated using an AC power supply (0-240V, 50Hz). The input specific energy density (SED), i.e. the discharge power supplied to the cold plasma reactor per unit of gas volume, was modified by adjusting the input voltage between 0-240V depending on the particular experimental conditions being tested but was kept constant for each particular experiment.

Non-cold plasma assisted thermal and catalytic pyrolysis of waste HDPE (chapter 5) and waste PP (chapter 6) were conducted in the two-stage quartz reactor as described above (Figure 3.11 and Appendix D) with the only difference that the electrodes and cold plasma system were not connected to the coaxial DBD reactor zone.

The solid residue and condensed fraction were collected and weighted for their yields once the system cooled down below 50 °C under N_2 atmosphere to minimise further decomposition of the products. The gas yield was calculated by mass balance. At the end of each experiment the wax collected in the condenser was quantitative analysed by gas chromatography. During each experiment the gas fraction was constantly collected from the point volatiles started to be released until the end of the experiment in four or five 0.6L Supelco Tedlar bags and analysed off-line by gas-chromatography.

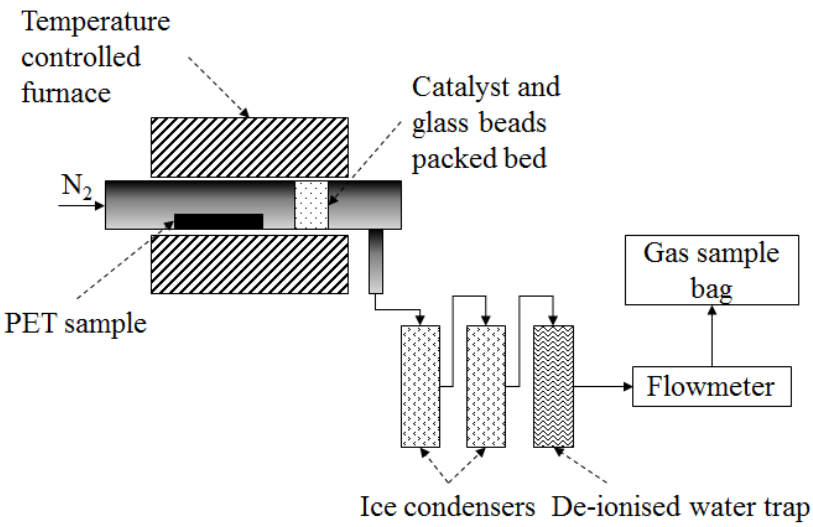

Figure 3.12 Catalytic pyrolysis in quartz glass reactor set-up (not to scale)

3.2.2 PET catalytic pyrolysis in quartz tube

Figure 3.12 shows the experimental set-up for thermal and catalytic PET waste pyrolysis. Appendix E has detailed drawings of the set-up and the reactor. The PET waste sample was evenly spread onto a quartz combustion boat placed at the centre of a quartz glass reactor (length of 300 mm long, 32 mm O.D. and 29 mm I.D.). SZ catalyst was packed in a 10 mm long catalyst bed created by mixing the desired amount of the SZ catalyst (3-10 wt%) with 10 g of 1 mm diameter glass beads (Sigma-Aldrich) as shown in Appendix E. This was done to obtain even distribution, uniform contact of the volatiles released from pyrolysis and the catalyst and to prevent the catalyst to flow out of the reactor with the volatiles. The catalyst bed was placed just after the sample crucible in the quartz glass reactor inside the furnace (Appendix E).
The pyrolysis reactor containing both the plastic waste sample and the catalyst bed was heated by a cylindrical horizontal Vecstar VCTF1 furnace. The reactor was purged with nitrogen at a flow rate of 20 mL/min for 1h prior to experiments to ensure an air-free system (confirmed by gas analysis). During experiments, the furnace was heated up to the desired pyrolysis temperature (450-700 °C) at a set heating rate (30-75 °C/min) and hold for 15 minutes before it was turned off to ensure full decomposition of the volatiles released. The residence time of the volatiles inside the heated zone was varied (10, 20 or 30s) modifying the nitrogen flow rate (40 mL/min, 20 mL/min and 13 mL/min respectively). Volatiles were condensed at the outlet in two condensers cooled with ice (0 °C). The gases out of the condenser (non-condensable gases) were passed through a water trap to ensure no residues enter the gas collection system. Gas samples were collected at regular time intervals in 0.6L Tedlar bags (Sigma-Aldrich) between 350 °C and the final pyrolysis temperature for off-line gas analysis. The solid residue in the combustion boat and the condensed fraction were collected and weighted for their yields once the system cooled down below 100 °C under N_2 atmosphere. The gas yield was calculated by mass balance. The catalyst was recovered from the catalyst bed and separated from the glass beads/rock wool by agitation.

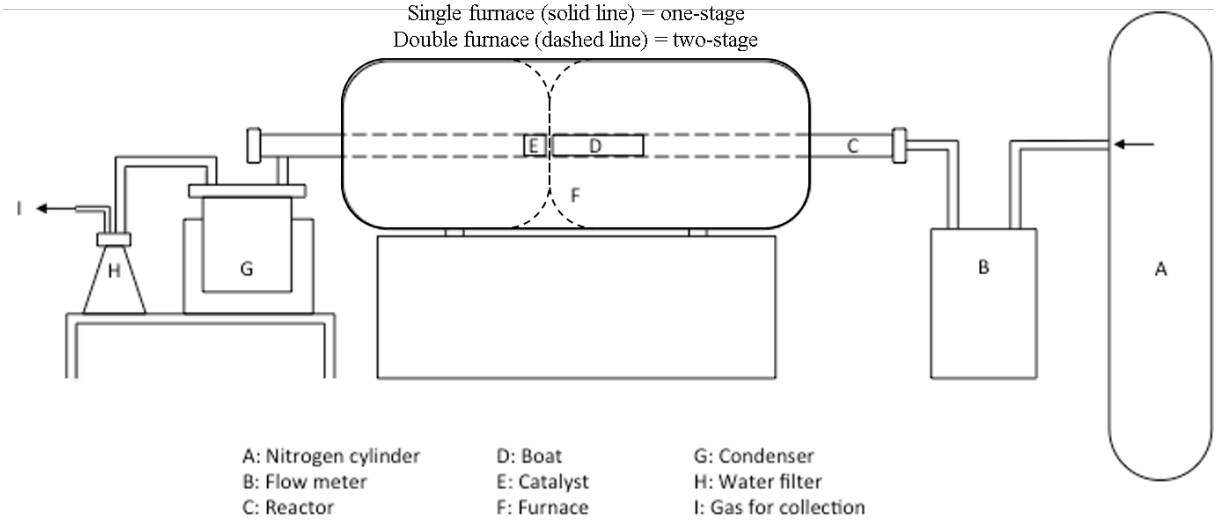

Figure 3.13 One and two-stage catalytic pyrolysis in stainless steel reactor set-up (not to scale)

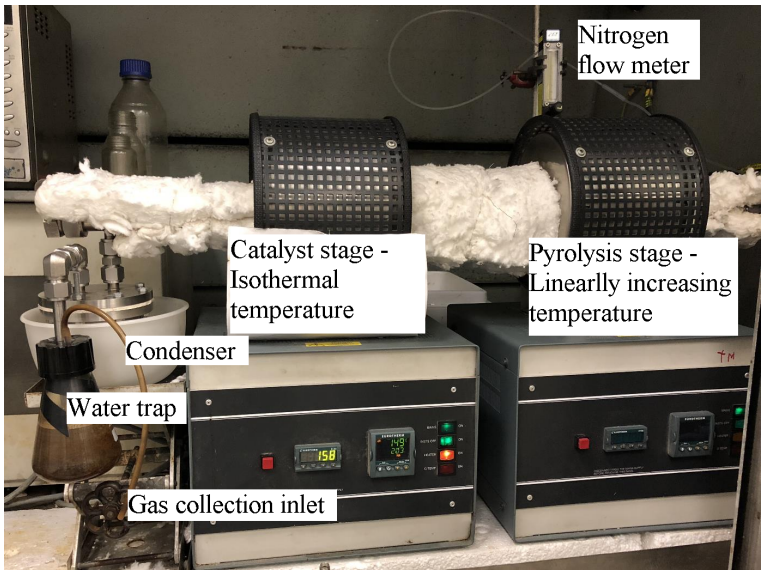

Figure 3.14 Two-stage catalytic pyrolysis in stainless steel reactor set-up after an experiment

3.2.3 Catalytic pyrolysis in stainless steel reactor

One-stage catalytic pyrolysis set-up of mixed plastic waste (Figure 3.13) comprised of a 22 mm inner diameter and 850 mm length 316L stainless steel reactor placed horizontally in an electric Vecstar VCTF4 furnace (heated length of 450 mm and a 36 mm diameter). Appendix F shows detailed drawings of the set-up and reactor used for mixed plastic waste pyrolysis. The outlet of the reactor was connected to a 316L stainless steel condenser inside an ice bath (0 °C) to collect the condensable fraction (wax). The non-condensable gas was collected by four 0.6L Supelco Tedlar gas bags. The four bags were collected one after the other starting when the pyrolysis temperature reached 375 °C and ending during the holding time at the final pyrolysis temperature. After collection, they were analysed off-line. About 4 g of mixed plastic waste were placed on a 316L stainless steel crucible and slid to the centre of the furnace heated length (Appendix F). The catalyst was packed in a 316L stainless steel mesh and pushed inside the

reactor immediately after the plastic waste sample (Appendix F). The bed of biochar had a volume of 6.3 cm^3 whilst the zeolite HY and Al_2O_3 catalyst bed, supported on 10 g of 1-2 mm borosilicate glass beads, had a volume of 18.8 cm^3. This was done to maintain the catalyst:plastic mass ratio constant for all tested catalysts. The apparent volatiles retention time was calculated based on the carrier gas flow rate (25 mL/min) resulting on 0.26 s for biochar and 0.75 s for zeolite HY and Al_2O_3.

The experimental set-up was purged with nitrogen prior to pyrolysis experiments until a non-oxidant atmosphere (confirmed by gas analysis) was obtained, after which the flow rate of nitrogen was fixed to 25.0±2.5 mL/min to convey gas and volatiles to the outlet. The temperature was increased at 25 °C/min up to the desired pyrolysis temperature (500-800 °C) and held for 15 minutes. After that, the furnace was switched off and the system was left to cool under nitrogen flow until the temperature dropped below 50 °C. The solid residue in combustion boat and the fraction in the condenser were collected and weighed to determine the solid residue and wax yields respectively before further analysis. The gas fraction was calculated by mass balance.

Two-stage isothermal catalytic pyrolysis experiments were carried out identically as described above with the only exception of the introduction of an additional Vecstar VCTF1 furnace (second stage) kept at constant temperature i.e. isothermal. Detailed drawings of the two-stage catalytic pyrolysis of mixed plastic waste are shown in Appendix F. Figure 3.14 shows a picture of two-stage isothermal catalytic pyrolysis of mixed plastic waste after an experiment. The second stage, containing only the catalyst bed, was heated to a desired temperature (500-800 °C) to activate the catalysts 30 minutes prior to pyrolysis experiments. From this point, the remaining set-up: condenser and gas collection, remained exactly as described above for one-stage catalytic pyrolysis of mixed plastic waste.

3.2.4 Gas Analysis

Non-condensable gases were collected during all pyrolysis experiments in 0.6L Tedlar bags and analysed off-line by gas chromatography. The gas collection system comprised of a digital flow meter (Agilent) to measure the gas flow at the outlet of the water trap, placed straight after the condenser; a Tedlar bag; and a timer. The gas flow coming out of the water trap was measured at regular time intervals for the full duration of each pyrolysis experiment. When the pyrolysis temperature was between 350-375 °C a Tedlar bag was connected to the outlet of the water trap collecting the gas for a certain amount time, measured with the timer. At the end of the gas collection interval, set by temperature limits, the timer was stopped; the Tedlar bag was sealed and disconnected from the water trap outlet pipe; and the gas flow measured again with the flow meter. This process was repeated with various Tedlar bags at regular temperature intervals until the end of each pyrolysis experiment.

Non-condensable gases were analysed off-line using a Varian 450 gas chromatography unit equipped with a TCD and an FID detectors to respectively analyse permanent gases (i.e. H_2, O_2, N_2, CH_4, CO and CO_2) and hydrocarbons (C_2-C_4). The TCD inlet, detector and oven

temperatures were kept constant at 250 °C, 175 °C and 100 °C respectively and connected to three columns: a Hayesep T ultimetal, a Hayesep Q ultimetal and a Molecular Sieve ultimetal. The gas sample from the TCD detector was passed into a CP-Sil 5CB 25m x 0.55mm x 40μm connected to the FID detector set at 255 °C. This column was kept in another oven programmed as follows: held at 40 °C for 2 minutes, ramped to 50 °C at 4 °C/min and held for 0.5 minutes, ramped to 100 °C at 8 °C/min and ramped to 120 °C at 10 °C/ min. The yield of all compounds in the gas identified by GC-TCD/FID are always referred to the initial plastic waste sample (i.e. mass of compound/mass of plastic waste sample).
The Varian 450 gas chromatography unit was connected to a Galaxy software which contained calibrations for the permanent gases and hydrocarbons. These calibrations calculated the mole percentage, for permanent gases, and the weight percentage, for hydrocarbons, based on the peak area of each compound detected. The calibrations were tested on a regular basis by injecting a sample of a standard gas mixture (2 % O_2, 3 % CH_4, 10 % CO_2, 15 % H_2, 20 % CO and 50 % N_2, all mole percentage) of known composition. The values obtained from the calibration were compared with the ones of the standard mixture injected and adjusted accordingly if required. The values obtained from the Galaxy software i.e. mole percentage of permanent gases and weight percentage of hydrocarbons, were further processed. To do so, first the total volume of gas sample (mL) in each bag was calculated by multiplying the total gas collection time (seconds) by the average gas flow measured before and after connecting the Tedlar gas (mL/s). From this point all the calculations made are summarised in Appendix G. The final values referred to as weight percentage of each compound referred to the initial plastic sample mass.

3.2.5 Wax Analysis

The fraction in the condenser, in a form of soft wax, was characterised by:

1. FT-IR (Agilent Cary 630 FTIR Spectrometer with spectra collected between 600 and 4000 cm^{-1}) to identify the functional groups

2. Gas Chromatography - Mass Spectrometry (GC-MS) to identify individual compounds (Agilent 5975C coupled with a mass spectrometer and a HP5 30m x 0.25mm x 25 μm with the inlet/detector set at 310/280 °C, 20:1 split ratio and oven initially set at 30 °C 5 min followed by a 5 °C/min ramp to 310 °C)

3. Gas Chromatography - Flame Ionisation Detector (GC-FID) to quantify the most abundant compounds.

A certain amount of wax collected from the condenser for each tested condition was dissolved in a 1:1 mixture of ethyl acetate an n-hexane and then injected in an Agilent 7820A coupled with an FID detector and a CP-Sil 5CB 25m x 0.55mm x 40 μm column. The inlet and detector temperatures were both set at 280 °C whilst the oven operated a temperature profile as follows: 60 °C with a 0.5 minute hold and ramped to 280 °C at 6.5 °C/min followed by a final 13min hold. The compounds in the wax identified by GC-FID were quantified using both an internal

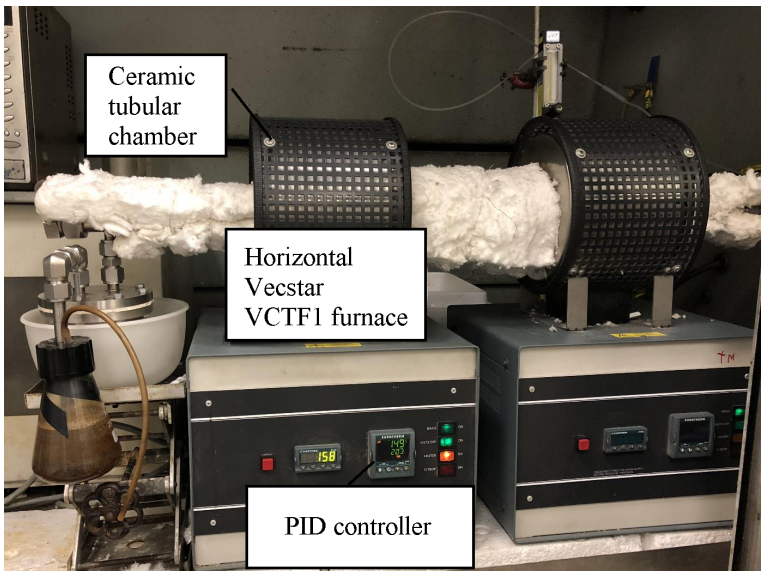

Figure 3.15 Horizontal Vecstar furnace, model VCTF1

(methyl heptadecanoate in n-hexane at 500ppm, Sigma Aldrich) and external standards (Agilent FID MDL comprised of 2.37±0.01 mg/L C_{13}, 2.37±0.01 mg/L C_{14}, 23.6±0.01 mg/L C_{15} and 23.7±0.01 mg/L C_{16}). Wax yield resulting from GC-FID analysis are calculated based on the initial plastic waste mass (i.e. mass of compound/mass of plastic waste sample).

3.2.6 Horizontal Vecstar furnaces calibration

Two horizontal Vecstar electric furnaces were used for the experiments involving heating. Their technical specifications are summarised in Table B.5 in Appendix B. The main parts of the furnaces consisted of a ceramic tubular chamber of varying length, depending on the model, and a PID controller used to regulate the temperature and heating rate during each experiment. Figure 3.15 shows a picture of a Vectar furnace model VCTF1. The other model used, Vectar VCTF4 was similar with the only difference of a longer ceramic tubular chamber: 17cm for the VCTF1 model and 45cm for the VCTF4 model.

All the Vecstar furnaces were equipped with a type K thermocouple built into the tubular chamber and connected to the PID controller. They were also equipped with a secondary type K thermocouple connected to a safety controller to prevent a thermal runaway. This safety controller was always set at 50 °C over the maximum temperature used in the experiment.

The furnace thermocouple was calibrated prior to conducting experiments using an external type K thermocouple (RS Components) connected to a data logger. The calibration was conducted by placing a reactor in the tubular chamber of the furnace and fixing the external (sample) thermocouple in the centre of the reactor, where the plastic waste combustion boat was going to be placed during experiments. The furnace set point temperature was then fixed at various at set values between 30-700 °C.

Vecstar horizontal furnaces provide heat to the chamber via an electric resistance. This resistance is controlled by the PID controller where the furnace set point temperature and the heating rate were fixed. The controller switched on and off the resistance depending on whether

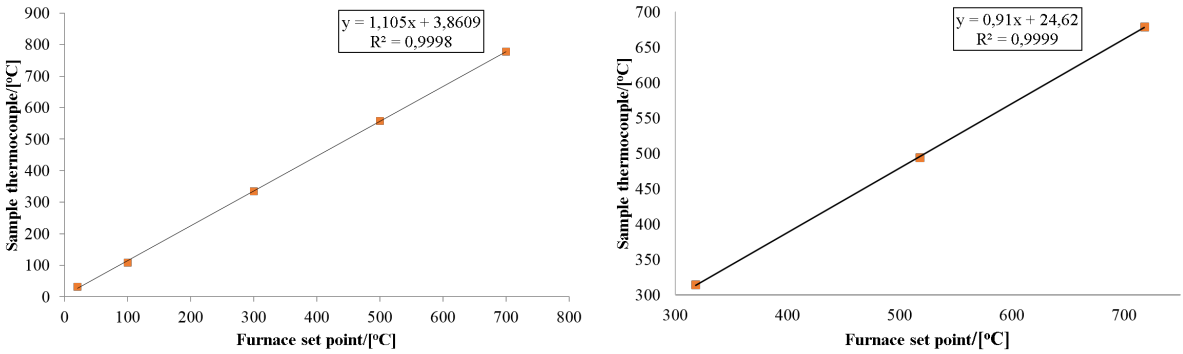

(a) VCTF1 Furnace

(b) VCTF4 furnace

Figure 3.16 Vectsar horizontal furnaces linear calibration (furnace set point versus Type K thermocouple measurements at the centre of reactor and heated length)

the temperature measured at the furnace thermocouple was or not the same as the furnace set point respectively.

Figure 3.16 shows the calibration obtained for the VCTF1 and VCTF4 furnaces. The y-axis represents the average temperature measured by the external thermocouple over a period of time (30min after the furnace reached the set point) and the x-axis the temperature fixed as set-point. All the temperatures in this thesis referred to the one measured at the centre of the reactor, calculated using the linear regression obtained in this calibration and shown in Figure 3.16. This calibration was repeated periodically to ensure it was valid and to detect any possible defects of the furnaces.

Chapter 4 Kinetic model of municipal plastic waste

Chapter 4 explores the thermal behaviour of plastic waste during pyrolysis via the development of a kinetic model for municipal plastic waste (HDPE, LDPE, PP, PET and PS) pyrolysis. Despite kinetic studies being popular in literature, only a few compile information about all the main plastic waste types like this one. In addition, most studies on this topic oversimplified the mechanism by assuming first order decomposition, leading to inaccurate predictions. This model was developed based on experimental data (thermogravimetric analysis (TGA)) and numerical calculations using Matlab. Unlike most kinetic studies in literature, this model used exhaustive methods (Kissinger–Akahira–Sunose, KAS, Málek method and linear model fitting) and validation through experimental data to obtain the full kinetic triplet (activation energy, pre-exponential factor and decomposition model) and predict the mechanism of municipal plastic waste (MPW) pyrolysis. All components in MPW were decomposed in N_2 atmosphere over various heating rates (5-40 °C/min), temperatures (30-700 °C) and for sample particle size 1–4 mm. Variation of the apparent activation energy with conversion and heating rate confirmed MPW thermal decomposition occurred via a mixture of series and parallel reactions as opposed to the simple 1^{st} order reaction proposed in literature. Predicted rate of reaction for all MPW obtained with the apparent activation energy results from linear model fitting agreed well with experimental data for heating rates <40 °C/min. The work presented in this chapter has been published in "Kinetic study of municipal plastic waste" at *International Journal of Hydrogen Energy* (Diaz-Silvarrey and Phan, 2016).

4.1 Kinetic model background

The kinetic model predicts the behaviour of MPW during thermal pyrolysis based on the calculation of the rate of reaction. The rate of a solid-state reaction (dα/dt), such as MPW pyrolysis, represents the instantaneous fraction of reacted material at each period of time and is expressed by Equation (4.1):

$$\frac{d\alpha}{dt} = k(T)\, f(\alpha) \tag{4.1}$$

where α is the reacted fraction or conversion, $k(T)$ a mathematical function of temperature and $f(\alpha)$ a mathematical expression of the conversion called kinetic model.
The function of the temperature in Equation (4.1) follows Arrhenius law as expressed by Equation (4.2):

$$k = A\ e^{(-Ea/RT)} \tag{4.2}$$

where k is reaction rate constant (s^{-1}), A the pre-exponential factor (s^{-1}), E_a the activation energy (J/mol), R the universal gas constant (8.314 J/mol·K) and T the temperature (K).
For a non-isothermal process at constant heating rate (β = dT/dt = constant), Equation (4.1) becomes Equation (4.3):

$$\frac{d\alpha}{dT} = \frac{A}{\beta}\ e^{(-E_a/R\ T)}\ f(\alpha) \tag{4.3}$$

where $d\alpha$/dT is the reaction rate under non-isothermal conditions and β the heating rate (°C/s or K/s).
Obtaining the kinetic triplet i.e. activation energy (E_a), pre-exponential factor (A) and kinetic model ($f(\alpha)$), allows the prediction of MPW pyrolysis reaction rate outside the experimental range tested. Several studies reported kinetic triplets for individual plastic types (Grammelis et al., 2009; Sorum et al., 2001; Westerhout et al., 1997; Wu et al., 1993) while a few others developed kinetic studies on simple binary and tertiary MPW mixtures (Albano and de Freitas, 1998; Bockhorn et al., 1999; Garcia et al., 1995; Hujuri et al., 2008; Kayacan and Dogan, 2008). The results were generally scattered and inconsistent. Simple decomposition mechanism (first order) and single heating rate experiments were used (Grammelis et al., 2009; Sorum et al., 2001) to obtain the kinetic triplet despite being inadvisable practices (Vyazovkin et al., 2011), leading to inexact results (Perez-Maqueda et al., 2014).
Modelling MPW thermal decomposition is not a simple task due to the complexity of the reaction mechanism. Hujuri et al. (2008) reported that a first order model (Equation 4.4) oversimplified MPW thermal decomposition because interactions between the residue and pyrolysis products varied the apparent activation energy as reaction proceeded. Vyazovkin et al. (2011) explained that variation due to the residue becoming more refractory and interfering with non-reacted MPW as temperatures increased.

$$Polymer \xrightarrow{k} Products \tag{4.4}$$

According to Simha and Wall (1952) MPW thermal decomposition mechanism follows a random chain scission. By using Simha & Wall, Vyazovkin (2015) predicted the reaction rate as a function of the fraction of broken bonds according to Equation (4.5):

$$\frac{dx}{dt} = A\ e^{(-E_a/R\ T)}\ (1-x) \tag{4.5}$$

where x is the fraction of broken bonds and dx/dt the rate of bond breaking.
However, the fraction of broken bonds (dx/dt) cannot be experimentally determined, limiting the applicability of Simha & Wall model. Sánchez-Jiménez et al. (2010) developed a correlation between dx/dt and α as presented in Equation (4.6):

$$\alpha = 1 - (1-x)^{L-1}\ [1 + x(L-1)] \tag{4.6}$$

where x is the fraction of broken bonds, L the number of monomer units in the shortest non volatilised chain fragment before further decomposition and α the fraction of reacted MPW or conversion.
Only at L=2, Equation (4.6) is simplified in such a way that x can be rewritten as a function of α to yield Equation (4.7). For L = 3 - 8, the relationship between x and α (Equation 4.6) has no symbolic solution and they can only be graphically/numerically correlated.

$$\alpha = 1-(1-x)(1+x) \quad \rightarrow \quad \alpha = 1-(1-x^2) \quad \rightarrow \quad x = \alpha^{1/2} \tag{4.7}$$

Combining Equations (4.7) and (4.5) for L=2 Sánchez-Jiménez et al. (2010) obtained Equation (4.8) that determines the reaction rate of MPW thermal decomposition:

$$\frac{d\alpha}{dt} = A\, e^{(-E_a/R\,T)}\, 2\, \left(\alpha^{1/2}-\alpha\right) \tag{4.8}$$

4.2 Modelling methodology

Westerhout et al. (1997) proved that non-oxidative thermal decomposition behaviour of HDPE, LDPE, PP and PS mixtures was similar to that of individual MPW. Hence, MPW mixtures can be simulated applying additive rule as presented in Equation (4.9):

$$\frac{d\alpha}{dt}_{mixture} = x_1\left(\frac{d\alpha}{dt}\right)_1 + x_2\left(\frac{d\alpha}{dt}\right)_2 + \ldots + x_n\left(\frac{d\alpha}{dt}\right)_n \tag{4.9}$$

where $(d\alpha/dt)_{mixture}$ represents the reaction rate of the MPW mixture, $(d\alpha/dt)_n$ the reaction rate of the n^{th} individual MPW and x_n the mass fraction the n^{th} individual MPW in the mix.
A four-step process was developed to obtain the kinetic triplet for individual MPW as shown in Figure 4.1, based on recommendations from The International Committee for Thermal Analysis and Calorimetry (ICTAC) (Vyazovkin et al., 2011). Knowing of the kinetic triplet, the reaction rate ($d\alpha/dt$) of each individual MPW was calculated with Equations (4.1) and (4.2).
Raw data from TGA analysis (obtained as described in section 3.1.1 in chapter 3) was carried at four heating rates (5, 10, 20 and 40 °C/min) to obtain weight loss, W (%), derivative weight loss, dW/dt (%/min) and heat flow, HF (mW) versus temperature, T (°C). Mass, m_i and reacted fraction, α were calculated by Equations (4.10) and (4.11) respectively.

$$m_i = W \cdot m_0 \tag{4.10}$$

$$\alpha = \frac{m_0 - m_i}{m_0 - m_f} \tag{4.11}$$

where m_0, m_i and m_f are the initial, remaining and final mass of individual MPW (g).
α versus temperature data from TGA analysis was then processed by two isoconversional methods: Kisinger-Akahira-Sunose (KAS) and Friedman to evaluate the apparent activation energy (E_a) and the apparent pre-exponential factor (A). Isoconversional methods are based on

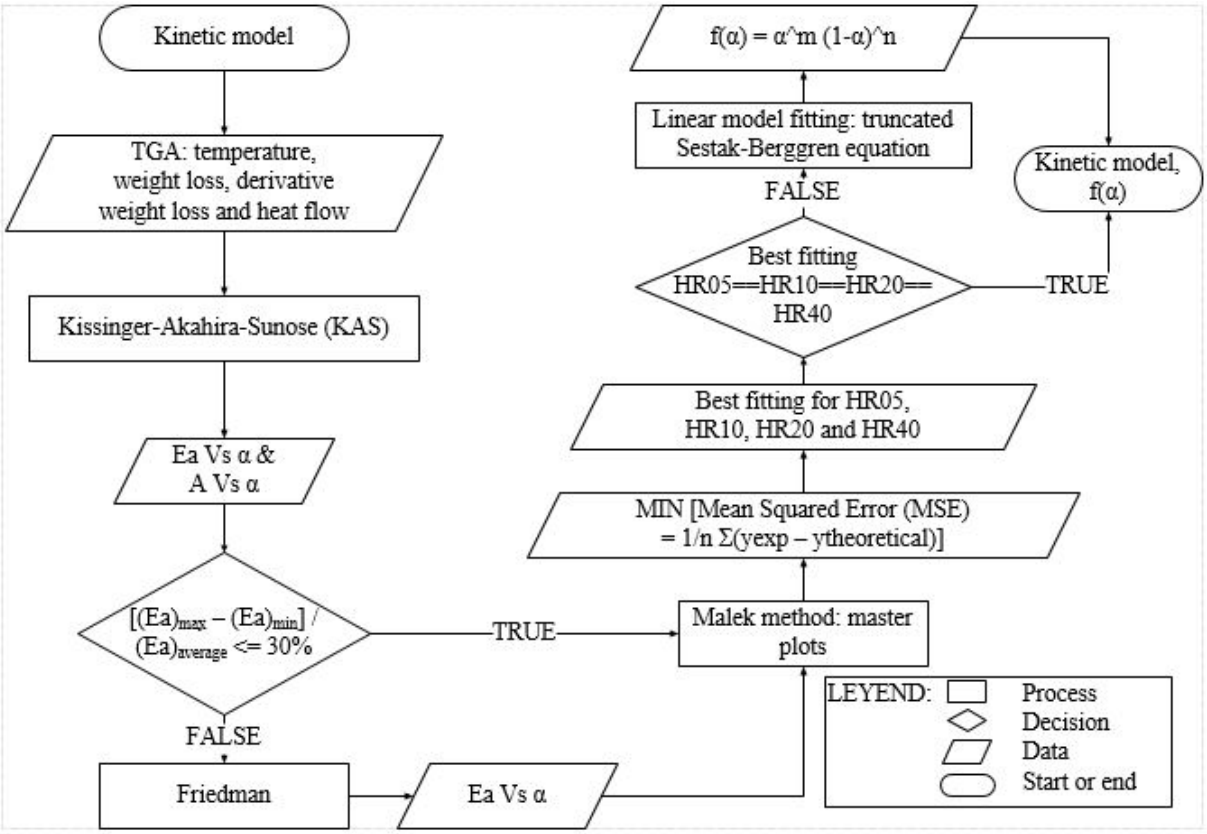

Figure 4.1 Steps to develop a kinetic model

the principle that when a certain amount of material has reacted (constant conversion, α) the reaction rate only depends on the temperature (Vyazovkin, 2006). As explained in Figure 4.2, at a certain extent of reaction (e.g. α_2), the rate of reaction (dα/dt) only changes with the heating rate (β_i).

KAS is one of the most popular isoconversional methods along with Flynn-Wall-Ozawa (FWO) and Friedman (Sbirrazzuoli et al., 2009; Vyazovkin et al., 2011). Of the three KAS is the easiest, most popular and the most accurate one (Vyazovkin et al., 2011) and therefore, was the selected one for the development of the model.

KAS equation is obtained by integration of Equation (4.3) at constant extents of conversion (Equation 4.12):

$$g(\alpha) = \int_0^{\alpha} \frac{d\alpha}{f(\alpha)} = \frac{A}{\beta} \int_0^{T} e^{(-E_a/R\,T)}\, dT \tag{4.12}$$

where g(α) is the integral form of the kinetic model, f(α).

The integral on the right side has no analytical solution. To approximate the value of that integral, the reduced activation energy ($c = E_a/R\,T$) is applied, yielding Equation (4.13):

$$g(\alpha) = \frac{A\,E_a}{\beta\,R} \left[\frac{e^{-c}}{c} - \int_c^{\inf} \frac{e^{-c}}{c} \right] = \frac{A\,E_a}{\beta\,R}\, p(c) \tag{4.13}$$

where c and p(c) are the reduced activation energy and an approximation of the integral in the right side of Equation (4.12).

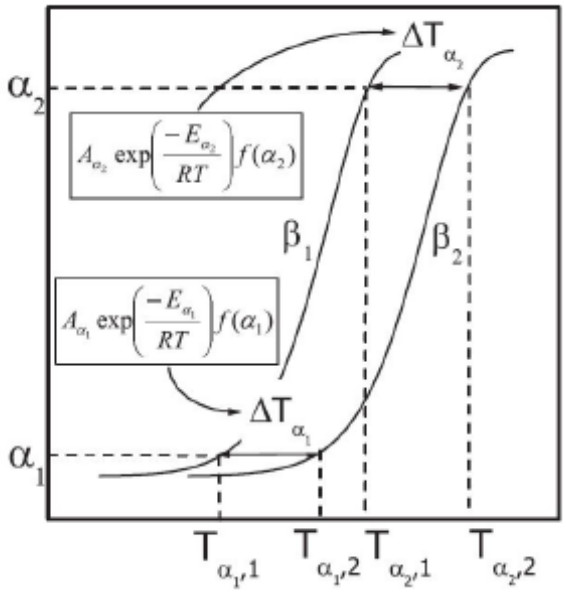

Figure 4.2 Isoconversional method (Vyazovkin, 2006)

KAS applies Murray and White approximation: $p(c) = e^{-c}/c^2$ with 20<c<50, producing Equation (4.14):

$$ln\left(\frac{\beta_i}{T_{\alpha,i}^2}\right) = ln\left(\frac{A_\alpha\, R}{E_{a,\alpha}}\right) - ln(g(\alpha)) - \left(\frac{E_a}{R\, T_{\alpha,i}}\right) \tag{4.14}$$

where β_i represents heating rate (K/s or °C/s), $T_{\alpha,i}$ the temperature of reaction at constant α for each of the β_i heating rates (K), $E_{a,\alpha}$ the apparent activation energy (J/mol), A_α the apparent pre-exponential factor (s^{-1}), $g(\alpha)$ the integral form of the kinetic model and R the universal gas constant (8.314 J/mol·K).

For a constant α, plots of the left side of Equation (4.14) i.e. $ln(\beta_i/T_{\alpha,i}^2)$ against the reciprocal of reaction temperature for all heating rates tested yields KAS linear plots. KAS linear plot are parallel line which correspond to each value of α and they are formed by as many points as heating rates tested. The apparent activation energy is obtained from the slope of KAS linear plots. Since $ln(g(\alpha))$ in Equation 4.14 is negligible compared to $ln\left(\frac{A_\alpha\, R}{E_{a,\alpha}}\right)$, the pre-exponential factor (A) was determined from the intercept of KAS linear plots.

Finally, the kinetic model ($f(\alpha)$) was determined by applying master plots, or Málek method, and linear model fitting. Master plots or Málek method is a very popular fitting method used for kinetic model determination. It consists of two master plots figures: one ($y(\alpha)$) based on Equation (4.15) and the other ($z(\alpha)$) on Equation (4.16). $y(\alpha)$ master plot is obtained rearranging Equation (4.1). $z(\alpha)$ master plot is obtained from a combination between Equations (4.1) and (4.13) (Málek, 1992; Vyazovkin, 2015).

$$y(\alpha) = \left(\frac{d\alpha}{dt}\right)_\alpha exp\left(\frac{E_{average}}{R\, T_\alpha}\right) = A\, f(\alpha) \tag{4.15}$$

$$z(\alpha) = f(\alpha)\ g(\alpha) = \left(\frac{d\alpha}{dt}\right)_{\alpha} T_{\alpha}^{2} \left[\frac{\pi(c)}{\beta\ T_{\alpha}}\right] \tag{4.16}$$

where $(d\alpha/dt)_{\alpha}$ is the reaction rate at conversion (α), $E_{average}$ and A the average apparent activation energy and pre-exponential factor obtained from isoconvensional methods (J/mol), R the universal gas constant (8.314 J/mol·K), $f(\alpha)$ a mathematical expression of conversion along the reaction, $g(\alpha)$ the integral form of $f(\alpha)$, T_{α} the reaction temperature at a constant α (K), β the heating rate (°C/s or K/s), c the reduced activation energy ($c = E_a/R\ T$) and $\pi(c)$ a mathematical expression used to approximate the value of the integral in the right side of Equation (4.13).

The middle term in Equation (4.15) ($(d\alpha/dt)_{\alpha}\ e^{E_{average}/R\ T_{\alpha}}$) represents the experimental values of the $y(\alpha)$ master plot. This term was calculated from experimental values of $(d\alpha/dt)_{\alpha}$ and T_{α} from TGA analysis at constants values of α along with the average E_a from isoconversional methods. Theoretical values of $y(\alpha)$, right side of Equation (4.15) ($A\ f(\alpha)$), were calculated by inserting different values of α into the theoretical expressions of $f(\alpha)$ illustrated in Table 4.1 for various theoretical kinetic models.

Table 4.1 Kinetic models most commonly used in solid state reactions (Vyazovkin et al., 2011)

Reaction model	Code	$f(\alpha)$
Power law (n = 2, 3, 4)	Pn	$n\ (\alpha)^{(n-1)/n}$
Random scission	RS	$2\ (\alpha^{1/2} - \alpha)$
Mampel (First order)	F1	$(1-\alpha)$
n^{th} order (n = 0.5, 2, 3)	Fn	$(1-\alpha)^{n}$
Avrami-Erofeev (nuclei growth) (n = 2, 3, 4)	An	$n\ (1-\alpha)\ (-ln(1-\alpha))^{(n-1)/n}$
One-dimensional diffusion	D1	$1/2\ \alpha^{1/2}$
Two-dimensional diffusion	D2	$(-ln(1-\alpha))^{-1}$
Three-dimensional diffusion (Jander equation)	D3	$3/2\ (1-\alpha)^{2/3}\ (1-(1-\alpha)^{1/3})^{-1}$
Contracting cylinder (contracting area)	R2	$2\ (1-\alpha)^{1/2}$
Contracting sphere (contracting volume)	R3	$3\ (1-\alpha)^{2/3}$

Both the theoretical and experimental values of $y(\alpha)$ were normalized to ease comparison so all the values range form 0 to 1 by feature scaling method (Equation (4.17)).

$$y'(\alpha) = \frac{y(\alpha) - y(\alpha)_{min}}{y(\alpha)_{max} - y(\alpha)_{min}} \tag{4.17}$$

where $y'(\alpha)$ corresponds to the normalized value, $y(\alpha)$ the experimental or theoretical value calculated as aforementioned, $y(\alpha)_{min}$ and $y(\alpha)_{max}$ the minimum and maximum value obtained respectively.

The $f(\alpha)$ selected was the one with minimum variance between the normalized theoretical and experimental $y(\alpha)$. The variance was measured by mean squared error (MSE) which is represented in Equation (4.18).

$$MSE(\%) = 100 * \frac{1}{j} \sum_{i=1}^{j} (y(\alpha)_{experimental} - y(\alpha)_{theoretical})^2 \tag{4.18}$$

where j is the length of the α vector studied e.g. 0.2<α<0.8, and y(α)$_{experimental}$ and y(α)$_{theoretical}$ are the experimental and theoretical values of y(α) respectively.
Experimental z(α) master plot values were calculated inserting only the experimental values of (dα/dt) and T_α in the right side of Equation (4.16) ($(d\alpha/dt)_\alpha \; T_\alpha^2 \; [\pi(c)/\beta \; T_\alpha]$) because the term $[\pi(c)/\beta \; T_\alpha]$ has no influence upon the shape of z(α) master plots. Theoretical values of z(α) were estimated by multiplying theoretical values of f(α) from Table 4.1 by the function g(α) defined by Equation (4.19).

$$g(\alpha) = \int_0^\alpha \frac{1}{f(\alpha)} \, d\alpha \tag{4.19}$$

where g(α) represents the integral from of f(α) and f(α)the kinetic model or mathematical function of α illustrated in Table 4.1.
Linear model fitting method applies linear regression techniques to Equation (4.1) to determine the kinetic model. For a general mechanism of reaction, Equation (4.1) can be represented as Equation (4.20) when $f(\alpha)$ is substituted by truncated Sestak-Berggren equation ($\alpha^m \; (1-\alpha)^n$).

$$\frac{d\alpha}{dt} = k \; f(\alpha) \;\; where \;\; f(\alpha) = C \; \alpha^m \; (1-\alpha)^n \tag{4.20}$$

where dα/dt is the reaction rate, k the reaction rate constant, α the conversion, f(α) a mathematical function of α, C an agglomeration of all constant values, n the order of reaction and m the order of nucleation.
The Truncated Sestak-Berggren equation (TSB) is a generalised form of any solid-state reaction mechanism such as MPW pyrolysis. For instance, when m = 0 and n = 1, TSB equation becomes $f(\alpha) = (1-\alpha)$ which corresponds to the first order reaction model. Therefore, different pairs of values of n and m in TSB equation yield all the theoretical models illustrated in Table 4.1. In addition, unlike master plots, the TSB equation is versatile to select values of n and m that may not be represented in Table 4.1 and therefore considered in Málek method.
In order to obtained the kinetic model from TSB equation, Equation (4.20) needs to be rearranged and linearised to obtain Equation (4.21).

$$ln\left(\frac{d\alpha}{dt} \; \frac{1}{\alpha^m \; (1-\alpha)^n}\right) = ln \; (C \; A) - \frac{E_a}{R \; T} \tag{4.21}$$

The model developed tested various n and m pairs of values into Equation (4.21) to produce a straight line with each pair when the left side of Equation (4.21) ($ln[(d\alpha/dt) \; 1/(\alpha^m \; (1-\alpha))^n]$) was plotted against the reciprocal temperature from TGA analysis. Each singular line obtained with each n and m pair is associated with a Pearson linear correlation coefficient to measure the goodness of the correlation. Since the slope of the linear plots was negative the maximum possible value of this coefficient was -1. Therefore, the selected pair of n and m, and thus the

correct kinetic model f(α), where those with the Pearson linear correlation coefficient closer to -1 (Vyazovkin et al., 2011).
Appendix A includes the Matlab code developed applying the kinetic methods describe in this section in order to obtain the kinetic triplet of MPW.

4.3 Results and discussion

4.3.1 Thermogravimetric analysis (TGA)

As shown in TGA plots i.e. W against T (Figure 4.3), all MPW presented a single weight loss step but the temperature range for that step shifted to higher temperatures as follows: PS < PET < PP < LDPE < HDPE. The shift was caused by the different structure of MPW. Substitution groups (-Ph in PS and -CH_3 in PP) provide weaker C-C bonds than those in linear MPW (HDPE and LDPE) meaning the former thermally decompose at lower temperatures. PET has a different structure as it is a polyester and the cleavage occurs at the ester group which again needs lower temperature than C-C bonds in both PEs. PP data at 20 °C/min was found not reliable due to lack of reproducibility despite multiple repetitions and therefore it was removed from the model. The residue remaining for each MPW at 700 °C was: 25-30 % for HDPE and PET and 0 % for LDPE, PP and PS. The difference was because of higher ash content of PET and HDPE than the other MPW (table 3.2 in chapter 3). Although PS residue was slightly below 0% due to the systematic error in Perkin Elmer STA6000 balance at low mass samples (PS initial mass = 1.672 - 1.714 mg), it was considered as 0 mg for further analysis.
Figure 4.4 represents DTG plots i.e. dW/dt versus T, for all MPW. Peak height increased with both heating rate and MPW type following the same trend as TGA plots: 40 °C/min > 20 °C/min > 10 °C/min > 5 °C/min and HDPE > LDPE > PP > PET > PS. Higher peaks indicated easier, more rapid decomposition thus, with lower energy requirements. Peak width represents the temperature range where MPW decomposed. When heating rate doubled, peak width increased around 20 °C. This pattern was equally followed by all MPW. DTG plots at 40 °C/min showed different peak shape implying different mechanism of reaction at low an high heating rates i.e. threshold between slow and fast pyrolysis.
The variance in the peak height observed in Figure 4.4 points to the dependency between the nature of plastic waste and their thermal behaviour. This means that the additives in plastic waste added to alter the properties of plastic products affect their thermal behaviour and, thus, it may have an effect during plastic waste pyrolysis. This signifies the importance of using plastic waste rather than virgin materials in further experiments in order to evaluate the real potential of the technologies studied. This opens up further work to study the effect of additives in plastic waste thermal behaviour via comparison of the kinetic triplet obtained using several different plastic waste products for each plastic waste type.
Figure 4.5 shows the variation of HF versus T. High heating rates (> 20 °C/min) presented a larger perturbation of the heat flow within MPW decomposition temperature range than low heating rates (< 20 °C/min). That perturbation was explained due to the low thermal

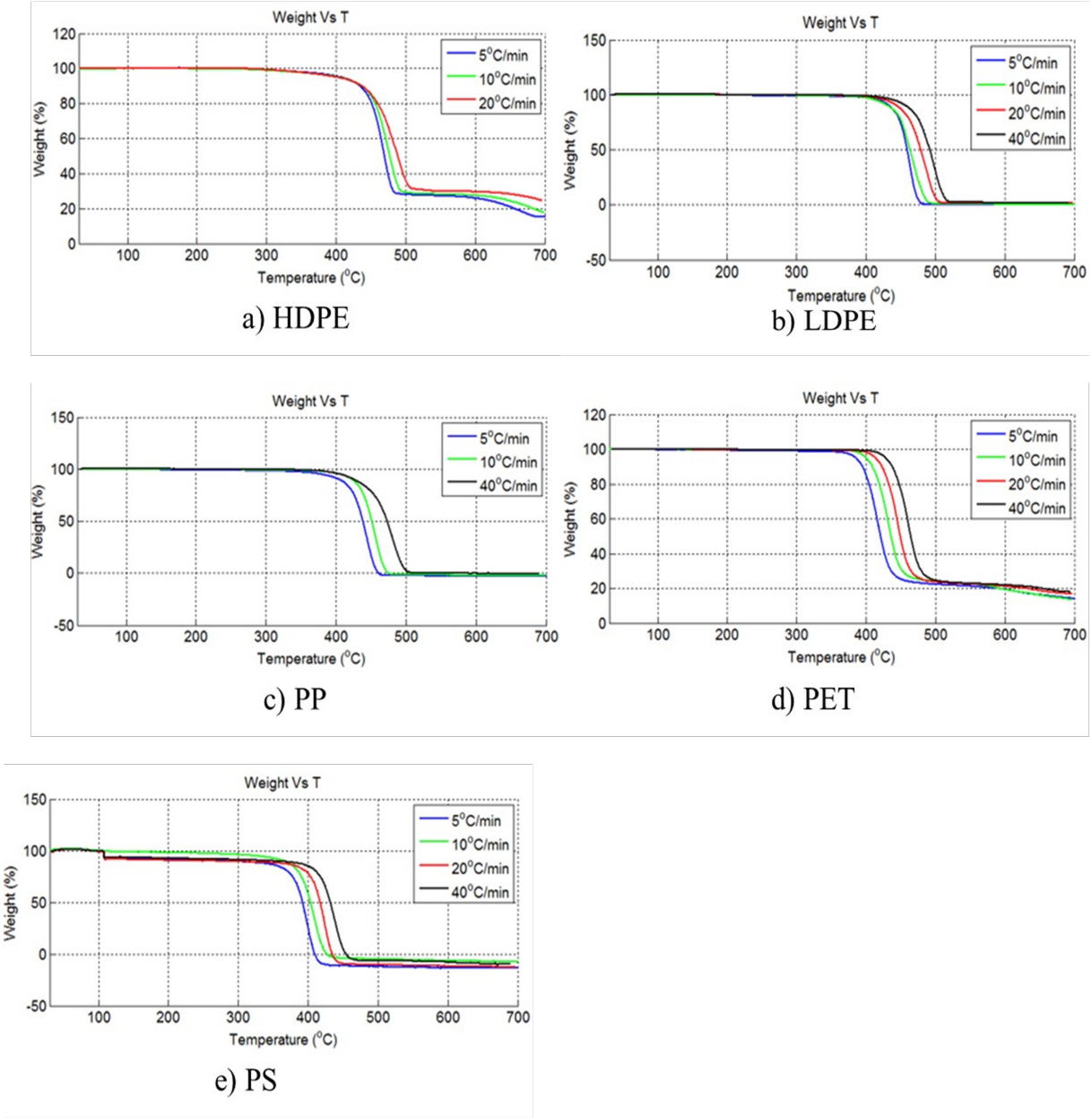

Figure 4.3 Weight loss (%) against temperature (°C) for (a) HDPE, (b) LDPE, (c) PP, (d) PET and (e) PS at 5 (blue), 10 (green), 20 (red) and 40 (black) °C/min between 30-700 °C

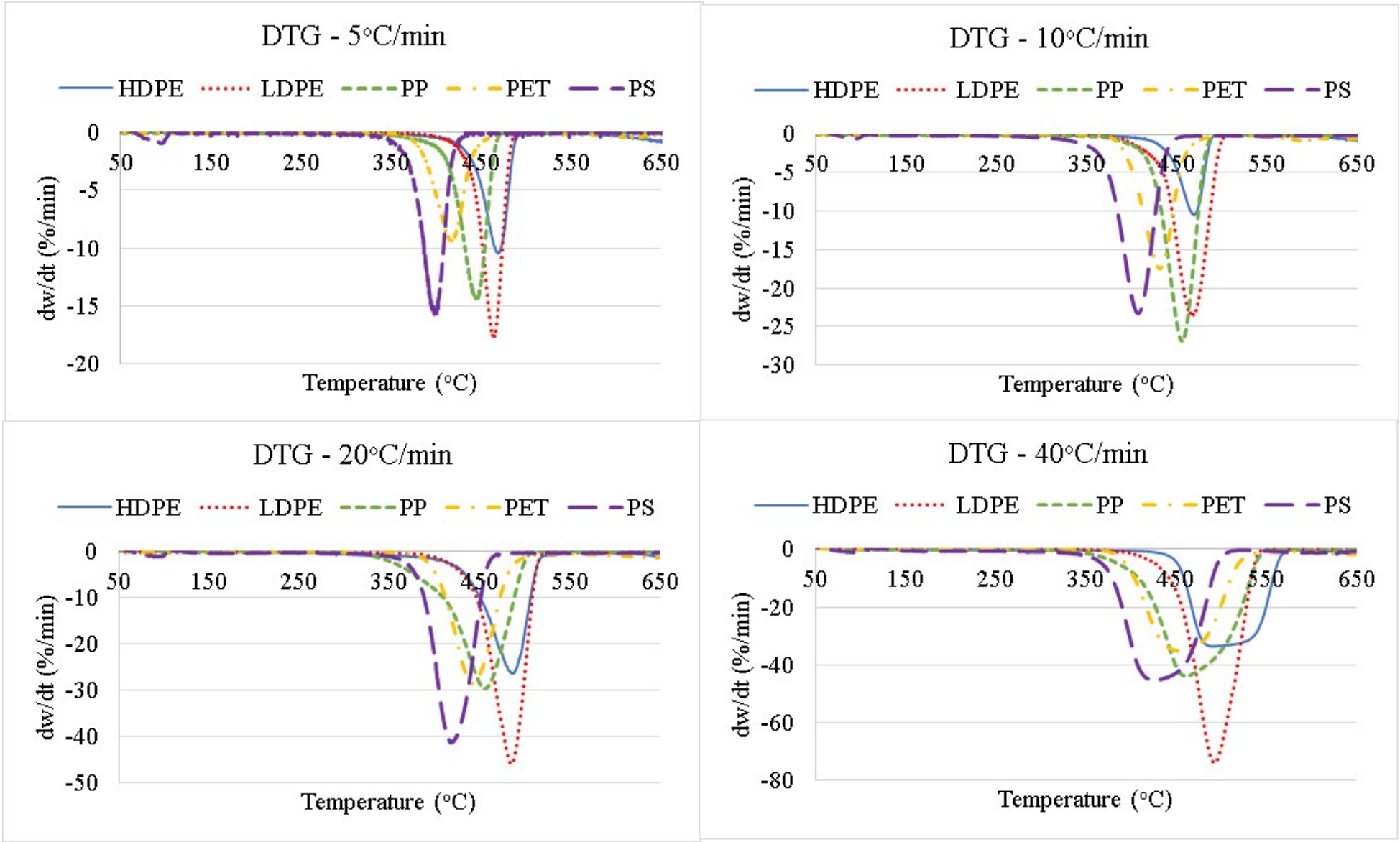

Figure 4.4 Derivative weight loss (DTG) versus temperature for (a) HDPE, (b) LDPE, (c) PP, (d) PS and (e) PET at 5, 10, 20 and 40 °C/min between 30-700 °C

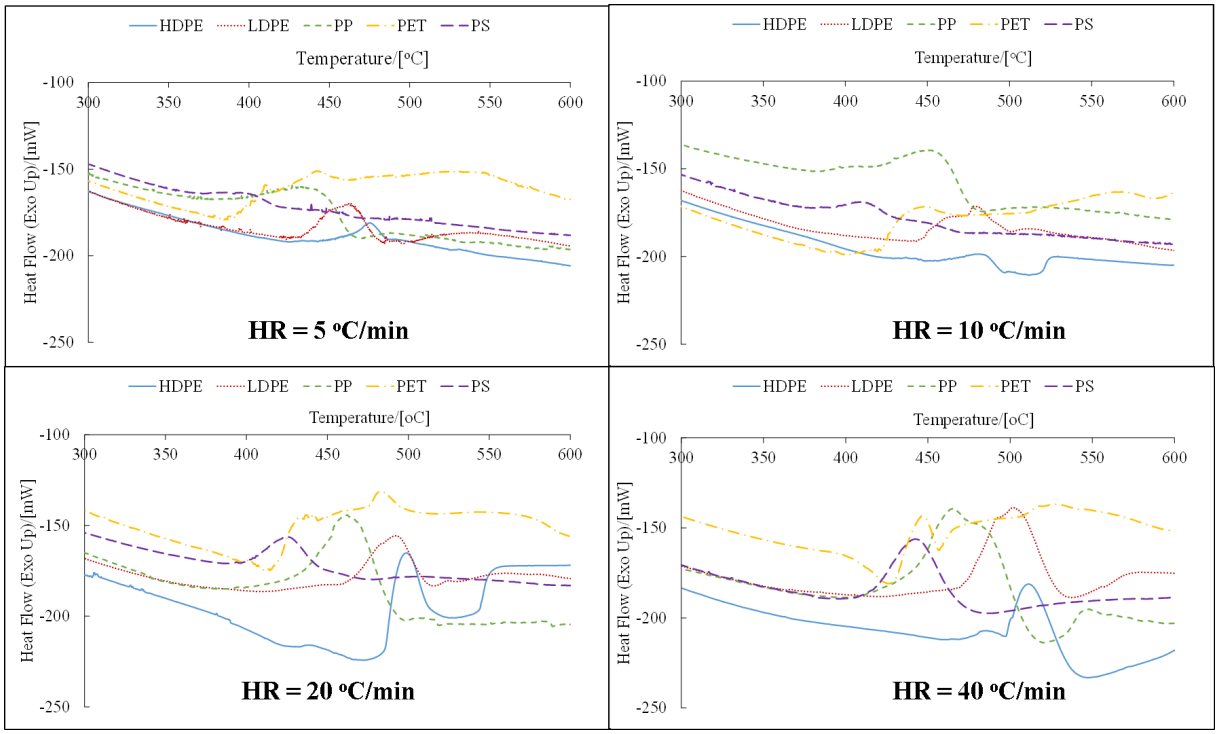

Figure 4.5 Heat flow against temperature for HDPE (blue), LDPE (red), PP (green), PET (yellow) and PS (purple) at 5, 10, 20 and 40 °C/min between 300-600 °C

conductivity of MPW. As heating rate increases, there was a less uniform heat distribution causing a temperature profile on individual particles and that perturbation. At a given instant of time at high heating rates, only part of MPW particles are melt due to the temperature profile. Therefore, there was a rapid partial thermal decomposition of the melted MPW particles while the remaining decomposed at a lower rate over longer time as part of that heat was transferred to cooler, non-melted fraction of MPW particles. The latter suggested heating rate plays a relevant role for future MPW pyrolysis experiments.

Pyrolysis temperature for experiments discussed in chapters 5 to 8 was set based on TGA results. The minimum pyrolysis temperature was selected to ensure more than 20 % MPW decomposition whereas the maximum pyrolysis temperature was selected to obtain complete MPW decomposition.

4.3.2 Isoconversional methods: Kissinger-Akahira-Sunose and Friedman

Figure 4.6 shows seven of the KAS linear plots obtained to illustrate how KAS method was applied. The model plots one line for each value α between 0.2 and 0.8 at a 0.01 interval. The apparent E_a and A were calculated as the average of all the slopes and intercepts of KAS linear plots and are shown in Figure 4.7.

Figure 4.7 shows no variation depending on the heating rate i.e. blue, green, red and black lines are superimposed. However, the results from KAS showed variation of E_a with α implying MPW pyrolysis consisted on multiple parallel reactions occurring as the reaction proceeded. KAS method assumed that the apparent E_a did not significantly vary with the conversion

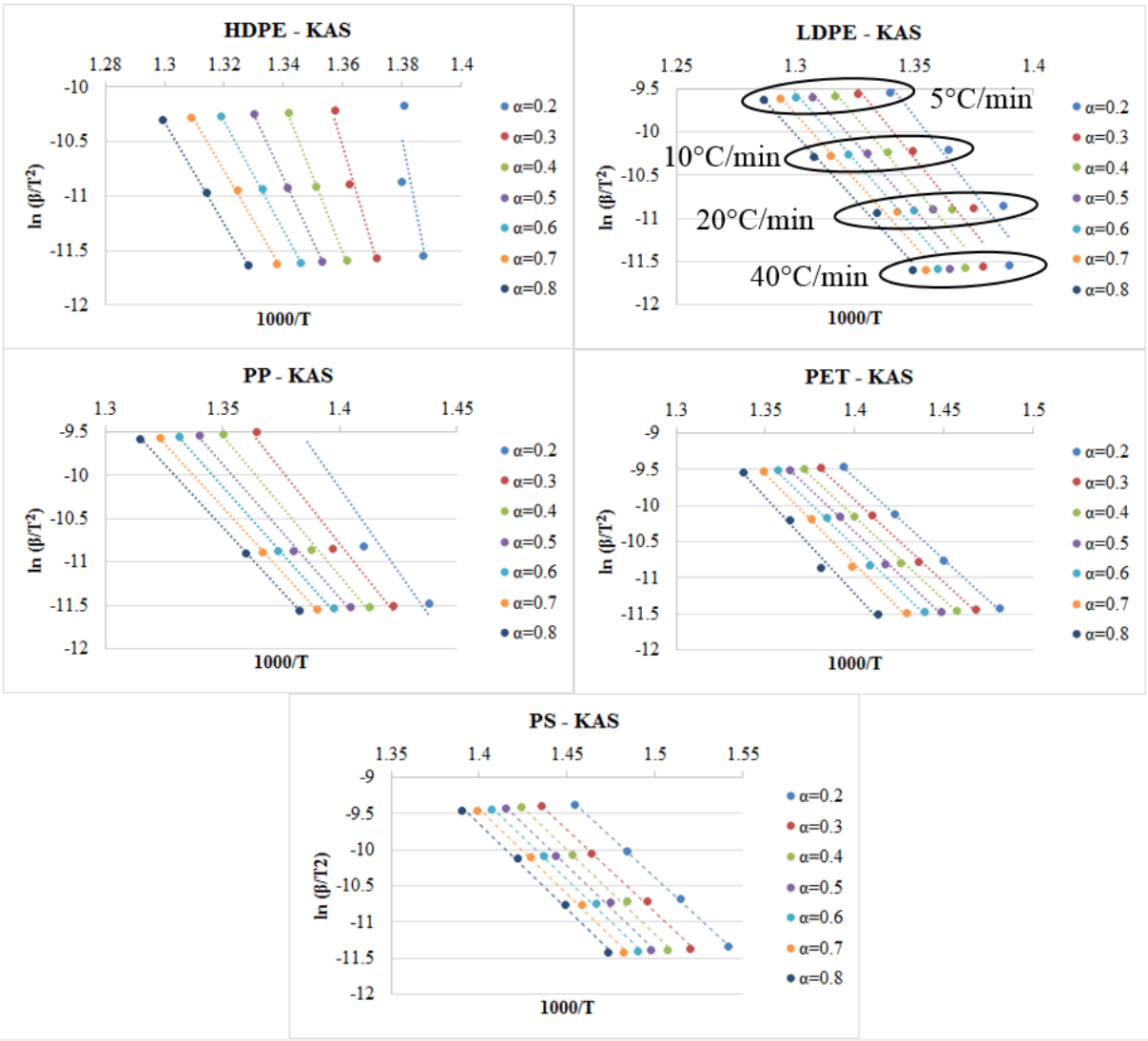

Figure 4.6 Kissinger-Akahira-Sunose linear plots for (a) HDPE, (b) LDPE, (c) PP, (d) PET and (e) PS

Table 4.2 Apparent activation energy and pre-exponential factor found in literature.

Literature values			
Reference	Polymer	E_a (kJ/mol)	A (s^{-1})
Sorum et al. (2001)	HDPE (virgin)	445.1	$4.34 \cdot 10^{12}$
	LDPE (virgin)	340.8	$3.51 \cdot 10^{9}$
	PP (virgin)	336.7	$4.29 \cdot 10^{9}$
	PS (virgin)	311.5	$3.05 \cdot 10^{9}$
Wu et al. (1993)	HDPE (virgin)	232.83	$1.17 \cdot 10^{6}$
	LDPE (virgin)	206.07	$1.76 \cdot 10^{5}$
	PP (virgin)	183.5	$4.90 \cdot 10^{4}$
	PS (virgin)	171.8	$4.44 \cdot 10^{4}$
Kayacan and Dogan (2008)	HDPE (virgin)	396 - 493	$9.04 \cdot 10^{11} - 1.58 \cdot 10^{13}$
	LDPE (virgin)	271 - 333	$4.10 \cdot 10^{7} - 5.05 \cdot 10^{8}$
Saha and Ghoshal (2005)	PET (waste drinking bottles)	162 - 339	$2.83 \cdot 10^{11}$ - $1.18 \cdot 10^{25}$

$(\frac{(E_a)_{maximum}-(E_a)_{minimum}}{(E_a)_{average}} < 0.3)$. HDPE presented higher variation of E_a versus α (around 60 %) therefore did not meet KAS assumption and was analysed via Friedman. The experimental data at 40 °C/min was rejected for Friedman analysis due to high level of noise.

Friedman method is similar to KAS. Apparent E_a was calculated from the slope of various plots of the left side of Equation (4.22) against the reciprocal temperature at several constant values of α.

$$ln\left(\frac{d\alpha}{dt}\right)_{\alpha,i} = ln(A_\alpha\ f(\alpha)) - \frac{E_a}{R\ T_\alpha, i} \tag{4.22}$$

where i represents the different heating rates studied and α the conversion. The value of f(α) can be neglected to obtain the pre-exponential factor (A) from the intercept of Friedman linear plots as A»>f(α) and so $ln(A\ f(\alpha)) = ln(A')$.

Literature values and the results obtained in this study for all polymers were compared in Tables 4.2 and 4.3. Table 4.3 shows that the apparent activation energy decreased with the following order HDPE>LDPE>PP>PET>PS as expected (Table 4.2). The only deviation observed was the apparent activation energy for HDPE using KAS method. This was caused by the fact that the data collected for HDPE did not did not meet KAS assumption as explained above. The expected pattern was observed for the values obtained using the Friedman method. Friedman results were also more similar to those already reported in literature (Table 4.2) compared to KAS results. The apparent E_a for HDPE, LDPE, PP, PET and PS obtained from KAS and the apparent E_a for HDPE obtained from Friedman are presented in Figure 4.8. HDPE exhibited a high variation for α<0.4 even using Friedman method, suggesting different mechanisms of reaction depending on how much HDPE has been decomposed. This variation can be explained by the formation of some residue which interfered with HDPE thermal decomposition at α>0.4. HDPE apparent E_a decreased from an average of 569.71 kJ/mol when α<0.4 to an average of 313.39 kJ/mol for α>0.4. The latter agreed well with the literature values reported by Sorum et al. (2001) (Table 4.2).

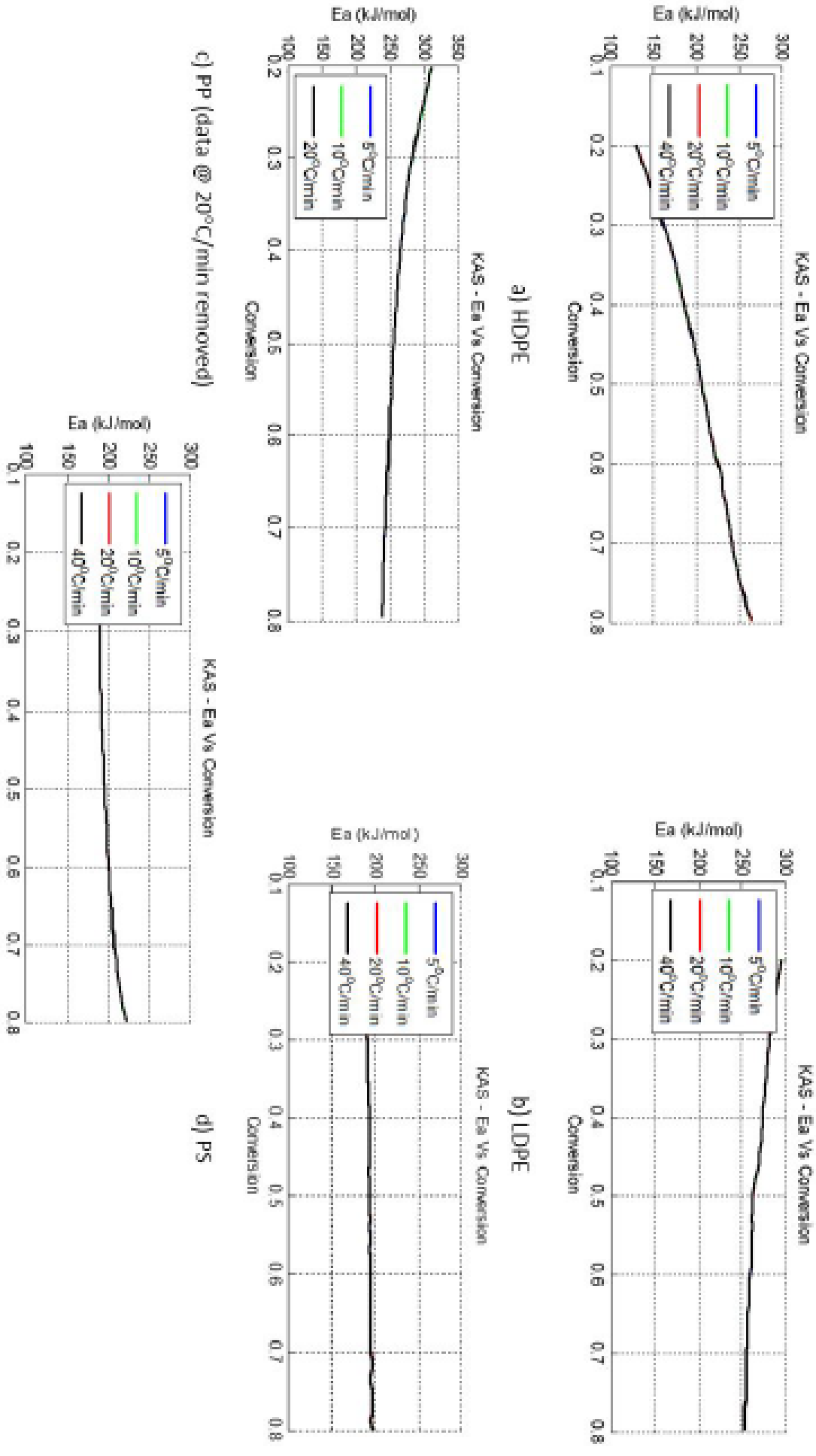

Figure 4.7 Variation of the apparent activation energy with conversion for (a) HDPE, (b) LDPE, (c) PP, (d) PS and (e) PET

Table 4.3 Average ± 95% confidence interval for apparent activation energy and pre-exponential factor.

KAS		
MPW	E_a± C.I. (kJ/mol)	A ± C.I. (s^{-1})
HDPE (0.2<α<0.8)	202.40 ± 9.47	$3.23 \cdot 10^{16} \pm 2.62 \cdot 10^{16}$
LDPE (0.2<α<0.8)	267.61 ± 3.23	$7.86 \cdot 10^{19} \pm 5.26 \cdot 10^{19}$
PP (0.2<α<0.8)	261.22 ± 5.13	$3.03 \cdot 10^{21} \pm 3.17 \cdot 10^{21}$
PET (0.2<α<0.8)	197.61 ± 2.27	$4.84 \cdot 10^{14} \pm 2.30 \cdot 10^{14}$
PS (0.2<α<0.8)	192.61 ± 0.76	$5.52 \cdot 10^{14} \pm 0.14 \cdot 10^{14}$
Friedman		
MPW	E_a± C.I. (kJ/mol)	A ± C.I. (s^{-1})
HDPE (0.2<α<0.8)	381.40 ± 38.80	$1.12 \cdot 10^{62} \pm 2.11 \cdot 10^{62}$
HDPE (α<0.4)	569.71 ± 78.04	$1.20 \cdot 10^{64} \pm 2.33 \cdot 10^{64}$
HDPE (α>0.4)	313.41 ± 8.62	$1.59 \cdot 10^{27} \pm 2.03 \cdot 10^{27}$
LDPE (0.2<α<0.8)	218.73 ± 6.28	$6.92 \cdot 10^{20} \pm 8.95 \cdot 10^{20}$
PP (0.2<α<0.8)	204.61 ± 14.29	$1.71 \cdot 10^{20} \pm 7.89 \cdot 10^{19}$
PET (0.2<α<0.8)	185.79 ± 5.71	$2.92 \cdot 10^{19} \pm 4.45 \cdot 10^{19}$
PS (0.2<α<0.8)	174.22 ± 7.71	$1.28 \cdot 10^{19} \pm 1.47 \cdot 10^{19}$

Comparison of Friedman results (Table 4.3) with those reported in literature (Table 4.2) showed some variation. This can be caused by the effect of the additives in plastic waste thermal behaviour. However, a similar difference was observed between values reported in literature for virgin polymers (Table 4.2). For example, Friedman method in this study found that for waste LDPE the E_a = 218.73 kJ/mol. Sorum et al. (2001) reported that for virgin LDPE E_a = 340.8 kJ/mol whilst Wu et al. (1993) showed an E_a = 206.07 KJ/mol for virgin LDPE and Kayacan and Dogan (2008) found that E_a = 271 - 333 kJ/mol also for virgin LDPE. This means that the additives in plastic products are only partially responsible for those deviations but there are other factors, yet unknown, that may also have a significant effect on the kinetic triplet of plastic products. As mentioned above, this uncertainty opens up further scope for research on the effect of additives to plastic waste behaviour.

4.3.3 y(α) and z(α) master plots for kinetic model, f(α)

Theoretical and experimental plots of y(α) against α represented in Figure 4.9 showed how experimental data fitted theoretical models. Table 4.4 summarises the best theoretical model that fitted each set of experimental data and the mean squared error for that fitting.
Results from y(α) master plot were scattered. The variation was found not only between MPW type but also between heating rates. As Málek method assumes single step decomposition with little variation of apparent E_a with α, all y(α) plots for each heating rate should be the same and overlap (Vyazovkin, 2015; Vyazovkin et al., 2011). However, as aforementioned and shown in Figure 4.8 this assumption was not met and thus, the method cannot be applied for this set of data.

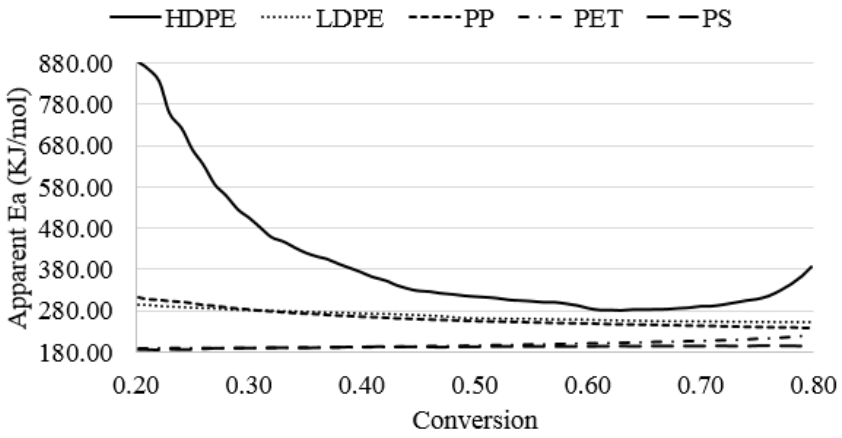

Figure 4.8 Comparison of apparent activation energy versus conversion obtained from KAS (LDPE, PP, PET and PS) and from Friedman (HDPE)

Figure 4.10 presents results of z(α) master plots which were more consistent between MPW and heating rates than y(α) master plot (Figure 4.9). Table 4.4 shows that random scission mechanism exhibited the best fitting between experimental and theoretical values for most cases, followed by second order Avrami-Erofeev. However, Avrami-Erofeev models describe crystallisation reactions (Vyazovkin, 2015) totally lacking from any physical meaning in regards to MPW thermal decomposition. DSC results (table 3.4 in chapter 3) showed that the melting point of all MPW was lower than onset temperature i.e. temperature where 10 % of total weight loss was achieved. Hence, all MPW melted and were in liquid not solid form when thermal decomposition started. Apart from the random scission model, the rest of theoretical f(α) in Table 4.1 were developed only for solid-state decompositions meaning their applicability to MPW thermal decomposition is limited (Vyazovkin, 2015).

It was observed in Figure 4.10 that both first order and Avrami-Erofeev models had a maximum at the same α and, when normalized, presented the same shape. As shown in Table 4.4, despite of the best fitting observed for HDPE, LDPE, PP and PS being Avrami-Erofeev, several theoretical models presented the same shape and thus, differentiation between them was random. Therefore, results cannot be admitted as conclusive.

Even though Málek method cannot be used to predict MPW thermal decomposition kinetic model, it can be concluded form the results that MPW thermal decomposition is not a simple mechanism. Instead, results suggested a multiple step mechanism similar to the one proposed in Figure 4.11. This mechanism agreed well with the one previously reported by Aguado et al. (2014*b*). Although via different methodology i.e. principal component analysis, Aguado et al. (2014*b*) concluded that HDPE thermal decomposition occurs by primary decomposition into waxes (C_{11+}) followed by secondary decomposition of the waxes into liquid (C_5-C_9), gas (C_1-C_4) and aromatics and final tertiary decomposition of aromatics into char.

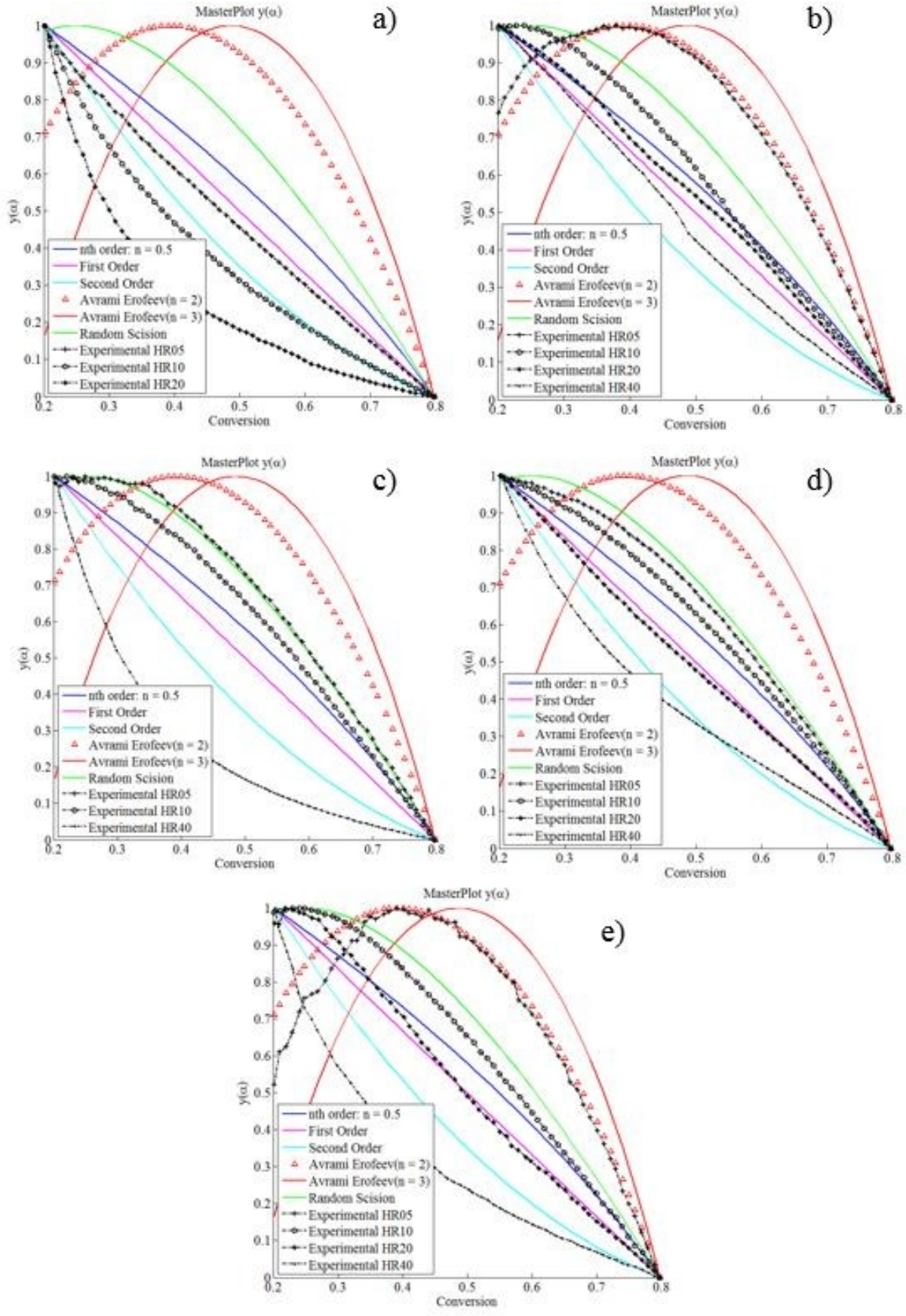

Figure 4.9 y(α) master plots for (a) HDPE, (b) LDPE, (c) PP, (d) PET and (e) PS

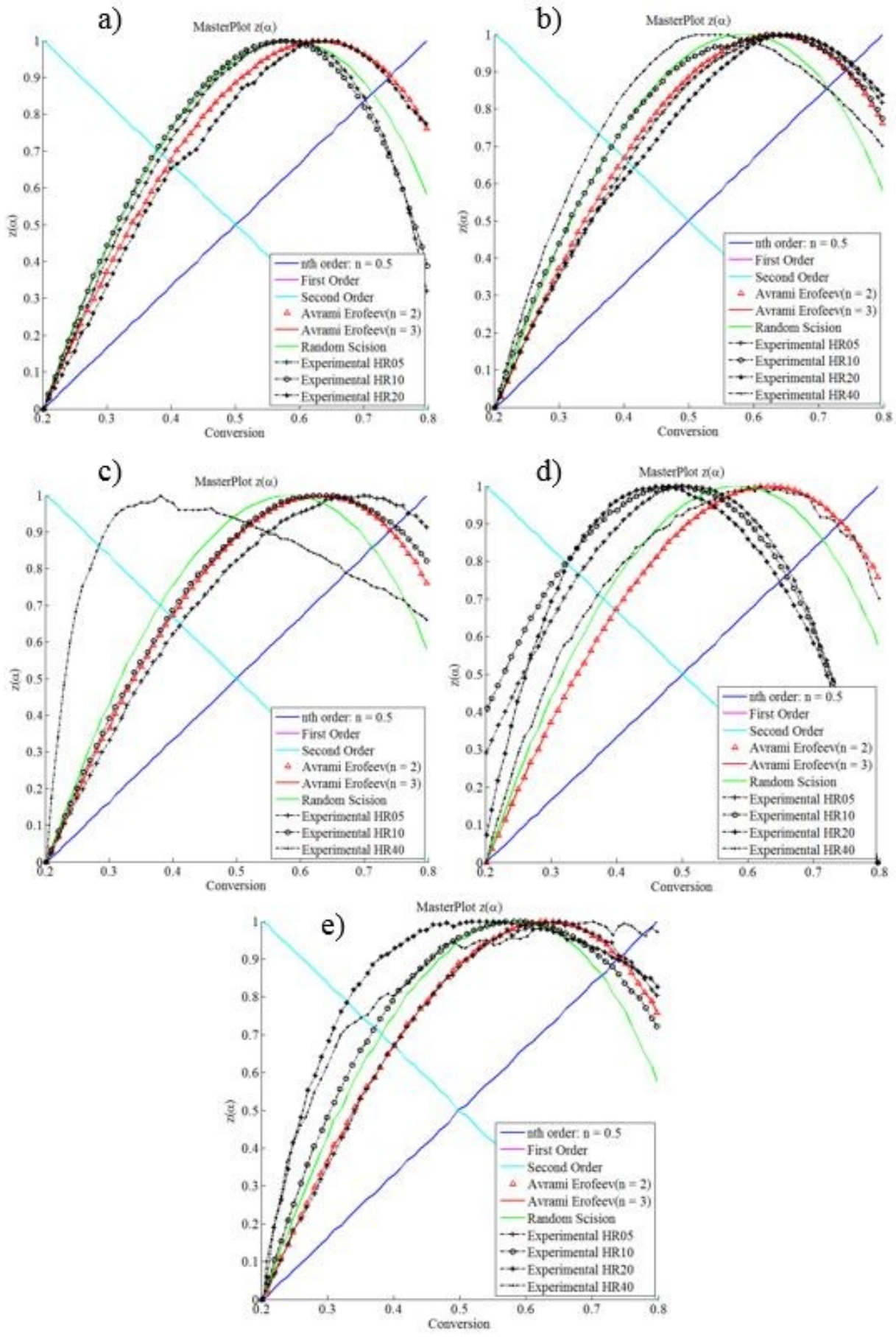

Figure 4.10 z(α) master plots for (a) HDPE, (b) LDPE, (c) PP, (d) PET and (e) PS

Table 4.4 Best Fitting between y(α) and z(α) theoretical and experimental master plots

y(α)				z(α)			
Plastic	β	Best Fitting f(α)	MSE(%)	Plastic	β	Best Fitting f(α)	MSE (%)
HDPE	5	F1	0.14	HDPE	5	RS	0.42
	10	F2	0.20		10	RS	0.32
	20	F2	2.71		20	A2	0.08
LDPE	5	A2	0.08	LDPE	5	F1	0.05
	10	F0.5	0.25		10	A2	0.21
	20	F0.5	0.08		20	A3	0.18
	40	F1	0.20		40	RS	0.35
PP	5	RS	0.01	PP	5	A2	0.33
	10	RS	0.24		10	A2	0.03
	40	F2	2.69		20	RS	5.85
PET	5	RS	0.09	PET	5	RS	5.35
	10	F0.5	0.15		10	RS	7.30
	20	F1	0.03		20	RS	6.20
	40	F2	0.20		40	RS	0.31
PS	5	A2	0.30	PS	5	A2	0.02
	10	RS	0.22		10	RS	0.21
	20	F1	0.13		20	RS	2.02
	40	F2	1.33		40	A2	1.90

4.3.4 Linear model-fitting method: Truncated Sestak-Berggren equation for kinetic model, f(α)

Table 4.5 illustrates the optimised values of n and m and the correspondent linear correlation Pearson coefficient obtained from linear model fitting and TSB equation (Equation (4.21)) as well as the resulting equation for MPW thermal decomposition (a is the intercept, $a = ln(A)$, and b the slope, $b = -E_a/R \cdot T$).

As mentioned in section 4.1, most literature on MPW thermal decomposition kinetics assumes first order reaction for all MPW but none present analytical confirmation. The results in Table 4.5 showed that LDPE, PP and PS order of reaction was close to first order. On the other hand,

Table 4.5 Truncated Sestak-Berggren equation results

Polymer	m	n	Pearson	Equation
HDPE	0.00	1.70	-0.9928	$ln[(d\alpha/dt)(1/(1-\alpha)^{1.70}] = a + b/T$
LDPE	0.00	0.95	-0.9968	$ln[(d\alpha/dt)(1/(1-\alpha)^{0.95}] = a + b/T$
PP	0.00	0.75	-0.9584	$ln[(d\alpha/dt)(1/(1-\alpha)^{0.75}] = a + b/T$
PET	0.00	2.80	-0.9650	$ln[(d\alpha/dt)(1/(1-\alpha)^{2.80}] = a + b/T$
PS	0.00	0.90	-0.9541	$ln[(d\alpha/dt)(1/(1-\alpha)^{0.90}] = a + b/T$

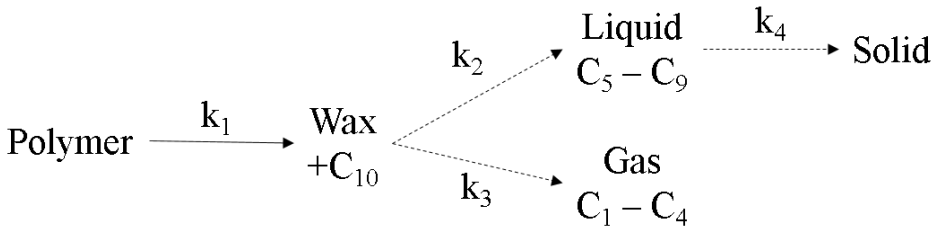

Figure 4.11 Proposed MPW thermal decomposition mechanism where solid lines are primary reactions and dashed lines secondary reactions

Table 4.6 Sum of Squared Error (SSE) and maximum α obtained from experimental ($\alpha_{p,exp}$) and predicted ($\alpha_{p,theo}$) rates of reaction

	HR = 5°C/min			HR = 10°C/min		
MPW	SSE	$\alpha_{p,exp}$	$\alpha_{p,theo}$	SSE	$\alpha_{p,exp}$	$\alpha_{p,theo}$
HDPE	4.17	0.57	0.40	2.30	0.56	0.40
LDPE	6.72	0.65	0.48	0.10	0.62	0.60
PP	1.55	0.57	0.65	0.003	0.62	0.63
PET	10.77	0.50	0.22	9.37	0.47	0.21
PS	1.52	0.63	0.54	0.30	0.57	0.55
	HR = 20°C/min			HR = 40°C/min		
MPW	SSE	$\alpha_{p,exp}$	$\alpha_{p,theo}$	SSE	$\alpha_{p,exp}$	$\alpha_{p,theo}$
HDPE	6.60	0.62	0.75	–	–	–
LDPE	0.20	0.64	0.63	0.46	0.51	0.57
PP	–	–	–	18.98	0.31	0.72
PET	8.86	0.43	0.20	8.95	0.43	0.20
PS	1.41	0.46	0.52	6.77	0.33	0.47

HDPE was almost second order and PET almost third order therefore, differing from literature assumptions. The coefficient m was zero for all MPW. This coefficient only differs from zero in autocatalytic reactions and, since MPW thermal decomposition is not an autocatalytic reaction, m must be zero for all MPW. No previous studies reporting this value for MPW thermal pyrolysis and therefore it was considered that the results obtained were correct.

Using the MPW thermal decomposition equation shown in Table 4.5 and the averages E_a and A obtained from isoconversional methods, the rate of reaction for all MPW was predicted. Figure 4.12 compares the normalised experimental (exp) and predicted (theo) rates of reaction for all MPW.

The closest predictions were found for LDPE, PP and PS. The predicted values for HDPE at low heating rates (5 and 10 °C/min) had a maximum reaction rate at lower temperatures than experimental values whilst the opposite was observed for 20 °C/min. In the case of PET predictions at all heating rates were deviated from experimental values by a constant amount of about 20 °C.

Table 4.6 summarise the mean squared error between experimental and theoretical rate of reaction. Completely accurate prediction would have a SSE = 0 and $\alpha_{p,exp} = \alpha_{p,theo}$.

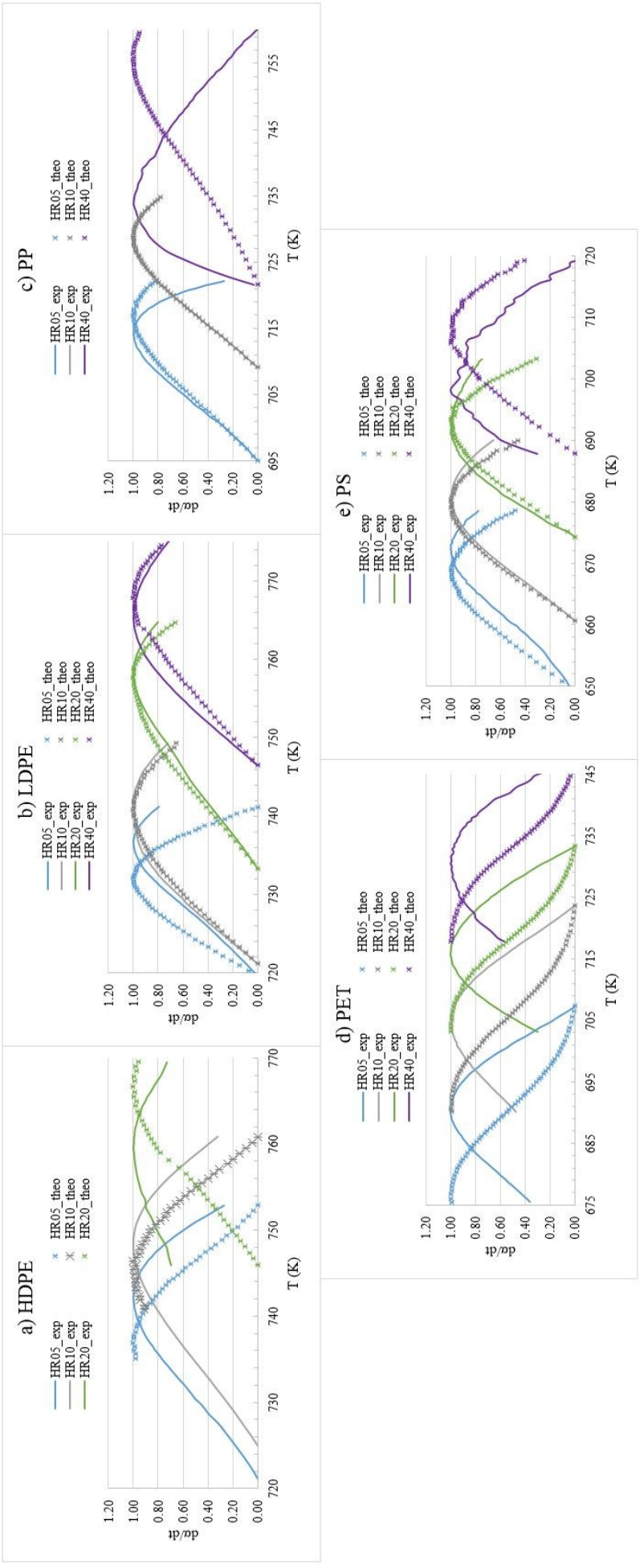

Figure 4.12 Comparison between experimental (exp) and predictions of rate of reaction (theo) for (a) HDPE, (b) LDPE, (c) PP, (d) PET and (e) PS

Predictions with SSE > 5 were considered too inaccurate and were rejected. Following this criteria, it was concluded that this kinetic model poorly predicted PET thermal decomposition, but provides acceptable (HDPE and PP) and good (LDPE and PS) predictions for the remaining MPW. The poor performance of PET was caused by the constant offset of predicted and experimental values. Despite the small variations, it was concluded that this kinetic model is able to predict MPW rate of reaction for low and intermediate heating rates (<20 °C/min) but not so well for high ones (40 °C/min). This lack of fitting for 40 °C/min was attributed to a temperature profile created in MPW particles meaning they are both in liquid and solid state at the same time. Therefore, the methods used to develop this model cannot be applied as they required uniformity and a single state.
As aforesaid, Aguado et al. (2014*b*) suggested the use of a multi-variable analysis i.e. principal component analysis, which has less assumptions than the methodology used in this study. However, this alternative method only allows determination of all the reaction pathways that conform the mechanism but gives no information on the kinetic triplet. A more suitable methodology, model-free isoconversional method, was applied to PS, PE and PP (Peterson et al., 2001) and polymers (Vyazovkin and Sbirrazzuoli, 2006) thermal degradation. Peterson et al. (2001) reported apparent E_a values of 200, 240 and 250 kJ/mol for PS, PE and PP respectively showing very little variation with the results from this study except for HDPE. However, the model-free isoconversional method is very computationally complex suggesting the question of whether the additional effort is worth it in terms of improving the accuracy of predictions.

4.4 Summary

MPW pyrolysis reaction mechanism cannot be modelled as a single first order decomposition. Pyrolysis liquid (C_5-C_9) and gas (C_1-C_4) are formed via two secondary parallel reactions from primary waxes (C_{11+}). KAS and Friedman methods provided values of apparent E_a and A of HDPE = 375.59 kJ/mol and $9.47 \cdot 10^{29}$ s^{-1}; LDPE = 267.61 kJ/mol and $7.86 \cdot 10^{19}$ s^{-1}; PP = 261.22 kJ/mol and $3.03 \cdot 10^{21}$ s^{-1}; PET = 197.61 kJ/mol and $4.84 \cdot 10^{14}$ s^{-1}; and PS = 192.61 kJ/mol and $5.52 \cdot 10^{14}$ s^{-1}. Although quick and simple, master plots or Málek method was very limited for MPW pyrolysis. The linear model fitting (TSB equation) provided MPW decomposition kinetic model by optimising the order of reaction (n) and the nucleation factor (m). The results showed that m=0 for all MPW whereas the order of reaction was: HDPE = 1.70, LDPE = 0.95, PP = 0.75, PET = 2.80, PS = 0.90. Prediction of the rate of reaction for all MPW were made using the calculated kinetic triplet. Predictions fitted poorly for PET but reasonably acceptably for all other MPW. They fitted experimental data accurately for low and intermediate heating rates however high heating rates were not well represented. Those predictions implied a more complex mechanism dependant on the heating rate as well as the type of MPW analysed.

Chapter 5 Monomer recovery through advanced pyrolysis of waste high density polyethylene (HDPE)

This chapter focuses on cold plasma thermal and catalytic pyrolysis of HDPE to maximise the yield of gas and ethylene for the first time. Waste HDPE was selected for an initial assessment of cold plasma because is easily handled, has the simplest structure with no functional groups and there is ample literature on waste and virgin HDPE pyrolysis to compare with. Due to the lack of information of cold plasma applied to PWP, this chapter started with the investigation of cold plasma power along with two effect-known parameters, temperature and heating rate, via a factorial design of experiments to directly crack heavier hydrocarbons into lighter ones. The synergistic effect of catalyst (HZ1, HZ2 and SZ) and cold plasma was also exploited for the time applied to PWP at 500 °C. Sulphated zirconia catalyst, an uncommon catalyst used for PWP, was used and compared with commercial zeolite HZSM-5 in terms of gas and monomer yield maximisation and reusability. SZ catalyst was selected for this study because: (i) it does not involve the use of toxic and/or corrosive reagents, (ii) it can be directly synthesised via solvent-free methods (Eterigho et al., 2011; Reddy et al., 2005) and (iii) limited research is available on the viability of SZ for waste HDPE, or other plastic waste, catalytic pyrolysis. Full characterisation of the three catalysts is available in chapter 3. The contents of this chapter have been published in "Monomer recovery through advanced pyrolysis of waste high density polyethylene (HDPE)" at *Green Chemistry* (Diaz-Silvarrey, Zhang and Phan, 2018).

5.1 Background

Waste HDPE thermal pyrolysis yields three fractions: gas (light hydrocarbons - C_1-C_4- and small amounts of hydrogen), liquid/wax/oil (mixture of alkanes ranging from C_6-C_{30+}) and solid residue (Miskolczi et al., 2004; Pinto et al., 1999*a*; Sakata et al., 1996; Williams and Williams, 1997*a*, 1999). Temperature, heating rate, reaction time and catalysts play an important role on product yields during waste HDPE pyrolysis (Lee, 2012). Mastral et al. (2002) reported that HDPE pyrolysis product yield and composition varied greatly with temperature: from 72.3 wt% wax and 22.1 wt% gas at 650 °C to 13.5 wt% wax and 76.16 wt% gas at 730 °C. HDPE thermal pyrolysis at 500 °C yields mostly wax (67 wt% C_{+20} aliphatic hydrocarbons, 25 wt% C_{12}-C_{20} hydrocarbons, 5 wt% C_5-C_{11} hydrocarbons) with very little gas produced (0.03 wt% methane, 0.15 wt% C_2, 0.57 wt% C_3 and 2.27 wt% C_4 (Elordi, Olazar, Lopez, Artetxe and Bilbao, 2011). The wide range of hydrocarbons in the wax decreases its quality due to the high

viscosity and high boiling point range and thus, is not suitable to be use directly as fuel without upgrading. The gas fraction also lacks from valuable products (e.g. hydrogen or ethylene) restricting the profitability of thermal HDPE pyrolysis. Zeolite catalysts e.g. HY, increases the C_5-C_{10} fraction to 44.55 wt% and the gas fraction to 24.44 wt% however the yield of ethylene is still low (0.62 wt%) (Elordi et al., 2007).

5.2 Experimental

Waste HDPE samples used on experiments were cut into 15x15mm size particles and characterised as described section 3.1.1 in chapter 3. The experimental set-up used for cold plasma assisted thermal and catalytic waste HDPE pyrolysis is illustrate in Figure 3.11 in chapter 3. Section 3.2.1 in chapter 3 describes the experimental procedure. Appendix D details the experimental set-up and reactor used. In this chapter, experiments were carried out using the reactor detailed in Appendix D. This reactor consisted on two joined sections, an initial pyrolysis reactor followed by a DBD reactor to generate the cold plasma.
Waste HDPE samples were placed inside the pyrolysis section of the reactor and heated up to a set pyrolysis temperature (500-700 °C) in a nitrogen atmosphere (20 mL/min) at a fixed heating rate (30-75 °C/min) and then hold at pyrolysis temperature for 15 min. The cold plasma input SED in the DBD section was varied between 90 J/mL (30 W supplied) and 180 J/mL (60 W supplied) but remained constant during each experiment. About 0-10 wt% of each of the three catalyst (HZ_1, HZ_2 and SZ) was packed into the DBD reactor gap as shown in Appendix D. The DBD reactor section with the catalyst was heated along with pyrolysis reactor up to 500 °C at 55 °C/min and an SED of 135 J/mL (45 W supplied).

5.3 Comparison of cold plasma assisted pyrolysis with thermal and catalytic pyrolysis

Columns 2, 5 and 6 in Figure 5.1 compare thermal and cold plasma assisted pyrolysis of waste HDPE at 600 °C showing a considerable increase in the gas yield (from 15 wt% in thermal pyrolysis to 44 wt% and 50 wt% at cold plasma SED of 90 and 180 J/mL respectively). Column 1 in Figure 5.1 (92 wt% wax yield and 6 wt% gas yield) showed similarity with previous thermal pyrolysis of waste HDPE at 500 °C (95 wt% wax and and low gas yield (Bagri and Williams, 2002)). The gas yield obtained from cold plasma assisted pyrolysis (columns 5 and 6 in Figure 5.1) was closer to catalytic pyrolysis (column 4 in Figure 5.1) and high temperature thermal pyrolysis (column 3 in Figure 5.1) than that of thermal pyrolysis at low and medium temperatures (columns 1 and 2 in Figure 5.1).
Results in Figure 5.1 suggested cold plasma enhanced secondary cracking reactions similarly to catalysts or high temperature. These results cannot be compared/validated because no other studies on cold plasma applied to plastic waste pyrolysis were found at the time this work was completed. However, previous studies (Dave and Joshi, 2010; Mazzoni and Janajreh, 2017; Park

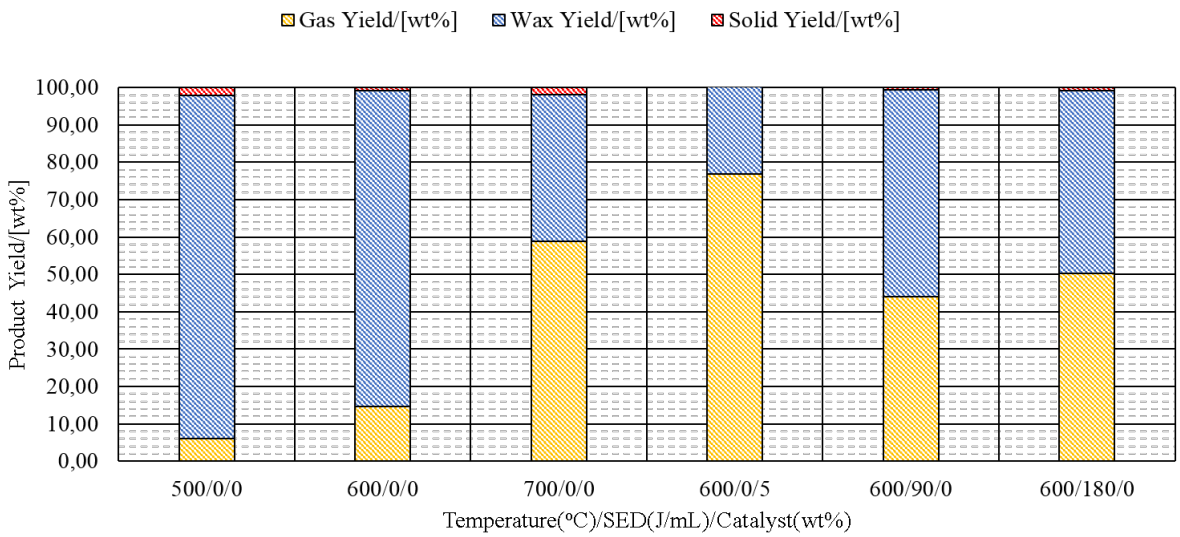

Figure 5.1 Comparison between waste HDPE thermal pyrolysis at temperatures between 500-700 °C and 45 °C/min (columns 1-3), catalytic pyrolysis at 600 °C, 45 °C/min and 5 wt% HZSM-5 (column 4) and cold plasma assisted pyrolysis at 600 °C, 30 °C/min and SED = 90-180 J/mL (columns 5 and 6)

et al., 2016; Punčochář et al., 2012) reported thermal plasma to produce syngas from plastic waste gasification/incineration implying the cracking ability of plasma technologies.
Some excited electrons in the cold plasma have higher energy (96-965 kJ/mol (Fan et al., 2018)) than waste HDPE bond dissociation energies (C-H = 415 kJ/mol and C-C = 331 kJ/mol (Fan et al., 2018)) promoting the C-C and C-H cracking process. In addition to the excited electrons, cold plasma generates an array of molecular N_2 excited species by electron impact dissociation (San Fabián and Pastor-Abia, 2007; Xiao et al., 2014): 1) N_2 second positive system in the UV region ($N_2(C^3\Pi_u\text{-}B^3\Pi_g)$), 2) N_2^+ first negative system ($N_2^+(B^2\sum_u\text{-}X^2\sum_g)$), 3) N_2 first positive system ($N_2(B^3\Pi_g\text{-}A^3\Pi_u)$) and 4) atomic nitrogen (N). As the scope of this thesis does not involve applied physics or quantum mechanics no more detail is provided regarding the different excited states of molecules, their nomenclature, etc. but extensive information is available elsewhere (Capitelli et al., 2015, 2011; Fridman, 2008). However, what is relevant to this work is that these excited species collide with the volatiles released from waste HDPE pyrolysis leading to the formation of carbenium-like ions and radicals along volatiles chains. These ions and radicals promote reaction pathways similar to secondary β-scission reactions and mimic the mechanism of thermal decomposition of hydrocarbons in the presence of acid catalysts i.e. HSZM-5 (section 2.3.4 in chapter 2 and Figure 5.2b).
Figure 5.1 shows the highest gas yield in thermal pyrolysis was obtained at high temperature (700 °C). Only 5 wt% HSZM-5 catalyst decreased the pyrolysis temperature for comparable yield of gas from 700 °C (59 wt% in thermal pyrolysis) to 600 °C (77 wt% in catalytic pyrolysis) due to the different mechanism between thermal (random chain scission (Ceamanos et al., 2002; Gascoin et al., 2012; Sobeih et al., 2008)) and catalytic pyrolysis (carbocation mechanism (Sobeih et al., 2008; Vogt and Weckhuysen, 2015; Weitkamp and Puppe, 2013)).

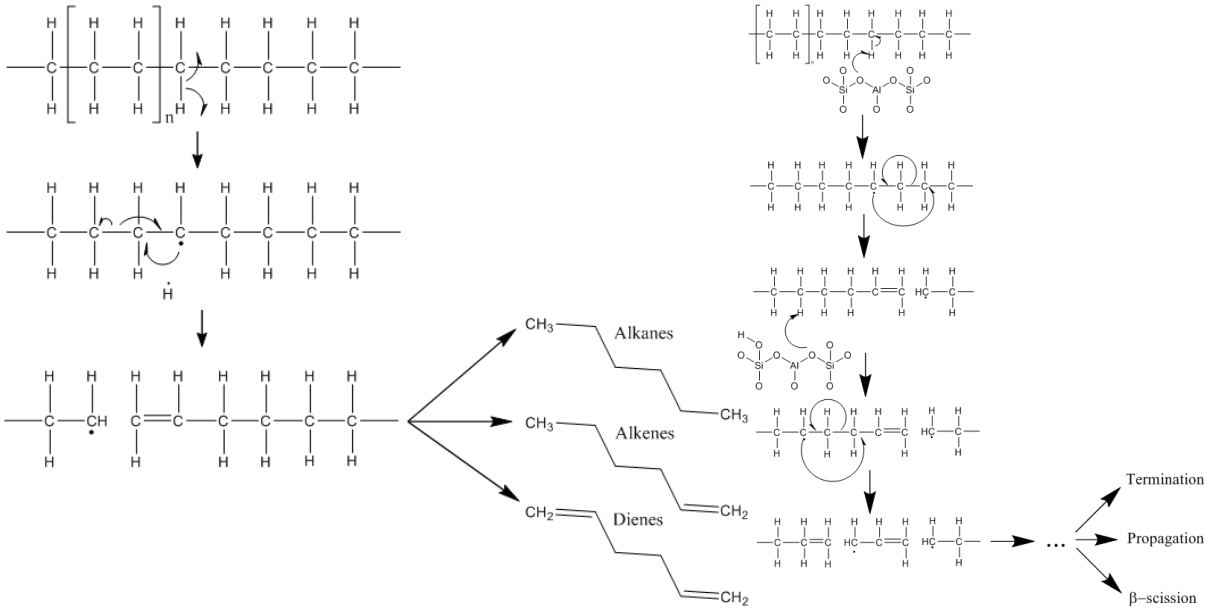

(a) Random chain scission mechanism (Beyler and Hirschler, 2015; CDS Solutions, 2017; Sobeih et al., 2008)

(b) Carbocation mechanism over zeolite (Sobeih et al., 2008; Weitkamp and Puppe, 2013)

Figure 5.2 Schematic representation to illustrate both random chain scission and carbocation mechanisms of HDPE

Waste HDPE thermal pyrolysis occurs via random scission mechanism (Figure 5.2a) consisting of three steps: 1) initiation (formation of a radical), 2) propagation (by intramolecular and intermolecular hydrogen transfer) and 3) termination (recombination of free radicals to form alkanes, alkenes and dienes). The amount of monomer formed through thermal pyrolysis of waste polyolefins (HDPE, LDPE, PP or PS) depends on the substitution group attached to the main plastic chain. Small groups e.g. hydrogen in HDPE and LDPE, do not interfere in the transfer of hydrogen from the weakest 4^{th} carbon counting from the carbon alpha (bond dissociation energy of 282.4 kJ/mol compared to 335 kJ/mol for terminal C-C bond (Dean, 1999)). This implies the chain cleavage is far away from the end and, therefore, the molecules formed will be larger. For large substitution groups e.g. a methyl in PP or phenyl in PS, the intermolecular hydrogen step is hindrance (steric hindrance) and the reaction occurs through reverse polymerisation or unzipping increasing the monomer yield (Beyler and Hirschler, 2015). This phenomena explains the low gas yield obtained with waste HDPE thermal pyrolysis unless the temperature is sufficiently high to reach the activation energy of secondary cracking reactions.

When a catalyst (HZ_1 and HZ_2) were added, waste HDPE pyrolysis occurred via carbocation formation (Figure 5.2b). Lewis acid sites of the zeolite can extract a proton (H^-) from a C-H bond in the waste HDPE chain creating a carbocation (carbon ion with positive charge) in the chain (Weitkamp and Puppe, 2013). Then, the carbocation can either: 1) accept a proton (H^+) from the Brønsted acid sites of the zeolite (termination to form another long alkane), 2) undergo propagation following a random scission mechanism or, more frequently, 3) suffer β-scission. The latter occurs when the C-C bond between the beta carbon (i.e. the one next to the

carbocation) and the next one is broken resulting in a smaller chain carbocation and a shorter olefin (Bruckner, 2001). This step enhances the formation of shorter hydrocarbon chains explaining the increased in the gas yield from 15 wt% to 77 wt% at 600 °C and 3 wt% of HZ_1 (Figure 5.1).
As mentioned, cold plasma enhanced the cracking of heavier hydrocarbons and increasing the gas yield compared to thermal pyrolysis. However, the lower gas yield in cold plasma compared to HZ_1 at the same temperature indicated that the cracking ability of cold plasma was lower than that of HZ_1. Therefore, β-scission reactions in cold plasma occurred less frequently than the formation of radical hydrocarbons leading to the formation of longer alkanes, alkenes and dienes.

5.4 Effect of cold plasma on HDPE pyrolysis

The effect of the temperature (600-700 °C), heating rate (30-75 °C/min) and SED (90-180 J/mL) was studied using a factorial design of experiments with one centre point. This design was not meant to develop an statistical model but only to minimise the number of experiments due to time constrains related to the use of the cold plasma system. The design explored the effect of cold plasma, temperature and heating rate on the yield of gas, wax and solid residue, as well as on the composition of each fraction.

5.4.1 Product Yields

Figure 5.3 shows that larger SED increased the gas yield at all tested temperatures and heating rates. The cause was higher discharge power and electron density in the discharge (Petrović et al., 2009; Tu and Whitehead, 2012), translating into a more energetic environment (Song et al., 2004). This environment enhanced the formation of carbocations and radicals in the hydrocarbon chains, promoted C-C bonds cleavage and therefore, a larger yield of lighter compounds e.g. gas and ethylene. The effect of temperature and heating rate was less than that of SED. For example at SED of 90 J/mL, higher heating rate (from 30 to 75 °C/min) only increased the gas yield 33.3 wt% to 43.5 wt% at 700 °C. Opposite, larger SED (from 90 to 180 J/mL) at constant temperature (700 °C) and heating rate (30 °C/min) doubled the gas yield (from 32 wt% to 62 wt%).
The test carried out at 700 °C, 30 °C/min and an SED of 90 J/mL was found to deviate from the overall trend found in the set of conditions shown in Figure 5.3. This is because for all other tested conditions, increasing the heating rate had a negative effect on the gas yield. When removing this experiment from the set, the trend follows for all other conditions. Therefore, this experiments is considered an outline and will not be consider further in the discussion.
High heating rate and temperature promoted the formation of primary products (Buekens, 2006). The effect of heating rate on waste HDPE thermal pyrolysis was discussed in Chapter 4 although TGA experiments slightly differ from real thermal pyrolysis so results should be taken with caution. Nevertheless, Figures 4.3 and 4.4 in Chapter 4 showed that at high heating rates (over

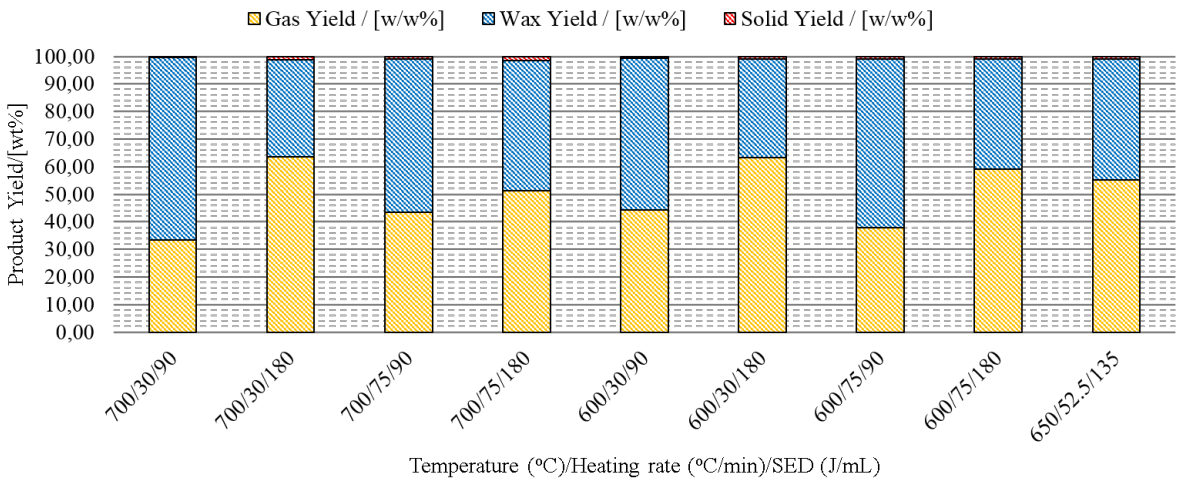

Figure 5.3 Effect of temperature (600-700 °C), heating rate (30-75 °C/min) and SED (90-180 J/mL) on the gas, wax and solid residue yield of waste HDPE cold plasma assisted pyrolysis

40 °/min) the temperature decomposition range increased and the same level of waste HDPE thermal decomposition into products was achieved at higher temperatures. In order to maximise the ethylene proportion in the gas, high heating rates should be used to favour the formation of smaller compounds. Thereby, later experiments testing the effect of the three catalysts in the cold plasma were performed at 55 °C/min.

The very small amount of solid residue produced for all tested temperatures, heating rates and SEDs (below 1 wt%) made collection and characterisation impossible. Nevertheless, the similarity with plastic waste ash content (average of 2.59 wt% for mixed plastic waste in equal proportion shown in Section 3.1.1 in Chapter 3) suggested that the solid residue was formed by inorganic materials added as pigments during plastic manufacture e.g. Cr, Cd, Mn, Co, Fe, etc. (Scheirs and Kaminsky, 2006).

5.4.2 Gas composition

Figure 5.4 shows that the gas fraction comprised of hydrogen (0.4-1.7 wt%), methane (9.0-19.3 wt%) and C_2-C_4 hydrocarbons (19.4-46.2 wt%) with predominance of CH_4 and C_2 for all tested conditions. Figure 5.5 shows the gas product distribution referred to a 100 % i.e. absolute composition not referred to the initial plastic waste mass. Figure 5.5 adds a reference to compare and evaluate the absolute change in the gas product distribution amongst conditions without the effect of the gas yield.

Figure 5.5 shows that increasing the three parameters (SED, temperature and heating rate) has a positive effect on the amount of C_2 in the gas fraction. In this case, the effect of heating rate was greater than that of SED (from 31.67 % at 700/30/180 to 48.88 % at 700/75/180 compared to 46.67 % at 700/75/90 [°C]/[°C/min]/[J/mL]). This is because the rapid volatilisation of hydrocarbon at higher heating rates promotes the formation of lighter compounds.

Compared to thermal pyrolysis, where the amount of C_2 is below 10 wt% (Williams and Williams, 1999), cold plasma doubled the yield of C_2 up to 20 wt% (Figure 5.4). This increased

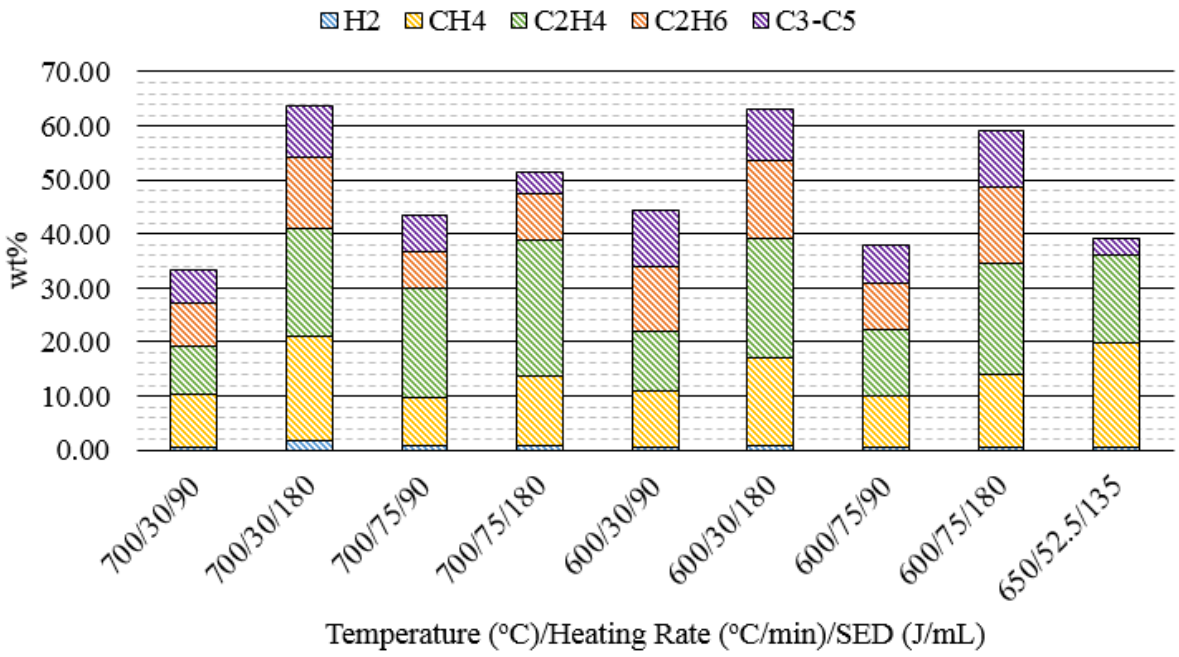

Figure 5.4 Effect of cold plasma SED (90-180 J/mL), temperature (500-700 °C) and heating rate (30-75 °C/min) on the gas composition (total amount represents the corresponding gas yield -wt%-)

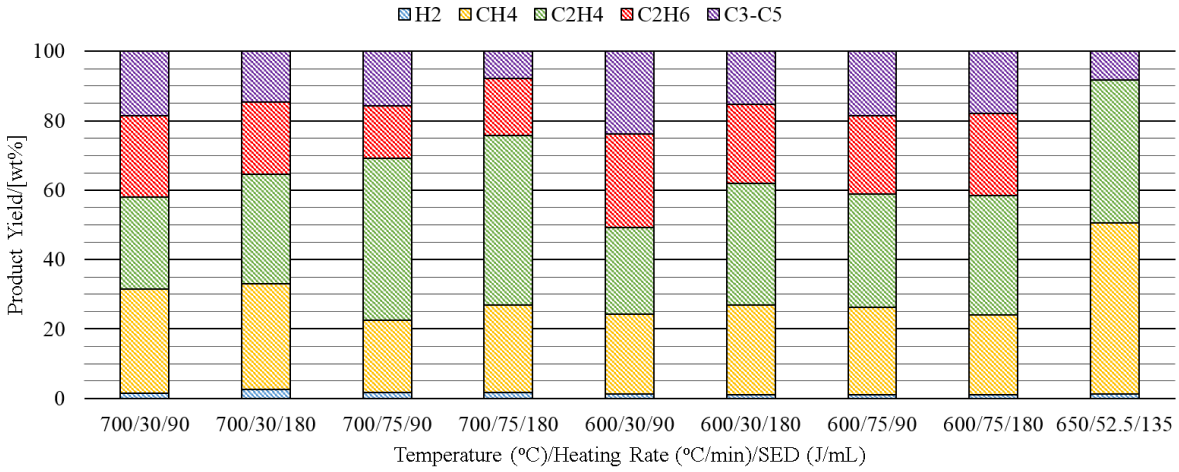

Figure 5.5 Effect of cold plasma SED (90-180 J/mL), temperature (500-700 °C) and heating rate (30-75 °C/min) on the gas composition (not referred to initial plastic waste sample mass)

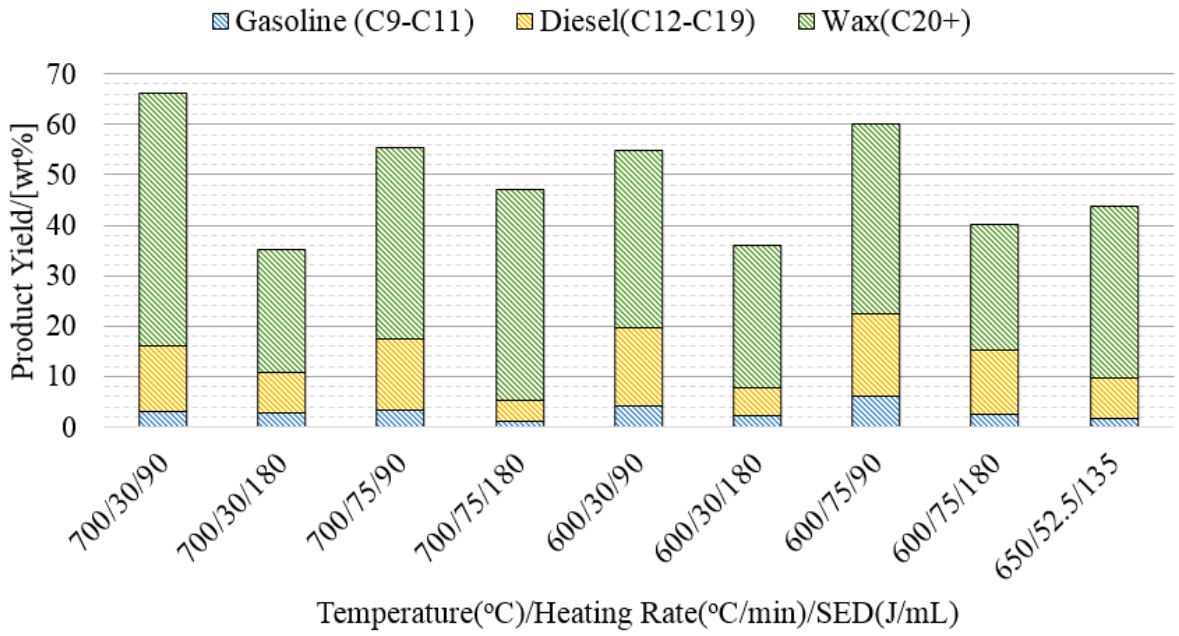

Figure 5.6 Effect of temperature (600-700 °C), heating rate (30-75 °C/min) and cold plasma SED (90-180 J/mL) on the wax composition (total amount represents the corresponding wax yield - wt%-)

the value of the gas stream as ethylene (CH_2=CH_2) is a key chemical blocks used in chemical processes. About 80 % of the global ethylene production is used for either HDPE or LDPE plastic products manufacture (Intratec, 2016; Wittcoff et al., 2013). Ethylene is mainly manufactured from fossil fuels via steam reforming of naphtha from crude oil (Intratec, 2016; Wittcoff et al., 2013) (Figure 2.1 in chapter 2). Increasing the amount of monomer i.e. ethylene, using cold plasma assisted PWP improves the profitability of the process with just a low increase in the energy consumption: cold plasma consumption during experiments of 72-108 kJ for 90 J/mL and 180 J/mL respectively compared with the 684 kJ needed for waste HDPE pyrolysis.

5.4.3 Wax composition

Figure 5.6 shows the wax composition referred to the initial plastic sample mass (the total amounts to the wax yield at each tested conditions) while Figure 5.7 shows the wax product distribution referred to a total of 100 % (the absolute amount of each product found in the wax fraction). As explained in section 5.4.2 with the gas product the purpose of Figure 5.7 is to allow the evaluation of the absolute change on each product at all tested conditions removing the effect of the wax yield.

Figure 5.7 shows again the deviation of 700/30/90 [°C]/[°C/min]/[J/mL] from the general trend. For all other tested conditions, increasing the SED from 90 to 180 J/mL produced an increased in the amount of C_{20+} hydrocarbons in the wax. This observation confirms that this experiment is an outline and needed to be discarded from the discussion.

Unlike the gas fraction, cold plasma had little effect on the distribution of hydrocarbons in the wax fraction: mostly C_{20+} followed by C_{12}-C_{19} and a small proportion of C_9-C_{11} as shown in

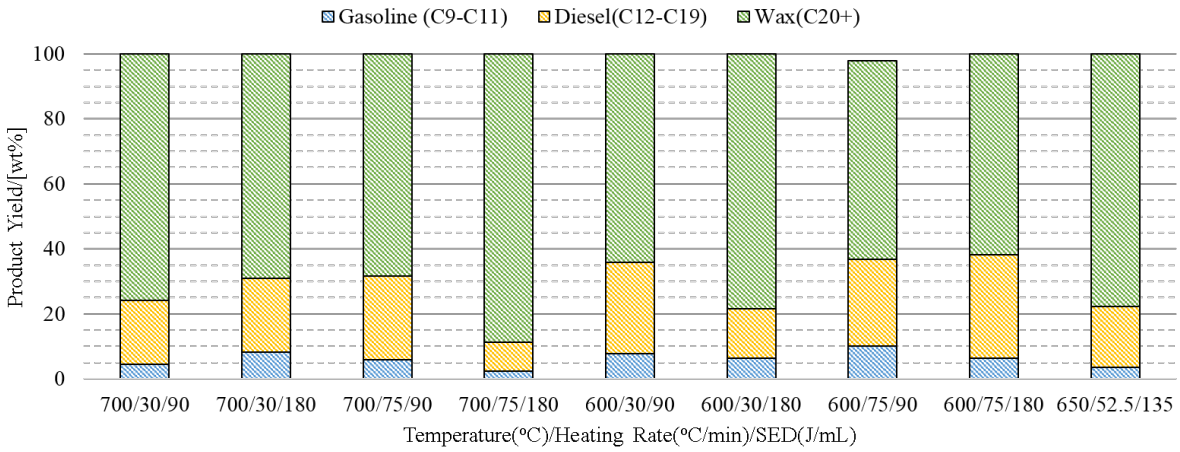

Figure 5.7 Effect of temperature (600-700 °C), heating rate (30-75 °C/min) and cold plasma SED (90-180 J/mL) on the wax composition (not referred to initial plastic waste sample mass)

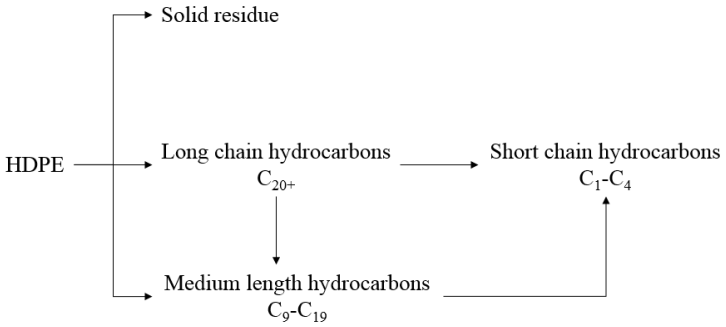

Figure 5.8 Proposed reaction pathway of waste HDPE cold plasma assisted pyrolysis

Figure 5.6. This is more easily seen in Figure 5.7. This behaviour suggested that the volatiles released (C_9-C_{20+}) from the pyrolysis undergoes secondary cleavage into C_1-C_4 because cold plasma promoted the β-scission step, yielding lighter hydrocarbons. Figure 5.8 shows a proposed reaction pathway according to product yields and composition.

Figure 5.9 shows comparison between the simulated distillation curves (SDC) i.e. cumulative mass percentage against boiling point temperature, of waste HDPE cold plasma assisted pyrolysis for all tested conditions and a Maya crude oil. Differences between conditions were very small and were mainly because of different wax yields rather than by a change in the boiling point distribution range. Fossil fuels e.g. gasoline, light naphtha or heavy naphtha, have a narrower boiling point distribution range than the ones obtained for the wax (Figure 5.9). For instance, unleaded gasoline boiling point distribution range is between 36-216 °C (equivalent to C_5-C_{12}) whilst light naphtha is between 216-271 °C (equivalent to C_{12}-C_{15}) and heavy naphtha is above 271 °C (equivalent to C_{20+}). Therefore, it suggests the wax obtained in these experiments resembles more a crude oil than fossil fuels and requires upgrading to be utilised as fuel.

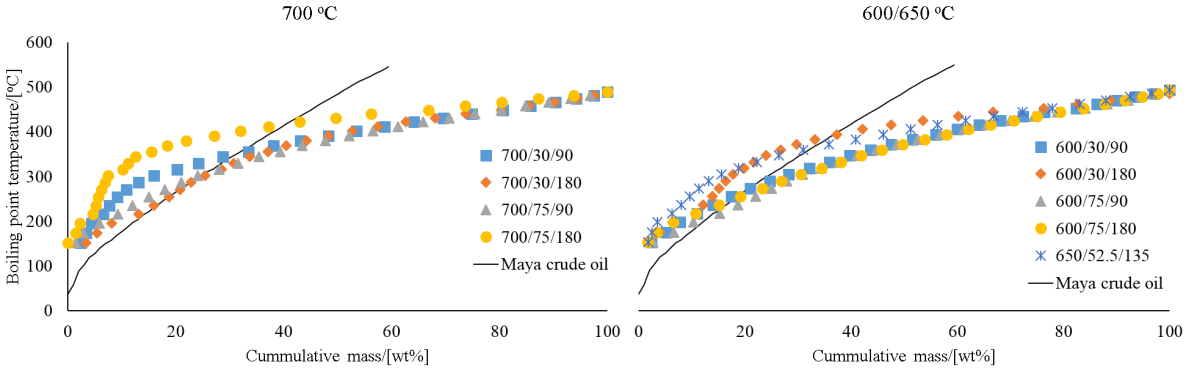

Figure 5.9 Comparison of simulated distillation curves from waste HDPE cold plasma assisted pyrolysis at various temperatures (600-700 °C), heating rates (30-75 °C/min) and cold plasma SEDs (90-180 J/mL) with Maya crude oil (Espinosa-Pena et al., 2004) (solid line). Legend: Temperature (°C)/Heating rate (°C/min)/SED (J/mL)

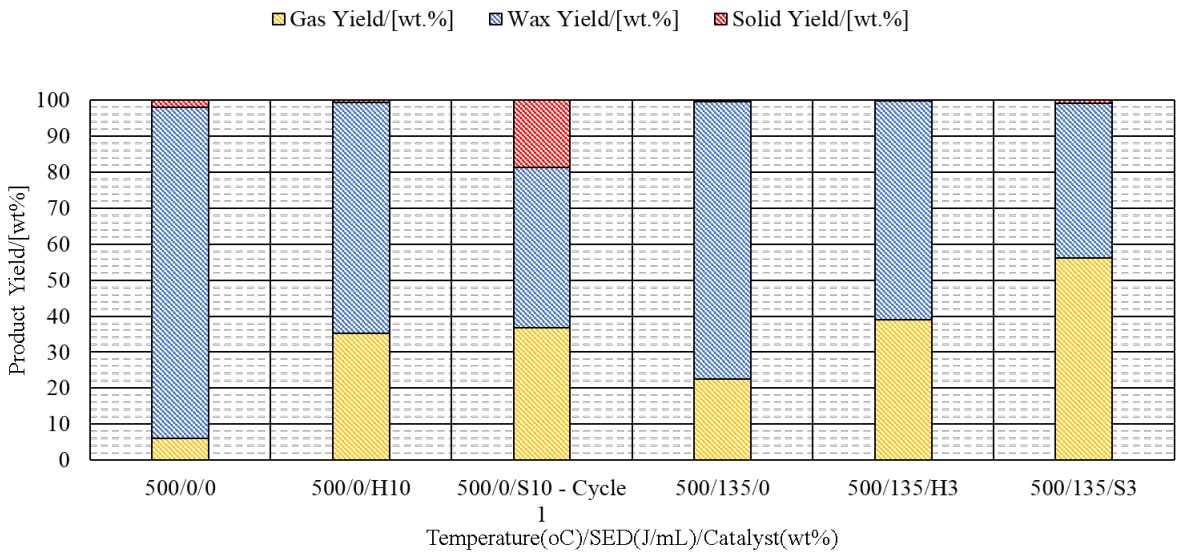

Figure 5.10 Effect of catalyst (H = HZSM-5 and S = SZ) on waste HDPE cold plasma assisted catalytic pyrolysis at 500 °C and 55 °C/min

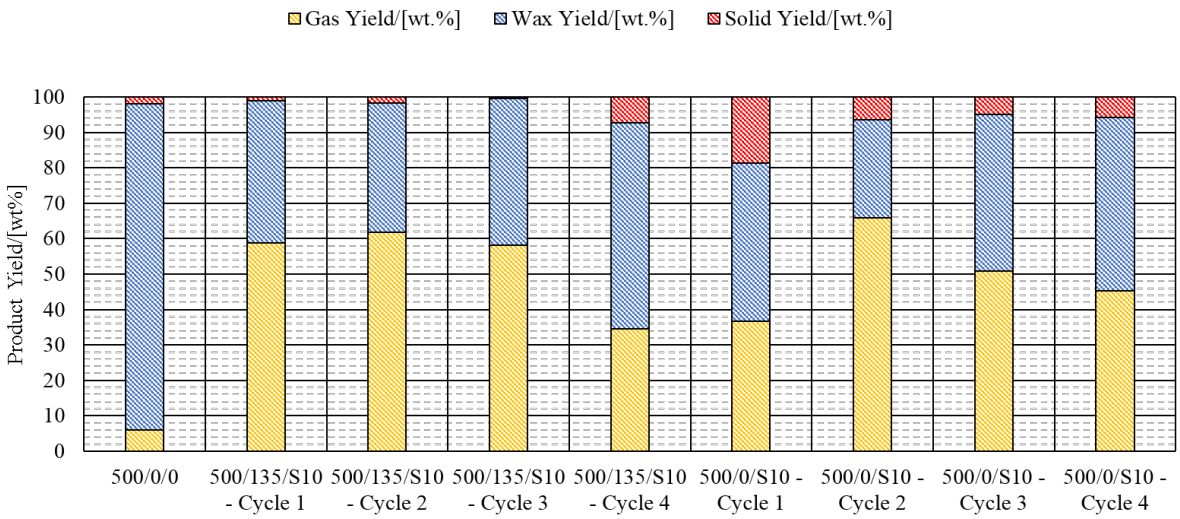

Figure 5.11 Re-usability of SZ catalyst under waste HDPE catalytic pyrolysis (columns 2 to 5) and cold plasma assisted catalytic pyrolysis (columns 6 to 9) at 500 °C and 55 °C/min. Legend: Temperature (°C)/SED (J/mL)/Catalyst weight (wt%)

5.5 Effect of the catalyst in cold plasma catalytic pyrolysis

Figure 5.10 compares the influence on product yields of thermal pyrolysis (column 1) with catalysts (HZ_2 in column 2 and SZ in column 3), cold plasma (column 4) and combined catalysts and cold plasma (columns 5 and 6). Waste HDPE catalytic pyrolysis (columns 2 and 3 in Figure 5.10) increased the gas yield over 35 wt% at low temperature (500 °C) compared to thermal pyrolysis (below 10 wt%). Compared to waste HDPE cold plasma assisted pyrolysis at 500 °C (column 4), Figure 5.10 shows that HZ_2 (column 5) and SZ (column 6) catalysts placed in the cold plasma discharge gap improved the gas yield from over 20 wt% up to 30 wt% and 40 wt% respectively.

Packing catalyst in the cold plasma discharge zone reduces the discharge gap, the breakdown voltage, enhances the average electron energy and improves the reaction performance. On the other hand, cold plasma can activate the catalysts and promote reactions on the catalyst surface. Therefore, cold plasma combined to acid catalysts increased in the monomer (C_2) recovered at lowered the energy requirements (500 °C) which is an improvement on PWP profitability. This makes the process more competitive with current plastic waste management e.g. incineration with energy recovery and landfill disposal.

Figure 5.11 shows the effect after four cycles of 10 wt% SZ catalyst alone (columns 2-5) and when added to cold plasma discharge gap (columns 6-9). SZ catalyst was re-used from one cycle to the next without adding any fresh catalyst. Further cycles with cold plasma could not be completed as coking on catalyst surface and discharge gap inhibited the formation of cold plasma. Columns 3 and 7 in Figure 5.11) show a rise in the gas yield on the second cycle for both scenarios with a reduction on further cycles. When the catalyst was in the cold plasma discharge gap, although reduced with cycles, the gas yield was higher and almost stable for longer (columns 6-8) than with catalyst SZ alone (columns 3-5).

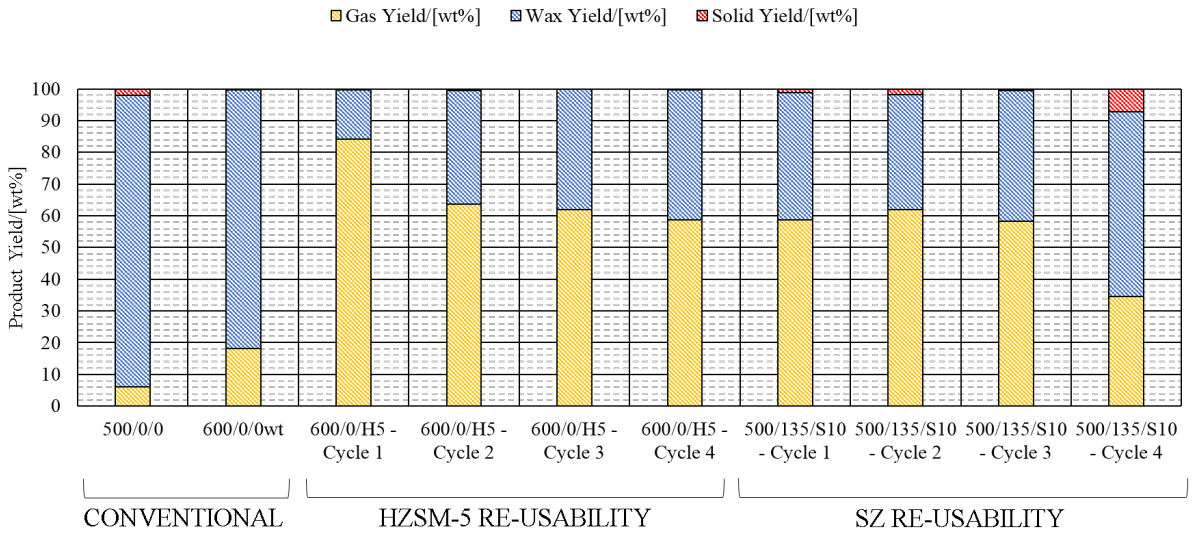

Figure 5.12 Re-usability of catalysts for waste HDPE catalytic pyrolysis at 600 °C and 40 °C/min (columns 3 to 6) and cold plasma assisted catalytic pyrolysis at 500 °C and 55 °C/min (columns 7 to 10). Legend: Temperature (°C)/SED (J/mL)/Catalyst weight (wt%) with H = HZSM-5 and S = SZ

This phenomena was caused by the synergistic effect of cold plasma and SZ catalyst. Catalyst can change the plasma discharge type e.g. filament discharge to the combination of micro and surface discharges inside the catalyst pores creating a more oxidative, and thus reactive, atmosphere (Van Durme et al., 2008). Also, cold plasma can vary the catalyst chemical composition, surface area and structure (Van Durme et al., 2008). The combination of these two effects explained the higher gas yield on the second cycle of SZ (columns 3 and 7 in Figure 5.11). Coking deactivated SZ catalyst with cycles reducing the gas yield from the third cycle onwards. However, because coking also occurs in zeolites and it is a reversible process (López, De Marco, Caballero, Adrados and Laresgoiti, 2011), SZ catalyst proved comparable catalytic activity to zeolites for PWP.

Figure 5.12 compares the re-usability study of the two catalyst, HZ_1 zeolite (columns 3-6, 600 °C and 40 °C/min) and SZ catalyst with cold plasma (columns 7-10, 500 °C and 55 °C/min) during four cycles. Despite operation at two different pyrolysis temperatures, comparison in terms of performance with number of cycles without losing activity is still valid. However, product distribution cannot be directly compared as differences in product yield were influenced by both the catalyst activity and temperature. HZ_1 catalyst improved the gas yield compared to thermal pyrolysis (84.11 wt% on first cycle, column 3, compared to 18.08 wt%, column 2). The use of spent zeolite in consecutive cycles (columns 4-6 in Figure 5.12) showed a decrease in the gas yield to about 60 wt% implying lower ethylene yield. HZ_1 catalyst was deactivated with cycles, similarly to SZ catalyst, by coking.

SZ catalyst distributed in the cold plasma discharge gap showed a more stable performance in terms of gas yield for the first three cycles. The gas yield (66 wt% on the first cycle) was higher than that of thermal pyrolysis at both 500 and 600 °C (6 and 18 wt% respectively) but lower than that of HZ_1 (84.11 wt% in the first cycle). However, further cycles showed that the gas yield in

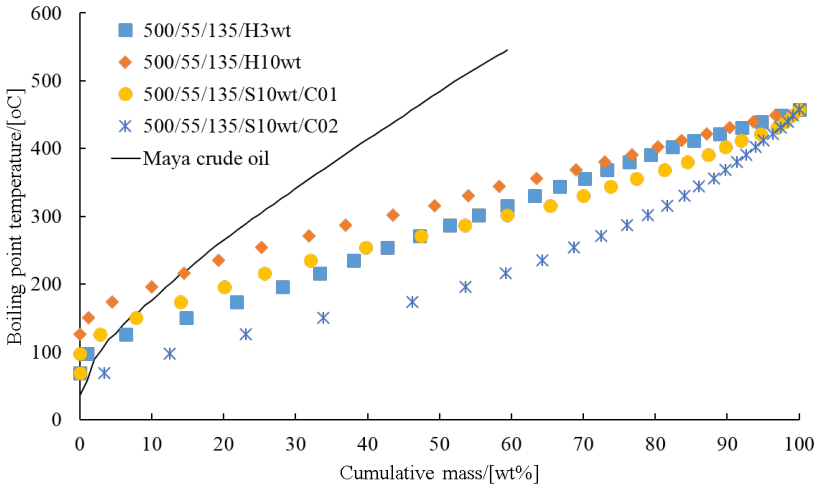

Figure 5.13 Comparison of simulated distillation curves of waste HDPE cold plasma catalytic pyrolysis and Maya crude oil (solid line). Legend: Temperature (°C)/Heating rate (°C/min)/SED (J/mL)/Catalyst weight (wt%) with H = HZSM-5, S = SZ and C0X = the X^{th} cycle of the catalyst

further cycles was equivalent (about 60-64 wt%) for both catalyst. Considering the energy requirements of the process, SZ (500 °C) was superior than HZ_1 (600 °C) in long term operation. Sections 2.3.4 and 2.3.4 in chapter 2 discussed the acidity and catalytic cracking mechanism of HZSM-5 and SZ catalysts respectively. It appears that, equally to zeolites, SZ presents Lewis and Brønsted acid sites (Son et al., 2001). The proportion of each type of acid site in SZ highly depends on the temperature at which the catalyst is under. Below 600 °C, SZ acidity is caused by three different acid sites: Brønsted, medium and strong Lewis acid sites. However, above that temperature, Brønsted acid sites disappeared (Srinivasan et al., 1996).

According to López, De Marco, Caballero, Laresgoiti, Adrados and Aranzabal (2011) ZSM-5 zeolites total acidity was 0.2 mmol-NH_3/g-catalyst with some weak acid sites between 100-250 °C and a majority of strong acid sites between 250-550 °C. On the other hand, Choudhary and Karkamkar (2003) reported SZ catalyst total acidity was about 0.4 mmol-NH_3/g-catalyst with some very weak acid sites between 50-150 °C, the majority of their acid sites between 150-500 °C and a small fraction above 500 °C. Therefore, even HZ_1 had stronger acid sites than SZ, explaining the initial higher gas yield, SZ total acidity was higher and therefore the catalyst was active at lower temperature. The higher gas yield of HZ_1 was also influenced by the higher pyrolysis temperature in HZ_1 re-usability study.

Figure 5.12 showed a significant proportion of wax formed (15-41 wt% for HZ_1 and 28-58 wt% for SZ) despite HZ_1 and SZ catalysts increasing the gas yield and the monomer recovered. As aforementioned, cold plasma had little effect on the product distribution of the wax other than decreasing its yield at the expense of the gas yield. The addition of a catalyst enhanced secondary cracking reactions producing more gas and lighter wax fractions.

Figure 5.13 compares the simulated distillation curves of the wax obtained for cold plasma assisted catalytic pyrolysis to Maya crude oil (Espinosa-Pena et al., 2004). Compared with the commercial Maya crude oil, the wax obtained in this study had a slightly narrower boiling point distribution (approximately 69-460 °C as opposed to 36-542 °C from the crude oil) and less

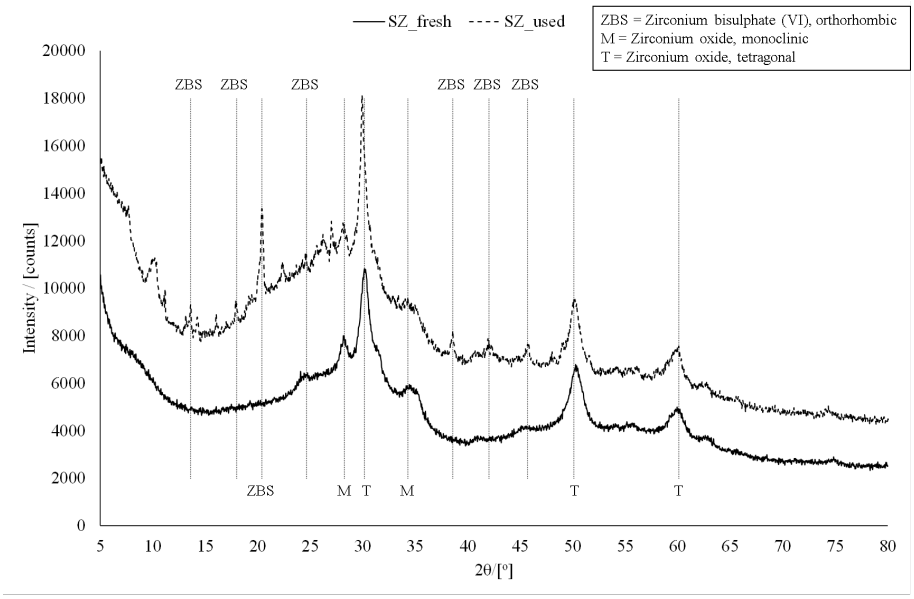

Figure 5.14 X-ray diffraction spectra of fresh (solid line) and used (dashed line) SZ after four waste HDPE cold plasma assisted catalytic pyrolysis cycles (T = tetragonal crystal, M = monoclinic crystal and ZBS = zirconium bisulphate (VI))

residue (the Maya crude oil had a 40 % residue). Except wax from the second SZ and cold plasma cycle (blue stars in Figure 5.13), the remaining wax distributions differed very little with about 10 wt% between 60-200 °C (gasoline-like), 20 wt% between 200-271 °C (light naphtha-like) and the remaining >271 °C (heavy naphtha-like). The second SZ cycle however presented about 60 wt% between 60-216 °C (gasoline-like), 13 wt% between 216-271 °C (light naphtha-like) and the remaining >271 °C (heavy naphtha-like) demonstrating a reduction in the amount of heavy compounds due to the combined effect of SZ and cold plasma. Therefore, it appears that the synergistic effect of cold plasma and SZ catalyst improved the wax product distribution with a composition resembling gasoline.

5.5.1 Characterisation of used sulphated zirconia catalyst

Figure 5.14 compares the XRD spectra (obtained following the method in section 3.1.2 in chapter 3) of fresh SZ (solid line) and used SZ after the four waste HDPE cold plasma assisted catalytic pyrolysis (dashed line). The spent SZ catalyst presented a small amount of orthorhombic zirconium bi-sulphate (VI) ($Zr(SO_4)_2$) crystalline phase not found in the fresh SZ catalyst. This zirconia polymorph only forms at elevated pressure but, the high energy environment of cold plasma, mimicked those conditions and altering SZ structure which explains the difference between SZ only and SZ and cold plasma re-usability studies (Figure 5.11). Figure 5.15 compares the FT-IR spectra of fresh (solid line) and used SZ (dashed line) after four waste HDPE cold plasma assisted catalytic pyrolysis cycles (obtained as described in section 3.1.2 in chapter 3). Both spectra presented bands at 992 and 1119 cm^{-1}, characteristic of the S-O stretching vibration modes of SO_4^{2-} species; 1425 cm^{-1}, corresponding to the stretching vibration of S=O bonds in sulphate groups; and at 1635 and 3207 cm^{-1}, caused by the δ_{O-H}

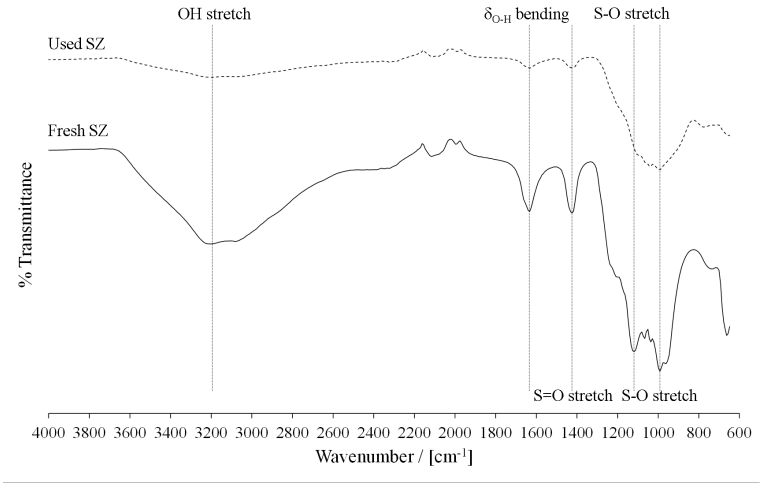

Figure 5.15 FTIR spectra of fresh (solid line) and used SZ (dashed line) after four waste HDPE cold plasma assisted catalytic pyrolysis cycles

bending frequency and the O-H stretch of the water molecules. These findings agreed with previous studies (Witoon et al., 2015). The relative intensity i.e. ratio of individual peak transmittance and total transmittance of all peaks, of bands at 1425, 1635 and 3207 cm^{-1} decreased from 24, 24 and 22 % in fresh SZ to 22, 22 and 21 % in used SZ respectively while remained the same for the 992 and 1119 cm^{-1} bands. This suggested some reduction in the oxidation state of S=O (S^{+6}) due to SZ catalyst deactivation and water removal during experiments.

5.6 Summary

Overall this chapter suggested a novel approach to plastic waste pyrolysis. The addition of cold plasma immediately following the pyrolysis of waste HDPE had a positive effect on monomer recovery (ethylene). This effect was further enhanced by the addition of an acid catalysts (SZ). This is because the cold plasma presented a synergistic effect with the catalyst providing activation of the active sites and enhancing its catalytic activity. This phenomenon allowed ethylene yields over 20 wt% at much lower temperatures (500 °C) than when cold plasma only assisted or thermal pyrolysis were tested. From all the tested parameters, the highest impact in terms of increasing the yield of ethylene was observed at: higher SED (180 J/mL), medium heating rates (52.5-55 °C/min) and low temperatures (500 °C) in the presence of SZ catalyst. This was considered the highest impact because of the biggest difference with thermal pyrolysis but still under moderate operational conditions i.e. lower operational costs.
Waste HDPE cold plasma assisted non-catalytic and catalytic pyrolysis doubled the amount of ethylene recovered in the gas up to 24 wt% compared with thermal pyrolysis (6 wt% at 500 °C) unless the operation temperature was over 700 °C (27 wt% ethylene yield). Very high temperature had a negative effect on the cold plasma but the reason is still unclear. One possibility is the change in the electrodes properties at this temperature (700 oC) but this issue needs more exhaustive investigation as future work.

Acid catalysts in the cold plasma decreased the temperature to maximise the gas yield even further (59 wt% gas yield at 500 °C and 10 wt% SZ). The ethylene yield recovered with SZ catalytic cold plasma HDPE pyrolysis (13 wt% on the first cycle increasing to 15 wt% on the second and decreased to 13 wt% again on the third cycle) was lower than that under non-catalytic cold plasma at higher temperature (16 wt% at 600 °C, 30 °C/min and 180 J/mL or 24 wt% at 700 °C, 75 °C/min and 180 J/mL). Although the ethylene yield recovered when SZ was added was 3 % below that at 600 °C, the energy requirements were reduced as operation was lower temperatures. Therefore, SZ proven to be an improvement over the use of only cold plasma assisted pyrolysis of waste HDPE.

Despite SZ suffering deactivation, its overall performance in terms of waste HDPE pyrolysis for ethylene recovery deserved to be considered. SZ deactivation was caused by coking and, to some extent, reduction of sulphate ion oxidation state. The former is reversible by combustion at temperatures below 550 °C to prevent thermal decomposition of sulphate ions into SO_x and hence, SZ catalytic activity can be partially recovered. Since catalytic experiments with SZ were performed below SO_4 decomposition temperature (>550 °C), it was not observed the release of any sulphur-based compounds. However, it is worth considering that if pyrolysis temperature is higher this could occur subtracting value to SZ catalyst. Regardless, SZ appeared as a suitable alternative to expensive zeolites to recover value from plastic waste. Further work with SZ catalyst is discussed in chapters 6, 7 and 8.

Chapter 6 Pyrolysis of polypropylene

This chapter extended the novel and successful approach to introduce cold plasma to assist plastic waste pyrolysis observed in chapter 5 via a response surface design of experiments (DoE) applied to waste PP cold plasma assisted catalytic pyrolysis using SZ as catalyst (section 6.3). An innovative method to recover high-value carbon products and hydrogen is also studied in this chapter (section 6.4) building on previous information on the synergy between cold plasma and catalysts, the use of plastic waste as carbon sources to recover high-value carbon products and the ability of Ni/Al_2O_3 catalyst to increase the yield of hydrogen. Some of the contents of this chapter (section 6.4) have been submitted for publication in "Direct production of carbon nanotubes and hydrogen from plastic waste using cold plasma pyrolysis" to *ACS Sustainable Chemistry & Engineering*.

6.1 Background

The study of the synergistic effect between SZ catalyst and cold plasma was extended from chapter 5 via a response surface method (RSM) applied to waste PP cold plasma assisted catalytic pyrolysis (CPCP). Design of experiments using RSM has been considered as a powerful problem-solving tool to compare, characterise, model or optimise a process with a minimum number of experiments and hence minimum time and costs (Antony, 2003; Davim, 2016; Greenfield and Metcalfe, 2006; Montgomery, 2017). RSM evaluates the effect and interactions of several input variables (factors) on the desired variables of interest (response variables). According to Miranda et al. (2010), RSM results showed mixed waste pyrolysis (30 wt% waste tyres and 70 wt% waste plastics - 20 wt% PE, 30 wt% PP and 20 wt% PS-) maximised the wax yield at 370 °C, 15 min reaction time and initial pressure of 0.48 MPa. Pinto et al. (2013) reported similar behaviour using also RSM applied to pyrolysis of a mixed wastes (10 % pine, 10 % scrap tyres and 80 % plastic waste - 56 % PE, 27% PP and 17% PS-) to maximise the wax yield (91.3 wt%): 350 °C, 30 min reaction time and initial pressure of 0.2 MPa. Opposite, Kumar and Singh (2014) applied RSM methodology to maximise the wax yield (78.7 wt%) obtained from catalytic pyrolysis of waste HDPE finding optimum temperature of 450 °C and catalyst:HDPE mass ratio of 1:4. The reduction in optimum pyrolysis temperature observed between Kumar and Singh (2014) and Miranda et al. (2010) and Pinto et al. (2013) was caused by the pressure and presence of waste tyres in the latter two studies. However, all showed that

RSM allowed the selection of optimum conditions and the study of the effect and interactions between factors to maximise the desired products with minimum experiments.
Several studies have studied the combined production of H_2 and high-value carbon products via thermal conversion in the presence of nickel catalyst (Ni/HY, Ni/HZSM-5, Ni/SiO_2 and Ni/SiO_2/Al_2O_3) at temperatures between 500-700 °C using CH_4 as carbon source (Ahmed et al., 2009; Choudhary and Goodman, 2006; Muradov and Veziroglu, 2005). The production of high-value carbon products e.g. CNTs, was also studied via plasma (glow discharge at high vacuum) assisted CVD showing plasma improved uniformity in terms of diameter, height (Teo et al., 2003) and alignment (Chhowalla et al., 2001). However, CVD is very energy intensive and requires complex set-ups difficult to scale-up hindering its development (Novoselov et al., 2012). Chung and Chang (2017) showed that atmospheric-pressure spark discharge plasma of CO_2/CH_4 at 1/3 ratio generated CNTs and syngas proving to be an alternative carbon capture, utilization and storage technique. Section 2.3.3 in chapter 2 reviews several studies reporting the recovery of CNTs and hydrogen from PP two-stage pyrolysis/gasification at temperatures between 500-800 °C using Ni-based catalysts (Bajad et al., 2016; Ksapabutr et al., 2013; Liu, Jiang, Yu and Tang, 2011; Mishra et al., 2012; Wu and Williams, 2009*a*). Therefore, waste PP appears as a suitable feedstock for catalytic pyrolysis to recover not only pyrolysis wax/liquid but also other high-value products e.g. hydrogen and CNTs.

6.2 Experimental

The pyrolysis set-up used in this chapter is illustrated in Figure 3.11 and explained in section 3.2.1 both in chapter 3. Detailed drawings of the experimental set-up and the reactor used are in Appendix D. In this chapter thermal and catalytic, in the presence or absence of cold plasma, were tested using waste PP as feedstock. Catalytic experiments involved the use of SZ and Ni/Al_2O_3.
Waste PP samples used on experiments were cut into 15x15mm size particles and characterised as described section 3.1.1 in chapter 3. Fresh SZ and Ni/Al_2O_3 catalysts were prepared and characterised by TEM, XRD and N_2 physisorption isotherms at 77K and BET equation (section 3.1.2 in chapter 3). Used Ni/Al_2O_3 catalyst was collected from the cold plasma zone and characterised (section 3.1.4 in chapter 3) by HRTEM and EDXS for morphology, XRD for nature of phases, Raman Spectroscopy for graphitation and TPO for amount and reactivity towards oxygen of the carbonaceous species deposited on the catalyst surface. Characterisation of spent SZ catalyst was previously discussed in chapter 5 and extended later in chapters 7 and 8. Experiments with Ni/Al_2O_3, discussed in section 6.4, were tested at varying temperatures between 450-600 °C and constant cold plasma power of 45 W (SED=135 J/mL) and catalyst mass fraction of 5 wt%. The experimental set-up used for these experiments was the same as the one used in chapter 5 and described in section 5.2 for waste HDPE. The reactor used comprised of a two section quartz reactor as detailed in Appendix D. The first section, pyrolysis section, contained the waste PP sample and was followed by the DBD reactor section which contained,

Table 6.1 Levels and codes for the three independent variables studied as factors for the RSM analysis to investigate yields for product distribution

Variable	Factor	Level		
		Low limit (-)	Centre level (0)	High limit (+)
Temperature/[°C]	x_1	500	600	700
Power/[W]	x_2	30	45	60
Catalyst/Plastic/[wt%]	x_3	0	5	10

for cold plasma assisted and catalytic experiments, the cold plasma and catalyst. For all tested conditions waste PP samples were placed inside the pyrolysis section of the reactor and heated up to a set pyrolysis temperature (400-700 °C) in a nitrogen atmosphere (20 mL/min) at a fixed heating rate (55 °C/min) and then hold at pyrolysis temperature for 15 min. The cold plasma input power in the DBD section was varied between 20 W and 70 W but remained constant during each experiment. About 0-10 wt% of each of the two catalysts (SZ and Ni/Al_2O_3) was packed into the DBD reactor gap as shown in Appendix D. During all tested conditions the gas fraction was collected in four gas samples. The gas collection was evenly distributed between 350 °C and the end of the experiment and analysed by off-line gas chromatography (section 3.2.4 in chapter 3). The wax fraction was analysed off-line by GC-FID (section 3.2.5 in chapter 3) to quantify the most abundant compounds.

The RSM used in this work, discussed in section 6.3, was designed and analysed using Minitab. The factors considered (x_i where i=1,2,3...) were the cold plasma power, pyrolysis temperature and amount of catalyst. The response variables (Y_i where i=1,2,3...) were the three product yields i.e. gas, wax and solid residue, as well as the yield of each compound in the products i.e. H_2, CH_4, CO, CO_2 and C_2-C_4 hydrocarbons in the gas and <C_{11}, C_{12}-C_{17}, C_{18}-C_{25} and C_{25+} fractions in the wax. Each Y_i was fitted by least-square to a second-order model following equation 6.1 where β_i represent the unknown parameters estimated and e the random error of the model.

$$Y_i = \beta_0 + \beta_1 x_1 + \beta_2 x_2 + \beta_3 x_3 + \beta_{12} x_1 x_2 + \beta_{13} x_1 x_3 + \beta_{23} x_2 x_3 + \beta_{11} x_1^2 + \beta_{22} x_2^2 + \beta_{33} x_3^2 + e \quad (6.1)$$

Limits for each of the three factors studies were set using experience from previous studies (Diaz-Silvarrey, Zhang and Phan, 2018) and are represented in Table 6.1.

Figure 6.1 illustrates the RSM experimental matrix which is a map of all tested conditions where each point represents a single experiment. RSM designs extends a basic factorial design (i.e. one experiment at each of the level limits) by introducing a centre point and four axial experiments forming a star centred around the initial factorial design. The automatic RSM design generated by Minitab presented negative catalyst mass values at the axial points. However, since this was not possible, the design was modified to set as zero all the negative values (first and second row in third column in Figure 6.1). After the modification the design was tested and found to be

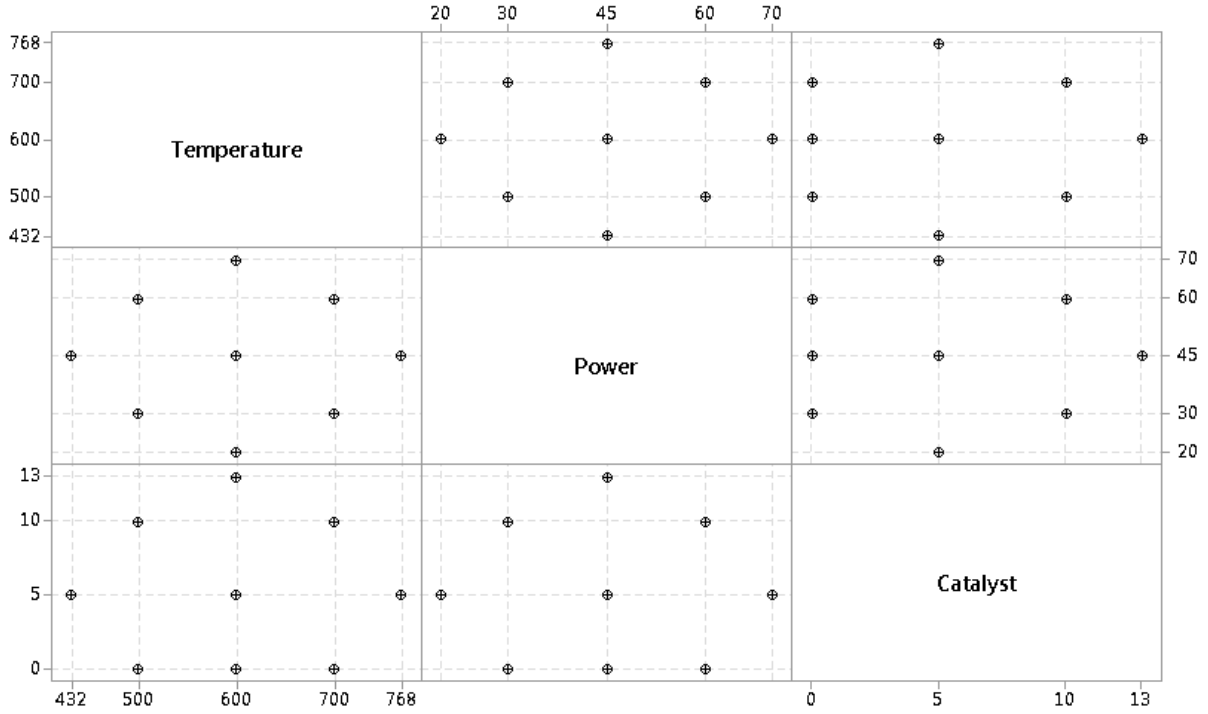

Figure 6.1 Response surface design matrix (temperature in °C, cold plasma power in W and catalyst mass in wt%)

orthogonal. Therefore, the predicted variance response was minimal and the regression coefficients could be assessed independently (Pinto et al., 2013).
Table 6.2 summarises the coded names and specific conditions for all the experiments performed.

6.3 Response surface design to investigate waste PP cold plasma assisted catalytic pyrolysis

Table 6.3 shows the response variable values i.e. product yield, obtained from all the experiments performed following the RSM design (Table 6.2).
Figure 6.2 shows the median and variation intervals of experimental gas (H_2, CH_4, C_2-C_5 hydrocarbons) and wax ($<C_{11}$, C_{12}-C_{17}, C_{18}-C_{25} and C_{25+}) product yields. The main product obtained from waste PP CPCP was propylene (C_3H_6) with a median yield of 32.40 wt%. C_3H_6 is the monomer used for PP manufacture suggesting that cold plasma enhanced the recovery of the monomer for PP. The other products recovered in descending order were: $<C_{11}$ (16.51wt%), C_{12}-C_{17} (10.77wt%), C_2 (10.74wt%), C_4 (7.64wt%), CH_4 (6.35wt%), C_{18}-C_{25} (3.93wt%), C_5 (2.84wt%), C_{25+} (2.53wt%) and H_2 (0.38wt%).
Table 6.4 summarises the effect coefficient obtained for each Y_i. This value is an indicator of the magnitude and direction of the relationship between each of the x_i and the Y_i. The magnitude represents the predicted change in the mean Y_i value when one x_i varies from the low to the high level and the other two factors remain constant. The direction represents the direct or inverse relationship between x_i and Y_i. Positive coefficients translate into a direct relationship where

Table 6.2 Response surface design (temperature in °C, cold plasma power in W and catalyst mass in wt%)

Order		Coded name	Factors		
Standard	Run		Temperature (x_1)	Power (x_2)	Catalyst (x_3)
15	1	PP/600/45/5wt	600	45	5
3	2	PP/500/60/0wt	500	60	0
2	3	PP/700/30/0wt	700	30	0
1	4	PP/500/30/0wt	500	30	0
13	5	PP/600/45/0wt	600	45	0
8	6	PP/700/60/10wt	700	60	10
6	7	PP/700/30/10wt	700	30	10
9	8	PP/432/45/5wt	432	45	5
5	9	PP/500/30/10wt	500	30	10
11	10	PP/600/20/5wt	600	20	5
14	11	PP/600/45/13wt	600	45	13
12	12	PP/600/70/5wt	600	70	5
4	13	PP/700/60/0wt	700	60	0
10	14	PP/768/45/5wt	768	45	5
7	15	PP/500/60/10wt	500	60	10

Table 6.3 Pyrolysis product yield (wt%) from waste PP cold plasma assisted catalytic using RSM design

[PP/°C/W/wt%]	H_2	CH_4	C_2	C_3	C_4	C_5	$<C_{11}$	C_{12}-C_{17}	C_{18}-C_{25}	C_{+25}
PP/600/45/5wt	0.38	8.59	24.29	13.92	7.64	9.25	2.73	17.59	10.55	3.74
PP/500/60/0wt	0.27	2.92	10.21	37.31	4.82	4.46	20.44	10.77	3.19	1.51
PP/700/30/0wt	0.33	6.58	17.11	35.15	4.66	4.97	7.34	14.49	3.96	3.02
PP/500/30/0wt	0.22	4.96	14.29	35.70	5.18	5.18	22.25	6.95	2.82	0.67
PP/600/45/0wt	0.13	3.38	10.74	32.40	4.67	6.39	15.14	20.58	3.93	1.18
PP/700/60/10wt	0.34	4.95	7.01	17.29	16.61	0.10	26.53	17.01	5.22	2.76
PP/700/30/10wt	0.57	8.85	9.93	29.69	14.96	0.13	1.97	10.81	10.73	2.99
PP/432/45/5wt	0.44	4.13	8.43	27.26	15.30	0.13	30.93	7.41	3.32	2.36
PP/500/30/10wt	0.13	2.85	9.52	32.48	5.16	5.20	16.51	13.56	6.58	2.54
PP/600/20/5wt	0.45	6.35	11.38	33.50	17.17	0.15	18.68	7.11	3.38	1.74
PP/600/45/13wt	0.56	8.51	11.03	24.71	17.30	0.19	20.78	8.27	2.96	2.53
PP/600/70/5wt	0.45	6.94	10.48	28.12	17.81	0.20	1.03	19.87	7.59	6.08
PP/700/60/0wt	0.42	7.22	14.76	34.43	7.32	2.84	18.02	7.92	1.83	1.62
PP/768/45/5wt	0.84	12.85	12.96	28.55	19.04	0.25	14.61	5.50	1.96	0.64
PP/500/60/10wt	0.09	1.34	6.79	54.31	3.87	4.11	0.52	8.54	8.55	5.43

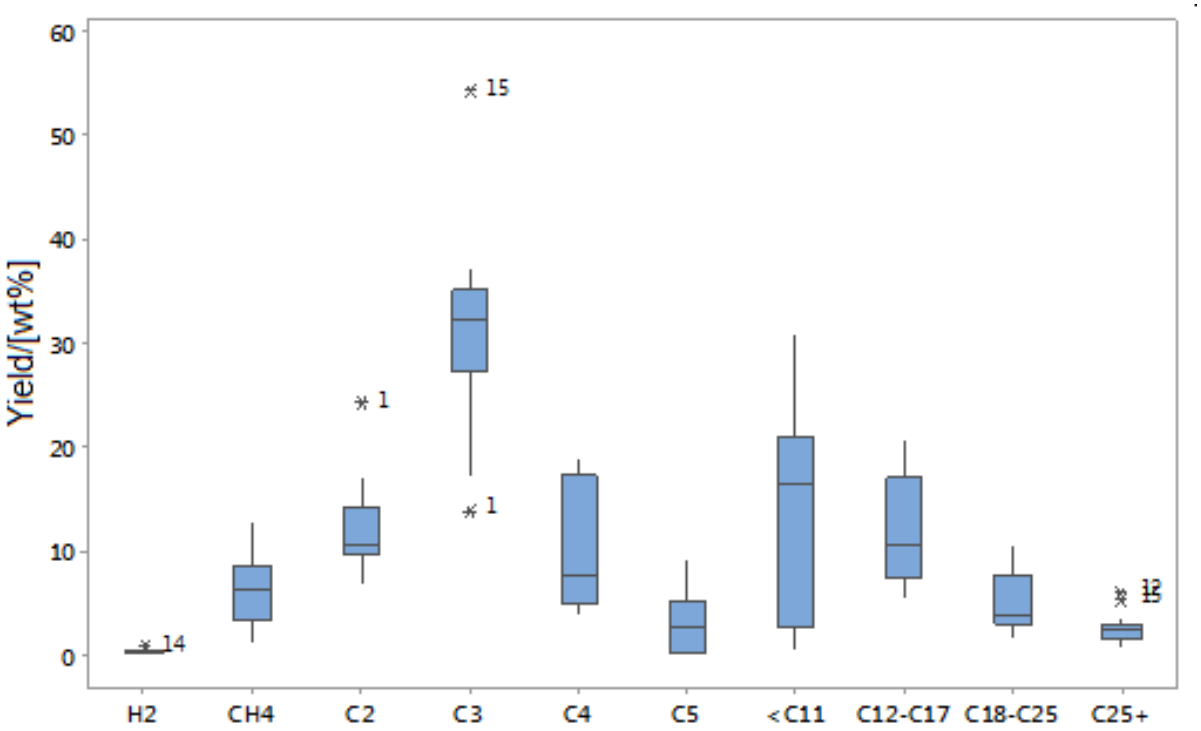

Figure 6.2 Median and variation intervals of experimental gas and wax products yield (asterisks=outlines and number=run order in table 6.2)

increasing the x_i increases the Y_i and negative coefficient represent and inverse relationship where increasing the x_i decreases the Y_i.

Pyrolysis temperature was included for all Y_i models confirming its importance on pyrolysis product distribution. Cold plasma power and amount of catalyst also significantly contributed to the yield of C_2-C_5 hydrocarbons. The light fraction of the wax ($<C_{11}$) was mostly influenced by temperature and cold plasma power whilst the amount of SZ presented an effect on the heavier fraction of the wax yield (C_{18}-C_{25} and C_{25+}). Two-way interactions ($x_i j$ with i,j = 1,2,3) and quadratic terms (x_i^2 with i = 1,2,3) had an important effect on the yield of C_2-C_5 hydrocarbons and the light and medium wax fractions ($<C_{25}$).

Table 6.4 Effect of temperature (x_1), cold plasma power (x_2), SZ catalyst amount (x_3), their two-way interactions (x_1x_2, x_1x_3 and x_2x_3) and quadratic terms (x_1^2, x_2^2 and x_3^2) on the response variables (N/E=no effect of the response variable)

	H_2	CH_4	C_2	C_3	C_4	C_5	$<C_{11}$	C_{12}-C_{17}	C_{18}-C_{25}	C_{25+}
x_1	0.40	7.43	3.84	-14.70	10.18	-2.64	-8.19	1.77	-0.41	-0.65
x_2	N/E	N/E	-3.34	0.33	N/E	-0.96	-2.95	N/E	N/E	2.30
x_3	N/E	N/E	-8.77	-4.57	4.57	-3.98	N/E	N/E	1.78	1.94
x_1x_2	N/E	N/E	N/E	-25.59	N/E	N/E	37.13	N/E	N/E	-3.75
x_1x_3	N/E	N/E	N/E	-19.86	11.23	N/E	N/E	N/E	N/E	N/E
x_2x_3	N/E	N/E	N/E	N/E	N/E	N/E	N/E	N/E	N/E	N/E
x_1^2	0.43	N/E	-16.30	N/E	N/E	-9.82	21.70	-16.64	-7.72	N/E
x_2^2	N/E	N/E	-15.81	N/E	N/E	-9.82	N/E	N/E	N/E	3.77
x_3^2	N/E	N/E	-9.78	N/E	-11.72	N/E	N/E	N/E	-6.59	N/E

$$H_2 = 2.31 - 0.008x_1 + 0.000008x_1^2 \quad (6.2)$$

$$CH_4 = -7.24 + 0.02x_1 \quad (6.3)$$

$$C_2 = -115.30 + 0.36x_1 + 1.07x_2 + 0.83\,x_3 - 0.0003x_1^2 - 0.013\,x_2^2 - 0.12x_3^2 \quad (6.4)$$

$$C_3 = -59.0 + 0.15x_1 + 1.83x_2 + 5.11\,x_3 - 0.003x_1x_2 - 0.009\,x_1x_3 \quad (6.5)$$

$$C_4 = 7.9 - 0.003x_1 - 0.93x_3 - 0.14\,x_3^2 + 0.005x_1x_3 \quad (6.6)$$

$$C_5 = -65.3 + 0.20x_1 + 0.69x_2 - 0.31\,x_3 - 0.0002x_1^2 - 0.008x_3^2 \quad (6.7)$$

$$< C_{11} = 286.0 - 0.69x_1 - 2.71\,x_2 + 0.0004x_1^2 + 0.004x_1x_2 \quad (6.8)$$

$$C_{12} - C_{17} = -94.80 + 0.36x_1 - 0.0003x_1^2 \quad (6.9)$$

$$C_{18} - C_{25} = -44.50 + 0.16x_1 + 1.15x_3 - 0.0001 * x_1^2 - 0.08x_3^2 \quad (6.10)$$

$$C_{25+} = -5.65 + 0.02x_1 + 0.04x_2 + 0.15x_3 + 0.003x_2^2 - 0.0004x_1x_2 \quad (6.11)$$

Equations 6.2 to 6.11 show the Y_i models calculated from the quadratic regression analysis of experimental data (Table 6.3). The Y_i models were determined via a stepwise method (α = 0.15) implemented on Minitab 17. The method performed a variance test on each x_i on each step to assess their statistic significance (p-value). The factors (x_1 = temperature / [°C], x_2 = cold plasma power / [W], and x_3 = SZ catalyst mass / [wt%]) included for each Y_i models varied depending on their statistical significance i.e. p-value<0.15. Equations 6.2 to 6.11 were used to predict the yield of waste PP CPCP products at different experimental conditions. Figures 6.3 and 6.4 show these predictions for the yield of gas and products respectively.
Figure 6.2 showed outlines (asterisks) for H_2, C_2, C_3 and C_{25+} in the following experiments: PP/600/45/5wt, PP/600/70/5wt, PP/768/45/5wt and PP/500/60/10wt. New Y_i models were calculated after removing these experiments from the RSM design; however, only C_2 and C_3 showed an improvement in terms of regression compared to the ones in equations 6.4 and 6.5. Equations 6.12 and 6.13 represent the equations for the new Y_i models to predict the yield of C_2 and C_3 without considering results for PP/600/45/5wt and for PP/500/60/10wt in the case of C_3.

$$C_2 = 9.25 + 0.01x_1 - 0.07x_2 - 0.40\,x_3 \quad (6.12)$$

$$C_3 = 32.18 + 0.05x_2 + 1.03x_3 - 0.04x_2x_3 \quad (6.13)$$

Compared to the original C_2 model (Equation 6.4), the new one (Equation 6.12) also depended on temperature, cold plasma power and SZ catalyst amount but presented different effect coefficient values: 1.92 for pyrolysis temperature, -1.67 for cold plasma power and -2.57 for SZ catalyst amount. Temperature was removed from the original C_3 model (Equation 6.5) being cold plasma power and catalyst amount the only two factors included in the new C_3 model (Equation 6.13). The new C_3 effect coefficients were -11.53 and -12.26 for cold plasma power and catalyst amount respectively. Cold plasma had a negative effect on the yield of C_3 i.e. higher

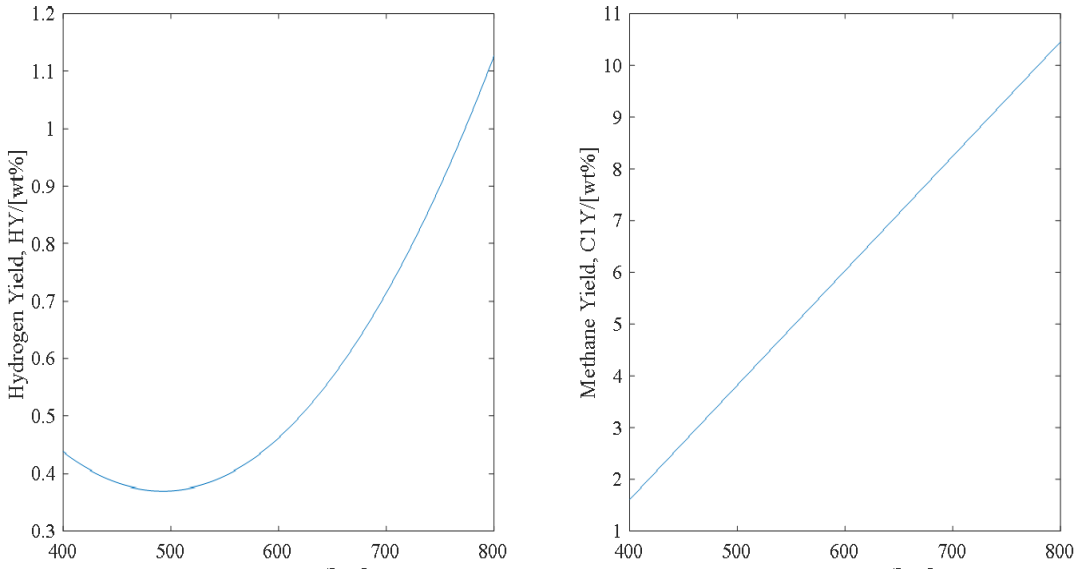

(a) Yield of H_2 (left) and CH_4 (right) predictions

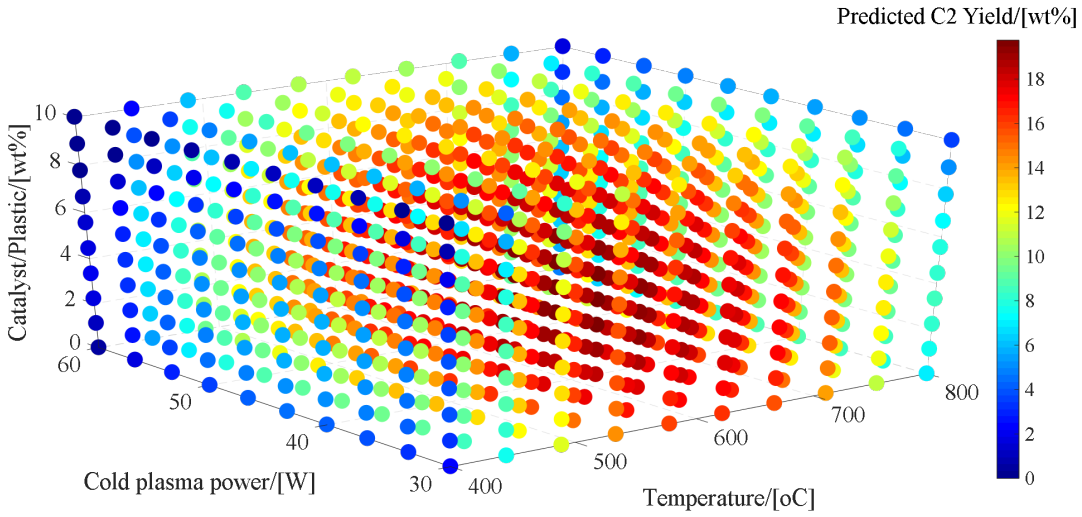

(b) Yield of C_2 predictions

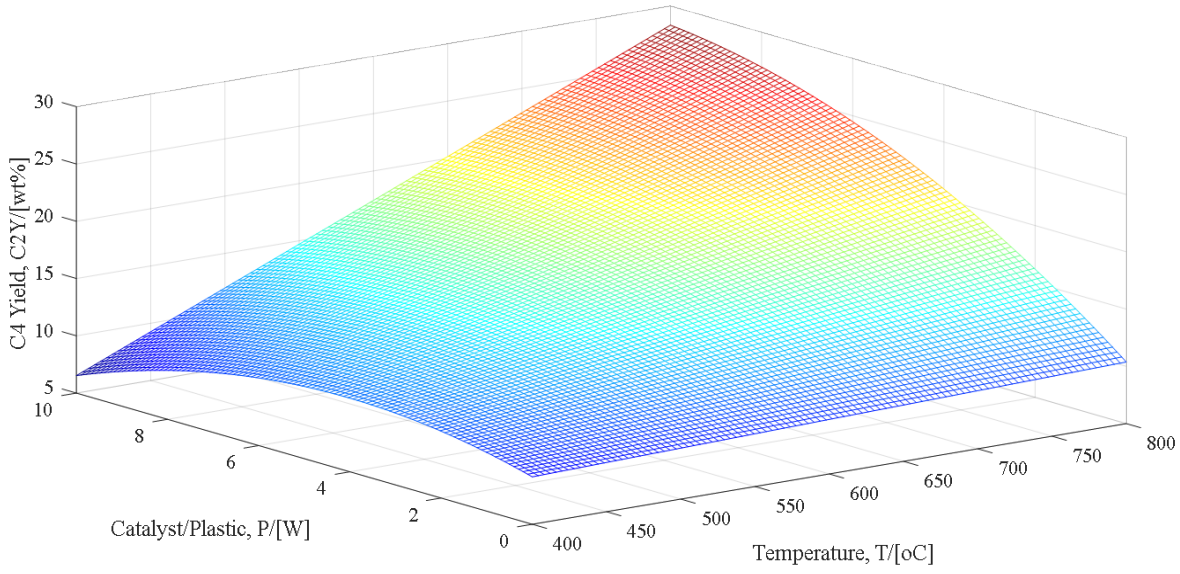

(c) Yield of C_4 predictions

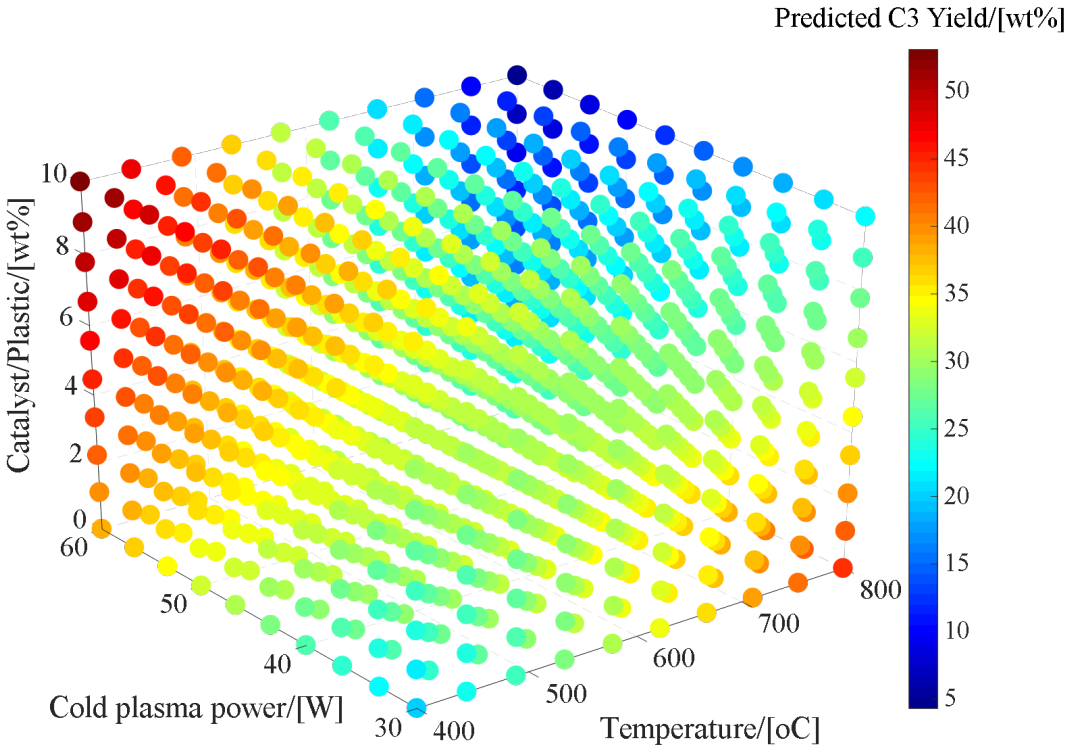

(d) Yield of C_3 predictions

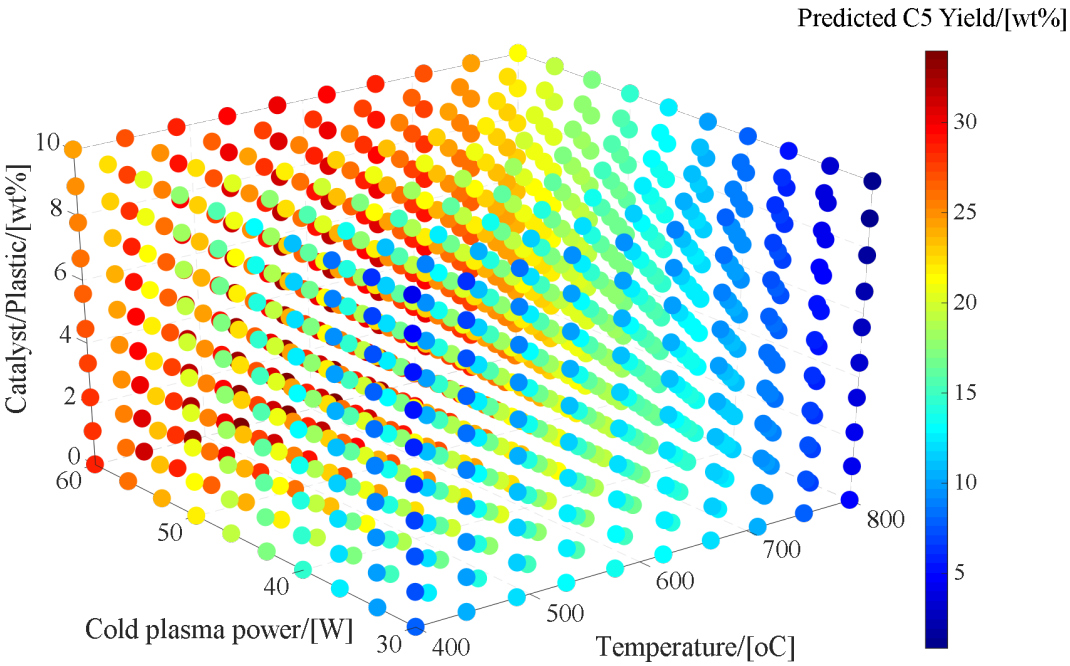

(e) Yield of C_5 predictions

Figure 6.3 Prediction plots of the yield of gas products: (a) H_2 and CH_4, (b) C_2, (c) C_3, (d) C_4 and (e) C_5

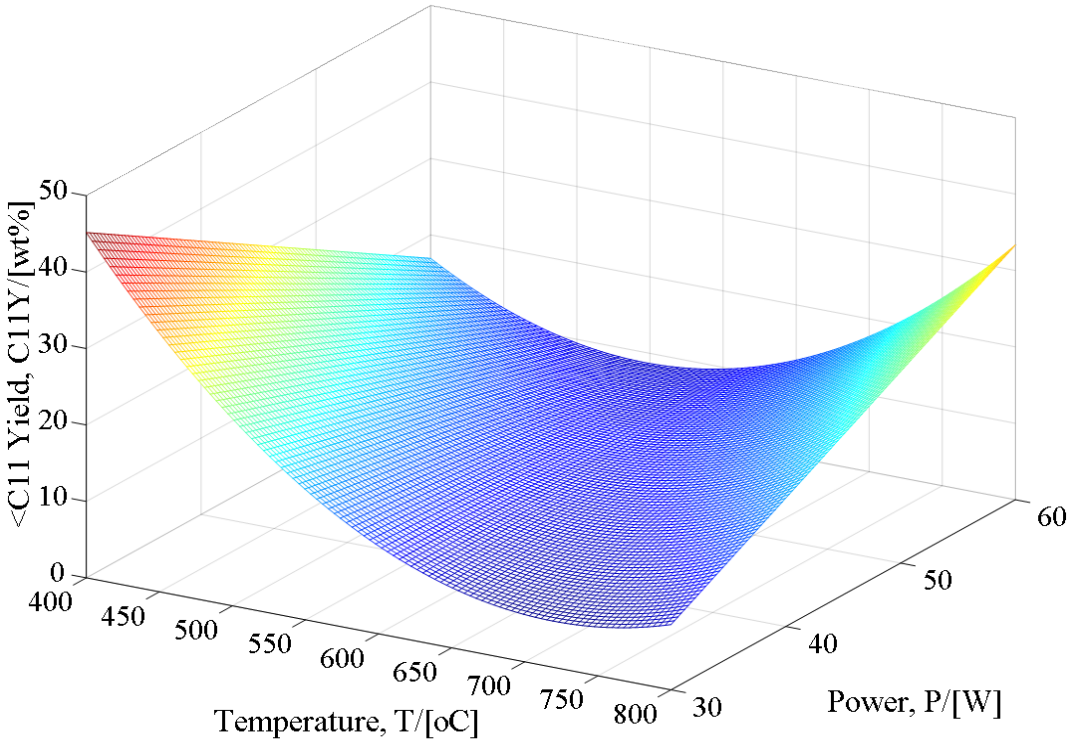

(a) Yield of $<C_{11}$ predictions

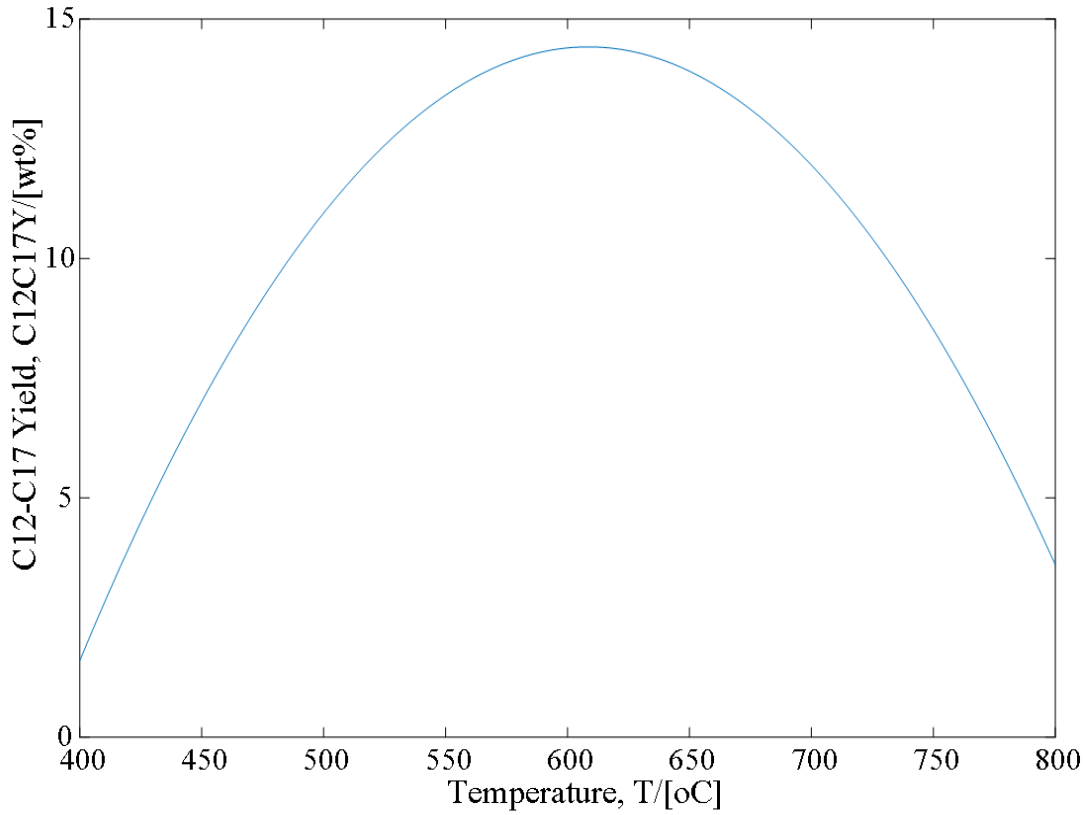

(b) Yield of C_{12}-C_{17} predictions

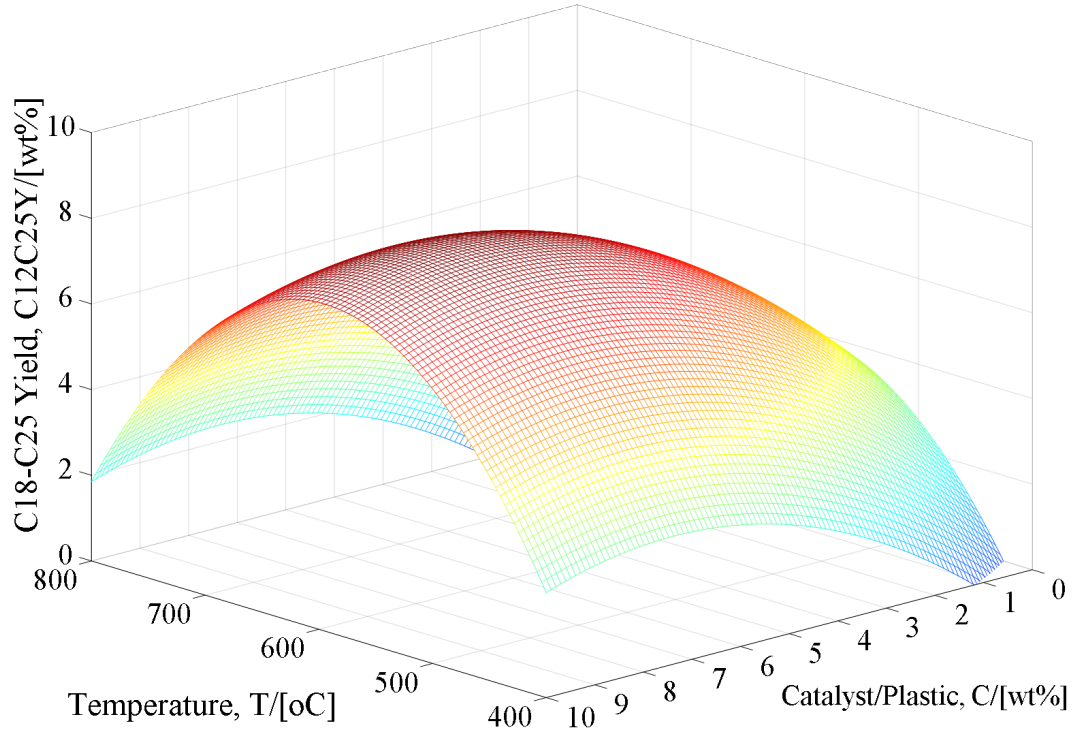

(c) Yield of C_{18}-C_{25} predictions

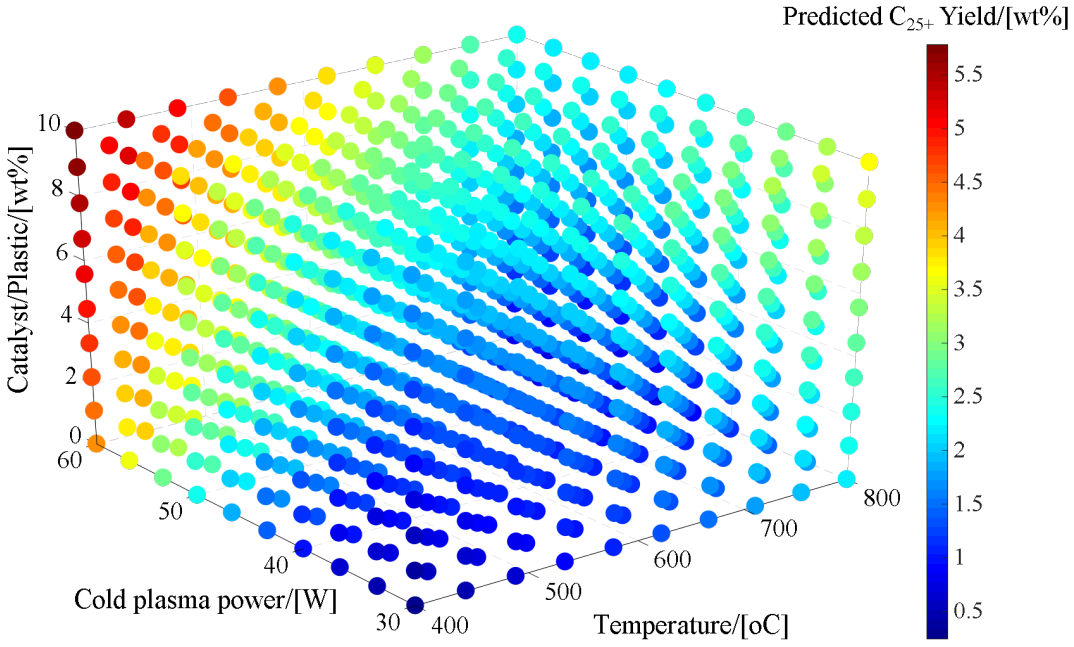

(d) Yield of C_{25+} predictions

Figure 6.4 Prediction plots of the yield of wax products: (a) $<C_{11}$, (b) C_{12}-C_{17}, (c) C_{18}-C_{25} and (d) C_{25+}

cold plasma power decomposed C_3 hydrocarbons into lower ones hydrocarbons e.g. C_2 and CH_4. Figure 6.5 shows the predictions for the yield of C_2 and C_3 obtained with the new models (Equations 6.12 and 6.13).
Figure 6.6 compares the fitting of experimental and predicted yields obtained using the old and new C_2 and C_3 models. The fitting for both C_2 models was very similar meaning the removal of the outlines was not necessary. Opposite, the new C_3 models showed better fitting than the old one.
All the results aforementioned showed the myriad of compounds obtained from CPCP. Due to this wide distribution of products, parameter optimisation to maximise the yield of desired products is essential. For instance, maximum yield of the monomer (C_3) was obtained at 70 W and 0 wt% catalyst amount for any tested temperature. Opposite, maximum yield of C_2, a key chemical block, was obtained at 768 °C, 20 W and 0 wt% catalyst amount. When the wax products were considered in the optimisation, maximum yield of the lighter fraction ($<C_{11}$) required operation at 432 °C and 20 W for any catalyst amount tested. Therefore, the models obtained through Equations 6.2 to 6.13 allowed parameter optimisation to maximise all the desired products instead of individual ones.
Overlaid contour plots (Figure 6.7) visually identified the operating areas to optimise one or more desired response variables at the same time. The white areas in Figure 6.7 represent the operating range at which the target yields set were obtained. Figure 6.7a shows that maximum amount of C_2 (12-15wt% target) and C_3 (30-35 wt% target) was obtained at cold plasma power below 45 W, catalyst amount below 4 wt% and 500 °C. Opposite, when the desired fraction was the wax, Figure 6.7b showed two optimum operating regions to maximise the lighter wax fraction ($<C_{11}$, 15-20 wt% target) while minimising the heavier wax fractions (C_{18}-C_{25}, 0-5 wt% target and C_{25+}, 0-2 wt% target): 500 °C, 45 W and catalyst amount below 2 wt% or 750 °C, 45 W and catalyst amount below 7 wt%.
Conditions on Figure 6.7 were selected to maximise the products with higher value i.e. ethylene, propylene and light wax. Results from this study suggested that waste PP CPCP using SZ as catalyst operated at optimum conditions at 500 °C, low to medium SZ catalyst loads (0-4 wt%) and medium cold plasma power (45 W).

6.4 Direct production of carbon nanotubes and hydrogen from waste PP cold plasma assisted catalytic pyrolysis

This section discusses the effect of pyrolysis temperature (450-600 °C) and the addition of 5 wt% Ni/Al_2O_3 catalyst to CPCP at SED=135 J/mL (45 W supplied) to study their influence over the yield of gas and CNTs growth.

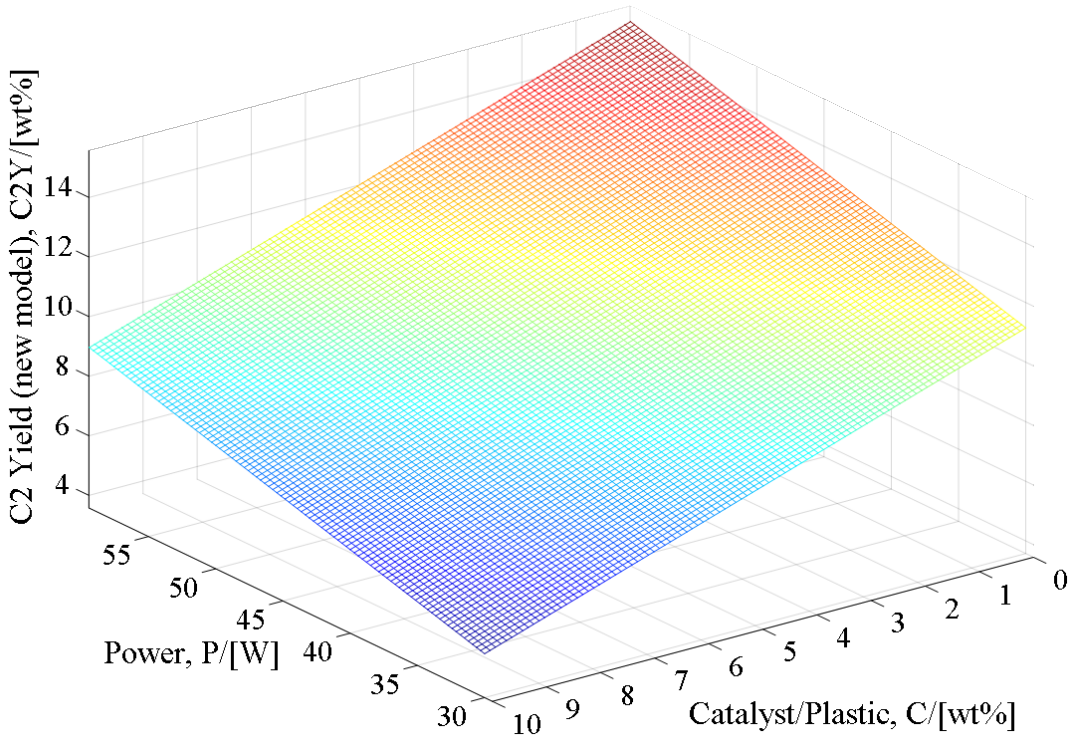

(a) C_2 yield predictions with new model

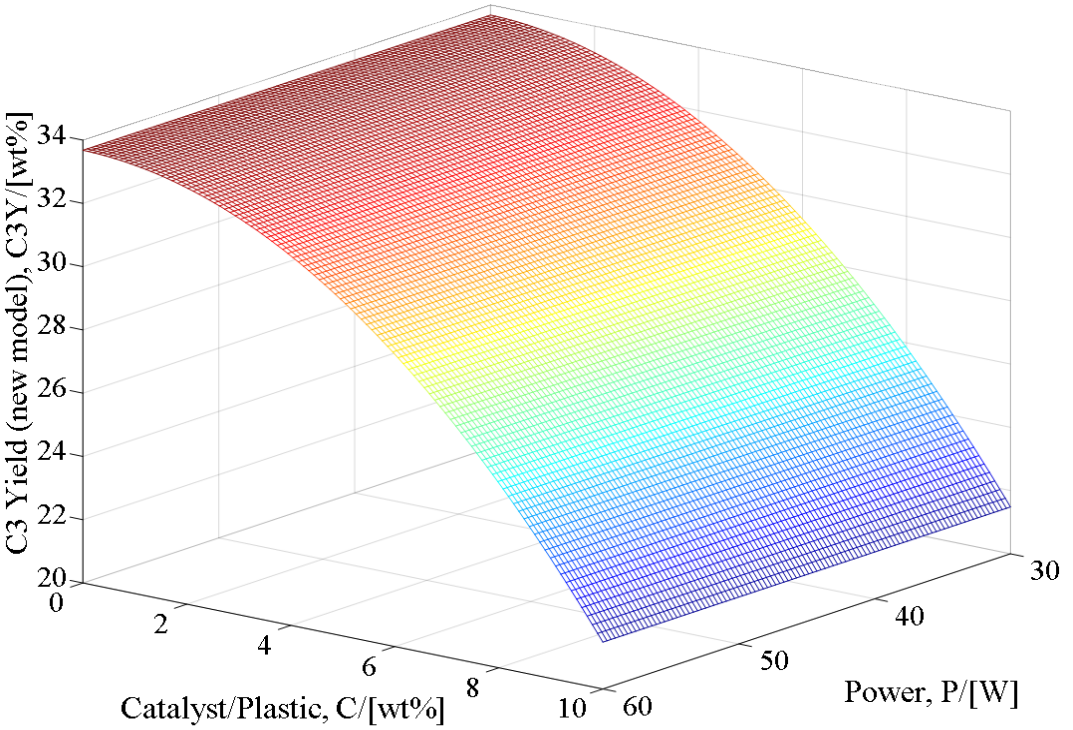

(b) C_3 yield predictions with new model

Figure 6.5 Prediction of the yield of (a) C_2 and (b) C_3 obtained with Equations 6.12 and 6.13

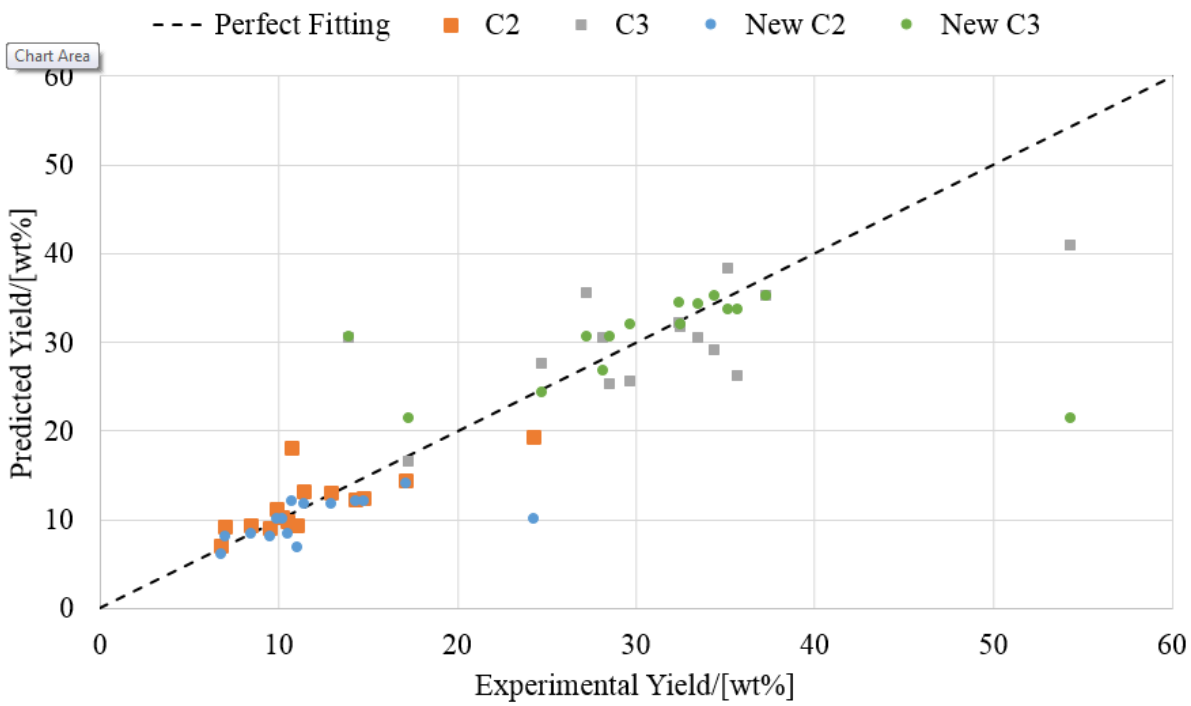

Figure 6.6 Fitting of experimental and predicted yield of C_2 and C_3 using the old (squares) and new (circles) models obtained with RSM

Table 6.5 Solid residue, wax and gas yields from waste PP cold plasma assisted catalytic pyrolysis compared to thermal pyrolysis and cold plasma assisted non-catalytic pyrolysis (N=Ni/Al_2O_3 catalyst)

[PP/(°C)/(°C/min)/(J/mL)/(wt%)]	Residue / [wt%]	Wax / [wt%]	Gas / [wt%]
PP/500/55/0/N0wt	0.65±0.20	77.76±1.89	21.60±1.69
PP/700/55/0/N0wt	0.49±0.28	67.81±3.17	31.41±3.30
PP/600/55/0/N5wt	0	36.66	63.34
PP/600/55/135/N0wt	1.46±0.47	40.82±0.10	57.72±0.57
PP/450/55/135/N5wt	9.06	29.39	61.55
PP/500/55/135/N5wt	0.97	27.28	71.75
PP/600/55/135/N5wt	0.07	38.00	61.93

6.4.1 Effect of Ni/Al_2O_3 catalyst and cold plasma on gas yield and hydrogen generation

Mass balance and gas composition for the cold plasma pyrolysis experiments are shown in Tables 6.5 and Figure 6.8 respectively.

Table 6.5 shows that 5 wt% of Ni/Al_2O_3 catalyst achieved a higher gas yield at lower temperatures (63.34 wt% at 600 °C and 5 wt% Ni/Al_2O_3) than thermal pyrolysis (31.41wt% at 700 °C and no catalyst). Cold plasma alone had a similar effect to Ni/Al_2O_3, increasing the gas yield to 57.72wt% (600 °C and 135 J/mL) compared to thermal pyrolysis at higher temperature. However, the highest gas yield was found when Ni/Al_2O_3 was distributed in the cold plasma discharge gap (71.75 wt% at 500 ∘C, 135 J/mL and 5 wt% Ni/Al_2O_3) at even lower temperatures than thermal, catalytic only and cold plasma alone pyrolysis.

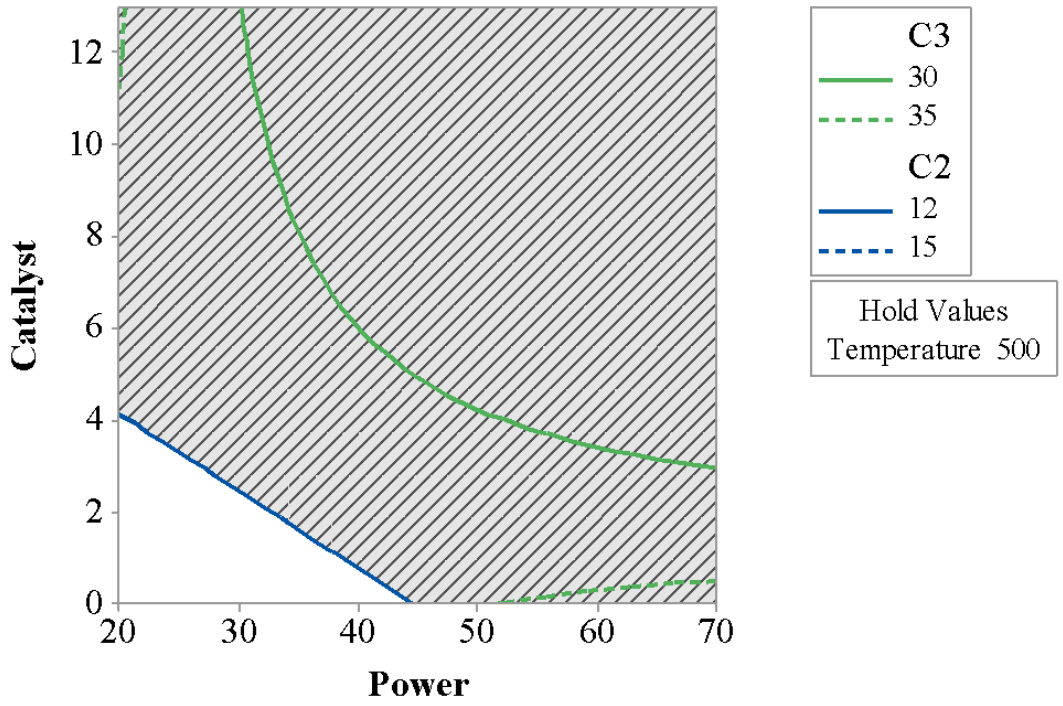

(a) Overlaid contour plot for maximum C_2 and C_3

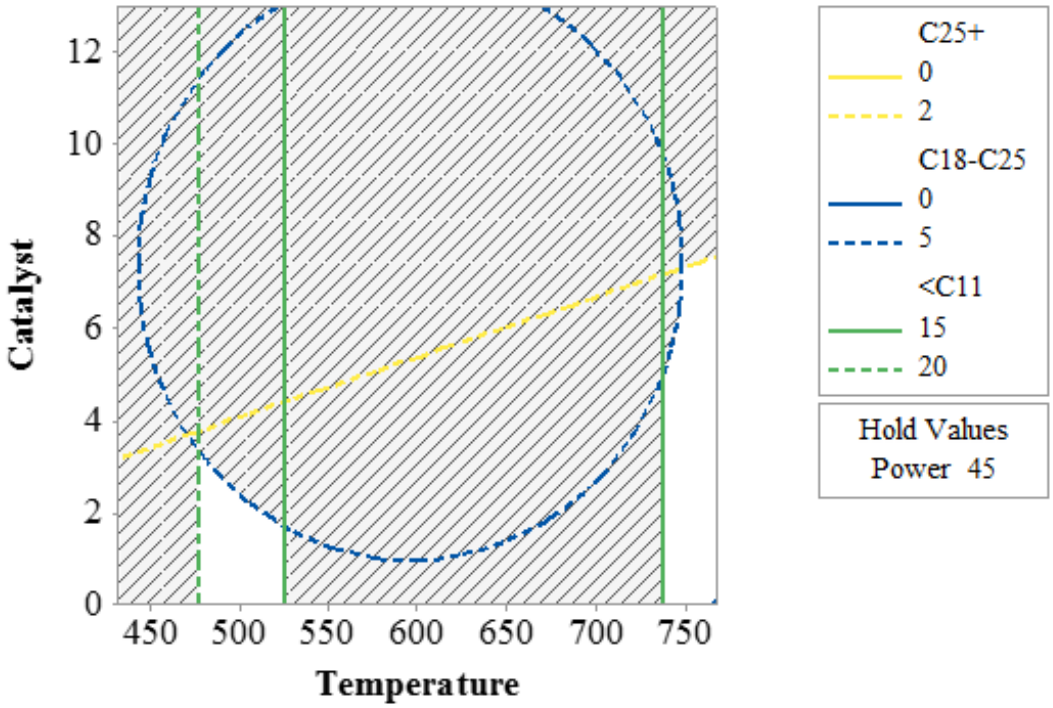

(b) Overlaid contour plot for maximum $<C_{11}$ and minimum C_{18}-C_{25} and C_{25+}

Figure 6.7 Overlaid contour plot for maximum C_2 (12-15wt%) and C_3 (30-35wt%) at fixed temperature (600 °C) and maximum $<C_{11}$ (15-20wt%) with minimum C_{18}-C_{25} (0-5wt%) and C_{25+} (0-2wt%) at fixed cold plasma power (45 W)

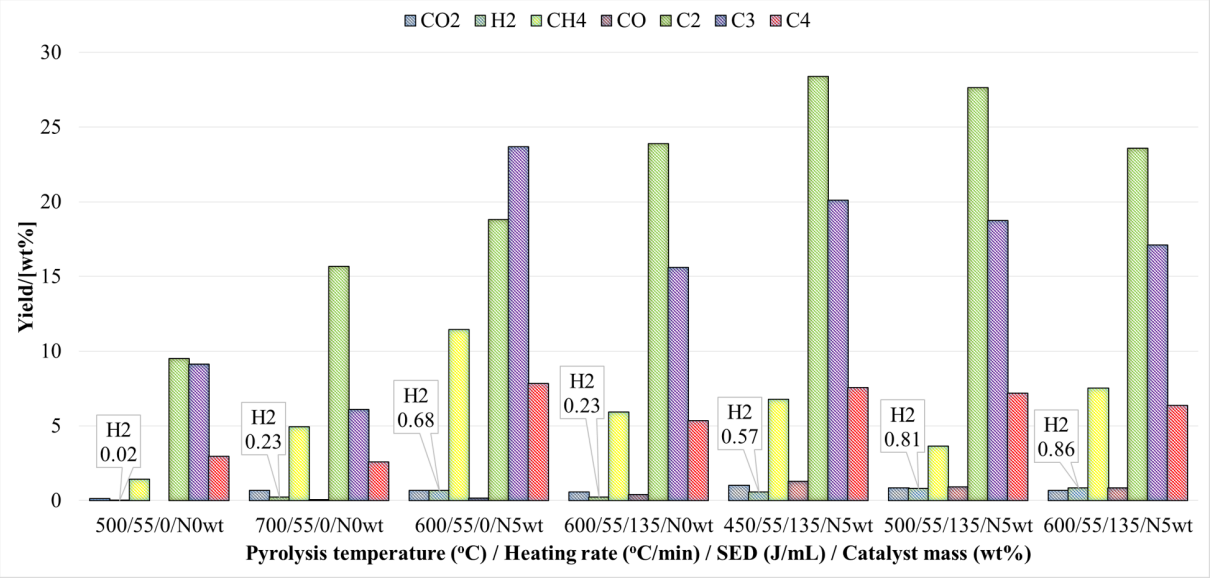

Figure 6.8 Comparison of gas composition at various conditions (N=Ni/Al_2O_3)

Both Ni/Al_2O_3 and cold plasma enhance the cracking compared to thermal pyrolysis and thus, promoted the formation of lighter products i.e. more gas (López, De Marco, Caballero, Laresgoiti, Adrados and Aranzabal, 2011). In the case of Ni/Al_2O_3, the cracking activity is caused by Al_2O_3 acidity. Cold plasma on the other hand provides a very reactive environment with higher energy species (electron=964.85 kJ/mol, ion=192.97 kJ/mol, excited particle=1929.71 kJ/mol and photon=289.46-3859.41 kJ/mol (Fan et al., 2018)) than the bond energies in waste PP (C-H=415 kJ/mol and C-C=331 kJ/mol (Fan et al., 2018)). Therefore, lower temperature is required to reach the activation energy of C-C and C-H bond cleavage forming more lighter products.

Figure 6.8 shows the product distribution in the gas fraction at various conditions. The gas fraction of waste PP thermal pyrolysis comprised of mostly C_2-C_4 hydrocarbons with little CH_4 and H_2. High temperature (700 °C) promoted the formation of CH_4 and C_2 at the expense of C_3 and C_4 through secondary cracking. However, the H_2 yield was low at any temperature (0.02 wt% 500 °C and 0.23 wt% at 700 °C). Ni/Al_2O_3 at 600 °C increased the yield of hydrogen (0.7 wt%) and C_1-C_4 hydrocarbons, especially the one of the monomer (C_3H_6) up to 23.7 wt%, compared to thermal pyrolysis (9.13 wt% at 500 °C and 6.09 wt% at 700 °C). This was caused by Ni/Al_2O_3 cracking and hydrogenation reactions enhancement. Cold plasma alone also increased the yield of light hydrocarbons, particularly C_2 (23.9 wt%), but not the hydrogen yield (0.2wt%). Combination of the catalyst and cold plasma resulted in a synergistic effect with a rise on both C_3H_6 and hydrogen yields (17.12 wt% and 0.9 wt% at 600 °C respectively) even at low temperatures (20.09 wt% and 0.8wt% at 450 °C respectively).

Figure 6.9 shows the total hydrogen flow recovered at various conditions and a comparison of the evolution of hydrogen flow between waste PP thermal pyrolysis and CPCP. As discussed above, Figure 6.9a shows that the total hydrogen flow recovered with only Ni/Al_2O_3 at 600 °C compared to thermal pyrolysis at 700 °C increased from 124.99 mL/s to 224.69 mL/s. Although cold plasma alone produced higher hydrogen flows than thermal pyrolysis (137.16 mL/min at

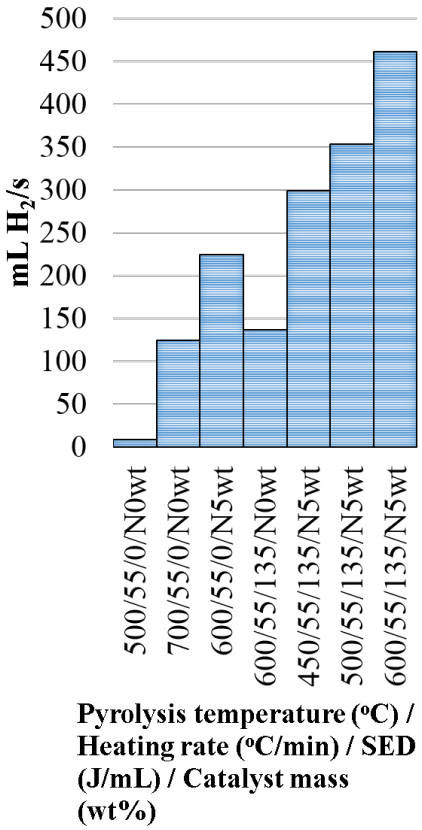

(a) Total hydrogen flow (mL/s) (N=Ni/Al_2O_3)

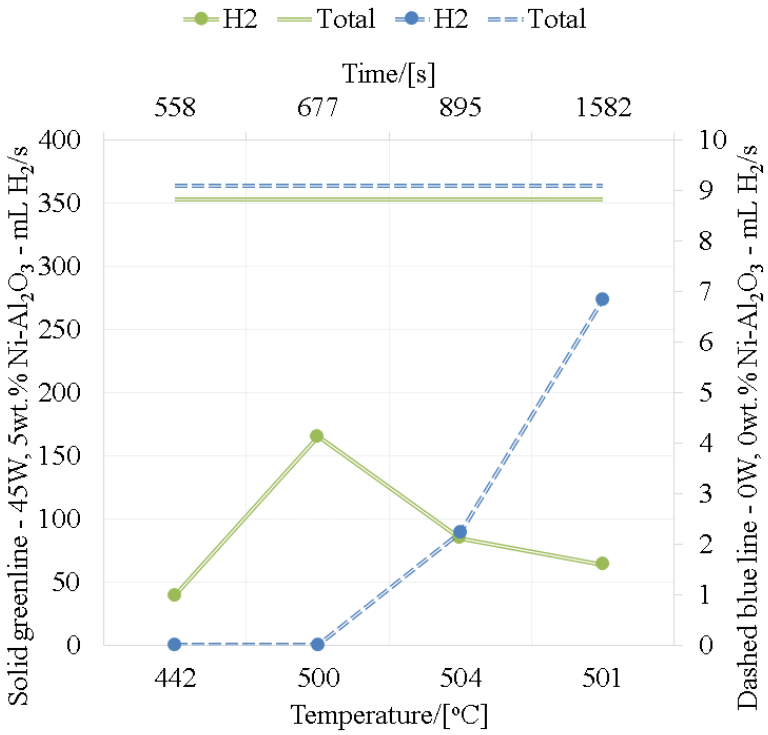

(b) Comparison of H_2 flow (mL/s) during reaction between catalytic (right, doted line) and cold plasma catalytic (left, solid line) pyrolysis

Figure 6.9 Comparison of hydrogen flow between waste PP thermal and cold plasma assisted catalytic pyrolysis

135 J/mL and 600 °C), the synergistic effect of Ni/Al_2O_3 and cold plasma was more significant with a total 461.50 mL/s of hydrogen at 600 °C. As expected, high temperature produced more hydrogen than low temperatures (461.50 mL/s at 600 °C compared to 299.22 mL/s at 450 °C both at 135 J/mL and 5 wt% Ni/Al_2O_3) since temperature also contributes to the increase in the cracking rate.
A direct comparison of hydrogen flow evolution during reaction at 500 °C (Figure 6.9b) showed that, although the temperature for maximum hydrogen flow was the same (about 500 °C), the time to obtain that amount decreased for waste PP CPCP (677 s) compared to thermal pyrolysis (1582 s). This effect was due to the increase in the cracking rate caused by the presence of Ni/Al_2O_3 and cold plasma. For CPCP, the amount of hydrogen decreased as reaction proceeded because hydrogen radicals generated by cold plasma recombined with the carbonium ions, created along the volatiles chain by Ni/Al_2O_3, forming alkenes products in the gas and wax.

6.4.2 Effect of cold plasma on CNTs growth

TEM images of used Ni/Al_2O_3 catalyst in Figure 6.10 show multiwalled CNTs formed with (a-c) and without (d-f) cold plasma. The multiwall CNTs diameter was around 40 nm (15 nm of wall thickness) in the presence of cold plasma and around 30 nm (11 nm of wall thickness) in the absence of cold plasma. Two types of carbon material were observed in Figure 6.10 according to the angle between the graphene layers and growth axis (Zhou et al., 2006): graphene layers were parallel to the growth axis in the presence of cold plasma (Figure 6.10c) and graphene layers at a 12 ± 3^o angle to the growth axis (fishbone) in the absence of cold plasma (Figure 6.10e).
It was found (Gallego et al., 2011; Zhou et al., 2006) that both the catalyst and the carbon source are vital parameters in the formation of the microstructure and morphology of CNTs. Therefore, is not surprising that the presence of cold plasma affected the precipitation of carbon on the catalyst metal (Ni) since it also altered the catalyst performed as aforesaid in section 6.4.1.

XRD analysis of used catalyst

Figure 6.11 shows the XRD spectrum of used Ni/Al_2O_3 after waste PP CPCP at 600 °C, 55 °C/min, 135 J/mL and 5 wt% Ni/Al_2O_3. The diffraction peak at 25^o indicated the presence of highly graphitized carbon i.e. CNTs. Pure graphene, identified by a diffraction peak at 54.5^o, was not present suggesting the amount of the perfect graphene layers was negligible agreeing well with previous studies where plastic waste were used as feedstock to produce CNTs (Wu et al., 2013).

Raman analysis of used catalyst

Graphitization of the CNTs i.e. the amount of free carbon or graphite, was determined by Raman spectroscopy via three bands: (i) the D-band at 1300 cm^{-1}, which indicates the disorder of carbons; (ii) the G-band at 1560 cm^{-1}, which measures the crystallinity or pristine arrangement of carbon atoms; and (iii) the G'-band at 2690 cm^{-1}, which indicates the purity of

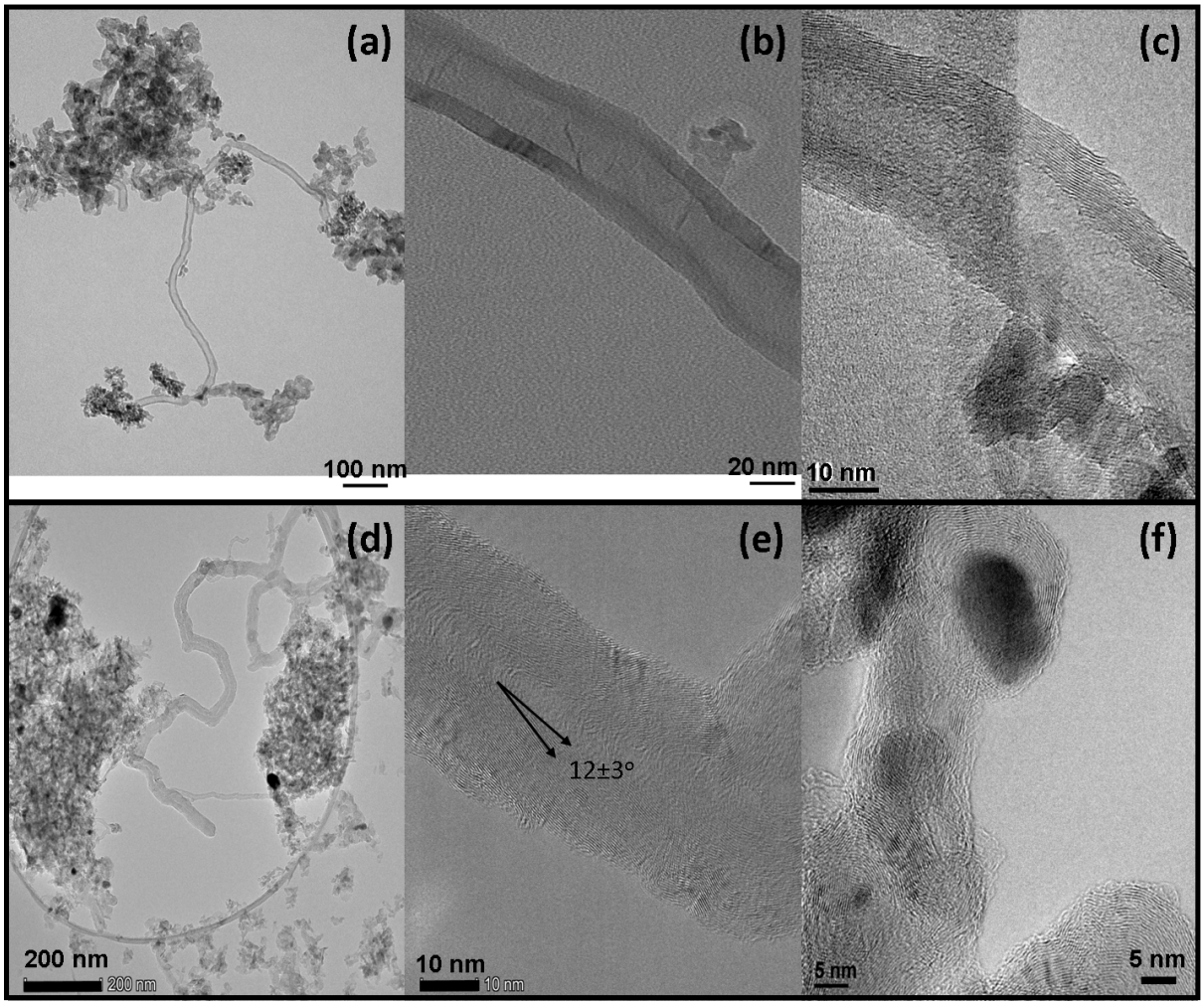

Figure 6.10 TEM images of used Ni/Al_2O_3 catalyst: (a-c) at 600 °C, 55 °C/min, 135 J/mL and 5 wt% Ni/Al_2O_3 and (d-f) at 600 °C, 55 °C/min, 0 J/mL and 5 wt% Ni/Al_2O_3

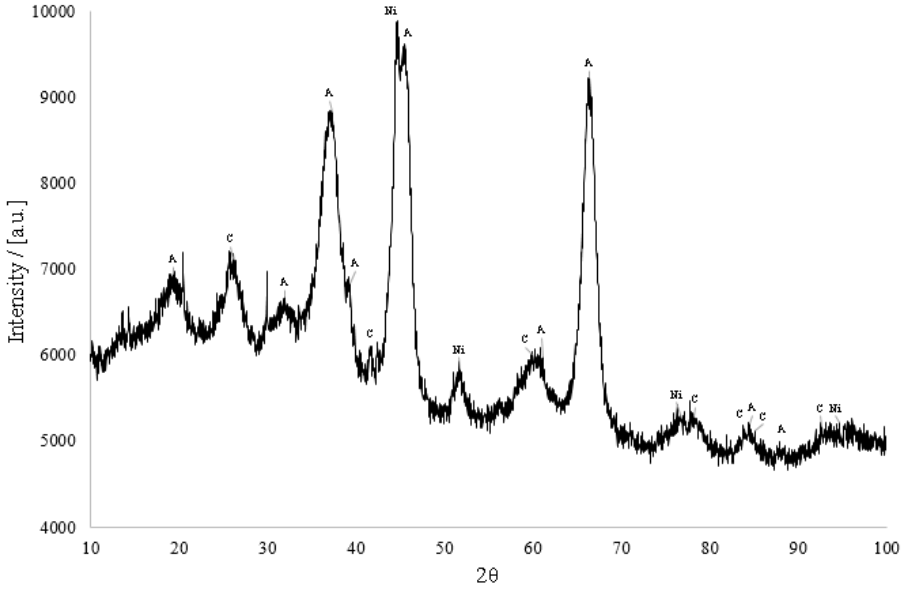

Figure 6.11 XRD spectrum of used Ni/Al_2O_3 catalyst after waste PP cold plasma assisted catalytic pyrolysis at 600 °C, 55 °C/min, 135 J/mL and 5 wt% Ni/Al_2O_3

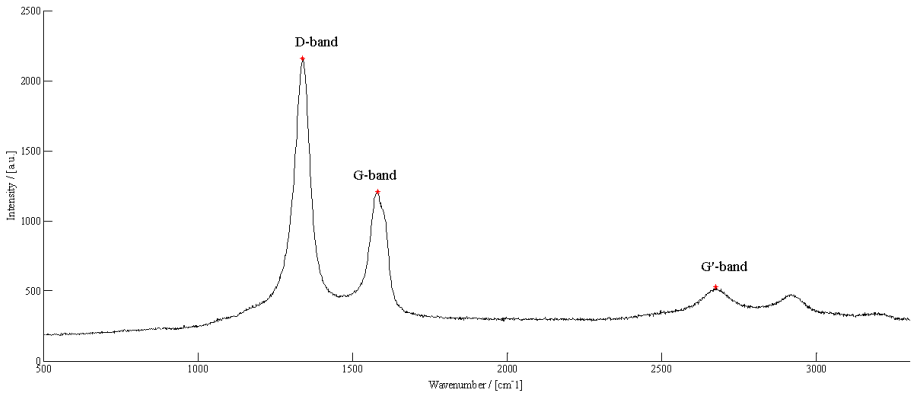

Figure 6.12 Example of Raman spectrum obtained for used Ni/Al_2O_3 catalyst after waste PP cold plasma assisted catalytic pyrolysis at 600 °C, 55 °C/min, 135 J/mL and 5 wt% Ni/Al_2O_3

Table 6.6 I_D/I_G and I'_G/I_G ratios obtained from Raman spectra of used Ni/Al_2O_3 catalyst (N = Ni/Al_2O_3)

[PP/(°C)/(°C/min)/(J/mL)/(wt%)]	I_D/I_G	I'_G/I_G
PP/600/55/135/N5wt	1.79	0.44
PP/450/55/135/N5wt	0.87	0.45
PP/600/55/0/N5wt	1.13	0.41

CNTs. CNTs were characterised by the ratio of intensity of the D to G band (I_D/I_G), and the ratio of intensity of the G' to G band (I'_G/I_G). Figure 6.12 shows an example (600 °C, 55 °C/min, 135 J/mL and 5 wt% Ni/Al_2O_3) of the Raman spectrum with the three bands present. Table 6.6 shows the results for all tested conditions.

The I_D/I_G ratio measures the ratio of disordered to graphitic carbon; therefore, the highest the value the more disordered CNTs are. Commercial multiwall CNTs have an I_D/I_G ratio between 0.63–1.5 (Zhang, Nahil, Wu and Williams, 2017) suggesting that results shown in Table 6.6 were within the commercial range. The I'_G/I_G ratio estimates the purity of carbon. The presence of the G'-band indicates defects in the graphitic crystallinity of the carbon and thus, the lower the I'_G/I_G ratio the less defects present. The most graphitic CNTs were found at high temperature and in the absence of cold plasma.

Temperature programmed oxidation (TPO) of used catalyst

Figure 6.13 shows the variation of the concentration of CO_2 produced and measured by mass spectroscopy during used Ni/Al_2O_3 catalyst TPO analysis at various temperatures. Each peak is formed by three carbonaceous fractions eluted at different temperatures: amorphous carbon (low temperature, eluted before 300 °C), graphitic (medium temperature, eluted up to 400 °C) and filamentous (high temperature, eluted at 500 °C). Table 6.7 shows the total carbon deposited on the surface of used Ni/Al_2O_3 and the relative amount of each of three aforementioned carbonaceous fractions.

The amount of total carbon deposited on Ni/Al_2O_3 catalyst was substantial for all tested conditions reaching almost double in the absence of cold plasma compared to the cases with of cold plasma. However, observing the three types of carbon individually, cold plasma eliminated

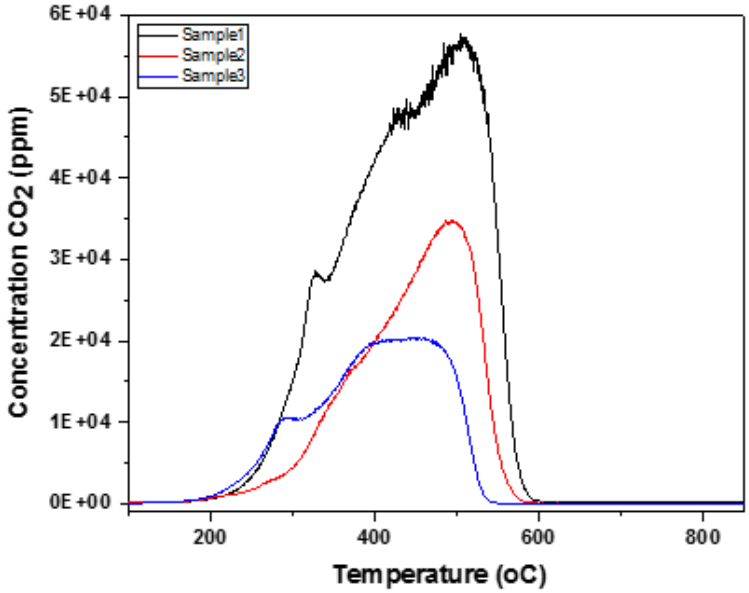

Figure 6.13 Cumulative temperature programmed oxidation patterns obtained from used Ni/Al_2O_3 catalyst: Sample 1=PP/600/55/0/N5wt, sample 2=PP/600/55/135/N5wt and sample 3=PP/450/55/135/N5wt (PP/XXX/YY/ZZ/AA: PP=polypropylene, XXX=pyrolysis temperature [°C], YY=heating rate [°C/min], ZZ=SED [J/mL] and AA=Ni/Al_2O_3 catalyst mass [wt%])

Table 6.7 Total amount of carbon deposited and relative amount of carbonaceous fractions deconvoluted from temperature programmed oxidation analysis peaks of used Ni/Al_2O_3 (PP/XXX/YY/ZZ/AA: PP=polypropylene, XXX=pyrolysis temperature [°C], YY=heating rate [°C/min], ZZ=SED [J/mL] and AA=Ni/Al_2O_3 catalyst mass [wt%])

Carbon	Total/[wt%]	Amorphous/[%]	Graphitic/[%]	Filamentous/[%]
PP/450/55/135/N5wt	14	23.53	56.86	19.61
PP/600/55/135/N5wt	18	0	52.38	47.62
PP/600/55/0/N5wt	38	28.21	46.15	25.64

the poorly organised amorphous carbon in favour of a more stable graphitic one characteristic of CNTs. Increasing the temperature of waste PP CPCP from 450 to 600 °C enhanced the formation of the more stable filamentous carbon over the amorphous one (from 19.61 % to 47.62 %). Therefore, the presence of cold plasma in waste PP catalytic pyrolysis promoted the growth of more stable forms of carbon (graphitic and filamentous) over the poorly organised amorphous carbon compared to catalytic only pyrolysis, improving the quality of the CNTs recovered. Previous studies on CNT recovery via waste plastic pyrolysis do not involve the use of cold plasma and therefore results cannot be directly compared. However, it has been reported that plasma improves the uniformity of CNTs diameter, height (Teo et al., 2003) and alignment (Chhowalla et al., 2001) when combined with CVD showing similarity to this study.

6.5 Summary

This chapter showed the positive effect of SZ catalyst and cold plasma to increase the recovery waste PP monomer (propylene) up to 54.31 wt% at 500 °C, SED of 180 J/mL and 10 wt% SZ catalyst and the amount of ethylene in the gas up to 24.29 wt% at 600 °C, SED of 135 J/mL and 5 wt% SZ catalyst. It also developed statistical models able to predict the yield of all the compounds in the gas and wax fractions. These models were used in parameter optimisation finding that optimum conditions to maximise the yield of C_2, C_3 and $<C_{11}$ hydrocarbons from waste PP cold plasma assisted catalytic pyrolysis using SZ as catalyst were 500 °C, medium cold plasma power (45 W) and low to medium SZ catalyst loads (0-4 wt%).
Long multiwall CNTs with relatively small diameters (30-40 nm) were produced on Ni/Al_2O_3 catalyst from waste PP cold plasma assisted catalytic pyrolysis. Cold plasma and Ni/Al_2O_3 presented a strong synergistic effect that increased the hydrogen flow recovered in the gas up to 461.50 mL/s compared to the individual conditions (227.97mL/s for catalytic alone and 137.16 mL/s for cold plasma alone) and reduced up to 50 % the reaction time for maximum hydrogen flow production compared to thermal pyrolysis. Cold plasma showed a positive effect on CNTs structure favouring parallel CNTs instead of the fishbone CNTs derived from catalytic pyrolysis in the absence of cold plasma. The structure would affect CNTs surface reactivity and therefore CNTs potential applications. However, this chapter shows only a preliminary study and further work is needed to fully understand the suitability of cold plasma assisted catalytic pyrolysis of plastic waste for hydrogen and high-value carbon products.

Chapter 7 Catalytic pyrolysis of polyethylene terephthalate to recover benzoic acid from pyrolysis wax

This chapter involves the use of waste PET, often forgotten in literature for plastic waste pyrolysis, to extend the investigation of SZ as a catalyst initiated on chapters 5 and 6. PET differs from the other plastic waste discussed so far i.e. HDPE and PP, due to the presence of aromatic rings and oxygenated groups (ester) therefore, different thermal behaviour and product distribution were expected. The effect of the catalyst, pyrolysis temperature and their interaction on waste PET catalytic pyrolysis were novelly assessed. In addition, this chapter turned the attention into the recovery of benzoic acid from waste PET catalytic pyrolysis wax which was not previously reported elsewhere. This constitutes a novel approach regarding the range of products recovered from PWP. The contents of this chapter have been published in "Benzoic acid recovery via waste poly(ethylene terephthalate) (PET) catalytic pyrolysis using sulphated zirconia catalyst" at *Journal of Analytical and Applied Pyrolysis* (Diaz-Silvarrey, McMahon and Phan, 2018).

7.1 Background

PET is widely used in the textile industry, for food packaging and the production of bottles (Bartolome et al., 2012). The products recovered from waste PET pyrolysis differ from those of other plastic waste types as they comprise of a range of aromatic and oxygenated compounds e.g. acetaldehyde, vinyl benzoate and benzoic acid (Dzięcioł and Trzeszczyński, 2000). Pyrolysis of waste PET occurs through the cleavage of the ester linkage via the effect of either temperature or both temperature and a catalyst resulting in the formation of vinyl ester and carboxyl compounds (e.g. benzoic acid). The vinyl ester decomposes further into other compounds e.g. acetaldehyde, acetophenone or light hydrocarbons (C_1-C_3) releasing CO_2 in the gas (Çit et al., 2010; Venkatachalam et al., 2012). Benzoic acid is a high-value chemical product used in the food and beverage industry and as a feedstock for phenol manufacture. It is often used as an intermediate in the manufacture of benazoates and other related antifungal preservatives (E210, E211, E212 and E213) found in numerous foods e.g. soft drinks, coffee, salad dressings, etc. (Global Market Insights, 2017), as well as a precursor of plasticizers, fungal ointments for medical use, and calibrating substance for bomb calorimeters (Global Market Insights, 2017). Its market size is expected to increase by almost 30 % in the next few years (from 480 ktons in 2014 to 620 ktons in 2023) (Global Market Insights, 2017) and its price is around $4000/Mton (Loong, 2011).

Therefore, the recovery of this compound is very important due to the potential economical improvement of the pyrolysis process.
Research on plastic waste pyrolysis has been discussed in section 2.3 in chapter 2. SZ was again chosen as a catalyst because: (i) its acidity (Srinivasan et al., 1996) activates light alkanes at room temperature (Li et al., 2005) proving effective for cracking of long chain hydrocarbons (triglycerides/vegetable oil (Eterigho et al., 2011; Helwani et al., 2009), waste PS (Lin and White, 1997) and waste HDPE (Diaz-Silvarrey, Zhang and Phan, 2018)); (ii) its cheaper than commercial zeolites; and (iii) there is limited research involving the use of SZ catalyst for plastic waste, particularly waste PET.

7.2 Experimental

Waste PET samples used in this chapter were cut into 1.5 x 1.5cm size particles.
Characterisation was discussed in section 3.1.1 in chapter 3. SZ catalyst was synthesised and characterised as described in section 3.1.3 in chapter 3 by a solvent-free method proposed by Eterigho et al. (2011). Experiments were conducted in a one-stage pyrolysis set-up (Figure 3.12 in chapter 3), explained in section 3.2.2 in chapter 3, using waste PET samples of approximately 5.04 ± 0.03g. The analysis of pyrolysis products was described in sections 3.2.4 and 3.2.5 in chapter 3. Gas samples, collected in one 0.6L Supelco Tedlar bag at the final pyrolysis temperature, were analysed by GC-TCD/FID. The wax fraction in the condenser was analysed by both GC-MS (qualitative analysis) and GC-FID (quantitative analysis) and ^{1}H-NMR and FT-IR to cross examine the GC-MS results.

7.3 Effect of operating conditions on decomposition of PET

Figure 7.1 shows the effect of temperature and catalyst:plastic mass ratio on the yield of gas (left), wax (middle) and solid residue (right) products. It was found that temperature had the strongest effect on the product yield followed by the catalyst:plastic mass ratio at all tested conditions: temperature (450-600 °C), volatile residence time in the heated zone (10-30 s) and catalyst:plastic mass ratio (3-10 wt%). Increasing temperature enhanced the production of the gas at the expense of wax. At low temperatures (450 °C) higher catalyst loads (10 wt%) increased the solid residue yield but did not have a clear effect on the gas and wax yields. At high temperature (600 °C), the gas yield was maximum and the wax yield minimum at medium catalyst loads (6.5 wt%). Opposite, at that temperature, the solid residue yield increased with catalyst (12.45 wt% with no catalyst, 13.37 wt% at 3 wt% catalyst and 20.28 wt% at 10 wt% catalyst). Since the solid residue represented only the residue recovered from the waste PET sample combustion boat after pyrolysis and it was never in contact with the catalyst bed, the variation of solid residue yield with catalyst was coincidental. Differences observed in the solid residue yield were mainly caused by the use of different waste PET products with different compositions e.g. drink bottles, ready-meal packets, etc.

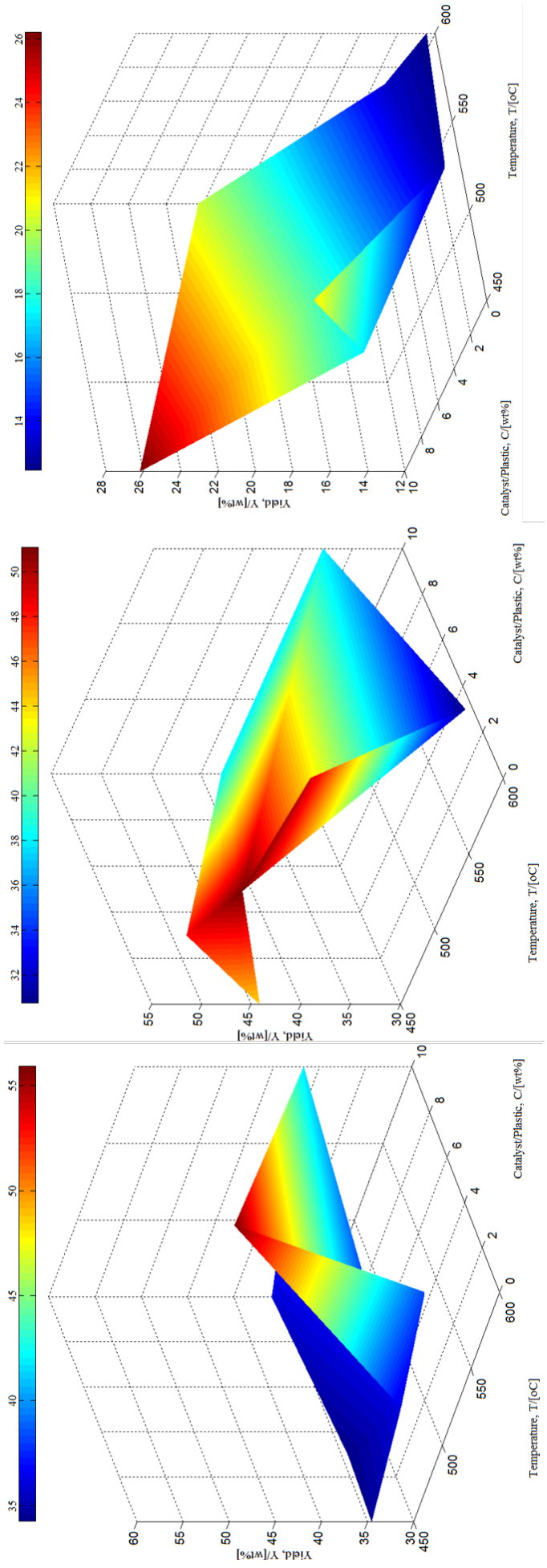

Figure 7.1 Effect of temperature and catalyst:plastic mass ratio on the yield of gas (left, ± 6.37 wt%), wax (middle, ± 7.60 wt%) and solid residue (right, ± 8.53 wt%) at volatile residence time of 20s (red areas represent higher values, blue areas lower values and geen and yellow areas are intermediate values)

The effect of SZ catalyst on waste PET catalytic pyrolysis was more prominent at high temperature (600 °C): increasing the catalyst load at 450 °C from 0 to 10 wt% resulted in a 3 % increase of the gas yield (from 34.54 wt% to 35.87 wt%) while at 600 °C the same variation in the catalyst load increased the gas yield by 29 % (from 38.19 wt% to 55.91 wt%). This suggested SZ catalyst required a minimum activation temperature above 450 °C to enhance secondary cracking.

The volatiles residence time i.e. the time volatiles remained inside the catalyst bed in contact with the catalyst, had little effect product yields in the tested range of 10-30s. This observation agreed well with Mastral et al. (2003) who observed that residence times between 0.81-1.45 s had no significant effect on the product distribution of plastic waste pyrolysis at temperatures below 685 °C. However, there is a general consensus that longer residence times of the volatiles in the reactor enhance the formation of light hydrocarbons and non-condensable gases due to secondary cracking reactions (Ludlow-Palafox and Chase, 2001; Sharuddin et al., 2016). Therefore, the little effect of the residence time on the product yields observed in this study was likely caused by the small range tested. Nevertheless, the residence time could not be altered over a wider range due to experimental restrictions so its effect was not further studied and results from this point forward referred to constant residence time of 20s.

7.4 Effect of operating conditions on the gas composition

As expected, high temperatures promote the cracking of heavier compounds into lighter ones thereby, increasing the gas yield and decreasing the wax yield as shown in Figure 7.1. Martín-Gullón et al. (2001) reported that an increase in temperature produced the decomposition of a fraction of the already formed solid residue increasing the proportion of CO and CO_2 in the gas product. Figure 7.2 shows the evolution of carbon dioxide and carbon monoxide in the gas fraction with temperature and catalyst:plastic ratio.

For catalyst loads of 0 wt%, higher temperature decreased the yield of CO_2 (from 19.4 wt% at 450 °C to 17.25 wt% at 600 °C) whereas the yield of CO remained almost constant (11.5 wt% at 450 °C to 11.6 wt% at 600 °C). CO_2 yield variation corresponded to the solid residue yield due to the reverse Boudouard reaction occurring to some extent at the tested conditions to transform CO_2 into CO (reaction (7.1)). At 450 °C (theoretical molar fraction: CO_2=0.969 and CO=0.031 (Reed, 2016)) the forward reaction was promoted towards the formation of CO_2 (Figure 7.2) and solid residue (Figure 7.1) whereas increasing temperature to 600 °C (theoretical molar fraction: CO_2=0.723 and CO=0.277 (Reed, 2016)) shifted the equilibrium of Boudouard reaction towards the formation of CO (Figure 7.2).

$$2CO \leftrightarrow CO_2 + C_{(s)} \tag{7.1}$$

Figure 7.2 initially suggested that SZ catalyst may affect the reverse Boudouard reaction to form CO from CO_2 and solid residue. Lahijani et al. (2015) observed that alkali and alkaline metals e.g. Na, Ca, Mg, etc., decreased the minimum temperature to promote the reverse Boudouard

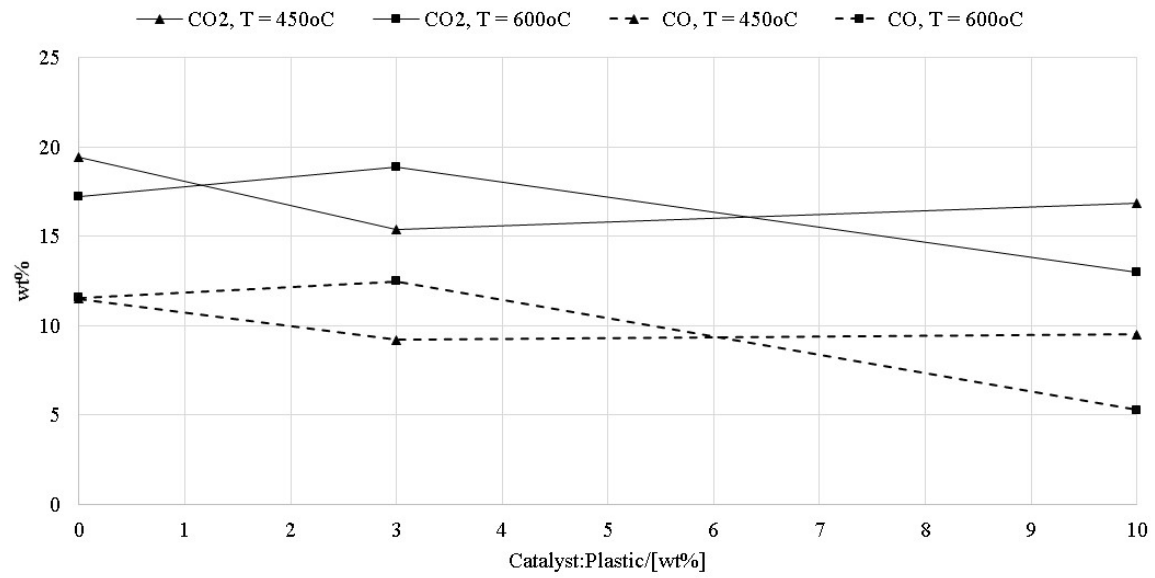

Figure 7.2 Effect of temperature (450-600 °C) and catalyst load (0-10 wt%) on the yield of CO_2 (solid line, ±2.70 wt%) and CO (dashed line, ±1.86 wt%) in the waste PET catalytic pyrolysis gas (triangles represent T=450 °C and squares represent T=600 °C

reaction from 700 °C to 580 °C. Kogler et al. (2016) observed also that the surface oxygen in metal oxides, like ZrO_2, can be a substrate for carbon residue deposition via Boudouard reaction (reaction (7.1)) at high temperature. However, no previous work involving SZ as a Boudouard reaction catalyst was found. Therefore, the CO_2 yield reduction at high temperature and high catalyst loads is suggested to be formed via the Boudouard reaction along with carbon residue but consumed by methane in an oxidative coupling with CO_2 as oxidant to form other light hydrocarbons. The carbon residue deposited on SZ surface deactivated the catalyst. Nevertheless, further work on the effect of SZ in the Boudouard reaction will be beneficial to consolidate these conclusions.

Figure 7.3 shows the variation of the remaining products in the gas product: H_2, CH_4 and C_2-C_5 hydrocarbons with temperature and catalyst mass percentage at constant volatiles residence time of 20s. The amount of C_2-C_5 hydrocarbons (left figure, dashed line, triangles for 450 °C and squares for 600 °C) increased with both the catalyst load (0 wt% to 10 wt%) and temperature (450 °C to 600 °C). At low temperature (450 °C) the amount of CO_2 and CO decreased with increasing the catalyst loading (Figure 7.2), leading to the formation of C_2-C_4 hydrocarbons and oxygen (Figure 7.3). At high temperature (600 °C), the formation of CO_2 and CH_4 was favoured at low catalyst loads whereas the formation of light hydrocarbons and oxygen increased with the catalyst load.

SZ catalyst contained tetragonal ZrO_2 (Figure 3.6 in chapter 3) providing surface oxygen which can interact with some of the reaction products e.g. CH_4. At high temperature (600 °C), a proportion of the CH_4 generated can react with CO_2 as an oxidant agent (reaction (7.2)) (Eliasson et al., 2000; Nishiyama and Aika, 1990).

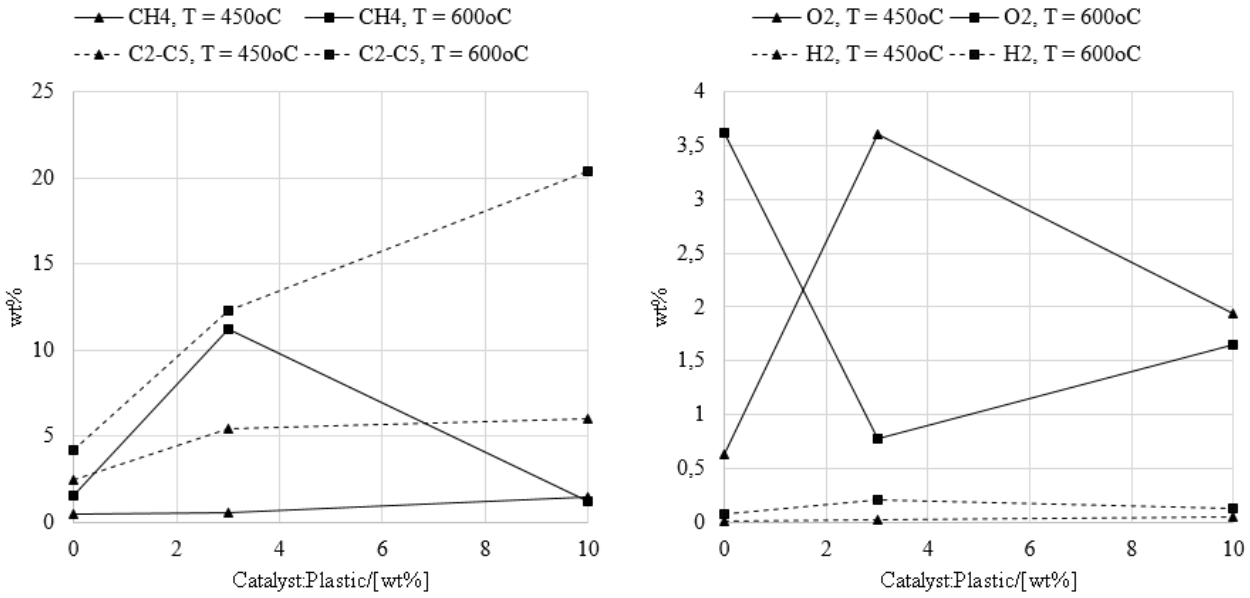

Figure 7.3 CH_4 (left, solid line, ±1.50 wt%), C_2-C_5 hydrocarbons (left, dashed line, ±2.73 wt%), O_2 (right, solid line, ±1.30 wt%) and H_2 (right, dashed line, ±0.09 wt%) yield (in wt%) at 450 °C (triangles) and 600 °C (squares) at constant volatiles residence time of 20s and SZ catalyst mass percentage of 0-10 wt%

$$2CH_4 + CO_2 \rightarrow CO + C_2H_6 + H_2O$$
$$C_2H_6 + CO_2 \rightarrow CO + C_2H_4 + H_2O \quad (7.2)$$

Reaction (7.2) requires oxygen to form a methyl radical intermediate (CH_3^*) which can undergo a chain reaction to form multiple hydrocarbons e.g. C_2, C_3 and C_4. The oxygen supply for reaction (7.2) can come from the gas phase, which reacts with CH_3^* to form CO_2 via CH_3O_2 and CH_2O radicals mechanism, or from the surface of a catalyst as in this case. The latter inhibits the formation of CO_2 and improves the selectivity of C_2-C_4 hydrocarbons (Nishiyama and Aika, 1990) explaining the reduction of CH_4 and CO_2 and the increase in C_2-C_5 yield at high temperature (600 °C) shown in Figure 7.3.

During these experiments, certain SZ catalyst weight loss was observed after catalytic pyrolysis. This was more prominent at temperatures above 525 °C, explaining the release of oxygen (Figure 7.3) as part of the SO_4 group decomposition into SOx. TGA analysis of SZ performed by Srinivasan et al. (1995) showed two weight loss regions for SZ in helium: 1) 10 wt% weight loss between 100-500 °C and 2) 6 wt% weight loss between 500-700 °C. Figure 3.7 in chapter 3 showed that SZ catalyst presented hydrated water loss between 80-455 °C and either formation of tetragonal ZrO_2 or decomposition of the sulphate into SO_x gases and O_2 between 455-525 °C. SZ thermal decomposition is further discussed later on in section 7.6, but so far it was observed that at temperatures >525 °C, higher catalyst loads were required to achieve equal results due to the catalyst decomposition and reduction of active sites.

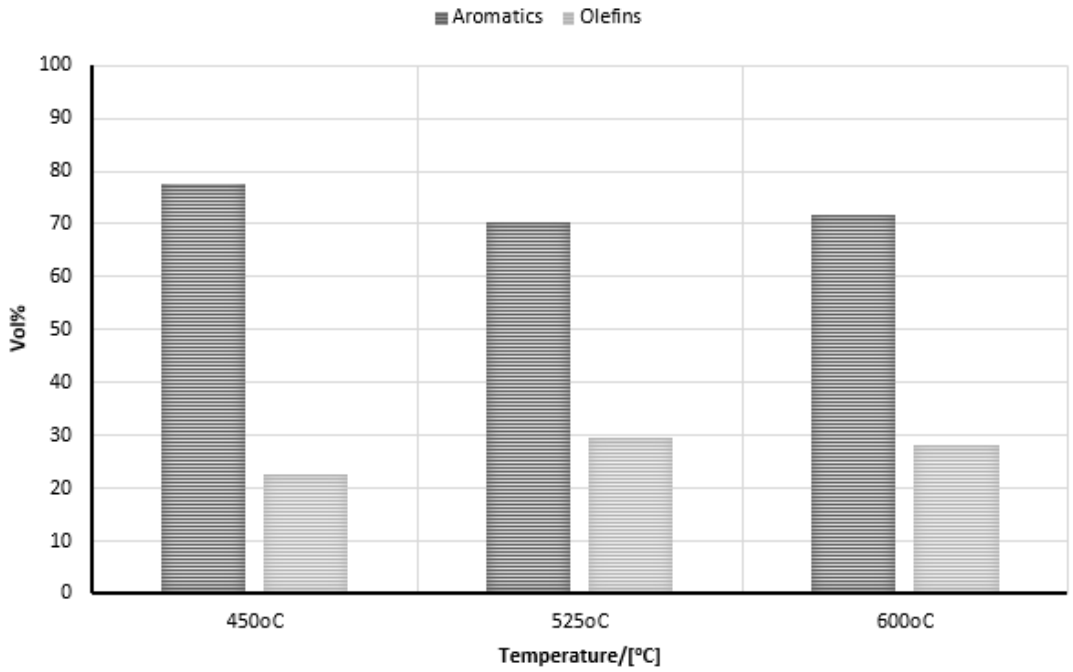

Figure 7.4 Proportion of aromatic and olefinic fraction in PET wax derived from pyrolysis at 450 °C, 525 °C and 600 °C at constant volatiles residence time of 20s and 6.5 wt% catalyst mass

7.5 Effect of operating conditions on the wax composition

Figure 7.4 represents the calculated proportion of aromatic and olefin compounds in waste PET catalytic pyrolysis wax via ^{1}H-NMR analysis based on the method proposed by Myers Jr. et al. (1975). ^{1}H-NMR showed PET wax comprised of aromatic compounds (most peaks within 6.6-8.3 ppm region).

The olefin proportion corresponded to the functional groups attached to aromatic rings. This confirmed the findings of GC-MS analysis where vinyl ester groups were found in the wax. The aromatic proportion corresponded to the hydrogen atoms attached to aromatic rings, implying that most of the wax was formed by aromatic compounds and agreeing with GC-MS analysis. Higher temperatures slightly increased the proportion of olefin functional groups at the expense of the aromatic one due to further decomposition of the primary compounds (Figure 7.5). However, ^{1}H-NMR show little difference between results as it did not provide information on the individual compounds or functional groups within those two wide fractions, just a general composition overview. Hence, the wax was also qualitatively analysed by FT-IR and GC-MS and quantified via GC-FID.

7.5.1 Functional groups in PET wax product

FT-IR analysis of the wax obtained at 450, 525 and 600 °C, catalyst mass of 0 wt% and 20s residence time are shown in Figure 7.6. Temperature had little effect on the functional groups distribution in the wax except for the presence of two small peaks between 3013-2815 cm^{-1} at 450 °C which were not found at 525 and 600 °C. These two peaks corresponded to the C-H

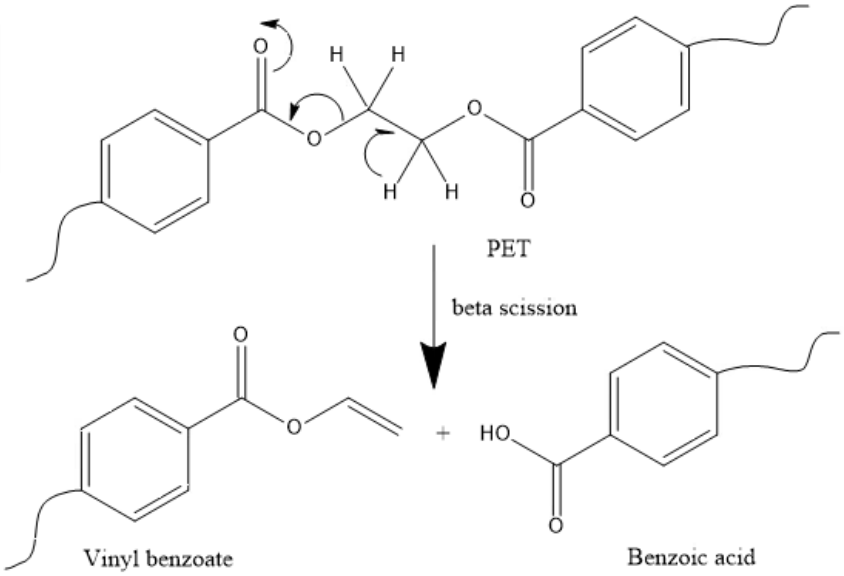

Figure 7.5 Beta scission mechanism of PET thermal degradation adapted from (Venkatachalam et al., 2012)

stretch in the methylene group (R=CH_2) suggesting that, as temperature increased, the vinyl ester bond broke into other compounds. The presence of the most predominant peak at 1730-1630 cm^{-1}, related to the C=O stretch, and the peak between 1330-1200 cm^{-1}, designated to the C-O stretch, implied the existence of either carboxylic acids (the second peak typically found between 1380-1210 cm^{-1}) or esters (the second peak usually between 1300-1100 cm^{-1}) (Larkin, 2011; Masuda et al., 1997).
FT-IR analysis agreed well with those obtained from ^{1}H-NMR and GC-MS with a significant proportion of aromatic compounds (70-80 vol%) and olefins (20-30 vol%). Peaks around 1000 cm^{-1} and 900 cm^{-1} corresponded to the C-C and C-H stretch in aromatic rings respectively. These findings confirmed that PET wax was formed mainly by aromatic compounds and had a low H/C ratio as expected. The FT-IR spectrum from waste PET catalytic pyrolysis wax showed in Figure 7.6 also agreed with previous spectra reported in literature (Çit et al., 2010).

7.5.2 Wax composition

^{1}H-NMR and FT-IR results showed that the majority of the wax comprised of aromatic compounds. GC-MS results confirmed that 90-95 % of the wax fraction was formed by: benzaldehyde, acetophenone, methoxybenzyl alcohol, benzoic ether, benzoic acid and 2-acetylbenzoic acid which agreed well with previous studies (Çit et al., 2010; Du et al., 2016; Dzięcioł and Trzeszczyński, 2000; Venkatachalam et al., 2012; Yoshioka et al., 2004). Table 7.1 shows that waste PET catalytic pyrolysis wax was formed by: 20.0-28.0 wt% of benzoic acid, 3.0-5.9 wt% of acetylbenzoic acid, 0.8-3.1 wt% of benzoic ether, 1.1-2.1 wt% of acetophenone, 0.5-1.0 wt% of methoxybenzyl alcohol, 0.5-1.0 wt% of styrene and 2.9-8.6 wt% of other unknown aromatic compounds. These results agreed well with waste PET pyrolysis wax composition previously reported (Dziwiński et al., 2018).

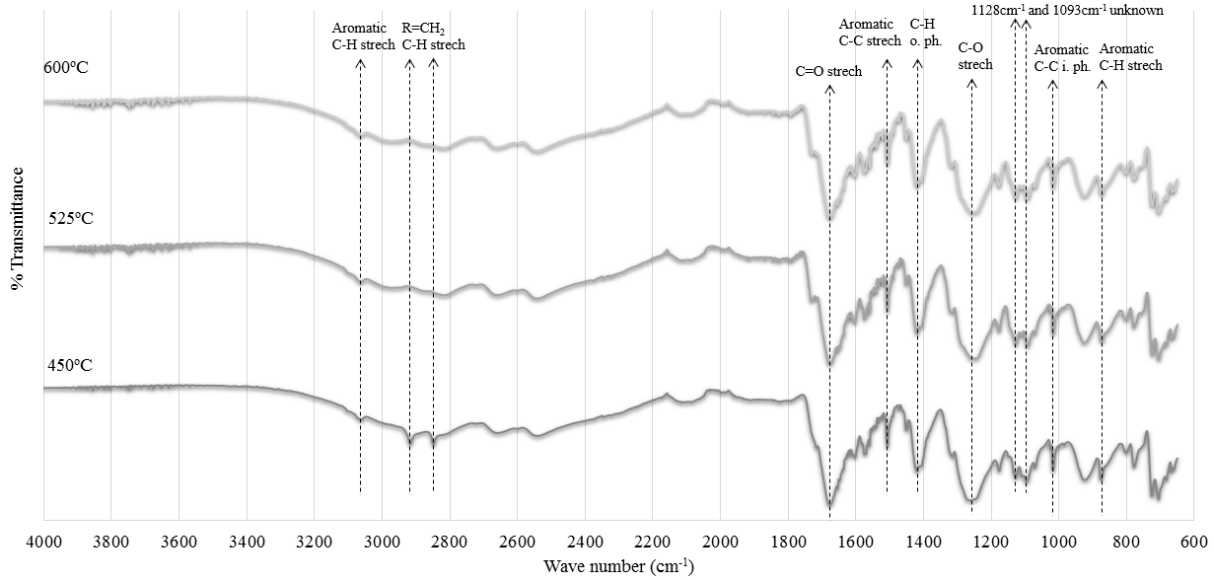

Figure 7.6 FT-IR spectra of the wax obtained from waste PET catalytic pyrolysis at 450 (bottom), 525 (middle) and 600 (top) °C, 0 wt% catalyst mass and 20s residence time

Table 7.1 Yield of wax products from waste PET catalytic pyrolysis at 450-600 °C, 0-10 wt% catalyst mass and constant volatile residence time of 20s: (a) Styrene (±0.44 wt%), (b) acetophenone (±0.61 wt%), (c) methoxybenzyl alcohol (±1.13 wt%), (d) benzoic ether (±1.54 wt%), (e) benzoic acid (±2.67 wt%), (f) acetylbenzoic acid (±0.07 wt%) and (g) other unknown aromatics (±4.84 wt%) calculated by mass difference (T=temperature/[°C] and C:P=catalyst mass/[wt%])

T	C:P	Product/[wt%]						
		(a)	(b)	(c)	(d)	(e)	(f)	(g)
450	0	0.59	1.84	0.90	1.36	27.13	1.66	1.82
	3	1.00	2.21	0.88	3.15	27.53	2.93	3.71
	10	0.40	1.05	0.04	0.99	25.24	1.18	2.69
525	0	0.79	1.21	0.06	2.73	23.91	1.95	3.62
600	0	1.22	2.10	0.08	3.22	31.64	5.88	5.21
	3	0.48	1.60	0.92	1.75	19.02	2.81	4.15
	10	0.45	1.10	0.45	0.72	25.91	2.86	6.47

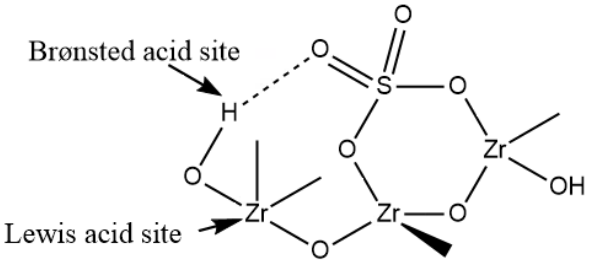

Figure 7.7 Scheme of the Brønsted and Lewis acid sites on sulphated zirconia. Adapted from (Wang and Xiao, 2015)

Figure 7.5 shows that, at temperatures >395 °C, waste PET decomposition was initiated via β-scission at the carboxylic group where the ester link was broken and formed benzoic acid and vinyl benzoate. As temperature kept increasing, the vinyl benzoate formed further decomposed into other aromatic compounds found in the wax fraction and lighter compounds in the gas phase. Theoretically, vinyl benzoate undergoes a McLafferty rearrangement yielding acetaldehyde and ethylene (Venkatachalam et al., 2012). However, acetaldehyde was not found for any tested condition and it was not previously reported as a product from either thermal or catalytic waste PET pyrolysis (Çit et al., 2010; Du et al., 2016; Dzięcioł and Trzeszczyński, 2000; Dziwiński et al., 2018; Yoshioka et al., 2004).

SZ catalyst presented both Brønsted (protons on the surface hydroxyl groups of sulphated zirconia oxide) and Lewis (Zr atoms) acid sites (Figure 7.7) (Srinivasan et al., 1996). SZ acid sites promoted the formation of carbocations on the species formed by thermal decomposition via either proton donation (Brønsted) or electron acceptance (Lewis) creating active species that further cracked into smaller molecules.

Table 7.1 showed rising the temperature from 450 to 600 °C decreased the yield of benzoic acid by 26 % at 3 wt% catalyst mass (26.9 wt% to 20.0 wt% $\pm$ 1.7 wt%) but remained constant at 10 wt% catalyst mass (27.4 wt% to 28.0 wt% $\pm$ 1.7 wt%). When the catalyst mass varied from 3-10 wt% at low temperature (450 °C) the amount of benzoic acid remain unchanged (26.9 wt%-27.5 wt% $\pm$ 1.7 wt%) whereas it increased by 40 % at high temperature i.e. 600 °C (20.0 wt% to 28.0 wt% $\pm$ 1.7 wt%).

Assuming an average 24 wt% benzoic acid yield recovered from waste PET catalytic pyrolysis, potentially about 408 ktonnes of benzoic acid could be recovered if all waste PET generated were managed by catalytic pyrolysis. This could suggest a recovery value of almost $1.8 million per year (assuming steady waste PET generation as in the UK in 2014 (Plastic Europe,, 2016)). In addition, waste PET catalytic pyrolysis could avoid the disposal of over 600 ktonnes of wastes in landfills (assuming an average plastic waste landfill disposal rate in the UK in 2014 of 38 wt% (Plastic Europe,, 2016)).

7.6 Sulphated zirconia thermal decomposition and deactivation

It was observed at temperatures above 525 °C that the weight of SZ catalyst recovered from the catalyst bed after experiments was lower than the initial load, suggesting the catalyst was either carried out of the reactor by volatiles or or decomposed by temperature. The latter explained the low benzoic acid yield at 600 °C and catalyst mass of 3 wt% compared to the equivalent at 450 °C (Table 7.1). Thermal transitions of SZ fresh catalyst, investigated by DSC (section 3.1.3 in chapter 3), showed the loss of hydrated water molecules between 80-180 °C and deactivation via either crystallisation of tetragonal ZrO_2 or decomposition of the sulphate into SO_x gases and O_2 between 455-525 °C. However, sulphate decomposition was previously reported to require temperatures above 700 °C (Sohn and Lee, 2003). Despite Wang et al. (2016) suggestion that, under N_2, the sulphur content of SZ decreases above 500 °C, no sulphur compounds were detected during waste PET catalytic pyrolysis experiments at any tested temperature in neither the gas not the wax fraction. Therefore, the SZ weight loss observed in this study was likely caused by the loss of hydrated water along with the crystallisation of tetragonal ZrO_2.
SZ deactivation occurs through either the reduction of the surface sulphate groups from S^{+6} to lower oxidation states, decreasing both the acidity and activity of the catalyst or through pore clogging via coking (Ng and Horvát, 1995). SZ deactivation was further studied through cold plasma assisted catalytic pyrolysis of waste HDPE (Diaz-Silvarrey, Zhang and Phan, 2018). In addition, SZ and zeolite HY were both re-used up to four consecutive cycles before they showed deactivation by coking (chapter 8).
Blank tests re-using SZ catalyst in several consecutive cold plasma assisted catalytic pyrolysis (500 °C, 55 °C/min, SED=135 J/mL, 1 g of SZ catalyst and 20 mL/min of N_2) showed an initial SZ catalyst weight loss of 62.2±7.3 % in the first cycle, a further 28.5±6.7 % weight loss in the second one and no further weight loss in consecutive cycles. During these experiments the gases generated were analysed on-line with GC-TCD finding that O_2 was released between 80-288 °C in the first cycle only. Other than N_2, only traces of CO_2 and CO were detected at any temperature in any cycle. Previous studies reported that thermochemical sulphate oxidation state reduction can occur at temperatures between 80-200 °C (Krouse et al., 1988; Machel et al., 1995) explaining the release of O_2 when sulphate oxidation state was reduced.
In addition, fresh SZ catalyst was analysed via TGA analysis coupled with a mass spectrometer (TGA/DSC 3+ coupled with MS Hiden HPR-20) in 50 mL/min of helium with initial isothermal step at 35 °C for 15 minutes followed by heating to 900 °C at 20 °C/min. Figure 7.8 shows four weight loss steps: about 10 wt% <80 °C, almost 5 wt% between 120-200 °C, just over 5 wt% between 400-430 °C and about 30 wt% between 580-710 °C. The total SZ weight loss at 500 °C was about 40 wt% suggesting cold plasma contributed to further SZ decomposition. The first, second and to less extent, third steps corresponded to H_2O released confirming hydrated water loss molecules at temperatures below 400 °C. CO_2 was only detected during the fourth step at temperatures >600 °C. Therefore, the aforementioned observations regarding SZ thermal

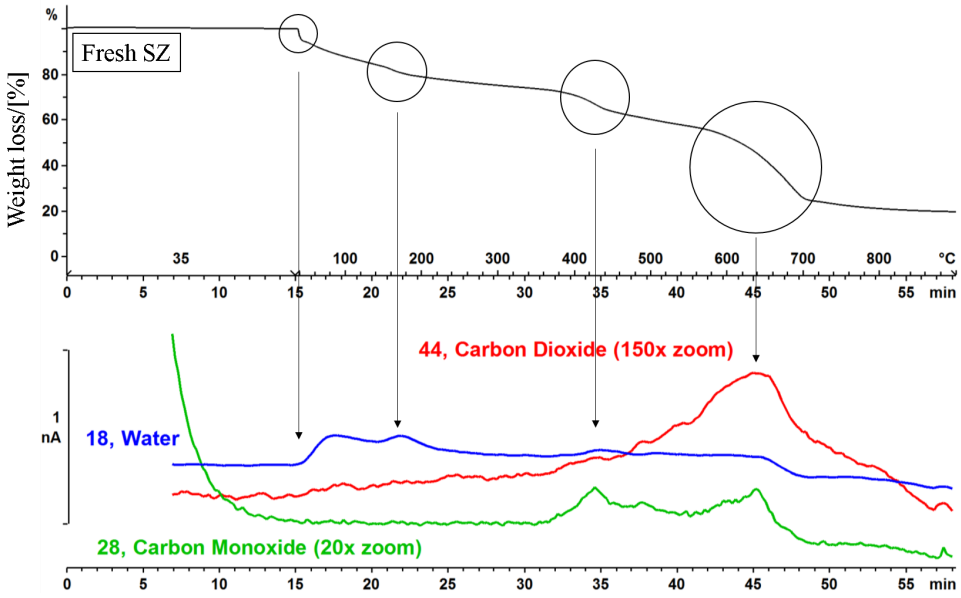

Figure 7.8 TGA-MS profile of fresh sulphated zirconia catalyst (masses: blue=H_2O (18), green=CO (28) and red=CO_2 (44))

decomposition were confirmed confirming that SZ deactivated above 500 °C due to thermochemical sulphate oxidation state reduction (CO_2 released) as well as coking. Despite the SZ deactivation, this catalyst has advantages in terms of cost and environmental impact compared to other commercial catalyst such as zeolites, even though it may be restricted for waste PET pyrolysis at high temperature (>525 °C). Catalytic pyrolysis at 450 °C and 3 wt% catalyst mass increased the yield of benzoic acid up to 27.53 ± 2.67 wt% without any catalyst decomposition observed. This yield was higher or comparable to the one obtained at high temperatures and no catalyst (23.91 ± 2.67 wt% at 525 °C and 31.64 ± 2.67 wt% at 600 °C). SZ is a solid catalyst placed on a separate bed and therefore not mixed with pyrolysis products. SZ deactivation was caused by coking and therefore is reversible through regeneration by combustion at 450 °C (Binghui, 1998; Li and Stair, 1996) or treatment with hydrogen (Yang and Weng, 2010), allowing the reutilization of the catalyst. From previous studies (Diaz-Silvarrey, Zhang and Phan, 2018), SZ was used for several pyrolysis cycles before deactivation. Therefore, the use of this catalyst showed some enhancement over thermal PET pyrolysis and could be considered as an alternative catalyst for low temperature PET pyrolysis.

7.7 Summary

PET is widely used in food packaging applications which have a very short life and therefore rapidly become waste PET. Currently, chemical recycling through glycolysis and landfill are the main approaches for PET waste management in some countries. Mechanical recycling of PET wastes accounted for only 29.2 % of total PET waste in the USA in 2017 (NAPCOR, 2018) compared to the almost 74 % of the total PET waste recycled in the EU in the same year (Plastic Recyclers Europe, 2018) or the outstanding 100 % recycling rate of PET bottles in China in 2012 (Zhang and Wen, 2014). However, despite the high recycling rate, the majority of the PET

waste recycling in China is unregulated and it is carried out in small unsupervised family business with little to none pollution control systems (Zhang and Wen, 2014). These issues make impossible to control the real amount of PET wastes that are recycled and the true environmental impact of this process. Pyrolysis of PET wastes is a promising alternative that recovers valuable chemicals without extra costs associated to cleaning and segregation. It may form a promising alternative to landfill or incineration for regions with low recycling rates. Results showed that both catalyst mass and temperature play an important role in the production of benzoic acid, a precursor widely used in the food and beverage industry. High temperature (600 °C) and no catalyst increased by 16 % the benzoic acid recovery in the wax product compared to the other conditions tested. However, operation at those conditions has a high energy consumption to achieve that pyrolysis temperature. The addition of SZ catalyst increased the amount of another valuable product i.e. light hydrocarbons (C_2-C_5) from 4 wt% without catalyst to 20 wt% at 10 wt% catalyst mass. SZ deactivated due to coking on the catalyst surface and partially decomposed at temperatures above 525 °C. This phenomena was not observed when pyrolysis was performed at low temperatures. Based on the costs of catalyst and energy (about $1.4/g (anhydrous) SZ versus $0.10/kW-h on average in 2015 in the IEA (UK Department for Business, Energy & Industrial Strategy, 2017)), results from this chapter suggested that waste PET catalytic pyrolysis in the presence of SZ should be carried out at low temperature (450 °C) and catalyst loads below 10 wt% to obtain high yields of benzoic acid and high-value products in the gas i.e. C_2-C_5 hydrocarbons.

Chapter 8 Catalytic pyrolysis of unsorted mixed plastic waste

This chapter introduced the use of char derived from waste biomass pyrolysis as a catalysts for catalytic pyrolysis of mixed plastic waste, simulating the EU/UK demand of plastic waste which comprises of 30 wt% PP, 20 wt% HDPE, 27 wt% LDPE, 13 wt% PET and 10 wt% PS (Plastic Europe,, 2016). The plastic waste mixture was prepared by direct mix of cleaned 15x15 mm squares cut from the individual plastic waste, characterised in chapter 3. Although PVC accounts up to 10 % of the EU/UK plastic demand it was disregard in this study as it is unsuitable for pyrolysis due to the formation of HCl which causes corrosion of the reactor and is detrimental for the wax composition. The work in this chapter was developed based on previous reports on the successful use of biomass char for tar removal in biomass pyrolysis as well as the use of other carbon-based catalysts for PWP. The combination of those two ideas yield a novel approach to utilise waste materials as catalysts to develop a sustainable and profitable process to reutilise plastic wastes.

This chapter is divided into two main sections. Section 8.1 discusses the effect of temperature and catalyst type on the yield and composition of pyrolysis products via comparison of char derived from waste biomass pyrolysis i.e. biochar, and two commercial catalysts (zeolite HY and alumina - Al_2O_3-). The main findings of this section were: 1) without catalyst, increasing temperature increased the gas yield (32 wt% to 52 wt%) but had little effect on the product composition; 2) biochar (isothermal at 800 °C) significantly enhanced cracking reactions resulting in a gas yield of 85 wt% with an increase in hydrogen yield (0.17 wt% to 3.25 wt%) and the removal of benzoic acid derived from PET in the wax; and 3) biochar improved the wax composition reducing heavier hydrocarbons compared to zeolite HY and Al_2O_3 catalysts. The contents of this section have been submitted for publication in "Waste to wealth: pyrolysis of unsorted plastic waste using a waste derived catalyst" to *Applied Energy* which is under review after revision. In addition, section 8.2 in this chapter includes a reusability assessment of three catalysts (biochar, zeolite HY and SZ using both nitrogen and CO_2 as carrier gases) which are scarce studies on literature. Finally, catalyst regeneration was investigated via two novel methods: cold plasma and CO_2 utilisation. The main findings from the reusability study were: 1) up to 77 % of the coke deposited on zeolite HY pores was removed using CO_2 as carrier gas and 2) no deactivation of biochar over five consecutive catalytic pyrolysis cycles was observed unlike zeolite HY and SZ catalysts.

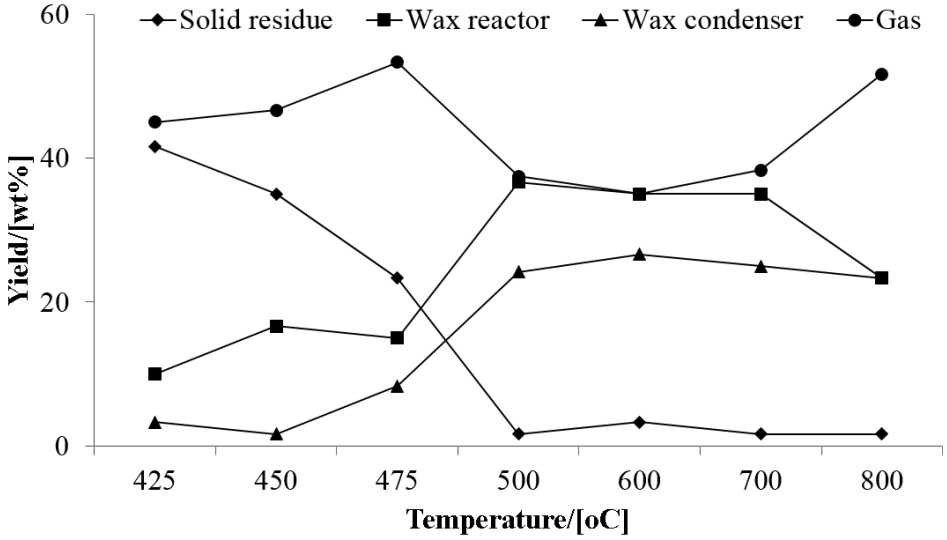

Figure 8.1 Solid residue (± 0 wt%), wax in the reactor (± 5.85 wt%), wax in the condenser (± 4.41 wt%) and gas (± 3.47 wt%) yield from mixed plastic waste thermal pyrolysis between 425-800 °C

8.1 Catalytic pyrolysis of unsorted mixed plastic using a waste derived catalyst

Thermal and catalytic pyrolysis experiments at a temperature range between 500-800 °C were carried out in both a one-stage (both plastic waste sample and catalyst heated at the same time) and a two-stage (catalyst held isothermally in a separate furnace) pyrolysis as described in section 3.2.3 in chapter 3. Biochar catalyst, derived from waste biomass pyrolysis at 900 °C, was the primary catalyst used. Other catalysts (Al_2O_3 and zeolite HY) were also studied for comparison purposes. Section 3.1.2 in chapter 3 described the characterisation of biochar and zeolite HY catalysts. Al_2O_3 catalyst was a commercial Al_2O_3 support (particle size <50 nm, surface area of 255 m^2/g, Sigma Aldrich).

8.1.1 Thermal pyrolysis

Figure 8.1 shows the direct effect of temperature on mixed plastic waste decomposition products: gas, wax in the condenser, wax in the reactor and solid residue. The gas yield increased from 37.50 wt% to 51.67 wt% when temperatures increased from 500 °C to 800 °C because higher temperatures enhance the cleavage of C-C bonds through a random scission mechanism in long chain carbon compounds (Miandad et al., 2016). The solid residue yield decreased considerably from 41.7 wt%, 35 wt% and 23.33 wt% at 425, 450 and 475 °C respectively to below 3 wt% at temperatures above 500 °C due to complete plastic waste thermal decomposition above 500 °C. The difference, in the solid residue yield was accounted for as an increase in the amount of wax recovered (from 15 wt% and 8.33 wt% at 475 °C to 36.67 wt% and 24.17 wt% at 500 °C for the wax in the reactor and condenser respectively). Above 500 ∘C, the solid residue remained almost constant at 1.67 wt% across the entire pyrolysis temperature range and agreed well with

literature (López, De Marco, Caballero, Laresgoiti and Adrados, 2011; Miandad et al., 2016; Yoshioka et al., 2004).

The solid residue was 2-3 times higher than the ash content (0.6 wt%, section 3.1.1 in chapter 3) and thereby, it is likely that the solid residue is formed by all the inorganic material present in the original plastic products along with the carbon content not volatilised at pyrolysis temperature. Although mixed plastic waste pyrolysis solid residue (char) could have some applications within the environmental and energy sectors, the extremely low yield obtained in these experiments meant that no further analysis of the char was conducted.

Compared to previous studies of mixed plastic waste mixtures (35 wt% PP, 40 wt% PE, 18 wt% PS, 4 wt% PET and 3 wt% PVC) (López, De Marco, Caballero, Laresgoiti and Adrados, 2011), results from this study were similar except for a higher solid residue yield at 450 °C (35 wt% compared to the 1.10 wt% at 460 °C reported by López, De Marco, Caballero, Laresgoiti and Adrados (2011)). The gas yield showed in Figure 8.1 increased with temperature (from 37.50 wt% at 500 to 51.67 wt% at 800 °C) agreeing with trends reported (Adrados et al., 2012; López, De Marco, Caballero, Laresgoiti and Adrados, 2011; Williams and Williams, 1997*a*). However, values differed from others found in literature: increased from 9.8 wt% at 500 °C to 68.8 wt% at 700 °C according to Williams and Williams (1997*a*) (7.3 wt% PP, 62.5 wt% PE, 13.5 wt% PS, 5.2 wt% PET and 11.5 wt% PVC). The latter suggests that there is a strong influence between feedstock composition, pyrolysis conditions and mixed plastic pyrolysis products yield.

There were two fractions in the total wax yield i.e. the wax in the reactor walls and that in the condenser. Figure 8.1 shows that increasing pyrolysis temperature up to 500 °C increase both fractions of the wax at the expense of solid residue (complete thermal decomposition). Opposite, increasing pyrolysis temperature above 500 °C decreased the wax in the condenser due to secondary cracking of volatiles to form non-condensible gases and lighter volatile compounds.

Figure 8.2a shows the gas composition at various pyrolysis temperatures in the absence of catalysts. Since HDPE, LDPE, PP and PS do not present oxygen in their structure, the formation of CO_2 and CO was entirely from the PET in the mixed plastic waste via decarboxylation at high temperature (Grause et al., 2011) to yield vinyl esters, carboxylic acids and some gases e.g. CO_2, CO, O_2 or C_2H_4. Although hydrogen was detected for all tested conditions, the yield was low (<0.4 wt%) as expected. High temperature used for plastic waste pyrolysis caused the cleavage of the C-C bonds at unpredictable points along the length of the chain (Wampler, 1989) (average C-C bond energy = 83 kcal/mol (Gerö, 1948)) by a random scission mechanism. As the reaction progressed all of the remaining bonds had the same probability of being broken hence forming an array of hydrocarbons ranging from C_1-C_{30+} (Williams, 2006). During this process, the cleavage of the C-H bond did not occur due to the higher bond energy (average C-H bond energy = 97 kcal/mol (Gerö, 1948)) and therefore the H_2 released was limited.

Apart from CO_2 and CO, the other main fraction in the pyrolysis gas were short chain olefin hydrocarbons produced from the C-C cleavage of long chain aliphatic hydrocarbons. Light hydrocarbons are predominant in polyolefins plastic pyrolysis i.e. HDPE, LDPE and PP. Therefore, the higher their presence in the mixed plastic waste feedstock, the higher the amount

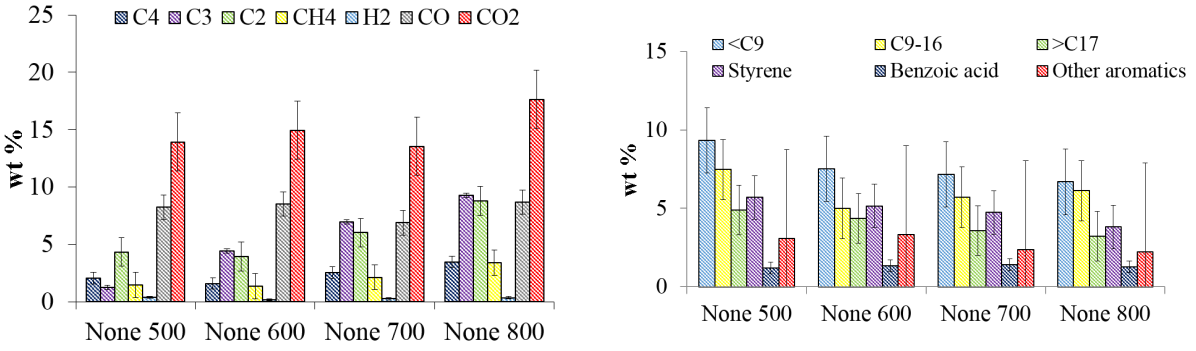

(a) Gas composition

(b) Wax composition

Figure 8.2 Thermal pyrolysis (a) gas yield and (b) wax yield at various temperatures (number refers to temperature [°C] and 'None' to no catalyst

of C_2-C_4 recovered. The amount of CO_2 and CO is directly related to the proportion of PET. Hydrocarbons in the gas and wax fractions were mainly alkenes (CH_2=CH-R, R-CH=CH-R). The higher percentage of alkenes (as opposed to alkanes) was caused by the presence of PP in the mixed feedstock. When the methyl group attached to PP chain is close to the radical carbon, formed after thermal pyrolysis initiation step, the formation of double C=C bonds is favoured over single C-C ones due to the higher energy associated with the former (Pinto et al., 1999*a*; Williams, 2006).

For all tested conditions, the gas yield had calorific value higher than commercial natural gas (Table 8.1), enough to subsidise the energy requirements of the highly endothermic pyrolysis process. According to Gao (2010), pyrolysis of PE requires 1.05 MJ/kg at 400 °C to produce 10 wt% C_1-C_4 (gas), 30 wt% C_5-C_{12} (gas), 40 wt% C_{13}-C_{22} (gas) and 20 wt% C_{23+} (liquid). Similar values were reported by Xingzhong (2006) (1.32 MJ/kg) to obtain 2 wt% C_1-C_4 (gas), 46 wt% C_5-C_{12} (gas), 34 wt% C_{13}-C_{22} (gas) and 18 wt% C_{23+} (liquid) at 200-300 °C.

The wax formed in thermal pyrolysis of mixed plastic waste comprised of at least 36 different compounds but many of which had had negligible concentrations. Therefore, hydrocarbons were grouped into three fractions according to their carbon number: $<C_9$, C_{10}-C_{16} and $>C_{17+}$. Figure 8.2b shows that the $<C_9$ fraction, corresponding to the gasoline carbon number range, was the predominant for all tested conditions. Despite the large proportion of HDPE, LDPE and PP in the mixed feedstock, there was a significant amount of aromatic compounds i.e. styrene (due to PS), benzoic acid (due to PET) and other aromatics compounds. A wide range of compounds in the wax is often reported from mixed plastic waste thermal pyrolysis (Almeida and Marques, 2016; Kim and Kim, 2004; López, De Marco, Caballero, Laresgoiti and Adrados, 2011) implying that the liquid/wax has low octane number and limited application as a burning fuel or wax. It was found that increasing the temperature did not noticeably change the wax composition but enhanced the gas yield at the expense of the wax yield.

Table 8.2 compares the composition of the wax inside the reactor and that in the condenser at pyrolysis temperature of 500 °C. It was found that the wax collected from the reactor walls had a higher fraction of heavier hydrocarbons (C_{10} - C_{16}) as well as benzoic acid derived from PET

Table 8.1 Summary of the pyrolysis gas low calorific value (LHV) calculated at 15 °C and 1 atmosphere (XXX=pyrolysis temperature [°C], YYY=NON for no catalyst and ISO for isothermal catalyst bed temperature, ZZZ=catalyst bed temperature [°C] and CAT=catalyst use i.e. biochar, zeolite HY and Al_2O_3)

XXX/YYY	ZZZ/CAT	LHV / [MJ/m^3]	LHV / [MJ/kg]	UK natural gas, LHV / [MJ/m^3]
500/NON		29.02	17.70	35.70 [ab]
600/NON		30.72	18.28	
700/NON		40.81	24.24	
800/NON		42.22	25.29	
600/ISO	500/CHAR	46.72	29.07	
600/ISO	600/CHAR	46.98	34.03	
600/ISO	700/CHAR	49.04	41.05	
600/ISO	800/CHAR	45.79	48.56	
600/ISO	500/HY	46.41	28.60	
600/ISO	500/Al2O3	41.90	25.23	

[a] Department Energy and Climate Change (2015)
[b] UK produced and imported gas as entering the National Transmission System. It can also be expressed as 11.007 kWh per cubic metre

Table 8.2 Comparison of reactor and condenser wax composition produced by thermal pyrolysis at 500 °C (wt%)

Wax	$<C_9$	C_{10}-C_{16}	$>C_{17+}$	Styrene	Benzoic Acid	Other aromatics
Reactor	5.63	10.48	9.35	4.02	2.74	2.77
Condenser	9.32	7.46	4.90	5.70	1.19	3.09

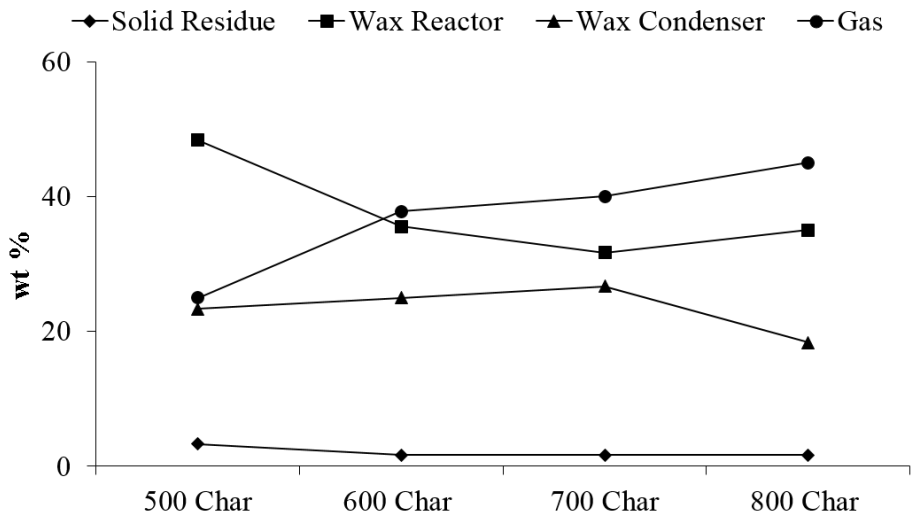

Figure 8.3 Solid residue (± 0 wt%), wax in the reactor (± 5.85 wt%), wax in the condenser (± 4.41 wt%) and gas (± 3.47 wt%) yield from mixed plastic waste one-stage catalytic pyrolysis at 500-800 °C ('XXX Char': XXX=catalyst bed temperature [°C])

than that in the condenser. Long chain hydrocarbons are less volatile and hence condense in the outskirts of the reactor (around 300 °C). In addition, subsequent random analysis of the wax in the reactor from thermal and catalytic experiments with with biochar and zeolite HY showed that its composition was fairly constant for all tested conditions. For this reason, this fraction was not further analysed. Results from this point forward refer solely to the wax in the condenser.
It can be concluded that temperature alone only affects the product yield but not the properties of the products. Increasing the temperature from 500 °C to 800 °C caused a larger degree of thermal cracking increasing the gas phase but not substantially modifying the distribution of compounds. Therefore, catalytic pyrolysis was investigated with the hypothesis to refine the gas and wax fractions and reduce the energy consumption and costs of operation.

8.1.2 Catalytic pyrolysis

Biochar

In this part both mixed plastic waste and biochar were heated in the same heating zone (one-stage pyrolysis). It was found little variation in product yields (Figure 8.3) and composition (Figure 8.4) occurred compared to the thermal process at equivalent conditions. This could be because the biochar was inactive during the temperature range when the volatile material was released (400-550 °C). This theory agreed well with tar cracking studies (Gilbert et al., 2009; Phan et al., 2009; Wang et al., 2014; Zhang et al., 2015), where biochar was activated at isothermal conditions above 700 °C. Therefore, two-stage pyrolysis experiments were conducted with the catalyst bed temperature constant an independently controlled between 500-800 °C. Figure 8.5 shows the product yields from two-stage catalytic pyrolysis at 600 °C.
The wax inside the reactor was reduced from 23-35 wt% to zero suggesting that biochar effectively cracked long chain hydrocarbons. Figure 8.6a shows that both the gas yield and

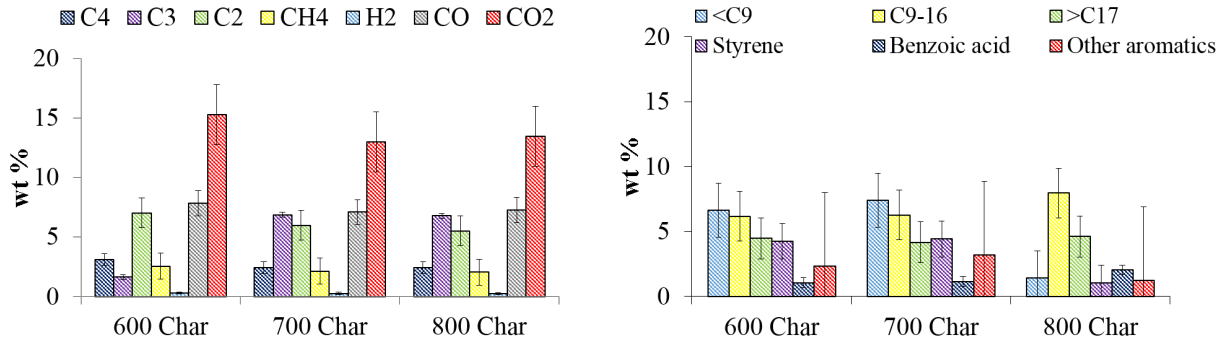

(a) Gas composition (b) Wax composition

Figure 8.4 Gas and wax composition from mixed plastic waste one-stage catalytic pyrolysis at 600-800 °C ('XXX Char': XXX=catalyst bed temperature [°C])

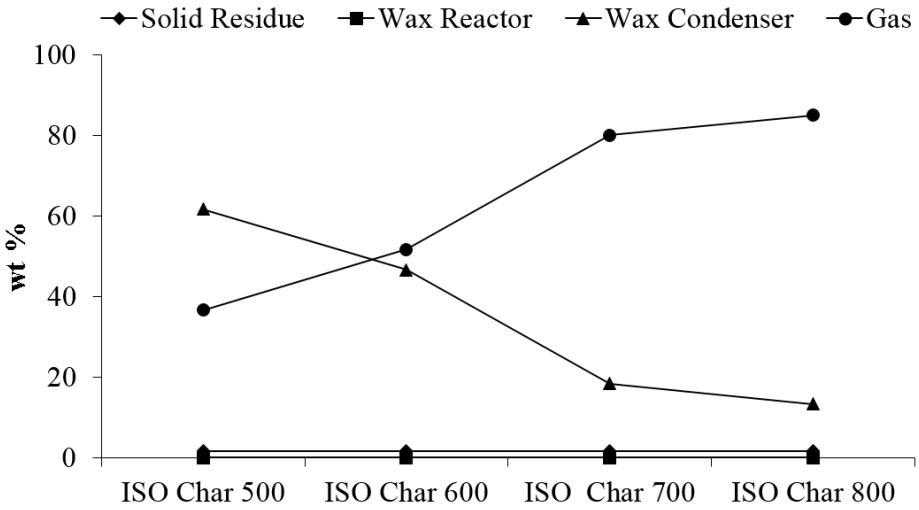

Figure 8.5 Solid residue (± 0 wt%), wax in the reactor (± 5.85 wt%), wax in the condenser (± 4.41 wt%) and gas (± 3.47 wt%) yield from mixed plastic waste two-stage catalytic pyrolysis at 600 °C ('ISO Char XXX': ISO=isothermal conditions and XXX=catalyst bed temperature [°C])

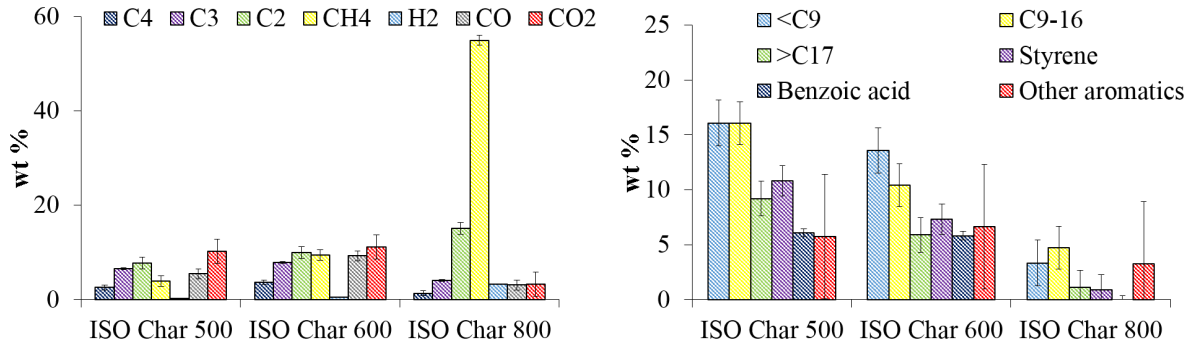

(a) Gas composition (b) Wax composition

Figure 8.6 Gas and wax composition from two-stage biochar catalytic pyrolysis at 600 °C ('ISO Char XXX': ISO=isothermal conditions and XXX=catalyst bed temperature [°C])

composition varied significantly compared to thermal and one-stage pyrolysis at 600 °C. For example, the gas yield increased from 35 wt% in thermal pyrolysis to 52, 80 and 85 wt% when biochar was kept isothermally at 600, 700 and 800 °C respectively. Biochar isothermally at 500 °C tripled the yield of methane to 3.9 wt% and decreased the yields of CO and CO_2 by approximately 36 % and 32 % respectively (CO_2: from 14.9 wt% to 10.2 wt% and CO: from 8.5 wt% to 5.5 wt%) compared to thermal pyrolysis at the same temperature (i.e. 600 °C). Increasing the temperature of the biochar bed to 800 °C, further decreased the yield of CO_2, C_3, C_4 and increased the yield of CH_4 and H_2 (Figure 8.6a).
These findings suggested that biochar was activated and cracked long chain hydrocarbons at temperatures above 700-800 °C. Biochar catalytic activity for biomass tar removal has been attributed to the active sites formed by AAEM metals (Na, Ca, Mg, etc.), the large pores enough to enable adsorption of bulky hydrocarbons and the acidic sites formed at the surface oxygen-containing groups (Klinghoffer, 2013; Wang et al., 2014). Biochar analysis showed the presence of Ca, K, Mg, Na and Si, high surface area (124 m^2/g) and pore volume (0.07 cm^3/g with 64 % <30 nm) and 10 wt% oxygen (section 3.1.3 in chapter 3) confirming the presence of active sites, large enough pores and acidic sites for biochar catalytic activity. The catalytic hydrocarbon cracking using biochar (section 2.3.4 in chapter 2) was initiated via hydrogen transfer from the hydrocarbon chain which is hydrogen-rich, into the biomass char which is hydrogen-deficient. The removal of the hydrogen created an a carbocation ion which underwent further cracking reaction like inter or intra molecular hydrogen transfer or β-scission.
Figure 8.6b showed the weight percentages of the main components in the wax fraction. Small variation was observed between different biochar conditions, except the disappearance of benzoic acid when biochar was isothermally kept at 800°C, suggesting that benzoic acid can undergo decarboxylation to form aromatic hydrocarbons, such as benzene (Du et al., 2016). In addition, all tested conditions produced a thick wax except for the use of biomass biochar under isothermal conditions at 800°C which produced a less viscous brown liquid.

Zeolite HY

The mechanism of zeolite catalytic plastic waste pyrolysis involves the acidity of the catalyst and pore size. Zeolites act as molecular sieves that are able to separate molecules based on their shape and size as well as possess a high number of active sites (Almeida and Marques, 2016). Both of these characteristics are equally important, as the un-cracked polymer chains are too large to enter the internal pores of the zeolite. Figure 8.7 compares the products yield of mixed plastic waste one and two-stage catalytic pyrolysis using zeolite as catalyst. Zeolite catalyst in one-stage pyrolysis at 500 °C presented almost identical yield to those of thermal pyrolysis at equivalent conditions however it increased the gas yield (35 wt% to 55 wt%) at 600 °C.
The results from Figure 8.7 indicate that zeolite HY required lower activation temperatures (600 °C) than biochar (700 °C). Therefore, zeolite HY was activated closer to the temperature range when volatiles were released agreeing with literature (López, De Marco, Caballero, Laresgoiti, Adrados and Torres, 2011). Under isothermal conditions (Figure 8.7), the gas yield remained

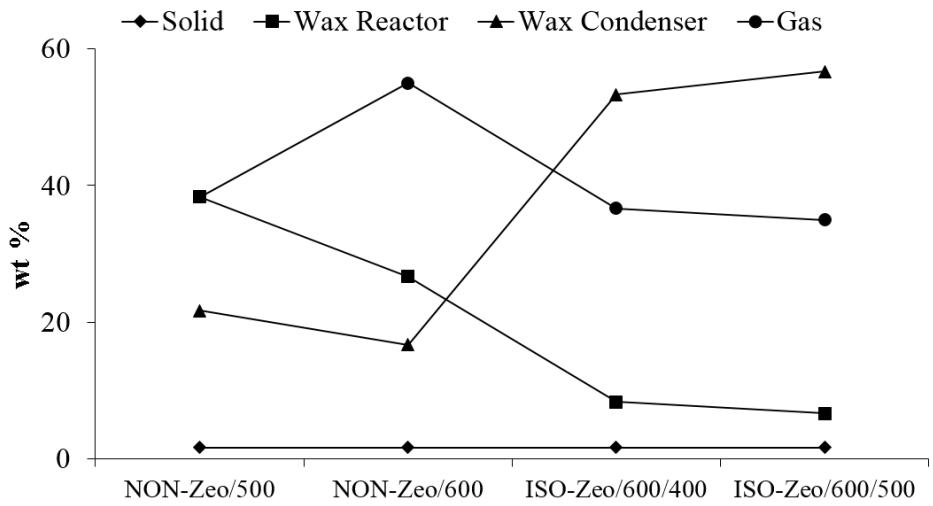

Figure 8.7 Solid residue (± 0 wt%), wax in the reactor (± 5.85 wt%), wax in the condenser (± 4.41 wt%) and gas (± 3.47 wt%) yield from mixed plastic waste one and two-stage catalytic pyrolysis at 600 °C ('XXX-Zeo/YYY/ZZZ': XXX=NON for one-stage and ISO for two-stage, Zeo=zeolite HY, YYY=pyrolysis temperature [°C] and ZZZ=catalyst bed temperature [°C] for isothermal experiments)

constant (approximately 35 wt%). There was a remarkable increase in the wax in the condenser at the expense of a reduction in that in the reactor compared to equivalent conditions in thermal and one-stage catalytic pyrolysis: 26.7 wt% for thermal pyrolysis at 600 °C, 16.67 wt% for one-stage catalytic pyrolysis at 600 °C and 56.7 wt% for two-stage catalytic pyrolysis at 600/500 °C in pyrolysis/catalyst bed. This suggested that zeolite HY cracked heavy volatiles in the reactor to lighter compounds.

Figure 8.8 shows that the zeolite HY catalyst increased the combined yield of C_2-C_4 hydrocarbons from 5.6 wt% in thermal pyrolysis (600 °C) to 16.4 wt% in one-stage catalytic pyrolysis (600 °C) and to 15.8 wt% in two-stage catalytic pyrolysis (600/500 °C in the first/second stage). In addition, zeolite HY decreased the amount of CO_2 in the gas phase, especially for two-stage pyrolysis (19.6 wt% with one-stage zeolite HY at 600 °C), compared to two-stage pyrolysis (9.6 wt%) at 500/600 °C catalyst/pyrolysis temperature. The pore structure of the zeolite favoured the production of C_3H_6 from the PE/PP in the mixture agreeing with previous studies (Li et al., 2016). Acidic cracking catalysts proceed by the formation of ions along hydrocarbon chains i.e. carbocation mechanism (Figure 2.7 in chapter 2), followed by β-scission, isomerization, oligoremization and/or hydrogen transfer to generate short-chained cracked products (Wei et al., 2010).

Catalyst comparison

Figure 8.9 compares the products yields obtained from thermal (600 °C) and two-stage catalytic pyrolysis (600 °C) with isothermal catalysts: biochar at 500-800 °C, zeolite and Al_2O_3 at 500 °C. Even though biochar needed temperatures over 800 °C to be activated (discussed in section 8.1.2), two-stage catalytic pyrolysis at just 500 °C showed similar catalytic activity as to that of

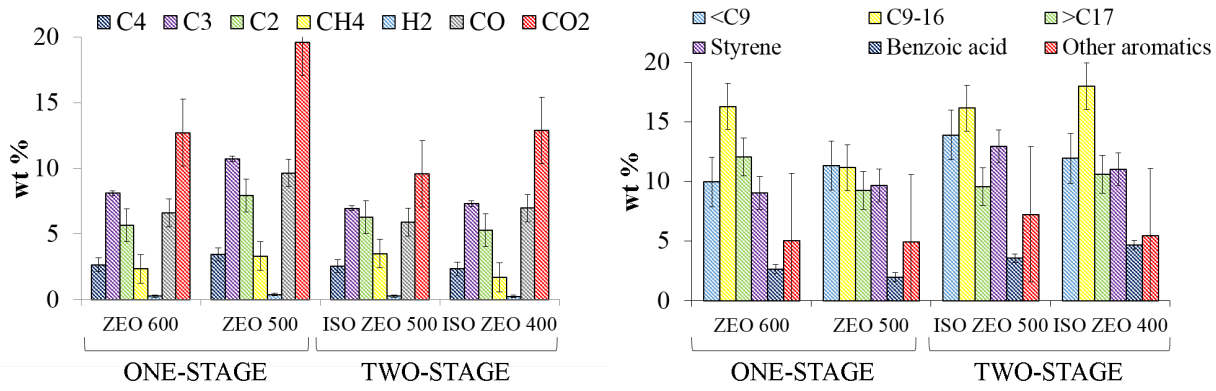

(a) Gas Yield (b) Wax Yield

Figure 8.8 Gas and wax composition from zeolite HY one and two-stage catalytic pyrolysis ('ISO ZEO XXX': ISO refers to isothermal conditions and XXX to the catalyst bed temperature [°C])

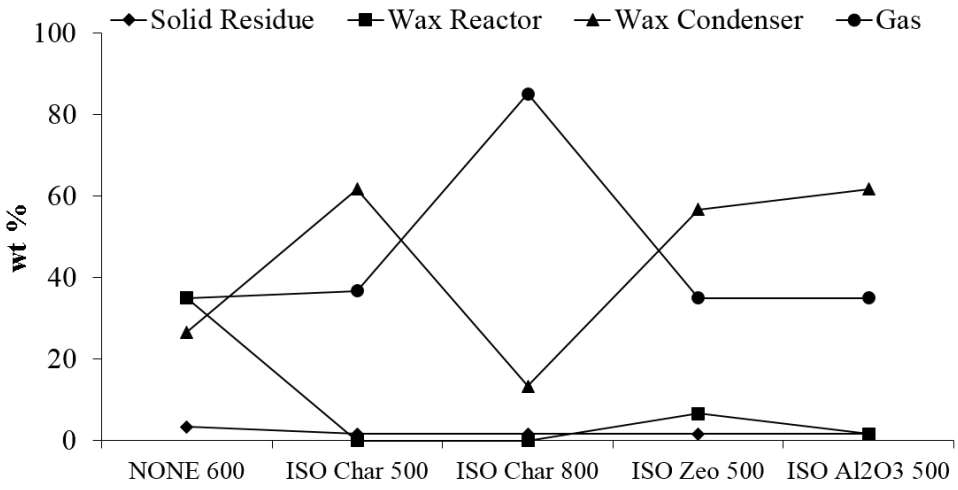

Figure 8.9 Comparison between thermal and two-stage catalytic pyrolysis at 600 °C products yield: solid residue (± 0 wt%), wax in the reactor (± 5.85 wt%), wax in the condenser (± 4.41 wt%) and gas (± 3.47 wt%) ('XXX Cat YYY': XXX=NON for thermal and ISO for isothermal, Cat=catalyst type i.e. biochar, zeolite HY or Al_2O_3 and YYY=catalyst bed temperature [°C])

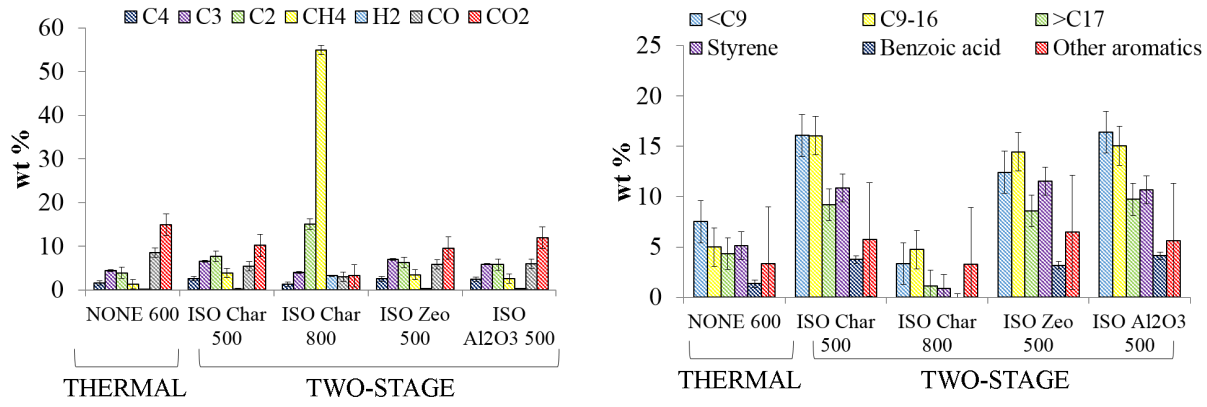

(a) Gas composition

(b) Wax composition

Figure 8.10 Comparison of gas and wax composition from thermal and two-stage catalytic pyrolysis at 600 °C ('XXX Cat YYY': XXX=NON for thermal and ISO for isothermal, Cat=catalyst type i.e. biochar, zeolite HY or Al_2O_3 and YYY=catalyst bed temperature [°C])

zeolite HY and Al_2O_3. The gas yield obtained with two-stage pyrolysis (600/500 °C in pyrolysis/catalyst bed) remained equal to that in thermal pyrolysis with the three catalysts. However, the three catalysts increased the wax in the condenser at the expense of that in the reactor (from 26.67/35.00 wt% wax condenser/reactor yield in thermal to 61.67/0.00 wt%, 56.67/6.67 wt% and 61.67/1.67 wt% in two-stage pyrolysis at 600/500 °C using biochar, zeolite HY and Al_2O_3 respectively).

The catalytic activity associated to the three catalysts promoted the decomposition of the heavier compounds, otherwise condensed in the reactor walls, into lighter molecules. Alumina is an amorphous acid catalyst which, similarly to zeolite HY, contains Lewis acid sites. Both zeolite HY and Al_2O_3 form carbenium ions along the chain of volatiles released from pyrolysis via abstraction of a hydride ion. Secondary reactions (aromatization, oligomerization, β-scission, etc.) occurring on these carbenium ions yield shorter olefin compounds and shorter carbenium ions until termination reactions (Figure 2.7 in section 2). Biochar catalytic cracking activity on the other hand is caused by the presence of acidic surface oxygen groups and AAEM metals (Klinghoffer, 2013).

Figure 8.10 compares the difference of the gas and wax composition between thermal and two-stage catalytic pyrolysis at 600 °C using biochar (isothermally at 500-800 °C), zeolite HY and Al_2O_3 (both isothermally at 500 °C).

Compared to thermal pyrolysis at 600 °C, an addition of biochar, zeolite HY and Al_2O_3: 1) reduced the amount of CO_2 (by 31, 35 and 20 % respectively) and CO (by 35, 31 and 30%), 2) increased the amount of hydrogen (by 52, 54 an 55 %) and 3) enhanced the formation of methane (by 186, 158 and 91 %) and C_2-C_4 (by 69, 58 and 42 %) hydrocarbons (Figure 8.10a). This could be because the addition of the catalyst alters the reaction pathway of PET decomposition from the decarboxylation which produced CO_2 and CO. Furthermore, Figure 8.10a showed that, when biochar was activated (800 °C), its performance was superior than zeolite HY, Al_2O_3 and thermal pyrolysis in terms of: 1) CO_2 and CO reduction to 3.3 wt% CO_2

and 3.1 wt% CO; 2) hydrogen production up to 3.2 wt%; and 3) hydrocarbons generation (up to 55 wt% CH_4 and 20.4 wt% C_2-C_4 hydrocarbons).

Figure 8.10a showed that biochar kept isothermal at 800 °C increased the yield of CH_4 over 50 wt% compared with thermal experiments (two-stage thermal pyrolysis at 500/800 °C) where the yield of CH_4 was about 25 wt% (shown later on in Figure 8.12a). Biochar doubled the amount of CH_4 produced. The heat of formation for CH_4 from carbon ($C + 2\,H_2 \rightarrow CH_4$) is about -74 kJ/mol (Chase, 1996). H_2 is also present at high temperature in more abundance than in the other temperatures tested. This suggested that the carbonaceous nature of biochar may have been contributed to its decomposition at high temperature (800 °C) and to the formation of CH_4.

Thermal pyrolysis at 600 °C yielded similar fractions of wax in the reactor (35 wt%) and in the condenser (26.67 wt%) (Figure 8.9). However, the presence of the three catalysts reduced the wax in the reactor to 6.67 wt% (zeolite HY), 1.67 wt% (Al_2O_3) and 0 wt% (biochar) when isothermally kept at 500 °C. This was due to the aforementioned differences in cracking mechanism between catalytic and thermal pyrolysis. The acidic sites in the catalysts promoted secondary cracking reactions and enhanced the formation of lighter compounds i.e. $<C_9$ collected in the condenser.

The three catalyst tested i.e. zeolite HY, Al_2O_3 and biochar, isothermally held at 500 °C, had only a small influence on the composition of the wax in the condenser compared to thermal pyrolysis at the same temperature (600 °C). However, as shown in Figure 8.10b, the yield of individual compounds increased as well as the wax collected in the condenser. This suggested the three catalysts had cracking catalytic activity to reduce heavier compounds. Biochar, activated at 800 °C, compared to thermal and two-stage (600/500 °C) catalytic pyrolysis with zeolite HY/Al_2O_3 considerable reduced: 1) >C17 hydrocarbons (from about 7.1-10.1 wt% to 1.1 wt%); 2) styrene (from 7.8-12.9 wt% to 0.9 wt%) and 3) benzoic acid (from 3.0-3.6 wt% to 0 wt%). This phenomenon was caused by a combination of high temperature (800 °C) and secondary cracking promoted by AAEM metals and surface oxygen-containing groups on biochar (Wang et al., 2014). As aforementioned, biochar was used for tar removal (organic compounds heavier than benzene, e.g. naphthalene, phenol, toluene) in biomass pyrolysis vapours (El-Rub et al., 2008; Zhang et al., 2014) and therefore it contributed in the same way to the reduction of styrene and benzoic acid in this study.

These results confirmed biochar as a suitable catalyst for mixed plastic waste pyrolysis. Compared to commercial catalyst (zeolite HY and Al_2O_3), biochar, derived from pyrolysis of waste biomass, showed a comparable performance. Therefore, biochar proved to be a potential alternative to conventional catalyst, reducing operating costs and improving the profitability of plastic waste pyrolysis plants.

8.2 Reusability and regeneration of biochar and zeolite HY for mixed plastic waste catalytic pyrolysis

This section is focused on reusability studies of biochar, zeolite HY and SZ. This section also studies two novel catalyst regeneration techniques: CO_2 utilisation and cold plasma. Reusability was investigated through five consecutive two-stage catalytic pyrolysis cycles in the same set-up as the one described in section 8.1. Mixed plastic waste were heated to 500 °C at 30-32 °C/min for all tested conditions while the catalysts were isothermally kept at 800 °C for biochar, 500 and 800 °C for zeolite HY and 400 °C for SZ. Two different five-cycles sets using biochar as a catalyst were conducted to test reproducibility and calculate errors which were extrapolated to the remaining tested conditions in this section.
Regeneration of used zeolite HY catalyst was investigated through: 1) cold plasma at room temperature in a DBD reactor at SED = 180 J/mL (60 W supplied) with CO_2 as discharge gas and 2) two-stage pyrolysis with CO_2 as carrier gas. The cold plasma system used for zeolite HY regeneration was identical to the one described in 3.2.1 in chapter 3. The discharge gap was filled with 1 mm borosilicate glass beads coated with the spent zeolite HY catalyst. Cold plasma was hold for 2h after which the catalyst was separated from the glass beads by agitation and sieving and weighted. Zeolite HY regeneration via CO_2 pyrolysis was conducted in the two-stage set-up already described in section 8.1 but using CO_2 instead of N_2 as carrier gas. The mixed plastic waste were heated up to 500 °C at 30-32 °C/min in the first stage (pyrolysis) followed by a second catalyst stage, containing the spent zeolite HY, isothermally kept at 600 °C. This procedure was repeated for two catalytic pyrolysis cycles. After the system was cooled down below 50 °C the second time, the catalyst was collected, separated via agitation and sieving, weighted and tested in two additional two-stage catalytic pyrolysis cycles.

8.2.1 Effect of temperature in mixed plastic waste pyrolysis products

Although having a different mechanism (random chain scission) to catalyst, high temperature has a similar cracking effect (Almeida and Marques, 2016) due to secondary cracking promotion. Two-stage pyrolysis with an isothermal second stage set at 500 and 800 °C without a catalyst was investigated to isolate the effect of high temperature from that of catalyst to C-C bond cleavage. These experiments (control) were used as a benchmark for comparison. Control experiments with N_2 at 800 °C were repeated three times to test reproducibility and for errors. Figure 8.11 shows the yield of products i.e. gas, wax and solid residue in the control experiments using both N_2 and CO_2 as carrier gases. The temperature in the second stage and the gas yield had a direct relation. Increasing the temperature from 500 to 800 °C, increased the gas yield from 37 wt% to over 74 wt% at the expense of the total wax yield i.e. wax in the condenser plus wax in the reactor (total 70 % reduction). CO_2 had a large effect on the gas and wax yield due to an almost complete conversion of the mixed plastic waste into gas (88.34 wt%). Unlike N_2, an inert environment, CO_2 is an oxidant agent which reacted with the volatile hydrocarbons via dry

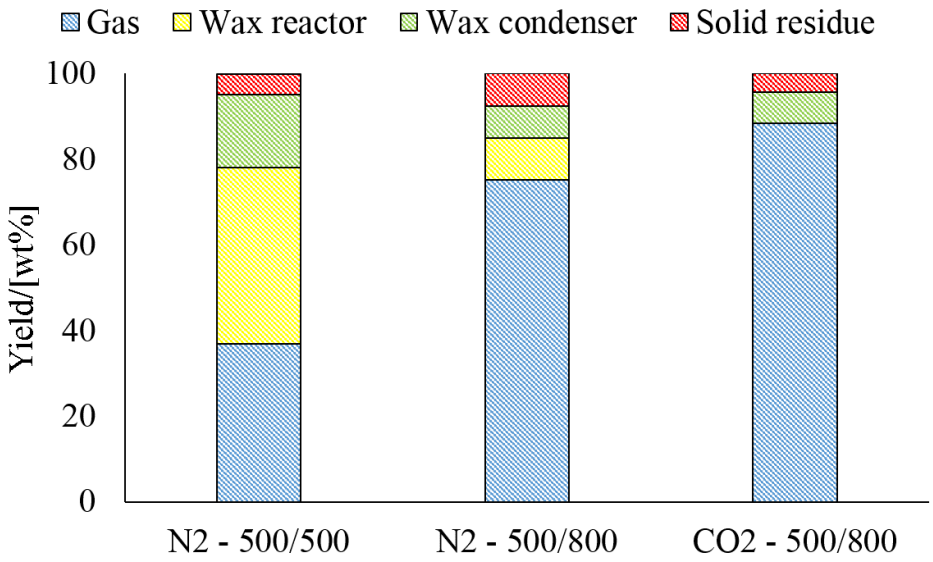

Figure 8.11 Yield of gas (±0.99 wt%), wax (±0.34 wt%) and solid residue (±0.66 wt%) products from mixed plastic waste two-stage thermal pyrolysis ('ZZ - XXX/YYY': ZZ=carrier gas (N_2 or CO_2) and XXX/YYY=pyrolysis/catalyst bed temperature [°C])

reforming into lighter compounds, or even H_2 and CO (reaction (8.1)). This was evidenced by the disappearance of the wax in the reactor (from 9.87 wt% with N_2 to 0 wt% with CO_2 at 800 °C). Opposite, the wax in the condenser (7.4-17.0 wt%) and the solid residue (4.3-7.6 wt%) remained almost constant during all control experiments for both carrier gases.

$$C_xH_y + xCO_2 \rightarrow 2xCO + \frac{y}{2}H_2 \tag{8.1}$$

A similar finding was reported (Saad and Williams, 2016) for a two-stage pyrolysis study of individual plastic waste (HDPE, LDPE, PP, PS and PET) conducted at 500/800 °C in the first/second stage. Injecting CO_2 between the first and second stage increased the gas yield by 1.4 - 5.3 times, depending on the type of plastic waste, at the expense of the wax yield.
Figure 8.12 shows the gas (Figure 8.12a) and condenser wax (Figure 8.12b) composition for the three control experiments. Increasing the temperature of the second furnace from 500 to 800 °C in N_2 reduced the amount of C_3-C_4 in the gas at the same time it increased the amount of CH_4 and C_2. The proportion of CH_4 and C_2 was lower for CO_2 as carrier gas than for N_2 while the amount of CO and H_2 increased according to reaction 8.1.
Low temperature favoured the yield of ethyl-benzene (3.38 wt%) and styrene (4.74 wt%) suggesting that they decomposed into non-condensible volatiles at higher temperatures. Ethyl-Benzene can be thermally decomposed into light hydrocarbons e.g. ethylene, and benzyl radicals, further explaining, the increased C_2 yield in the gas fraction (Figure 8.12a). The wax collected in the reactor was significantly higher at 500 °C than at 800 °C. The wax in the reactor had a higher boiling point explaining why it condensed at the high temperatures of the outskirts of the reactor (approximately 300 °C). Therefore, it is predicted that it was comprised of C_{17+} hydrocarbons, giving a much broader range in chain length than that collected at 800 °C. Results from columns 2 and 3 in Figure 8.12b showed negligible difference in the condenser wax

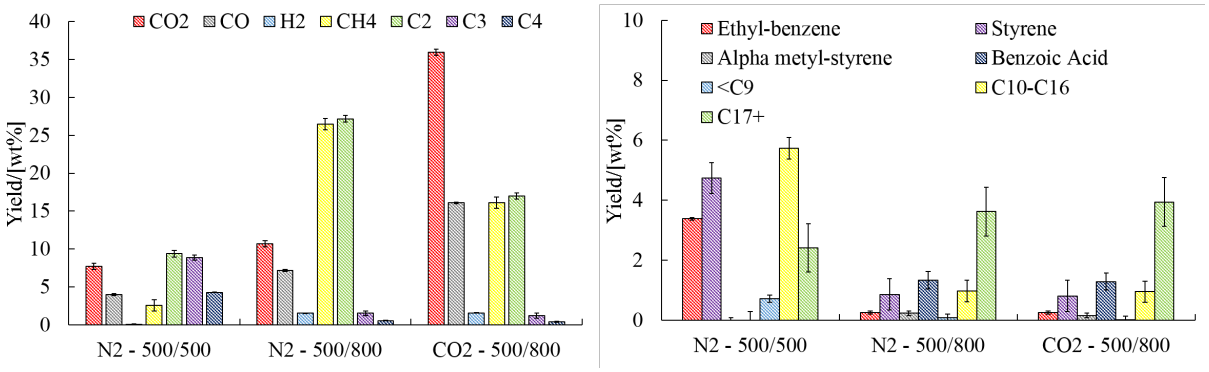

(a) Gas composition

(b) Wax in the condenser composition

Figure 8.12 Yield of products from the gas and wax in the condenser obtained in mixed plastic waste two-stage thermal pyrolysis ('ZZ - XXX/YYY': ZZ=carrier gas (N_2 or CO_2) and XXX/YYY=pyrolysis/catalyst bed temperature [°C])

composition when CO_2 (column 3) was used as carrier gas compared to N_2 (column 2). However, CO_2 eliminated the fraction of wax in the reactor hence suggesting that CO_2 enhances the thermal degradation of heavier hydrocarbons (C_{17+}) through dry reforming (reaction 8.1).

8.2.2 Reusability of biochar in a two-stage pyrolysis with N_2 and CO_2 as carrier gases

As shown in previous section (section 8.1), biochar catalyst activated above 700 °C. This catalyst showed in Figure 8.6 an effective cracking of long chain hydrocarbons due to the acidic centres formed at surface oxygen-containing groups in biochar (Klinghoffer, 2013; Wang et al., 2014). Figure 8.13 shows products yield for N_2 (Figure 8.13a) and CO_2 (Figure 8.13b) as carrier gases over five consecutive mixed plastic waste two-stage catalytic pyrolysis (500/800 °C) cycles using biochar as a catalyst. The fourth cycle in Figure 8.13b was discarded due to a failure in the pyrolysis furnace during the experiment and it is not shown here. However, the biochar sample used in the fourth cycle was not affected by that failure and therefore was reused in the fifth cycle.

When N_2 was used as carrier gas, the yield of gas and wax, in the condenser and the reactor, remained almost constant for the first three cycles. After that, the gas yield increased at the expense of the wax in the condenser. The amount of residue deposited on biochar surface increased after the first cycle, then remained stable before decreasing in the last cycle. The solid residue yield varied slightly between cycles however, as the temperature in the pyrolysis stage was constant at 500 °C for all cycles, this difference resulted from external contaminants e.g. adhesives, ink, etc., in the plastic waste sample. Comparison of Figure 8.13a and Figure 8.11 suggests that, even though the gas yield in the first cycle with biochar was equal to that of the control, biochar increased the wax in the condenser (from 7.41 to 20.08 wt%) at the expense of all the wax in the reactor. The gas yield increased in the third and fourth cycles at the expense of the wax in the condenser. Up to this point, a total of 4.89 wt% of carbon residue was deposited on the surface of the catalyst hence likely contributing to the activity of the catalyst. The delay

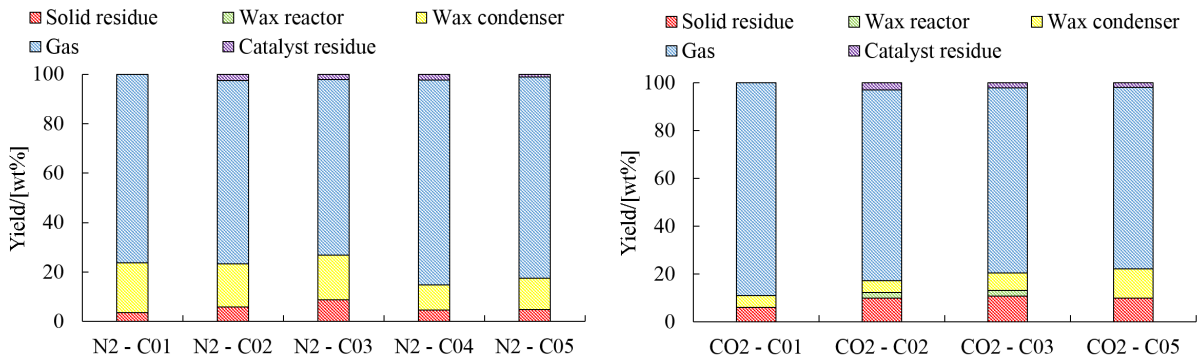

(a) N_2 carrier gas (b) CO_2 carrier gas

Figure 8.13 Yield of gas (±0.84 wt%), wax in the condenser (±1.41 wt%), solid residue (±0.61 wt%) and catalyst residue (±0.53 wt%) products from five cycles of mixed plastic waste two-stage catalytic pyrolysis at 500/800 °C using biochar as catalyst kept isothermal in the second stage ('ZZ - XXX': ZZ=carrier gas (N_2 or CO_2) and XXX=cycle number)

observed in biochar catalytic activity until the third cycle implied that thermal/chemcial activation of biochar prior to pyrolysis could improve its catalytic activity and allow its use in one-stage systems.

Comparison of Figure 8.13b and Figure 8.11 suggests that, during the first cycle in CO_2, biochar slightly increased the gas yield (from 88.3 to 89.1 wt%) at the expense of the wax in the condenser (from 7.4 to 5.0 wt%). It can be concluded that, in addition to the dry reforming effect of CO_2 at high temperature, biochar enhanced even more the cracking of the heavy hydrocarbons. Following cycles (Figure 8.13b), showed an increasing trend in the total wax yield at the expense of the gas yield indicating a loss in biochar catalytic activity. Biochar comprised of 87.88 wt% carbon (section 3.1.3 in chapter 3), therefore according to the Boudouard reaction (reaction 8.2), carbon residue can react with CO_2 to form CO decomposing part of catalyst and reducing biochar catalytic activity. Conventionally, the equilibrium of the Boudouard reaction is highly displaced towards the formation of CO_2 from CO. However, it has been proven (Lahijani et al., 2015) that alkali and alkaline metals (i.e. Na, Ca, etc.), like the ones present in biochar, decrease the minimum temperature to promote the Boudouard reaction from 700 °C to only 580 °C favouring the formation of CO from CO_2.

$$C_{(s)} + CO_2 \leftrightarrow 2CO \tag{8.2}$$

Alternatively, Figure 8.13b showed that carbon deposited on biochar surface after the second, third and fourth cycles. This carbon deposits could clogged biochar pores hindering the access of large compounds to the pores and, therefore reducing another source of biochar catalytic activity (Klinghoffer, 2013; Wang et al., 2014).

In addition, above 600 °C, a proportion of the CH_4 generated reacted with the CO_2 (oxidant agent) as shown in reaction (8.3). This reaction is catalysed by the surface oxygen-containing groups in biochar (Eliasson et al., 2000; Nishiyama and Aika, 1990), via the formation of an intermediate methyl radical (CH_3^*), to form C_2, C_3 and C_4 hydrocarbons after a chain reaction

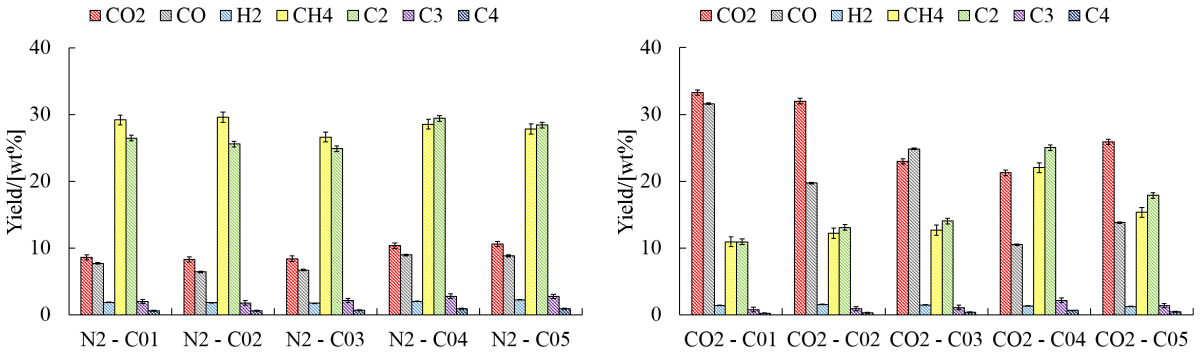

(a) N_2 carrier gas (b) CO_2 carrier gas

Figure 8.14 Gas composition obtained from mixed plastic waste two-stage catalytic pyrolysis at 500/800 °C using biochar as catalyst kept isothermal in the second stage ('ZZ - XXX': ZZ=carrier gas (N_2 or CO_2) and XXX=cycle number)

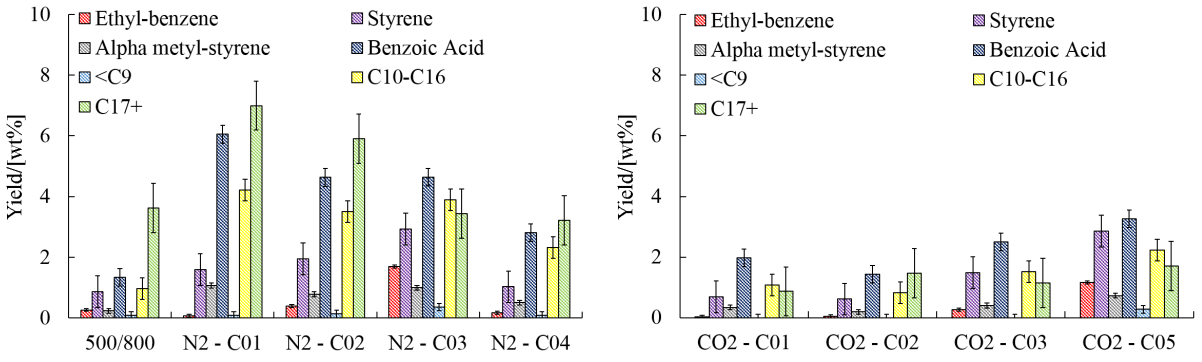

(a) N_2 carrier gas (b) CO_2 carrier gas

Figure 8.15 Wax composition obtained from mixed plastic waste two-stage catalytic pyrolysis at 500/800 °C using biochar as catalyst kept isothermal in the second stage ('ZZ - XXX': ZZ=carrier gas (N_2 or CO_2) and XXX=cycle number)

mechanism. Figure 8.14b confirms the yield of light hydrocarbons in the gas fraction, particularly C_2, increased with the number of cycles as CO_2 decreased. When N_2 was used as carrier gas (Figure 8.14a), the same effect was observed however the increase in the yield was lower e.g. C_2 yield increased by 2 wt% with N_2 compared to 7 wt% with CO_2.

$$\begin{aligned} xCH_4 + CO_2 &\rightarrow CO + C_xH_{(4x-2)} + H_2O \\ C_xH_{(4x-2)} + CO_2 &\rightarrow CO + C_xH_{(4x-4)} + H_2O \end{aligned} \tag{8.3}$$

Figure 8.15 shows the yield of the compounds in the wax fraction in the condenser. Compared to the control at equivalent conditions (Figure 8.12b), biochar (with N_2 as carrier gas, Figure 8.15a) exhibited cracking catalytic activity evidenced by a reduction of the C_{17+} hydrocarbons proportion in favour of C_{10}-C_{16} hydrocarbons. Biochar also promoted the formation of styrene (from PS) and benzoic acid (from PET) in the wax fraction compared with the control experiments. The amount of ethyl-benzene, alpha-methyl styrene and $<C_9$ remained invariable.

Parallel trends were observed for biochar with CO_2 as carrier gas (Figure 8.15b), with the exception of an additional increase in the ethyl-benzene proportion.
Acidic catalyst such as zeolites (Akubo et al., 2017), clay-based catalyst (Auxilio et al., 2017) or sulphated zirconia (Almustapha et al., 2017) can increase the aromatic content of plastic waste pyrolysis wax fraction due to the formation of carbenium ions via Lewis acid sites or protonation of hydrocarbons at Brønsted acid sites (Akubo et al., 2017) followed by dehydrocyclisation and aromatisation reactions (Akubo et al., 2017; Almustapha et al., 2017). However, the higher amount of styrene and benzoic acid found with biochar compared to the control for both N_2 (Figure 8.15a) and CO_2 (Figure 8.15b) was not caused by Lewis or Brønsted acid sites. Instead, biochar adsorbed the aromatic compounds i.e. ethyl-benzene, styrene and benzoic acid, (Klinghoffer et al., 2012) avoiding their decomposition at high temperature into lighter molecules e.g. C_2.

Characterisation of spent biochar

Catalysts often deactivate over time due to coke deposition on their surface, poisoning of the surface, morphological changes as a result of sintering or alteration in their oxidation state (Klinghoffer et al., 2012). As shown in Figure 8.13 (section 8.2.2), biochar catalytic activity slightly decreased over five cycles when CO_2 was used as carrier gas. This was caused by either reaction of the carbonaceous catalyst with the CO_2 or pore saturation with the mixed plastic waste pyrolysis products i.e. solid residue or wax. Klinghoffer et al. (2012) found that catalysts made of biomass char changed their composition during thermal treatments due to decomposition of the amorphous carbon at temperatures above 300 °C (Papadopoulou et al., 2012). As the amorphous carbon was removed, the oxygen-containing groups and the AAEM metals in biochar migrated to the surface and, eventually sintering and forming agglomerations if temperatures rose up to 1000 °C.
Figure 8.16 compares SEM images of fresh (left) and spent (right) biochar showing small bright spots (examples circled in Figure 8.16). According to Klinghoffer et al. (2012), these spots correspond to AAEM metals and oxygen-containing groups. ICP/MS analysis of biochar confirmed the presence of Ca, K, Mg, Na and Si alongside traces of other AAEM (section 3.1.3 in chapter 3). However, the number of bright sport observed in the fresh and spent catalyst SEM images (Figure 8.16) appeared to be similar. This observation confirmed that rather than deactivation through reaction of the carbonaceous catalyst with the CO_2 or removal of the amorphous carbon with temperature biochar was more likely deactivated by a reduction in the surface area and pore size and volume. Table 8.3 compares surface area, pore volume and pore distribution of fresh and spent biochar after five pyrolysis cycles in N_2.
The surface area of biochar considerably decreased after five consecutive pyrolysis cycles in N_2 carrier gas explaining the loss of biochar catalytic activity with cycles. Referring back to Figure 8.13, the catalyst residue increased from the second cycle forward. This suggests that biochar was progressively saturated with pyrolysis residue or wax losing catalytic activity because less area was available for the pyrolysis volatiles to react. In addition, the total pore volume of the

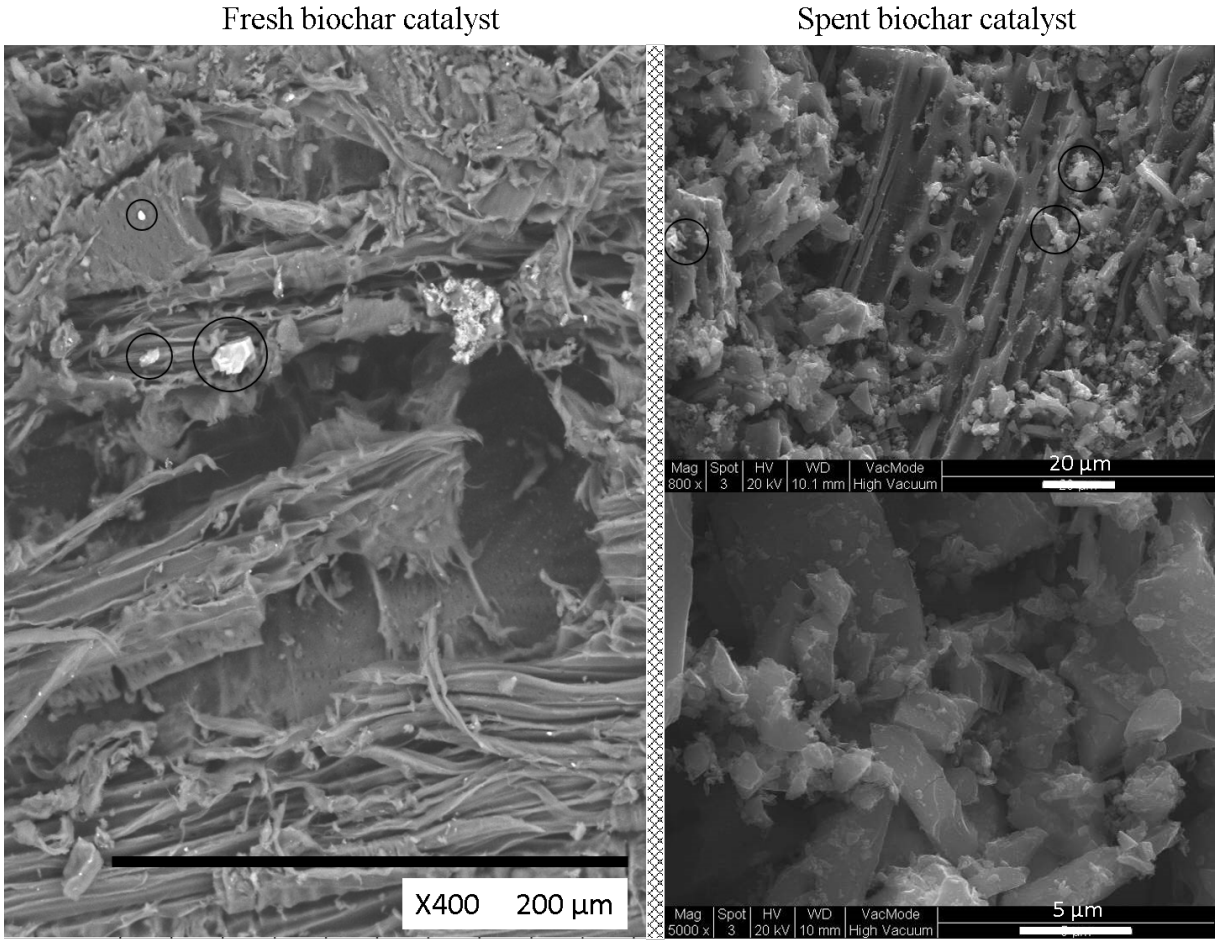

Figure 8.16 SEM images of fresh (left) and spent (right) biochar after five consecutive two-stage pyrolysis of mixed plastic waste at 500/800 °C in N_2 carrier gas (circles are examples of AAEM and oxygen-containing groups)

Table 8.3 Properties of fresh and spent biochar after five consecutive two-stage pyrolysis of plastic waste at 500/800 °C in N_2 carrier gas

	Fresh biochar	Spent biochar
Surface area/[m^2/g]	124.00 ± 12.10	3.08 ± 1.66
Total pore volume/[cm^3/g]	0.07	0.006
Pore size distribution/[nm]		
2.9 - 3.2 nm	-	5 %
3.2 - 18.0 nm	-	95 %
<30 nm	65 %	-
>30 nm	36 %	-

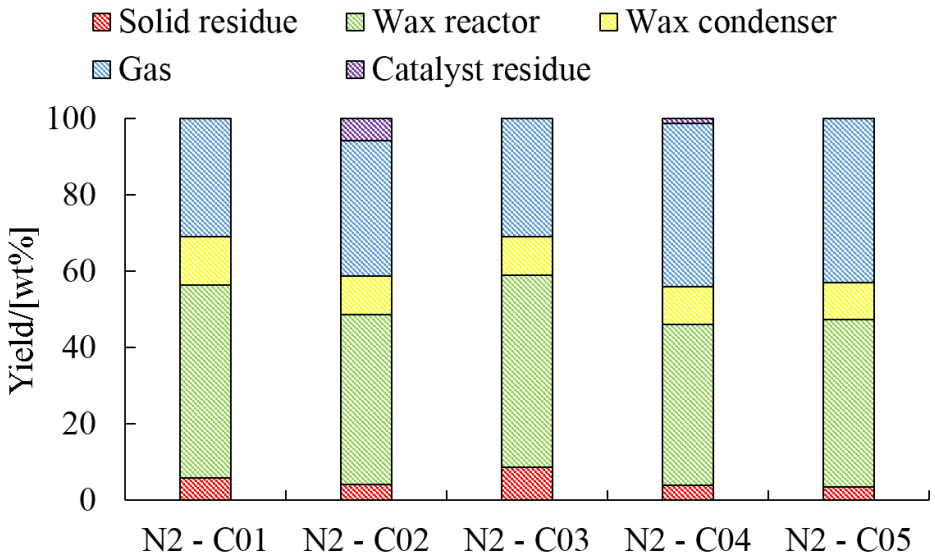

Figure 8.17 Gas (±0.84), wax in the reactor (±5.93), wax in the condenser (±1.41), solid residue (±0.61) and carbon residue on catalyst (±0.53) yield obtained in mixed plastic waste two-stage catalytic pyrolysis using SZ catalyst at 500/400 °C in the first/second stages ('N2 - C0X': C0X refers to the cycle number

catalyst decreased by 91 % meaning again that less catalyst was available for reaction. The pore size distribution became smaller (2.94-17.96 nm) than in the fresh catalyst (larger than 30 nm). This suggests that the large pores of biochar responsible for heavy compounds cracking were blocked preventing the cracking process.

8.2.3 Reusability of sulphated zirconia in a two-stage pyrolysis

Figure 8.17 shows the products yield for each cycle presented some variation compared to the control at 500 °C (Figure 8.11). SZ catalyst first cycle exhibited a higher proportion of wax in the reactor (from 41.27 wt% in the control to 50.63 wt% in the first SZ cycle) and a lower proportion of wax in the condenser (from 17.00 wt% in the control to 12.66 wt% in the first SZ cycle). As SZ was re-used, the gas yield increased from 30.98 wt% in the first cycle up to 42.99 wt% in the fifth one at the expense of the wax in the reactor (from 50.63 wt% in the first cycle up to 43.89 wt% in the fifth one) and in the condenser (from 12.66 wt% in the first cycle up to 9.75 wt% in the last cycle). The solid residue remained almost constant and similar to the control test as expected since the pyrolysis temperature remained the same and the catalyst was placed downstream. The solid residue, however increased up to 8.53 wt% in the third cycle. This was caused by a higher presence of contaminants/additives in the mixed plastic waste feedstock. The residue deposited on the surface of the catalyst was only detected on the second and fourth cycles. In the other three cycles (first, third and fifth) the catalyst bed presented a weight loss at the end of each cycle of 20.8, 21.2 and 13.7 wt% respectively (calculated from the initial amount of catalyst weighted at the beginning of each cycle). This suggested either catalyst thermal decomposition or powder loss between cycles. As mentioned, thermal analysis of fresh SZ showed four peaks occurring between 80 and 525 °C (section 3.1.3 in chapter 3). The first two

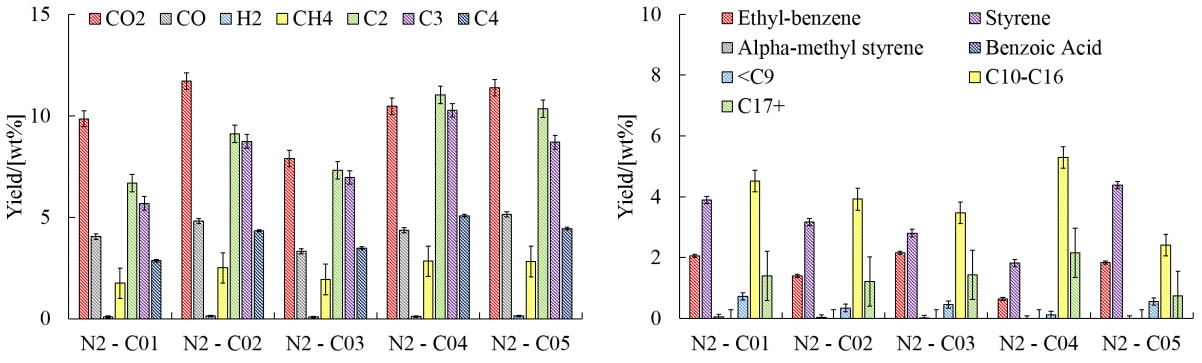

(a) Gas yield

(b) Wax yield

Figure 8.18 Gas and wax composition from mixed plastic waste two-stage catalytic pyrolysis using SZ catalyst at 500/400 °C in the first/second stages ('N2 - C0X': C0X refers to the cycle number)

(80-180 °C) were caused by the loss of hydrated water molecules explaining the weight loss: $Zr(SO_4)_2 \cdot x\mathrm{H_2O} \rightarrow Zr(SO_4)_2 \cdot y\mathrm{H_2O}$ where y<x. Since the catalyst bed was not heated above 400 °C no other thermal transitions applied in these experiments. The latter along with the fact that SZ did not show a loss of activity in Figure 8.17, confirmed that the weight loss observed was caused by the loss of hydrated water.

Figure 8.18 shows the composition of the gas (Figure 8.18a) and the wax in the condenser (Figure 8.18b). Higher yield of CO_2 (9.86-11.39 wt%), C_2 (6.69-10.35 wt%) and C_3 (5.69-8.70 wt%) were observed in SZ pyrolysis cycles than in the control test (7.69, 9.39 and 8.85 wt% respectively) at 500 °C (Figure 8.12a). Opposite, lower yield of ethyl-benzene (2.06-1.84 wt%) than that in the control test at 500 °C (3.38 wt%) was observed (Figure 8.12b). According to Park et al. (2000), the tetragonal crystalline ZrO_2 at the surface of SZ can catalyse the oxidative dehydrogenation of ethyl-benzene into styrene in the presence of the CO_2 (oxidant agent) according to reaction 8.4.

$$Ph-CH_2-CH_3+CO_2 \leftrightarrow Ph-CH=CH_2+H_2O+CO \tag{8.4}$$

However, the small variations in products yield and the low proportion of tetragonal ZrO_2 found in the catalyst analysis (Figure 3.6 in chapter 3), suggested that reaction (8.4) only occurred to a very low extent or not at all. The remaining fractions in the wax in the condenser were not significantly altered by the introduction of SZ.

Base on the yield and composition of products, it can be concluded that SZ cracking activity at 400 °C is much lower than that of biochar. Nevertheless, previous work at higher temperature (450-600 °C) (Diaz-Silvarrey, McMahon and Phan, 2018; Diaz-Silvarrey, Zhang and Phan, 2018) supported the use of SZ as a cracking catalyst for plastic waste. This suggests that SZ catalyst requires temperatures above 400 °C to be activated. However, as it suffers thermal decomposition above 525 °C (Diaz-Silvarrey, McMahon and Phan, 2018), SZ optimum catalytic pyrolysis temperature is very restricted.

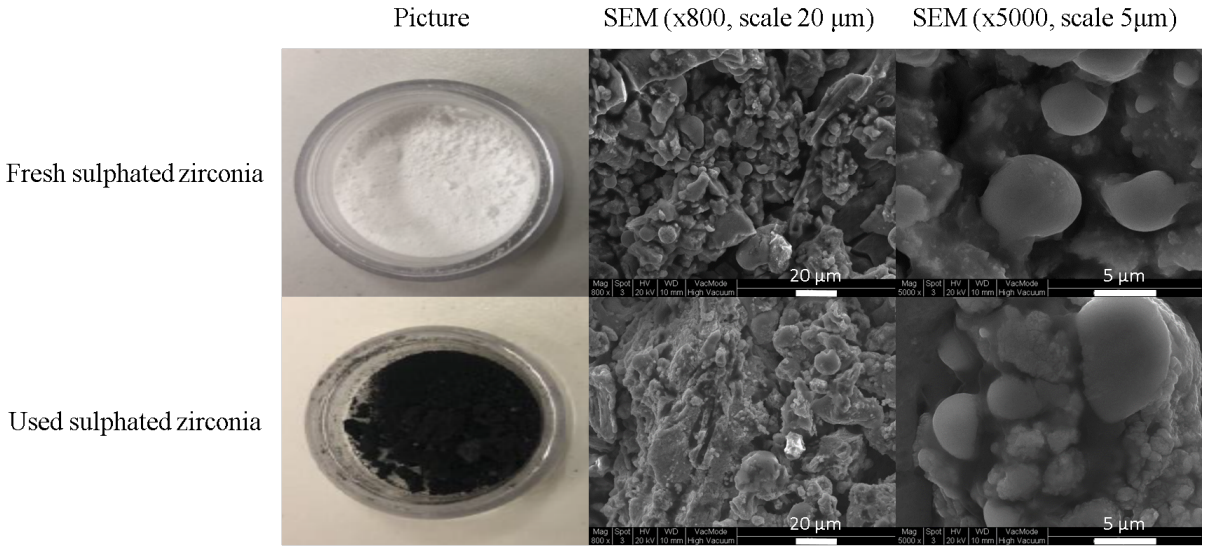

Figure 8.19 Pictures (left column) and SEM images (middle and right columns) of fresh (top) and spent (bottom) sulpated zirconia catalyst after five mixed plastic waste two-stage catalytic pyrolysis at 500/400 °C (pyrolysis/catalyst bed temperature)

Table 8.4 Properties of fresh and spent sulphated zirconia after five consecutive two-stage pyrolysis of plastic waste at 500/400 °C in N_2 carrier gas

	Fresh	Spent
EDX analysis		
Zr	43 wt%	41 wt%
O	39 wt%	39 wt%
S	18 wt%	20 wt%
Zr/S	0.18 mole/mole	0.25 mole/mole
SO_4	9 mol%	12 mol%
Surface area/[m^2/g]	10.62 $\pm$ 0.21	2.97 $\pm$ 1.68
Total pore volume/[cm^3/g]	0.06	0.005
Pore size distribution		
<4.1 nm	0 %	18 %
4.1 - 16.4 nm	32 %	65 %
16.4 - 34.4 nm	68 %	17 %

Characterisation of spent sulphated zirconia

SZ showed a reduction between the initial and final weight of 20.8, 21.2 and 13.7 % on the first, third and fifth cycles respectively with a total weight loss between the weight at the end of cycle five and the initial amount of SZ loaded before cycle one of 26 %.

As observed in Figure 8.19 left column pictures, the coke deposition on the surface of SZ catalyst was obvious at plain sight due to the colour change from white (top) to black (bottom). SEM images (middle and right columns in Figure 8.19) show more detail on the change in the catalyst surface. The sputtered circular granules, formed by tetragonal ZrO_2 (Ewais et al., 2014), were less prominent and more sintered to the surface in the spent SZ catalyst than in the fresh one. This could be a result of a rearrangement of the surface due to the migration of hydrated water molecules from deep inside the catalyst to the surface between 80-180 °C.

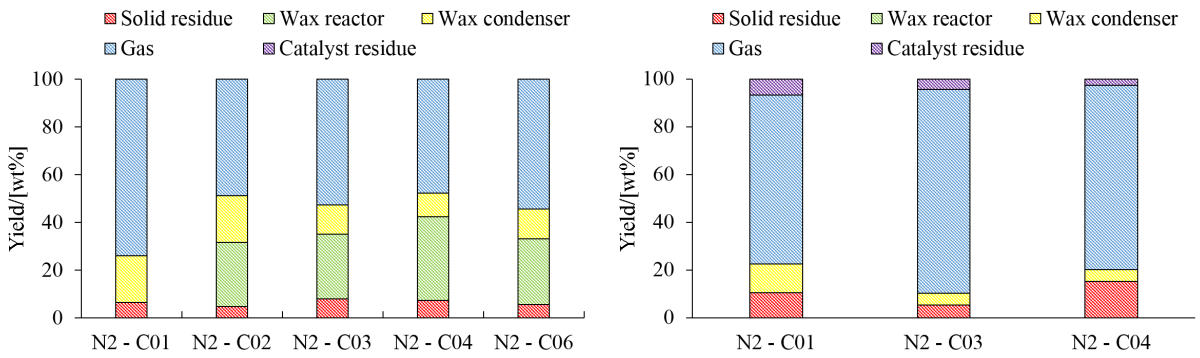

(a) Catalyst temperature = 500 °C

(b) Catalyst temperature = 800 °C

Figure 8.20 Gas (±0.84 wt%), wax in the reactor (±5.93 wt%), wax in the condenser (±0.1.41 wt%), solid residue (±0.0.61 wt%) and catalyst residue (±0.53 wt%) yield obtained in mixed plastic waste two-stage catalytic pyrolysis at 500/500 °C and 500/800 °C (pyrolysis/catalyst bed temperatures) ('N2 - C0X': C0X=refers to the cycle number)

As illustrated in Table 8.4, the composition of the fresh and spent catalysts appeared almost identical therefore, confirming that SZ did not suffer thermal decomposition at the operating temperature. The differences in the surface showed in Figure 8.19 were confirmed to be caused by the migration of hydrated water molecules to the surface due to their evaporation between 80-180 °C and the coke deposits. CN analysis confirmed that spent SZ catalyst presented a 14.79 wt% of carbon and BET analysis confirmed that larger pores (>16.4 nm) were clogged, decreasing the total pore volume and surface area hence, deactivating the catalyst with cycles.

8.2.4 Reusability of zeolite HY in a two-stage pyrolysis

Figure 8.20 shows the products yield for all completed cycles. Figure 8.20a shows that an extra sixth cycle was carried out at 500/500 °C due to the fifth one being discarded because the mixed plastic waste sample crucible slid out of the pyrolysis furnace. The same reason explains the elimination of the second cycle at 500/800 °C. Only four cycles instead of five were conducted at 500/800 °C (Figure 8.20b) as the coke on the surface of the catalyst and borosilicate beads covered all the void volume blocking the pass of gas/volatiles after four cycles. The effect of zeolite HY catalyst on the yield of pyrolysis products compared to control tests at equivalent conditions was more prominent when the catalyst was isothermally kept at 500 °C (Figure 8.20a) than at 800 °C (Figure 8.20b). This was caused by the destruction of some of the carbocations formed by zeolite HY at the high temperatures before they underwent secondary reactions (Guisnet et al., 1992).

At low temperature (500 °C), zeolite HY increased the yield of both the gas and the wax in the condenser in detriment of the wax in the reactor compared with the control test (Figure 8.20a). The reaction between zeolite HY and volatiles from mixed plastic waste pyrolysis starts when the volatiles are adsorbed at zeolite HY acid sites at the surface or entrance of pores (Serrano et al., 2012). Then hydrogen atoms are exchanged between the acid sites and the volatile chain forming carbonium (Brønsted acid sites via protonation) or carbenium (Lewis acid sites via

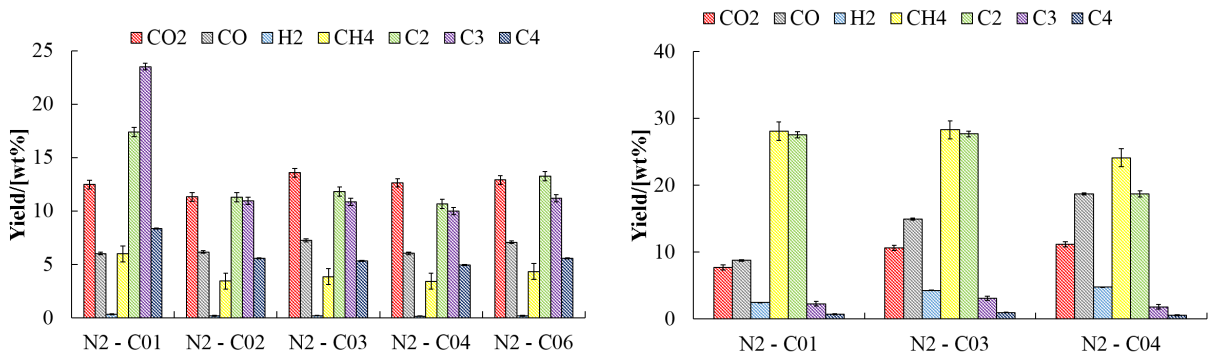

(a) Catalyst temperature = 500 °C

(b) Catalyst temperature = 800 °C

Figure 8.21 Gas composition obtained in mixed plastic waste two-stage catalytic pyrolysis at 500/500 °C and 500/800 °C/min (pyrolyis/catalyst bed temperature) ('N2 - C0X': C0X=cycle number)

abstraction) (Figure 2.7 in chapter 2). These ions promote the cleavage of C-C bonds via β-scission in particular forming shorter molecules. Opposite, thermal cracking occurs through the random formation of radicals along the volatiles chain which does not promote β-scission reactions. The latter hinders the formation of shorter hydrocarbons and explains the larger yield of gas and wax in the condenser in the presence of zeolite HY.

Figure 8.20 shows that the amount of catalyst residue after the first cycle was larger at high temperature (6.81 wt%) than at low temperature (0.67 wt%). Coke deposition, one of the main well-known disadvantages of zeolite catalysts (Magnoux et al., 1987; Marcilla et al., 2004; Masuda et al., 1999; Uemichi et al., 1998), poisons zeolite HY acid sites via the adsorption of polyaromatic compounds and the blockage of the pores. The large amount of catalyst residue observed in Figure 8.20 during pyrolysis cycles at high temperature deactivated the zeolite HY catalyst (6.81 wt% on first cycle, 3.15 wt% on second cycle, 4.33 wt% on third cycle and 2.77 wt% on fourth cycle). This contributes to the explanation on the low catalytic performance at 800 °C compared to the control at equivalent conditions. When acid catalysts like zeolite HY are exposed to high temperature a fraction of the carbocations are destroyed reducing the activity of the catalyst (Guisnet et al., 1992).

Figure 8.21 breaks down the composition of the gas fraction at both temperatures. There was a clear difference between the amount of CH_4 and C_2-C_4 hydrocarbons in the gas at the first and at the remaining four cycles at 500 °C (Figure 8.21a). The amount of CO_2, CO and H_2 also increased with zeolite HY compared with the control test (7.69, 4.00 and 0.09 wt% respectively) but remained relatively constant across all five cycles (11.30-12.62, 6.01-7.24 and 0.12-0.32 wt% respectively). At 800 °C, the yield of hydrocarbons in the gas was higher than that in the control test (from 16.99, 1.23 and 0.41 wt% for C_2, C_3 and C_4 respectively in the control to about 18.69-27.54, 1.79-3.08 and 0.56-0.96 wt% respectively in the three cycles at 800 °C). In particular, the amount of CH_4 and C_2 almost doubled compared to both the control and experiments with zeolite HY at 500 °C. The most significant variation was observed in the H_2 yield, which tripled at 800 °C compared to the control and by almost 40 times compared with zeolite HY experiments at 500 °C according to reaction 8.5.

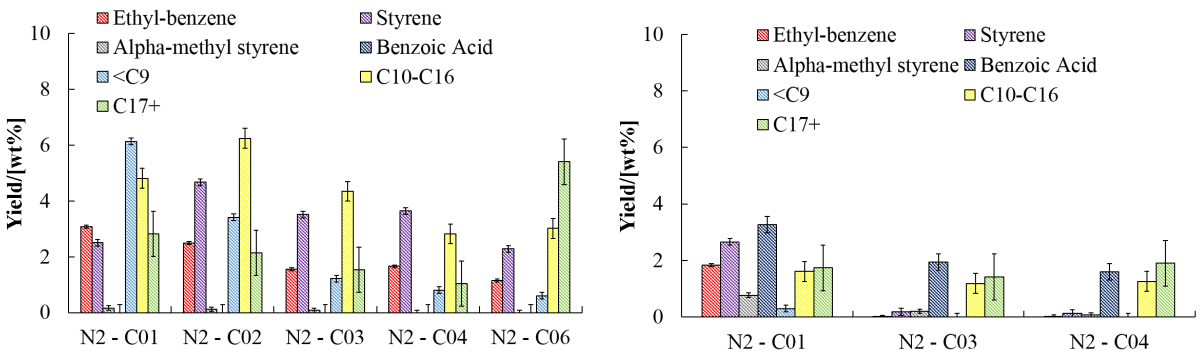

(a) Catalyst temperature = 500 °C (b) Catalyst temperature = 800 °C

Figure 8.22 Composition of the wax in the reactor collected from mixed plastic waste two-stage catalytic pyrolysis at : first stage = pyrolysis at 500/500 °C and 500/800 °C/min (pyrolyis/catalyst bed temperature) ('N2 - C0X': C0X=cycle number)

$$C_xH_y \rightarrow xC_{(s)} + \frac{y}{2}H_2 \tag{8.5}$$

Reaction (8.5) shows that C_3 and C_4 hydrocarbons at 800 °C in the presence of zeolite HY decomposed into H_2 and catalyst residue. In addition, a portion of the generated CH_4 and CO_2 reacted (reaction (8.3) in section 8.2.2). These two reactions explained the larger amount of C_2, CO, H_2, and catalyst residue and the reduction of C_3-C_4, CH_4 and CO_2 (Figure 8.20b) compared with the control (Figure 8.11) and zeolite HY experiments at 800 °C (Figure 8.21a). As the catalyst was re-used over cycles it was poisoned with coke explaining the subsequent increase in the CO_2 yield and the decrease in the C_2 yield due to catalyst deactivation.
Figure 8.22a shows that the first and second cycle conducted at 500 °C significantly increase the yield of $<C_9$, compared to the control test (Figure 8.12b), at the expense of C_{10}-C_{17+} hydrocarbons. As the catalyst was re-used the product distribution shifted to the opposite trend due to the deactivation of zeolite HY. Ethyl-benzene yield steadily decreased across all five cycles at 500 °C from 3.07 wt% (similar to the control test: 3.38 wt%) to 0.93 wt%. This suggested that, unlike SZ catalyst, zeolite HY may catalysed the oxidative dehydrogenated of ethyl-benzene into styrene and CO (reaction (8.4)). The reduction of styrene yield from the third cycle onwards suggested the cracking of styrene into benzene and alkylbenzenes at zeolite HY acid sites (Marczewski et al., 2013).
At 800 °C, following the behaviour showed in the control test (Figure 8.11), zeolite HY significantly decreased the amount of wax in the reactor (from 26.91-44.59 wt% to 0.00 wt%) compared to that when zeolite HY was heated at 500 °C. The presence of zeolite HY increased the amount of aromatic compounds i.e. ethyl-benzene, styrene, α-methyl styrene and benzoic acid in the first cycle.
Plastic waste pyrolysis wax main application is the use as transportation fuel. This requires a high content of aromatic, naphthenes and iso-alkanes (Buekens and Huang, 1998). Table 8.5 shows that zeolite HY, isothermally kept at 500 °C, decreased the aromatic content compared to the control test. Although it has been previously reported that zeolite HY increases the aromatic

Table 8.5 Comparison of the proportion of aliphatic (<C_9, C_{10}-C_{16}, C_{17+}) and aromatic (ethylbenzene, styrene, α-methyl styrene and benzoic acid) compounds in the condenser wax fraction from mixed plastic waste two-stage catalytic pyrolysis at 500/500 °C and 500-800 °C (pyrolysis/catalyst bed temperatures) (C0X=number of cycle)

		Aliphatic / [%]	Aromatic / [%]
Control - 500/500		52.23	47.78
HY - 500/500	C01	70.56	29.44
HY - 500/500	C02	61.81	38.19
HY - 500/500	C03	57.92	42.08
HY - 500/500	C04	46.87	53.13
HY - 500/500	C06	72.43	27.57
Control - 500/800		63.73	36.29
HY - 500/800	C01	29.90	70.10
HY - 500/800	C03	52.74	47.26
HY - 500/800	C04	63.65	36.35

content in pyrolysis wax/liquid (Akubo et al., 2017; Buekens and Huang, 1998; López, De Marco, Caballero, Laresgoiti, Adrados and Aranzabal, 2011; Pinto et al., 1999*b*), those studies were performed on individual aliphatic plastic waste i.e. HDPE, PP and PS. Hence, the main difference was the presence of PET in the feedstock and the generation of CO_2 in the gas. CO_2 can act as an oxidant agent and, in the presence of zeolite HY, oxidise the aromatics compounds formed. As zeolite HY deactivated with cycles, the aromatic content increased up to 53.13 % in the fourth cycle (compared to 47.78 % in the control test) due to a reduction in the oxidative dehydrogenation of aromatic compounds. In the sixth cycle however, the proportion of aromatics sharply decreased (to 27.57 %) again due to a sharp increase in the C_{17+} fraction from 9.97 wt% to 12.45 wt% (Figure 8.22a).

At high 800 °C, the proportion of aromatic compounds in the wax in the condenser increased sharply in the first cycle (70.10 %) compared to both the control (36.29 %) and two-stage catalytic pyrolysis at 500 °C (29.44 %). This proportion then decreased considerably with cycles (to 47.26 and 36.35 % in the third and fourth cycles respectively). The aforementioned high amount of coke on zeolite HY after the first cycle (6.81 wt%) blocked zeolite HY pores. This hindered the entrance of compounds into the catalyst and thus, the occurrence of secondary reactions such as aromatization.

Characterisation of spent zeolite HY

Figure 8.23 shows at first sight that spent zeolite HY (bottom left) was darker than fresh catalyst (top left). The amount of carbon, measure by elemental analysis, increased from 0 % in fresh zeolite HY up to 15.70 % for used zeolite HY after the six cycles at 500 °C confirming deposits of coke. No difference was observed in Figure 8.23 between SEM images of fresh (top middle) and used (bottom middle and right) zeolite HY suggesting that pyrolysis did not had an effect on the catalyst morphology. EDX analysis (Table 8.6) was almost identical for the fresh and used catalyst confirming that temperature did not affect the composition of the catalyst.

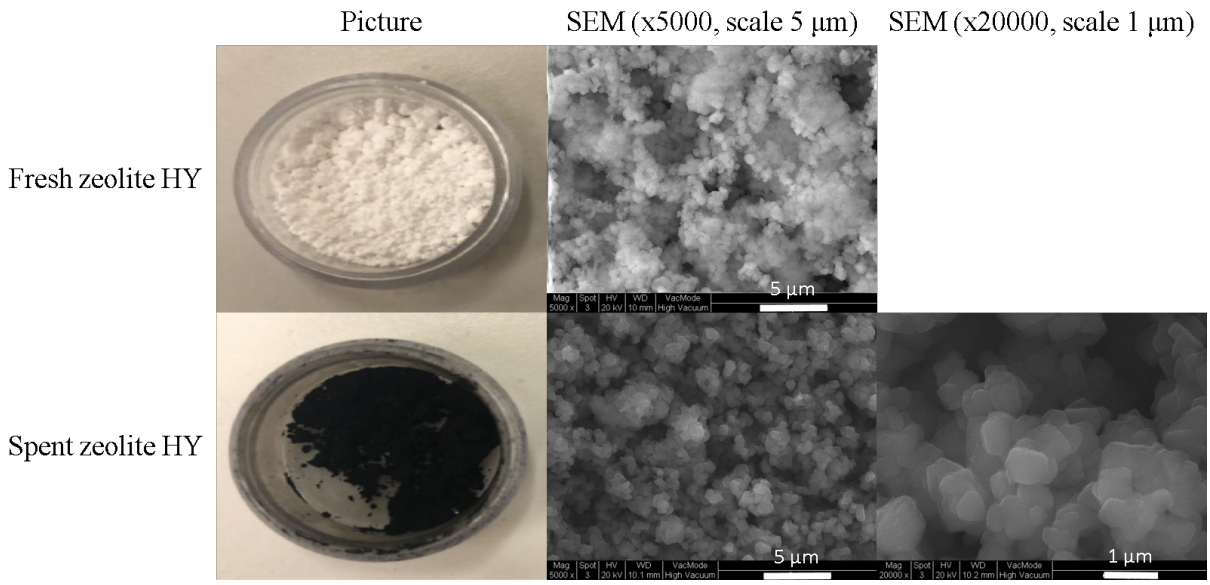

Figure 8.23 Pictures (left column) and SEM images (middle and right columns) of fresh (top) and spent (bottom) zeolite HY catalyst after six consecutive mixed plastic waste two-stage pyrolysis at 500/500 °C (pyrolysis/catalyst bed temperatures) in N_2 carrier gas

Table 8.6 Properties of fresh and spent zeolite HY catalyst after six consecutive mixed plastic waste two-stage pyrolysis at 500/500 °C in N_2 carrier gas

	Fresh	Spent
EDX analysis		
Al	11 wt%	9 wt%
Si	34 wt%	32 wt%
O	55 wt%	59 wt%
SiO_2/Al_2O_3	5.17	5.78
Surface area/[m^2/g]	666.82 ± 31.13	4.03 ± 0.82
Total pore volume/[cm^3/g]	0.117 ± 0.001	0.01
Pore size distribution		
2.7 - 4.2 nm	14.15 ± 4.19 %	0 %
4.2 - 16.4 nm	63.76 ± 4.88 %	53.14 %
16.4 - 34.4 nm	22.09 ± 1.83 %	46.86 %

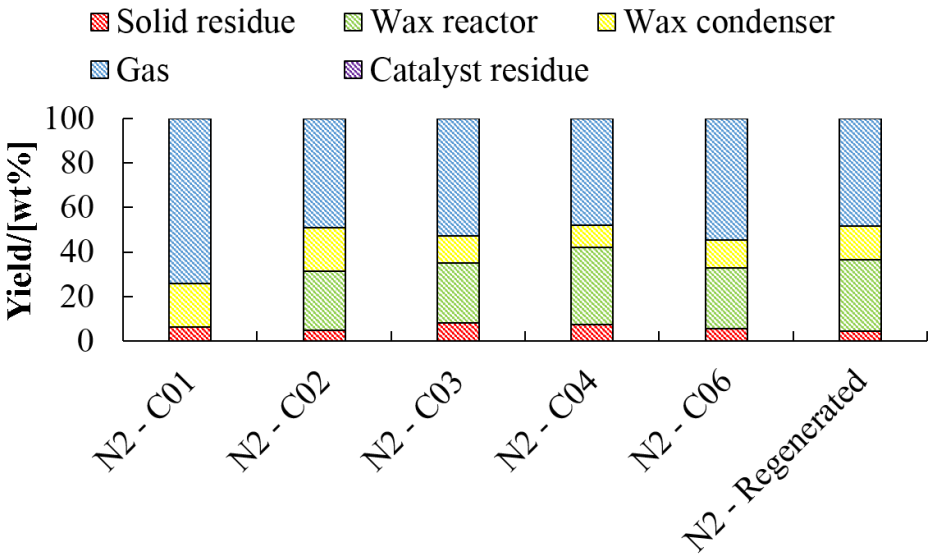

Figure 8.24 Gas (±0.84 wt%), wax in the reactor (±5.93 wt%), wax in the condenser (±0.1.41 wt%), solid residue (±0.0.61 wt%) and catalyst residue (±0.53 wt%) yield obtained with cold plasma regenerated zeolite HY in a two-stage catalytic pyrolysis at 500/500 °C (pyrolysis/catalyst bed temperature) (C0X=cycle number)

The spent catalyst had much lower surface area (4.03 m^2/g) and pore volume (0.01 cm^3/g) than the fresh catalyst (666.82 m^2/g and 0.12 cm^3/g) as shown in Table 8.6. Table 8.6 also shows that after the six cycles at 500 °C, zeolite HY small pores (2.7-4.2 nm) disappeared. These findings confirm that the deactivation of the catalyst was caused by the blockage of pores via coking.

Regeneration of used zeolite HY via cold plasma treatment and CO_2 pyrolysis

The spent zeolite HY collected after six cycles of mixed plastic waste two-stage catalytic pyrolysis at 500/500 °C was treated under cold plasma (SED = 180 mL/min, 60 W supplied) in a CO_2 stream (20 mL/min) for 2 hours. A total of 4.60 wt% of the original carbon present in the spent zeolite HY sample was removed after the two-hour period, suggesting the use of cold plasma for catalyst regeneration. The regenerated zeolite HY from cold plasma was tested on a two-stage catalytic pyrolysis cycle using N_2 as carrier gas at 500/500 °C.
Figure 8.24 shows that the products yield obtained from the regenerated zeolite HY test followed the trend of the previous two-stage catalytic pyrolysis six cycles. Therefore, cold plasma was not able to remove enough carbon residue to reactivate zeolite HY catalyst.
The composition of the gas obtained from the regenerated catalyst (Figure 8.25a) resembled the trend of the previous six cycles at 500 °C, showing little effect of cold plasma reactivating the catalyst. However, the yield of C_{17+} hydrocarbons decreased from 5.40 wt% in the six cycle to 1.60 wt% in the regenerated catalyst cycle (Figure 8.25b) in favour of the C_{10}-C_{16} hydrocarbons yield (from 3.02 wt% in the six cycle to 5.80 wt% in the regenerated catalyst cycle). This suggests that cold plasma removed some of the superficial carbon recovering the catalyst activity at the surface. Longer treatment time or higher temperature would improve the removal of carbon via cold plasma.

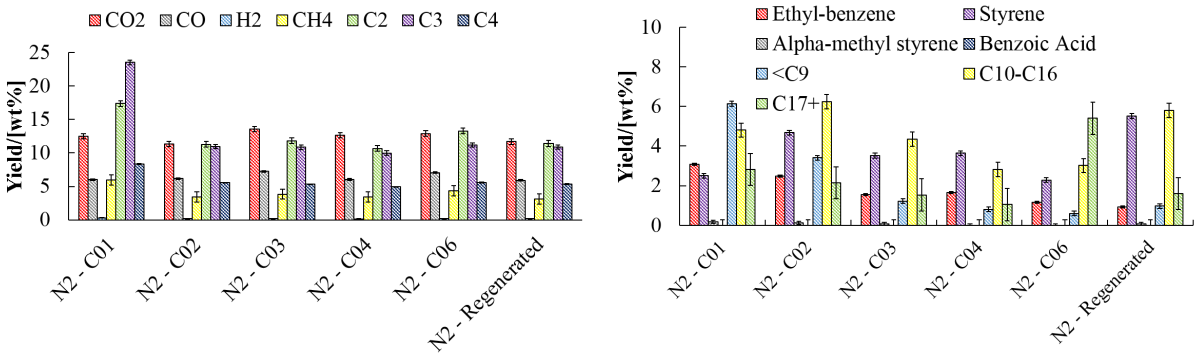

(a) Gas yield

(b) Wax yield

Figure 8.25 Gas and wax composition obtained with cold plasma regenerated zeolite HY in a two-stage catalytic pyrolysis at 500/500 °C (pyrolysis/catalyst bed temperature) (C0X=cycle number)

Zeolite HY, recovered from the extra two-stage catalytic pyrolysis cycle, was re-used in another two two-stage catalytic pyrolysis cycles at 500/600 °C in the first/second stage respectively with CO_2 as carrier gas.

Figure 8.26 shows that the gas yield obtained using the regenerated zeolite HY with CO_2 on the first (70.18 wt%) and second (75.00 wt%) cycle was as high as the one obtained in the first cycle with fresh zeolite HY (74.02 wt%) and higher than that of further cycles (47.78-54.49 wt%) and the control test at 500 °C (36.87 wt%). This difference was caused by the slightly higher temperature used in the catalyst bed (600 °C) and the oxidant atmosphere of CO_2. The wax in the reactor was reduced by 70-80 % in the two CO_2 regenerated zeolite HY cycles compared to the sixth previous cycle at 500 °C (27.47 wt%) in favour of the wax in the condenser (increased by 58 % from 12.48 wt%) and gas yield. The solid residue yield remained the same as previous zeolite HY experiments at around 5 wt%. However, the weight of carbon deposited on the catalyst surface was reduced by 6 % on the first CO_2 regeneration cycle and by 0.06 % on the second one.

According to Boudouard reaction (reaction 8.2), at temperatures above 600 °C, CO_2 can react with the carbon residue at the surface of zeolite HY catalyst to produce CO. However, Figure 8.27a show little variation in the yield of CO (from 5.9 wt% at the previous sixth cycle to 5.43 wt% and 6.66 wt% at the first and second cycles using regenerated zeolite HY and CO_2). A higher catalyst bed temperature (>600 °C) may favoured the Boudouard reaction to produce CO from CO_2 and zeolite HY carbon residue. These findings open up a potential new research path on a novel CO_2 utilisation alternative that, at the same time, provides a sustainable plastic waste management process.

Figure 8.27b shows the regenerated zeolite HY with CO_2 cycles increased the yield of $<C_9$ (2.50 wt% and 1.57 wt% in the first and second respectively) compared to the previous sixth cycle at 500 °C (0.60 wt%) at the expense of the yield of C_{17+} (reduced from 5.40 wt% on the sixth previous cycle to 2.29 wt% and 0.92 wt% on the first and second regenerated zeolite HY cycles with CO_2 respectively). Even though the regenerated zeolite HY recovered a small catalytic cracking effect, the slightly higher temperature of the catalyst bed (600 °C) also promoted the

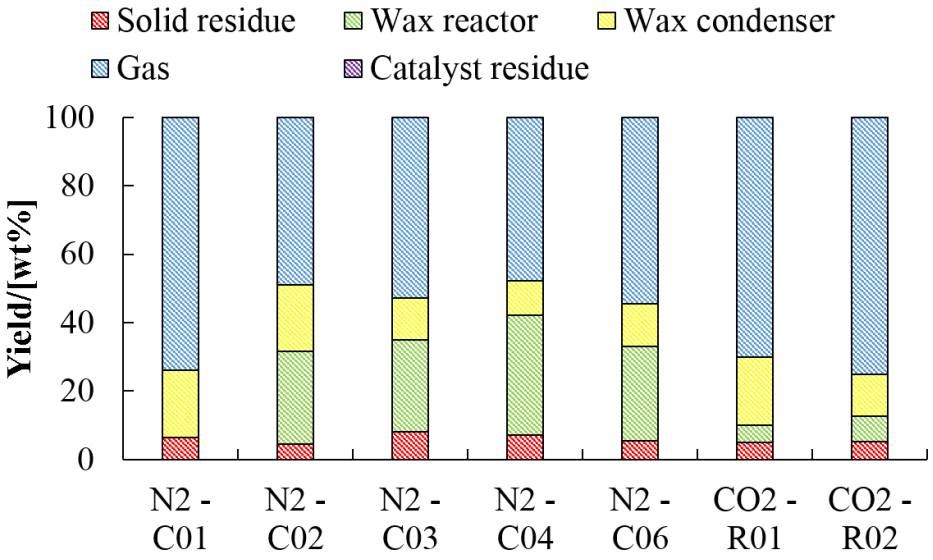

Figure 8.26 Gas (±0.84 wt%), wax in the reactor (±5.93 wt%), wax in the condenser (±0.1.41 wt%), solid residue (±0.0.61 wt%) and catalyst residue (±0.53 wt%) yield obtained with zeolite HY in a two-stage catalytic pyrolysis at 500/600 °C (pyrolysis/catalyst bed temperatures) with CO_2 as carrier gas (C0X=cycle number)

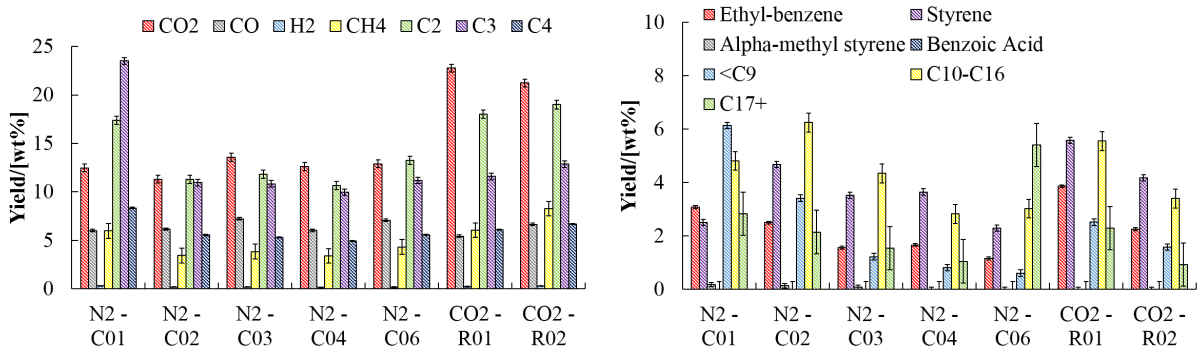

(a) Gas yield

(b) Wax yield

Figure 8.27 Gas and wax composition obtained with regenerated zeolite HY in two-stage catalytic pyrolysis at 500 °C and a 30-32 °C/min (first stage) and 500 °C (second stage)

cracking of heavy compounds. It appears that, even though promising, regeneration of spent zeolite HY catalyst via CO_2 pyrolysis would require high temperature to promote the formation of CO via Boudouard reaction (reaction 8.2).

8.3 Summary

The results in section 8.1 showed that 10 wt% biochar was able to remarkably increase the yield of CH_4 (up to 55 wt%) and H_2 (up to 3.2 wt%) and reduce the CO_2 and CO yields (to 3.3 wt% and 3.1 wt% respectively) via mixed plastic waste pyrolysis two-stage catalytic pyrolysis (600 °C) with biochar isothermally held at 800 °C. This suggested that, additionally to the recovery of the wax fraction for transportation fuels, biochar as a catalyst could expand the array of chemicals recovered from mixed plastic waste pyrolysis. The major effect of biochar on the wax product was the reduction of styrene (to 0.9 wt%) and $>C_{17+}$ (to 1.1 wt%) and the complete removal of benzoic acid and wax deposited inside the reactor. Therefore, biochar presented great potential as a cracking catalyst for mixed plastic waste pyrolysis. Even though high temperature was required for biochar activation (>700 °C), increasing operational costs, biochar is a by-product from waste biomass pyrolysis and therefore much cheaper than other catalysts, such as zeolites or alumina, providing an economical advantage.
The second section of this chapter showed that biochar was able to maintain catalytic performance over five consecutive two-stage catalytic pyrolysis cycles while SZ and zeolite HY showed deactivation with cycles due to coking. Cold plasma and CO_2 pyrolysis were assessed to remove the coke deposits from the surface of zeolite HY catalyst and recover the catalyst activity. The two technologies proved suitable for the removal of carbon: 1) 4.60 wt% with cold plasma after two hours and SED = 180 J/mL or 60 W and 2) 5.67 wt% on the first and an additional 0.06 wt% on the second CO_2 catalytic pyrolysis cycle with regenerated zeolite HY. These findings open up a new path for both plastic waste management and CO_2 utilisation.

Chapter 9 Outlook of technical, economic and environmental aspects of plastic waste pyrolysis

Pyrolysis is a mature and well-known technology developed during the II World War which has been extensively researched since then. Pyrolysis is an endothermic process and thus, requires heat supply (temperatures above 450 °C). That, along with the simplicity and low costs of mechanical recycling and landfill disposal, hindered pyrolysis development after its first appearance. However, due to their convenience, plastic products usage has dramatically increased over the past few decades and so has the amount of plastic waste generated (from about 8.3 billion tonnes of plastic waste generated in the 68 years since early 1950s up to over 25 billion tonnes predicted for 2050 (Jambeck, J., 2018)). Currently, there is a very growing public and governmental concern about plastic waste management. It has been reported on literature, the news etc. how plastic waste escape their management ending up into the environment, specially water bodies, causing great harm to wildlife and, potentially, humans. Therefore, several Governments are now introducing policies and bans on certain plastic products such as plastic bags, straws, food packaging, etc. Hence, research on plastic waste management is currently an up-to-date research topic worth pursuing.

9.1 Action plan for plastic waste management

The EU has identified plastic waste as a key priority in the 2015 Circular Economy Plan which aims to utilise resources more sustainably (European Economic and Social Committee, 2018). This lead to the publication of the 'European Strategy for Plastics in a Circular Economy' (European Commission, 2018) in early 2018 which sets out the guidelines for the design, production, use and recycling of plastic waste in all Member States. This documents is focused on transitioning plastic products from the current linear system (production $\rightarrow$ consumption $\rightarrow$ disposal) into a circular system (Figure 9.1) where the value of resources and products is perpetuated in time. This type of strategy requires an increase in the European recycling capacity and the development of new plastic waste management technologies amongst other approaches, such as new products design.

The UK has adopted the EU approach and this has been reflected in the 'Plastic Pollution Bill' draft which, at the time this thesis was written (April 2019), has already passed the first reading in the House of Commons. The aim of this Bill is again a transition into a circular strategy whit targets for plastic waste reduction; the development of a strategy and annual reports on plastic

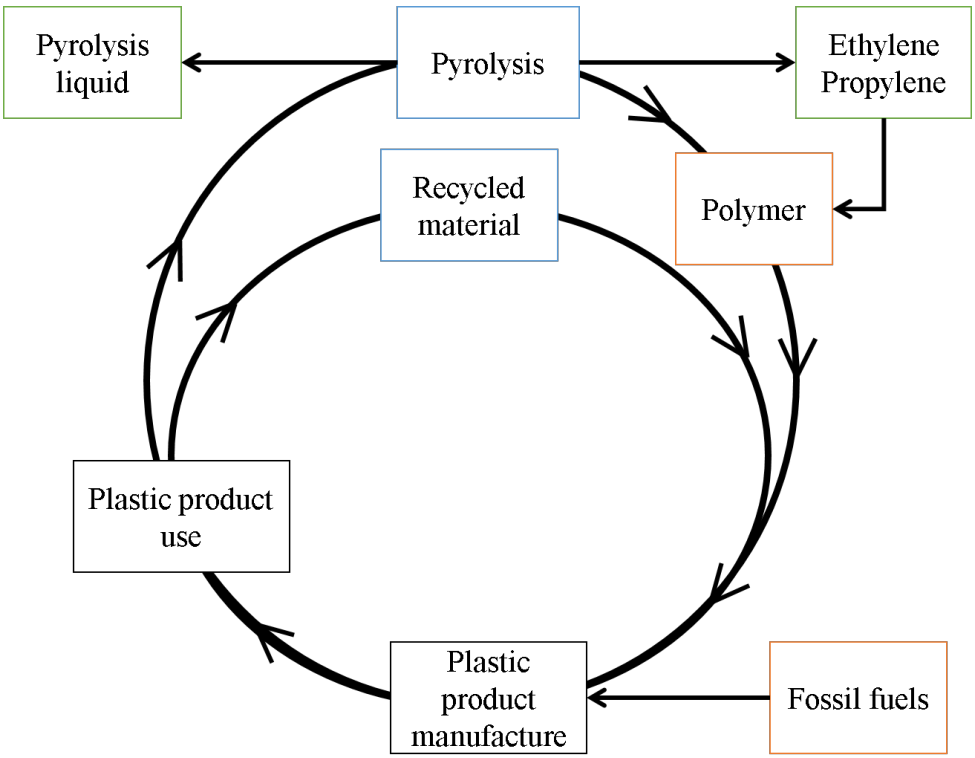

Figure 9.1 Schematic representation of an example of how plastic waste pyrolysis fits into a circular economy

waste pollution; and the creation of an advisory committee on plastic waste pollution (Parliament.co.uk, 2019). This means that the UK has started a great effort to lead the world to introduce legislation that tackles plastic waste pollution. Despite this great effort to minimise or replace plastic products, there is still a gap in regard to the management of all plastic waste generated from the use of essential plastic products (e.g. hospital and research plastic materials or socially and environmentally valuable plastic product harder to replace with other materials). Pyrolysis of plastic waste could very well be one the technologies use to fill this gap. The current action plan for the EU and the UK does not mention any specifics in regard to the management of plastic waste. This opens up a new line of research in relation to potential policies and how all the available plastic waste technologies (e.g. waste-to-energy, landfill, recycling, gasification, pyrolysis etc.) could fit into a circular strategy.

Despite all the awareness and efforts to reduce plastics consumption, there is another issue that is not so broadly tackled. The action plans mentioned above set out targets in relation to the manufacture of plastic products so all are produced only from recyclable materials. This aims to promote the recycling of the plastic waste that could not be avoided. However, a large number of the EU Member States lack from domestic recycling capacity. Currently, about a third of plastic wastes collected to be recycled are shipped to other countries. The strategy aforementioned will put even more strain in the domestic recycling capacity creating a need to introduce alternative management methods.

Up until China introduced a ban on imported plastic waste in early 2018, it was the main importer; however, Malaysia has taken now that position. The biggest issue with exported plastic

waste for recycling is the complete lack of knowledge on the recycling method, often carried out in small family business lacking from pollution controls, and thereby the real environmental impact of plastic waste recycling. In addition, a vast majority of daily consumed plastic products e.g. yoghurt and margarine pots, films, black food containers, etc. are manufactured from a mixture of several plastic types and thus, cannot be recycled neither domestically not abroad and are disposed in landfills/incinerated.
The reality of plastic waste management is that, more often than not, plastic waste are disposed in landfills or, even worst, in the environment. As an example, it has been estimated that by 2050 for every tonne of fish in the oceans there will be at least 0.3 tonnes of plastic waste. Aside from environmental issues, there are also economic ones with the current plastic waste management scenario. Although considered a residue, plastic waste are still a very rich material and disposing them in landfills or incinerating them to only recover energy is a big waste of high-value resources contravening the aim of a circular strategy. Therefore, there is a need to develop and introduce alternative and sustainable mixed plastic waste management technologies to tackle the aforesaid issues.

9.2 Plastic waste pyrolysis in a circular economy strategy

Interest on plastic waste pyrolysis to produce fuel-like compounds and other high-value products has awaken again in recent years. The main focus of plastic waste pyrolysis research and operational plants still remains the production of fuel-like products for transportation. However, this traditional approach to plastic waste pyrolysis of focusing only on the liquid as the main product has hindered its implementation in the past. This is because the fuel-like product recovered:

i. is not standardised and therefore cannot be registered under REACH (Registration, Evaluation, Authorisation & restriction of Chemicals) blocking its market outside the country where it was produced;

ii. lacks from regulatory and fiscal incentives (Renewable Transport Fuels Obligation (RTFO), Feed-in Tariff (FiT) or Renewable Heat Incentive (RHI)) as opposed to fuels from thermal treatment of biogenic material (e.g. biomass);

iii. has a composition highly dependant on the ever changing distribution of plastic waste types in the feedstock;

iv. often cannot be fed to engines in isolation;

v. emits even more contaminants than diesel when fed to engines; and

vi. depending on composition can be more expensive than fossil fuels.

Following modern trends on plastic waste pyrolysis, this thesis has showed that plastic waste pyrolysis yields a myriad of high-value products (e.g. ethylene, hydrogen, CNTs and benzoic

acid) in addition to a fuel-like product. This offers the opportunity to utilise plastic waste pyrolysis in a circular economy where the negative impacts of plastic are minimised while their positive impacts are maximised. This means that plastic waste pyrolysis could be considered into the EU or the UK future action plan for plastic waste management.

Ethylene and propylene are the monomers used to manufacture HDPE, LDPE and PP which account for about two thirds of the total plastic products consumed in most countries. These products are often manufactured from naphtha, natural gas or coal at the moment and they have a high market value (estimated up to $248 billion in 2021 for ethylene (Business Wire, 2018) and over $99 billion in 2022 for propylene (Markets and Markets, 2018)). The addition of cold plasma to plastic waste pyrolysis increased the amount of both ethylene and propylene recovered from waste HDPE (Chapter 5) and waste PP (Chapter 6) respectively. Sulphated zirconia combined with cold plasma showed a synergistic effect to recover ethylene from waste HDPE at low temperature (500 °C), which was not achievable with thermal or catalytic-only pyrolysis (Chapter 5).

This novel finding contributes to the idea of implementing plastic waste pyrolysis, assisted by cold plasma, into a circular economy strategy, fitting into the future action plan of the EU and the UK for plastics. Plastic waste pyrolysis assisted by cold plasma can be incorporated along with other measures, e.g. production of plastic products only made of recyclable materials; increase the demand of recycled plastic to manufacture new products, in particular packaging; or introduction of regulatory measures to support a plastic waste circular economy. Incorporating plastic waste pyrolysis into a circular economy strategy is particularly relevant for wastes made from a mixture of polymers (e.g. yoghurt pots are often manufactured from PP, HDPE and PS), or for non-recyclable but widely used products (e.g. plastic films in food packaging). The replacement of the aforementioned products is not foreseen in the middle to long term future. This means that other plastic waste management technologies, such as plastic waste pyrolysis, need to be considered, fully researched and introduced into the plastic circular economy.

One example of how plastic waste pyrolysis could be utilise to recover value from plastic waste is the meat industry. The meat industry generates large amounts of plastic films (over 30000 tonnes of packaging (Polymer Solutions Incorporated, 2013)) when the larger cuts of meat are cut into retail cuts. These films often comprised of a mixture of plastic and are contaminated with biological residue which limits their management through mechanical recycling. Pyrolysis is a process that often accepts contaminated and mixed-composition feedstock solving these issues. Therefore cold plasma assisted pyrolysis of these types of plastic packaging wastes could be a very promising alternative to recover the monomer which could be utilise to manufacture new plastic products (i.e. circular economy approach). There is further scope to research potential similar applications and to investigate how this new technology compares with current waste management methods e.g. through life cycle analysis studies.

9.3 Scale-up of cold plasma assisted pyrolysis of plastic waste

One of the uncertainties when investigating how novel processes would be integrated into industry is their scalability. As mentioned before in this thesis, pyrolysis is a mature process which has been extensively studied and scaled-up. Opposite, cold plasma is a very novel process which carries more uncertainties. Despite its novelty, DBD systems (cold plasma) have already being scaled-up for nanoparticles synthesis (Cole et al., 2017). The simplicity of the system allows its scale-up by increasing the total gas volume that passes through the reactor but maintaining the gap constant. For example, the experimental DBD (cold plasma) reactor used in Chapter 5 and Chapter 6 comprised of two co-axial tubes with a 12cm length and a 1.5mm gap. This reactor could be easily scaled-up, for instance, by increasing the length of the reactor but keeping the 1.5mm gap; by creating several 12cm long parallel DBD reactors with a 1.5mm gap; or simply, by increasing the outer and inner electrode diameter while keeping a 1.5mm gap. Dimensionless parameters are often used in several engineering fields e.g. heat transfer, mass transfer etc to scale-up processes. Following this route, Lim et al. (2017) have developed a dimensionless parameter (δ, energy ratio) based on the geometrical features of DBD reactors so they can be scaled-up. They showed that the energy ratio (Equation 9.1) categorised DBD reactors into three separate groups according to their efficiency.

$$\delta = \frac{P_d/f}{0.5 C_{eg} V_{in}^2} \tag{9.1}$$

$$C_{eg} = \frac{2\pi L 8.854 \dot{1}0^{-12}}{ln(r_i/r_o} \tag{9.2}$$

where P_d is the DBD reactor discharge power (W), f the frequency (Hz), V_{in} the input voltage (V), C_{eg} the estimated gap distance (Equation 9.2), L the length of the DBD reactor, r_i the inner radii of the outer co-axial tube and r_o the outer radii of the inner co-axial tube.
This parameter can be used to investigate how the dimensions of the DBD reactor could affect its efficiency when attached to a plastic waste pyrolysis reactor. This finding opens up a new research path extending the work done in this thesis.
Due to their simplicity, atmospheric cold plasma systems could be implemented into plastic waste pyrolysis plants. The simple design suggests low capital costs for cold plasma system (Niemira, 2012). Unfortunately, no specific economic details are available therefore it is difficult to really assess the profitability improvement and further work on this regard is much needed. Nevertheless, this thesis showed that the energy consumption of cold plasma (72-108 kJ for 90-180 J/mL) was only a fraction of the energy requirements of pyrolysis (684 kJ) but the value of the products increased considerably (e.g. about 20wt% of ethylene recovered from waste HDPE which has a very high market value). Therefore, the capital and operational costs could easily be overcome by the high value of the products yielded.
Unlike DBD reactors, the scale-up of plastic waste pyrolysis is more complex. The low thermal conductivity of plastic waste restricts scalability of pyrolysis reactors to maintain uniform

heating limiting their maximum capacity to 1 tonne/h (around 8000 tonnes/year). The minimum capacity to cover capital and operational costs (capital costs for 27000 tonnes/year are £20-30 million for an average fuel yield of 50-70 wt%) by exploiting the liquid/wax as fuel is 12-16 ktonnes/year. Hence, parallel operation is mandatory. This could be avoided by recovering other products from the gas. Aside ethylene and propylene, this thesis also showed an increase in the amount of hydrogen recovered and the production of good quality CNTs from the synergistic effect of cold plasma and Ni/Al_2O_3 catalyst in waste PP pyrolysis. Both products have high market value ($155 billion in 2022 (IEA Hydrogen, 2017) for H_2 and $8 billion in 2014 (Global Market Insight Inc., 2018) for CNTs) that could decrease the minimum capacity to cover costs minimising the number of parallel reactors.

9.4 Operational plastic waste pyrolysis plants

Despite all the constraints aforementioned the future of plastic waste pyrolysis is not completely dark. This technology has already been used in operational plants all over the world such as:

- Sapporo Plastics Recycling, Mitsui & Co. Ltd. (Hokkaido, Japan) established since 2000: 50 tonnes/day of mixed PE, PP and PS with up to 20 wt% of PET and PVC and up to 40-50 wt% of other municipal solid waste to recover light oil (virgin plastic manufacture), medium fuel oil (diesel-like) and heavy fuel oil (electricity).
- Newalta plant (Greater Vancouver, Canada) currently under development: pyrolysis of up to 5000 tonnes per year of non-recyclable plastic (layer films or laminates, contaminated plastics, industrial waste and residual plastic waste from recycling) to recover up to 5 million L/year of high-grade diesel.
- New Klean Industries and Greenfuels plant (East Germany): 35000 tonnes per year of mixed plastic waste to produce 33 million L/year of diesel-like fuel.
- New plant to be constructed in Perth (Scotland) by Recycling Technologies and Zero Waste Scotland using patented fluidised bed technology, called RT7000. Designed to process up to 7000 tonnes of mixed plastic per year to produce about 5000 tonnes/year of oil (Plaxx, sold at £300/tonne) that can be used to manufacture plastics or as a shipping fuel. There are also plans to implement another 17 new plants across Scotland in the future.
- Other operational plants but with no further details available include: Agilyx, Cynar & Envion, Global Climax Energy & Natural State Research and Plastic2Oil in USA; two Cynar plant in Spain; another Cynar plant in Ireland; Alphakat in Germany; Ventana Cleantech in India and Niutech Energy Limited in China.

Although catalytic pyrolysis of plastic waste is extensively researched all of the operational plants above are reported as thermal pyrolysis plants. This thesis showed that waste PET

catalytic pyrolysis using sulphated zirconia could produced about 408 ktonnes/year of benzoic acid, assuming all waste PET were managed by catalytic pyrolysis. This could suggest a recovery value of almost $1.8 million per year which is comparable to the £1.5 million estimated from Plaxx in the new Perth plant mentioned above. Considering most plastic waste pyrolysis plants only accept a limited amount of PET due to the increase in the liquid/wax acidity, it appears to be reasonable the development of distributed plants tuned for the feedstock composition at the plastic waste origin. In addition, the implementation of cold plasma at the outlet of the pyrolysis reactor could very much improve the profitability of plastic waste pyrolysis plants by increasing the value of all the products recovered.

Conclusively, despite current constraints, plastic waste pyrolysis is a mature and suitable alternative to tackle the growing and worrying plastic waste issue. However, it is very important to keep the focus not only on the environmental benefits of pyrolysis but also on the profitability of the process if this technology is to be successful. Further research on the novel technologies presented in this thesis is recommended from a life cycle assessment perspective.

Chapter 10 Conclusions and recommendations for future work

10.1 General conclusions

The popularity of plastic products has dramatically increase the global generation of plastic waste transforming them into a key global environmental issue. The large amount of plastic products consumed, the transfer of plastic waste into the environment and their harmful effect on wild and human life, and the lack of their recycling capacity has triggered plastic products bans and research of alternative management technologies like pyrolysis. The vast majority of plastic waste pyrolysis research and plants focus on maximising the liquid/wax/oil fraction to substitute fossil fuels; however, low pyrolysis capacity and fuel value hinder the industrial implementation of pyrolysis plants. Despite technology constraints, there is a rising number of plastic waste pyrolysis plants operating all over the world proving the suitability of the technology. However, it is imperative to shift the attention into the recovery of other high-value products (e.g. hydrogen, CNTs, ethylene, propylene, etc.) from plastic waste pyrolysis to improve the profitability of the process and fully exploit the high value of plastic waste.
This thesis shows the promising use of cold plasma to assist plastic waste pyrolysis for ethylene, hydrogen and CNTs production for the first time. It explores the use of SZ as a cracking catalyst for plastic waste pyrolysis. Although SZ presented thermal instabilities, it proved a catalytic activity almost comparable to the more expensive zeolite catalysts opening up further research on reusability, thermal decomposition and synergy with cold plasma. Finally, biomass char form waste biomass pyrolysis was positively used as a cracking catalyst for mixed plastic waste pyrolysis opening up new research paths on the topic.

10.2 Conclusions from chapters 4 to 8

- The kinetic model developed found that plastic waste pyrolysis (thermal decomposition) entails a complex reaction mechanism involving at least three different parallel stages. Linear model fitting (via optimisation of the order of reaction and the nucleation factor), combined with isoconversional methods, was found to be a more suitable method to obtain plastic waste thermal decomposition kinetic model than master plots. The kinetic model results showed that only LDPE and PS order of reaction (HDPE = 1.70, LDPE = 0.95, PP = 0.75, PET = 2.80, PS = 0.90) could be considered as first order reaction, as often assumed in literature. KAS and Friedman isoconversional methods provided values

of Ea and A of HDPE = 375.59 kJ/mol and $3.23 \cdot 10^{16}$ s^{-1}, LDPE = 267.61 kJ/mol and $7.86 \cdot 10^{19}$ s^{-1}, PP = 261.22 kJ/mol and $3.03 \cdot 10^{21}$ s^{-1}, PS = 192.61 kJ/mol and $5.52 \cdot 10^{14}$ s^{-1} and PET = 197.61 kJ/mol and $4.84 \cdot 10^{14}$ s^{-1}. The kinetic model allowed prediction of the rate of reaction for individual and plastic waste mixtures which is essential to set plastic waste pyrolysis operation conditions and to design pyrolysis reactors.

- Cold plasma assisted pyrolysis with and without a catalyst proved a suitable technology for waste HDPE (ethylene recovery) and waste PP (hydrogen and CNTs) pyrolysis. Cold plasma increased the ethylene recovered from waste HDPE pyrolysis by a 55 times fold (24 wt%) compared to thermal pyrolysis at equivalent pyrolysis conditions. It was found that the cold plasma altered the structure of the CNTs found from waste PP catalytic pyrolysis (parallel CNTs instead of fishbone CNTs found with catalyst alone), affecting CNTs surface reactivity and applications.

- A synergistic effect between cold plasma and acid catalysts (SZ and Ni/Al_2O_3 for waste HDPE and waste PP respectively) was observed in terms of: (i) equivalent ethylene yield (13 wt%) at lower temperatures (500 °C) than catalytic-only waste HDPE pyrolysis (600 °C); and (ii) higher H_2 flow rate in the gas (461.50 mL/s) compared to the individual conditions (227.97 mL/s for catalytic only and 137.16 mL/s for cold plasma only) using waste PP. This three products present a high market value (ethylene = $248 billion in 2021 (Business Wire, 2018), hydrogen = $155 billion in 2022 (IEA Hydrogen, 2017) and CNTs = $8 billion in 2014 (Global Market Insight Inc., 2018)) which could improve the profitability of conventional plastic waste pyrolysis processes.

- It was found that both, SZ catalyst:plastic mass ratio and temperature played important roles to maximise benzoic acid yield. Thermal pyrolysis at 600 °C increased the yield of benzoic acid by 16 % compared to the other conditions tested while 10 wt% SZ catalyst increased the total amount of methane and light hydrocarbons (C_2–C_4) to 20 wt% compared to thermal pyrolysis (4 wt%) at the same temperature. SZ catalyst deactivated due to coking as well as partially decomposed at high pyrolysis temperatures, therefore, PET catalytic pyrolysis using SZ should be carried out at temperatures below 525 °C and catalyst loads below 10 wt% to obtain high yields of benzoic acid and high value of gas products i.e. high proportion of hydrocarbons. Based on an average 24 wt% benzoic acid yield, potentially about 408 ktonnes of benzoic acid could be recovered (estimated value of $1.8 million/year) avoiding the disposal of over 600 ktonnes of waste PET in landfills.

- Biochar, derived from waste biomass pyrolysis, proved to be a suitable cracking catalyst when activated at temperatures above 800 °C via two-stage catalytic pyrolysis of mixed plastic waste. About 10 wt% biochar remarkably increased methane (up to 55 wt%) and hydrogen (up to 3.2 wt%) yield and lowered CO_2 and CO yield to 3.3 wt% and 3.1 wt% respectively alongside styrene and $>C_{17}$ hydrocarbons yield from 11.9 wt% to 0.9 wt% and from 10.0 wt% to 1.1 wt% respectively. Reusability tests showed that biochar could be used for two-stage mixed plastic waste catalytic pyrolysis over five consecutive cycles

while SZ and zeolite HY deactivated due to coking. These results showed that an inexpensive waste material can be used as a cracking catalyst, rather than the more expensive traditional alternatives, for plastic waste pyrolysis, reducing operational costs.

- Two novel regeneration alternatives i.e. cold plasma and CO_2 pyrolysis, were assessed to remove the coke from zeolite HY surface and recover its catalyst activity. The two technologies were partially successful showing carbon removal of: 1) 4.60 wt% with cold plasma after two hours and SED = 180 J/mL or 60 W and 2) 5.67 wt% in the first CO_2 catalytic pyrolysis cycle and an additional 0.06 wt% on the second one. The two regeneration techniques opened up new research paths for both plastic waste management and CO_2 utilisation.

10.3 Recommendations for future work

- Despite the potential shown by cold plasma, further work is needed to fully assess its suitability combined with plastic waste pyrolysis for hydrogen and high-value carbon products production. In particular, studies on scalability of cold plasma applied to plastic waste pyrolysis are necessary to fully assess the potential industrial implementation of cold plasma.

- SZ catalyst for cold plasma assisted pyrolysis of waste HDPE showed promising results; however, catalyst characterisation after every pyrolysis cycles and not only at the end of the five cycles as in this work would be advantageous to truly comprehend how cold plasma affects its morphology. In addition, there is still room for research regarding SZ thermal behaviour and deactivation mechanisms if SZ is to be implemented in plastic waste catalytic pyrolysis.

- Biochar, derived from waste biomass pyrolysis, turned out as an cheap alternative to traditional cracking catalysts. Nevertheless, further research testing biochar performance after chemical or thermal activation on plastic waste pyrolysis would provide a more complete picture before it can be considered for industrial use.

- A new research path combining CO_2 utilisation and plastic waste management opened up after zeolite HY regeneration via CO_2 pyrolysis. Although showing favourable results, further investigation at different temperatures, CO_2 flow rates, feedstock composition, etc. would be beneficial.

References

Aboul-Enein, A., Awadallah, A., Abdel-Rahman, A. and Haggar, A. (2018), 'Synthesis of multi-walled carbon nanotubes via pyrolysis of plastic waste using a two-stage process', *Fullerenes, Nanotubes and Carbon Nanostructures* **26**(7), 443–450.

Abu El-Rub, Z., Bramer, E. and Brem, G. (2004), 'Review of catalysts for tar elimination in biomass gasification processes', *Industrial & engineering chemistry research* **43**(22), 6911–6919.

Achilias, D., Roupakias, C., Megalokonomos, P., Lappas, A. and Antonakou, E. (2007), 'Chemical recycling of plastic wastes made from polyethylene (LDPE and HDPE) and polypropylene (PP)', *Journal of Hazardous Materials* **149**(3), 536–542.

Acomb, J., Wu, C. and Williams, P. (2014), 'Control of steam input to the pyrolysis-gasification of waste plastics for improved production of hydrogen or carbon nanotubes', *Applied Catalysis B: Environmental* **147**, 571–584.

Acomb, J., Wu, C. and Williams, P. (2016), 'The use of different metal catalysts for the simultaneous production of carbon nanotubes and hydrogen from pyrolysis of plastic feedstocks', *Applied Catalysis B: Environmental* **180**, 497–510.

Adrados, A., De Marco, I., Caballero, B., López, A., Laresgoiti, M. and Torres, A. (2012), 'Pyrolysis of plastic packaging waste: A comparison of plastic residuals from material recovery facilities with simulated plastic waste', *Waste Management* **32**(5), 826–832.

Aguado, J. and Serrano, D. (1999), *Feedstock recycling of plastic wastes*, Royal Society of Chemistry, Cambridge, UK.

Aguado, J., Serrano, D. and Escola, J. (2006), Catalytic upgrading of plastic wastes, *in* 'in Feedstock recycling and pyrolysis of waste plastics', John Wiley & Sons, Oxford, chapter 3, pp. 73–110.

Aguado, J., Serrano, D., Escola, J. and Peral, A. (2009), 'Catalytic cracking of polyethylene over zeolite mordenite with enhanced textural properties', *Journal of Analytical and Applied Pyrolysis* **85**(1), 352–358.

Aguado, J., Serrano, D., San Miguel, G., Rodríguez, J. et al. (2007), 'Catalytic activity of zeolitic and mesostructured catalysts in the cracking of pure and waste polyolefins', *Journal of analytical and applied pyrolysis* **78**(1), 153–161.

Aguado, R., Elordi, G., Arrizabalaga, A., Artetxe, M., Bilbao, J. and Olazar, M. (2014*a*), 'Principal component analysis for kinetic scheme proposal in the thermal pyrolysis of waste HDPE plastics', *Chemical Engineering Journal* **254**, 357–364.

Aguado, R., Elordi, G., Arrizabalaga, A., Artetxe, M., Bilbao, J. and Olazar, M. (2014*b*), 'Principal component analysis for kinetic scheme proposal in the thermal pyrolysis of waste HDPE plastics', *Chemical Engineering Journal* **254**, 357–364.

Aguado, R., Olazar, M., Gaisan, B., Prieto, R. and Bilbao, J. (2003), 'Kinetics of polystyrene pyrolysis in a conical spouted bed reactor', *Chemical Engineering Journal* **92**(1-3), 91–99.

Ahmed, S., Aitani, A., Rahman, F., Al-Dawood, A. and Al-Muhaish, F. (2009), 'Decomposition of hydrocarbons to hydrogen and carbon', *Applied Catalysis A: General* **359**(1), 1–24.

Akubo, K., Nahil, M. and Williams, P. (2017), 'Aromatic fuel oils produced from the pyrolysis-catalysis of polyethylene plastic with metal-impregnated zeolite catalysts', *Journal of the Energy Institute* .

Al-Salem, S., Evangelisti, S. and Lettieri, P. (2014), 'Life cycle assessment of alternative technologies for municipal solid waste and plastic solid waste management in the Greater London area', *Chemical Engineering Journal* **244**, 391–402.

Al-Salem, S., Lettieri, P. and Baeyens, J. (2009), 'Recycling and recovery routes of plastic solid waste (PSW): A review', *Waste management* **29**(10), 2625–2643.

Al-Salem, S., Lettieri, P. and Baeyens, J. (2010), 'The valorization of plastic solid waste (PSW) by primary to quaternary routes: from re-use to energy and chemicals', *Progress in Energy and Combustion Science* **36**(1), 103–129.

Albano, C. and de Freitas, E. (1998), 'Thermogravimetric evaluation of the kinetics of decomposition of polyolefin blends', *Polymer degradation and stability* **61**(2), 289–295.

Ali, S., Garforth, A., Harris, D., Rawlence, D. and Uemichi, Y. (2002), 'Polymer waste recycling over used catalysts', *Catalysis Today* **75**(1-4), 247–255.

Almeida, D. and Marques, M. (2016), 'Thermal and catalytic pyrolysis of plastic waste', *Polímeros* **26**(1), 44–51.

Almustapha, M., Farooq, M. and Andresen, J. (2017), 'Sulphated zirconia catalysed conversion of high density polyethylene to value-added products using a fixed-bed reactor', *Journal of Analytical and Applied Pyrolysis* **125**, 296–303.

Almutairi, S. (2013), The role of Lewis and Brønsted acidity for alkane activation over zeolites, PhD thesis, Technische Universiteit Eindhoven, Eindhoven, The Netherlands.

Alvarez, J., Kumagai, S., Wu, C., Yoshioka, T., Bilbao, J., Olazar, M. and Williams, P. (2014), 'Hydrogen production from biomass and plastic mixtures by pyrolysis-gasification', *International Journal of Hydrogen Energy* **39**(21), 10883–10891.

Ángel-Soto, J., Martínez-Rosales, M., Ángel-Soto, P. and Zamorategui-Molina, A. (2017), 'Synthesis, characterization and catalytic application of Ni catalysts supported on alumina–zirconia mixed oxides', *Bulletin of Materials Science* **40**(7), 1309–1318.

Angyal, A., Miskolczi, N. and Bartha, L. (2007), 'Petrochemical feedstock by thermal cracking of plastic waste', *Journal of Analytical and Applied Pyrolysis* **79**, 409–414.

Antony, J. (2003), *Design of experiments for engineers and scientists*, Butterworth-Heinemann, Oxford.

Arata, K. and Hino, M. (1990), 'Solid catalyst treated with anion: XVIII. Benzoylation of toluene with benzoyl chloride and benzoic anhydride catalysed by solid superacid of sulfate-supported alumina', *Applied Catalysis* **59**(1), 197–204.

Artetxe, M., López, G., Amutio, M., Barbarias, I., Arregi, A., Aguado, R., Bilbao, J. and Olazar, M. (2015), 'Styrene recovery from polystyrene by flash pyrolysis in a conical spouted bed reactor', *Waste Management* **45**, 126–133.

Artetxe, M., Lopez, G., Amutio, M., Elordi, G., Olazar, M. and Bilbao, J. (2010), 'Operating conditions for the pyrolysis of poly(ethylene terephthalate) in a conical spouted-bed reactor', *Industrial and Engineering Chemistry Research* **49**(5), 2064–2069.

Auxilio, A., Choo, W., Kohli, I., Srivatsa, S. and Bhattacharya, S. (2017), 'An experimental study on thermo-catalytic pyrolysis of plastic waste using a continuous pyrolyser', *Waste Management* **67**, 143–154.

Aziz, K., Miessner, H., Mueller, S., Kalass, D., Moeller, D., Khorshid, I. and Rashid, M. (2016), 'Degradation of pharmaceutical diclofenac and ibuprofen in aqueous solution, a direct comparison of ozonation, photocatalysis, and non-thermal plasma', *Chemical Engineering Journal* **313**, 1033–1041.

Babu, B. and Chaurasia, A. (2003), 'Modeling, simulation and estimation of optimum parameters in pyrolysis of biomass', *Energy Conversion and Management* **44**(13), 2135–2158.

Bagri, R. and Williams, P. (2002), 'Catalytic pyrolysis of polyethylene', *Journal of Analytical and Applied Pyrolysis* **63**(1), 29–41.

Bajad, G., Guguloth, V., Vijayakumar, R. and Bose, S. (2016), 'Conversion of plastic waste into cnts using ni/mo/mgo catalyst—an optimization approach by mixture experiment', *Fullerenes, Nanotubes and Carbon Nanostructures* **24**(2), 162–169.

Balat, M. (2008), 'Potential importance of hydrogen as a future solution to environmental and transportation problems', *International Journal of Hydrogen Energy* **33**(15), 4013–4029.

Barbarias, I., López, G., Alvarez, J., Artetxe, M., Arregi, A., Bilbao, J. and Olazar, M. (2016), 'A sequential process for hydrogen production based on continuous hdpe fast pyrolysis and in-line steam reforming', *Chemical Engineering Journal* **296**, 191–198.

Barbarias, I., Lopez, G., Artetxe, M., Arregi, A., Bilbao, J. and Olazar, M. (2018), 'Valorisation of different waste plastics by pyrolysis and in-line catalytic steam reforming for hydrogen production', *Energy Conversion and Management* **156**, 575–584.

Barnes, D., Galgani, F., Thompson, R. and Barlaz, M. (2009), 'Accumulation and fragmentation of plastic debris in global environments', *Philosophical Transactions of the Royal Society of London B: Biological Sciences* **364**(1526), 1985–1998.

Bartholomew, C. and Farrauto, R. (1976), 'Chemistry of nickel-alumina catalysts', *Journal of Catalysis* **45**(1), 41–53.

Bartolome, L., Cho, B., Do, H., Imran, M. and Al-Masry, W. (2012), *Recent Developments in the Chemical Recycling of PET*, INTECH Open Access Publisher.

Bazargan, A. and McKay, G. (2012), 'A review–synthesis of carbon nanotubes from plastic wastes', *Chemical Engineering Journal* **195**, 377–391.

Benbenek, S., Fedoryńska, E. and Winiarek, P. (1993), 'Investigation of the acidity of Ni/Al_2O_3 and Ni/SiO_2 - Al_2O_3 catalysts', *Reaction Kinetics and Catalysis Letters* **51**(1), 189–195.

Benedetti, M., Cafiero, L., De Angelis, D., Dell'Era, A., Pasquali, M., Stendardo, S., Tuffi, R. and Ciprioti, S. (2017), 'Pyrolysis of WEEE plastics using catalysts produced from fly ash of coal gasification', *Frontiers of Environmental Science & Engineering* **11**(5), 11.

Bernardo, M. (2011), Physico-chemical characterization of chars produced in the co-pyrolysis of wastes and possible routes of valorisation, PhD thesis, Faculdade de Ciências e Tecnologia, Universidade Nova de Lisboa, Lisboa, Portugal.

Beyler, C. and Hirschler, M. (2015), *Thermal decomposition of polymers*, SFPE, chapter 7, pp. 1–110.

Bhaskar, T., Kaneko, J., Muto, A., Sakata, Y., Jakab, E., Matsui, T. and Uddin, M. (2004), 'Pyrolysis studies of PP/PE/PS/PVC/HIPS-Br plastics mixed with PET and dehalogenation (Br, Cl) of the liquid products', *Journal of Analytical and Applied Pyrolysis* **72**(1), 27–33.

Bhaskar, T., Muto, A., Sakata, Y. and Uddin, M. (2005), Feedstock recycling of electric and electronic waste plastics: Fundamental investigation for feasibility studies, *in* 'REWAS'04 - Global Symposium on Recycling, Waste Treatment and Clean Technology', Madrid, pp. 1489–1498.

Bhaskar, T., Uddin, M., Murai, K., Kaneko, J., Hamano, K., Kusaba, T., Muto, A. and Sakata, Y. (2003), 'Comparison of thermal degradation products from real municipal waste plastic and model mixed plastics', *Journal of Analytical and Applied Pyrolysis* **70**(2), 579–587.

Binghui, L. (1998), Deactivation and regeneration of sulfated zirconia, PhD thesis, Tulane University, New Orleans, USA.

Bockhorn, H., Hornung, A. and Hornung, U. (1999), 'Mechanisms and kinetics of thermal decomposition of plastics from isothermal and dynamic measurements', *Journal of Analytical and Applied Pyrolysis* **50**(2), 77–101.

Bogaerts, A., Neyts, E., Gijbels, R. and Van der Mullen, J. (2002), 'Gas discharge plasmas and their applications', *Spectrochimica Acta Part B: Atomic Spectroscopy* **57**(4), 609–658.

Borsodi, N., Miskolczi, N., Angyal, A., Gerencser, A., Lazar, I. and Bartha, L. (2011), 'Environmental saving disposal of contaminated plastic wastes by their pyrolysis', *Chemical Engineering Transactions* **24**, 1183–1188.

Bridjesh, P., Periyasamy, P., Chaitanya, A. and Geetha, N. (2018), 'MEA and DEE as additives on diesel engine using waste plastic oil diesel blends', *Sustainable Environment Research* **28**(3), 142–147.

British Plastics Federation (BPF) (2019), 'Recycling My Plastic?'. Accessed: 06/05/2019. **URL:** *https://www.bpf.co.uk/recycling/where-can-i-recycle-my-plastic.aspx*

Bruckner, R. (2001), *Advanced organic chemistry: reaction mechanisms*, Academic Press, Orlando.

Bruggeman, P. and Leys, C. (2009), 'Non-thermal plasmas in and in contact with liquids', *Journal of Physics D: Applied Physics* **42**(5), 1–28.

Buekens, A. (2006), Introduction to feedstock recycling of plastics, *in* 'in Feedstock recycling and pyrolysis of waste plastics', John Wiley & Sons, Oxford, chapter 1, pp. 1–41.

Buekens, A. and Huang, H. (1998), 'Catalytic plastics cracking for recovery of gasoline-range hydrocarbons from municipal plastic wastes', *Resources, Conservation and Recycling* **23**(3), 163–181.

Bukkarapu, K., Gangadhar, D., Jyothi, Y. and Kanasani, P. (2018), 'Management, conversion, and utilization of waste plastic as a source of sustainable energy to run automotive: a review', *Energy Sources, Part A: Recovery, Utilization, and Environmental Effects* **40**(14), 1681–1692.

Burange, A., Gawande, M., Lam, F., Jayaram, R. and Luque, R. (2015), 'Heterogeneously catalyzed strategies for the deconstruction of high density polyethylene: plastic waste valorisation to fuels', *Green Chemistry* **17**(1), 146–156.

Business Wire (2018), 'Global Ethylene Market Worth USD 248 Billion by 2021 - Analysis, Technologies & Forecast Report 2016-2021 - Key Vendors: Akzo Nobel, China Energy & Royal Dutch Shell - Research and Markets'. Accessed: 18/09/2018. **URL:** *https://www.businesswire.com/news/home/20160218006473/en/Global-Ethylene-Market-Worth-USD-248-Billion*

Capitelli, M., Celiberto, R., Colonna, G., Esposito, F., Gorse, C., Hassouni, K., Laricchiuta, A. and Longo, S. (2015), *Fundamental aspects of plasma chemical physics: Kinetics*, Vol. 85, Springer Science & Business Media.

Capitelli, M., Colonna, G. and D'Angola, A. (2011), *Fundamental aspects of plasma chemical physics: thermodynamics*, Vol. 66, Springer Science & Business Media.

Cardona, S. and Corma, A. (2000), 'Tertiary recycling of polypropylene by catalytic cracking in a semibatch stirred reactor: use of spent equilibrium FCC commercial catalyst', *Applied Catalysis B: Environmental* **25**(2), 151–162.

Carta, D., Cao, G. and D'Angeli, C. (2003), 'Chemical recycling of poly(ethylene terephthalate)(PET) by hydrolysis and glycolysis', *Environmental Science and Pollution Research* **10**(6), 390–394.

Castaño, P., Elordi, G., Olazar, M., Aguayo, A., Pawelec, B. and Bilbao, J. (2011), 'Insights into the coke deposited on HZSM-5, Hβ and HY zeolites during the cracking of polyethylene', *Applied Catalysis B: Environmental* **104**(1-2), 91–100.

CDS Solutions (2017), 'Degradation Mechanism - Random Scission'. Accessed: 25/04/2017. **URL:** *http://www.analytix.co.uk/wp-content/uploads/2015/02/Degradation-mechanisms-random-scission.pdf*

Ceamanos, J., Mastral, J., Millera, A. and Aldea, M. (2002), 'Kinetics of pyrolysis of high density polyethylene. Comparison of isothermal and dynamic experiments', *Journal of Analytical and Applied Pyrolysis* **65**(2), 93–110.

Chaianansutcharit, S., Katsutath, R., Chaisuwan, A., Bhaskar, T., Nigo, A., Muto, A. and Sakata, Y. (2007), 'Catalytic degradation of polyolefins over hexagonal mesoporous silica: Effect of aluminum addition', *Journal of Analytical and Applied Pyrolysis* **80**(2), 360–368.

Chandrasekaran, S., Kunwar, B., Moser, B., Rajagopalan, N. and Sharma, B. (2015), 'Catalytic thermal cracking of postconsumer waste plastics to fuels. 1. Kinetics and optimization', *Energy & Fuels* **29**(9), 6068–6077.

Chase, M. (1996), 'NIST-JANAF thermochemical tables for oxygen fluorides', *Journal of physical and chemical reference data* **25**(2), 551–603.

Chen, D., Yin, L., Wang, H. and He, P. (2014), 'Pyrolysis technologies for municipal solid waste: A review', *Waste management* **38**, 68–94.

Chen, F., Coudurier, G., Joly, J. and Vedrine, J. (1993), 'Superacid and catalytic properties of sulfated zirconia', *Journal of catalysis* **143**(2), 616–626.

Chen, H., H.M., L., S.H., C., Y., C. and M.B., C. (2008), 'Review of plasma catalysis on hydrocarbon reforming for hydrogen production - interaction, integration, and prospects', *Applied Catalysis B: Environmental* **85**(1), 1–9.

Chhowalla, M., Teo, K., Ducati, C., Rupesinghe, N., Amaratunga, G., Ferrari, A., Roy, D., Robertson, J. and Milne, W. (2001), 'Growth process conditions of vertically aligned carbon nanotubes using plasma enhanced chemical vapor deposition', *Journal of Applied Physics* **90**(10), 5308–5317.

Choudhary, T. and Goodman, D. (2006), 'Methane decomposition: production of hydrogen and carbon filaments', *Catalysis* **19**, 164–183.

Choudhary, V. and Karkamkar, A. (2003), 'Temperature-programmed desorption of water and ammonia on sulphated zirconia catalysts for measuring their strong acidity and acidity distribution', *Journal of Chemical Sciences* **115**(4), 281–286.

Chung, W. and Chang, M. (2017), 'Simultaneous Generation of Syngas and Multiwalled Carbon Nanotube via CH_4/CO_2 Reforming with Spark Discharge', *ACS Sustainable Chemistry & Engineering* **5**(1), 206–212.

Ciesielski, P., Pecha, M., Bharadwaj, V., Mukarakate, C., Leong, G., Kappes, B., Crowley, M., Kim, S., Foust, T. and Nimlos, M. (2018), 'Advancing catalytic fast pyrolysis through integrated multiscale modeling and experimentation: Challenges, progress, and perspectives', *Wiley Interdisciplinary Reviews: Energy and Environment* **7**(4), e297.

Ciliz, N., Ekinci, E. and Snape, C. (2004), 'Pyrolysis of virgin and waste polypropylene and its mixtures with waste polyethylene and polystyrene', *Waste Management* **24**(2), 173–181.

Çit, I., Sınağ, A., Yumak, T., Uçar, S., Mısırlıoğlu, Z. and Canel, M. (2010), 'Comparative pyrolysis of polyolefins (PP and LDPE) and PET', *Polymer Bulletin* **64**(8), 817–834.

Cole, J., Zhang, Y., Liu, T., Liu, C. and Sankaran, R. (2017), 'Process scale-up considerations for non-thermal atmospheric-pressure plasma synthesis of nanoparticles by homogenous nucleation', *Journal of Physics D: Applied Physics* **50**(30), 304001.

Comelli, R., Vera, C. and Parera, J. (1995), 'Influence of ZrO_2 crystalline structure and sulfate ion concentration on the catalytic activity of SO_4^{2-}–ZrO_2', *Journal of Catalysis* **151**(1), 96–101.

Costa, P., Pinto, F., Ramos, A., Gulyurtlu, I., Cabrita, I. and Bernardo, M. (2007), 'Kinetic evaluation of the pyrolysis of polyethylene waste', *Energy and Fuels* **21**(5), 2489–2498.

Costa, P., Pinto, F., Ramos, A., Gulyurtlu, I., Cabrita, I. and Bernardo, M. (2010), 'Study of the pyrolysis kinetics of a mixture of polyethylene, polypropylene, and polystyrene', *Energy and Fuels* **24**(12), 6239–6247.

Coster, D., Blumenfeld, A. and Fripiat, J. (1994), 'Lewis acid sites and surface aluminum in aluminas and zeolites: a high-resolution nmr study', *The Journal of Physical Chemistry* **98**(24), 6201–6211.

Csukas, B., Varga, M., Miskolczi, N., Balogh, S., Angyal, A. and Bartha, L. (2013), 'Simplified dynamic simulation model of plastic waste pyrolysis in laboratory and pilot scale tubular reactor', *Fuel Processing Technology* **106**, 186–200.

Daramola, M., Aransiola, E. and Ojumu, T. (2012), 'Potential applications of zeolite membranes in reaction coupling separation processes', *Materials* **5**(11), 2101–2136.

Dave, P. and Joshi, A. (2010), 'Plasma pyrolysis and gasification of plastics waste - A review', *Journal of Scientific and Industrial Research* **69**(3), 177–179.

David Shukman, BBC News (2018), 'Indonesian study into health risks of microplastics'. Accessed: 15/08/2018.
URL: *https://www.bbc.co.uk/news/science-environment-43913597*

Davim, J. (2016), *Design of experiments in production engineering*, Springer, New York.

Davis, B., Keogh, R. and Srinivasan, R. (1994), 'Sulfated zirconia as a hydrocarbon conversion catalyst', *Catalysis Today* **20**(2), 219–256.

de Marco, I., Caballero, B., López, A., Laresgoiti, M., Torres, A. and Chomón, M. (2009), 'Pyrolysis of the rejects of a waste packaging separation and classification plant', *Journal of Analytical and Applied Pyrolysis* **85**(1), 384–391.

Dean, J. (1999), *Lange's handbook of chemistry*, McGraw-Hill, New York.

Deminsky, M., Jivotov, V., Potapkin, B. and Rusanov, V. (2002), 'Plasma-assisted production of hydrogen from hydrocarbons', *Pure and applied chemistry* **74**(3), 413–418.

Demirbas, A. (2004), 'Pyrolysis of municipal plastic wastes for recovery of gasoline–range hydrocarbons', *Journal of Analytical and Applied Pyrolysis* **72**(1), 97–102.

Department Energy and Climate Change (2015), 'DUKES: Calorific Values'. Accessed: 14/04/2015.
URL: *https://www.gov.uk/government/statistics/dukes-calorific-values*

Department for Environment Food & Rural Affairs (2011), Final Report to DEFRA: WR 1002 Detailed compositional assessment for municipal residual waste and recycling streams in England, Technical report, DEFRA.

Department for Environment Food & Rural Affairs (DEFRA) (2013), Waste management plan for England, Legal rule or regulation, DEFRA.

Diaz-Silvarrey, L., McMahon, A. and Phan, A. (2018), 'Benzoic acid recovery via waste poly(ethylene terephthalate)(PET) catalytic pyrolysis using sulphated zirconia catalyst', *Journal of Analytical and Applied Pyrolysis* **134**, 621–631.

Diaz-Silvarrey, L. and Phan, A. (2016), 'Kinetic study of municipal plastic waste', *International Journal of Hydrogen Energy* **41**(37), 16352–16364.

Diaz-Silvarrey, L., Zhang, K. and Phan, A. (2018), 'Monomer recovery through advanced pyrolysis of waste high density polyethylene (hdpe)', *Green Chemistry* **20**, 1813–1823.

Du, S., Valla, J., Parnas, R. and Bollas, G. (2016), 'Conversion of polyethylene terephthalate based waste carpet to benzene-rich oils through thermal, catalytic, and catalytic steam pyrolysis', *ACS Sustainable Chemistry & Engineering* **4**(5), 2852–2860.

Ducousso, M., Weiss-Hortala, E., Nzihou, A. and Castaldi, M. (2015), 'Reactivity enhancement of gasification biochars for catalytic applications', *Fuel* **159**, 491–499.

Dupont, C., Nocquet, T., Da Costa Jr, J. and Verne-Tournon, C. (2011), 'Kinetic modelling of steam gasification of various woody biomass chars: influence of inorganic elements', *Bioresource technology* **102**(20), 9743–9748.

Duque-Ingunza, I., López-Fonseca, R., De Rivas, B. and Gutiérrez-Ortiz, J. (2014), 'Process optimization for catalytic glycolysis of post–consumer PET wastes', *Journal of Chemical Technology and Biotechnology* **89**(1), 97–103.

Dzięcioł, M. and Trzeszczyński, J. (2000), 'Volatile products of poly(ethylene terephthalate) thermal degradation in nitrogen atmosphere', *Journal of Applied Polymer Science* **77**(9), 1894–1901.

Dziwiński, E., Iłowska, J. and Gniady, J. (2018), 'Py-GC/MS analyses of poly(ethylene terephthalate) film without and with the presence of tetramethylammonium acetate reagent. Comparative study', *Polymer Testing* **65**, 111–115.

El-Rub, Z., Bramer, E. and Brem, G. (2008), 'Experimental comparison of biomass chars with other catalysts for tar reduction', *Fuel* **87**(10-11), 2243–2252.

Eliasson, B., Liu, C. and Kogelschatz, U. (2000), 'Direct conversion of methane and carbon dioxide to higher hydrocarbons using catalytic dielectric-barrier discharges with zeolites', *Industrial & Engineering Chemistry Research* **39**(5), 1221–1227.

Eliezer, S. and Eliezer, Y. (2001), *The fourth state of matter: an introduction to plasma science*, Institute of Physiscs Publishing Bristol and Philadelphia, CRC Press.

Elordi, G., Olazar, M., Aguado, R., Lopez, G., Arabiourrutia, M. and Bilbao, J. (2007), 'Catalytic pyrolysis of high density polyethylene in a conical spouted bed reactor', *Journal of Analytical and Applied Pyrolysis* **79**(1), 450–455.

Elordi, G., Olazar, M., Lopez, G., Artetxe, M. and Bilbao, J. (2011), 'Product yields and compositions in the continuous pyrolysis of high-density polyethylene in a conical spouted bed reactor', *Industrial & Engineering Chemistry Research* **50**(11), 6650–6659.

Elordi, G., Olazar, M., Lopez, G., Castaño, P. and Bilbao, J. (2011), 'Role of pore structure in the deactivation of zeolites (HZSM-5, Hβ and HY) by coke in the pyrolysis of polyethylene in a conical spouted bed reactor', *Applied Catalysis B: Environmental* **102**(1-2), 224–231.

Environment and Plastics Industry Council (EPIC) (2004), 'A review of the options for the thermal treatment of plastics', *Canadian Plastics Industry Association (CPIA)* .

Espinosa-Pena, M., Figueroa-Gómez, Y. and Jiménez-Cruz, F. (2004), 'Simulated distillation yield curves in heavy crude oils: A comparison of precision between ASTM D-5307 and ASTM D-2892 physical distillation', *Energy & fuels* **18**(6), 1832–1840.

Eterigho, E. (2012), Development and application of heterogeneous catalysts for direct cracking of triglycerides for biodiesel production, phdthesis, Newcastle University, Newcastle upon Tyne, United Kingdom.

Eterigho, E., Lee, J. and Harvey, A. (2011), 'Triglyceride cracking for biofuel production using a directly synthesised sulphated zirconia catalyst', *Bioresource Technology* **102**(10), 6313 – 6316.

European Comission (2015), 'Review of waste policy and legislation'. Accessed: 10/04/2015.
URL: *http://ec.europa.eu/environment/waste/target_review.htm*

European Commission (2018), A European Strategy for Plastics in a Circular Economy, Technical report, European Commission. Accessed: 27/04/2019.
URL: *http://ec.europa.eu/environment/circular-economy/pdf/plastics-strategy-swd.pdf*

European Economic and Social Committee (2018), 'EU Strategy for Plastics in a Circular Economy'. Accessed: 27/04/2019.
URL: *https://www.eesc.europa.eu/en/agenda/our-events/events/eu-strategy-plastics-circular-economy*

European Environmental Agency (EEA) (2013), Managing municipal solid waste - a review of achivements in 32 european countries, Technical report, EEA.

EuroStat (2015*a*), Environment in the EU: Each person in the EU generated 481 kg of municipal waste in 2013, Technical report, Eurostat. Accessed: 23/03/2015.
URL: *http://ec.europa.eu/eurostat/documents/2995521/6757479/8-26032015-AP-EN.pdf/a2982b86-9d56-401c-8443-ec5b08e543cc*

Eurostat (2015*b*), 'Municipal Waste'. Accessed: 10/04/2015.
URL: *http://ec.europa.eu/eurostat/c/portal/layout?p_l_id=629266&p_v_l_s_g_id=0*

Eurostat (2015*c*), 'Recycling rate of municipal waste'. Accessed: 10/04/2015.
URL:
http://ec.europa.eu/eurostat/tgm/table.do?tab=table&init=1&plugin=1&pcode=t2020_-rt120&language=en

Eurostat (n.d.), 'Municipal waste'. Accessed: 30/05/2016.
URL: *http://ec.europa.eu/eurostat/cache/metadata/en/env_wasmun_esms.htm*

Ewais, O., Al Abbassy, F., Ghoneim, M. and Aboushelib, M. (2014), 'Novel zirconia surface treatments for enhanced osseointegration: laboratory characterization', *International journal of dentistry* **2014**, 1–8.

Ewan, B. and Allen, R. (2005), 'A figure of merit assessment of the routes to hydrogen', *International Journal of Hydrogen Energy* **30**(8), 809–819.

Fan, Y., Cai, Y., Li, X., Yin, H., Chen, L. and Liu, S. (2015), 'Regeneration of the HZSM-5 zeolite deactivated in the upgrading of bio-oil via non-thermal plasma injection (NTPI) technology', *Journal of Analytical and Applied Pyrolysis* **111**, 209–215.

Fan, Y., Zhao, W., Shao, S., Cai, Y., Chen, Y. and Jin, L. (2018), 'Promotion of the vapours from biomass vacuum pyrolysis for biofuels under non-thermal Plasma synergistic catalysis (NPSC) system', *Energy* **142**, 462–472.

Fridman, A. (2008), *Plasma chemistry*, Cambridge University press, New York, USA.

Fridman, G., Peddinghaus, M., Balasubramanian, M., Ayan, H., Fridman, A., Gutsol, A. and Brooks, A. (2006), 'Blood coagulation and living tissue sterilization by floating-electrode dielectric barrier discharge in air', *Plasma Chemistry and Plasma Processing* **26**(4), 425–442.

Gallego, J., Sierra, G., Mondragon, F., Barrault, J. and Batiot-Dupeyrat, C. (2011), 'Synthesis of MWCNTs and hydrogen from ethanol catalytic decomposition over a Ni-La_2O_3 catalyst produced by the reduction of $LaNiO_3$', *Applied Catalysis A: General* **397**(1–2), 73–81.

Gao, F. (2010), Pyrolysis of waste plastics into fuels, PhD thesis, University of Canterbury, Christchurch, New Zealand.

Garcia, A., Marcilla, A. and Font, R. (1995), 'Thermogravimetric kinetic study of the pyrolysis of municipal solid waste', *Thermochimica Acta* **254**, 277–304.

Garcia, C., Teixeira, S., Marciniuk, L. and Schuchardt, U. (2008), 'Transesterification of soybean oil catalyzed by sulfated zirconia', *Bioresource Technology* **99**(14), 6608–6613.

Gascoin, N., Navarro-Rodriguez, A., Gillard, P. and Mangeot, A. (2012), 'Kinetic modelling of high density polyethylene pyrolysis: Part 1. Comparison of existing models', *Polymer degradation and stability* **97**(8), 1466–1474.

Gayubo, A., Aguayo, A., Atutxa, A., Prieto, R. and Bilbao, J. (2004), 'Deactivation of a HZSM-5 zeolite catalyst in the transformation of the aqueous fraction of biomass pyrolysis oil into hydrocarbons', *Energy & Fuels* **18**(6), 1640–1647.

Gear, M., Sadhukhan, J., Thorpe, R., Clift, R., Seville, J. and Keast, M. (2018), 'A life cycle assessment data analysis toolkit for the design of novel processes–A case study for a thermal cracking process for mixed plastic waste', *Journal of Cleaner Production* **180**, 735–747.

Gent, M., Menendez, M., Toraño, J. and Diego, I. (2009), 'Recycling of plastic waste by density separation: prospects for optimization', *Waste management & research* **27**(2), 175–187.

Gerö, L. (1948), 'Bond energies of hydrocarbons', *The Journal of Chemical Physics* **16**(11), 1011–1013.

Gilbert, P., Ryu, C., Sharifi, V. and Swithenbank, J. (2009), 'Tar reduction in pyrolysis vapours from biomass over a hot char bed', *Bioresource technology* **100**(23), 6045–6051.

Global Market Insight Inc. (2018), 'Carbon Nanotubes Market size worth over USD 8bn by 2024'. Accessed: 18/09/2018.
URL: *https://www.gminsights.com/pressrelease/carbon-nanotubes-market*

Global Market Insights (2017), 'Benzoic Acid Market Size, Industry Analysis Report, Regional Outlook (U.S., Germany, UK, Italy, Russia, China, India, Japan, South Korea, Brazil, Mexico, Saudi Arabia, UAE, South Africa), Application Development, Price Trend, Competitive Market Share and Forecast, 2016 – 2023'. Accessed: 25/01/2017.
URL: *https://www.gminsights.com/industry-analysis/benzoic-acid-market*

González, Y., Costa, C., Márquez, M. and Ramos, P. (2011), 'Thermal and catalytic degradation of polyethylene wastes in the presence of silica gel, 5A molecular sieve and activated carbon', *Journal of Hazardous Materials* **187**(1-3), 101–112.

Gopu, C., Gao, L., Volpe, M., Fiori, L. and Goldfarb, J. (2018), 'Valorizing municipal solid waste: Waste to energy and activated carbons for water treatment via pyrolysis', *Journal of Analytical and Applied Pyrolysis* **133**, 48–58.

Grammelis, P., Basinasa, P., Malliopouloua, A. and Sakellaropoulos, G. (2009), 'Pyrolysis kinetics and combustion characteristics of waste recovered fuels', *Fuel* **88**, 195–205.

Grause, G., Matsumoto, S., Kameda, T. and Yoshioka, T. (2011), 'Pyrolysis of mixed plastics in a fluidized bed of hard burnt lime', *Industrial & Engineering Chemistry Research* **50**(9), 5459–5466.

Greenfield, T. and Metcalfe, A. (2006), *Design and analyse your xperiment using Minitab*, Hodder Arnold, London.

Guczi, L. and Erdôhelyi, A. (2012), *Catalysis for alternative energy generation*, Springer Science & Business Media.

Guddeti, R., Knight, R. and Grossmann, E. (2000*a*), 'Depolymerization of polyethylene using induction–coupled plasma technology', *Plasma Chemistry and Plasma Processing* **20**(1), 37–64.

Guddeti, R., Knight, R. and Grossmann, E. (2000*b*), 'Depolymerization of polypropylene in an induction-coupled plasma (ICP) reactor', *Industrial & engineering chemistry research* **39**(5), 1171–1176.

Guisnet, M., Gnep, N., Aittaleb, D. and Doyemet, Y. (1992), 'Conversion of light alkanes into aromatic hydrocarbons: VI. Aromatization of C_2-C_4 alkanes on H-ZSM-5 reaction mechanisms', *Applied Catalysis A: General* **87**(2), 255–270.

Hackam, R. and Aklyama, H. (2000), 'Air pollution control by electrical discharges', *IEEE Transactions on Dielectrics and Electrical Insulation* **7**(5), 654–683.

Hamouda, L., Ghorbel, A. and Figueras, F. (2000), 'Study of acidic and catalytic properties of sulfated zirconia prepared by sol-gel process: Influence of preparation conditions', *Studies in Surface Science and Catalysis* **130**, 971–976.

Hao, H., Wu, B., Yang, J., Guo, Q., Yang, Y. and Li, Y. (2015), 'Non-thermal plasma enhanced heavy oil upgrading', *Fuel* **149**, 162–173.

Harling, A., Demidyuk, V., Fischer, S. and Whitehead, J. (2008), 'Plasma-catalysis destruction of aromatics for environmental clean-up: Effect of temperature and configuration', *Applied Catalysis B: Environmental* **82**(3), 180–189.

Helwani, Z., Othman, M., Aziz, N., Fernando, W. and Kim, J. (2009), 'Technologies for production of biodiesel focusing on green catalytic techniques: a review', *Fuel Processing Technology* **90**(12), 1502–1514.

Hervy, M., Villot, A., Gérente, C., Minh, D., Weiss-Hortala, E., Nzihou, A. and Le Coq, L. (2018), 'Catalytic cracking of ethylbenzene as tar surrogate using pyrolysis chars from wastes', *Biomass and Bioenergy* **117**, 86–95.

Hopewell, J., Dvorak, R. and Kosior, E. (2009), 'Plastics recycling: challenges and opportunities', *Philosophical Transactions of the Royal Society of London B: Biological Sciences* **364**(1526), 2115–2126.

Huang, H. and Tang, L. (2007), 'Treatment of organic waste using thermal plasma pyrolysis technology', *Energy Conversion and Management* **48**(4), 1331–1337.

Hujuri, U., Ghoshal, A. K. and Gumma, S. (2008), 'Modeling pyrolysis kinetics of plastic mixtures', *Polymer Degradation and Stability* **93**(10), 1832–1837.

IEA Hydrogen (2017), Global trends and outlook for hydrogen, Technical report, IEA Hydrogen. Accessed: 18/09/2018.
URL:
http://ieahydrogen.org/pdfs/Global-Outlook-and-Trends-for-Hydrogen_Dec2017_WEB.aspx

Iglesia, E., Soled, S. and Kramer, G. (1993), 'Isomerization of alkanes on sulfated zirconia: promotion by Pt and by adamantyl hydride transfer species', *Journal of Catalysis* **144**(1), 238–253.

Institut für Arbeitsschutz der Deutschen Gesetzlichen Unfallversicherung (2015), 'Polyethyle terephthalate'. Accessed: 21/06/2015.
URL: *http://gestis-en.itrust.de/nxt/gateway.dll/gestis_-en/530566.xml?f=templatesfn = default.htm3.0*

Intratec (2016), Ethylene Production via Steam Cracking of Naphtha - Cost Analysis. Ethylene E72A, Techreport, Intratec.
URL: *https://www.intratec.us/analysis/ethylene-e72b*

Jambeck, J. (2018), 'Global plastic waste totals 4.9 billion tonnes'. Accessed: 19/09/2018.
URL: *https://cosmosmagazine.com/society/global-plastic-waste-totals-4-9-billion-tonnes*

Jambeck, J., Geyer, R., Wilcox, C., Siegler, T., Perryman, M., Andrady, A., Narayan, R. and Law, K. (2015), 'Plastic waste inputs from land into the ocean', *Science* **347**(6223), 768–771.

Jiao, Y., Zhang, J., Du, Y., Li, F., Li, C., Lu, J., Wang, J. and Chen, Y. (2016), 'Hydrogen production by catalytic steam reforming of hydrocarbon fuels over Ni/Ce-Al_2O_3 bifunctional catalysts: Effects of SrO addition', *International Journal of Hydrogen Energy* **41**(31), 13436–13447.

Juliastuti, S., Hisbullah, M. and Abdillah, M. (2018), High density polyethylene plastic waste treatment with microwave heating pyrolysis method using coconut-shell activated carbon to produce alternative fuels, *in* 'IOP Conference Series: Materials Science and Engineering', Vol. 334, IOP Publishing, p. 012015.

Jung, J. and Kim, J. (2017), 'An indoor air purification technology using a non-thermal plasma reactor with multiple-wire-to-wire type electrodes and a fiber air filter', *Journal of Electrostatics* **86**, 12–17.

Jung, S., Cho, M., Kang, B. and Kim, J. (2010), 'Pyrolysis of a fraction of waste polypropylene and polyethylene for the recovery of BTX aromatics using a fluidized bed reactor', *Fuel Processing Technology* **91**(3), 277–284.

Kalargaris, I., Tian, G. and Gu, S. (2017), 'The utilisation of oils produced from plastic waste at different pyrolysis temperatures in a DI diesel engine', *Energy* **131**, 179–185.

Kalpakjian, S., Schmid, S. R. and Kok, C. W. (2008), *Manufacturing processes for engineering materials*, Pearson-Prentice Hall.

Kaminsky, W. (1991), 'Recycling of polymeric materials by pyrolysis', *Makromolekulare Chemie. Macromolecular Symposia* **48-49**(1), 381–393.

Kaminsky, W. and Kim, J. (1999), 'Pyrolysis of mixed plastics into aromatics', *Journal of Analytical and Applied Pyrolysis* **51**(1-2), 127–134.

Kaminsky, W. and Zorriqueta, I. (2007), 'Catalytical and thermal pyrolysis of polyolefins', *Journal of Analytical and Applied Pyrolysis* **79**(1), 368–374.

Kang, S., Seo, S., Kim, Y., Shin, Y., Koh, Y., Lee, C., Yang, S., Lee, J., Moon, E., Kang, H., Ryeo, J., Lee, Y. and Kim, C. (2017), 'Comparative effects of non-thermal atmospheric pressure plasma on migration and invasion in oral squamous cell cancer, by cas type', *Yonsei Medical Journal* **58**(2), 272–281.

Karak, T., Bhagat, R. and Bhattacharyya, P. (2012), 'Municipal solid waste generation, composition, and management: the world scenario', *Critical Reviews in Environmental Science and Technology* **42**(15), 1509–1630.

Karayannidis, G. and Achilias, D. (2007), 'Chemical recycling of poly(ethylene terephthalate)', *Macromolecular Materials and Engineering* **292**(2), 128–146.

Kassargy, C., Awad, S., Burnens, G., Kahine, K. and Tazerout, M. (2018), 'Gasoline and diesel-like fuel production by continuous catalytic pyrolysis of waste polyethylene and polypropylene mixtures over USY zeolite', *Fuel* **224**, 764–773.

Kayacan, I. and Dogan, O. M. (2008), 'Pyrolysis of low and high density polyethylene. Part I: Non-isothermal pyrolysis kinetics', *Energy sources, Part A* **30**, 385–391.

Khani, M., Khosravi, A., Dezhbangooy, E., Hosseini, B. and Shokri, B. (2014), 'Study on the feasibility of plasma (DBD Reactor) cracking of different hydrocarbons (n-hexadecane, lubricating oil, and heavy oil)', *IEEE Transactions on Plasma Science* **42**(9), 2213–2220.

Khoo, H. (2019), 'LCA of plastic waste recovery into recycled materials, energy and fuels in Singapore', *Resources, Conservation and Recycling* **145**, 67–77.

Khoonkari, M., Haghighi, A., Sefidbakht, Y., Shekoohi, K. and Ghaderian, A. (2015), 'Chemical recycling of PET wastes with different catalysts', *International Journal of Polymer Science* **2015**.

Kim, S. and Kim, S. (2004), 'Pyrolysis characteristics of polystyrene and polypropylene in a stirred batch reactor', *Chemical engineering journal* **98**(1), 53–60.

Kissin, Y. (2001), 'Chemical mechanisms of catalytic cracking over solid acidic catalysts: alkanes and alkenes', *Catalysis Reviews* **43**(1-2), 85–146.

Klinghoffer, N. (2013), Utilization of char from biomass gasification in catalytic applications, PhD thesis, Columbia University, New York, USA.

Klinghoffer, N., Castaldi, M. and Nzihou, A. (2012), 'Catalyst properties and catalytic performance of char from biomass gasification', *Industrial & Engineering Chemistry Research* **51**(40), 13113–13122.

Knight, R., Grossmann, E. and Guddeti, R. (2002), 'Thermal plasma process for recovering monomers and high value carbons from polymeric materials'. US Patent 6,444,864.

Kogelschatz, U. (2003), 'Dielectric-barrier discharges: their history, discharge physics, and industrial applications', *Plasma chemistry and plasma processing* **23**(1), 1–46.

Kogelschatz, U., Eliasson, B. and Egli, W. (1997), 'Dielectric-barrier discharges. Principle and applications', *Le Journal de Physique IV* **7**(C4), C4–47.

Kogler, M., Köck, E., Klötzer, B., Schachinger, T., Wallisch, W., Henn, R., Huck, C., Hejny, C. and Penner, S. (2016), 'High-temperature carbon deposition on oxide surfaces by CO disproportionation', *The Journal of Physical Chemistry C* **120**(3), 1795–1807.

Kosuth, M., Mason, S. and Wattenberg, E. (2018), 'Anthropogenic contamination of tap water, beer, and sea salt', *PloS one* **13**(4), e0194970.

Kowalska, E., Opalińska, T., Radomska, J. and Ulejczyk, B. (2008), 'Non-thermal plasma for oxidation of gaseous products originating from thermal treatment of wastes', *Vacuum* **82**(10), 1069–1074.

Kraus, M., Eliasson, B., Kogelschatz, U. and Wokaun, A. (2001), 'CO_2 reforming of methane by the combination of dielectric-barrier discharges and catalysis', *Physical Chemistry Chemical Physics* **3**(3), 294–300.

Kreith, F. and Tchobanoglous, G. (1994), *Handbook of Solid Waste Management*, McGraw-Hill, New York.

Krouse, H., Viau, C., Eliuk, L., Ueda, A. and Halas, S. (1988), 'Chemical and isotopic evidence of thermochemical sulphate reduction by light hydrocarbon gases in deep carbonate reservoirs', *Nature* **333**(6172), 415.

Ksapabutr, B., Chalermkiti, T. and Panapoy, M. (2013), 'Facile and low-cost synthesis of Ni/NiO catalyst by microwave plasma method for carbon nanotubes growth using plastic waste as carbon source', *Advanced Science Letters* **19**(1), 268–272.

Kumar, P., Bharathikumar, M., Prabhakaran, C., Vijayan, S. and Ramakrishnan, K. (2017), 'Conversion of waste plastics into low-emissive hydrocarbon fuels through catalytic depolymerization in a new laboratory scale batch reactor', *International Journal of Energy and Environmental Engineering* **8**(2), 167–173.

Kumar, S. and Singh, R. (2014), 'Optimization of process parameters by response surface methodology (RSM) for catalytic pyrolysis of waste high-density polyethylene to liquid fuel', *Journal of Environmental Chemical Engineering* **2**(1), 115–122.

Kyrikou, I. and Briassoulis, D. (2007), 'Biodegradation of agricultural plastic films: a critical review', *Journal of Polymers and the Environment* **15**(2), 125–150.

Lahijani, P., Zainal, Z., Mohammadi, M. and Mohamed, A. (2015), 'Conversion of the greenhouse gas CO_2 to the fuel gas co via the boudouard reaction: A review', *Renewable and Sustainable Energy Reviews* **41**, 615–632.

Larkin, P. (2011), General Outline and Strategies for IR and Raman Spectral Interpretation, *in* 'Infrared and Raman Spectroscopy', Elsevier, Oxford, chapter 7, pp. 117–133.

Lee, K. (2008), 'Composition of aromatic products in the catalytic degradation of the mixture of waste polystyrene and high-density polyethylene using spent FCC catalyst', *Polymer Degradation and Stability* **93**(7), 1284–1289.

Lee, K. (2009), 'Thermal and catalytic degradation of pyrolytic oil from pyrolysis of municipal plastic wastes', *Journal of Analytical and Applied Pyrolysis* **85**(1), 372–379.

Lee, K. (2012), Pyrolysis of waste polystyrene and high-density polyethylene, *in* 'Material Recycling-Trends and Perspectives', InTech, pp. 175–192.

Li, A., Li, X., Li, S., Ren, Y., Chi, Y., Yan, J. and Cen, K. (1999), 'Pyrolysis of solid waste in a rotary kiln: influence of final pyrolysis temperature on the pyrolysis products', *Journal of Analytical and Applied Pyrolysis* **50**(2), 149–162.

Li, C. and Stair, P. (1996), 'Ultraviolet Raman spectroscopy characterization of sulfated zirconia catalysts: fresh, deactivated and regenerated', *Catalysis letters* **36**(3), 119–123.

Li, G., Hu, L. and Hill, J. (2006), 'Comparison of reducibility and stability of alumina-supported Ni catalysts prepared by impregnation and co-precipitation', *Applied Catalysis A: General* **301**(1), 16–24.

Li, K., Lee, S., Yuan, G., Lei, J., Lin, S., Weerachanchai, P., Yang, Y. and Wang, J. (2016), 'Investigation into the catalytic activity of microporous and mesoporous catalysts in the pyrolysis of waste polyethylene and polypropylene mixture', *Energies* **9**(6), 431.

Li, X., Nagaoka, K., Simon, L., Lercher, J., Wrabetz, S., Jentoft, F., Breitkopf, C., Matysik, S. and Papp, H. (2005), 'Interaction between sulfated zirconia and alkanes: prerequisites for active sites-formation and stability of reaction intermediates', *Journal of Catalysis* **230**(1), 214–225.

Li, X., Shimizu, Y., Pyatenko, A., Wang, H. and Koshizaki, N. (2012), 'Tetragonal zirconia spheres fabricated by carbon-assisted selective laser heating in a liquid medium', *Nanotechnology* **23**(11), 115602–115610.

Lie, L., Bin, W., Chi, Y. and Chengkang, W. (2006), 'Characteristics of gliding arc discharge plasma', *Plasma Science and Technology* **8**(6), 653.

Lim, M., Shah Zulkifli, A., Jayapalan, K. and Chin, O. (2017), 'Development of a dimensionless parameter for characterization of dielectric barrier discharge devices with respect to geometrical features', *Plasma Science and Technology* **19**(9), 095402.

Lin, R. and White, R. (1997), 'Acid-catalyzed cracking of polystyrene', *Journal of applied polymer science* **63**(10), 1287–1298.

Lin, Y. and Yang, M. (2007*a*), 'Catalytic conversion of commingled polymer waste into chemicals and fuels over spent FCC commercial catalyst in a fluidised-bed reactor', *Applied Catalysis B: Environmental* **69**(3-4), 145–153.

Lin, Y. and Yang, M. (2007*b*), 'Catalytic pyrolysis of polyolefin waste into valuable hydrocarbons over reused catalyst from refinery FCC units', *Applied Catalysis A: General* **328**(2), 132–139.

Lin, Y. and Yang, M. (2008), 'Chemical catalysed recycling of polypropylene over a spent FCC catalyst and various commercial cracking catalysts using TGA', *Thermochimica Acta* **470**(1-2), 52–59.

Liu, C., Ye, J., Jiang, J. and Pan, Y. (2011), 'Progresses in the preparation of coke resistant ni-based catalyst for steam and CO_2 reforming of methane', *ChemCatChem* **3**(3), 529–541.

Liu, J., Jiang, Z., Yu, H. and Tang, T. (2011), 'Catalytic pyrolysis of polypropylene to synthesize carbon nanotubes and hydrogen through a two–stage process', *Polymer degradation and stability* **96**(10), 1711–1719.

Liu, K. and Meuzelaar, H. (1996), 'Catalytic reactions in waste plastics, HDPE and coal studied by high-pressure thermogravimetry with on-line GC/MS', *Fuel processing technology* **49**(1-3), 1–15.

Long, H., Shang, S., Tao, X., Yin, Y. and Dai, X. (2008), 'CO_2 reforming of CH_4 by combination of cold plasma jet and Ni/γ-Al_2O_3 catalyst', *International Journal of Hydrogen Energy* **33**(20), 5510–5515.

Loong, C. (2011), *Simulation: Optimize the production of benzoic acid by using benzene and acetic anhydride*, Universiti Tunku Abdul Rahman.

López, A., De Marco, I., Caballero, B., Adrados, A. and Laresgoiti, M. (2011), 'Deactivation and regeneration of ZSM-5 zeolite in catalytic pyrolysis of plastic wastes', *Waste Management* **31**(8), 1852–1858.

López, A., De Marco, I., Caballero, B., Laresgoiti, M. and Adrados, A. (2011), 'Influence of time and temperature on pyrolysis of plastic wastes in a semi-batch reactor', *Chemical Engineering Journal* **173**(1), 62–71.

López, A., De Marco, I., Caballero, B., Laresgoiti, M., Adrados, A. and Aranzabal, A. (2011), 'Catalytic pyrolysis of plastic wastes with two different types of catalysts: ZSM-5 zeolite and Red Mud', *Applied Catalysis B: Environmental* **104**(3), 211–219.

López, A., De Marco, I., Caballero, B., Laresgoiti, M., Adrados, A. and Torres, A. (2011), 'Pyrolysis of municipal plastic wastes II: Influence of raw material composition under catalytic conditions', *Waste management* **31**(9-10), 1973–1983.

Lopez, D., Goodwin Jr, J., Bruce, D. and Furuta, S. (2008), 'Esterification and transesterification using modified-zirconia catalysts', *Applied Catalysis A: General* **339**(1), 76–83.

Lopez, D., Goodwin Jr, J., Bruce, D. and Lotero, E. (2005), 'Transesterification of triacetin with methanol on solid acid and base catalysts', *Applied Catalysis A: General* **295**(2), 97–105.

Lopez, G., Artetxe, M., Amutio, M., Bilbao, J. and Olazar, M. (2017), 'Thermochemical routes for the valorization of waste polyolefinic plastics to produce fuels and chemicals. a review', *Renewable and Sustainable Energy Reviews* **73**, 346–368.

Lopez-Urionabarrenechea, A., De Marco, I., Caballero, B., Laresgoiti, M. and Adrados, A. (2012), 'Catalytic stepwise pyrolysis of packaging plastic waste', *Journal of analytical and applied pyrolysis* **96**, 54–62.

Lu, P., Huang, Q., Chi, Y. and Yan, J. (2017), 'Preparation of high catalytic activity biochar from biomass waste for tar conversion', *Journal of Analytical and Applied Pyrolysis* **127**, 47–56.

Ludlow-Palafox, C. and Chase, H. (2001), 'Microwave-induced pyrolysis of plastic wastes', *Industrial & engineering chemistry research* **40**(22), 4749–4756.

Machel, H., Krouse, H. and Sassen, R. (1995), 'Products and distinguishing criteria of bacterial and thermochemical sulfate reduction', *Applied Geochemistry* **10**(4), 373–389.

Madorsky, S. (1964), *Thermal degradation of organic polymers*, Polymer reviews, Interscience Publishers, New York,.

Magnoux, P., Cartraud, P., Mignard, S. and Guisnet, M. (1987), 'Coking, aging, and regeneration of zeolites: III. Comparison of the deactivation modes of H-mordenite, HZSM-5, and HY during n-Heptane cracking', *Journal of Catalysis* **106**(1), 242–250.

Málek, J. (1992), 'The kinetic analysis of non-isothermal data', *Thermochimica acta* **200**, 257–269.

Mani, M., Nagarajan, G. and Sampath, S. (2011), 'Characterisation and effect of using waste plastic oil and diesel fuel blends in compression ignition engine', *Energy* **36**(1), 212–219.

Marcilla, A., Beltrán, M., Hernández, F. and Navarro, R. (2004), 'HZSM5 and HUSY deactivation during the catalytic pyrolysis of polyethylene', *Applied Catalysis A: General* **278**(1), 37–43.

Marczewski, M., Kamińska, E. and Marczewska, H. (2013), 'Decomposition of styrene dimers: the influence of the acid strength of the catalyst', *Reaction Kinetics, Mechanisms and Catalysis* **108**(1), 59–68.

Mark, J. (2007), *Physical properties of polymers handbook*, Vol. 1076, Springer, New York, USA.

Markets and Markets (2018), 'Polypropylene Market by Type (Homopolymer, Copolymer), Application (Injection Molding, Fiber & Raffia, Film & Sheet, and Blow Molding), End-Use Industry (Packaging, Automotive, Building & Construction, Medical), and Region - Global Forecast to 2022'. Accessed: 19/09/2018.
URL: *https://www.prnewswire.com/news-releases/polypropylene-market-worth-9917-billion-usd-by-2022-671001263.html*

Martín-Gullón, I., Esperanza, M. and Font, R. (2001), 'Kinetic model for the pyrolysis and combustion of poly(ethylene terephthalate)(PET)', *Journal of Analytical and Applied Pyrolysis* **58**, 635–650.

Mason, S., Welch, V. and Neratko, J. (2018), 'Synthetic polymer contamination in bottled water', *Available from: Department of Geology and Environmental Sciences, Fredonia University, New York [Accessed 15 August 2018] http://news.bbc.co.uk/2/shared/bsp/hi/pdfs/14_03_13_finalbottled. pdf* .

Mastral, F., Esperanza, E., Berrueco, C., Juste, M. and Ceamanos, J. (2003), 'Fluidized bed thermal degradation products of HDPE in an inert atmosphere and in air–nitrogen mixtures', *Journal of Analytical and Applied Pyrolysis* **70**(1), 1–17.

Mastral, F., Esperanza, E., Garcıa, P. and Juste, M. (2002), 'Pyrolysis of high-density polyethylene in a fluidised bed reactor. Influence of the temperature and residence time', *Journal of Analytical and Applied Pyrolysis* **63**(1), 1–15.

Masuda, T., Miwa, Y., Tamagawa, A., Mukai, S., Hashimoto, K. and Ikeda, Y. (1997), 'Degradation of waste poly(ethylene terephthalate) in a steam atmosphere to recover terephthalic acid and to minimize carbonaceous residue', *Polymer Degradation and Stability* **58**(3), 315–320.

Masuda, T., Tomita, P., Fujikata, Y. and Hashimoto, K. (1999), Deactivation of hy-type zeolite catalyst due to coke deposition during gas-oil cracking, *in* 'Studies in Surface Science and Catalysis', Vol. 126, Elsevier, pp. 89–96.

Mat, R., Samsudin, R., Mohamed, M., Johari, A., Kamaruddin, M. and Ali, A. (2014), 'Trans-esterification of triglycerides with methanol on sulfated zirconia prepared with different concentration of sulfuric acid', *Applied Mechanics and Materials* **493**, 15–20.

Mazzoni, L. and Janajreh, I. (2017), 'Plasma gasification of municipal solid waste with variable content of plastic solid waste for enhanced energy recovery', *International Journal of Hydrogen Energy* **42**(30), 19446–19457.

Meichsner, J., Schmidt, M., Schneider, R. and Wagner, H. (2012), *Non-thermal plasma chemistry and physics*, CRC Press.

Meier, D., Van de Beld, B., Bridgewater, A., Elliott, D., Oasmaa, A. and Prieto, F. (2013), 'State-of-the-art of fast pyrolysis in IEA bioenergy member countries', *Renewable and Sustainable Energy Reviews* **20**, 619–641.

Miandad, R., Barakat, M., Aburiazaiza, A., Rehan, M. and Nizami, A. (2016), 'Catalytic pyrolysis of plastic waste: a review', *Process Safety and Environmental Protection* **102**, 822–838.

Miranda, M., Pinto, F. and Gulyurtlu, I. (2011), Polymer wastes pyrolysis, *in* C. Nielsen, ed., 'Recycling: Processes, costs and benefits', INETI, chapter 4, pp. 141–166.

Miranda, M., Pinto, F. and Gulyurtlu, I. (2012), Polymer wastes pyrolysis for liquid fuel production, *in* D. Carasillo, ed., 'Liquid Fuels: Types, Properties and Production', LNEG-LEN-UEZ, chapter 4, pp. 147–167.

Miranda, M., Pinto, F., Gulyurtlu, I., Cabrita, I., Nogueira, C. and Matos, A. (2010), 'Response surface methodology optimization applied to rubber tyre and plastic wastes thermal conversion', *Fuel* **89**(9), 2217–2229.

Mishra, N., Das, G., Ansaldo, A., Genovese, A., Malerba, M., Povia, M., Ricci, D., Di Fabrizio, E., Di Zitti, E., Sharon, M. and Sharon, M. (2012), 'Pyrolysis of waste polypropylene for the synthesis of carbon nanotubes', *Journal of analytical and applied pyrolysis* **94**, 91–98.

Miskolczi, N. (2014), 'Hydrocarbons obtained by pyrolysis of waste materials', *Proceedings of Institution of Civil Engineers: Waste and Resource Management* **167**, 6–14.

Miskolczi, N., Angyal, A., Bartha, L. and Valkai, I. (2009), 'Fuels by pyrolysis of waste plastics from agricultural and packaging sectors in a pilot scale reactor', *Fuel Processing Technology* **90**(7-8), 1030–1040.

Miskolczi, N., Bartha, L., Angyal, A. and Valkai, I. (2008), Hydrocarbon fractions from plastic wastes for refinery and petrochemical industry, *in* 19th World Petroleum Congress 2008: A World in Transition: Delivering Energy for Sustainable Growth, ed., 'Energy Institute - 19th World Petroleum Congress 2008: A World in Transition: Delivering Energy for Sustainable Growth', Vol. 2, Madrid, pp. 822–831.

Miskolczi, N., Bartha, L. and Deák, G. (2006), 'Thermal degradation of polyethylene and polystyrene from the packaging industry over different catalysts into fuel-like feed stocks', *Polymer Degradation and Stability* **91**(3), 517–526.

Miskolczi, N., Barthaa, L., Deaka, G. and Jover, B. (2004), 'Thermal degradation of municipal plastic waste for production of fuel-like hydrocarbons', *Polymer Degradation and Stability* **86**(2), 357–366.

Miskolczi, N. and Nagy, R. (2012), 'Hydrocarbons obtained by waste plastic pyrolysis: Comparative analysis of decomposition described by different kinetic models', *Fuel Processing Technology* **104**, 96–104.

Mitsuoka, K., Hayashi, S., Amano, H., Kayahara, K., Sasaoaka, E. and Uddin, M. (2011), 'Gasification of woody biomass char with CO_2: The catalytic effects of K and Ca species on char gasification reactivity', *Fuel Processing Technology* **92**(1), 26–31.

Mo, Y., Kibria, A. and Nahm, K. (2001), 'The growth mechanism of carbon nanotubes from thermal cracking of acetylene over nickel catalyst supported on alumina', *Synthetic Metals* **122**(2), 443–447.

Montgomery, D. (2017), *Design and analysis of experiments*, 8 edn, John wiley & sons, New York.

Mordor Intelligence (2016), 'Global Thermoplastics Market - Segmented by type, application and geography - Trends and forecasts (2015-2020)'. Accessed: 18/10/2016.
URL: *www.mordorintelligence.com/industry-reports/global-thermoplastics-market-industry*

Mortimer, M. and Taylor, P. (2002), *Chemical kinetics and mechanism*, Vol. 1 of *The Molecular World*, The Royal Society of Chemistry.

Muradov, N. and Veziroglu, T. (2005), 'From hydrocarbon to hydrogen–carbon to hydrogen economy', *International Journal of Hydrogen Energy* **30**(3), 225–237.

Mustafa, M., Fu, X., Liu, Y., Abbas, Y., Wang, H. and Lu, W. (2018), 'Volatile organic compounds (VOCs) removal in non-thermal plasma double dielectric barrier discharge reactor', *Journal of Hazardous Materials* **347**, 317–324.

Myers Jr., M., Stollsteimer, J. and Wims, A. (1975), 'Determination of hydrocarbon-type distribution and hydrogen/carbon ratio of gasolines by nuclear magnetic resonance spectrometry', *Analytical Chemistry* **47**(12), 2010–2015.

Na, J., Jeong, B., Chung, S. and Kim, S. (2006), 'Pyrolysis of low-density polyethylene using synthetic catalysts produced from fly ash', *Journal of Material Cycles and Waste Management* **8**(2), 126–132.

Nabid, M., Bide, Y., Fereidouni, N. and Etemadi, B. (2017), 'Maghemite/nitrogen–doped graphene hybrid material as a reusable bifunctional catalyst for glycolysis of polyethylene terephthalate', *Polymer Degradation and Stability* **144**, 434–441.

Namioka, T., Saito, A., Inoue, Y., Park, Y., Min, T., Roh, S. and Yoshikawa, K. (2011), 'Hydrogen-rich gas production from waste plastics by pyrolysis and low-temperature steam reforming over a ruthenium catalyst', *Applied Energy* **88**(6), 2019–2026.

NAPCOR (2018), Report on Postconsumer PET Container Recycling Activity in 2017, Technical report, National Association for PET Container Resources (NAPCOR). Accessed: 15/11/2018.
URL: *https://www.plasticsrecycling.org/images/pdf/resources/reports/Rate-Reports/Reports-on-Postconsumer-PET-Container-Recycling-Activity*

Nascimento, P., Akratopoulou, C., Oszagyan, M., Coudurier, G., Travers, C., Joly, J. and Vedrine, J. (1993), ZrO_2-SO_4^{2-} Catalysts. Nature and Stability of Acid Sites Responsible for n-Butane Isomerization, *in* 'Studies in Surface Science and Catalysis', Vol. 75, pp. 1185–1197.

National Energy Technology Laboratory (NETL) (2017), 'Non-thermal plasma for fossil energy related applications'. Accessed: 03/02/2017.
URL: *https://www.netl.doe.gov/research/on-site-research/research-portfolio/coal-research/carbon-storage/non-thermal-plasma-for-fossil-energy-related-applications*

Nema, S. and Ganeshprasad, K. (2002), 'Plasma pyrolysis of medical waste', *Current science* **83**(3), 271–278.

Ng, F. and Horvát, N. (1995), 'Sulfur removal from ZrO_2/so_4^{2-} during n-butane isomerization', *Applied Catalysis A: General* **123**(2), L197–L203.

Niemira, B. (2012), 'Cold plasma decontamination of foods', *Annual review of food science and technology* **3**, 125–142.

Nishiyama, T. and Aika, K. (1990), 'Mechanism of the oxidative coupling of methane using C_{02} as an oxidant over PbO–MgO', *Journal of Catalysis* **122**(2), 346–351.

Novoselov, K., Falko, V., Colombo, L., Gellert, P., Schwab, M. and Kim, K. (2012), 'A roadmap for graphene', *Nature* **490**(7419), 192–200.

Olabisi, O. and Adewale, K. (2016), *Handbook of thermoplastics*, Vol. 41, CRC press.

Olazar, M., López, G., Amutio, M., Elordi, G., Aguado, R. and Bilbao, J. (2009), 'Influence of FCC catalyst steaming on HDPE pyrolysis product distribution', *Journal of Analytical and Applied Pyrolysis* **85**(1), 359–365.

Ono, Y. (2003), 'A survey of the mechanism in catalytic isomerization of alkanes', *Catalysis Today* **81**(1), 3–16.

Onwudili, J., Insura, N. and Williams, P. (2009), 'Composition of products from the pyrolysis of polyethylene and polystyrene in a closed batch reactor: Effects of temperature and residence time', *Journal of Analytical and Applied Pyrolysis* **86**(2), 293–303.

Panda, A., Singh, R. and Mishra, D. (2010), 'Thermolysis of waste plastics to liquid fuel: a suitable method for plastic waste management and manufacture of value added products – a world prospective', *Renewable and Sustainable Energy Reviews* **14**(1), 233–248.

Papadopoulou, C., Matralis, H. and Verykios, X. (2012), Utilization of biogas as a renewable carbon source: Dry reforming of methane, *in* 'in Catalysis for alternative energy generation', Springer Science & Business Media, London, chapter 3, pp. 57–128.

Park, J., Noh, J., Chang, J. and Park, S. (2000), 'Ethylbenzene to styrene in the presence of carbon dioxide over zirconia', *Catalysis Letters* **65**(1-3), 75–78.

Park, J., Park, H., Choi, S. and Park, D. (2016), 'Effects of blend ratio between high density polyethylene and biomass on co-gasification behaviour in a two-stage gasification system', *International Journal of Hydrogen Energy* **41**(38), 16813–16822.

Parliament.co.uk (2019), 'Plastic Pollution Bill 2017-19'. Accessed: 27/04/2019.
URL: *https://services.parliament.uk/bills/2017-19/plasticpollution.html*

Paszun, D. and Spychaj, T. (1997), 'Chemical recycling of poly(ethylene terephthalate)', *Industrial & Engineering Chemistry Research* **36**(4), 1373–1383.

Paulmier, T. and Fulcheri, L. (2005), 'Use of non-thermal plasma for hydrocarbon reforming', *Chemical Engineering Journal* **106**(1), 59–71.

Penetrante, B., Hsiao, M., Bardsley, J., Merritt, B., Vogtlin, G., Kuthi, A., Burkhart, C. and Bayless, J. (1997), 'Identification of mechanisms for decomposition of air pollutants by non-thermal plasma processing', *Plasma Sources Science and Technology* **6**(3), 251.

Perez-Maqueda, L., Sanchez-Jimenez, P., Perejón, A., García-Garrido, C., Criado, J. and Benítez-Guerrero, M. (2014), 'Scission kinetic model for the prediction of polymer pyrolysis curves from chain structure', *Polymer Testing* **37**, 1–5.

Peterson, J., Vyazovkin, S. and Wight, C. (2001), 'Kinetics of the thermal and thermo-oxidative degradation of polystyrene, polyethylene and poly(propylene)', *Macromolecular Chemistry and Physics* **202**(6), 775–784.

Petitpas, G., Rollier, J., Darmon, A., Gonzalez-Aguilar, J., Metkemeijer, R. and Fulcheri, L. (2007), 'A comparative study of non-thermal plasma assisted reforming technologies', *International Journal of Hydrogen Energy* **32**(14), 2848–2867.

Petrović, D., Martens, T., Van Dijk, J., Brok, W. and Bogaerts, A. (2009), 'Fluid modelling of an atmospheric pressure dielectric barrier discharge in cylindrical geometry', *Journal of Physics D: Applied Physics* **42**(20), 205–206.

Phan, A., Sharafi, V. and Swithenbank, J. (2009), 'Effect of bed depth on characterisation of slow pyrolysis products', *Fuel* **88**(8), 1383–1387.

Pinto, F., Costa, P., Gulyurtlu, I. and Cabrita, I. (1999*a*), 'Pyrolysis of plastic wastes. 1. Effect of plastic waste composition on product yield', *Journal of Analytical and Applied Pyrolysis* **51**(1), 39–55.

Pinto, F., Costa, P., Gulyurtlu, I. and Cabrita, I. (1999*b*), 'Pyrolysis of plastic wastes: 2. Effect of catalyst on product yield', *Journal of Analytical and Applied Pyrolysis* **51**(1), 57–71.

Pinto, F., Paradela, F., Gulyurtlu, I. and Ramos, A. (2013), 'Prediction of liquid yields from the pyrolysis of waste mixtures using response surface methodology', *Fuel Processing Technology* **116**, 271–283.

Plastic Europe (2015), Plastics – the Facts 2015, Technical report, Plastics Europe. Accessed: 12/06/2015.
URL: *http://www.plasticseurope.org/Document/plastics—the-facts-2015.aspx*

Plastic Europe, (2016), Plastics - the Facts 2014-2015, Technical report, Plastics Europe.
URL: *https://www.plasticseurope.org/application/files/5515/1689/9220/2014plastics_the_-facts_PubFeb2015.pdf*

Plastic Europe (2017), 'Plastics - The Facts, 2017'. Accessed: 05/03/2018.
URL: *http://www.plasticseurope.org/application/files/5715/1717/4180/Plastics_the_facts_-2017_FINAL_for_website_one_page.pdf*

Plastic Recyclers Europe (2018), PET Recycling industry installed capacity reviewed, Technical report, Plastic recyclers Europe. Accessed: 03/07/2018.
URL: *https://www.plasticsrecyclers.eu/pet-recycling-industry-installed-capacity-reviewed*

Pol, V. and Thiyagarajan, P. (2010), 'Remediating plastic waste into carbon nanotubes', *Journal of environmental monitoring* **12**(2), 455–459.

Polymer Solutions Incorporated (2013), 'U.K. Grapples with recycling meat packaging waste'. Accessed: 06/05/2019.
URL:
https://www.polymersolutions.com/blog/uk-grapples-with-recycling-meat-packaging-waste/

Prathiba, R., Shruthi, M. and Miranda, L. (2018), 'Pyrolysis of polystyrene waste in the presence of activated carbon in conventional and microwave heating using modified thermocouple', *Waste Management* **76**, 528–536.

Prieto, G., Okumoto, M., Shimano, K., Takashima, K., Katsura, S. and Mizuno, A. (2001), 'Reforming of heavy oil using nonthermal plasma', *IEEE Transactions on industry applications* **37**(5), 1464–1467.

Punčochář, M., Ruj, B. and Chatterj, P. (2012), 'Development of process for disposal of plastic waste using plasma pyrolysis technology and option for energy recovery', *Procedia Engineering* **42**, 420–430.

Qi, X., Watanabe, M., Aida, T. and Smith J., R. L. (2009), 'Sulfated zirconia as a solid acid catalyst for the dehydration of fructose to 5-hydroxymethylfurfural', *Catalysis Communications* **10**(13), 1771–1775.

Rahimi, N. and Karimzadeh, R. (2011), 'Catalytic cracking of hydrocarbons over modified ZSM-5 zeolites to produce light olefins: A review', *Applied Catalysis A: General* **398**(1), 1–17.

Ratnasari, D., Nahil, M. and Williams, P. (2017), 'Catalytic pyrolysis of waste plastics using staged catalysis for production of gasoline range hydrocarbon oils', *Journal of Analytical and Applied Pyrolysis* **124**, 631 – 637.

Raynaud, J. (2014), Valuing Plastics: The Business Case for Measuring, Managing and Disclosing Plastic Use in the Consumer Goods Industry, Techreport, Truecost – UNEP.
URL: *www.unep.org/pdf/ValuingPlastic/*

Reddy, B., Sreekanth, P. and Lakshmanan, P. (2005), 'Sulfated zirconia as an efficient catalyst for organic synthesis and transformation reactions', *Journal of molecular catalysis A: Chemical* **237**(1), 93–100.

Reed, T. (2016), 'The Boudouard Equilibrium - Gasifiers'. Accessed: 12/01/2016.
URL: *http://gasifiers.bioenergylists.org/files/boudouard_reaction.xls*

Robinson, P. (2010), Studies on the preparation of supported nickel catalysts using bis(ethylenediamine) nickel (II) complexes as precursors, PhD thesis, Cochin University of Science and Technology, Kerala, India.

Rostrup-Nielsen, J. (1973), 'Activity of nickel catalysts for steam reforming of hydrocarbons', *Journal of Catalysis* **31**(2), 173–199.

Rotliwala, Y. and Parikh, P. (2012), 'Thermal co-processing of high density polyethylene with coal, fly ashes, and biomass: characterization of liquid products', *Energy Sources, Part A: Recovery, Utilization, and Environmental Effects* **34**(11), 1055–1066.

Rouquerol, J., Avnir, D., Fairbridge, C., Everett, D., Haynes, J., Pernicone, N., Ramsay, J., Sing, K. and Unger, K. (1994), 'Recommendations for the characterization of porous solids (Technical Report)', *Pure and Applied Chemistry* **66**(8), 1739–1758.

Saad, J. and Williams, P. (2016), 'Pyrolysis-catalytic-dry reforming of waste plastics and mixed waste plastics for syngas production', *Energy & Fuels* **30**(4), 3198–3204.

Saha, B. and Ghoshal, A. (2005), 'Thermal degradation kinetics of poly(ethylene terephthalate) from waste soft drinks bottles', *Chemical Engineering Journal* **111**(1), 39–43.

Sakata, Y., Uddin, M., Koizumi, K. and Murata, K. (1996), 'Thermal degradation of polyethylene mixed with poly (vinyl chloride) and poly(ethyleneterephthalate)', *Polymer Degradation and Stability* **53**(1), 111–117.

Sakata, Y., Uddin, M. and Muto, A. (1999), 'Degradation of polyethylene and polypropylene into fuel oil by using solid acid and non-acid catalysts', *Journal of Analytical and Applied Pyrolysis* **51**(1), 135–155.

Salmiaton, A. and Garforth, A. (2007), 'Waste catalysts for waste polymer', *Waste Management* **27**(12), 1891–1896.

San Fabián, E. and Pastor-Abia, L. (2007), 'Theoretical investigation of excited states of molecules. an application on the nitrogen molecule', *Theoretical Chemistry Accounts* **118**(3), 637–642.

San Miguel, G., Serrano, D. and Aguado, J. (2009), 'Valorization of waste agricultural polyethylene film by sequential pyrolysis and catalytic reforming', *Industrial & Engineering Chemistry Research* **48**(18), 8697–8703.

Sánchez-Jiménez, P. E., Pérez-Maqueda, L. A., Perejón, A. and Criado, J. M. (2010), 'Generalized kinetic master plots for the thermal degradation of polymers following a random scission mechanism', *The Journal of Physical Chemistry A* **114**(30), 7868–7876.

Sarker, M., Rashid, M. and Molla, M. (2011), 'Abundant high-density polyethylene (HDPE-2) turns into fuel by using of HZSM-5 catalyst', *Journal of Fundamentals of Renewable Energy and Applications* **1**, 1–12.

Sbirrazzuoli, N., Vincent, L., Mija, A. and Guigo, N. (2009), 'Integral, differential and advanced isoconversional methods - Complex mechanisms and isothermal predicted conversion-time curves', *Chemometrics and Intelligent Laboratory Systems* **96**, 219–226.

Scheirs, J. and Kaminsky, W. (2006), *Feedstock recycling and pyrolysis of waste plastic: converting waste plastic into diesel and other fuels*, John Wiley & Sons.

Schirinzi, G., Pérez-Pomeda, I., Sanchís, J., Rossini, C., Farré, M. and Barceló, D. (2017), 'Cytotoxic effects of commonly used nanomaterials and microplastics on cerebral and epithelial human cells', *Environmental research* **159**, 579–587.

Schutze, A., Jeong, J., Babayan, S., Park, J., Selwyn, G. and Hicks, R. (1998), 'The atmospheric-pressure plasma jet: a review and comparison to other plasma sources', *IEEE Transactions on Plasma Science* **26**(6), 1685–1694.

Sehested, J. (2006), 'Four challenges for nickel steam-reforming catalysts', *Catalysis Today* **111**(1-2), 103–110.

Serrano, D., Aguado, J. and Escola, J. (2000), 'Catalytic conversion of polystyrene over HMCM-41, HZSM-5 and amorphous SiO_2/Al_2O_3: comparison with thermal cracking', *Applied Catalysis B: Environmental* **25**(2), 181–189.

Serrano, D., Aguado, J. and Escola, J. (2012), 'Developing advanced catalysts for the conversion of polyolefinic waste plastics into fuels and chemicals', *ACS Catalysis* **2**(9), 1924–1941.

Serrano, D., Aguado, J., Garagorri, E., Rodríguez, J., Morselli, L., Palazzi, G., Orsi, R. et al. (2004), 'Feedstock recycling of agriculture plastic film wastes by catalytic cracking', *Applied Catalysis B: Environmental* **49**(4), 257–265.

Serrano, D., Aguado, J., Rodríguez, J. and Peral, A. (2007), 'Catalytic cracking of polyethylene over nanocrystalline HZSM-5: Catalyst deactivation and regeneration study', *Journal of Analytical and Applied Pyrolysis* **79**(1), 456–464.

Sharuddin, S., Abnisa, F., Daud, W. and Aroua, M. (2016), 'A review on pyrolysis of plastic wastes', *Energy conversion and management* **115**, 308–326.

Shonfield, P. (2008), 'LCA of management options for mixed waste plastics', *WRAP, UK* .

Siddiqui, M. and Redhwi, H. (2009), 'Pyrolysis of mixed plastics for the recovery of useful products', *Fuel Processing Technology* **90**(4), 545–552.

Simha, R. and Wall, L. A. (1952), 'Kinetics of chain depolymerization', *The Journal of Physical Chemistry* **56**(6), 707–715.

Singh, R., Ruj, B., Sadhukhan, A. and Gupta, P. (2019), 'Impact of fast and slow pyrolysis on the degradation of mixed plastic waste: Product yield analysis and their characterization', *Journal of the Energy Institute* .

Singh, S., Wu, C. and Williams, P. (2012), 'Pyrolysis of waste materials using TGA-MS and TGA-FTIR as complementary characterisation techniques', *Journal of Analytical and Applied Pyrolysis* **94**, 99–107.

Sobeih, K., Baron, M. and Gonzalez-Rodriguez, J. (2008), 'Recent trends and developments in pyrolysis–gas chromatography', *Journal of Chromatography A* **1186**(1-2), 51–66.

Sohn, J. and Lee, D. (2003), 'Characterization of zirconium sulfate supported on TiO_2 and activity for acid catalysis', *Korean Journal of Chemical Engineering* **20**(6), 1030–1036.

Son, J., Gwon, T. and Kim, S. (2001), 'Characterization of zirconium sulfate supported on zirconia and activity for acid catalysis', *Bulletin of the Korean Chemical Society* **22**(12), 1309–1315.

Song, H., Choi, J., Yue, S., Lee, H. and Na, B. (2004), 'Synthesis gas production via dielectric barrier discharge over Ni/γ-Al_2O_3 catalyst', *Catalysis Today* **89**(1), 27–33.

Sorum, L., Gronli, M. and Hustad, J. (2001), 'Pyrolysis characteristics and kinetics of municipal solid wastes', *Fuel* **80**, 1217–1227.

Srinivasan, R., Keogh, R. and Davis, B. (1996), 'Sulfated zirconia catalysts: Are Brønsted acid sites the source of the activity?', *Catalysis letters* **36**(1-2), 51–57.

Srinivasan, R., Keogh, R., Milburn, D. and Davis, B. (1995), 'Sulfated zirconia catalysts: Characterization by TGA/DTA mass spectrometry', *Journal of Catalysis* **153**(1), 123–130.

Staffell, I. and Dodds, P. (2017), 'The role of hydrogen and fuel cells in future energy systems', *H2FC SUPERGEN, London, UK* .

Stephenson, W. (2018), 'Why plastic recycling is so confusing'. Accessed: 06/05/2019. **URL:** *https://www.bbc.co.uk/news/science-environment-45496884*

Stichert, W. and Schüth, F. (1998), 'Synthesis of catalytically active high surface area monoclinic sulfated zirconia', *Journal of Catalysis* **174**(2), 242–245.

Strydom, C. and Pretorius, G. (1993), 'The thermal decomposition of zirconium sulphate hydrate', *Thermochimica acta* **223**, 223–232.

Sun, K., Huang, Q., Ali, M., Chi, Y. and Yan, J. (2018), 'Producing aromatic-enriched oil from mixed plastics using activated biochar as catalyst', *Energy & Fuels* **32**(4), 5471–5479.

Sushil, S. and Batra, V. (2008), 'Catalytic applications of red mud, an aluminium industry waste: A review', *Applied Catalysis B: Environmental* **81**(1), 64–77.

Takeguchi, T., Kani, Y., Yano, T., Kikuchi, R., Eguchi, K., Tsujimoto, K., Uchida, Y., Ueno, A., Omoshiki, K. and Aizawa, M. (2002), 'Study on steam reforming of CH_4 and C_2 hydrocarbons and carbon deposition on Ni-YSZ cermets', *Journal of Power Sources* **112**(2), 588–595.

Tang, L. and Huang, H. (2007), 'Decomposition of polyethylene in radio-frequency nitrogen and water steam plasmas under reduced pressures', *Fuel Processing Technology* **88**(6), 549–556.

Tang, L., Huang, H., Zhao, Z., Wu, C. and Chen, Y. (2003), 'Pyrolysis of polypropylene in a nitrogen plasma reactor', *Industrial & Engineering Chemistry Research* **42**(6), 1145–1150.

Tangchupong, N., Khaodee, W., Jongsomjit, B., Laosiripojana, N., Praserthdam, P. and Assabumrungrat, S. (2010), 'Effect of calcination temperature on characteristics of sulfated zirconia and its application as catalyst for isosynthesis', *Fuel Processing Technology* **91**(1), 121–126.

Ten Brink, P., Schweitzer, J., Watkins, E., Janssens, C., De Smet, M., Leslie, H. and Galgani, F. (2018), Circular economy measures to keep plastics and their value in the economy, avoid waste and reduce marine litter, Technical report, Economics Discussion Papers.

Tendero, C., Tixier, C., Tristant, P., Desmaison, J. and Leprince, P. (2006), 'Atmospheric pressure plasmas: A review', *Spectrochimica Acta Part B: Atomic Spectroscopy* **61**(1), 2–30.

Teo, K., Lee, S., Chhowalla, M., Semet, V., Binh, V., Groening, O., Castignolles, M., Loiseau, A., Pirio, G., Legagneux, P., Pribat, D., Hasko, D., Ahmed, H., Amaratunga, G. and Milne, W. (2003), 'Plasma enhanced chemical vapour deposition carbon nanotubes/nanofibres—how uniform do they grow?', *Nanotechnology* **14**, 204–211.

Teuten, E., Saquing, J., Knappe, D., Barlaz, M., Jonsson, S., Björn, A., Rowland, S., Thompson, R., Galloway, T., Yamashita, R., Ochi, D., Watanuki, Y., Moore, C., Viet, P., Tana, T., Prudente, M., Boonyatumanond, R., Zakaria, M., Akkhavong, K., Ogata, Y., Hirai, H., Iwasa, S., Mizukawa, K., Hagino, Y., Imamura, A., Saha, M. and Takada, H. (2009), 'Transport and release of chemicals from plastics to the environment and to wildlife', *Philosophical Transactions of the Royal Society of London B: Biological Sciences* **364**(1526), 2027–2045.

Themelis, N. and Mussche, C. (2014), 2014 Energy and economic value of municipal solid waste (MSW), including non-recycled plastics (NRP), currently landfilled in the fifty States, Technical report, Earth Engineering Center - Columbia University. Accessed: 10/04/2015. **URL:** *https://www.americanchemistry.com/policy/energy/energy-recovery/2014-update-of-potential-for-energy-recovery-from-municipal-solid-waste-and-non-recycled-plastics.pdf*

Thompson, R., Moore, C., Vom Saal, F. and Swan, S. (2009), 'Plastics, the environment and human health: current consensus and future trends', *Philosophical Transactions of the Royal Society B: Biological Sciences* **364**(1526), 2153–2166.

Tripathi, P., Durbach, S. and Coville, N. (2017), 'Synthesis of Multi-Walled Carbon Nanotubes from Plastic Waste Using a Stainless-Steel CVD Reactor as Catalyst', *Nanomaterials* **7**(10), 284–301.

Tu, X. and Whitehead, J. (2012), 'Plasma-catalytic dry reforming of methane in an atmospheric dielectric barrier discharge: Understanding the synergistic effect at low temperature', *Applied Catalysis B: Environmental* **125**, 439–448.

Uemichi, Y., Hattori, M., Itoh, T., Nakamura, J. and Sugioka, M. (1998), 'Deactivation behaviors of zeolite and silica- alumina catalysts in the degradation of polyethylene', *Industrial & Engineering Chemistry Research* **37**(3), 867–872.

Uemichi, Y., Makino, Y. and Kanazuka, T. (1989), 'Degradation of polyethylene to aromatic hydrocarbons over metal-supported activated carbon catalysts', *Journal of analytical and applied pyrolysis* **14**(4), 331–344.

UK Department for Business, Energy & Industrial Strategy (2017), 'Industrial electricity prices in the IEA (QEP 5.3.1)'. Accessed: 25/01/2017.
URL:
https://www.gov.uk/government/statistical-data-sets/international-industrial-energy-prices

Urashima, K. and Chang, J. (2000), 'Removal of volatile organic compounds from air streams and industrial flue gases by non-thermal plasma technology', *IEEE Transactions on Dielectrics and Electrical Insulation* **7**(5), 602–614.

U.S. Environmental Protection Agency (EPA) (2016), 'Together, we can make a difference'. Accessed: 13/06/2016.
URL:
https://www.epa.gov/sites/production/files/2015-09/documents/advncng_smm_infogrphc.pdf

Van Cauwenberghe, L. and Janssen, C. (2014), 'Microplastics in bivalves cultured for human consumption', *Environmental pollution* **193**, 65–70.

Van der Stelt, M., Gerhauser, H., Kiel, J. and Ptasinski, K. (2011), 'Biomass upgrading by torrefaction for the production of biofuels: A review', *Biomass and bioenergy* **35**(9), 3748–3762.

Van Durme, J., Dewulf, J., Leys, C. and Van Langenhove, H. (2008), 'Combining non-thermal plasma with heterogeneous catalysis in waste gas treatment: a review', *Applied Catalysis B: Environmental* **78**(3), 324–333.

Vasile, C., Pakdel, H., Mihai, B., Onu, P., Darie, H. and Ciocâlteu, S. (2001), 'Thermal and catalytic decomposition of mixed plastics', *Journal of analytical and Applied Pyrolysis* **57**(2), 287–303.

Velis, C. (2014), Global recycling markets – plastic waste: A story for one player – China, Technical report, Prepared by FUELogy and formatted by D-waste on behalf of International Solid Waste Association, Vienna. Accessed: 30/09/2014.
URL: *https://www.iswa.org/fileadmin/galleries/Task_Forces/TFGWM_Report_GRM_-Plastic_China_LR.pdf*

Venkatachalam, S., Kelkar, A. K., Labde, J. V., Rao, K., Gharal, P. R. and Nayak, S. G. (2012), Degradation and recyclability of Poly(ethylene terephthalate), *in* H. Saleh, ed., 'Polyester', INTECH Open Access Publisher, chapter 4.

Verma, R., Vinoda, K., Papireddy, M. and Gowda, A. (2016), 'Toxic Pollutants from Plastic Waste-A Review', *Procedia Environmental Sciences* **35**, 701–708.

Virta, R. (1997), Zeolites, Technical report, U.S. Geological Survey - Minerals Information.

Vishwanathan, V., Balakrishna, G., Rajesh, B., Jayasri, V., Sikhwivhilu, L. and Coville, N. (2008), 'Alkylation of catechol with methanol to give guaiacol over sulphate-modified zirconia solid acid catalysts: The influence of structural modification of zirconia on catalytic performance', *Catalysis Communications* **9**(14), 2422–2427.

Vitolo, S., Bresci, B., Seggiani, M. and Gallo, M. (2001), 'Catalytic upgrading of pyrolytic oils over HZSM-5 zeolite: behaviour of the catalyst when used in repeated upgrading–regenerating cycles', *Fuel* **80**(1), 17–26.

Vogt, E. and Weckhuysen, B. (2015), 'Fluid catalytic cracking: recent developments on the grand old lady of zeolite catalysis', *Chemical Society Reviews* **44**(20), 7342–7370.

Vyas, D., Dave, U. and Parekh, H. (2011), Plasma pyrolysis: an innovative treatment to solid waste of plastic material, *in* 'National conference on recent trends in engineering & technology, NCRTET, Gujarat'.

Vyazovkin, S. (2006), 'Model-free kinetics: Staying free of multiplying entities without necessity', *Journal of Thermal Analysis and Calorimetry* **83**, 45 – 51.

Vyazovkin, S. (2015), *Isoconversional Kinetics of Thermally Stimulated Processes*, Springer.

Vyazovkin, S., Burnham, A. K., Criado, J. M., Pérez-Maqueda, L. A., Popescu, C. and Sbirrazzuoli, N. (2011), 'ICTAC Kinetics Committee recommendations for performing kinetic computations on thermal analysis data', *Thermochimica Acta* **520**(1–2), 1 – 19.

Vyazovkin, S. and Sbirrazzuoli, N. (2006), 'Isoconversional Kinetic Analysis of Thermally Stimulated Processes in Polymers', *Macromolecular Rapid Communications* **27**(18), 1515–1532.

Wampler, T. (1989), 'Thermometric behaviour of polyolefins', *Journal of Analytical and Applied Pyrolysis* **15**, 187–195.

Wang, F., Zhang, S., Chen, Z., Liu, C. and Wang, Y. (2014), 'Tar reforming using char as catalyst during pyrolysis and gasification of Shengli brown coal', *Journal of Analytical and Applied Pyrolysis* **105**, 269–275.

Wang, J. and Wang, L. (2011), 'Catalytic pyrolysis of municipal plastic waste to fuel with nickel-loaded silica-alumina catalysts', *Energy Sources, Part A: Recovery, Utilization, and Environmental Effects* **33**(21), 1940–1948.

Wang, L. and Xiao, F. (2015), 'Nanoporous catalysts for biomass conversion', *Green Chemistry* **17**(1), 24–39.

Wang, P., Zhang, J., Wang, G., Li, C. and Yang, C. (2016), 'Nature of active sites and deactivation mechanism for n-butane isomerization over alumina-promoted sulfated zirconia', *Journal of Catalysis* **338**, 124–134.

Ward, J. (1970), 'The nature of active sites on zeolites: XI. The effects of the silica-to-alumina ratio on the acidity and catalytic activity of synthetic faujasite-type zeolites', *Journal of Catalysis* **17**(3), 355–358.

Wei, T., Wu, K., Lee, S. and Lin, Y. (2010), 'Chemical recycling of post-consumer polymer waste over fluidizing cracking catalysts for producing chemicals and hydrocarbon fuels', *Resources, Conservation and Recycling* **54**(11), 952–961.

Weitkamp, J. and Puppe, L. (2013), *Catalysis and zeolites: fundamentals and applications*, Springer Science & Business Media, New York, USA.

Wen, G., Xu, Y., Xu, Z. and Tian, Z. (2009), 'Characterization and catalytic properties of the ni/Al_2O_3 catalysts for aqueous-phase reforming of glucose', *Catalysis letters* **129**(1-2), 250–257.

Westerhout, R., Waanders, J., Kuipers, J. and Van Swaaij, W. (1997), 'Kinetics of the low-temperature pyrolysis of polyethene, polypropene, and polystyrene modeling, experimental determination, and comparison with literature models and data', *Industrial & Engineering Chemistry Research* **36**, 1955–1964.

Williams, E. and Williams, P. (1997*a*), 'Analysis of products derived from the fast pyrolysis of plastic waste', *Journal of Analytical and Applied Pyrolysis* **40**, 347–363.

Williams, E. and Williams, P. (1997*b*), 'The pyrolysis of individual plastics and a plastic mixture in a fixed bed reactor', *Journal of Chemical Technology & Biotechnology: International Research in Process, Environmental and Clean Technology* **70**(1), 9–20.

Williams, P. and Bagri, R. (2004), 'Hydrocarbon gases and oils from the recycling of polystyrene waste by catalytic pyrolysis', *International Journal of Energy Research* **28**, 31–44.

Williams, P. and Slaney, E. (2007), 'Analysis of products from the pyrolysis and liquefaction of single plastics and waste plastic mixtures', *Resources, Conservation and Recycling* **51**(4), 754–769.

Williams, P. T. (2006), Yield and composition of gases and oils/waxes from the feedstock recycling of waste plastic, *in* 'Feedstock Recycling and Pyrolysis of Waste Plastics: Converting waste plastic into diesel and other fuels', John Wiley & Sons, chapter 11, pp. 285 – 314.

Williams, P. and Williams, E. (1998), 'Recycling plastic waste by pyrolysis', *Journal of the Institute of Energy* **71**(487), 81–93.

Williams, P. and Williams, E. (1999), 'Interaction of plastics in mixed-plastics pyrolysis', *Energy & Fuels* **13**(1), 188–196.

Witoon, T., Permsirivanich, T., Kanjanasoontorn, N., Akkaraphataworn, C., Seubsai, A., Faungnawakij, K., Warakulwit, C., Chareonpanich, M. and Limtrakul, J. (2015), 'Direct synthesis of dimethyl ether from CO_2 hydrogenation over cu-zno-ZrO_2/so_4^{2-}-ZrO_2 hybrid catalysts: effects of sulfur-to-zirconia ratios', *Catalysis Science & Technology* **5**(4), 2347–2357.

Wittcoff, H., Reuben, B. and Plotkin, J. (2013), *Industrial Organic Chemicals*, 3 edn, Wiley Online Library, New Jersey.

Wrap (2018), 'Carrier bags - material matters'. Accessed: 14/09/2018.
URL: *http://www.wrap.org.uk/content/carrier-bags-material-matters-0*

Wu, C., Chang, C., Hor, J., Shih, S., Chen, L. and Chang, F. (1993), 'On the thermal treatment of plastic mixtures of MSW: Pyrolysis kinetics', *Waste Management* **13**(3), 221–235.

Wu, C., Nahil, M., Miskolczi, N., Huang, J. and Williams, P. (2013), 'Processing real–world waste plastics by pyrolysis-reforming for hydrogen and high–value carbon nanotubes', *Environmental science & technology* **48**(1), 819–826.

Wu, C., Nahil, M., Miskolczi, N., Huang, J. and Williams, P. (2014), 'Processing real-world waste plastics by pyrolysis-reforming for hydrogen and high-value carbon nanotubes', *Environmental Science and Technology* **48**(1), 819–826.

Wu, C., Nahil, M., Miskolczi, N., Huang, J. and Williams, P. (2016), 'Production and application of carbon nanotubes, as a co-product of hydrogen from the pyrolysis-catalytic reforming of waste plastic', *Process Safety and Environmental Protection* **103**, 107–114.

Wu, C., Wang, Z., Wang, L., Williams, P. and Huang, J. (2012), 'Sustainable processing of waste plastics to produce high yield hydrogen-rich synthesis gas and high quality carbon nanotubes', *RSC Advances* **2**(10), 4045–4047.

Wu, C. and Williams, P. (2009*a*), 'Hydrogen production by steam gasification of polypropylene with various nickel catalysts', *Applied Catalysis B: Environmental* **87**(3-4), 152–161.

Wu, C. and Williams, P. (2009*b*), 'Investigation of Ni-Al, Ni-Mg-Al and Ni-Cu-Al catalyst for hydrogen production from pyrolysis–gasification of polypropylene', *Applied Catalysis B: Environmental* **90**(1-2), 147–156.

Wu, C. and Williams, P. (2010*a*), 'Pyrolysis–gasification of post–consumer municipal solid plastic waste for hydrogen production', *International Journal of Hydrogen Energy* **35**(3), 949–957.

Wu, C. and Williams, P. (2010*b*), 'Pyrolysis-gasification of post-consumer municipal solid plastic waste for hydrogen production', *International Journal of Hydrogen Energy* **35**(3), 949–957.

Xiao, D., Cheng, C., Shen, J., Lan, Y., Xie, H., Shu, X., Meng, Y., Li, J. and Chu, P. (2014), 'Characteristics of atmospheric-pressure non-thermal N_2 and N_2/O_2 gas mixture plasma jet', *Journal of Applied Physics* **115**(3), 033303–1–033303–10.

Xingzhong, Y. (2006), *Feedstock Recycling and Pyrolysis of Waste Plastics: Converting Waste Plastics into Diesel and Other Fuels*, Wiley Online Library, chapter 28 - Converting waste plastics into liquid fuel by pyrolysis: developments in China, pp. 729–755.

Yadav, G. and Nair, J. (1999), 'Sulfated zirconia and its modified versions as promising catalysts for industrial processes', *Microporous and mesoporous materials* **33**(1-3), 1–48.

Yadav, G. and Sengupta, S. (2002), 'Friedel- Crafts alkylation of diphenyl oxide with benzyl chloride over sulphated zirconia', *Organic Process Research & Development* **6**(3), 256–262.

Yamaguchi, T. (1990), 'Recent progress in solid superacid', *Applied Catalysis* **61**(1), 1–25.

Yang, Y.-C. and Weng, H.-S. (2010), 'Regeneration of coked Al-Promoted sulfated zirconia catalysts by high pressure hydrogen', *Industrial & Engineering Chemistry Research* **49**(4), 1982–1985.

Yanik, J., Uddin, M., Ikeuchi, K. and Sakata, Y. (2001), 'The catalytic effect of Red Mud on the degradation of poly(vinyl chloride) containing polymer mixture into fuel oil', *Polymer Degradation and Stability* **73**(2), 335–346.

Yao, D., Zhang, Y., Williams, P., Yang, H. and Chen, H. (2018), 'Co-production of hydrogen and carbon nanotubes from real-world waste plastics: Influence of catalyst composition and operational parameters', *Applied Catalysis B: Environmental* **221**, 584–597.

Yori, J., Luy, J. and Parena, J. (1989), 'Deactivation of H-mordenite and ZrO_2/SO_4^{2-} during n-butane isomerization', *Applied Catalysis* **46**(1), 103–112.

Yoshioka, T., Grause, G., Eger, C., Kaminsky, W. and Okuwaki, A. (2004), 'Pyrolysis of poly(ethylene terephthalate) in a fluidised bed plant', *Polymer Degradation and Stability* **86**(3), 499–504.

Yue, L., Li, G., He, G., Guo, Y., Xu, L. and Fang, W. (2016), 'Impacts of hydrogen to carbon ratio (H/C) on fundamental properties and supercritical cracking performance of hydrocarbon fuels', *Chemical Engineering Journal* **283**, 1216–1223.

Yue, Q., Wang, C., Zhang, L., Ni, Y. and Jin, Y. (2011), 'Glycolysis of poly(ethylene terephthalate)(PET) using basic ionic liquids as catalysts', *Polymer degradation and stability* **96**(4), 399–403.

Yue, Q., Xiao, L., Zhang, M. and Bai, X. (2013), 'The glycolysis of poly(ethylene terephthalate) waste: lewis acidic ionic liquids as high efficient catalysts', *Polymers* **5art**(4), 1258–1271.

Zhang, H. and Wen, Z. (2014), 'The consumption and recycling collection system of PET bottles: A case study of Beijing, China', *Waste Management* **34**(6), 987–998.

Zhang, K., Zhang, G., Liu, X., Phan, A. and Luo, K. (2017), 'A study on CO_2 decomposition to co and O_2 by the combination of catalysis and dielectric-barrier discharges at low temperatures and ambient pressure', *Industrial & Engineering Chemistry Research* **56**(12), 3204–3216.

Zhang, Y., Luo, Y., Wu, W., Zhao, S. and Long, Y. (2014), 'Heterogeneous cracking reaction of tar over biomass char, using naphthalene as model biomass tar', *Energy & Fuels* **28**(5), 3129–3137.

Zhang, Y., Nahil, M., Wu, C. and Williams, P. (2017), 'Pyrolysis–catalysis of waste plastic using a nickel–stainless-steel mesh catalyst for high–value carbon products', *Environmental technology* **38**(22), 2889–2897.

Zhang, Y., Wu, W., Zhao, S., Long, Y. and Luo, Y. (2015), 'Experimental study on pyrolysis tar removal over rice straw char and inner pore structure evolution of char', *Fuel Processing Technology* **134**, 333–344.

Zhou, J., Sui, Z., Li, P., Chen, D., Dai, Y. and Yuan, W. (2006), 'Structural characterization of carbon nanofibers formed from different carbon-containing gases', *Carbon* **44**(15), 3255–3262.

Appendix A Matlab code for kinetic model

```
%%%%%%%%%%%%%%%%%%%%%%%%%%%%%%%%%%%%%%%%%%%%%%%%%%%%%%%%%%%%%%%%%%%%%%%%%%%%
%%
%%file dialogue to get the polymer data
function a = kinetics()
%% KAS and FWO methods for determination of kinetic parameters
% This programme will extract TGA data from Excel into Matlab and analyse
% it following KAS, FWO and master plots methods to determine Ea
(activation energy), A
% (pre-exponential factor) and n (order of reaction).
%%%%%%%%%%%%%%%%%%%%%%%%%%%%%%%%%%%%%%%%%%%%%%%%%%%%%%%%%%%%%%%%%%%%%%%%%%%%
%%
%% DELETE PREVIOUS VARIABLES AND COMMAND WINDOW
    clear all; %Clear all variables
    close all; %Close all open windows (figures, etc.)
    clc;       %Delete Command Window
%%%%%%%%%%%%%%%%%%%%%%%%%%%%%%%%%%%%%%%%%%%%%%%%%%%%%%%%%%%%%%%%%%%%%%%%%%%%
%%
%% DEFINE GLOBAL VARIABLES AND CONSTANTS
    global HR05;
    global HR10;
    global HR20;
    global HR40;

    global HR05Clean;
    global HR10Clean;
    global HR20Clean;
    global HR40Clean;

    global HR05IsoConv;
    global HR10IsoConv;
    global HR20IsoConv;
    global HR40IsoConv;
    global isoConversion;
    global sourceConsts;
    global R;
    R = 8.314;
%%%%%%%%%%%%%%%%%%%%%%%%%%%%%%%%%%%%%%%%%%%%%%%%%%%%%%%%%%%%%%%%%%%%%%%%%%%%
%%
%%PROGRAMME
goOnWhile = true;
while goOnWhile
        close all; %Close all open windows (figures, etc.)
        Log('Select Excel Data File <or cancel to exit>...');
        excelPath = GetDataFilePath();
        %%excelPath = 'H:\MATLAB\data\PETdata.xlsx';

        Log('Parsing Excel Data File...');
        [sourceConsts, HR05, HR10, HR20, HR40] =
GetDataFromFile(excelPath);

        Log('Plotting data...');
        PlotAllInputData(HR05, HR10, HR20, HR40);

        Log('Data Sanitization by Conversion...');
        prompt  = '  ->Enter the minimum relevant conversion: ';
        %%minConversion = input(prompt);
```

```
        minConversion = 0.2;

        prompt  = '  ->Enter the maximum relevant conversion: ';
        %%maxConversion = input(prompt);
        maxConversion = 0.8;
        [HR05Clean, HR10Clean, HR20Clean, HR40Clean] = ...
            SanitizeDataByConversion(HR05, HR10, HR20, HR40,
minConversion, maxConversion);

        Log('Sampling for Relevant Data...');
        [HR05IsoConv, HR10IsoConv, HR20IsoConv, HR40IsoConv,
isoConversion] = ...
            CalculateIsoConversion(HR05Clean, HR10Clean, HR20Clean,
HR40Clean, minConversion, maxConversion);
        [pKAS, KASR2] = ...
            LinearRegression(HR05IsoConv, HR10IsoConv, HR20IsoConv,
HR40IsoConv);

        Log('Calculate Ea...');
        %KAS --> ln(HR/T^2)=ln(AR/Ea)-Ea/RT:
        %FWO --> ln(HR)=ln(A·Ea/R)-5.331-1.0516*Ea/RT:
        EaKAS        = (-pKAS(:,1) * R)/1000;
        AKAS         = exp(pKAS(:,2)) .* (EaKAS .* 1000) ./ R;
        AverageEaKAS = mean(EaKAS);

        %%sdd%% EaFWO  = (-pFWO(:,1) * R/1.0516)/1000;
        %%sdd%% AFWO   = exp(pFWO(:,2) + 5.331) .* R ./ (EaFWO .* 1000);

        Log('Plotting Ea Vs conversion...');
        PlotEaVsConversion(EaKAS, KASR2, HR05IsoConv, HR10IsoConv,
HR20IsoConv, HR40IsoConv);

        Log('Plotting Master Plots...');
        [BestHR05Fit, BestHR10Fit, BestHR20Fit, BestHR40Fit,
BestHR05Fit2, BestHR10Fit2, BestHR20Fit2, BestHR40Fit2] = ...
            MasterPlot(EaKAS, AverageEaKAS, HR05IsoConv, HR10IsoConv,
HR20IsoConv, HR40IsoConv, minConversion, maxConversion);

        Log('Linear model fitting...');
        [best_m, best_n, bestOptimal] = ...
            ModelFitting(HR05IsoConv, HR10IsoConv, HR20IsoConv,
HR40IsoConv);


fprintf('%%%%%%%%%%%%%%%%%%%%%%%%%%%%%%%%%%%%%%%%%%%%%%%%%%%%%%%%%%%%%%%%
%%%%%%%%%%%%%%%%%%%%%%%%%%%%%%%%%%%%%%%%\n');
        fprintf(' Presenting best fitting models for y(alpha) and
z(alpha) master plots respectively: %s:\n', excelPath);
        fprintf('  |->Best Model for HR05 :........ %s , %s.\n',
BestHR05Fit.Name{1},BestHR05Fit2.Name{1} );
        fprintf('     |->MSE     : %.4f , %.4f.\n', BestHR05Fit.MSE,
BestHR05Fit2.MSE);
        fprintf('  |->Best Model for HR10 :........ %s , %s.\n',
BestHR10Fit.Name{1},BestHR10Fit2.Name{1} );
```

```
        fprintf('     |->MSE     : %.4f , %.4f.\n', BestHR10Fit.MSE,
BestHR10Fit2.MSE);
        fprintf('  |->Best Model for HR20 :........ %s , %s.\n',
BestHR20Fit.Name{1},BestHR20Fit2.Name{1} );
        fprintf('     |->MSE     : %.4f , %.4f.\n', BestHR20Fit.MSE,
BestHR20Fit2.MSE);
        fprintf('  |->Best Model for HR40 :........ %s , %s.\n',
BestHR40Fit.Name{1},BestHR40Fit2.Name{1} );
        fprintf('     |->MSE     : %.4f , %.4f.\n', BestHR40Fit.MSE,
BestHR40Fit2.MSE);

fprintf('%%%%%%%%%%%%%%%%%%%%%%%%%%%%%%%%%%%%%%%%%%%%%%%%%%%%%%%%%%%%%%%%
%%%%%%%%%%%%%%%%%%%%%%%%%%%%%%%%%%%%%%%%\n');


fprintf('%%%%%%%%%%%%%%%%%%%%%%%%%%%%%%%%%%%%%%%%%%%%%%%%%%%%%%%%%%%%%%%%
%%%%%%%%%%%%%%%%%%%%%%%%%%%%%%%%%%%%%%%%\n');
        fprintf(' Presenting m and n that maximise Pearson linear
coefficient for truncated Sestak-Berggren: %s:\n', excelPath);
        fprintf('  |->Best Fitting:........ m  ,  n , Pearson\n');
        fprintf('     |->Results        : %.4f , %.4f , %.4f.\n', best_m,
best_n, bestOptimal);

fprintf('%%%%%%%%%%%%%%%%%%%%%%%%%%%%%%%%%%%%%%%%%%%%%%%%%%%%%%%%%%%%%%%%
%%%%%%%%%%%%%%%%%%%%%%%%%%%%%%%%%%%%%%%%\n');


%%%%%%%%%%%%%%%%%%%%%%%%%%%%%%%%%%%%%%%%%%%%%%%%%%%%%%%%%%%%%%%%%%%%%%%%%
%%
        prompt    = 'Do you want to process more data(y/n)?: ';
        val  = input(prompt, 's');
        goOnWhile = strcmp(lower(val), 'y') ||  strcmp(lower(val),
'yes');

%%%%%%%%%%%%%%%%%%%%%%%%%%%%%%%%%%%%%%%%%%%%%%%%%%%%%%%%%%%%%%%%%%%%%%%%%
%%
    end
end

%%This function writes the corrent step number on Command Window when
function "kinetics" is run
function Log(message)
    persistent logCounter;
    if isempty(logCounter)
        logCounter = 1;
    end

    fprintf('%d. %s\n',logCounter,message);
    logCounter = logCounter + 1;
end

%% This function extracts the Excel path and name of the selected file
and store them in a variable
function excelPath = GetDataFilePath()
    filename = 0;
    [filename, pathname] = uigetfile('*.xlsx', 'Select the data source');
```

```
    if filename == 0
        error('No file');
    end
    excelPath = fullfile(pathname, filename);
end

%% This function extracts data from Excel file selected. Inputs are the
file name and path obtained with previous function. Outputs are four
structures (one for each heating rate) with temperature, weight,
derivative weight, and heat flow and one structure with constants
(initial and final mass).
function [sourceConsts, HR05, HR10, HR20, HR40] =
GetDataFromFile(excelPath)
    ExcelSourceConsts = xlsread(excelPath,'Constants');
    ExcelSourceData   = xlsread(excelPath,'Data');
    % Get the constants out of the excel
    assert(ExcelSourceConsts(1, 1) == 5 , 'Wrong heating rate provided,
expected 5^{o}C/min');
    assert(ExcelSourceConsts(2, 1) == 10, 'Wrong heating rate provided,
expected 10^{o}C/min');
    assert(ExcelSourceConsts(3, 1) == 20, 'Wrong heating rate provided,
expected 20^{o}C/min');
    assert(ExcelSourceConsts(4, 1) == 40, 'Wrong heating rate provided,
expected 40^{o}C/min');

        sourceConsts.HR05.initialMass  = ExcelSourceConsts(1,2);
    sourceConsts.HR05.finalMass    = ExcelSourceConsts(1,3);
    sourceConsts.HR10.initialMass = ExcelSourceConsts(2,2);
    sourceConsts.HR10.finalMass   = ExcelSourceConsts(2,3);
    sourceConsts.HR20.initialMass = ExcelSourceConsts(3,2);
    sourceConsts.HR20.finalMass   = ExcelSourceConsts(3,3);
    sourceConsts.HR40.initialMass = ExcelSourceConsts(4,2);
    sourceConsts.HR40.finalMass   = ExcelSourceConsts(4,3);


%%%%%%%%%%%%%%%%%%%%%%%%%%%%%%%%%%%%%%%%%%%%%%%%%%%%%%%%%%%%%%%%%%%%%%%%
%%
    %Indexing excel data into Matlab for easy reading of the loop
    ColumnIndex.KtemperatureHR05 = 1;
    ColumnIndex.WeightHR05      = 2;
    ColumnIndex.dw_dtHR05       = 3;
    ColumnIndex.heatFlowHR05    = 4;

    ColumnIndex.KtemperatureHR10 = 5;
    ColumnIndex.WeightHR10      = 6;
    ColumnIndex.dw_dtHR10       = 7;
    ColumnIndex.heatFlowHR10    = 8;

    ColumnIndex.KtemperatureHR20 = 9;
    ColumnIndex.WeightHR20      = 10;
    ColumnIndex.dw_dtHR20       = 11;
    ColumnIndex.heatFlowHR20    = 12;

    ColumnIndex.KtemperatureHR40 = 13;
    ColumnIndex.WeightHR40      = 14;
    ColumnIndex.dw_dtHR40       = 15;
```

```
    ColumnIndex.heatFlowHR40    = 16;

    ColumnIndex.massHR05        = 17;
    ColumnIndex.massHR10        = 18;
    ColumnIndex.massHR20        = 19;
    ColumnIndex.massHR40        = 20;

    ColumnIndex.conversionHR05  = 21;
    ColumnIndex.conversionHR10  = 22;
    ColumnIndex.conversionHR20  = 23;
    ColumnIndex.conversionHR40  = 24;

%%%%%%%%%%%%%%%%%%%%%%%%%%%%%%%%%%%%%%%%%%%%%%%%%%%%%%%%%%%%%%%%%%%%%%%%%%%%
%%
    %Storing data into structures
    for i=1:length(ExcelSourceData)
        fprintf('.');
        HR05(i).Ktemperature =
ExcelSourceData(i,ColumnIndex.KtemperatureHR05) + 273;
        HR05(i).mass         = ExcelSourceData(i,ColumnIndex.WeightHR05)
/ 100 * sourceConsts.HR05.initialMass;
        HR05(i).conversion   = (sourceConsts.HR05.initialMass -
HR05(i).mass)  / (sourceConsts.HR05.initialMass -
sourceConsts.HR05.finalMass);
        HR05(i).weight       = ExcelSourceData(i,ColumnIndex.WeightHR05);
        HR05(i).dw_dt        = ExcelSourceData(i,ColumnIndex.dw_dtHR05);
        HR05(i).dalpha_dt    = -(sourceConsts.HR05.initialMass) *
HR05(i).dw_dt;
        HR05(i).dx_dt        = (sourceConsts.HR05.initialMass) *
HR05(i).dw_dt;


        HR10(i).Ktemperature =
ExcelSourceData(i,ColumnIndex.KtemperatureHR10) + 273;
        HR10(i).mass         = ExcelSourceData(i,ColumnIndex.WeightHR10)
/ 100 * sourceConsts.HR10.initialMass;
        HR10(i).conversion   = (sourceConsts.HR10.initialMass -
HR10(i).mass) / (sourceConsts.HR10.initialMass -
sourceConsts.HR10.finalMass);
        HR10(i).weight       = ExcelSourceData(i,ColumnIndex.WeightHR10);
        HR10(i).dw_dt        = ExcelSourceData(i,ColumnIndex.dw_dtHR10);
        HR10(i).dalpha_dt    = -(sourceConsts.HR10.initialMass) *
HR10(i).dw_dt;
        HR10(i).dx_dt        = (sourceConsts.HR10.initialMass) *
HR10(i).dw_dt;


        HR20(i).Ktemperature =
ExcelSourceData(i,ColumnIndex.KtemperatureHR20) + 273;
        HR20(i).mass         = ExcelSourceData(i,ColumnIndex.WeightHR20)
/ 100 * sourceConsts.HR20.initialMass;
        HR20(i).conversion   = (sourceConsts.HR20.initialMass -
HR20(i).mass)  / (sourceConsts.HR20.initialMass  -
sourceConsts.HR20.finalMass);
        HR20(i).weight       = ExcelSourceData(i,ColumnIndex.WeightHR20);
        HR20(i).dw_dt        = ExcelSourceData(i,ColumnIndex.dw_dtHR20);
```

```
        HR20(i).dalpha_dt    = -(sourceConsts.HR20.initialMass) *
HR20(i).dw_dt;
        HR20(i).dx_dt        = (sourceConsts.HR20.initialMass) *
HR20(i).dw_dt;


        HR40(i).Ktemperature =
ExcelSourceData(i,ColumnIndex.KtemperatureHR40) + 273;
        HR40(i).mass         = ExcelSourceData(i,ColumnIndex.WeightHR40)
/ 100 * sourceConsts.HR40.initialMass;
        HR40(i).conversion   = (sourceConsts.HR40.initialMass -
HR40(i).mass) / (sourceConsts.HR40.initialMass  -
sourceConsts.HR40.finalMass);
        HR40(i).weight       = ExcelSourceData(i,ColumnIndex.WeightHR40);
        HR40(i).dw_dt        = ExcelSourceData(i,ColumnIndex.dw_dtHR40);
        HR40(i).dalpha_dt    = -(sourceConsts.HR40.initialMass) *
HR40(i).dw_dt;
        HR40(i).dx_dt        = (sourceConsts.HR40.initialMass) *
HR40(i).dw_dt;

    end
    fprintf('\n');
end

%% This function plots Weight and Conversion Vs Temperature for a single
heating rate so appropriate conversion range for analysis can be chosen
function PlotSingleHRData(fig, HRData, color)
    subplot(2,2,1)
    title('Weight Vs T')
    hold on
    grid on
    plot([HRData.Ktemperature] - 273,  [HRData.weight],
color,'LineWidth',2);
    xlabel('Temperature (^{o}C)');
    ylabel('Weight (%)');
    xlim([30 700]);
    hold off

    subplot(2,2,2)
    hold on
    grid on
    title('Conversion Vs T')
    plot([HRData.Ktemperature] -273, [HRData.conversion],
color,'LineWidth',2)
    xlabel('Temperature (^{o}C)');
    ylabel('Conversion (-)');
    xlim([30 700]);
    ylim([0 1]);
    hold off

    subplot(2,2,3:4)
    hold on
    grid on
    title('Conversion Vs T')
    plot([HRData.Ktemperature] -273, [HRData.dw_dt], color,'LineWidth',2)
    xlabel('Temperature (^{o}C)');
```

```
    ylabel('dw/dt (%/min)');
    xlim([30 700]);
    %ylim([0 1]);
    hold off

end

%% This function compiles previous plots for all heating rates (to
facilitate debugging of the programme)
function PlotAllInputData(HR05, HR10, HR20, HR40)
    fig1=figure;
    set(fig1,'Color','w');
    PlotSingleHRData(fig1, HR05, 'b');
    PlotSingleHRData(fig1, HR10, 'g');
    PlotSingleHRData(fig1, HR20, 'r');
    PlotSingleHRData(fig1, HR40, 'k');
    subplot(2,2,1)

legend('5^{o}C/min','10^{o}C/min','20^{o}C/min','40^{o}C/min','Location',
'NorthEast');
    subplot(2,2,2)

legend('5^{o}C/min','10^{o}C/min','20^{o}C/min','40^{o}C/min','Location',
'NorthWest');
    subplot(2,2,3:4)

legend('5^{o}C/min','10^{o}C/min','20^{o}C/min','40^{o}C/min','Location',
'NorthWest');
end

%% This function sanitize data: remove data out of selected range and
sorts data in ascending order of conversion
function [HR05Clean, HR10Clean, HR20Clean, HR40Clean] =
SanitizeDataByConversion(HR05, HR10, HR20, HR40, minConversion,
maxConversion)
    HR05CleanTemp = HR05([HR05(:).conversion] >= minConversion &
[HR05(:).conversion] <= maxConversion);
    HR10CleanTemp = HR10([HR10(:).conversion] >= minConversion &
[HR10(:).conversion] <= maxConversion);
    HR20CleanTemp = HR20([HR20(:).conversion] >= minConversion &
[HR20(:).conversion] <= maxConversion);
    HR40CleanTemp = HR40([HR40(:).conversion] >= minConversion &
[HR40(:).conversion] <= maxConversion);

    Log('Sorting Data by Mass Conversion...');
    [preSort, postSort] = sort([HR05CleanTemp(:).conversion],'ascend');
    HR05Clean = HR05CleanTemp(postSort);
    [preSort, postSort] = sort([HR10CleanTemp(:).conversion],'ascend');
    HR10Clean = HR10CleanTemp(postSort);
    [preSort, postSort] = sort([HR20CleanTemp(:).conversion],'ascend');
    HR20Clean = HR20CleanTemp(postSort);
    [preSort, postSort] = sort([HR40CleanTemp(:).conversion],'ascend');
    HR40Clean = HR40CleanTemp(postSort);
end
```

```
%% This function obtains all the values of temperature, weight,
derivative weight and heat flow in the range of conversion +- threshold
(e.g. form 0.045 to 0.055) and calculate the median which is assigned as
the values for that level of conversion (e.g. the median of all entries
within the range 0.045 to 0.055 are assigned to conversion = 0.05). The
loop runs from selected values of minimum and maximum conversion
previously selected.
function [HR05IsoConv, HR10IsoConv, HR20IsoConv,
HR40IsoConv,isoConversion] = CalculateIsoConversion(HR05, HR10, HR20,
HR40, minConversion, maxConversion)
    threshold = 0.004;
    i = 0;
    for conversionIter = minConversion:0.01:maxConversion
        fprintf('.');
        i = i + 1 ;

        HR05Sampled  = HR05([HR05(:).conversion] >= (conversionIter -
threshold) & [HR05(:).conversion] <= (conversionIter + threshold));
        HR10Sampled  = HR10([HR10(:).conversion] >= (conversionIter -
threshold) & [HR10(:).conversion] <= (conversionIter + threshold));
        HR20Sampled  = HR20([HR20(:).conversion] >= (conversionIter -
threshold) & [HR20(:).conversion] <= (conversionIter + threshold));
        HR40Sampled  = HR40([HR40(:).conversion] >= (conversionIter -
threshold) & [HR40(:).conversion] <= (conversionIter + threshold));

        isoConversion(i).HR05 =  struct( 'Ktemperature',
median(table2array(table(HR05Sampled.Ktemperature)))...
                                        , 'mass'        ,
median(table2array(table(HR05Sampled.mass)))...
                                        , 'conversion'  ,
median(table2array(table(HR05Sampled.conversion)))...
                                        , 'weight'      ,
median(table2array(table(HR05Sampled.weight)))...
                                        , 'dw_dt'       ,
median(table2array(table(HR05Sampled.dw_dt)))...
                                        , 'dalpha_dt'   ,
median(table2array(table(HR05Sampled.dalpha_dt)))...
                                        , 'KAS'         , 0 ...
                                        , 'NumEntries'  ,
length(HR05Sampled));

        isoConversion(i).HR10 =  struct( 'Ktemperature',
median(table2array(table(HR10Sampled.Ktemperature)))...
                                        , 'mass'        ,
median(table2array(table(HR10Sampled.mass)))...
                                        , 'conversion'  ,
median(table2array(table(HR10Sampled.conversion)))...
                                        , 'weight'      ,
median(table2array(table(HR10Sampled.weight)))...
                                        , 'dw_dt'       ,
median(table2array(table(HR10Sampled.dw_dt)))...
                                        , 'dalpha_dt'   ,
median(table2array(table(HR10Sampled.dalpha_dt)))...
                                        , 'KAS'         , 0 ...
                                        , 'NumEntries'  ,
length(HR10Sampled));
```

```
        isoConversion(i).HR20 =  struct( 'Ktemperature',
median(table2array(table(HR20Sampled.Ktemperature))),...
                                        , 'mass'        ,
median(table2array(table(HR20Sampled.mass))),...
                                        , 'conversion'  ,
median(table2array(table(HR20Sampled.conversion))),...
                                        , 'weight'      ,
median(table2array(table(HR20Sampled.weight))),...
                                        , 'dw_dt'       ,
median(table2array(table(HR20Sampled.dw_dt))),...
                                        , 'dalpha_dt'   ,
median(table2array(table(HR20Sampled.dalpha_dt))),...
                                        , 'KAS'         , 0 ...
                                        , 'NumEntries'  ,
length(HR20Sampled));

        isoConversion(i).HR40 =  struct( 'Ktemperature',
median(table2array(table(HR40Sampled.Ktemperature))),...
                                        , 'mass'        ,
median(table2array(table(HR40Sampled.mass))),...
                                        , 'conversion'  ,
median(table2array(table(HR40Sampled.conversion))),...
                                        , 'weight'      ,
median(table2array(table(HR40Sampled.weight))),...
                                        , 'dw_dt'       ,
median(table2array(table(HR40Sampled.dw_dt))),...
                                        , 'dalpha_dt'   ,
median(table2array(table(HR40Sampled.dalpha_dt))),...
                                        , 'KAS'         , 0 ...
                                        , 'NumEntries'  ,
length(HR40Sampled));

        isoConversion(i).HR05.KAS =  log(05 /
((isoConversion(i).HR05.Ktemperature)^2));
        isoConversion(i).HR10.KAS =  log(10 /
((isoConversion(i).HR10.Ktemperature)^2));
        isoConversion(i).HR20.KAS =  log(20 /
((isoConversion(i).HR20.Ktemperature)^2));
        isoConversion(i).HR40.KAS =  log(40 /
((isoConversion(i).HR40.Ktemperature)^2));

        %%sdd%% isoConversion(i).HR05.FWO =  log(05);
        %%sdd%% isoConversion(i).HR10.FWO =  log(10);
        %%sdd%% isoConversion(i).HR20.FWO =  log(20);
        %%sdd%% isoConversion(i).HR40.FWO =  log(40);
    end

    %%NOTE 1: this can be removed; is kept here to make sure the data is
valid and that there are not
    %values of conversion with 0 entries in the database
    tempHR05        = [isoConversion.HR05];
    HR05IsoConv     = tempHR05([tempHR05.NumEntries] >= 1 );
    notHR05IsoConv  = tempHR05([tempHR05.NumEntries] == 0 );

    tempHR10        = [isoConversion.HR10];
```

```
    HR10IsoConv     = tempHR10([tempHR10.NumEntries] >= 1 );
    notHR10IsoConv  = tempHR10([tempHR10.NumEntries] == 0 );

    tempHR20        = [isoConversion.HR20];
    HR20IsoConv     = tempHR20([tempHR20.NumEntries] >= 1 );
    notHR20IsoConv  = tempHR20([tempHR20.NumEntries] == 0 );

    tempHR40        = [isoConversion.HR40];
    HR40IsoConv     = tempHR40([tempHR40.NumEntries] >= 1 );
    notHR40IsoConv  = tempHR40([tempHR40.NumEntries] == 0 );

    fprintf('.\n');

    assert(length(HR05IsoConv) + length(notHR05IsoConv) ==
length(tempHR05));
    assert(length(HR10IsoConv) + length(notHR10IsoConv) ==
length(tempHR10));
    assert(length(HR20IsoConv) + length(notHR20IsoConv) ==
length(tempHR20));
    assert(length(HR40IsoConv) + length(notHR40IsoConv) ==
length(tempHR40));
end

%% This function calculates the linear regression of isoconversion plots
function [pKAS, KASR2] =  LinearRegression(HR05, HR10, HR20, HR40)
    assert(length(HR05) == length(HR10) ...
        && length(HR05) == length(HR20) ...
        && length(HR05) == length(HR40));

    len = length(HR05);
    for j=1:len
        %KAS
        x(j,:)              =
([HR05(j).Ktemperature,HR10(j).Ktemperature,HR20(j).Ktemperature,HR40(j).
Ktemperature]);
        yKAS(j,:)           = ([HR05(j).KAS,                HR10(j).KAS,
HR20(j).KAS,                HR40(j).KAS]);
        xReciprocal         = 1./x;
        pKAS(j,:)           = polyfit(xReciprocal(j,:),yKAS(j,:),1);
        yKASFits(j,:)       = pKAS(j,2) + pKAS(j,1) .* xReciprocal(j,:);
        KASResiduals        = yKAS - yKASFits;
        KASSSResiduals(j)   = sum(KASResiduals(j,:).^2);
        KASSSTotal(j)       = (length(yKAS(j,:)) - 1) * var(yKAS(j,:));
        KASR2(j)            = 1-(KASSSResiduals/KASSSTotal);

        %FWO
        %%sdd%% yFWO(j,:)           = ([HR05(j).FWO, HR10(j).FWO,
HR20(j).FWO, HR40(j).FWO]);
        %%sdd%% pFWO(j,:)           =
polyfit(xReciprocal(j,:),yFWO(j,:),1);
        %%sdd%% yFWOFits(j,:)       = pFWO(j,2) + pFWO(j,1) .*
xReciprocal(j,:);
        %%sdd%% FWOResiduals        = yFWO - yFWOFits;
        %%sdd%% FWOSSResiduals(j)   = sum(FWOResiduals(j,:).^2);
        %%sdd%% FWOSSTotal(j)       = (length(yFWO(j,:)) - 1) *
var(yFWO(j,:));
```

```
        %%sdd%% FWOR2(j)            = 1-(FWOSSResiduals/FWOSSTotal);
    end
end

%% This function plots the variation of activation energy with conversion
and the goodness of fit obtain from the linear regression for every value
of conversion
function PlotEaVsConversion(EaKAS, KASR2, HR05, HR10, HR20, HR40)
    fig2=figure;
    set(fig2,'Color','w');
    %set(fig1, 'Units', 'pixels', 'Position', [100, 100, 1000, 400]);
    subplot(2,1,1)
    title('KAS - Ea Vs Conversion')
    hold on
    grid on
    plot([HR05.conversion], EaKAS, 'b','LineWidth',2)
    plot([HR10.conversion], EaKAS, 'g','LineWidth',2)
    plot([HR20.conversion], EaKAS, 'r','LineWidth',2)
    plot([HR40.conversion], EaKAS, 'k','LineWidth',2)

legend('5^{o}C/min','10^{o}C/min','20^{o}C/min','40^{o}C/min','Location',
'NorthWest');
    xlabel('Conversion');
    ylabel('Ea (kJ/mol)');
    xlim([0.1 0.8]);
    ylim([100 300]);
    hold off

    %conv = [0.05:0.02:0.83];
    subplot(2,1,2)
    title('KAS - R^2')
    hold on
    grid on
    %plot(conv, KASR2, 'b','LineWidth',2)
    plot([HR05.conversion], KASR2, 'b*','LineWidth',2)
    plot([HR10.conversion], KASR2, 'g*','LineWidth',2)
    plot([HR20.conversion], KASR2, 'r*','LineWidth',2)
    plot([HR40.conversion], KASR2, 'k*','LineWidth',2)

    xlabel('Conversion');
    ylabel('R^2');
    xlim([0.1 0.8]);
    hold off

    %%sdd%% subplot(2,2,3)
    %%sdd%% title('FWO - Ea Vs Conversion')
    %%sdd%% hold on
    %%sdd%% grid on
    %%sdd%% plot([HR05.conversion], EaFWO, 'b','LineWidth',2)
    %%sdd%% plot([HR10.conversion], EaFWO, 'g','LineWidth',2)
    %%sdd%% plot([HR20.conversion], EaFWO, 'r','LineWidth',2)
    %%sdd%% plot([HR40.conversion], EaFWO, 'k','LineWidth',2)
    %%sdd%%
legend('5^{o}C)/min','10^{o}C)/min','20^{o}C)/min','40^{o}C)/min','Locati
on','NorthWest');
    %%sdd%% xlabel('Conversion');
```

```
    %%sdd%% ylabel('Ea (J/mol)');
    %%sdd%% xlim([0.1 0.8]);
    %%sdd%% hold off

    %%sdd%% subplot(2,2,4)
    %%sdd%% title('KAS - R^2')
    %%sdd%% hold on
    %%sdd%% grid on
    %plot(conv, FWOR2, 'b','LineWidth',2)
    %%sdd%% plot([HR05.conversion], FWOR2, 'b*','LineWidth',2)
    %%sdd%% plot([HR10.conversion], FWOR2, 'g*','LineWidth',2)
    %%sdd%% plot([HR20.conversion], FWOR2, 'r*','LineWidth',2)
    %%sdd%% plot([HR40.conversion], FWOR2, 'k*','LineWidth',2)

    xlabel('Conversion');
    ylabel('R^2');
    xlim([0.1 0.8]);
    hold off
    drawnow;
end

function BestFit = FindBestFit(FitData)
    assert(length(FitData.FitObject) == length(FitData.GoF));
    assert(length(FitData.FitObject) == length(FitData.Names));
    bestFitScore = 0;
    bestFitIndex = 1;
    for i=1:length(FitData.GoF)
        if(FitData.GoF{i}.sse < 1)
            if(FitData.GoF{i}.rsquare > bestFitScore)
                bestFitScore = FitData.GoF{i}.rsquare;
                bestFitIndex = i;
            end
        end
    end
    BestFit.Name      = FitData.Names{bestFitIndex};
    BestFit.GoF       = FitData.GoF{bestFitIndex};
    BestFit.FitObject = FitData.FitObject{bestFitIndex};

end
function BestFit = FindBestFitAlternate(FitData)
    assert(length(FitData.FitObject) == length(FitData.GoF));
    assert(length(FitData.FitObject) == length(FitData.Names));
    bestFitScore = 5000;
    bestFitIndex = 1;
    for i=1:length(FitData.GoF)
        if(FitData.GoF{i}.rsquare > 0.95)
            if(FitData.GoF{i}.sse < bestFitScore)
                bestFitScore = FitData.GoF{i}.sse;
                bestFitIndex = i;
            end
        end
    end
    BestFit.Name      = FitData.Names{bestFitIndex};
    BestFit.GoF       = FitData.GoF{bestFitIndex};
    BestFit.FitObject = FitData.FitObject{bestFitIndex};
```

```
end

%% "new" MasterPlot
function [BestHR05Fit, BestHR10Fit, BestHR20Fit,
BestHR40Fit,BestHR05Fit2, BestHR10Fit2, BestHR20Fit2, BestHR40Fit2] =
MasterPlot(EaKAS, AverageEaKAS, HR05, HR10, HR20, HR40, minConversion,
maxConversion)
    %%%%%%%%%%%%%%%%%%%%%%%%%%%%%%%%%%%%%%%%%%%%%%%%%%%%%%%%%%%%%%%%%%%
    %% Experimental data
    %%%%%%%%%%%%%%%%%%%%%%%%%%%%%%%%%%%%%%%%%%%%%%%%%%%%%%%%%%%%%%%%%%%
    R = 8.314;
    HR05ConversionInRange              = HR05([HR05(:).conversion] >=
minConversion & [HR05(:).conversion] <= maxConversion);
    HR10ConversionInRange              = HR10([HR10(:).conversion] >=
minConversion & [HR10(:).conversion] <= maxConversion);
    HR20ConversionInRange              = HR20([HR20(:).conversion] >=
minConversion & [HR20(:).conversion] <= maxConversion);
    HR40ConversionInRange              = HR40([HR40(:).conversion] >=
minConversion & [HR40(:).conversion] <= maxConversion);

    %% Fill data for first plot
    expYHR05Graph1                     =
[HR05ConversionInRange.dalpha_dt] .* exp(AverageEaKAS * 1000 ./ (R .*
[HR05ConversionInRange.Ktemperature]));
    expYHR10Graph1                     =
[HR10ConversionInRange.dalpha_dt] .* exp(AverageEaKAS * 1000 ./ (R .*
[HR10ConversionInRange.Ktemperature]));
    expYHR20Graph1                     =
[HR20ConversionInRange.dalpha_dt] .* exp(AverageEaKAS * 1000 ./ (R .*
[HR20ConversionInRange.Ktemperature]));
    expYHR40Graph1                     =
[HR40ConversionInRange.dalpha_dt] .* exp(AverageEaKAS * 1000 ./ (R .*
[HR40ConversionInRange.Ktemperature]));

    %% Fill data for plot 2
    expYHR05Graph2                     =
[HR05ConversionInRange.dalpha_dt] .*
[HR05ConversionInRange.Ktemperature].^ 2;
    expYHR10Graph2                     =
[HR10ConversionInRange.dalpha_dt] .*
[HR10ConversionInRange.Ktemperature].^ 2;
    expYHR20Graph2                     =
[HR20ConversionInRange.dalpha_dt] .*
[HR20ConversionInRange.Ktemperature].^ 2;
    expYHR40Graph2                     =
[HR40ConversionInRange.dalpha_dt] .*
[HR40ConversionInRange.Ktemperature].^ 2;


%%%%%%%%%%%%%%%%%%%%%%%%%%%%%%%%%%%%%%%%%%%%%%%%%%%%%%%%%%%%%%%%%%%%%%%%
%%%%%%%%%%%%%%%
    %% Graph 1: y(alpha)

    %HR05theoZeroOrderGraph1       = [HR05ConversionInRange.conversion];
    HR05theoN_05_OrderGraph1     = sqrt(1 -
[HR05ConversionInRange.conversion]);
```

```
    HR05theoFirstOrderGraph1     = (1 -
[HR05ConversionInRange.conversion]);
    HR05theoSecondOrderGraph1    = power(1 -
[HR05ConversionInRange.conversion],2);
    HR05theoAvramiErofeev2Graph1 = 2 .* (1 -
[HR05ConversionInRange.conversion]) .* power(-log(1 -
[HR05ConversionInRange.conversion]), 1 / 2);
    HR05theoAvramiErofeev3Graph1 = 3 .* (1 -
[HR05ConversionInRange.conversion]) .* power(-log(1 -
[HR05ConversionInRange.conversion]), 2 / 3);
    HR05theoRandomScisionGraph1  = 2 .*
(sqrt([HR05ConversionInRange.conversion]) -
[HR05ConversionInRange.conversion]);

    %HR10theoZeroOrderGraph1      = [HR10ConversionInRange.conversion];
    HR10theoN_05_OrderGraph1     = sqrt(1 -
[HR10ConversionInRange.conversion]);
    HR10theoFirstOrderGraph1     = (1 -
[HR10ConversionInRange.conversion]);
    HR10theoSecondOrderGraph1    = power(1 -
[HR10ConversionInRange.conversion],2);
    HR10theoAvramiErofeev2Graph1 = 2 .* (1 -
[HR10ConversionInRange.conversion]) .* power(-log(1 -
[HR10ConversionInRange.conversion]), 1 / 2);
    HR10theoAvramiErofeev3Graph1 = 3 .* (1 -
[HR10ConversionInRange.conversion]) .* power(-log(1 -
[HR10ConversionInRange.conversion]), 2 / 3);
    HR10theoRandomScisionGraph1  = 2 .*
(sqrt([HR10ConversionInRange.conversion]) -
[HR10ConversionInRange.conversion]);

    %HR20theoZeroOrderGraph1      = [HR20ConversionInRange.conversion];
    HR20theoN_05_OrderGraph1     = sqrt(1 -
[HR20ConversionInRange.conversion]);
    HR20theoFirstOrderGraph1     = (1 -
[HR20ConversionInRange.conversion]);
    HR20theoSecondOrderGraph1    = power(1 -
[HR20ConversionInRange.conversion],2);
    HR20theoAvramiErofeev2Graph1 = 2 .* (1 -
[HR20ConversionInRange.conversion]) .* power(-log(1 -
[HR20ConversionInRange.conversion]), 1 / 2);
    HR20theoAvramiErofeev3Graph1 = 3 .* (1 -
[HR20ConversionInRange.conversion]) .* power(-log(1 -
[HR20ConversionInRange.conversion]), 2 / 3);
    HR20theoRandomScisionGraph1  = 2 .*
(sqrt([HR20ConversionInRange.conversion]) -
[HR20ConversionInRange.conversion]);

    %HR40theoZeroOrderGraph1      = [HR40ConversionInRange.conversion];
    HR40theoN_05_OrderGraph1     = sqrt(1 -
[HR40ConversionInRange.conversion]);
    HR40theoFirstOrderGraph1     = (1 -
[HR40ConversionInRange.conversion]);
    HR40theoSecondOrderGraph1    = power(1 -
[HR40ConversionInRange.conversion],2);
```

```
    HR40theoAvramiErofeev2Graph1 = 2 .* (1 -
[HR40ConversionInRange.conversion]) .* power(-log(1 -
[HR40ConversionInRange.conversion]), 1 / 2);
    HR40theoAvramiErofeev3Graph1 = 3 .* (1 -
[HR40ConversionInRange.conversion]) .* power(-log(1 -
[HR40ConversionInRange.conversion]), 2 / 3);
    HR40theoRandomScisionGraph1  = 2 .*
(sqrt([HR40ConversionInRange.conversion]) -
[HR40ConversionInRange.conversion]);


%%%%%%%%%%%%%%%%%%%%%%%%%%%%%%%%%%%%%%%%%%%%%%%%%%%%%%%%%%%%%%%%%%%%%%%%%%%%%%%%
%%%%%%%%%%%%%%
    %% Graph 2: z(alpha)

    HR05theoN_05_OrderGraph2         = power((1 -
[HR05ConversionInRange.conversion]),0.5) ...
                                     .* - 2 .* power((1 -
[HR05ConversionInRange.conversion]),0.5);
    HR05theoFirstOrderZGraph2        = (1 -
[HR05ConversionInRange.conversion]) ...
                                     .* - log(1 -
[HR05ConversionInRange.conversion]);
    HR05theoSecondOrderZGraph2       = power((1 -
[HR05ConversionInRange.conversion]),2) ...
                                     .* (1 ./ (1 -
[HR05ConversionInRange.conversion]));
    HR05theoAvramiErofeev_n_2ZGraph2 = 2 .* (1 -
[HR05ConversionInRange.conversion]) .* power(- log(1-
[HR05ConversionInRange.conversion]),1/2) ...
                                     .* power(- log(1-
[HR05ConversionInRange.conversion]) ,1/2);
    HR05theoAvramiErofeev_n_3ZGraph2 = 3 .* (1 -
[HR05ConversionInRange.conversion]) .* power(- log(1-
[HR05ConversionInRange.conversion]),2/3)...
                                     .* power(- log(1-
[HR05ConversionInRange.conversion]),1/3);
    HR05theoRandomScisionZGraph2     = 2 .*
(power([HR05ConversionInRange.conversion],0.5) -
[HR05ConversionInRange.conversion]) ...
                                     .* - log(1-
power([HR05ConversionInRange.conversion], 0.5));

    HR10theoN_05_OrderGraph2         = power((1 -
[HR10ConversionInRange.conversion]),0.5) ...
                                     .* - 2 .* power((1 -
[HR10ConversionInRange.conversion]),0.5);
    HR10theoFirstOrderZGraph2        = (1 -
[HR10ConversionInRange.conversion]) ...
                                     .* - log(1 -
[HR10ConversionInRange.conversion]);
    HR10theoSecondOrderZGraph2       = power((1 -
[HR10ConversionInRange.conversion]),2) ...
                                     .* (1 ./ (1 -
[HR10ConversionInRange.conversion]));
```

```
    HR10theoAvramiErofeev_n_2ZGraph2 = 2 .* (1 -
[HR10ConversionInRange.conversion]) .* power(- log(1-
[HR10ConversionInRange.conversion]),1/2) ...
                                      .* power(- log(1-
[HR10ConversionInRange.conversion]) ,1/2);
    HR10theoAvramiErofeev_n_3ZGraph2 = 3 .* (1 -
[HR10ConversionInRange.conversion]) .* power(- log(1-
[HR10ConversionInRange.conversion]),2/3)...
                                      .* power(- log(1-
[HR10ConversionInRange.conversion]),1/3);
    HR10theoRandomScisionZGraph2     = 2 .*
(power([HR10ConversionInRange.conversion],0.5) -
[HR10ConversionInRange.conversion]) ...
                                      .* - log(1-
power([HR10ConversionInRange.conversion], 0.5));

    HR20theoN_05_OrderGraph2         = power((1 -
[HR20ConversionInRange.conversion]),0.5) ...
                                      .* - 2 .* power((1 -
[HR20ConversionInRange.conversion]),0.5);
    HR20theoFirstOrderZGraph2        = (1 -
[HR20ConversionInRange.conversion]) ...
                                      .* - log(1 -
[HR20ConversionInRange.conversion]);
    HR20theoSecondOrderZGraph2       = power((1 -
[HR20ConversionInRange.conversion]),2) ...
                                      .* (1 ./ (1 -
[HR20ConversionInRange.conversion]));
    HR20theoAvramiErofeev_n_2ZGraph2 = 2 .* (1 -
[HR20ConversionInRange.conversion]) .* power(- log(1-
[HR20ConversionInRange.conversion]),1/2) ...
                                      .* power(- log(1-
[HR20ConversionInRange.conversion]) ,1/2);
    HR20theoAvramiErofeev_n_3ZGraph2 = 3 .* (1 -
[HR20ConversionInRange.conversion]) .* power(- log(1-
[HR20ConversionInRange.conversion]),2/3)...
                                      .* power(- log(1-
[HR20ConversionInRange.conversion]),1/3);
    HR20theoRandomScisionZGraph2     = 2 .*
(power([HR20ConversionInRange.conversion],0.5) -
[HR20ConversionInRange.conversion]) ...
                                      .* - log(1-
power([HR20ConversionInRange.conversion], 0.5));

    HR40theoN_05_OrderGraph2         = power((1 -
[HR40ConversionInRange.conversion]),0.5) ...
                                      .* - 2 .* power((1 -
[HR40ConversionInRange.conversion]),0.5);
    HR40theoFirstOrderZGraph2        = (1 -
[HR40ConversionInRange.conversion]) ...
                                      .* - log(1 -
[HR40ConversionInRange.conversion]);
    HR40theoSecondOrderZGraph2       = power((1 -
[HR40ConversionInRange.conversion]),2) ...
                                      .* (1 ./ (1 -
[HR40ConversionInRange.conversion]));
```

```
    HR40theoAvramiErofeev_n_2ZGraph2 = 2 .* (1 -
[HR40ConversionInRange.conversion]) .* power(- log(1-
[HR40ConversionInRange.conversion]),1/2) ...
                                      .* power(- log(1-
[HR40ConversionInRange.conversion]) ,1/2);
    HR40theoAvramiErofeev_n_3ZGraph2 = 3 .* (1 -
[HR40ConversionInRange.conversion]) .* power(- log(1-
[HR40ConversionInRange.conversion]),2/3)...
                                      .* power(- log(1-
[HR40ConversionInRange.conversion]),1/3);
    HR40theoRandomScisionZGraph2     = 2 .*
(power([HR40ConversionInRange.conversion],0.5) -
[HR40ConversionInRange.conversion]) ...
                                      .* - log(1-
power([HR40ConversionInRange.conversion], 0.5));



%%%%%%%%%%%%%%%%%%%%%%%%%%%%%%%%%%%%%%%%%%%%%%%%%%%%%%%%%%%%%%%%%%%%%%%%%%%%%%%%
%%%%%%%%%%%%%%%
    %% MSE against graph 1, "Y"

%%%%%%%%%%%%%%%%%%%%%%%%%%%%%%%%%%%%%%%%%%%%%%%%%%%%%%%%%%%%%%%%%%%%%%%%%%%%%%%%
%%%%%%%%%%%%%%%
        FitNames = {'N_05', 'FirstOrder', 'SecondOrder', 'Avrami
Erofeev2', 'Avrami Erofeev3', 'Random Scision'};

    HR05Fit(1).MSE = sum((NormalizeData(expYHR05Graph1) -
NormalizeData(HR05theoN_05_OrderGraph1     )).^2) /
length(expYHR05Graph1);
    HR05Fit(2).MSE = sum((NormalizeData(expYHR05Graph1) -
NormalizeData(HR05theoFirstOrderGraph1     )).^2) /
length(expYHR05Graph1);
    HR05Fit(3).MSE = sum((NormalizeData(expYHR05Graph1) -
NormalizeData(HR05theoSecondOrderGraph1    )).^2) /
length(expYHR05Graph1);
    HR05Fit(4).MSE = sum((NormalizeData(expYHR05Graph1) -
NormalizeData(HR05theoAvramiErofeev2Graph1 )).^2) /
length(expYHR05Graph1);
    HR05Fit(5).MSE = sum((NormalizeData(expYHR05Graph1) -
NormalizeData(HR05theoAvramiErofeev3Graph1 )).^2) /
length(expYHR05Graph1);
    HR05Fit(6).MSE = sum((NormalizeData(expYHR05Graph1) -
NormalizeData(HR05theoRandomScisionGraph1  )).^2) /
length(expYHR05Graph1);

    HR10Fit(1).MSE = sum((NormalizeData(expYHR10Graph1) -
NormalizeData(HR10theoN_05_OrderGraph1     )).^2) /
length(expYHR10Graph1);
    HR10Fit(2).MSE = sum((NormalizeData(expYHR10Graph1) -
NormalizeData(HR10theoFirstOrderGraph1     )).^2) /
length(expYHR10Graph1);
    HR10Fit(3).MSE = sum((NormalizeData(expYHR10Graph1) -
NormalizeData(HR10theoSecondOrderGraph1    )).^2) /
length(expYHR10Graph1);
```

```
    HR10Fit(4).MSE = sum((NormalizeData(expYHR10Graph1) -
NormalizeData(HR10theoAvramiErofeev2Graph1 )).^2) /
length(expYHR10Graph1);
    HR10Fit(5).MSE = sum((NormalizeData(expYHR10Graph1) -
NormalizeData(HR10theoAvramiErofeev3Graph1 )).^2) /
length(expYHR10Graph1);
    HR10Fit(6).MSE = sum((NormalizeData(expYHR10Graph1) -
NormalizeData(HR10theoRandomScisionGraph1  )).^2) /
length(expYHR10Graph1);

    HR20Fit(1).MSE = sum((NormalizeData(expYHR20Graph1) -
NormalizeData(HR20theoN_05_OrderGraph1     )).^2) /
length(expYHR20Graph1);
    HR20Fit(2).MSE = sum((NormalizeData(expYHR20Graph1) -
NormalizeData(HR20theoFirstOrderGraph1     )).^2) /
length(expYHR20Graph1);
    HR20Fit(3).MSE = sum((NormalizeData(expYHR20Graph1) -
NormalizeData(HR20theoSecondOrderGraph1    )).^2) /
length(expYHR20Graph1);
    HR20Fit(4).MSE = sum((NormalizeData(expYHR20Graph1) -
NormalizeData(HR20theoAvramiErofeev2Graph1 )).^2) /
length(expYHR20Graph1);
    HR20Fit(5).MSE = sum((NormalizeData(expYHR20Graph1) -
NormalizeData(HR20theoAvramiErofeev3Graph1 )).^2) /
length(expYHR20Graph1);
    HR20Fit(6).MSE = sum((NormalizeData(expYHR20Graph1) -
NormalizeData(HR20theoRandomScisionGraph1  )).^2) /
length(expYHR20Graph1);

    HR40Fit(1).MSE = sum((NormalizeData(expYHR40Graph1) -
NormalizeData(HR40theoN_05_OrderGraph1     )).^2) /
length(expYHR40Graph1);
    HR40Fit(2).MSE = sum((NormalizeData(expYHR40Graph1) -
NormalizeData(HR40theoFirstOrderGraph1     )).^2) /
length(expYHR40Graph1);
    HR40Fit(3).MSE = sum((NormalizeData(expYHR40Graph1) -
NormalizeData(HR40theoSecondOrderGraph1    )).^2) /
length(expYHR40Graph1);
    HR40Fit(4).MSE = sum((NormalizeData(expYHR40Graph1) -
NormalizeData(HR40theoAvramiErofeev2Graph1 )).^2) /
length(expYHR40Graph1);
    HR40Fit(5).MSE = sum((NormalizeData(expYHR40Graph1) -
NormalizeData(HR40theoAvramiErofeev3Graph1 )).^2) /
length(expYHR40Graph1);
    HR40Fit(6).MSE = sum((NormalizeData(expYHR40Graph1) -
NormalizeData(HR40theoRandomScisionGraph1  )).^2) /
length(expYHR40Graph1);

    BestHR05Fit = FindBestFitMSE(HR05Fit, FitNames);
    BestHR10Fit = FindBestFitMSE(HR10Fit, FitNames);
    BestHR20Fit = FindBestFitMSE(HR20Fit, FitNames);
    BestHR40Fit = FindBestFitMSE(HR40Fit, FitNames);

    %% MSE against graph 2, "z"
```

```
    FitNames = {'N_05', 'FirstOrder', 'SecondOrder', 'Avrami Erofeev2',
'Avrami Erofeev3', 'Random Scision'};

    HR05Fit2(1).MSE = sum((NormalizeData(expYHR05Graph2) -
NormalizeData(HR05theoN_05_OrderGraph2         )).^2) /
length(expYHR05Graph2);
    HR05Fit2(2).MSE = sum((NormalizeData(expYHR05Graph2) -
NormalizeData(HR05theoFirstOrderZGraph2        )).^2) /
length(expYHR05Graph2);
    HR05Fit2(3).MSE = sum((NormalizeData(expYHR05Graph2) -
NormalizeData(HR05theoSecondOrderZGraph2       )).^2) /
length(expYHR05Graph2);
    HR05Fit2(4).MSE = sum((NormalizeData(expYHR05Graph2) -
NormalizeData(HR05theoAvramiErofeev_n_2ZGraph2 )).^2) /
length(expYHR05Graph2);
    HR05Fit2(5).MSE = sum((NormalizeData(expYHR05Graph2) -
NormalizeData(HR05theoAvramiErofeev_n_3ZGraph2 )).^2) /
length(expYHR05Graph2);
    HR05Fit2(6).MSE = sum((NormalizeData(expYHR05Graph2) -
NormalizeData(HR05theoRandomScisionZGraph2     )).^2) /
length(expYHR05Graph2);

    HR10Fit2(1).MSE = sum((NormalizeData(expYHR10Graph2) -
NormalizeData(HR10theoN_05_OrderGraph2         )).^2) /
length(expYHR10Graph2);
    HR10Fit2(2).MSE = sum((NormalizeData(expYHR10Graph2) -
NormalizeData(HR10theoFirstOrderZGraph2        )).^2) /
length(expYHR10Graph2);
    HR10Fit2(3).MSE = sum((NormalizeData(expYHR10Graph2) -
NormalizeData(HR10theoSecondOrderZGraph2       )).^2) /
length(expYHR10Graph2);
    HR10Fit2(4).MSE = sum((NormalizeData(expYHR10Graph2) -
NormalizeData(HR10theoAvramiErofeev_n_2ZGraph2 )).^2) /
length(expYHR10Graph2);
    HR10Fit2(5).MSE = sum((NormalizeData(expYHR10Graph2) -
NormalizeData(HR10theoAvramiErofeev_n_3ZGraph2 )).^2) /
length(expYHR10Graph2);
    HR10Fit2(6).MSE = sum((NormalizeData(expYHR10Graph2) -
NormalizeData(HR10theoRandomScisionZGraph2     )).^2) /
length(expYHR10Graph2);

    HR20Fit2(1).MSE = sum((NormalizeData(expYHR20Graph2) -
NormalizeData(HR20theoN_05_OrderGraph2         )).^2) /
length(expYHR20Graph2);
    HR20Fit2(2).MSE = sum((NormalizeData(expYHR20Graph2) -
NormalizeData(HR20theoFirstOrderZGraph2        )).^2) /
length(expYHR20Graph2);
    HR20Fit2(3).MSE = sum((NormalizeData(expYHR20Graph2) -
NormalizeData(HR20theoSecondOrderZGraph2       )).^2) /
length(expYHR20Graph2);
    HR20Fit2(4).MSE = sum((NormalizeData(expYHR20Graph2) -
NormalizeData(HR20theoAvramiErofeev_n_2ZGraph2 )).^2) /
length(expYHR20Graph2);
    HR20Fit2(5).MSE = sum((NormalizeData(expYHR20Graph2) -
NormalizeData(HR20theoAvramiErofeev_n_3ZGraph2 )).^2) /
length(expYHR20Graph2);
```

```
    HR20Fit2(6).MSE = sum((NormalizeData(expYHR20Graph2) -
NormalizeData(HR20theoRandomScisionZGraph2     )).^2) /
length(expYHR20Graph2);

    HR40Fit2(1).MSE = sum((NormalizeData(expYHR40Graph2) -
NormalizeData(HR40theoN_05_OrderGraph2         )).^2) /
length(expYHR40Graph2);
    HR40Fit2(2).MSE = sum((NormalizeData(expYHR40Graph2) -
NormalizeData(HR40theoFirstOrderZGraph2        )).^2) /
length(expYHR40Graph2);
    HR40Fit2(3).MSE = sum((NormalizeData(expYHR40Graph2) -
NormalizeData(HR40theoSecondOrderZGraph2       )).^2) /
length(expYHR40Graph2);
    HR40Fit2(4).MSE = sum((NormalizeData(expYHR40Graph2) -
NormalizeData(HR40theoAvramiErofeev_n_2ZGraph2 )).^2) /
length(expYHR40Graph2);
    HR40Fit2(5).MSE = sum((NormalizeData(expYHR40Graph2) -
NormalizeData(HR40theoAvramiErofeev_n_3ZGraph2 )).^2) /
length(expYHR40Graph2);
    HR40Fit2(6).MSE = sum((NormalizeData(expYHR40Graph2) -
NormalizeData(HR40theoRandomScisionZGraph2     )).^2) /
length(expYHR40Graph2);

    BestHR05Fit2 = FindBestFitMSE(HR05Fit2, FitNames);
    BestHR10Fit2 = FindBestFitMSE(HR10Fit2, FitNames);
    BestHR20Fit2 = FindBestFitMSE(HR20Fit2, FitNames);
    BestHR40Fit2 = FindBestFitMSE(HR40Fit2, FitNames);

    %%%%%%%%%%%%%%%%%%%%%%%%%%%%%%%%%%%%%%%%%%%%%%%%%%%%%%%%%%%%%%%%%%%%%%%
    %% Plot graphs
    %%%%%%%%%%%%%%%%%%%%%%%%%%%%%%%%%%%%%%%%%%%%%%%%%%%%%%%%%%%%%%%%%%%%%%%
    masterPlotFigure = figure;
    set(masterPlotFigure,'Color','w');
    %%%%%%%%%%%%%%%%%%%%%%%%%%%%%%%%%%%%%%%%%%%%%%%%%%%%%%%%%%%%%%%%%%%%%%%
    %% Draw first graph
    subplot(1,2,1)
        hold on
        grid on

        title('MasterPlot y(\alpha)');
        %plot([HR05ConversionInRange.conversion],
NormalizeData(HR05theoZeroOrderGraph1)          , 'y','LineWidth',2)
        plot([HR05ConversionInRange.conversion],
NormalizeData(HR05theoN_05_OrderGraph1)         , 'b','LineWidth',2)
        plot([HR05ConversionInRange.conversion],
NormalizeData(HR05theoFirstOrderGraph1)         , 'm','LineWidth',2)
        plot([HR05ConversionInRange.conversion],
NormalizeData(HR05theoSecondOrderGraph1)        , 'c','LineWidth',2)
        plot([HR05ConversionInRange.conversion],
NormalizeData(HR05theoAvramiErofeev2Graph1)     , 'r^','LineWidth',2)
        plot([HR05ConversionInRange.conversion],
NormalizeData(HR05theoAvramiErofeev3Graph1)     , 'r','LineWidth',2)
        plot([HR05ConversionInRange.conversion],
NormalizeData(HR05theoRandomScisionGraph1)      , 'g','LineWidth',2)
```

```
        plot([HR05ConversionInRange.conversion],
NormalizeData(expYHR05Graph1), '-.k+','LineWidth',2)
        plot([HR10ConversionInRange.conversion],
NormalizeData(expYHR10Graph1), '-.ko','LineWidth',2)
        plot([HR20ConversionInRange.conversion],
NormalizeData(expYHR20Graph1), '-.k*','LineWidth',2)
        plot([HR40ConversionInRange.conversion],
NormalizeData(expYHR40Graph1), '-.k.','LineWidth',2)

        legend('nth order: n = 0.5'     , ...
               'First Order'            , ...
               'Second Order'           , ...
               'Avrami Erofeev(n = 2)'  , ...
               'Avrami Erofeev(n = 3)'  , ...
               'Random Scision'         , ...
               'Experimental HR05'      , ...
               'Experimental HR10'      , ...
               'Experimental HR20'      , ...
               'Experimental HR40'      , ...
               'Location', 'SouthWest');
        xlim([minConversion maxConversion]);
        xlabel('Conversion');
        ylabel('y(\alpha)');
        grid off
        hold off

    %%%%%%%%%%%%%%%%%%%%%%%%%%%%%%%%%%%%%%%%%%%%%%%%%%%%%%%%%%%%%%%%%%%%%%%
    %% Draw second graph
    subplot(1,2,2)
        hold on
        grid on
        title('MasterPlot z(\alpha)');

        plot([HR05ConversionInRange.conversion],
NormalizeData(HR40theoN_05_OrderGraph2)         , 'b','LineWidth',2)
        plot([HR05ConversionInRange.conversion],
NormalizeData(HR40theoFirstOrderZGraph2)        , 'm','LineWidth',2)
        plot([HR05ConversionInRange.conversion],
NormalizeData(HR40theoSecondOrderZGraph2)       , 'c','LineWidth',2)
        plot([HR05ConversionInRange.conversion],
NormalizeData(HR40theoAvramiErofeev_n_2ZGraph2) , 'r^','LineWidth',2)
        plot([HR05ConversionInRange.conversion],
NormalizeData(HR40theoAvramiErofeev_n_3ZGraph2) , 'r','LineWidth',2)
        plot([HR05ConversionInRange.conversion],
NormalizeData(HR40theoRandomScisionZGraph2)     , 'g','LineWidth',2)

        plot([HR05ConversionInRange.conversion],
NormalizeData(expYHR05Graph2), '-.k+','LineWidth',2)
        plot([HR10ConversionInRange.conversion],
NormalizeData(expYHR10Graph2), '-.ko','LineWidth',2)
        plot([HR20ConversionInRange.conversion],
NormalizeData(expYHR20Graph2), '-.k*','LineWidth',2)
        plot([HR40ConversionInRange.conversion],
NormalizeData(expYHR40Graph2), '-.k.','LineWidth',2)

        legend('nth order: n = 0.5'     , ...
```

```
                'First Order'            , ...
                'Second Order'           , ...
                'Avrami Erofeev(n = 2)'  , ...
                'Avrami Erofeev(n = 3)'  , ...
                'Random Scision'         , ...
                'Experimental HR05'      , ...
                'Experimental HR10'      , ...
                'Experimental HR20'      , ...
                'Experimental HR40'      , ...
                'Location', 'SouthEast');

        xlim([minConversion maxConversion]);
        xlabel('Conversion');
        ylabel('z(\alpha)');

        grid off
        hold off

end

function [best_m, best_n, bestOptimal] = ModelFitting(HR05, HR10, HR20,
HR40)
    %%ln(dalpha_dt * 1 / (conversion ^ m * (1 - conversion) ^ n)) =
ln(cA) - (AverageEaKAS * 1000) / (R * Ktemperature)
    assert(length(HR05) == length(HR10) ...
        && length(HR05) == length(HR20) ...
        && length(HR05) == length(HR40));

%%%%%%%%%%%%%%%%%%%%%%%%%%%%%%%%%%%%%%%%%%%%%%%%%%%%%%%%%%%%%%%%%%%%%%%%%%%%
%%
    % Linear search of m and n that maximise Pearson linear correlation
    % coefficient on Equation above
    bestOptimal = 0;
    best_m  = 0;
    best_n  = 0;


    for m = 0.5:0.05:1.5
        for n = 0:0.05:3
            YFittingHR05.Funct = log([HR05.dalpha_dt] ./
(([HR05.conversion] .^ m .* (1 - [HR05.conversion]) .^ n))); %Calculus of
right side eq sestak-bergger
            YFittingHR10.Funct = log([HR10.dalpha_dt] ./
(([HR10.conversion] .^ m .* (1 - [HR10.conversion]) .^ n)));
            YFittingHR20.Funct = log([HR20.dalpha_dt] ./
(([HR20.conversion] .^ m .* (1 - [HR20.conversion]) .^ n)));
            YFittingHR40.Funct = log([HR40.dalpha_dt] ./
(([HR40.conversion] .^ m .* (1 - [HR40.conversion]) .^ n)));

            [YFittingHR05.Pearson,YFittingHR05.PValue] = corr((1 ./
[HR05.Ktemperature]).',[YFittingHR05.Funct].'); %Evaluate Pearson coeff
and p-value for pair of m and n
            [YFittingHR10.Pearson,YFittingHR10.PValue] = corr((1 ./
[HR10.Ktemperature]).',[YFittingHR10.Funct].');
            [YFittingHR20.Pearson,YFittingHR20.PValue] = corr((1 ./
[HR20.Ktemperature]).',[YFittingHR20.Funct].');
```

```
            [YFittingHR40.Pearson,YFittingHR40.PValue] = corr((1 ./
[HR40.Ktemperature]).',[YFittingHR40.Funct].');

            if YFittingHR05.Pearson < 0 && YFittingHR10.Pearson < 0 &&
YFittingHR20.Pearson < 0 && YFittingHR40.Pearson < 0 %Check all Pearson
coeff are <0 as slope has to be <0, otherwise Ea<0
                optimal = YFittingHR05.Pearson * YFittingHR10.Pearson *
YFittingHR20.Pearson * YFittingHR40.Pearson; %Evaluate global optimum for
all four HR (this value is >0)
                if abs(optimal) > abs(bestOptimal) %Overwrite optimal
only if value in next iteration is best than previous iteration
                    best_m = m;
                    best_n = n;
                    bestOptimal = optimal;
                    fprintf('*');
                end
            end

          fprintf('.');
        end
        fprintf('\n');
    end


%%%%%%%%%%%%%%%%%%%%%%%%%%%%%%%%%%%%%%%%%%%%%%%%%%%%%%%%%%%%%%%%%%%%%%%%
%%
        % Ploting optimun n and m
        BestYHR05 = log([HR05.dalpha_dt] ./ (([HR05.conversion] .^ best_m
.* (1 - [HR05.conversion]) .^ best_n)));
        BestYHR10 = log([HR10.dalpha_dt] ./ (([HR10.conversion] .^ best_m
.* (1 - [HR10.conversion]) .^ best_n)));
        BestYHR20 = log([HR20.dalpha_dt] ./ (([HR20.conversion] .^ best_m
.* (1 - [HR20.conversion]) .^ best_n)));
        BestYHR40 = log([HR40.dalpha_dt] ./ (([HR40.conversion] .^ best_m
.* (1 - [HR40.conversion]) .^ best_n)));

        figure3 = figure;
        set(figure3,'Color','w');

        hold on
        plot((1 ./ [HR05.Ktemperature]), BestYHR05, 'b*','LineWidth',2)
        plot((1 ./ [HR10.Ktemperature]), BestYHR10, 'g*','LineWidth',2)
        plot((1 ./ [HR20.Ktemperature]), BestYHR20, 'r*','LineWidth',2)
        plot((1 ./ [HR40.Ktemperature]), BestYHR40, 'k*','LineWidth',2)
        hold off
        xlabel('1/Temperature (1/^{o}C)');
        ylabel('ln[(d\alpha/dt) * 1/(\alpha^m * (1-\alpha)^n)] (-)');
        legend('5^{o}C/min'     , ...
               '10^{o}C/min'    , ...
               '20^{o}C/min'    , ...
               '40^{o}C/min'    , ...
               'Location', 'NorthWest');


%%%%%%%%%%%%%%%%%%%%%%%%%%%%%%%%%%%%%%%%%%%%%%%%%%%%%%%%%%%%%%%%%%%%%%%%
%%
```

```
        % Linear regression with best n and m for Ea (slope) and A
        % (intercept)


end

function BestFit = FindBestFitMSE(FitData, FitNames)
    [val, index] = min([FitData.MSE]);
    BestFit.Name = FitNames(index);
    BestFit.MSE  = FitData(index).MSE;
end

function dataNormalized = NormalizeData(Data)
    dataNormalized  =  (Data - min(Data)) ./ (max(Data) - min(Data));
end
```

Appendix B Technical Specifications

Table B.1 CAL2k-ECO technical specifications and dimensions

Type	CAL2k-ECO
Power	90-260VAC 50/60Hz
Ambient temperature	0-60 $^{\circ}C$
Repeatability	0.1 (%RSD)
Resolution	0.01 (MJ/kg)
Temperature resolution	0.000006 $^{\circ}C$

Table B.2 TA instrument DSC Q20 technical specifications

Cooling accessory	RCS90
Temperature range	Amb to 725 $^{\circ}C$
With cooling accessory	-90 to 400 $^{\circ}C$
Temperature precision	$\pm$ 0.05 $^{\circ}C$
Temperature accuracy	$\pm$ 0.1 $^{\circ}C$
Calorimetric reproducibility (indium metal)	$\pm$ 1 $^{\circ}C$
Calorimetric precision (indium metal)	$\pm$ 1 $^{\circ}C$
Dynamic measurement range	+/- 350mW
Digital resolution	>0.04 μW
Baseline curvature (-50 to 300 $^{\circ}C$)	<0.15 mW
Baseline reproducibility	<0.04 mW
Sensitivity	1.0 μW
Indium height/width	8.0 mW/$^{\circ}C$

Table B.3 Perkin Elmer STA 6000 Thermal Analyser technical specifications

Sensor	Pure platinum pan holder and reference ring
Furnace design	Vertical
Balance design	Top loading, single beam
Balance resolution	0.2 μg
Balance measurement range	Up to 1500 mg
Temperature range	15-1000 $^{\circ}C$
Heating rate	Ambient to 1000 $^{\circ}C$/min 0.1 to 100$^{\circ}C$/min
Cooling rates	From 1000^{o}C to 30^{o}C Under 10 minutes
Temperature calibration	Metal standards such as Indium and Silver
Temperature accuracy/reproducibility	$\pm$ 0.5 $^{\circ}C$
Calorimetric accuracy/reproducibility	$\pm$ 2%
Balance precision	$\pm$ 0.02%
Thermocouples	PT-PT/Rh (Type R)
Sample pans	Alumina 180 μL
Dimensions (HxWxD)	17x38x41 cm 6.7x15x16.5 in
Weight	12 - 16 kg
Instrument control	Pyris software

Table B.4 Carlo Erba EA 1108 technical specifications

Combustion furnace temperature	1000 °C
Measuring range	100 ppm - 100 %
Detection limits	10 ppm
Accuracy	0.3-0.5 % absolute
Repeatability	0.2 % absolute
Sample size in capsules	0.1-100 mg (usual - 1.5 mg)

Table B.5 Vecstar horizontal electric furnace technical specifications

Model	VCTF1	VCTF4
Maximum temperature	1200 ° C	1200 ° C
Maximum continuous working temperature	1150 ° C	1150 ° C
Chamber diameter	38 cm	36 cm
Heated length	17 cm	45 cm
Power	0.4 kW	2.5 kW
Holding power	0.16 kW	1 kW
Thermocouple type	K	K

Table B.6 Philips CM100 TEM with Compustage technical specifications

Acceleration voltage	40-100 kV
Gun	Tungsten
Resolution	0.34 nm point to point at 100 kV spot size 1 μmW
	$1.33 \cdot 10^{-5}$ Pa
Column Pressure	$6.67 \cdot 10^{-5}$ Pa (Ultra high vacuum)
	$6.67 \cdot 10^{-4}$ Pa (Working vacuum)

Table B.7 JEOL JSM-5610LV SEM microscope technical specifications

Resolution	4 nm at 20 kV
Magnification	x5 to x300000
Speciment size	Up to 150 mm diameter
Stage type	Eucentric goniometer type
Accelerating Voltage	500 V to 20 kV
Imaging modes	Low vacuum (variable pressure)

Table B.8 Hitachi S2400 SEM microscope technical specifications

Resolution	40 Å
Magnification	Up to x300000
Specimen size	Up to 150 mm diameter
Accelerating Voltage	0 V to 25 kV

Table B.9 Thermo Scientific Surfer porosimeter technical specifications

Analytical capability	Physisorption and Chemisorption capability One analysis port and three independent outgassing ports
Specific surface area	Minimum 0.01 m^2/g
Specific pore volume	From 0.0001 cm^3/gamma
Pore size range	0.32-500 nm pore diameter
Inlet pressure	Maximum 150 kPa
Accepted adsorbates	N_2, Ar, CO_2, He, Kr, H_2, O_2, CO, CH_4, light hydrocarbons
Typical temperature set point	35.0 °C
Temperature stability	± 0.1 °C
Temperature reading resolution	0.1 °C
Degasser temperature	Room temperature to 450 °C
Degasser temperature accuracy	± 1% full scale temperature

Table B.10 Malvern Panalytical X'pert Pro Multipurpose Diffractometer technical specifications

X-ray generator	Philips PW3040/60
Detector	X'Celerator using real time multiple strip
Radiation	Cu-K_α
Wavelength	1.5418 Å
X-ray generator	Cu anode with 40 kV and 40 mA
Spectra analysis	PANalytical High Score Plus
Database	ICDD Powder Diffraction File 2 Database (1999) ICDD Powder Diffraction File 4 - Minerals (2012) American Mineralogist Crystal Structure Database (March 2010) Crystallography Open Database (February 2012)

Table B.11 Elementar Vario MICRO Cube technical specifications

Combustion furnace temperature	1200 °C
Sample size	From <1-800 mg (soil) and up to 20 mg organic matter
Element detection range	Up to 7 mg carbon and 10 mg nitrogen

Table B.12 Perkin Elmer Sciex Elan 6000 ICP-MS technical specifications

Resolution	0.3 - 3.0 amu
Mass range	1-270
Carrier gas	Argon = 16mL/min
Detector	Dual-stage discrete dynode electron multiplier
ICP generator	Free-running
Frequency	40.68 MHz
Power	1500 W
Torch	Demountable

Table B.13 Agilent Cary 630 FT-IR technical specifications

Spectral range	KBr 6300–350 cm^{-1}
Spectral resolution	<2 cm^{-1}
Wavenumber accuracy	0.05 cm^{-1}
Wavenumber reproducibility	0.005 cm^{-1}

Table B.14 Agilent 7820A GC-FID technical specifications

Retention time repeatability	<0.06 %
Peak area repeatability	<2%
Temperature set point resolution	1 °C
Maximum temperature ramp rate	75 °C/min
Maximum run time	999.99 min
Temperature programming rumps	5
Maximum oven temperature	400 °C
Maximum column flow	100 mL/min
Maximum split ratio	250:1
Maximum inlet temperature	400 °C
Maximum FID detector temperature	425 °C
Maximum FID detector data acquisition range	100 Hz

Table B.15 Varian 450 GC-TCD/FID/FID technical specifications

Temperature set point resolution	1 °C
Maximum temperature ramp rate	120 °C/min
Oven cool down rate	400 to 50 °C in 4.5 minutes
Maximum oven temperature	450 °C
Split range	1-10000 (column dependant)
Maximum inlet temperature	450 °C
Maximum FID detector temperature	450 °C
Maximum TCD detector temperature	450 °C
FID detector detectivity	2 pg C/s
TCD detector detectivity	300 pg/s (butane)

Table B.16 FEI Tecnai T20 HRTEM microscope technical specifications

Acceleration voltage	80-200 kV
Gun	LaB6 $\pm$ 80^o tilt
Resolution	Up to 200 nm
Additional equipment	TIETZ F415MP 4k x 4k multiport CCD camera

Table B.17 Hiden Analytical Mass Spectrometer technical specifications

Operating temperature	200 °C
Inlet	2 m capillary
Response time	300 ms
Mass range	200 amu
Detection capability	5 ppb - 100 %

Table B.18 Horiba HR800 Confocal Raman technical specifications

Spectral range	200-2100 nm
Spectral resolution	Up to 1.5 cm^{-1}
Spatial resolution	Up to 1 μm
Minimum frequency	3.5 cm^{-1}
Accuracy of wavenumber	1 cm^{-1}
Laser	Tunable Ar+ laser up to 50 mW with notch filters at 488 nm and 514 nm He-Ne at 632 nm and 10mW

Appendix C BS 1016-104.3:1998 Standard

BRITISH STANDARD

BS 1016-104.3:
1998
ISO 562:1998

Methods for analysis and testing of coal and coke —

Part 104: Proximate analysis —

Section 104.3: Determination of volatile matter content

ICS 73,040; 75.160.10

National foreword

This British Standard is the UK implementation of ISO 562:1998. It supersedes BS 1016-104.3:1991 which is withdrawn.

The UK participation in its preparation was entrusted to Technical Committee SFI/3, Analysis and testing of coal and coke, which has the responsibility to:

— aid enquirers to understand the text;

— present to the responsible international/European committee any enquiries on the interpretation, or proposals for change, and keep the UK interests informed;

— monitor related international and European developments and promulgate them in the UK.

A list of organizations represented on this committee can be obtained on request to its secretary.

Cross-references

The British Standards which implement international or European publications referred to in this document may be found in the BSI Standards Catalogue under the section entitled "International Standards Correspondence Index", or by using the "Find" facility of the BSI Standards Electronic Catalogue.

A British Standard does not purport to include all the necessary provisions of a contract. Users of British Standards are responsible for their correct application.

Compliance with a British Standard does not of itself confer immunity from legal obligations.

Summary of pages

This document comprises a front cover, an inside front cover, pages i and ii, the ISO title page, page ii, pages 1 to 6 and a back cover.

This standard has been updated (see copyright date) and may have had amendments incorporated. This will be indicated in the amendment table on the inside front cover.

This British Standard, having been prepared under the direction of the Sector Board for Materials and Chemicals, was published under the authority of the Standards Board and comes into effect on 15 April 1998

ISBN 0 580 29677 6

Amendments issued since publication

Amd. No.	Date	Comments

Contents

blank

BS 1016-104.3:1998

INTERNATIONAL STANDARD

ISO 562

Second edition
1998-02-01

Hard coal and coke — Determination of volatile matter

Houille et coke — Détermination des matières volatiles

Reference number
ISO 562:1998(E)

Foreword

ISO (the International Organization for Standardization) is a worldwide federation of national standards bodies (ISO member bodies). The work of preparing International Standards is normally carried out through ISO technical committees. Each member body interested in a subject for which a technical committee has been established has the right to be represented on that committee. International organizations, governmental and non-governmental, in liaison with ISO, also take part in the work. ISO collaborates closely with the International Electrotechnical Commission (IEC) on all matters of electrotechnical standardization.

Draft International Standards adopted by the technical committees are circulated to the member bodies for voting. Publication as an International Standard requires approval by at least 75 % of the member bodies casting a vote.

International Standard ISO 562 was prepared by Technical Committee ISO/TC 27, *Solid mineral fuels*, Subcommittee SC 5, *Methods of analysis*.

This second edition cancels and replaces the first edition (ISO 562:1981), which has been technically revised.

Annex A of this International Standard is for information only.

Descriptors: Solid fuels, fossil fuels, coal, pit-coal, coke, tests, determination of content, volatile matter, gravimetric analysis, test equipment.

Introduction

The volatile matter is determined as the loss in mass, less that due to moisture, when coal or coke is heated out of contact with air under standardized conditions. The test is empirical and, in order to ensure reproducible results, it is essential that the rate of heating, the final temperature and the overall duration of the test are carefully controlled. It is also essential to exclude air from the coal or coke during heating to prevent oxidation. The fit of the crucible lid is therefore critical. The moisture content of the sample is determined at the same time as the volatile matter so that the appropriate correction can be made.

Mineral matter associated with the sample may also lose mass under the conditions of the test, the magnitude of the loss being dependent on both the nature and the quantity of the minerals present.

NOTE When applying this International Standard for classification purposes, to samples obtained directly from coal seams, special care has to be given to the ash content.

The apparatus and procedure are specified so that one or more determinations may be performed simultaneously in the furnace.

1 Scope

This International Standard specifies a method of determining the volatile matter of hard coal and of coke. It is not applicable to brown coals and lignites.

2 Normative references

The following standards contain provisions which, through reference in this text, constitute provisions of this International Standard. At the time of publication, the editions indicated were valid. All standards are subject to revision, and parties to agreements based on this International Standard are encouraged to investigate the possibility of applying the most recent editions of the standards indicated below. Members of IEC and ISO maintain registers of currently valid International Standards.

ISO 331:1983, *Coal — Determination of moisture in the analysis sample — Direct gravimetric method.*

ISO 687:1974, *Coke — Determination of moisture in the analysis sample.*

ISO 11722:—[1)], *Solid mineral fuels — Hard coal — Determination of moisture in the analysis sample by drying in nitrogen.*

3 Principle

A portion of the sample is heated out of contact with air at 900 °C for 7 min. The percentage of volatile matter is calculated from the loss in mass of the test portion after deducting the loss in mass due to moisture.

4 Reagent

Cyclohexane of recognized analytical grade.

5 Apparatus

5.1 *Furnace,* heated by electricity, in which a zone of uniform temperature of 900 °C ± 5 °C can be maintained. It may be of the stop-ended type or fitted at the back with a flue approximately 25 mm diameter and 150 mm long (see Figure 1).

NOTE It is important for furnaces with flues that the furnace door seal well. The flue should not reach far out of the oven and should be fitted with a butterfly valve to restrict airflow through the furnace.

Its heat capacity shall be such that, with an initial temperature of 900 °C, the temperature is regained within 4 min after insertion of a cold stand and its crucibles. The temperature is measured with a thermocouple, as described in **5.2**.

Normally the furnace will be designed specifically either for multiple determinations using a number of crucibles in one stand or for receiving one crucible and its stand. In the first case, the zone of uniform temperature shall be at least 160 mm × 100 mm; in the latter case, a zone of diameter 40 mm will be sufficient.

A position for the crucible stand shall be chosen within the zone of uniform temperature and this position shall be used for all determinations. The temperature of 900 °C shall be attained as closely as possible with a specified tolerance of ± 5 °C in order to compensate for inherent errors in the temperature measurement and lack of uniformity in the temperature distribution.

5.2 *Thermocouple,* unsheathed, of wire no thicker than 1 mm. It should be long enough to reach the centre of the underside of each crucible when placed in the zone of uniform temperature on being inserted through the front or rear of the furnace. The thermojunction shall be placed midway between the base of the crucible in its stand and the floor of the furnace. If the stand holds more than one crucible, the temperature under each crucible shall be checked in the same manner.

[1)] To be published.

If desired, a sheathed thermocouple may be permanently installed in the furnace (see Figure 1) with its thermojunction as close as possible to the centre of the zone of uniform temperature; in this case furnace temperature readings shall be correlated at frequent intervals with those of the unsheathed thermocouple, which is thus inserted only when necessary.

NOTE The temperature/electromotive force relationship of a thermojunction maintained at elevated temperatures gradually changes with time.

5.3 *Crucible,* cylindrical, with a well-fitting lid, both of fused silica. The crucible with lid shall have a mass between 10 g and 14 g and dimensions approximating to those shown in Figure 2. The fit of the lid on the crucible is critical to the determination and a lid shall be selected to match the crucible so that the horizontal clearance between them is no greater than 0,5 mm. After selection, the crucible and the lid shall be ground together to give smooth surfaces and then be given a common distinguishing mark.

NOTE When performing multiple determinations on highly swelling coals, it may be necessary to use taller crucibles; these may be up to 45 mm in height without affecting the determined volatile matter, provided that the specified rate of temperature recovery be maintained.

5.4 *Crucible stand,* on which the crucible is placed in the furnace, such that the appropriate rate of heating can be achieved. For example, it may consist of the following:

a) for single determinations, a ring of heat-resistant steel wire as shown in Figure 3 a) with ceramic discs, 25 mm diameter and 2 mm thick, resting on the inner projection of its legs or

b) for multiple determinations, a tray of heat-resistant steel wire as shown in Figure 3 b), of appropriate size, with ceramic plates 2 mm thick supporting the crucibles.

5.5 *Balance,* capable of reading to the nearest 0,1 mg.

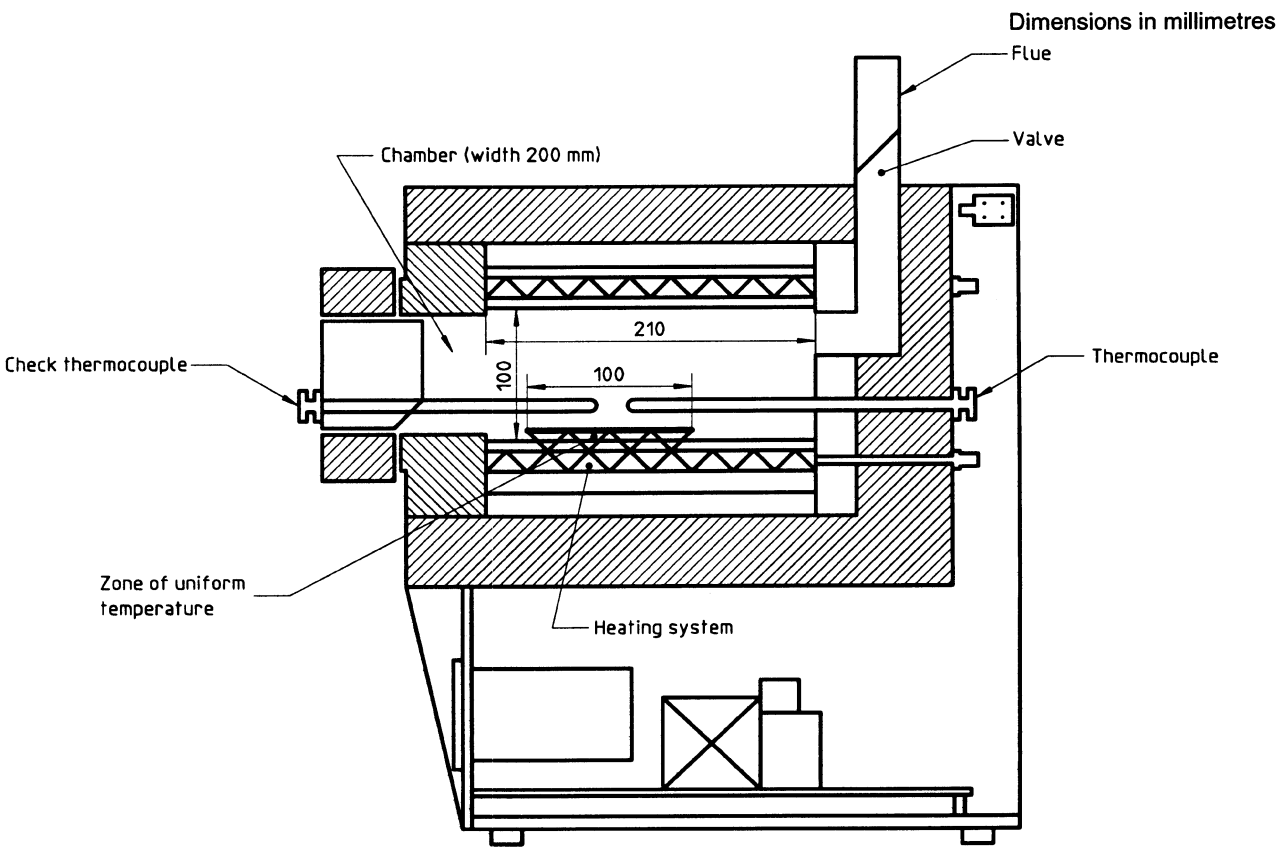

Figure 1 — Example of suitable furnace

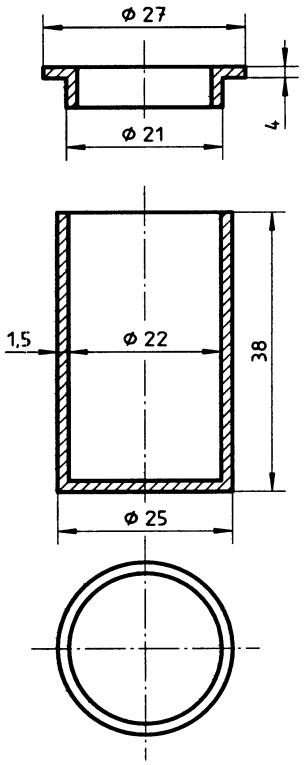

Figure 2 — Silica crucible and lid

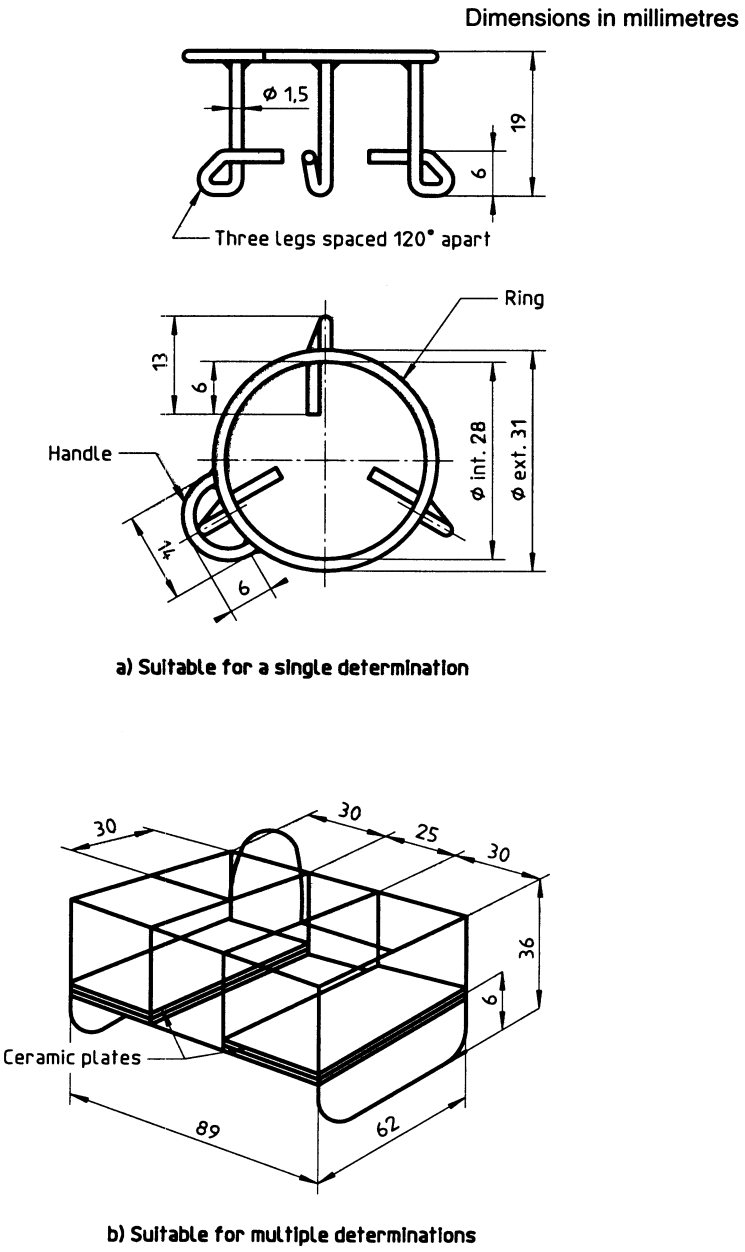

Figure 3 — Crucible stands

6 Preparation of the test sample

The coal or coke used for the determination of volatile matter is the general analysis test sample (ground to pass a sieve of 212 µm aperture).

The sample shall be well mixed and in moisture equilibrium with the laboratory atmosphere.

A test portion from the same test sample is separated for determination of moisture parallel to the determination of volatile matter.

7 Procedure

7.1 Furnace temperature checking

Adjust the temperature of the zone in the furnace (**5.1**), containing either a stand with one crucible and lid [Figure 3 a)] or a stand with the requisite number of crucibles and lids [Figure 3 b)], to 900 °C ± 5 °C as indicated by the correctly located thermocouple (**5.2**). Check that the temperature under each crucible, at the same height, lies within the temperature tolerance of the uniform zone.

NOTE Temperature checking should be made before starting determinations. However, when several analyses are performed per day, a daily temperature check is sufficient. The check of the temperature recovery criterion (**5.1**) should be dealt with in a similar way.

7.2 Volatile matter determination

Fill either a stand with one empty crucible and lid [Figure 3 a)] or a stand with the requisite number of empty crucibles and lids [Figure 3 b)] and insert in the oven. Maintain at 900 °C ± 5 °C for 7 min. Remove the crucible(s) from the furnace and allow to cool to room temperature on a thick metal plate.

As soon as they are cool, weigh each empty crucible and lid and weigh into each crucible, to the nearest 0,1 mg, 1 ± 0,1 g of test sample. Replace the lid and tap each crucible on a clean hard surface until the test portion forms a layer of even thickness on the bottom of the crucible. If the sample is of coke, remove the lid of the charged crucible, add 2 to 4 drops of cyclohexane (4) and replace the lid.

NOTE The addition of cyclohexane prevents oxidation of the coke but does not prevent adsorption of gases, e.g. nitrogen.

Place the charged crucible(s) in a cold stand, transfer to the furnace, close the door and leave for 7 min ± 5 s. Remove and allow to cool to room temperature. When cool, weigh the crucible(s) to the nearest 0,1 mg in the same manner as for the empty crucible(s).

NOTE 1 The same treatment of the crucible before and after the determination minimizes the effect of any film of water adsorbed on its surface, while the rapid cooling reduces absorption of moisture by the coal or coke residue.

NOTE 2 If multiple determinations are being made, any vacant places in the stand should be filled with empty crucibles.

8 Expression of results

The volatile matter V in the sample as analysed, expressed as a percentage by mass, is given by the equation:

$$V = \frac{100(m_2 - m_3)}{(m_2 - m_1)} - M$$

where

m_1 is the mass, in grams, of the empty crucible and lid;

m_2 is the mass, in grams, of the crucible and lid and test portion before heating;

m_3 is the mass, in grams, of the crucible and lid and contents after heating;

M is the moisture, as a percentage by mass, in the sample as analysed, determined according to the method specified in ISO 331 (to be superseded by ISO 11722) or ISO 687.

Report the result, as the mean of duplicate determinations, to the nearest 0,1 % (m/m). The results of the determination described in this International Standard are reported on the "air-dried" basis. Calculation of the results to other bases is dealt with in ISO 1170.

9 Precision

Table 1

Volatile matter	Maximum acceptable differences between, results obtained (calculated to the same moisture content)	
	Repeatability limit	Reproducibility critical difference
Hard coal of volatile matter < 10 %	0,3 % absolute	0,5 % absolute
Hard coal of volatile matter ⩾10 %	3 % of the mean result	0,5 % absolute or 4 % of the mean result, whichever is greater
Coke	0,2 % absolute	0,3 % absolute

9.1 Repeatability limit

The results of the duplicate determinations (performed within a short period of time, but not simultaneously) in the same laboratory by the same operator using the same apparatus on two representative test portions taken from the same general analysis test sample, shall not differ by more than the values given in Table 1.

9.2 Reproducibility critical difference

The means of the results of duplicate determinations, performed in each of two different laboratories on representative test portions taken from the same general analysis test sample shall not differ by more than the above values.

10 Test report

The test report shall include the following information:

a) the identification of the sample tested;

b) the method used;

c) the date of the determination;

d) results of the determination performed, together with the relevant analysis basis (e.g. air dry);

e) any unusual features noted during the determination;

f) a reference to this International Standard;

g) any operation not included in this International Standard or regarded as optional.

Annex A (informative)
Bibliography

[1] ISO 1170:1977, *Coal and coke — Calculation of analyses to different bases.*

[2] ISO 1213-2:1992, *Solid mineral fuels — Vocabulary — Part 2: Terms relating to sampling testing and analysis.*

blank

BSI — British Standards Institution

BSI is the independent national body responsible for preparing British Standards. It presents the UK view on standards in Europe and at the international level. It is incorporated by Royal Charter.

Revisions

British Standards are updated by amendment or revision. Users of British Standards should make sure that they possess the latest amendments or editions.

It is the constant aim of BSI to improve the quality of our products and services. We would be grateful if anyone finding an inaccuracy or ambiguity while using this British Standard would inform the Secretary of the technical committee responsible, the identity of which can be found on the inside front cover. Tel: 020 8996 9000. Fax: 020 8996 7400.

BSI offers members an individual updating service called PLUS which ensures that subscribers automatically receive the latest editions of standards.

Buying standards

Orders for all BSI, international and foreign standards publications should be addressed to Customer Services. Tel: 020 8996 9001. Fax: 020 8996 7001.

In response to orders for international standards, it is BSI policy to supply the BSI implementation of those that have been published as British Standards, unless otherwise requested.

Information on standards

BSI provides a wide range of information on national, European and international standards through its Library and its Technical Help to Exporters Service. Various BSI electronic information services are also available which give details on all its products and services. Contact the Information Centre. Tel: 020 8996 7111. Fax: 020 8996 7048.

Subscribing members of BSI are kept up to date with standards developments and receive substantial discounts on the purchase price of standards. For details of these and other benefits contact Membership Administration. Tel: 020 8996 7002. Fax: 020 8996 7001.

Copyright

BSI
389 Chiswick High Road
London
W4 4AL

Appendix D Thermal/Catalytic cold plasma assisted pyrolysis set-up

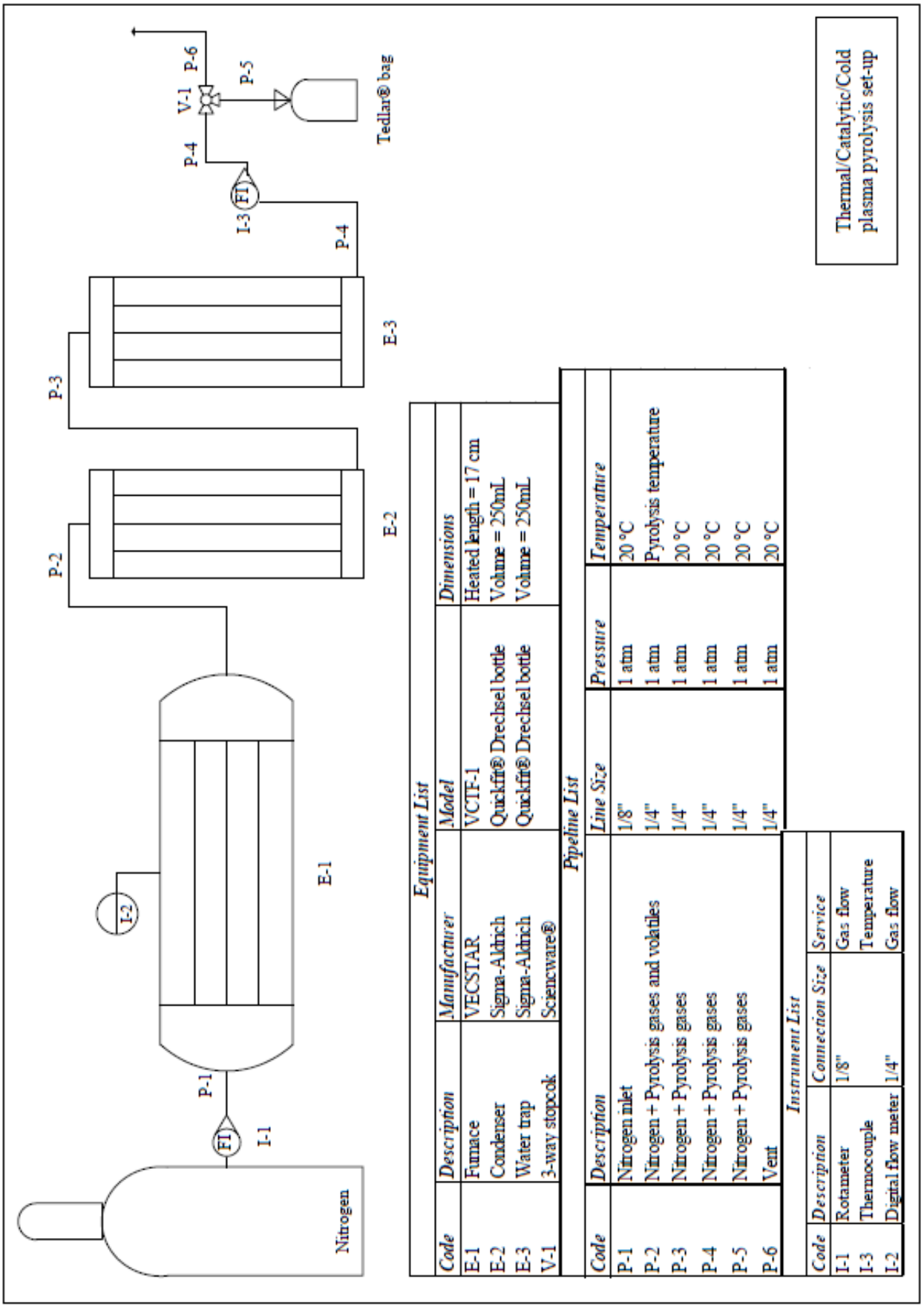

Equipment List

Code	*Description*	*Manufacturer*	*Model*	*Dimensions*
E-1	Furnace	VECSTAR	VCTF-1	Heated length = 17 cm
E-2	Condenser	Sigma-Aldrich	Quickfit® Drechsel bottle	Volume = 250mL
E-3	Water trap	Sigma-Aldrich	Quickfit® Drechsel bottle	Volume = 250mL
V-1	3-way stopcok	Sciencware®		

Pipeline List

Code	*Description*	*Line Size*	*Pressure*	*Temperature*
P-1	Nitrogen inlet	1/8"	1 atm	20 °C
P-2	Nitrogen + Pyrolysis gases and volatiles	1/4"	1 atm	Pyrolysis temperature
P-3	Nitrogen + Pyrolysis gases	1/4"	1 atm	20 °C
P-4	Nitrogen + Pyrolysis gases	1/4"	1 atm	20 °C
P-5	Nitrogen + Pyrolysis gases	1/4"	1 atm	20 °C
P-6	Vent	1/4"	1 atm	20 °C

Instrument List

Code	*Description*	*Connection Size*	*Service*
I-1	Rotameter	1/8"	Gas flow
I-3	Thermocouple		Temperature
I-2	Digital flow meter	1/4"	Gas flow

E-1 – VECSTAR Furnace Front and side view

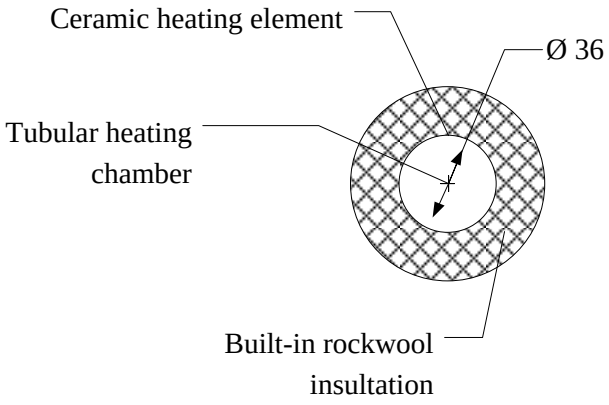

E-1 - Pyrolysis-cold plasma reactor side view

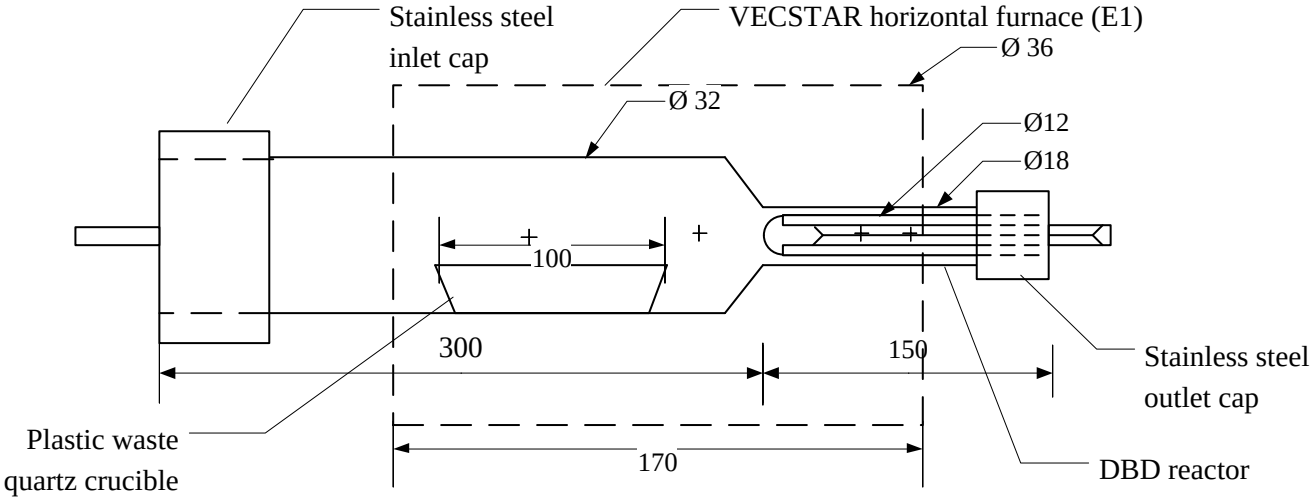

DBD reactor front view

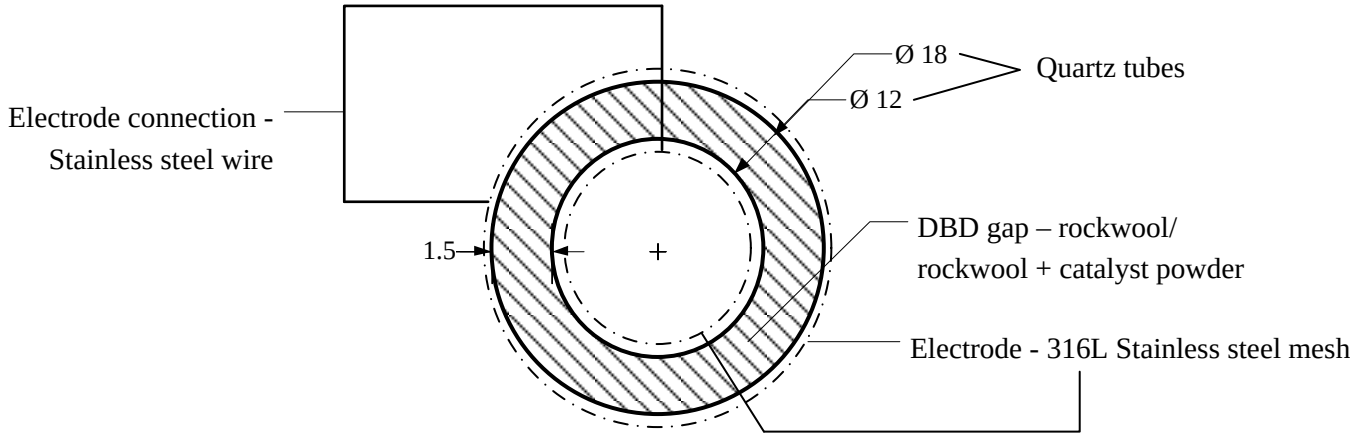

DBD reactor side view

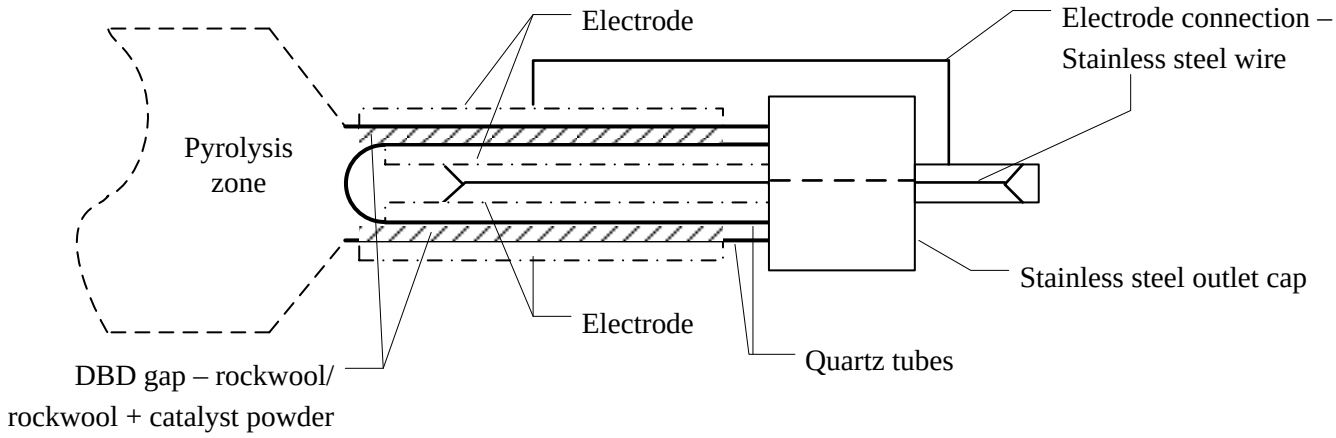

Appendix E Thermal/Catalytic PET pyrolysis set-up

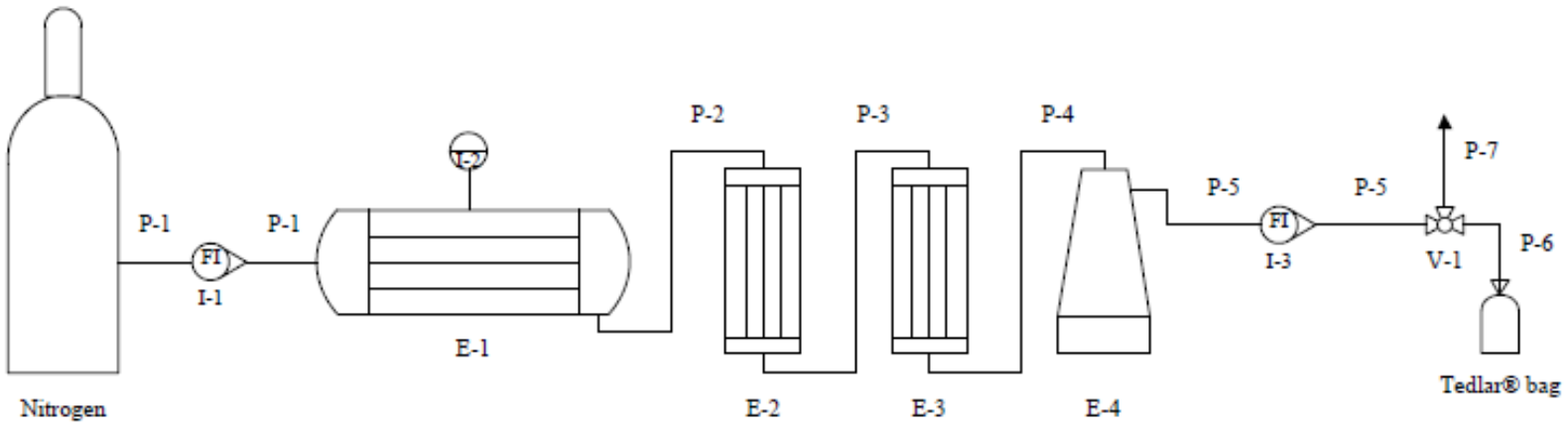

Equipment List				
Code	***Description***	***Manufacturer***	***Model***	***Dimensions***
E-1	Furnace	VECSTAR	VCTF-1	Heated length = 17cm
E-2	Condenser	Sigma-Aldrich	Quickfit® Drechsel bottle	Volume = 250mL
E-3	Condenser	Sigma-Aldrich	Quickfit® Drechsel bottle	Volume = 250mL
E-4	De-ionised water trap	Sigma-Aldrich	Quickfit® Drechsel bottle	Volume = 250mL
V-1	3-way stopcok	Scienceware®		

Pipeline List				
Code	***Description***	***Line Size***	***Pressure***	***Temperature***
P-1	Nitrogen inlet	1/8"	1 atm	20 °C
P-2	Nitrogen + Pyrolysis gases and volatiles	1/4"	1 atm	Pyrolysis temperature
P-3	Nitrogen + Pyrolysis gases and volatiles	1/4"	1 atm	< Pyrolysis temperature > 20 °C
P-4	Nitrogen + Pyrolysis gases	1/4"	1 atm	20 °C
P-5	Nitrogen + Pyrolysis gases	1/4"	1 atm	20 °C
P-6	Nitrogen + Pyrolysis gases	1/4"	1 atm	20 °C
P-7	Vent	1/4"	1 atm	20 °C

Instrument List			
Code	***Description***	***Connection Size***	***Service***
I-1	Rotameter	1/8"	Gas flow
I-2	Thermocouple		Temperature
I-3	Digital flow meter	1/4"	Gas flow

One-stage catalytic PET pyrolysis set-up

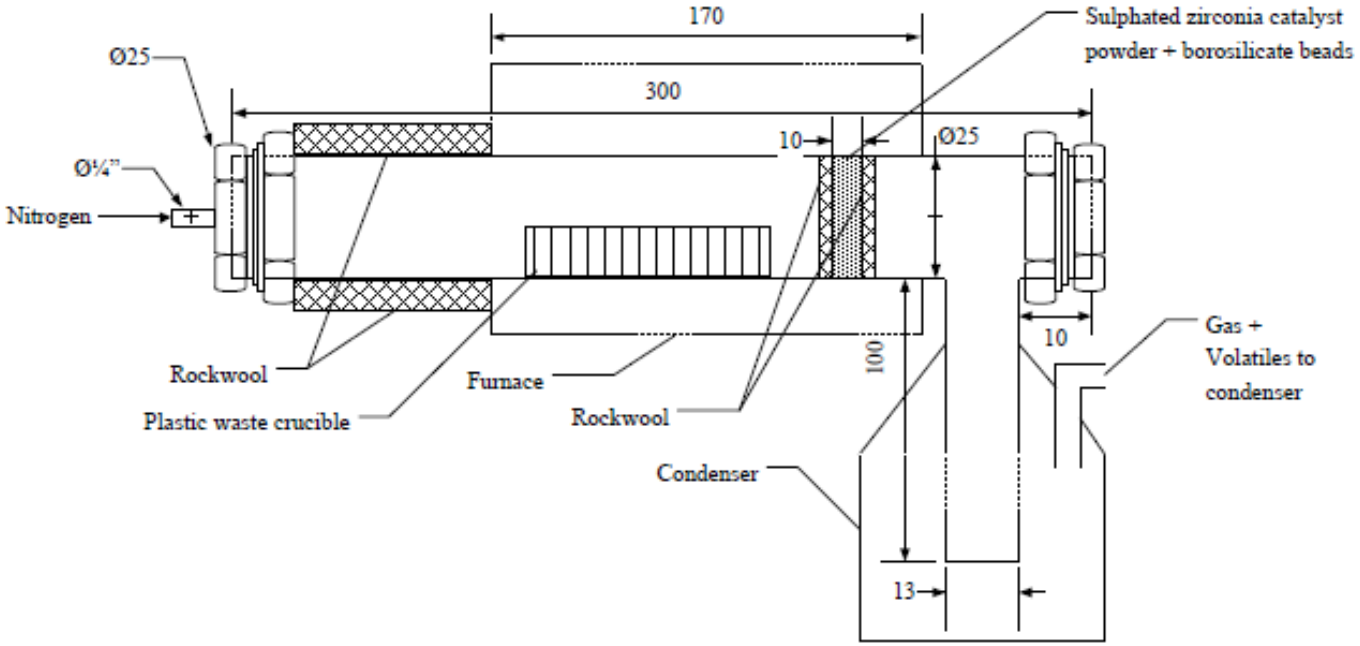

Side view of pyrolysis reactor

Appendix F Thermal/Catalytic one and two-stage pyrolysis set-up

One-stage pyrolysis

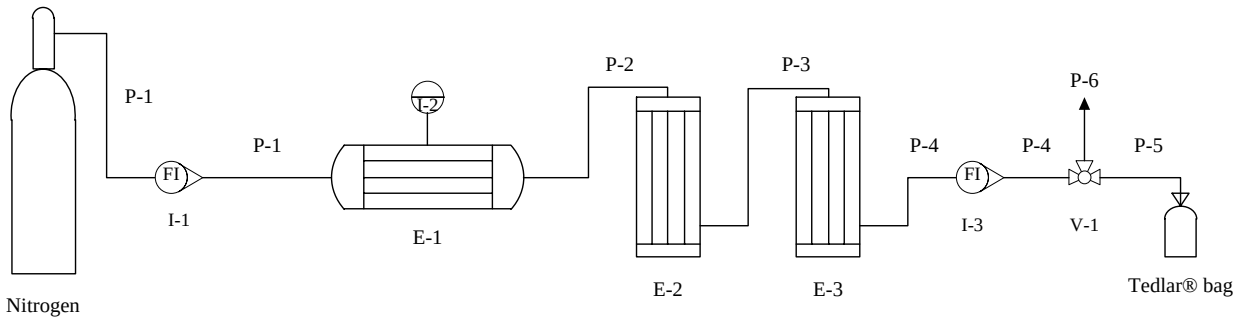

Two-stage pyrolysis

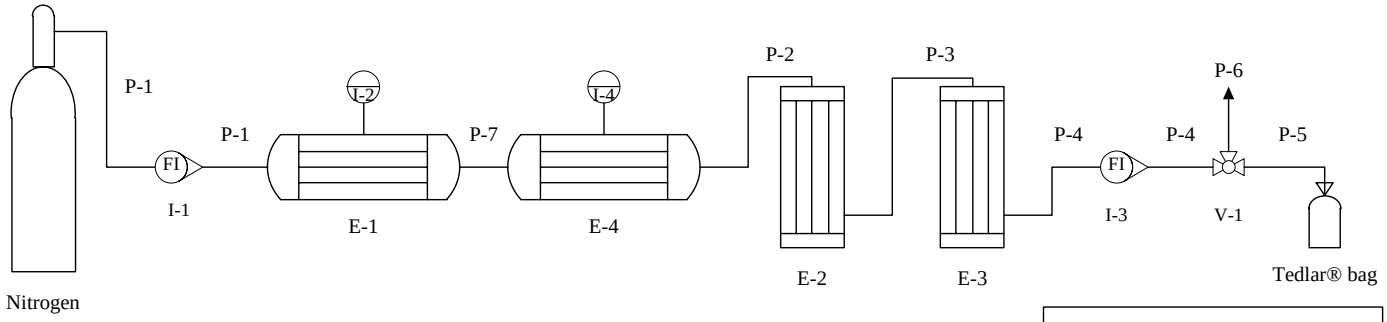

One and two stage catalytic pyrolysis

Equipment List					
Code	***Description***	***Manufacturer***	***Model***	***Dimensions***	***Material***
E-1	Pyrolysis furnace	VECSTAR	VCTF-1/VCTF-4	Heated length = 170mm (VCTF-1)/430mm (VCTF-4)	
E-2	Condenser	Swagelock		O.D. = 80mm, length = 120mm	316L Stainless steel
E-3	Water trap	Sigma-Aldrich	Quickfit® Drechsel bottle	Volume = 250mL	Borosilicate glass
E-4	Catalyst furnace	VECSTAR	VCTF-1	Heated length = 170mm	

Code	***Description***	***Line Size***	***Pressure***	***Temperature***
P-1	Nitrogen	1/8"	1 atm	20 ^{o}C
P-2	N_2 + Pyrolysis gases and volatiles	1/4"	1 atm	Same as furnce internal temperature
P-3	N_2 + Pyrolysis gases	1/4"	1 atm	20 ^{o}C
P-4	N_2 + Pyrolysis gases	1/4"	1 atm	20 ^{o}C
P-5	N_2 + Pyrolysis gases	1/4"	1 atm	20 ^{o}C
P-6	Vent	1/4"	1 atm	20 ^{o}C
P-7	N_2 + Pyrolysis gases and volatiles	1"	1 atm	300-350 ^{o}C

Instrument List			
Code	***Description***	***Connection Size***	***Service***
I-1	Rotameter	1/8"	Gas flow
I-2	Thermocouple		Temperature
I-3	Digital flow meter	1/4"	Gas flow
I-4	Thermocouple		Temperature

One and two stage catalytic pyrolysis

Side view one-stage pyrolysis reactor

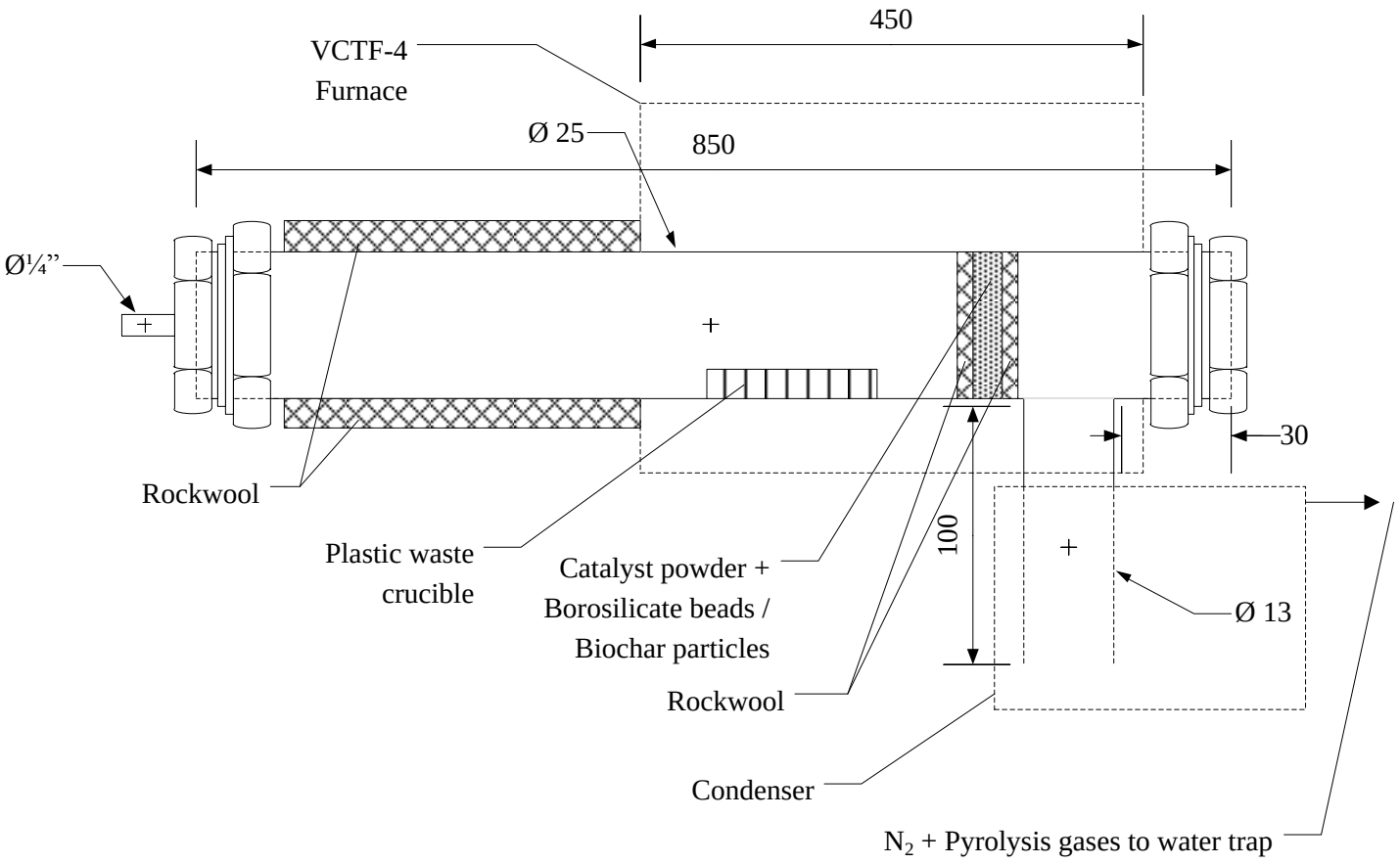

Side view two-stage pyrolysis reactor

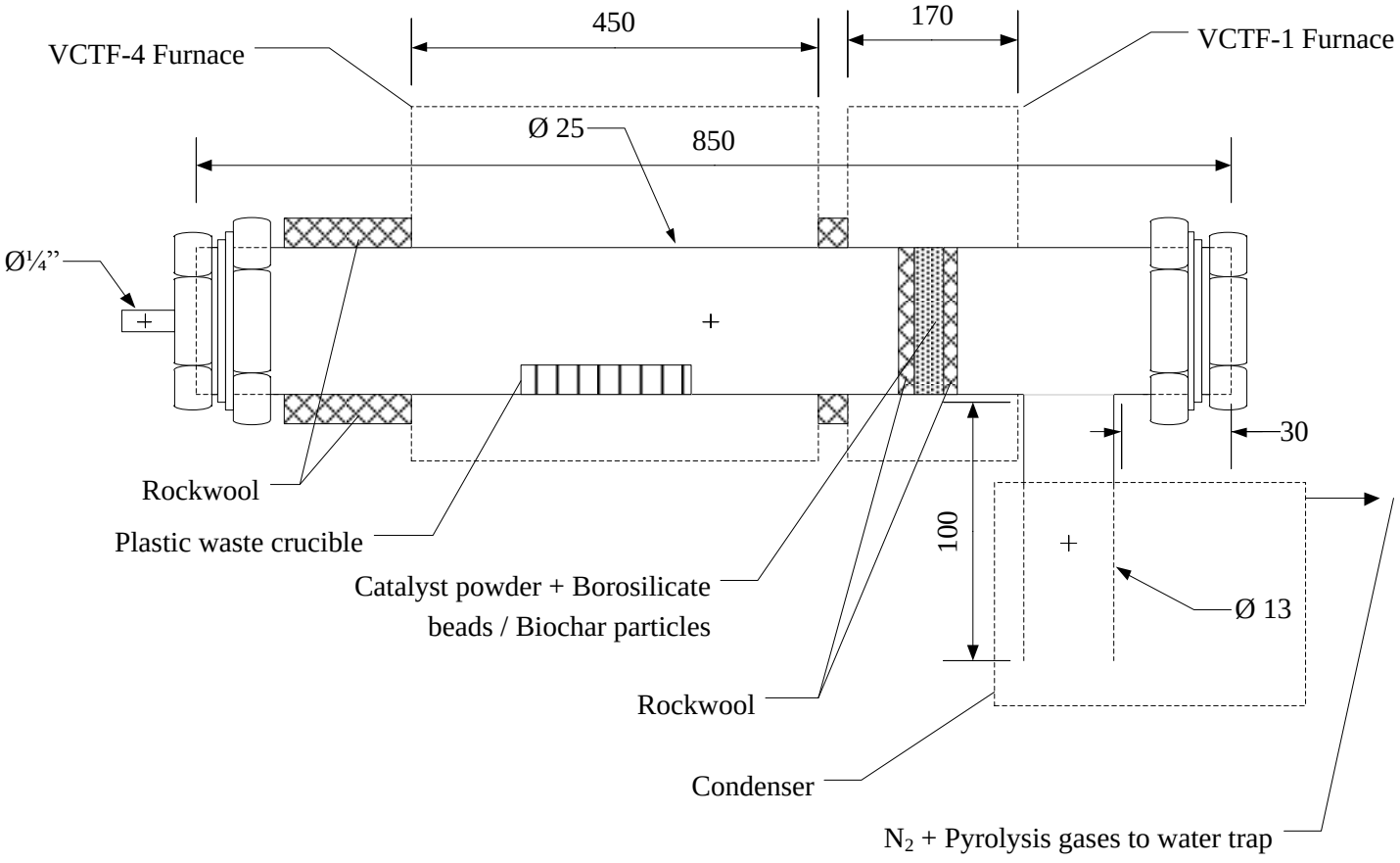

Appendix G Gas composition calculations

	A	B	C	D	E
1	*CATALYST*		g	wt%	Avg N2
2	*RXX, GAS*	Gas	0.383166666666582	18.080437894203	20
3	=(C3+D3)/2	BAG_01	530	566	=(G3+H3)/2
4	[%mol]	Name	Quantity [%mol]	Quantity [wt %]	
5		CO2	0.74	=IFERROR(C5*($W3/$AC$20),0)	
6		H2	0.08	=IFERROR(C6*($W4/$AC$20),0)	
7		O2	4.04	=IFERROR(C7*($W5/$AC$20),0)	
8		N2	73.16	=IFERROR(C8*($W6/$AC$20),0)	
9		CH4	0.17	=IFERROR(C9*($W7/$AC$20),0)	
10		CO	0	=IFERROR(C10*($W8/$AC$20),0)	
11					
12	Total		=SUM(C5:C10)	=SUM(D5:D10)	Total
13	[%wt]	Name	Quantity [mol %]	Quantity [wt %]	
14		Ethene	=IFERROR(D14/(W9/AC$20),0)	0	
15		Ethane	=IFERROR(D15/(W10/AC$20),0)	0.37	
16		Propene	=IFERROR(D16/(W11/AC$20),0)	0.03	
17		Propane	=IFERROR(D17/(W12/AC$20),0)	0	
18		Butene	=IFERROR(D18/(W13/AC$20),0)	0.02	
19		Butane	=IFERROR(D19/(W14/AC$20),0)	0	
20		Pentene	=IFERROR(D20/(W15/AC$20),0)	0	
21		Pentane	=IFERROR(D21/(W16/AC$20),0)	0	
22	Total		=IFERROR(SUM(C14:C21),0)	=SUM(D14:D21)	Total
23	Total (TCD+FID)		=C12+C22	=D12+D22	
24					
25					
26	RED VALUES - TO FILL				
27	BLACK VALUES - DO NOT ALTER				
28					

ASUS: From gas yield and initial plastic waste mass

Nitrogen inlet flow, fixed at rotameter

Gas yield

Values from GC - Permanent gases

ASUS: Values from GC - Hydrocarbons

	F	G	H	I	J
1	***Fill all the numbers in red***				
2	***DO NOT MODIFY VALUES IN BLACK***				
3	BAG_02	567	570	=(K3+L3)/2	BAG_03
4	Name	Quantity [%mol]	Quantity [wt %]		Name
5	CO2	3.63	=IFERROR(G5*($W3/$AC$21),0)		CO2
6	H2	0.23	=IFERROR(G6*($W4/$AC$21),0)		H2
7	O2	5.02	=IFERROR(G7*($W5/$AC$21),0)		O2
8	N2	66.22	=IFERROR(G8*($W6/$AC$21),0)		N2
9	CH4	1	=IFERROR(G9*($W7/$AC$21),0)		CH4
10	CO	0	=IFERROR(G10*($W8/$AC$21),0)		CO
11					
12		=SUM(G5:G10)	=SUM(H5:H10)	Total	
13	Name	Quantity [mol %]	Quantity [wt %]		Name
14	Ethene	=IFERROR(H14/(W9/AC$21),0)	0		Ethene
15	Ethane	=IFERROR(H15/(W10/AC$21),0)	0.36		Ethane
16	Propene	=IFERROR(H16/(W11/AC$21),0)	0.01		Propene
17	Propane	=IFERROR(H17/(W12/AC$21),0)	0		Propane
18	Butene	=IFERROR(H18/(W13/AC$21),0)	0		Butene
19	Butane	=IFERROR(H19/(W14/AC$21),0)	0		Butane
20	Pentene	=IFERROR(H20/(W15/AC$21),0)	0		Pentene
21	Pentane	=IFERROR(H21/(W16/AC$21),0)	0		Pentane
22		=SUM(G14:G21)	=SUM(H14:H21)	Total	
23		=G12+G22	=H12+H22		
24					
25					
26					
27					
28					

	K	L	M	N	O
1					
2					
3			=(O3+P3)/2	BAG_04	
4	Quantity [%mol]	Quantity [wt %]		Name	Quantity [%mol]
5		=IFERROR(K5*($W3/$AC$22),0)		CO2	
6		=IFERROR(K6*($W4/$AC$22),0)		H2	
7		=IFERROR(K7*($W5/$AC$22),0)		O2	
8		=IFERROR(K8*($W6/$AC$22),0)		N2	
9		=IFERROR(K9*($W7/$AC$22),0)		CH4	
10		=IFERROR(K10*($W8/$AC$22),0)		CO	
11					
12	=SUM(K5:K10)	=SUM(L5:L10)	Total		=SUM(O5:O10)
13	Quantity [mol %]	Quantity [wt %]		Name	Quantity [mol %]
14	=IFERROR(L14/(W9/AC$22),0)			Ethene	=IFERROR(P14/(W9/AC$23),)
15	=IFERROR(L15/(W10/AC$22),0)			Ethane	=IFERROR(P15/(W10/AC$23),0)
16	=IFERROR(L16/(W11/AC$22),0)			Propene	=IFERROR(P16/(W11/AC$23),0)
17	=IFERROR(L17/(W12/AC$22),0)			Propane	=IFERROR(P17/(W12/AC$23),0)
18	=IFERROR(L18/(W13/AC$22),0)			Butene	=IFERROR(P18/(W13/AC$23),0)
19	=IFERROR(L19/(W14/AC$22),0)			Butane	=IFERROR(P19/(W14/AC$23),0)
20	=IFERROR(L20/(W15/AC$22),0)			Pentene	=IFERROR(P20/(W15/AC$23),0)
21	=IFERROR(L21/(W16/AC$22),0)			Pentane	=IFERROR(P21/(W16/AC$23),0)
22	=SUM(K14:K21)	=SUM(L14:L21)	Total		=SUM(O14:O21)
23	=K12+K22	=L12+L22			=O12+O22
24					
25					
26					
27					
28					

	P	Q	R	S	T	U
1						
2						
3		=(S3+T3)/2	BAG_05			
4	Quantity [wt %]		Name	Quantity [%mol]	Quantity [wt %]	
5	=IFERROR(O5*($W3/$AC$24),0)		CO2		=IFERROR(S5*($W3/$AC$24),0)	
6	=IFERROR(O6*($W4/$AC$24),0)		H2		=IFERROR(S6*($W4/$AC$24),0)	
7	=IFERROR(O7*($W5/$AC$24),0)		O2		=IFERROR(S7*($W5/$AC$24),0)	
8	=IFERROR(O8*($W6/$AC$24),0)		N2		=IFERROR(S8*($W6/$AC$24),0)	
9	=IFERROR(O9*($W7/$AC$24),0)		CH4		=IFERROR(S9*($W7/$AC$24),0)	
10	=IFERROR(O10*($W8/$AC$24),0)		CO		=IFERROR(S10*($W8/$AC$24),0)	
11						
12	=SUM(P5:P10)	Total		=SUM(S5:S10)	=SUM(T5:T10)	
13	Quantity [wt %]		Name	Quantity [mol %]	Quantity [wt %]	
14			Ethene	=IFERROR(T14/(W9/AC$24),0)		
15			Ethane	=IFERROR(T15/(W10/AC$24),0)		
16			Propene	=IFERROR(T16/(W11/AC$24),0)		
17			Propane	=IFERROR(T17/(W12/AC$24),0)		
18			Butene	=IFERROR(T18/(W13/AC$24),0)		
19			Butane	=IFERROR(T19/(W14/AC$24),0)		
20			Pentene	=IFERROR(T20/(W15/AC$24),0)		=B3
21			Pentane	=IFERROR(T21/(W16/AC$24),0)		=F3
22	=SUM(P14:P21)	Total		=SUM(S14:S21)	=SUM(T14:T21)	=J3
23	=P12+P22			=S12+S22	=T12+T22	=N3
24						=R3
25						Total
26						
27						
28						

	V	W	X	Y	Z	AA
1			=B3		=F3	
2		MWi	Correc/[%mol]	Correc/[wt.%]	Correc/[%mol]	Correc/[wt.%]
3	CO2	=12+2*16	=C5*100/C$23	=D5*100/D$23	=G5*100/G$23	=H5*100/H$23
4	H2	=2*1	=C6*100/C$23	=D6*100/D$23	=G6*100/G$23	=H6*100/H$23
5	O2	=16*2	=C7*100/C$23	=D7*100/D$23	=G7*100/G$23	=H7*100/H$23
6	N2	=14*2	=C8*100/C$23	=D8*100/D$23	=G8*100/G$23	=H8*100/H$23
7	CH4	=12+4	=C9*100/C$23	=D9*100/D$23	=G9*100/G$23	=H9*100/H$23
8	CO	=12+16	=C10*100/C$23	=D10*100/D$23	=G10*100/G$23	=H10*100/H$23
9	Ethene	=12*2+4	=C14*100/C$23	=D14*100/D$23	=G14*100/G$23	=H14*100/H$23
10	Ethane	=12*2+6	=C15*100/C$23	=D15*100/D$23	=G15*100/G$23	=H15*100/H$23
11	Propene	=12*3+6	=C16*100/C$23	=D16*100/D$23	=G16*100/G$23	=H16*100/H$23
12	Propane	=12*3+8	=C17*100/C$23	=D17*100/D$23	=G17*100/G$23	=H17*100/H$23
13	Butene	=12*4+8	=C18*100/C$23	=D18*100/D$23	=G18*100/G$23	=H18*100/H$23
14	Butane	=12*4+10	=C19*100/C$23	=D19*100/D$23	=G19*100/G$23	=H19*100/H$23
15	Pentene	=12*5+10	=C20*100/C$23	=D20*100/D$23	=G20*100/G$23	=H20*100/H$23
16	Pentane	=12*5+12	=C21*100/C$23	=D21*100/D$23	=G21*100/G$23	=H21*100/H$23
17	Total		=SUM(X3:X16)	=SUM(Y3:Y16)	=SUM(Z3:Z16)	=SUM(AA3:AA16)
18	Total no N2, O2		=X17-X6-X5	=Y17-Y6-Y5	=Z17-Z6-Z5	=AA17-AA6-AA5
19	Avg T	Avg collect Time/[s]	Collec time/[s]	Avg Flow/[mL/s]	Volume/[mL]	P/RT
20	=A3		=7*60	=AVERAGE(31.4,31.4,31.4,31.4,193)/60	=Y20*X20	=1/(0.082*(A3+273))
21	=E3		=10*60	=AVERAGE(193,133)/60	=Y21*X21	=1/(0.082*(E3+273))
22	=I3				=Y22*X22	=1/(0.082*(I3+273))
23	=M3				=Y23*X23	=1/(0.082*(M3+273))
24	=Q3				=Y24*X24	=1/(0.082*(Q3+273))
25					=SUM(Z20:Z24)	
26						
27						
28						

	AB
1	=J3
2	Correc/[%mol]
3	=K5*100/K$23
4	=K6*100/K$23
5	=K7*100/K$23
6	=K8*100/K$23
7	=K9*100/K$23
8	=K10*100/K$23
9	=K14*100/K$23
10	=K15*100/K$23
11	=K16*100/K$23
12	=K17*100/K$23
13	=K18*100/K$23
14	=K19*100/K$23
15	=K20*100/K$23
16	=K21*100/K$23
17	=SUM(AB3:AB16)
18	=AB17-AB6-AB5
19	mol gas
20	=AA20*Z20/1000
21	=AA21*Z21/1000
22	=AA22*Z22/1000
23	=AA23*Z23/1000
24	=AA24*Z24/1000
25	
26	
27	
28	

	AC
1	
2	Correc/[wt.%]
3	=L5*100/L$23
4	=L6*100/L$23
5	=L7*100/L$23
6	=L8*100/L$23
7	=L9*100/L$23
8	=L10*100/L$23
9	=L14*100/L$23
10	=L15*100/L$23
11	=L16*100/L$23
12	=L17*100/L$23
13	=L18*100/L$23
14	=L19*100/L$23
15	=L20*100/L$23
16	=L21*100/L$23
17	=SUM(AC3:AC16)
18	=AC17-AC6-AC5
19	Mwgas
20	=C$5/100*W3+C6/100*W4+C7/100*W5+C8/100*W6+C9/100*W7+C10/100*W8+D14/100*W9+D15/100*W10+D16/100*W11+D17/100*W12+D18/100*W13
21	=G$5/100*W3+G6/100*W4+G7/100*W5+G8/100*W6+G9/100*W7+G10/100*W8+H14/100*W9+H15/100*W10+H16/100*W11+H17/100*W12+H18/100*W1
22	=K$5/100*W3+K6/100*W4+K7/100*W5+K8/100*W6+K9/100*W7+K10/100*W8+L14/100*W9+L15/100*W10+L16/100*W11+L17/100*W12+L18/100*W13+L
23	=O$5/100*W3+O6/100*W4+O7/100*W5+O8/100*W6+O9/100*W7+O10/100*W8+P14/100*W9+P15/100*W10+P16/100*W11+P17/100*W12+P18/100*W1
24	=S$5/100*W3+S6/100*W4+S7/100*W5+S8/100*W6+S9/100*W7+S10/100*W8+T14/100*W9+T15/100*W10+T16/100*W11+T17/100*W12+T18/100*W13+T
25	
26	
27	
28	

	AD	AE	AF	AG	AH	AI	AJ
1	=N3		=R3			=B3	
2	Correc/[%mol]	Correc/[wt.%]	Correc/[%mol]	Correc/[wt.%]		Correc/[mol]	Correc/[g]
3	=O5*100/O$23	=P5*100/P$23	=S5*100/S$23	=T5*100/T$23	CO2	=X3/100*$AB$20	=Y3/100*$AG$20
4	=O6*100/O$23	=P6*100/P$23	=S6*100/S$23	=T6*100/T$23	H2	=X4/100*AB$20	=Y4/100*$AG$20
5	=O7*100/O$23	=P7*100/P$23	=S7*100/S$23	=T7*100/T$23	O2	=X5/100*AB$20	=Y5/100*$AG$20
6	=O8*100/O$23	=P8*100/P$23	=S8*100/S$23	=T8*100/T$23	N2	=X6/100*AB$20	=Y6/100*$AG$20
7	=O9*100/O$23	=P9*100/P$23	=S9*100/S$23	=T9*100/T$23	CH4	=X7/100*AB$20	=Y7/100*$AG$20
8	=O10*100/O$23	=P10*100/P$23	=S10*100/S$23	=T10*100/T$23	CO	=X8/100*AB$20	=Y8/100*$AG$20
9	=O14*100/O$23	=P14*100/P$23	=S14*100/S$23	=T14*100/T$23	Ethene	=X9/100*AB$20	=Y9/100*$AG$20
10	=O15*100/O$23	=P15*100/P$23	=S15*100/S$23	=T15*100/T$23	Ethane	=X10/100*AB$20	=Y10/100*$AG$20
11	=O16*100/O$23	=P16*100/P$23	=S16*100/S$23	=T16*100/T$23	Propene	=X11/100*AB$20	=Y11/100*$AG$20
12	=O17*100/O$23	=P17*100/P$23	=S17*100/S$23	=T17*100/T$23	Propane	=X12/100*AB$20	=Y12/100*$AG$20
13	=O18*100/O$23	=P18*100/P$23	=S18*100/S$23	=T18*100/T$23	Butene	=X13/100*AB$20	=Y13/100*$AG$20
14	=O19*100/O$23	=P19*100/P$23	=S19*100/S$23	=T19*100/T$23	Butane	=X14/100*AB$20	=Y14/100*$AG$20
15	=O20*100/O$23	=P20*100/P$23	=S20*100/S$23	=T20*100/T$23	Pentene	=X15/100*AB$20	=Y15/100*$AG$20
16	=O21*100/O$23	=P21*100/P$23	=S21*100/S$23	=T21*100/T$23	Pentane	=X16/100*AB$20	=Y16/100*$AG$20
17	=SUM(AD3:AD16)	=SUM(AE3:AE16)	=SUM(AF3:AF16)	=SUM(AG3:AG16)	Total	=SUM(AI3:AI16)	=SUM(AJ3:AJ16)
18	=AD17-AD6-AD5	=AE17-AE6-AE5	=AF17-AF6-AF5	=AG17-AG6-AG5	Total No N2,O2	=AI17-AI6-AI5	=AJ17-AJ6-AJ5
19	Vol N2/[mL]	Vol gas/[mL]	%vol. gas	tot g	tot g (no N2,O2)	bag wt%	
20	=X20*E$2/60	=Z20-AD20	=AE20/AE$25*100	=AB20*AC20	=AG20-AJ5-AJ6	=AG20/$AG$25*100	
21	=X21*E$2/60	=Z21-AD21	=AE21/AE$25*100	=AB21*AC21	=AG21-AL6-AL7	=AG21/$AG$25*100	
22	=X22*E$2/60	=Z22-AD22	=AE22/AE$25*100	=AB22*AC22	=AG22-AN5-AN6	=AG22/$AG$25*100	
23	=X23*E$2/60	=Z23-AD23	=AE23/AE$25*100	=AB23*AC23	=AG23-AP5-AP6	=AG23/$AG$25*100	
24	=X24*E$2/60	=Z24-AD24	=AE24/AE$25*100	=AB24*AC24	=AG24-AR5-AR6	=AG24/$AG$25*100	
25	=SUM(AD20:AD24)	=SUM(AE20:AE24)	=SUM(AF20:AF24)	=SUM(AG20:AG24)	=SUM(AH20:AH24)	=SUM(AI20:AI24)	
26							
27							
28							

	AK	AL	AM	AN	AO	AP
1	=F3		=J3		=N3	
2	Correc/[mol]	Correc/[g]	Correc/[mol]	Correc/[g]	Correc/[mol]	Correc/[g]
3	=Z3/100*$AB$21	=AA3/100*$AG$21	=AB3/100*$AB$22	=AC3/100*$AG$22	=AD3/100*$AB$23	=AE3/100*$AG$23
4	=Z4/100*$AB$21	=AA4/100*$AG$21	=AB4/100*$AB$22	=AC4/100*$AG$22	=AD4/100*$AB$23	=AE4/100*$AG$23
5	=Z5/100*$AB$21	=AA5/100*$AG$21	=AB5/100*$AB$22	=AC5/100*$AG$22	=AD5/100*$AB$23	=AE5/100*$AG$23
6	=Z6/100*$AB$21	=AA6/100*$AG$21	=AB6/100*$AB$22	=AC6/100*$AG$22	=AD6/100*$AB$23	=AE6/100*$AG$23
7	=Z7/100*$AB$21	=AA7/100*$AG$21	=AB7/100*$AB$22	=AC7/100*$AG$22	=AD7/100*$AB$23	=AE7/100*$AG$23
8	=Z8/100*$AB$21	=AA8/100*$AG$21	=AB8/100*$AB$22	=AC8/100*$AG$22	=AD8/100*$AB$23	=AE8/100*$AG$23
9	=Z9/100*$AB$21	=AA9/100*$AG$21	=AB9/100*$AB$22	=AC9/100*$AG$22	=AD9/100*$AB$23	=AE9/100*$AG$23
10	=Z10/100*$AB$21	=AA10/100*$AG$21	=AB10/100*$AB$22	=AC10/100*$AG$22	=AD10/100*$AB$23	=AE10/100*$AG$23
11	=Z11/100*$AB$21	=AA11/100*$AG$21	=AB11/100*$AB$22	=AC11/100*$AG$22	=AD11/100*$AB$23	=AE11/100*$AG$23
12	=Z12/100*$AB$21	=AA12/100*$AG$21	=AB12/100*$AB$22	=AC12/100*$AG$22	=AD12/100*$AB$23	=AE12/100*$AG$23
13	=Z13/100*$AB$21	=AA13/100*$AG$21	=AB13/100*$AB$22	=AC13/100*$AG$22	=AD13/100*$AB$23	=AE13/100*$AG$23
14	=Z14/100*$AB$21	=AA14/100*$AG$21	=AB14/100*$AB$22	=AC14/100*$AG$22	=AD14/100*$AB$23	=AE14/100*$AG$23
15	=Z15/100*$AB$21	=AA15/100*$AG$21	=AB15/100*$AB$22	=AC15/100*$AG$22	=AD15/100*$AB$23	=AE15/100*$AG$23
16	=Z16/100*$AB$21	=AA16/100*$AG$21	=AB16/100*$AB$22	=AC16/100*$AG$22	=AD16/100*$AB$23	=AE16/100*$AG$23
17	=SUM(AK3:AK16)	=SUM(AL3:AL16)	=SUM(AM3:AM16)	=SUM(AN3:AN16)	=SUM(AO3:AO16)	=SUM(AP3:AP16)
18	=AK17-AK6-AK5	=AL17-AL6-AL5	=AM17-AM6-AM5	=AN17-AN6-AN5	=AO17-AO6-AO5	=AP17-AP6-AP5
19						
20	[g]	=B3	=F3	=J3	=N3	=R3
21	H2	=AJ4*1000	=AL4*1000	=AN4*1000	=AP4*1000	=AR4*1000
22	[mg/s]	=AL20	=AM20	=AN20	=AO20	=AP20
23	H2	=Y20*AL$21/Z20*1000	=Y21*AM$21/Z21*1000	=Y22*AN$21/Z22*1000	=Y23*AO$21/Z23*1000	=Y24*AP$21/Z24*1000
24	[mmol/s]	=AL22	=AM22	=AN22	=AO22	=AP22
25	H2	=AL23/2	=AM23/2	=AN23/2	=AO23/2	=AP23/2
26	**[mL/s]**	**=AL24**	**=AM24**	**=AN24**	**=AO24**	**=AP24**
27	**H2**	**=AL25/$AA20**	**=AM25/$AA21**	**=AN25/$AA22**	**=AO25/$AA23**	**=AP25/$AA24**
28						

	AQ	AR	AS	AT	AU
1	=R3		Total		No, N2, O2
2	Correc/[mol]	Correc/[g]	Correc/[mol]	Correc/[g]	gi/tot bag
3	=AF3/100*$AB$24	=AG3/100*$AG$24	=SUM(AI3,AK3,AM3,AO3,AQ3)	=SUM(AJ3,AL3,AN3,AP3,AR3)	CO2
4	=AF4/100*$AB$24	=AG4/100*$AG$24	=SUM(AI4,AK4,AM4,AO4,AQ4)	=SUM(AJ4,AL4,AN4,AP4,AR4)	H2
5	=AF5/100*$AB$24	=AG5/100*$AG$24	=SUM(AI5,AK5,AM5,AO5,AQ5)	=SUM(AJ5,AL5,AN5,AP5,AR5)	CH4
6	=AF6/100*$AB$24	=AG6/100*$AG$24	=SUM(AI6,AK6,AM6,AO6,AQ6)	=SUM(AJ6,AL6,AN6,AP6,AR6)	CO
7	=AF7/100*$AB$24	=AG7/100*$AG$24	=SUM(AI7,AK7,AM7,AO7,AQ7)	=SUM(AJ7,AL7,AN7,AP7,AR7)	Ethene
8	=AF8/100*$AB$24	=AG8/100*$AG$24	=SUM(AI8,AK8,AM8,AO8,AQ8)	=SUM(AJ8,AL8,AN8,AP8,AR8)	Ethane
9	=AF9/100*$AB$24	=AG9/100*$AG$24	=SUM(AI9,AK9,AM9,AO9,AQ9)	=SUM(AJ9,AL9,AN9,AP9,AR9)	Propene
10	=AF10/100*$AB$24	=AG10/100*$AG$24	=SUM(AI10,AK10,AM10,AO10,AQ10)	=SUM(AJ10,AL10,AN10,AP10,AR10)	Propane
11	=AF11/100*$AB$24	=AG11/100*$AG$24	=SUM(AI11,AK11,AM11,AO11,AQ11)	=SUM(AJ11,AL11,AN11,AP11,AR11)	Butene
12	=AF12/100*$AB$24	=AG12/100*$AG$24	=SUM(AI12,AK12,AM12,AO12,AQ12)	=SUM(AJ12,AL12,AN12,AP12,AR12)	Butane
13	=AF13/100*$AB$24	=AG13/100*$AG$24	=SUM(AI13,AK13,AM13,AO13,AQ13)	=SUM(AJ13,AL13,AN13,AP13,AR13)	Pentene
14	=AF14/100*$AB$24	=AG14/100*$AG$24	=SUM(AI14,AK14,AM14,AO14,AQ14)	=SUM(AJ14,AL14,AN14,AP14,AR14)	Pentane
15	=AF15/100*$AB$24	=AG15/100*$AG$24	=SUM(AI15,AK15,AM15,AO15,AQ15)	=SUM(AJ15,AL15,AN15,AP15,AR15)	Total
16	=AF16/100*$AB$24	=AG16/100*$AG$24	=SUM(AI16,AK16,AM16,AO16,AQ16)	=SUM(AJ16,AL16,AN16,AP16,AR16)	
17	=SUM(AQ3:AQ16)	=SUM(AR3:AR16)	=SUM(AS3:AS16)	=SUM(AT3:AT16)	
18	=AQ17-AQ6-AQ5	=AR17-AR6-AR5	=AS17-AS6-AS5	=AT17-AT6-AT5	
19					
20	Total				
21	=SUM(AL21:AP21)				
22	Total				
23	=SUM(AL23:AP23)				
24	Total				
25	=SUM(AL25:AP25)				
26	**Total**				
27	**=SUM(AL27:AP27)**				
28					

	AV	AW	AX	AY
1	=F3	=F3	=J3	=N3
2	Correc/[%wt.]	Correc/[%wt.]	Correc/[%wt.]	Correc/[%wt.]
3	=IF(AJ$18,AJ3/AJ$18*100,0)	=IF(AL$18,AL3/AL$18*100,0)	=IF(AN$18,AN3/AN$18*100,0)	=IF(AP$18,AP3/AP$18*100,0)
4	=IF(AJ$18,AJ4/AJ$18*100,0)	=IF(AL$18,AL4/AL$18*100,0)	=IF(AN$18,AN4/AN$18*100,0)	=IF(AP$18,AP4/AP$18*100,0)
5	=IF(AJ$18,AJ7/AJ$18*100,0)	=IF(AL$18,AL7/AL$18*100,0)	=IF(AN$18,AN7/AN$18*100,0)	=IF(AP$18,AP7/AP$18*100,0)
6	=IF(AJ$18,AJ8/AJ$18*100,0)	=IF(AL$18,AL8/AL$18*100,0)	=IF(AN$18,AN8/AN$18*100,0)	=IF(AP$18,AP8/AP$18*100,0)
7	=IF(AJ$18,AJ9/AJ$18*100,0)	=IF(AL$18,AL9/AL$18*100,0)	=IF(AN$18,AN9/AN$18*100,0)	=IF(AP$18,AP9/AP$18*100,0)
8	=IF(AJ$18,AJ10/AJ$18*100,0)	=IF(AL$18,AL10/AL$18*100,0)	=IF(AN$18,AN10/AN$18*100,0)	=IF(AP$18,AP10/AP$18*100,0)
9	=IF(AJ$18,AJ11/AJ$18*100,0)	=IF(AL$18,AL11/AL$18*100,0)	=IF(AN$18,AN11/AN$18*100,0)	=IF(AP$18,AP11/AP$18*100,0)
10	=IF(AJ$18,AJ12/AJ$18*100,0)	=IF(AL$18,AL12/AL$18*100,0)	=IF(AN$18,AN12/AN$18*100,0)	=IF(AP$18,AP12/AP$18*100,0)
11	=IF(AJ$18,AJ13/AJ$18*100,0)	=IF(AL$18,AL13/AL$18*100,0)	=IF(AN$18,AN13/AN$18*100,0)	=IF(AP$18,AP13/AP$18*100,0)
12	=IF(AJ$18,AJ14/AJ$18*100,0)	=IF(AL$18,AL14/AL$18*100,0)	=IF(AN$18,AN14/AN$18*100,0)	=IF(AP$18,AP14/AP$18*100,0)
13	=IF(AJ$18,AJ15/AJ$18*100,0)	=IF(AL$18,AL15/AL$18*100,0)	=IF(AN$18,AN15/AN$18*100,0)	=IF(AP$18,AP15/AP$18*100,0)
14	=IF(AJ$18,AJ16/AJ$18*100,0)	=IF(AL$18,AL16/AL$18*100,0)	=IF(AN$18,AN16/AN$18*100,0)	=IF(AP$18,AP16/AP$18*100,0)
15	=SUM(AV3:AV14)	=SUM(AW3:AW14)	=SUM(AX3:AX14)	=SUM(AY3:AY14)
16				
17				
18				
19				
20				
21				
22				
23				
24				
25				
26				
27				
28				

	AZ	BA	BB	BC
1	=R3	*No, N2, O2*	*=B3*	*=F3*
2	Correc/[%wt.]	*gi/g PP*	*Correc/[%wt.]*	*Correc/[%wt.]*
3	=IF(AR$18,AR3/AR$18*100,0)	*CO2*	*=AV3*($AH$20/$AH$25)*($D$2/100)*	*=AW3*($AH$21/$AH$25)*($D$2/100)*
4	=IF(AR$18,AR4/AR$18*100,0)	*H2*	*=AV4*($AH$20/$AH$25)*($D$2/100)*	*=AW4*($AH$21/$AH$25)*($D$2/100)*
5	=IF(AR$18,AR7/AR$18*100,0)	*CH4*	*=AV5*($AH$20/$AH$25)*($D$2/100)*	*=AW5*($AH$21/$AH$25)*($D$2/100)*
6	=IF(AR$18,AR8/AR$18*100,0)	*CO*	*=AV6*($AH$20/$AH$25)*($D$2/100)*	*=AW6*($AH$21/$AH$25)*($D$2/100)*
7	=IF(AR$18,AR9/AR$18*100,0)	*Ethene*	*=AV7*($AH$20/$AH$25)*($D$2/100)*	*=AW7*($AH$21/$AH$25)*($D$2/100)*
8	=IF(AR$18,AR10/AR$18*100,0)	*Ethane*	*=AV8*($AH$20/$AH$25)*($D$2/100)*	*=AW8*($AH$21/$AH$25)*($D$2/100)*
9	=IF(AR$18,AR11/AR$18*100,0)	*Propene*	*=AV9*($AH$20/$AH$25)*($D$2/100)*	*=AW9*($AH$21/$AH$25)*($D$2/100)*
10	=IF(AR$18,AR12/AR$18*100,0)	*Propane*	*=AV10*($AH$20/$AH$25)*($D$2/100)*	*=AW10*($AH$21/$AH$25)*($D$2/100)*
11	=IF(AR$18,AR13/AR$18*100,0)	*Butene*	*=AV11*($AH$20/$AH$25)*($D$2/100)*	*=AW11*($AH$21/$AH$25)*($D$2/100)*
12	=IF(AR$18,AR14/AR$18*100,0)	*Butane*	*=AV12*($AH$20/$AH$25)*($D$2/100)*	*=AW12*($AH$21/$AH$25)*($D$2/100)*
13	=IF(AR$18,AR15/AR$18*100,0)	*Pentene*	*=AV13*($AH$20/$AH$25)*($D$2/100)*	*=AW13*($AH$21/$AH$25)*($D$2/100)*
14	=IF(AR$18,AR16/AR$18*100,0)	*Pentane*	*=AV14*($AH$20/$AH$25)*($D$2/100)*	*=AW14*($AH$21/$AH$25)*($D$2/100)*
15	=SUM(AZ3:AZ14)	*Total*	*=SUM(BB3:BB14)*	*=SUM(BC3:BC14)*
16		*C2*	*=BB7+BB8*	*=BC7+BC8*
17		*C3*	*=BB9+BB10*	*=BC9+BC10*
18		*C4*	*=BB11+BB12*	*=BC11+BC12*
19				
20				
21				
22				
23				
24				
25				
26				
27				
28				

	BD	BE	BF	BG
1	=J3	=N3	=R3	Total
2	Correc/[%wt.]	Correc/[%wt.]	Correc/[%wt.]	Correc/[%wt.]
3	=AX3*($AH$22/$AH$25)*($D$2/100)	=AY3*($AH$23/$AH$25)*($D$2/100)	=AZ3*($AH$24/$AH$25)*($D$2/100)	=SUM(BB3:BF3)
4	=AX4*($AH$22/$AH$25)*($D$2/100)	=AY4*($AH$23/$AH$25)*($D$2/100)	=AZ4*($AH$24/$AH$25)*($D$2/100)	=SUM(BB4:BF4)
5	=AX5*($AH$22/$AH$25)*($D$2/100)	=AY5*($AH$23/$AH$25)*($D$2/100)	=AZ5*($AH$24/$AH$25)*($D$2/100)	=SUM(BB5:BF5)
6	=AX6*($AH$22/$AH$25)*($D$2/100)	=AY6*($AH$23/$AH$25)*($D$2/100)	=AZ6*($AH$24/$AH$25)*($D$2/100)	=SUM(BB6:BF6)
7	=AX7*($AH$22/$AH$25)*($D$2/100)	=AY7*($AH$23/$AH$25)*($D$2/100)	=AZ7*($AH$24/$AH$25)*($D$2/100)	=SUM(BB7:BF7)
8	=AX8*($AH$22/$AH$25)*($D$2/100)	=AY8*($AH$23/$AH$25)*($D$2/100)	=AZ8*($AH$24/$AH$25)*($D$2/100)	=SUM(BB8:BF8)
9	=AX9*($AH$22/$AH$25)*($D$2/100)	=AY9*($AH$23/$AH$25)*($D$2/100)	=AZ9*($AH$24/$AH$25)*($D$2/100)	=SUM(BB9:BF9)
10	=AX10*($AH$22/$AH$25)*($D$2/100)	=AY10*($AH$23/$AH$25)*($D$2/100)	=AZ10*($AH$24/$AH$25)*($D$2/100)	=SUM(BB10:BF10)
11	=AX11*($AH$22/$AH$25)*($D$2/100)	=AY11*($AH$23/$AH$25)*($D$2/100)	=AZ11*($AH$24/$AH$25)*($D$2/100)	=SUM(BB11:BF11)
12	=AX12*($AH$22/$AH$25)*($D$2/100)	=AY12*($AH$23/$AH$25)*($D$2/100)	=AZ12*($AH$24/$AH$25)*($D$2/100)	=SUM(BB12:BF12)
13	=AX13*($AH$22/$AH$25)*($D$2/100)	=AY13*($AH$23/$AH$25)*($D$2/100)	=AZ13*($AH$24/$AH$25)*($D$2/100)	=SUM(BB13:BF13)
14	=AX14*($AH$22/$AH$25)*($D$2/100)	=AY14*($AH$23/$AH$25)*($D$2/100)	=AZ14*($AH$24/$AH$25)*($D$2/100)	=SUM(BB14:BF14)
15	=SUM(BD3:BD14)	=SUM(BE3:BE14)	=SUM(BF3:BF14)	=SUM(BG3:BG14)
16	=BD7+BD8	=BE7+BE8	=BF7+BF8	=SUM(BB16:BF16)
17	=BD9+BD10	=BE9+BE10	=BF9+BF10	=SUM(BB17:BF17)
18	=BD11+BD12	=BE11+BE12	=BF11+BF12	=SUM(BB18:BF18)
19				
20				
21				
22				
23				
24				
25				
26				
27				
28				